NORTHWESTERN UNIVERSITY

Interference Measurement of the $\chi_{c0}(1^3P_0)$ in Proton-Antiproton Annihilation into Two Neutral Pseudoscalar Mesons

A DISSERTATION

SUBMITTED TO THE GRADUATE SCHOOL

IN PARTIAL FULFILLMENT OF THE REQUIREMENTS

for the degree

DOCTOR OF PHILOSOPHY

Field of Physics and Astronomy

By

Paolo Giuseppe Rumerio

EVANSTON, ILLINOIS

June 2003

Abstract of the Dissertation

Interference Measurement of the $\chi_{c0}(1^3P_0)$ in Proton-Antiproton Annihilation into Two Neutral Pseudoscalar Mesons

by

Paolo Giuseppe Rumerio

Doctor of Philosophy in Physics

Northwestern University, 2003

Professor Jerome L. Rosen, Chair

Fermilab experiment E835 has observed $\bar{p}p$ annihilation production of the charmonium state χ_{c0} and its subsequent decay into $\pi^0\pi^0$. Although the resonant amplitude is an order of magnitude smaller than that of the non-resonant continuum production of $\pi^0\pi^0$, an enhanced interference signal is evident. A partial wave expansion is used to extract physics parameters. The amplitudes $J = 0$ and 2, of comparable strength, dominate the expansion. Both are accessed by $L = 1$ in the entrance $\bar{p}p$ channel. The product of the input and output branching fractions is determined to be $B(\bar{p}p \to \chi_{c0}) \times B(\chi_{c0} \to \pi^0\pi^0) = (5.09 \pm 0.81 \pm 0.25) \times 10^{-7}$. An interference signal is also measured in the $\eta\eta$ channels and provides $B(\bar{p}p \to \chi_{c0}) \times B(\chi_{c0} \to \eta\eta) = (4.0 \pm 1.2^{+0.5}_{-0.3}) \times 10^{-7}$. The control channel $\pi^0\eta$, into which the χ_{c0} decay is suppressed by isospin conservation, is analyzed and a 90% confidence level upper limit, $B(\chi_{c0} \to \bar{p}p) \times B(\chi_{c0} \to \pi^0\eta) < 4 \times 10^{-8}$, is established.

A Margo, ai miei genitori ed alla mia famiglia.

Acknowledgements

I would like to thank my advisor, Professor Jerome Rosen, for his support and guidance. The study performed in this dissertation has been in his mind for many years. The frequent, instructive conversations with him have been fundamental for myself and for the completion of this work.

Thanks to Rosanna Cester and Stephen Pordes for their committed leadership in the experiment E835, and to all collaborators, whose work has been precious for the realization of this project. Particularly, I have benefited from frequent consultations in Fermilab with Stephen Pordes, Keith Gollwitzer, Jason Kasper, Ted Vidnovic, Roger Rusack and Wilhelm Roethel. The teachings, help and always available opinions of Keith and Stephen have been essential to me. I have also worked for short but profitable periods in Torino, where I have intensively collected important suggestions from Rosanna Cester, Giovanni Borreani, Ezio Menichetti, Flavio Marchetto, Nadia Pastrone, Roberto Mussa, and Margherita Obertino; I am grateful to them for both their professional help and friendship, other than hospitality at the Dipartimento di Fisica. Nadia and Margherita, in particular, have always been close and supportive friends. The help and friendship of Gabriele Garzoglio, since the very beginning of my work at Fermilab, and Ismail Uman and Dave Joffe in the last years at Northwestern, have been constant and very important. Special acknowledgments go also to Michelle Stancari, Claudia Patrignani and Marco Pallavicini. It has been a pleasure to work with all E835 collaborators; I would like to remember especially Giovanni Lasio, Giulio Stancari, Stefano Bagnasco, Wander Baldini, Gigi Cibinetto, Matteo Negrini, Mirco Andreotti, Peter Zweber, Seon-Hee Seo, and Matt Graham.

I would like to thank the members of my Ph.D. committee, Professors Kamal Seth and Gregory Anderson, for their helpful comments, and the Physics Department of Northwestern University.

Il ringraziamento maggiore va a Margo (who by now has learned Italian), a mia madre Santina ed alla mia famiglia, che sopportando la lontananza non mi hanno mai fatto mancare il loro affetto ed indispensabile sostegno.

Contents

List of Figures

List of Tables

Chapter 1

Introduction

The strong interaction is one of the four forces known in physics. Its name reflects the fact that the strength of the interaction, which is confined within distances of approximately one fermi (10^{-15} meters), is more intense than the electromagnetic, the weak, and the gravitational forces. The strong force is responsible for keeping together the constituents of the atomic nuclei, that is the protons and the neutrons (also called nucleons). It is also responsible for keeping together the constituents of the nucleons themselves, the quarks. The strong interaction is not as easily noticeable in the everyday life as the gravitational force or the electromagnetic force, but in the 20th century plenty of experimental evidence have become available to study this force, and theories have been formulated.

One of the possibilities to confront a theory with experimental observations is provided by spectroscopy studies. That is true for instance for the electromagnetic interaction. Spectroscopic observations in general and, in particular, the spectrum of the hydrogen atom and the positronium (the bound state between an electron and its antiparticle, the positron) have given an enormous contribution to the understanding of electromagnetism and, eventually, to the development of a successful theory, Quantum Electrodynamics (QED). In the same way, the study of systems bound by the strong interaction, such as quark-antiquark bound states, has provided important experimental evidence to help develop a theory for this force, and hopefully will continue to do so.

The experiment E835 at the Fermilab Antiproton Accumulator was designed and has been dedicated to charmonium spectroscopy. Charmonium is the name given to the bound state of the charm quark (c) and its antiquark ($\bar{c}$), which was experimentally observed for the first time in 1974. The charmonium spectrum presents several similarities with the positronium spectrum, demonstrating the existence of some analogies between the electromagnetic and strong forces. Such analogies have been one of the reasons to develop a theory for the strong interaction which is closely related to QED. Quantum Chromodynamics (QCD) is such a theory.

This dissertation is devoted to the study of the χ_{c0} state of charmonium; the analyzed data sample was collected in the E835 run of the year 2000. The χ_{c0} is the state where the $\bar{c}c$ bound pair has one unit of orbital angular momentum and in a triplet spin. The relative orientation of these angular momenta is such that the total angular momentum of the bound state is equal to zero. The reactions $\bar{p}p \to \pi^0\pi^0$ and $\bar{p}p \to \eta\eta$ are analyzed. In both of them, a clear signal due to the presence of the χ_{c0} resonance is observed. It will be shown in detail that, in both cases, the measured signal is enhanced and re-shaped by the interference between the resonant production of the final state (through the intermediate χ_{c0} state) and the more copious non-resonant production of that same final state. As a control channel, the reaction $\bar{p}p \to \pi^0\eta$ was also analyzed. The decay of the χ_{c0} into this final state is suppressed by isospin conservation, and no resonant signal is observed. The original motivation for attempting an interference study of the χ_{c0} in the pseudoscalar - pseudoscalar meson final channel was the investigation of an alternative technique to search for hadromolecular states at charmonium energies ($c\bar{c}q\bar{q}$ bound states, where q represents a light quark). Such states should decay into $\pi^0\pi^0$ and $\eta\eta$ (those states with isospin=0) or $\pi^0\eta$ (those with isospin=1) and could give rise to a detectable interference pattern similar to those observed for the χ_{c0}. These $\bar{p}p \to \pi^0\pi^0$ and $\eta\eta$ studies complements the already published χ_{c0} study performed by E835 in the channel $\bar{p}p \to J/\psi\,\gamma$, $J/\psi \to e^+e^-$ using simultaneously recorded data [1].

The first chapter of this thesis presents a short overview, in historical prospective, of the strong interaction, the quark model, the theoretical introduction of the charm quark and its discovery. The physics motivations for studying charmonium and the current status of our knowledge of it is described. The E835 experimental technique of producing charmonium in proton-antiproton annihilation is then briefly described. Finally, the phenomenological reaction formalism is introduced. The angular distribution partial wave analysis is presented and the phenomenon of the interference discussed.

The experimental apparatus is presented in the second chapter. The characteristics of the antiproton beam and their measurements are discussed. The hydrogen jet target, which intersects the $\bar{p}$-beam and provides the protons, is described. Then, the E835 detector, the trigger and data acquisition system are presented. The Central Calorimeter is described more in detail since that is the fundamental detector for the neutral analyses presented herein (the π^0's and η's are detected via their decay into two photons).

The third chapter presents in detail the analysis of the final state $\pi^0\pi^0$. This process and its analysis are quite unusual. A resonant process $\bar{p}p \to \chi_{c0} \to \pi^0\pi^0$ competes with a non-resonant process $\bar{p}p \to \pi^0\pi^0$ that dominates by orders of magnitudes. Still, an interference-enhanced resonant signal is evident in the measured cross section. A partial wave expansion fit and the extraction of the product of the branching ratios $B(\chi_{c0} \to \bar{p}p) \times B(\chi_{c0} \to \pi^0\pi^0)$ are discussed in detail. In a section of the third chapter, the already published results for the χ_{c0} mass ($M_{\chi_{c0}}$) and width ($\Gamma_{\chi_{c0}}$) from the process $\bar{p}p \to \chi_{c0} \to J/\psi\,\gamma$ are shortly presented. These results for $M_{\chi_{c0}}$ and $\Gamma_{\chi_{c0}}$ are used in fitting the $\bar{p}p \to \pi^0\pi^0$ cross section to extract a more precise value for $B(\chi_{c0} \to \bar{p}p) \times B(\chi_{c0} \to \pi^0\pi^0)$. At the end of the chapter, the same fit is also repeated with $M_{\chi_{c0}}$ and $\Gamma_{\chi_{c0}}$ left as free parameters, to prove the consistency and validity of our analysis.

The fourth chapter presents the analysis of the $\pi^0\eta$ final state. The χ_{c0}, as all charmonium states, cannot decay into this channel unless violating the isospin conservation. This analysis provides an important control reaction. No signal from the χ_{c0} is detected and an upper limit to the product $B(\chi_{c0} \to \bar{p}p) \times B(\chi_{c0} \to \pi^0\eta)$ is established.

The last analysis, the $\eta\eta$ final channel, is presented in the fifth chapter. The number of events is ~ 20 times smaller than in the $\pi^0\pi^0$ channel and the statistical fluctuations are larger, but an interference-enhanced resonant signal is still detected. The analysis follows closely that of the $\pi^0\pi^0$, and a measurement of $B(\chi_{c0} \to \bar{p}p) \times B(\chi_{c0} \to \eta\eta)$ is performed constraining the χ_{c0} mass and width to the values obtained from the process $\bar{p}p \to \chi_{c0} \to J/\psi\gamma$. Even with this limited sample of $\eta\eta$ events, the determination of the χ_{c0} mass and width is then attempted using the $\eta\eta$ sample alone and the results are in substantial agreement with those determined in the $J/\psi\gamma$ and $\pi^0\pi^0$ channels.

The sixth and last chapter summarizes and discusses the results presented in the previous chapters. Then, the E835 results are used along with those available in the literature to extract additional information on charmonium. In addition to the measurements specific to the $\bar{c}c$ states, this work has provided insights on the proton-antiproton annihilation into a pseudoscalar meson pair; these are discussed, as well. Finally, the original motivations for this work are re-discussed and possible future uses of the developed technique are suggested.

1.1 Historical Overview.

1.1.1 The quark model

During the 1950's and 1960's a growing number of resonances, or hadrons, participating in strong interactions was observed. The large number of particles and the fact that their characteristics could be arranged in schemes presenting clear regularities strongly suggested that they were not elementary objects. It was then proposed that these particles were made by a limited number of elementary constituents, the quarks, which would combine among themselves to form all existent hadrons. The first model, introduced by Gell-Mann and Zweig in 1964 [2, 3], assumed the existence of three quarks: the u (up), the d (down) and the s (strange). The first two of them constitute a doublet in the isospin quantum number, while the third one is an isospin singlet but with a newly introduced quantum number called strangeness. These three quarks are now often referred to as the light quarks and the symbol q may be used to indicate any of them. A fourth, more massive quark, the c (charm), was introduced and observed in 1974, as discussed in Section 1.1.5. The complete, current model includes the even more massive quarks b (bottom) and t (top). Each one of the six quark comes with its own antiquark: $\bar{u}$, $\bar{d}$, $\bar{s}$, $\bar{c}$, $\bar{b}$ and $\bar{t}$. The three later-introduced quarks may be referred to as the heavy quarks. The existence of each of them was experimentally observed whenever particle accelerators become as powerful as needed to generate the high-mass resonances that contain them.

The type of quark, u, d, s, c, b and t, is considered an additional quantum number named flavor. Their masses and the other quantum numbers are listed in Table 1.1.

Flavor	Charge (Q/e)	Mass	I (I_3)	S	C	B	T
u	$2/3$	~ 300 MeV	$\frac{1}{2}$ $(\frac{1}{2})$	0	0	0	0
d	$-1/3$	~ 300 MeV	$\frac{1}{2}$ $(\frac{-1}{2})$	0	0	0	0
s	$-1/3$	~ 500 MeV	0 (0)	-1	0	0	0
c	$2/3$	~ 1.5 GeV	0 (0)	0	1	0	0
b	$-1/3$	~ 5 GeV	0 (0)	0	0	-1	0
t	$2/3$	~ 175 GeV	0 (0)	0	0	0	1

Table 1.1: The approximate "constituent" quark masses (that is extrapolated from the values of the hadron masses, as opposed to the "current" quark masses [39]) and quantum numbers: the isospin (I) and its third component (I_3), the strangeness (S), charm (C), bottom or beauty (B), and top (T).

In addition to the numbers shown in the table, each quark is given a baryon number of 1/3 and a spin of 1/2, which implies that the quarks are fermions.

In the original three-quark model, many of the characteristics of the hadrons could be explained by assuming that they are a bound state of 3 quarks (the baryons), three antiquarks (antibaryons), or a quark-antiquark pair (mesons). The lowest-mass baryons are arranged into an octet of $J^P = \frac{1}{2}^+$ states and a decuplet of $J^P = \frac{3}{2}^+$, where J and P are the spin and parity quantum numbers. Only the above multiplets exist in nature because they are those, of the 27 possible combinations of three different quarks, that have a defined symmetry under the interchange of any pair of quarks. The lowest-mass mesons are arranged into two nonets with $J^P = 0^-$ and $J^P = 1^-$.

1.1.2 The color hypothesis

The existence of states interpreted as made of ddd (the baryon Δ^-), uuu (the Δ^{++}) or sss (the Ω^-) with parallel spins and zero orbital angular momentum, which implies that they are symmetric under the interchange of any of the constituent quarks, raised the problem that a fermion system must have a globally antisymmetric wavefunction. The hypothesis of an additional quantum number, named *color*, was then introduced. If a quark comes in one of three possible colors, red (r), blue (b) and green (g), and the new color wavefunction is the color singlet antisymmetric

$$\frac{rbg + grb + bgr - gbr - brg - rgb}{\sqrt{6}}, \tag{1.1}$$

then the total wavefunction of the Δ^-, Δ^{++}, and Ω^- (as well as the one of the other baryons) is globally antisymmetric.

The meson are also color singlet states, and their color wavefunction is

$$\frac{r\bar{r} + b\bar{b} + g\bar{g}}{\sqrt{3}}, \tag{1.2}$$

Experimental observations brought further evidence in favor of the color hypothesis. One of them is that the ratio,

$$R = \frac{\sigma(e^+e^- \to \text{hadrons})}{\sigma(e^+e^- \to \mu^+\mu^-)}, \tag{1.3}$$

between the cross section of the processes $e^+e^- \to$ hadrons and $e^+e^- \to \mu^+\mu^-$ should be proportional to

$$R \simeq \sum_i z_{q_i}^2 . \tag{1.4}$$

The index i runs over the different quarks that can be produced at energy the reaction takes place. Different color makes the quark different. The quantity z_{q_i}

is the charge of the considered quark. The measured R stabilizes at a value in agreement with equation 1.4 each time the energy exceeds the threshold of the production of a quark.

1.1.3 A Theory for the Strong Interaction

The Quantum Chromodynamics (QCD) is the currently accepted theory for the description of the strong interaction. It is built in analogy to the Quantum Electrodynamics (QED), the theory that successfully describes the electromagnetic interactions. The fundamental hypothesis of QCD are that the source of the strong field (the analogue of the electric charge in QED) is the color, and that the bosons mediating the interaction are vector particles which are called gluons. These bosons are the analogue of the photon of QED, but differently from the photon, they carry themselves the field source. The interaction is invariant under color interchange and the gluons are postulated to belong to an octet representation of the symmetry group SU(3). The color state of the gluons are

$$r\bar{b},\ r\bar{g},\ b\bar{g},\ b\bar{r},\ g\bar{r},\ g\bar{b},\ \frac{r\bar{r}-b\bar{b}}{\sqrt{2}},\ \text{ and } \frac{r\bar{r}+b\bar{b}-2g\bar{g}}{\sqrt{6}}. \tag{1.5}$$

The fact that the gluons carry color determines a major difference between QCD and QED. In QED there is only one fundamental vertex of the interaction, among a photon and a particle-antiparticle pair. In QCD, other that the analogue of the above (the quark-antiquark-gloun vertex), there are two additional vertices: one among three gluons and another among four gluons. As a consequence of this, the strong coupling constant, α_s, of the strong interaction behaves differently from the electromagnetic coupling constant α.

The value of α for small values of the squared four-momentum (q^2) transferred in the interaction (which means large distances) tends to the value 1/137 of the fine structure constant. In QCD, instead, the value of α_s tends to infinity for small q^2, which is supported by the experimental non-observation of free quarks. This limits the success of the QCD as compared to QED. In QED calculations can be performed using a perturbative method. Since α is much smaller than one, terms involving higher powers of α become increasingly less important and can be neglected. In QCD, perturbative calculations may be used only when α_s becomes smaller, which happens for large values of q^2 (short distances).

1.1.4 The Introduction of the *Charm* Quark.

In the 60's, when the three-quark model was reasonably well established, the introduction of a fourth quark was proposed [5] to establish a symmetry between quarks and leptons. At that time, four leptons were known and they were arranged in two doublets composed by the electron (e) with its associate neutrino (ν_e), and the muon (μ) with its neutrino (ν_μ):

$$\begin{pmatrix} e \\ \nu_e \end{pmatrix} \quad \begin{pmatrix} \mu \\ \nu_\mu \end{pmatrix}$$

The proposed *charm* quark (c) would have been associated in a doublet with the quark s on a side of the quark doublet made by u and d:

$$\begin{pmatrix} u \\ d \end{pmatrix} \quad \begin{pmatrix} c \\ s \end{pmatrix}$$

In 1963, before the c was introduced, Cabibbo proposed [7] that the quark states actually participating in the weak interaction were the u and an admixture, $d_c = d \cos\theta_c + s \sin\theta_c$, of the physical quarks d and s. Then, he showed that the experimentally-observed suppression of the strangeness-changing ($\Delta S = 1$) semileptonic weak decays with respect to the strangeness-conserving ($\Delta S = 0$) decays would be understood. The experimental value of the Cabibbo angle θ_c is about 0.25 rad.

However, a consequence of the Cabibbo theory was the existence of neutral currents with $\Delta S = 1$, which on the contrary are not observed in nature. A famous paper from Glashow, Iliopoulos and Maiani [6] in 1970 brought the solution to this problem and stronger support for the existence of the c. The authors proposed that the quark c would participate to the weak interaction in a doublet with a state, $s_c = s \cos\theta_c - d \sin\theta_c$, orthogonal to the d_c state. Hence the two quark doublet for weak interaction would be:

$$\begin{pmatrix} u \\ d_c = d\,\cos\theta_c + s\,\sin\theta_c \end{pmatrix} \quad \begin{pmatrix} c \\ s_c = s\,\cos\theta_c - d\,\sin\theta_c \end{pmatrix} ,$$

which determine a vanishing term for the neutral currents with $\Delta S = 1$, in agreement with the experimental observations.

1.1.5 The Discovery of Charmonium.

In 1974 the hypothesis of the existence of the quark c found experimental confirmation. A very narrow resonance at 3.1 GeV was discovered independently at Brookhaven National Laboratory in the reaction $p + p \to e^+e^- +$ anything [8] and at Stanford Linear Accelerator Center (SLAC) in the reaction $e^+e^- \to +$hadrons [9], soon confirmed in Frascati [10]. The new particle was called J/ψ .

A few days after the discovery of the J/ψ, another narrow resonance with some 600-MeV higher mass was found at SLAC [11]. It was named ψ' .

The properties of these two states were quite remarkable. They displayed large masses extremely narrow widths (Γ), particularly the J/ψ with its Γ of less than one hundred keV. Lighter strong interaction resonances were generally as wide as a few hundred MeV's and the widths seemed to increase with the increasing masses. The mass and width of the J/ψ and ψ' made these resonances non-compatible with the hypothesis that their constituents were the light quarks.

By introducing the quark c, interpreting the new particles as charm-anticharm ($\bar{c}c$) bound states, and appealing to the Okubo-Zweig-Iizuka (OZI) rule [12, 3, 13], the narrowness of these states could be explained.

The OZI rule states that processes described by diagrams with only disconnected lines between the initial and the final state (for example the diagram of $J/\psi \to \pi^-\pi^0\pi^+$ in Figure 1.1) would be suppressed as compared to processes with connected lines (for example the diagram of $\psi''(3770) \to D^+D^-$ in Figure 1.1 [1]).

[1]The $\psi''(3770)$ was discovered later; however, their occurrences of the OZI rule were known, for example the suppression of the decay $\phi \to \pi^-\pi^0\pi^+$ versus the decay $\phi \to K^+K^-$.

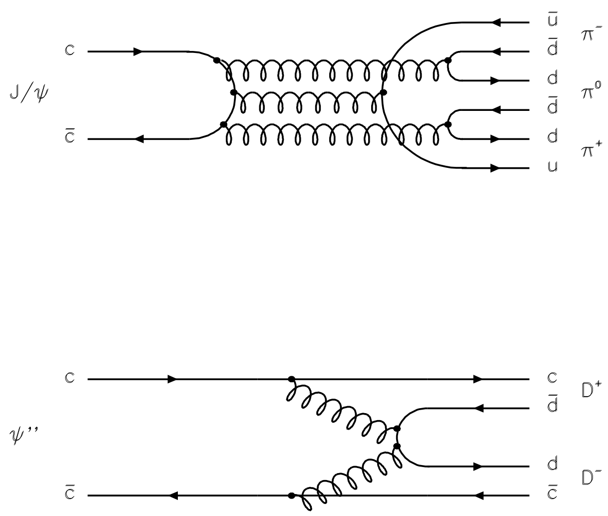

Figure 1.1: Above: the disconnected diagram of the decay $J/\psi \to \pi^- \pi^0 \pi^+$. Below: the connected diagram of the decay $\psi''(3770) \to D^+ D^-$.

The OZI rule can be intuitively explained. Disconnected lines requires the emission of "hard" gluons (that is very energetic) since they have to carry the the four-momentum of the annihilating quarks. These gluons, being far from their mass-shell, are less likely to be produced than "soft" gluons emitted from a quark that continue to exist in the final state (a connected line in the diagram). In addition, in order for a $\bar{q}q$ pair to annihilate, the q and $\bar{q}$ need to find each other in the same place.

In the case of the the J/ψ decay, three hard gluons need to be produced. That has a small probability to occur fast. The connected decays into final states where the c and $\bar{c}$ separate and persist in the final state (such as the decay into $D^+ D^-$) are energetically forbidden. The relatively low probability of $\bar{c}c$ annihilation makes the lifetime of the J/ψ unusually long for an hadronic resonance and, consequently, its width exceptionally small.

Both the J/ψ and ψ' are copiously produced in e^+e^- annihilation, which proceeds by the creation of a virtual photon. Consequently, they were assigned the quantum number of the photon: $J^{PC} = 1^{--}$ (J is the spin, P the parity and C the charge conjugation).

1.2 The Study of Charmonium.

Any theory conceived to describe the strong interaction should be able, in the first place, to describe a system such as the quark-antiquark bound states. Charmonium, with its narrow resonances well separated in energy (see Figure 1.2), is well suited for formulating and testing such a theory. In addition, given that a comprehensive and completely satisfying theory has not been reached yet[2], charmonium presents a few other advantages. In the framework of Quantum Chromodynamics, the value of the strong coupling constant α_s for the typical momentum exchanged between charmed quark and antiquark is not yet so large ($0.3 \div 0.35$) to invalidate the employment of Perturbative Quantum Chromodynamics. Also, the relatively small binding energy, compared to the rest mass of its constituents, allows $c\bar{c}$ states to be described using a non-relativistic approach (v^2/c^2 is about 0.25). Finally, the fact that the charmonium states are eigenstates of J^{PC} produces symmetry conserving simplifications.

On the contrary, the energy spectrum of the resonances composed by the three light quarks is much more confused. A larger number of particles populate the energy range for light quark spectroscopy and the width of the particles are often overlapping. Also, the light quarks in these bound states are highly relativistic.

1.2.1 The Charmonium Spectrum.

In the years after the discovery of the J/ψ and the ψ, several other charmonium states were found. Yet, a substantial part of the charmonium spectrum has not been

[2]The problems appear to be mainly computational. Unlike QED, QCD perturbative calculations are more difficult and converge much more slowly.

revealed or precisely measured. Figure 1.2 shows what is known, or in some cases expected, of the spectrum of the charmonium. The measured or expected value of the masses is plotted on the vertical axis versus the J^{PC} quantum number on the horizontal axis. The width of the resonances are indicated by the thickness given to the associated horizontal bars. The spectroscopic notation, $n^{2s+1}L_J$, is given: n is the number of nodes in radial wave function plus one, s is the combined spin of the two quarks, L is the orbital angular momentum, and J is the total angular momentum. Parity and charge conjugation, as in any fermion-antifermion state, are given by $P = (-1)^{L+1}$ and $C = (-1)^{L+S}$, respectively.

The most effective tools to calculate predictions of the masses, total and partial widths are models of the potential between the two quarks. Generally these potentials consists of a Coulomb-like term, which dominates at short distances and arises from a single-gluon exchange, and a linear term that dominates at larger distances and is responsible for the quark confinement. The nature of the linear or confinement term is less well understood. It is believed to originate from the gluon-gluon direct strong interaction. The most commonly used is the Cornell potential [14, 15]:

$$V(r) = -\frac{4}{3}\frac{\alpha_s}{r} + kr \,, \tag{1.6}$$

where α_s is the strong coupling constant, r is the distance between the two quarks, k is a constant of magnitude ~ 1 GeV/fm, and the factor 4/3 is an artifact of color symmetry.

In a perturbative approach to a quark-antiquark system, the perturbative part of the Hamiltonian can be written as a sum of a spin-independent (H_{SI}), a spin-orbit (H_{LS}), a tensor (H_T), and a spin-spin (H_{SS}) term [16, 17, 18]:

$$H = 2m + \frac{p^2}{m} - \frac{p^4}{4m^3} + V(r) + H_{SI} + H_{LS} + H_T + H_{SS} \,. \tag{1.7}$$

The above equation is the Breit-Fermi Hamiltonian. See the references given above for the formulas for the specific terms.

Precise measurements of the resonance masses, or more exactly the differences

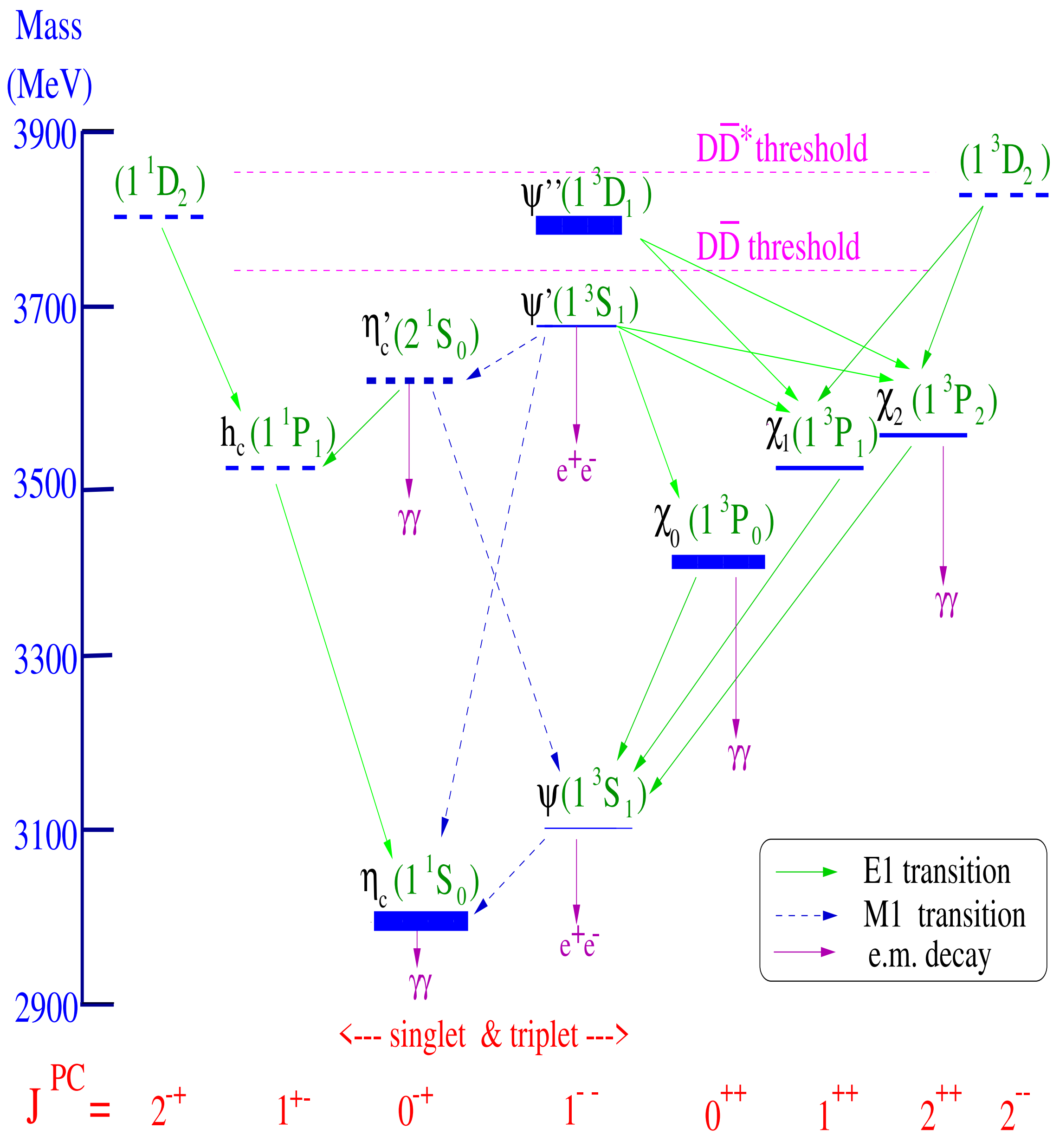

Figure 1.2: The Spectrum of Charmonium.

between them, are a very effective way to test the above models. For instance, the tensor and spin-orbit interaction split the masses of the χ_{cJ} ($1^3P_J,\ J = 0, 1, 2$) and other $L > 1$ states. The spin-spin force splits the vector and pseudo-scalar states and thus is responsible for the mass difference between J/ψ and η_c, and between ψ' and η_c'. A measurement of a deviation of the h_c mass from the center of gravity of the χ_{cJ} states would indicate departure from first order perturbation theory.

A precise knowledge of the partial widths and the branching ratios can be used to extract other important pieces of information on the dynamic of the strong interaction. From the ratio of the branching ratios of two appropriately chosen decay channels, an estimate of the strong coupling constant α_s can be derived [19]. Unknown quantities (such as the squared absolute value of the wave function at the origin $|\psi(0)|^2$) or poorly measured quantities (such as the branching ratio between resonance and initial state) often cancel in the ratio, leaving α_s as the only unknown. For example, in the case of η_c, η_c', χ_{c0}, and χ_{c2}, this occurs upon taking the ratio of the decays into two photons and into two gluons. Also, potential models provide predictions for the radiative partial widths that can be compared to the experimental results. Important decays for this comparison are the electric dipole transitions of the three χ_{cJ} states to J/ψ, and the magnetic dipole transition of J/ψ to η_c and ψ' to η_c'.

Table 1.2 lists the $c\bar{c}$ states that have been observed so far with information from the Particle Data Book (PDG) 2002 [39], including those states, such as η_c' and h_c, that have not been confirmed after the first observation. For many of the states, the total width is known with a large uncertainty. Improving the precision of that is the first requirement to enable the extraction of partial widths, using the experimentally determined branching ratios, with satisfying precision. Except for the J/ψ and, to a certain extent, the ψ', most of the decay channels of the charmonium states are poorly measured or not at all observed. A closer investigation shows that the actual situation is even less positive than depicted in the table. Important issues exist on the values of the masses and widths of those particles marked with an asterisk in the table.

The following part of this section presents a short overview of the several charmo-

Reson.	Mass (MeV)	Total Width (MeV)
η_c (*)	2979.7 ± 1.5	$16.0^{+3.6}_{-3.2}$
η_c' (*)	3594 ± 5	< 8 $(CL = 95\%)$
J/ψ	3096.87 ± 0.04	0.087 ± 0.005
χ_0	$3415.4 \pm 0.4 \pm 0.2$	$9.8 \pm 1.0 \pm 0.1$
χ_1	3510.51 ± 0.12	0.92 ± 0.12
χ_2	3556.18 ± 0.13	2.08 ± 0.17
h_c (*)	3526.14 ± 0.24	< 1.1 $(CL = 90\%)$
ψ'	3685.96 ± 0.09	0.300 ± 0.025
$\psi(3770)$	3769.9 ± 2.5	23.6 ± 2.7
$\psi(3836)$	3836 ± 13	?
$\psi(4040)$	4040 ± 10	52 ± 10
$\psi(4160)$	4159 ± 20	78 ± 20
$\psi(4415)$	4415 ± 6	43 ± 15

Table 1.2: Summary of charmonium masses and total widths [39]. The values for the χ_{c0} are from [1].

nium resonances, noting in particular their study by means of the technique adopted by the experiment E835: formation by proton-antiproton annihilation.

The 1^1S_0 state (η_c)

The η_c is the charmonium ground state. It can be directly formed via $\bar{p}p$ annihilation into two gluons, or reached by magnetic dipole transition of the J/ψ and ψ'. It cannot be reached by the J/ψ and ψ' electric dipole transition, nor formed in e^+e^- annihilation.

Even though its mass and total width have been measured, different experiments' measurements are in disagreement. The PDG [39] average for the η_c mass is 2979.7 ± 1.5 MeV/c^2, but the confidence level is 0.001! The measurements used to calculate the average are distributed over a range of ~ 20 MeV. It has to be pointed out that, in order to investigate the spin-spin interaction, the η_c mass has to be compared to the J/ψ mass, which is just ~ 120 MeV away.

The total width is even more unsettled. E760 determined a value $\Gamma_{\eta_c} = 23.9^{+12.6}_{-7.1}$ MeV [20] which was more than a factor 2 larger than the average of the 3 previously existing measurements. The result of E835 run 1996/97, $\Gamma_{\eta_c} = 20.4^{+7.7}_{-6.7} \pm 2.0$ MeV, agrees with E760. The experiments Belle [21] and BES [22] have recently provided new measurements.

Another important quantity is the partial width for the process $\eta_c \to \gamma\gamma$. In principle, perturbative QCD calculations can directly relate the ratio between the η_c partial widths to 2 photons ($\Gamma_{\gamma\gamma}$) and to two gluons (Γ_{gg}) to the value of the strong coupling constant α_s, since all of the unknown dynamics cancel in the ratio [19].

The 2^1S_0 state (η_c')

Among the charmonium states that lie below the "open charm" threshold (the energy value above which the decays into two charmed mesons are energetically allowed) there are two states that the PDG [39] still lists as needing confirmation. One of them is the η_c': the radially excited counterpart of the η_c. Similarly to the η_c, the η_c' can be produced via $\bar{p}p$ annihilations into two gluons or reached by magnetic dipole transition of the ψ'.

The only observation of this state came from a measurement performed with the Crystal Ball detector in 1982 [23], observing the magnetic dipole transition of the ψ'. So far, none of the subsequent experiments have succeeded in confirming that observation. A reliable determination of the mass of the η_c' would bring a second measurement of the hyperfine splitting between the S-wave states ($M_{\psi_c'} - M_{\eta_c'}$, in this case). In 1996/97, E835 performed a 35 pb^{-1} search for the η_c', in the channel $p\bar{p} \to \gamma\gamma$. It has set an upper limit for the product of the branching ratios $B(p\bar{p} \to \eta_c')$ and $B(\eta_c' \to \gamma\gamma)$ of 12.0×10^{-8}, 5.9×10^{-8}, and 4.8×10^{-8} assuming a total width $\Gamma(\eta_c')$ of 5 MeV, 10 MeV, and 15 MeV, respectively [24]. These upper limits are from ~ 2 to ~ 5 times smaller than the measurement of the same quantity for the ground state η_c (1^1S_0). The search has been carried out scanning the energy region between 3526 MeV and 3686 MeV, with steps of about 5 MeV. This region includes the energy of the Crystal Ball observation.

Recent observations of the η_c' have been reported by Belle [25, 26].

The 1^1P_1 state (h_c)

The second one of the $c\bar{c}$ state below "open charm" threshold that needs confirmation is the P-wave singlet state of charmonium. It has quantum number $J^{PC} = 1^{+-}$ and cannot be resonantly produced by e^+e^- annihilation. Also, it cannot be reached by a radiative transition from a charmonium vector states. Proton-antiproton annihilation can generate the h_c resonantly, by annihilating into 3 gluons.

The 1^1P_1 is expected to have a mass within a few MeV range from the center of gravity of the χ_c (1^3P_J) states, a small width of less than 1 MeV, and a peak cross-section from $p\bar{p}$ smaller than 10^{-6} of the $p\bar{p}$ cross-section to hadrons. Due to the above characteristic, the h_c state has proven to be difficult to observe and, in spite of an E760 earlier claim.

A determination of the mass of the h_c and, in particular, how it relates to the χ_{cJ} (1^3P_J) masses is clearly important

Another possibility would be the search for h_c in the channel $\phi\phi + \gamma$ with the ϕ's detected through their decay into K^+K^-. The detection of this channel would certainly benefit from the use of a magnetic field to discriminate among charged particles.

The 1^3P_{cJ} states (χ_{cJ}, $J = 0, 1, 2$)

The masses and total widths of the χ_{cJ} states are reasonably well determined. A strong contribution has come from E760/E835. Measurements of the mass and width of the χ_{c1} and χ_{c2} were performed with high precision during the E760 run [27].

E835 performed a first scan of the χ_{c0} in 1996/97 with limited luminosity and energy settings [28]. Both during the E760 and the E835-1996/97 runs, the transition energy[3] of the antiproton accumulator of Fermilab had a value corresponding

[3] The transition energy of the Fermilab antiproton accumulator, as for any synchrotron machine, is a value of the beam energy for which the beam is unstable. The value of the transition energy is determined by the value of the γ_t parameter of the machine lattice, introduced in equation 2.9.

to a center of mass energy of the $\bar{p}p$ system of $E_{cm} \simeq 3.4$ MeV. That posed technical difficulties in scanning the χ_{c0} resonance. During the accelerator upgrades of 1998 and 1999, the Fermilab Beams Division moved the transition energy to $E_{cm} \simeq 3.6$ MeV [29], so that most of the resonances (except the ψ') studied by the experiment lay below it. In particular, the scan of the χ_{c0} could be performed again in year 2000 without the previously existing difficulties. A larger amount of luminosity was invested and the mass and the width measured with high precision [1] (See also Section 3.12).

There are still several interesting partial widths and branching ratios to be measured or improved. As already mentioned, the two-photon branching ratios of χ_{c0} and χ_{c2} are interesting. PDG reports $B(\chi_{c0} \rightarrow \gamma\gamma) = (1.9 \pm 0.4) \times 10^{-4}$, and $B(\chi_{c2} \rightarrow \gamma\gamma) = (2.19 \pm 0.32) \times 10^{-4}$. A result for $B(\chi_{c0} \rightarrow p\bar{p}) \times B(\chi_{c0} \rightarrow \gamma\gamma)$ from the E835 2000 exists and is going to be published soon.

The radiative decays χ_{cJ} to J/ψ (electric dipole transitions) are important for obtaining information on the wave function of both the initial and final resonance. One of these three decays, the $B(\chi_{c0} \rightarrow J/\psi\,\gamma)$, had been anomalous for over 20 years. As it will be discussed in the conclusion chapter, the E835-2000 study of the χ_{c0} has brought agreement among the measured partial widths into $J/\psi\,\gamma$ of the three χ_{cJ} states.

The vector states 1^3S_1 and 2^3S_1 (J/ψ and ψ')

The J/ψ is the most extensively studied state of the charmonium spectrum. The mass is known with an excellent precision and the width is reasonably well determined. The same considerations apply to mass and width of the ψ'. Still, especially for the ψ', several useful partial widths and branching ratios need to be measured better. In particular, the radiative decays of J/ψ to η_c and ψ' to η_c' could help investigate about a possible anomalous magnetic moment of the charm quark. These branching ratios are known with an uncertainty of $\sim 30\%$ and $\sim 20\%$, respectively. Also, the branching ratio $B(\psi' \rightarrow p\bar{p}) = (2.07 \pm 0.31) \times 10^{-4}$ could be better mea-

The beam has to pass quickly across this instability point in order to avoid losses or deterioration of its quality.

sured since it is important, as far as $p\bar{p}$ experiments are concerned, to study processes such as $p\bar{p} \to \psi' \to \chi_{cJ}\,\gamma \to J/\psi\,\gamma\,\gamma$.

The states above the "open charm" threshold

The "open charm" threshold is the minimum energy ($\sim$ 3.74 GeV) required to generate a pair of $D^0\overline{D}^0$ charmed mesons. Very little charmonium physics has been carried out in this energy region. A few observations of charmonium states with mass above this threshold have been reported [39]. Almost all of them refers to states with quantum numbers $J^{PC} = 1^{--}$, allowed to be formed by e^+e^- annihilation, and actually observed by experiments using this techniques. Since these resonances can decay in a pair of charmed mesons, their total widths are relatively large: tens of MeV.

The situation of the spin-two D-wave states (the singlet 1^1D_2, with $J^{PC} = 2^{-+}$, and the triplet 1^3D_2, with $J^{PC} = 2^{--}$) is even worse, as is often the case when the considered states cannot be produced by e^+e^- annihilation. None of them have been found. The measurement of the mass splitting of these two states would provide information to investigate the spin-spin interaction.

In spite of having a mass above open charm threshold, 1^1D_2 and 1^3D_2 cannot decay into $D^0\overline{D}^0$, which is a spin-zero boson-antiboson pair. In fact, a spin-zero boson-antiboson pair generated by the decay of a J=2 state would be forced to be in a relative D wave, which has P=+1, and such a decay would violate parity conservation. Consequently, the 1^1D_2 and 1^3D_2 total widths are expected to be narrow. In particular, the 1^3D_2 state cannot even decay into two gluons and its width is estimated to be approximately 1 MeV. The 1^1D_2, instead, is allowed to decay into two gluons and its total width might be around 3 MeV [30]. Using a detector able to select electromagnetic final states, the $^1D_2$ and $^3D_2$ states could be searched by means of decay channels with a J/ψ decaying into e^+e^-.

1.3 The E835 Experimental Technique.

The experiment E835 has performed charmonium spectroscopy by means of proton-antiproton annihilations. The experimental apparatus used to be installed in the Antiproton Accumulator of the Fermi National Accelerator Laboratory (FNAL or Fermilab). It collected data in three different runs. The first run took place in 1990/91, when the experiment was called E760. After several technical upgrades, the name was changed into E835 and a second run was performed in 1996/97. Finally, further upgrades were implemented and E835 recorded new data in year 2000. This last run provided the sample analyzed in this dissertation.

The first experiment of this kind was R704 at the CERN Intersecting Storage Ring at the beginning of the 1980s [18]. R704 and E760/E835 exploited the technique of the stochastic cooling [31], which greatly reduces the momentum spread of the antiproton beam and allows precision studies of even the narrowest charmonium resonances. A target of protons was provided by a jet of hydrogen which intersected the $\bar{p}$-beam. A more detailed description of the Fermilab Antiproton Accumulator, the E835 experimental apparatus and hydrogen jet target is given in Chapter 2.

1.3.1 Charmonium Formation by $\bar{p}p$ annihilations

Before describing the $\bar{p}p$ process a few aspects of the charmonium study by means of the e^+e^- technique will be noted, since it has been the most extensively employed method to produce charmonium.

Electron-positron annihilation is the most most efficient process to produce the vector states of charmonium J/ψ and ψ'. It proceeds through e^+e^- annihilation into a virtual photon which subsequently generates the $\bar{c}c$ pair[4]. As a consequence, the quantum numbers of the formed charmonium states are constrained to match those of the virtual photon ($J^{PC} = 1^{--}$), and only the vector states J/ψ and ψ' (or higher radial excitations) can be directly produced. The other $\bar{c}c$ resonances must

[4]More rarely, two photons may be emitted by the e^+e^- pair (without annihilation) and generate charmonium by $\gamma\gamma$ fusion. In this case, the quantum number of the $\bar{c}c$ state are constrained to be $C = +$, such as for the η_c, η_c' and χ_{cJ} states.

be observed through the ψ' or J/ψ transitions. For instance, the χ_{cJ} states are reached by the radiative electric dipole transition of the ψ', while the η_c and η_c' by the magnetic dipole. The precision of the measurement of the resonance parameters is diminished by the detector resolution for the emitted photon.

In the proton-antiproton process, charmonium resonances are produced by complete annihilation of the three valence quark-antiquark pairs of the initial state. Strong interaction processes dominates. The $\bar{p}p$ state may annihilate into two or three intermediary gluons (see Figure 1.3) and all charmonium resonances can be produced directly[5].

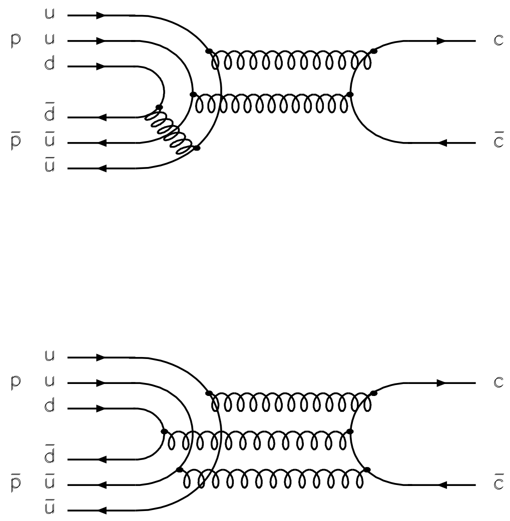

Figure 1.3: Above: charmonium formation through $\bar{p}p$ annihilation into two gluons ($C = +$). Below: charmonium formation through $\bar{p}p$ annihilation into three gluons ($C = -$).

States with even charge conjugation quantum number (C), such as the η_c, the η_c', and the three χ_{cJ}'s, are reached by the two-gluon process[6]. States with odd C,

[5]A single-gluon process is forbidden since a gluon carries color while the hadrons are colorless.

[6]The formation of the χ_{c1} state through two gluons is reduced but not forbidden by the Yang

such as the J/ψ, the ψ', and the h_c are formed through the three-gluon process.

Since all the $\bar{c}c$ states can be accessed directly, and given the excellent energy resolution available for stochastically cooled antiproton beams (bremsstrahlung radiation is greatly reduced, as compared to electron or positron beams, by the ~ 2000 times larger mass of the antiproton), the mass and width parameters of the resonances can be measured with a precision that cannot be reached using other techniques.

The counterpart of these advantages is the enormous hadronic non-resonant continuum ($\sim$ 60 mbarn, depending on the center of mass energy) compared to the product of the resonant cross-sections involved in the charmonium production ($\sim 1\mu$ barn) and the branching ratio to the analyzed final state (as low as 10^{-4} for certain electromagnetic decays).

The $\bar{p}p$ process can be classified according to the number of valence $\bar{q}q$ pairs that annihilate [7]:

Class 0 None of the valence $\bar{q}q$ pairs annihilate, but rearrangement may occur.

Class 1 One pair annihilates, the other two pairs are "spectators"; this category dominates for very high energy collisions.

Class 2 Two pairs annihilate, the remaining pair is a spectator.

Class 3 All three pairs annihilate; this is the total $\bar{p}p$ annihilation and charmonium production is required to belong to this category.

In spite of this large hadronic continuum, techniques exist to efficiently select the events of interest for charmonium studies, particularly for $c\bar{c}$ decays involving electromagnetic processes. These techniques have been extensively exploited by the experiment E760/E835 at Fermilab and its predecessor R704 at CERN.

---

theorem [32]. In fact, a particle with spin equal to one cannot annihilate into two massless identical particles, but the intermediate gluons may be neither massless nor identical.

[7] A classification often used by my Ph.D. advisor.

1.3.2 The Resonance Scanning Technique

To study a resonance, an energy scan is performed by varying the momentum of the stochastically cooled antiproton beam. At each energy point, the events in the chosen final channel are selected, counted and corrected for acceptance and efficiency. The corrected number of events is then normalized to the luminosity collected at that energy point to determine the excitation curve $F(E_{cm})$ as a function of the energy in the center of mass E_{cm}.

In the optimal condition, the chosen final state has negligible non-resonant production and background[8], the measured cross section is fitted to the convolution of the Breit-Wigner cross section, σ_{BW}, and the antiproton beam energy distribution, $G(E - E_{cm})$:

$$F(E_{cm}) = \int_0^\infty \sigma_{BW}(E)\; G(E - E_{cm})\; dE\ . \tag{1.8}$$

The Breit-Wigner cross section for an unpolarized $\bar{p}p$ initial state is given by:

$$\sigma_{BW}(E_{cm}) = (2J+1)\,\pi\,\lambda\!\!\!^{-2}\,\frac{B_{in}\,B_{out}}{x^2+1}\ , \tag{1.9}$$

where J is the spin of the resonance, $\lambda\!\!\!^{-}$ is the center of mass de Broglie wavelength of the initial state, B_{in} and B_{out} are the input and output branching ratios, and $x \equiv 2(E_{cm} - M)/\Gamma$ (M and Γ are the mass and the width of the resonance, respectively). The beam energy distribution $G(E - E_{cm})$ may be approximated with a Gaussian function or, if the resonance is much larger than the beam energy spread, treated as a delta function. This is the case for the χ_{c0} resonance, where the beam can be safely treated as virtually monochromatic.

Completely or partially electromagnetic final states have generally little non-resonant contribution from the hadronic initial state $\bar{p}p$, and the E835 detector was optimized for the detection of such channels. In addition, the selection of an e^+e^- pair from the J/ψ decay makes the background very small. A notable instance is the scan of the χ_{c0} performed in the year 2000 using the process $\bar{p}p \to J/\psi\,\gamma$,

[8] I call background those events from different final states that simulates the channel under study. The background should not be confused with the non-resonant production (also called continuum) of the same final state, which plays an important role in this dissertation.

$J/\psi \rightarrow e^+e^-$ [1]. The excitation curve is shown in Figure 3.22; a very small background is accounted for in the fit parameterization.

Using the resonance scanning technique, the precision achievable for the determination of the resonance parameters is not directly diminished by the resolution of the detector. The detector is only used to select and count the number of events in the examined final state. The resonance parameters are extracted from the excitation curve and the energy of the data points of the scan are determined with high precision from the knowledge of the beam momentum.

The experimental conditions for the channels $\pi^0\pi^0$, $\pi^0\eta$ and $\eta\eta$ is very different. The background is not an issue (particularly in the $\pi^0\pi^0$ final state), but a large non-resonant cross section is present. These processes are introduced in the following sections.

1.4 The Processes $\bar{p}p \rightarrow \pi^0\pi^0$, $\pi^0\eta$ and $\eta\eta$.

The $\pi^0\pi^0$, $\pi^0\eta$ and $\eta\eta$ can be copiously produced from proton-antiproton annihilation. This is especially true since there is overlap in the valence quark flavor between the initial and final states. The process may occur following many different paths. For $\pi^0\pi^0$ and $\eta\eta$, class 1, 2 and 3 (according to the definitions given on page 22) are all contributing to the non-resonant production of the final state; only class 0 is excluded. Rather than attempting to draw a full complex set of Feynman graphs, this process is simply represented by a filled ellipses in Figure 1.4 . The isospin-one state $\pi^0\eta$ can be accessed through classes 1 and 2, but not 3 since gluons do not carry isospin. At the χ_{c0} energies, the differential cross section for these non-resonant processes is of the order of tens of nanobarns at large angles in the center of mass and larger at small angles (a forward peak is present since the non-annihilating quarks tend to retain their original large longitudinal component of momentum). This can be seen in Figures 3.17, 3.18, 4.9, 4.10, 5.12, and 5.13, and also in Reference [33] (even if in that publication the cross section was measured not exactly at the energies studied in this thesis).

On the other hand, the resonant production of the final states $\pi^0\pi^0$ and $\eta\eta$

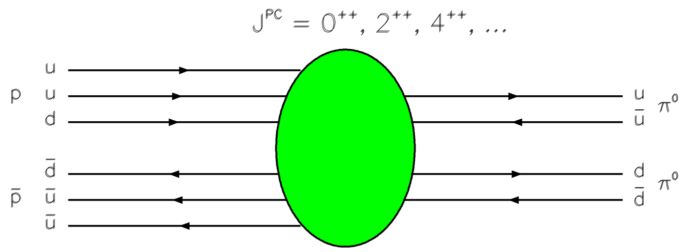

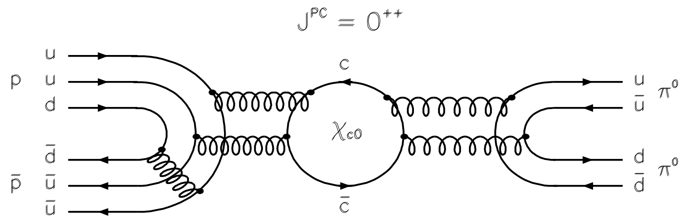

Figure 1.4: Two competing (and interfering) processes that contribute to the production of the $\pi^0\pi^0$ (or $\eta\eta$) final state. Above: the non-resonant production of the final state; this process can occur through many different possibilities represented by the filled ellipses. Below: the resonant production of the final state through the formation of the χ_{c0}; this process has a much smaller probability to occur than the above.

through the formation of the χ_{c0} may only proceed by complete annihilation of the initial state (class 3). This resonant process should be dominated by a two-gluon intermediary state both toward the input and output channels, and is sketched in the bottom drawing of Figure 1.4. The PDG 2002 [39] reports a value for $B(\chi_{c0} \to p\bar{p})$ of $(2.2 \pm 0.5) \times 10^{-4}$. In addition, the χ_{c0} decay rate into $\pi^0\pi^0$ and $\eta\eta$ is of the order of 10^{-3}, as recently reported by the BES collaboration [34]. With these values and without considering the interference with the non-resonant production of the final states, the Breit-Wigner cross section would be of the order of the tenths of nanobarns (distributed isotropically, since the χ_{c0} has spin equal to zero). This would be two orders of magnitude smaller than the non-resonant cross section. In spite of this unfavorable ratio, an interference-enhanced resonant signal is evident in the measured cross section of both $\pi^0\pi^0$ and $\eta\eta$ channels. This enhancent occurs through the mechanism described in Sections 1.4.2 and 1.4.3.

1.4.1 The Angular Distribution

The general expression of the angular distribution of $\bar{p}p \to \pi^0\pi^0$ holds for the other two final states examined in this dissertation ($\pi^0\eta$ and $\eta\eta$), since π^0 and η have common J^{PC} values[9]. The subsequent decay of the π^0 (or η) into 2 photons (which is isotropic in the parent particle rest frame) needs only to be considered for acceptance determination, since the photons' energy and direction are used only for reconstructing the parent particles' four-momenta.

The angular distribution, calculated in Appendix A using the formalism of M. Jacob and G. C. Wick [35], is expressed as a partial wave expansion on the total angular momentum J:

$$\frac{d\sigma}{dz}(z) =$$

$$= \Big| \sum_{J=0,2,4,\ldots}^{J_{max}} (2J+1)\; C_J\; e^{i\delta_J}\; P_J(z) \Big|^2 + \Big| \sum_{J=2,4,\ldots}^{J_{max}} \frac{2J+1}{\sqrt{J(J+1)}}\; C_J^1\; e^{i\delta_J^1}\; P_J^1(z) \Big|^2 . \quad (1.10)$$

The variable z is defined as

$$z \equiv |\cos\theta^*| \;, \quad (1.11)$$

where θ^* is the production polar angle of the two final state particles in the center of mass frame. The first term in equation 1.10 is generated from the initial $\bar{p}p$ state with helicity $\lambda_i \equiv \lambda_p - \lambda_{\bar{p}} = 0$ (helicity-0), where λ_p and $\lambda_{\bar{p}}$ are the proton and antiproton helicities, respectively. The positive real numbers C_J and the real numbers δ_J are the helicity-0 coefficients and phases of the expansion, respectively, and $P_J(z)$ are Legendre polynomials. The second term is generated from the initial $\bar{p}p$ state with helicity $|\lambda_i| \equiv |\lambda_p - \lambda_{\bar{p}}| = 1$ (helicity-1). The positive real numbers C_J^1 and the real numbers δ_J^1 are the helicity-1 coefficients and phases of the expansion, respectively,

[9]The spin (J), Parity (P) and Charge Conjugation (C) of the π^0 and the η are $J^{PC} = 0^{-+}$.

and $P_J^1(z)$ are Legendre associate functions of order 1. Alternatively, the two terms in equation 1.10 can be regarded as $M = 0$ and $|M| = 1$ contributions, respectively, where M is the third component of the total angular momentum J.

In Table 1.3, all the possible J^{PC} numbers of the initial $\bar{p}p$ state are built (see Appendix A.4 for more details). For each of them, it is indicated which charmonium state can be formed, if any, and whether the final $\pi^0\pi^0$, $\pi^0\eta$, or $\eta\eta$ states can be produced.

		$\bar{p}p$		$\bar{c}c$		$\pi^0\pi^0$, $\pi^0\eta$,
S	L	J^{PC}	$^{2S+1}L_J$	resonance	$n^{2S+1}L_J$	or $\eta\eta$
0	0	0^{-+}	$^1S_0$	η_c (η_c')	1^1S_0 (2^1S_0)	
1	0	1^{--}	$^3S_1$	J/ψ (ψ')	1^3S_1 (2^3S_1)	
0	1	1^{+-}	$^1P_1$	h_c	$^1P_1$	
1	1	0^{++}	$^3P_0$	χ_{c0}	$^3P_0$	✓
1	1	1^{++}	$^3P_1$	χ_{c1}	$^3P_1$	
1	1	2^{++}	$^3P_2$	χ_{c2}	$^3P_2$	✓
0	2	2^{-+}	$^1D_2$			
1	2	1^{--}	$^3D_1$	J/ψ (ψ')	1^3S_1 (2^3S_1)	
1	2	2^{--}	$^3D_2$			
1	2	3^{--}	$^3D_3$			
0	3	3^{+-}	$^1F_3$			
1	3	2^{++}	$^3F_2$	χ_{c2}	$^3P_2$	✓
1	3	3^{++}	$^3F_3$			
1	3	4^{++}	$^3F_4$			✓
0	4	4^{-+}	$^1G_4$			
1	4	3^{--}	$^3G_3$			
1	4	4^{--}	$^3G_4$			
1	4	5^{--}	$^3G_5$			

Table 1.3: How the spin S and the orbital angular momentum L of the $\bar{p}p$ in the initial state combine to make different J^{PC} values. It is indicated whether a charmonium resonance and/or the final $\pi^0\pi^0$, $\pi^0\eta$ or $\eta\eta$ (by a ✓) states are *accessible*. The spectroscopic notation is also given for $\bar{p}p$ ($^{2S+1}L_J$) and $\bar{c}c$ ($n^{2S+1}L_J$).

The symbol S represents the total spin of the two particles; $\bar{p}p$ and $\bar{c}c$ can combine in a singlet ($S = 0$) or triplet ($S = 1$) state, while $\pi^0\pi^0$, $\pi^0\eta$ and $\eta\eta$ are $S = 0$. The orbital angular momentum L between the two particles combines with the spin to make a total angular momentum $J = L, L \pm 1$ for triplet $\bar{p}p$ or $\bar{c}c$; and $J = L$ for singlet $\bar{p}p$ or $\bar{c}c$, and $\pi^0\pi^0$, $\pi^0\eta$ and $\eta\eta$. The J^{PC} values listed for $\bar{p}p$ apply for the intermediate and final states, as well, since they are conserved throughout the process.

Since $\bar{p}p$ and $\bar{c}c$ are both a fermion-antifermion pair, they are described in a completely equivalent way, as far as the angular momentum quantum numbers (spin S, orbital L, and total J), the parity (P) and the charge conjugation (C) are concerned. The only difference is that the initial $\bar{p}p$ state is not bound while the intermediate $\bar{c}c$ is. Thus the principal quantum number n that describes the radial excitation of $\bar{c}c$ does not apply to $\bar{p}p$.

The last column indicates that only even values of J can produce the final states, and that the only possibility for PC is $++$. The χ_{c0} resonance has $J^{PC} = 0^{++}$ and can be formed only by the $\bar{p}p$ state with $L = 1$ and $S = 1$; hence, it can decay into $\pi^0\pi^0$ or $\eta\eta$. As is the case for all charmonium resonances, the χ_{c0} does not carry isospin ($I = 0$); therefore, its decay into $\pi^0\eta$ ($I = 1$) is suppressed by isospin conservation.

Is has to be pointed out that the $L_{\bar{p}p} = 1$ initial state "feeds" the $J = 0, 2$ final states; $L_{\bar{p}p} = 3$ feeds $J = 2, 4$; $L_{\bar{p}p} = 5$ feeds $J = 4, 6$; etcetera. Since the entrant channel impact parameter (b) correlates with $L_{\bar{p}p}$ through the relation $\hbar L_{\bar{p}p} \simeq bp_i$ (wave mechanically smeared), where p_i is the momentum or the proton or the antiproton in the center of mass frame, increasing values of $L_{\bar{p}p}$ correspond to increasingly peripheral collisions.

1.4.2 Interference between the Resonant and the Non-Resonant Production of the Final State.

The E835 data sample herein analyzed has been collected at energies close to the χ_{c0} mass. As the χ_{c0} is formed in the $J^{PC} = 0^{++}$ channel, the complex coefficient $C_0\, e^{i\delta_0}$ is actually made by two components. The first component, analogous to all other $C_J\, e^{i\delta_J}$ and $C_J^1\, e^{i\delta_J^1}$ coefficients, is due to the non-resonant production of $\pi^0\pi^0$. The second component is due to the resonant production of $\pi^0\pi^0$ through the χ_{c0} intermediate state. By splitting these two components and parameterizing the χ_{c0} resonant production by a Breit-Wigner amplitude (with no z dependence, since the spin of the χ_{c0} is zero), equation 1.10 becomes:

$$\frac{d\sigma}{dz}(z) =$$

$$= \Big| -\frac{A_R}{x+i} + \sum_{J=0,2,4,...}^{J_{max}} (2J+1)\; C_J\; e^{i\delta_J}\;\; P_J(z)\Big|^2 + \Big| \sum_{J=2,4,...}^{J_{max}} \frac{2J+1}{\sqrt{J(J+1)}}\; C_J^1\; e^{i\delta_J^1}\;\; P_J^1(z)\Big|^2, \tag{1.12}$$

where x is defined as

$$x \equiv \frac{E_{cm} - M_{\chi_{c0}}}{\Gamma_{\chi_{c0}}/2}, \tag{1.13}$$

and $M_{\chi_{c0}}$ and $\Gamma_{\chi_{c0}}$ are the mass and width of the χ_{c0}.

The partial wave expansions over J can be summarized as

$$A\; e^{i\delta_A} \equiv \sum_{J=0,2,4,...}^{J_{max}} (2J+1)\; C_J\;\; e^{i\delta_J}\;\; P_J(z) \tag{1.14}$$

and

$$B\; e^{i\delta_B} \equiv \sum_{J=2,4,...}^{J_{max}} \frac{2J+1}{\sqrt{J(J+1)}}\; C_J^1\;\; e^{i\delta_J^1}\;\; P_J^1(z), \tag{1.15}$$

where A, B, δ_A, and δ_B are real numbers ($A, B > 0$), so that

$$\frac{d\sigma}{dz}(z) = \Big| -\frac{A_R}{x+i} + A\; e^{i\delta_A}\Big|^2 + \Big|B\; e^{i\delta_B}\Big|^2. \tag{1.16}$$

The amplitude $Ae^{i\delta_A}$ is the component of the non-resonant $\pi^0\pi^0$ production generated by the helicity-0 initial $\bar{p}p$ state[10]. The amplitude $Be^{i\delta_B}$ is the component

[10]Notice that in the first term of equation 1.12 the phase of the resonant amplitude at $x \ll -1$ has been factorized out. Therefore, δ_A is the phase of the helicity-0 non-resonant amplitude minus the phase of the resonant amplitude at $x = 0$ plus $90°$.

of the non-resonant $\pi^0\pi^0$ production generated by the helicity-1 initial $\bar{p}p$ state. Both of them have a slowly varying (on the scale of the χ_{c0} width) dependence on E_{cm}, and a dependence on z given by the Legendre polynomials. The non-resonant cross section will also be referred to as "continuum"; even though it does presents structures[11], they are on a larger scale than the χ_{c0} width.

The amplitudes $\frac{-A_R}{x+i}$ and $Ae^{i\delta_A}$ are added coherently because they are generated from the same helicity-0 initial state and interfere with each other. The amplitude $Be^{i\delta_B}$ is added incoherently because it is generated from the helicity-1 initial state and does not interfere with the helicity-0 terms.

Since $Ae^{i\delta_A}$ and $Be^{i\delta_B}$ do not change markedly when E_{cm} varies in the resonance region, it is useful to rewrite equation 1.16 as

$$\frac{d\sigma}{dz} = \frac{A_R^2}{x^2+1} + A^2 + \underbrace{2A_R A\,\frac{\sin\delta_A - x\cos\delta_A}{x^2+1}}_{interference-term} + B^2. \tag{1.17}$$

At a fixed value of z and for E_{cm} varying across the resonance (x passes through zero), even a very small resonant contribution can lead to a large signal, albeit superimposed on a large continuum[12], due to the magnifying effect of the interference. For example, if the contribution A_R^2 from the resonance at the resonance peak energy is 1% of the size of the cross section from the helicity-0 continuum A^2, the contribution from the factor $2A_RA$ of the interference term of equation 1.17 is as high as 20% of A_R^2. The factor $(\sin\delta_A - x\cos\delta_A)/(x^2+1)$ determines the functional shape of the interference pattern without modifying its size, as it will be illustrated in Section 1.4.3.

The term B^2 just provides an additional contribution to the cross section, which is slowly varying with x. Of course, if B^2 is too large compared to the interference term, it may hide completely the presence of the resonance. It is quite helpful that

[11]For example there is a significant dip in $\frac{d\sigma}{dz}\big|_{z=0}$ at $\sim 3000-3100$ MeV [33]. This is most likely due to a cancellation of $C_0\,e^{i\delta_0}$ and $C_2\,e^{i\delta_2}$ (the dominant terms in the sum, as it will be shown in Section 3.13).

[12]That is often the case when searching for charmonium formed in $\bar{p}p$ annihilation by selecting a hadronic final channel, and it will be shown that it is the case for the analyses presented herein.

all of the associated Legendre polynomials of order 1, which are the constituents of the amplitude $Be^{i\delta_B}$, share a common factor z which causes them to vanish at $z = 0$ (see Table 1.4 and Figure 1.5). Considering that the polynomials P_J^1 are

P_J^M	$M = 0$	$M = 1$
$J = 0$	$P_0 = 1$	/
$J = 2$	$P_2 = -\frac{1}{2}(1 - 3z^2)$	$P_2^1 = -3z\sqrt{1 - z^2}$
$J = 4$	$P_4 = \frac{1}{8}(3 - 30z^2 + 35z^4)$	$P_4^1 = \frac{5}{2}z(3 - 7z^2)\sqrt{1 - z^2}$
$J = 6$	$P_6 = \frac{1}{16}(-5 + 105z^2 - 315z^4 + 231z^6)$	$P_6^1 = -\frac{21}{8}z(5 - 30z^2 + 33z^4)\sqrt{1 - z^2}$

Table 1.4: The first Legendre polynomials and associated polynomials of order $M = 1$.

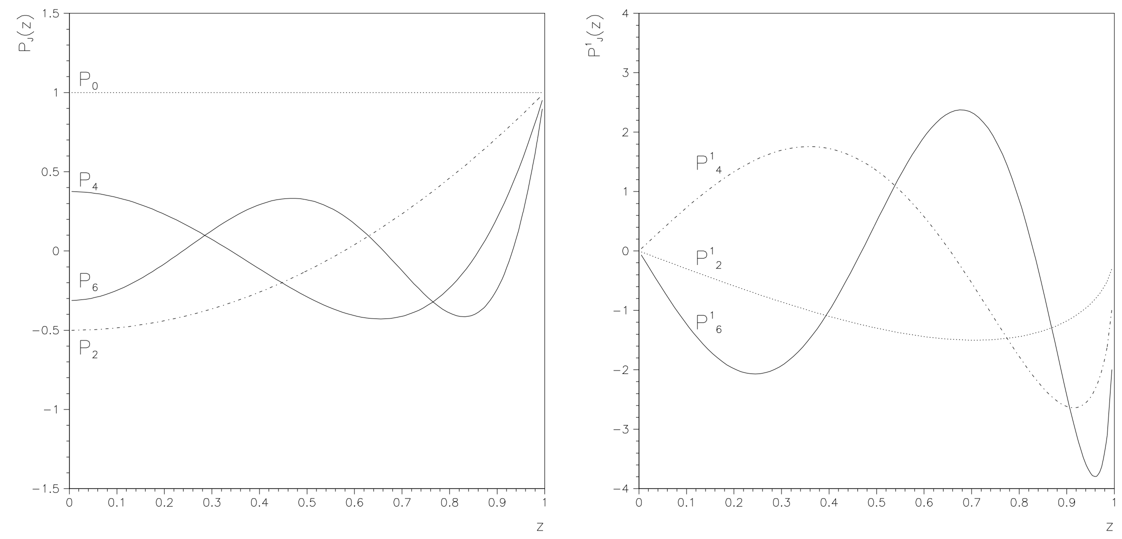

Figure 1.5: Plots of the first Legendre polynomials (left) and associated polynomials of order $M = 1$ (right).

either squared or multiplied by each other, the suppression factor of B^2 with respect to A^2 is z^2 at small z. This is very convenient. In order to measure the value of the resonant amplitude A_R, it is critical to know the relative size of the helicity-0 continuum, which is responsible for the magnifying effect of the interference, and the helicity-1 continuum, which does not interfere.

The region at small z is therefore the most natural place to concentrate on for the determination of A_R, which is constant throughout the whole range of z. Notice that small z corresponds to $\pi^0\pi^0$ events emitted at 90° with respect to the beam axis in the center of mass frame, that is toward the central part of the detector.

1.4.3 A Resonant Amplitude Added Coherently to a Larger Non-Resonant Amplitude.

A Breit-Wigner amplitude is parameterized by a vector $\boldsymbol{P}(x) = \frac{-A_R}{x+i}$ in the complex plane or Argand diagram. As illustrated in Figure 1.6 , $\boldsymbol{P}$ traces out a circle of diameter A_R as x varies[13] from $-\infty$ to $+\infty$. The rotation of the vector $\boldsymbol{P}(x)$ is counterclockwise. A more intuitive visualization of the circle is obtained by introducing an angle α through the definition $A_R \tan(\alpha/2) \equiv x$, so that $\boldsymbol{P}(x) = A_R \frac{i}{2}(1 + e^{i\alpha})$.

The range of energy of our data sample is from $E_{cm} \simeq$ 3340 MeV to $E_{cm} \simeq$ 3470 MeV. That corresponds to a range of x from $x \simeq -15$ to $x \simeq 11$, which implies that the Argand circle is traced almost completely.

What happens when $\frac{-A_R}{x+i}$ is added to another amplitude, A, which is approximately constant with x? The case of interest to us is when the A_R^2, the cross section due to the Breit-Wigner at its maximum, is much smaller than A^2, the (coherent) non-resonant cross section. This case is illustrated in Figure 1.7 (top) for a generic phase δ_A. The total amplitude, $-\frac{A_R}{x+i} + A\ e^{i\delta_A}$, reaches its maximum magnitude at the point $\boldsymbol{Q}$, which in general does not necessarily occurs at $x = 0$. There appears also a minimum at finite x at the point $\boldsymbol{R}$. The effect on the cross section σ, which is the square of the total amplitude, is shown in Figure 1.7 (bottom) as a function of x.

[13] The parameter x can be visualized as the distance (in units of A_R) between the point $(0, A_R)$ and the intersection between the continuation of the vector $\boldsymbol{P}$ and the axis $Im(\frac{-A_R}{x+i}) = A_R$; the sign of x is negative if the intersection lies on the positive $Re(\frac{-A_R}{x+i})$ semi-plane and positive if it lies on the negative semi-plane.

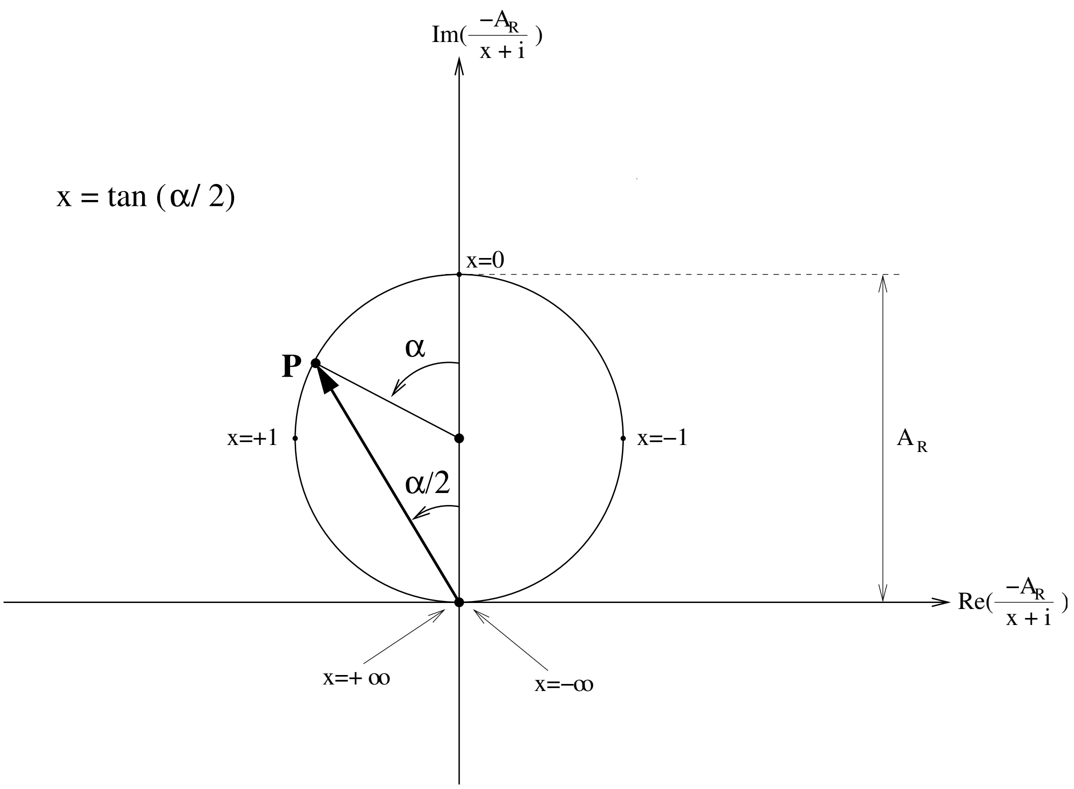

Figure 1.6: The visualization of a Breit-Wigner resonant amplitude $\frac{-A_R}{x+i}$ in the Argand diagram.

The shape of the signal observed in the cross section is determined by the value of the difference of phase δ_A between the non-resonant and the resonant amplitudes, and may vary from a depression, an enhancement, or both. Figure 1.8 illustrates, for four values of δ_A, the resulting shape of the interfering pattern. However, the size $\Delta\sigma$ of the signal due to the interference is basically independent on δ_A in the limit $A_R^2 \ll A^2$, and is approximately equal to $2A_R A$, apart from second powers of A_R. In fact, Figure 1.7 (top) shows that the difference between the maximum, $\sigma(Q)$, and the minimum, $\sigma(R)$, values of the cross section is

$$\Delta\sigma = \sigma(Q) - \sigma(R) = (A - \Delta A + A_R)^2 - (A - \Delta A)^2 = A_R^2 + 2\, A_R\, A - 2\Delta A\, A_R\,. \quad (1.18)$$

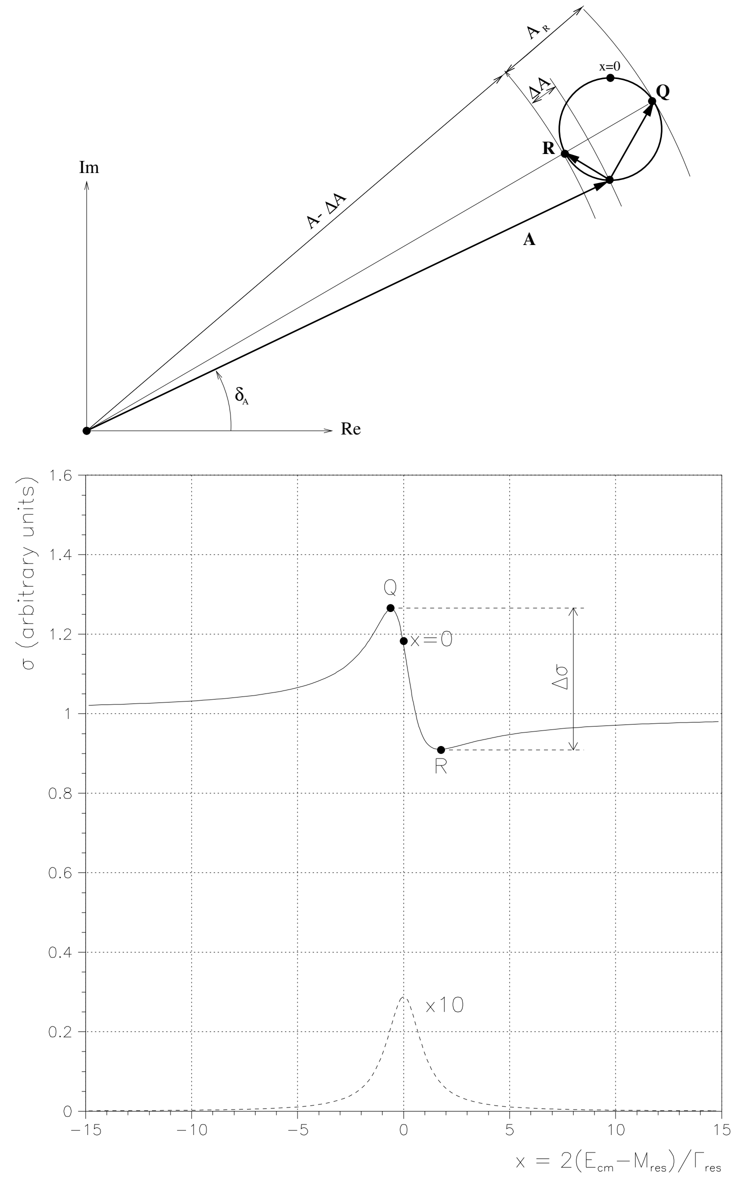

Figure 1.7: Top: The resonant amplitude $-\frac{A_R}{x+i}$ (which describes a circle of diameter A_R as x varies from $-\infty$ to $+\infty$) added to a non-resonant amplitude $A\ e^{i\delta_A}$ in the case $A_R^2 \ll A^2$ for a generic value of δ_A. Bottom: The interference pattern that the above configuration produces in the cross section $\sigma = \left| -\frac{A_R}{x+i} + A\ e^{i\delta_A} \right|^2$; the clean Breit-Wigner cross section $\sigma_{BW} = \left| -\frac{A_R}{x+i} \right|^2 = \frac{A_R^2}{x^2+1}$ is also shown (dashed line) multiplied by a factor 10 to make it comparable to the size of the interference signal.

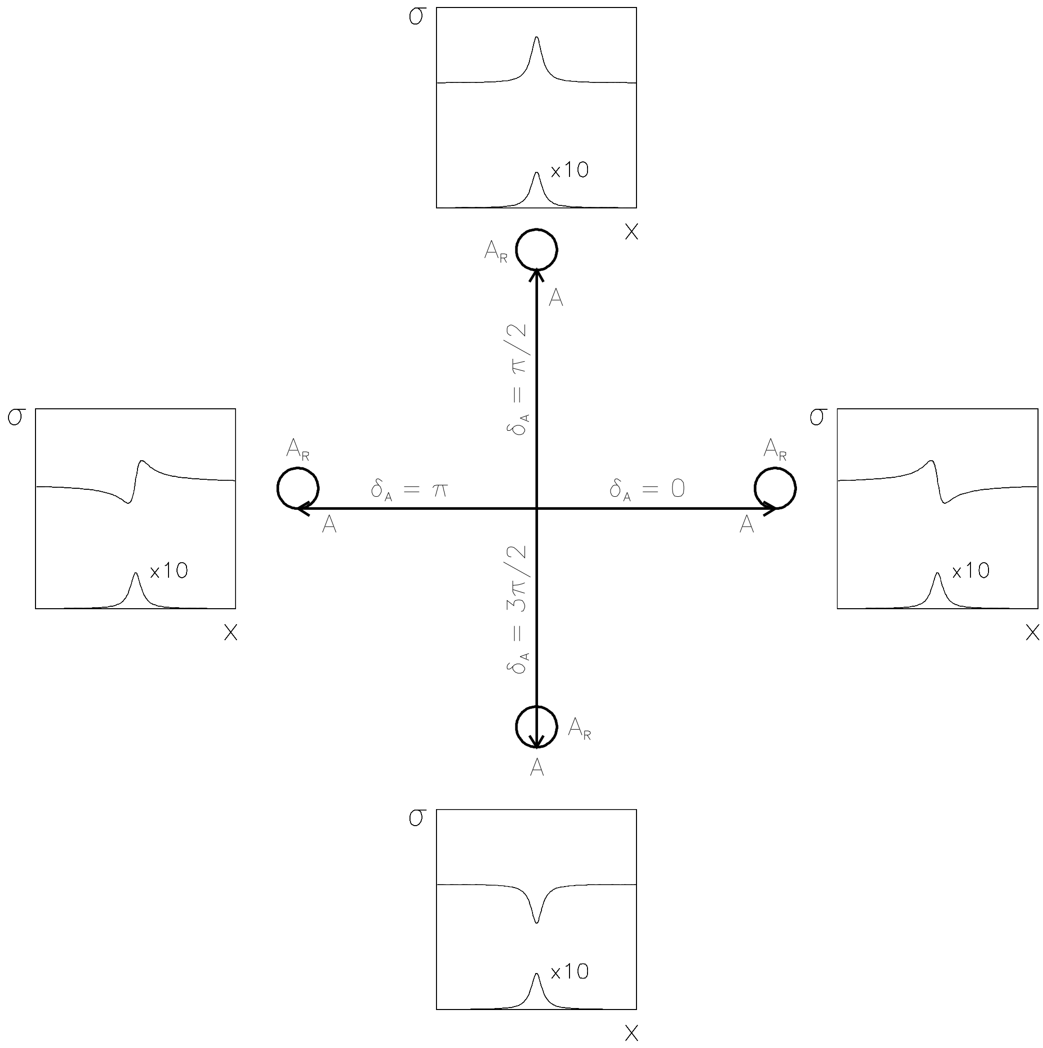

Figure 1.8: As in Figure 1.7, but for four different values of the phase δ_A. In the limit $A_R^2 \ll A^2$, the size of the interference pattern is independent from δ_A and approximately equal to $2\,A\,A_R$.

Even though ΔA depends on the phase δ_A, it never exceeds A_R. Therefore, apart from terms involving second powers of A_R, it holds

$$\Delta\sigma \simeq 2\, A_R\, A. \tag{1.19}$$

As mentioned on page 30, the size of the signal due to the interference is considerably larger than the Breit-Wigner maximum cross section $\sigma_{BW} = A_R^2$ by itself, in the case $A_R^2 \ll A^2$. To give a feeling of the magnifications involved, if $A_R^2 = \frac{1}{10}A^2$ then the interference signal size, $\Delta\sigma$, is ~ 6 times larger than σ_{BW} and corresponds to 63% of the non-resonant cross section A^2. If $A_R^2 = \frac{1}{100}A^2$ then $\Delta\sigma$ is 20 times σ_{BW} and corresponds to 20% of A^2. Finally, if $A_R^2 = \frac{1}{1000}A^2$ then $\Delta\sigma$ is ~ 60 times σ_{BW} and corresponds to $\sim 6\%$ of A^2, which may still be detectable.

It should also be noticed that for a given value of A_R^2 and considering only the statistical fluctuations, the precision of the measurement [14] of A_R^2 is independent on the size of A^2 (provided that the condition $A_R^2 \ll A^2$ still holds).

[14]Performed in an angular range, such as $z \simeq 0$, where the non-interfering continuum B^2 is small compared to the interfering continuum A^2.

Chapter 2

The Experimental Apparatus

The E835 experimental apparatus consists of three major components. The Antiproton Accumulator provides an intense beam of $\bar{p}$'s with very low momentum spread about a set value. The jet target injects a flow of hydrogen gas that intersects the $\bar{p}$ beam, so that proton-antiproton collisions take place. Finally, the detector, complemented by the trigger and data acquisition systems, discriminates, selects, and records events with specific characteristics.

2.1 The Antiproton Accumulator

The chain of production of the antiprotons, $\bar{p}$, begins with a bottle of hydrogen. By injecting the hydrogen atoms in a ion source, negatively charged H^- ions are obtained and then brought to about 750 keV of kinetic energy by means of a Cockcroft-Walton accelerator. A subsequent Linac accelerates them to 400 MeV toward a carbon foil that strips off the electrons, leaving bare protons. Two synchrotrons, first the Booster and subsequently the Main Injector, accelerate the protons to an energy of 8 GeV and 120 GeV, respectively.

The 120 GeV protons impinge on a Nickel target where many kinds of secondary particles are generated. For every million impinging protons, about 20 secondary particles are antiprotons with a momentum of about 8 GeV. A lithium lens focuses the (negatively charged) secondary particles toward a magnet set to bend the antiprotons in the direction of the Debuncher. The antiprotons are accompanied by a larger number of pions, muons and electrons. The pions and muons are unstable and decay, while the electrons synchrotron radiate and go out of the beam aperture. The generated beam of antiprotons inherits the bunched structure of the proton beam. The Debuncher reduces both the momentum spread and the bunched structure of the $\bar{p}$ beam, so that it matches the requirements for being successfully injected into the Antiproton Accumulator [36, 37]. Figure 2.1 illustrate the chain of accelerators involved in the antiproton production.

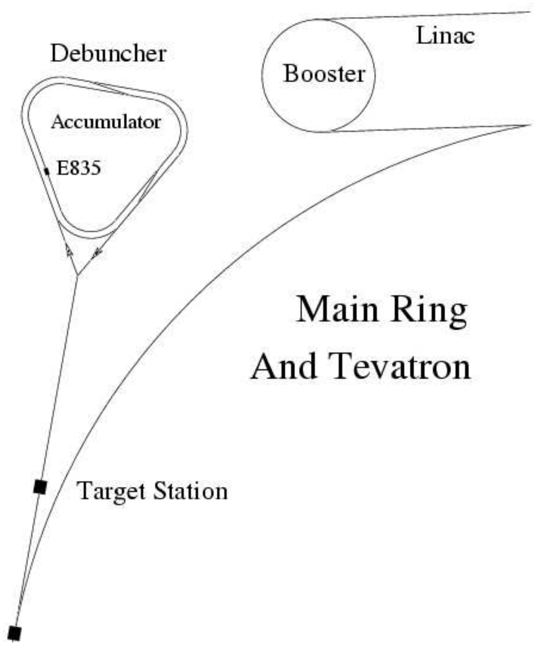

Figure 2.1: Sketch of the antiproton production and accumulation chain. The location of the E835 experiment in the Antiproton Accumulator is also shown.

The process of injecting $\bar{p}$ into the Accumulator, called stacking, continue for several hours at a stacking rate of $\sim 3 \times 10^{10}$ $\bar{p}$/hour, until a beam of $\sim 50 \times 10^{10}$ $\bar{p}$ is available to E835. During the stacking process, the Accumulator further reduces the momentum spread using the technique of *stochastic cooling* [31, 38]. Upon completion of the stacking, the beam is decelerated from the injection momentum of 8 GeV/c to the momentum requested by E835, which varied from 4915 GeV/c to 6840 GeV/c for the charmonium studies performed during the year 2000. The deceleration process occurs at a rate of approximately 20 MeV/s and is divided in several steps, called ramps. At the end of each ramp, the beam parameters are measured and corrected. When the requested momentum is reached, and during the E835 data taking, the beam is again stochastically cooled to re-establish and maintain a small momentum spread: $\sim 2 \times \times 10^{-4}$. At the E835 interaction region, where the beam is intersected by a proton jet, 95% of the beam is contained in an approximately circular cross section with a diameter of 5 mm.

2.1.1 Measurement of the Center of Mass Energy

The energy in the center of mass frame, E_{cm}, is determined by measuring the velocity[1], $v_{\bar{p}}$, of the antiprotons circulating in the accumulator and using the relation

$$E_{cm}^2 = 2m_p c^2 \left(m_p c^2 + E_{\bar{p}}\right) , \tag{2.1}$$

where $E_{\bar{p}}$ is the $\bar{p}$ energy:

$$E_{\bar{p}} = \frac{m_p c^2}{\sqrt{1-(v_{\bar{p}}/c)^2}} . \tag{2.2}$$

The most precise way to determine $v_{\bar{p}}$ is through the measurement of the revolution frequency, f, and the length of the orbit, L:

$$v_{\bar{p}} = f \times L . \tag{2.3}$$

The uncertainties on f and L (δf and δL, respectively) affect E_{cm} according to:

$$\frac{dE_{cm}}{E_{cm}} = \frac{\beta_{\bar{p}}^2 \gamma_{\bar{p}}^3}{2 \times (1+\gamma_{\bar{p}})} \sqrt{\left(\frac{\delta L}{L}\right)^2 + \left(\frac{\delta f}{f}\right)^2} , \tag{2.4}$$

[1] If not otherwise labelled, quantities in this section and its subsections are defined in the laboratory frame.

where δE_{cm} is the uncertainty on E_{cm}. The impact of δf and δL on δE_{cm} is calculated in table 2.1 at two energies of interest.

	Resonance (E_{cm})	
	ψ' (3686 MeV)	χ_{c0} (3415 MeV)
$\frac{d(\delta E_{cm})}{df}$	113.2 keV/Hz	74.0 keV/Hz
$\frac{d(\delta E_{cm})}{dL}$	149.3 keV/mm	93.7 keV/mm

Table 2.1: How the uncertainties on orbit length and revolution frequency affect the precision on E_{cm} .

The next two sections describe how f, L and their uncertainties, δf and δL, are determined. Both f and L depend on the energy of the beam; their values are approximately 474 m and 0.6 MHz, respectively. The uncertainties are $\delta f \simeq 0.1$ Hz and $\delta L \simeq 1.2$ mm, with the latter dominant. The resulting uncertainty on E_{cm} is contained within 200 keV.

Measurement of the Revolution Frequency

The spectrum, dN/df, of the revolution frequency of the $\bar{p}$ beam is determined by means of the Schottky noise power spectrum (figure 2.2), which is measured by using a Schottky pickup and a spectrum analyzer. The Schottky noise is the sum of the pulses generated by the passage of each particle in the pickup, and its spectrum, $P(f)$, is proportional to dN/df through the relation:

$$P(f) = 2\pi\ (ef)^2\ \frac{dN}{df}\ , \tag{2.5}$$

where e is the charge of an antiproton. The revolution frequency f is determined online by the spectrum analyzer as the average value of the spectrum[2]. The uncer-

[2]Notice the logarithmic scale (dB) of the ordinate axis in Figure 2.2: the tails of the spectrum are negligible.

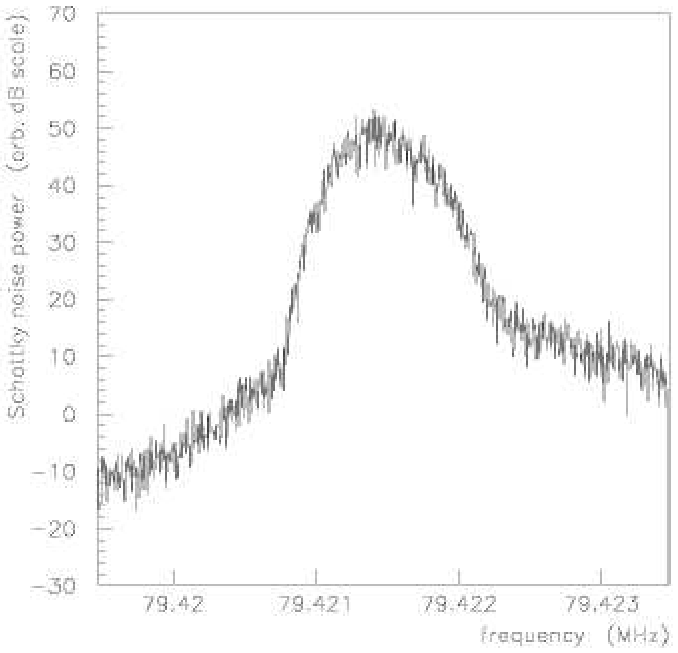

Figure 2.2: Measured Schottky noise power spectrum of the 127^{th} harmonic of the antiproton beam with momentum 6232 MeV/c (the ψ' resonance).

tainty, δf, on its value is approximately 0.1 Hz, corresponding to a measurement with precision of $\delta f/f \simeq 10^{-7}$.

A standard deviation, σ_f, is associated to the frequency spectrum by selecting the frequency range, centered about the average frequency, that makes the integral of the spectrum equal to 68% of the full spectrum.

Measurement of the Orbit Length

The most precise method to measure the orbit length consists in two steps. First, the length, L_{ref} , of a reference orbit is determined by scanning a narrow and well-known resonance through a copious and efficiently detected decay channel. Second, the difference between L_{ref} and the length, L, of the orbit actually used during a specific data taking is measured by a system of 48 Beam Position Monitors (BPMs).

For the run 2000 the resonance is the ψ' , observed through its inclusive decay into J/ψ , with subsequent J/ψ decay into e^+e^-. The length L_{ref} is determined by the Equation

$$M_{\psi'}^2 = 2 \times (m_p c^2)^2 \times \left(1 + \frac{1}{\sqrt{1-(f \times L_{ref}/c)^2}}\right) , \tag{2.6}$$

which is obtained from Equations 2.1 and 2.2 by setting $E_{cm} = M_{\psi'}$ and $L = L_{ref}$. The uncertainty, $\delta M_{\psi'}$, on the knowledge of the mass of the resonance[3] dominates on the statistical error from the determination of excitation curve and generates an uncertainty on L_{ref} equal to

$$\delta L_{ref} = L_{ref} \times \frac{M_{\psi'}}{\gamma_{\bar{p}}^3 \ \beta_{\bar{p}}^3 \ m_p^2} \times \delta M_{\psi'} \ = \ 0.6 \text{ mm} . \tag{2.7}$$

A detailed description of the determination of the difference, $\Delta L \equiv L - L_{ref}$, between the actual and the reference orbits is given in [40]. The difference ΔL can be as much as 2 mm, and the overall uncertainty δL is estimated to be of the order of 1.2 mm.

Measurement of Energy Spectrum

The spectrum of the beam energy is determined from the frequency spectrum (measured through the Schottky noise power spectrum, already shown in Figure 2.2) and by the fact that the momentum of the beam, $p_{\bar{p}}$, is related to the frequency through the Equation

$$\frac{dp_{\bar{p}}}{p_{\bar{p}}} = -\frac{1}{\eta} \times \frac{df}{f} . \tag{2.8}$$

The parameter η is called slip factor and is defined as

$$\eta = \frac{1}{\gamma_t^2} - \frac{1}{\gamma_{\bar{p}}^2} , \tag{2.9}$$

[3]The PDG [39] reports $M_{\psi'} = (3685.96 \pm 0.09)$ MeV/c^2 .

where γ_t is a parameter that depends on the lattice of the accumulator [41] and is measured with techniques described in [42].

In general, the spectrum of the energy in the center of mass is approximated by a Gaussian with central value, E_{cm} , determined as described at the beginning of this section. The standard deviation, $\sigma_{E_{cm}}$, is related to the standard deviation of the frequency, defined on page 41, by the expression

$$\sigma_{E_{cm}} = \frac{\beta_{\bar{p}}\; m_p\; c^2}{E_{cm}} \times \frac{p_{\bar{p}}}{\eta} \times \frac{\sigma_f}{f}\ . \tag{2.10}$$

In the case of the scan of the χ_{c0} , the subject of this dissertation, the width of the resonance is about 25 times larger than the typical standard deviation of the energy in the center of mass (generally $\sigma_{E_{cm}}$ is close to 400 keV). Thus, in extracting the excitation curve of the χ_{c0}, the beam can be treated as monochromatic.

2.2 The Hydrogen Jet target

E835 belongs to the category of the fixed target experiments; such a definition indicates that the kinetic energy of the target, if any, is negligible in the calculation of the total collision energy. Having said that, the E835 target [43] is anything but fixed. It consists of a jet of clusters of hydrogen, moving horizontally at speeds of the order of 1000 m/s, that intersects perpendicularly the antiproton beam.

The density of the jet can be varied up to a maximum of 6.5×10^{14} atoms/cm^3 [44]. A variable jet density allows compensating for the decrease of the antiproton beam intensity that occurs as the data taking proceeds and the $\bar{p}$'s are consumed. Therefore, the instantaneous luminosity, which is proportional to both jet density and beam intensity, can be maintained approximately constant throughout the data taking. A constant instantaneous luminosity, close to the maximum sustainable by the detector and data acquisition (generally between 2 and 3 $\times 10^{31}$ s^{-1}cm^{-2}) obviously optimizes the usage of the accelerator time allotted to E835. Furthermore, variations of apparatus performances and effects such as event contamination due to pileup of $p\bar{p}$ collisions are better understood and corrected for when the interaction rate is kept approximately constant.

The choice of the hydrogen as target fluid is dictated by the fact that the broadening of the energy resolution, due to Fermi motion of nucleons in higher-Z nuclei, would not be negligible with respect to the widths of the narrower charmonium resonances.

The layout of the jet target is schematically represented in Figure 2.3. The hydrogen gas is kept at a high pressure and low temperature and then let expand through a convergent-divergent nozzle (see detail in Figure 2.4). The isentropic expansion of the gas favors the formation of a core jet of clusters, made of $10^7 - 10^8$ molecules.

A system of turbo-molecular pumps, placed upstream (acting on chambers J1, J2, and J3 in Figure 2.3) and downstream (chambers R1, R2, and R3) the intersection with the antiproton beam, maintains the high vacuum in the beam pipe that is necessary to preserve a long-life and high-quality $\bar{p}$-beam. Upstream pumps remove that part of the gas that do not clusterize in the core of the jet, while downstream pumps remove the jet after it has crossed the $\bar{p}$ beam (only a small fraction of the protons interacts with the antiprotons).

The plot in Figure 2.5 is the curve of the values of temperature and pressure that an automatic control system sets to increase the jet density, which is also shown in the plot. As an example of the typical E835-2000 running conditions, Figure 2.6 shows, throughout some 30 hours of data taking, how the enforced increase of the jet density compensates for the unavoidable decrease of the beam current[4] to keep the instantaneous luminosity approximately constant.

In general, with the jet target on, a typical 50 mA beam may yield 2 or 3 days of data taking; with target off, the beam life time is 5 to 10 times longer.

[4]The $\bar{p}$-beam current, I, is given by $I = N_{\bar{p}} \times e \times f$, where $N_{\bar{p}}$ is the number of circulating antiprotons, e is the antiproton charge, and f is the revolution frequency; the rule of thumb is that 1×10^{10} $\bar{p}$'s correspond to 1 mA.

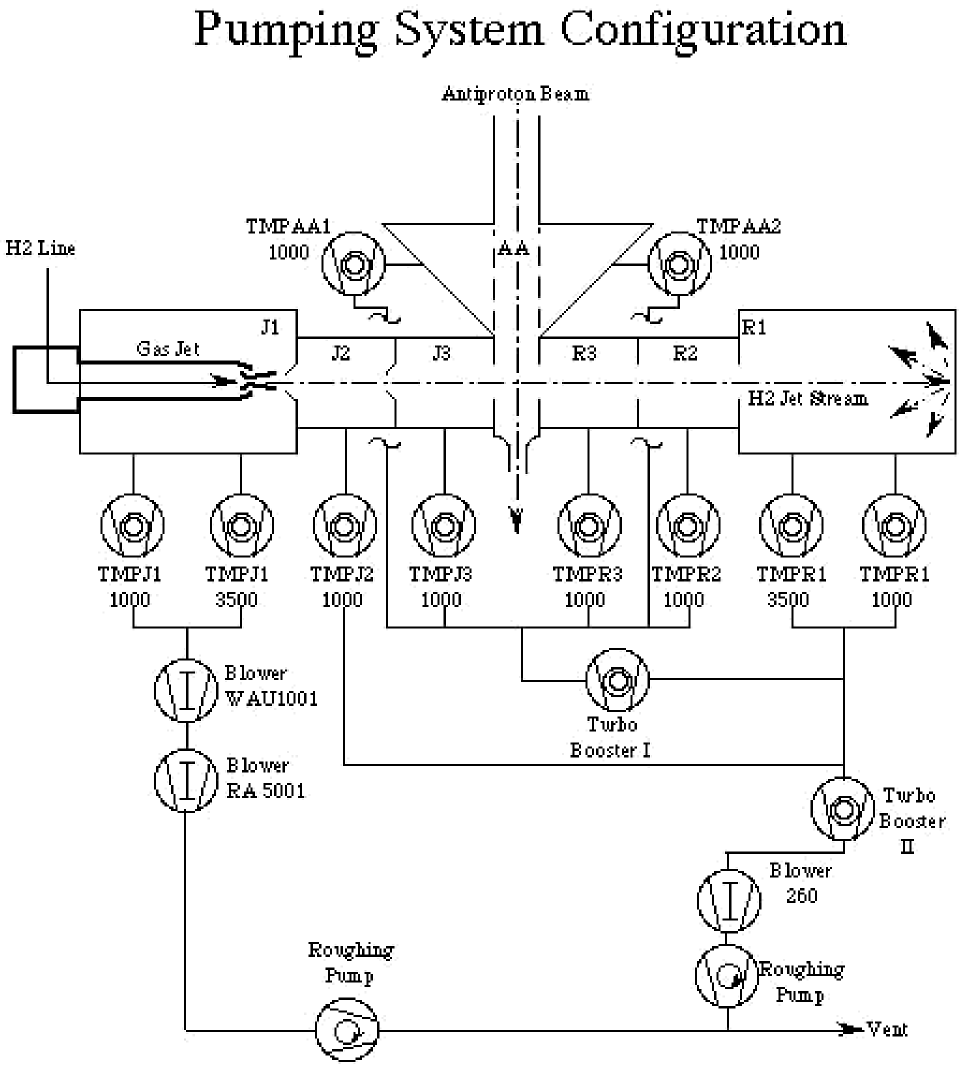

Figure 2.3: Layout of the jet target and pumping system.

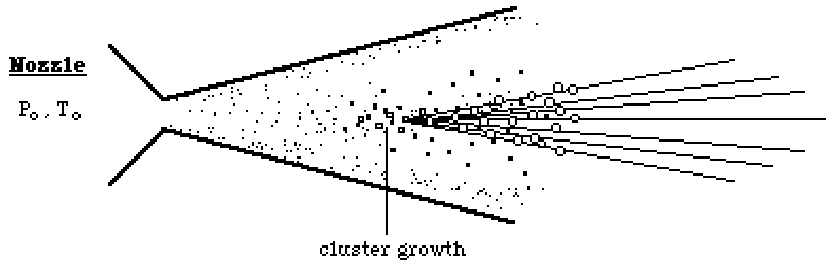

Figure 2.4: Detail of the nozzle and the formation of clusters of hydrogen.

2.3 The Detector

The non-magnetic spectrometer of E835 has been designed to efficiently detect electromagnetic final states, charged and neutral, at a high interaction rate. Its structure has a cylindrical geometry about the antiproton beam axis, defined as the z-axis of a spherical coordinate system with origin in the center of the proton-antiproton interaction region. The coverage of the detector is full in the azimuthal angle ϕ, and from $\sim 2°$ and $\sim 70°$ in the polar angle θ.

Several detectors compose the whole spectrometer, as shown in Figure 2.7: a central and a forward electromagnetic shower calorimeters, to measure energy and position of electrons and photons; a system of inner detectors, to track charged particles; a Čerenkov counter, to discriminate electrons and positrons from other charge particles; and a luminosity monitor, to measure the instantaneous luminosity. The detectors are highly segmented and equipped with time-to-digital converters (TDC) to reject out-of-time signals.

The neutral analyses presented in this dissertation are performed using the central calorimeter (CCAL), a system of scintillation counters (which are part of the inner detectors), and the luminosity monitor.

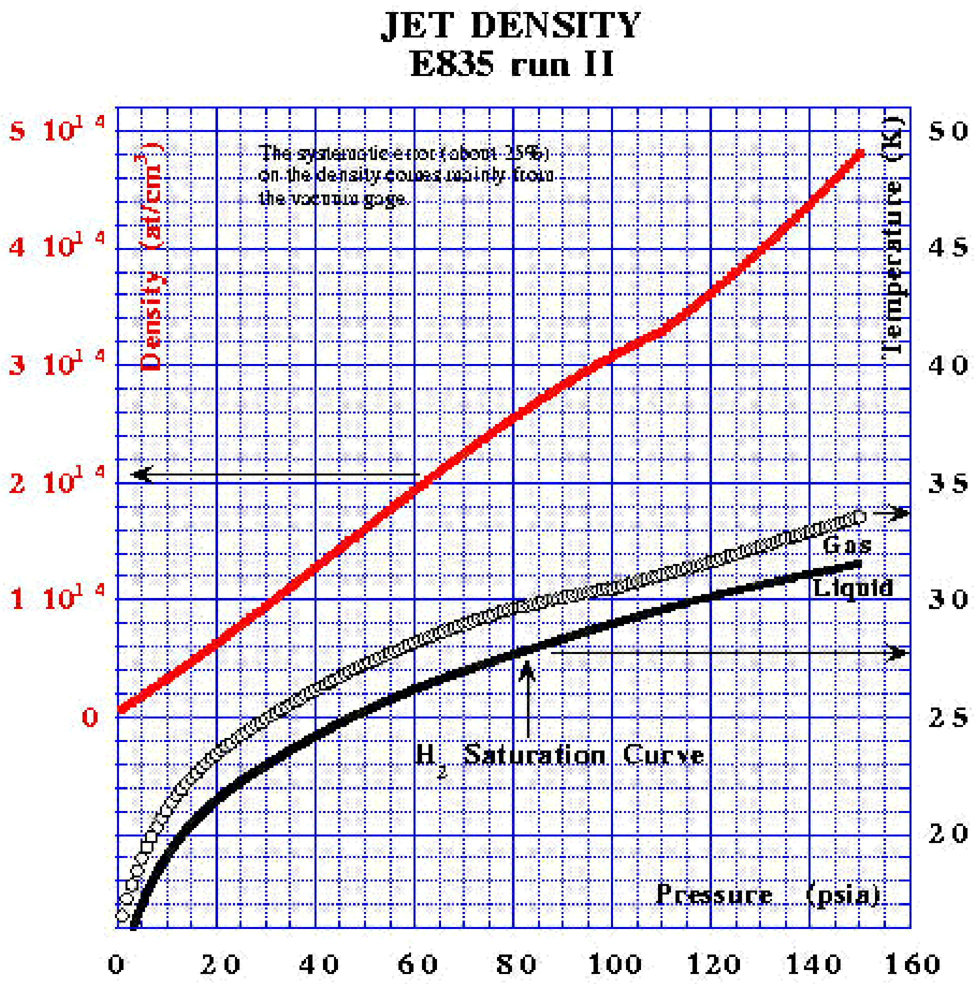

Figure 2.5: Sequence of temperature-pressure set points followed by the jet target control system to induce the increase of jet density. The set points lay just above the H_2 saturation curve.

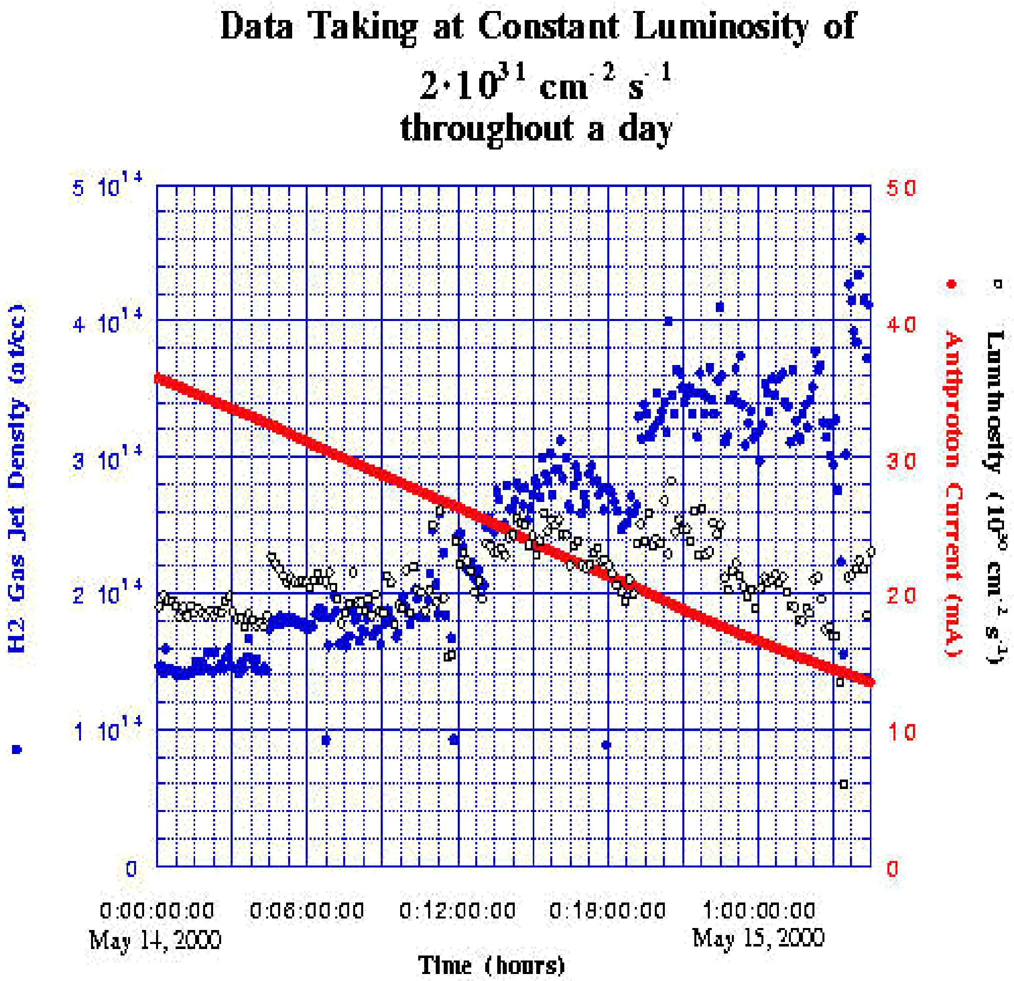

Figure 2.6: Jet target density and antiproton beam current during $\sim$ 30 hours of data taking at E_{cm} = 3526 MeV. As the beam is used (the current steadily decreases), the jet density is increased to maintain an approximately constant instantaneous luminosity.

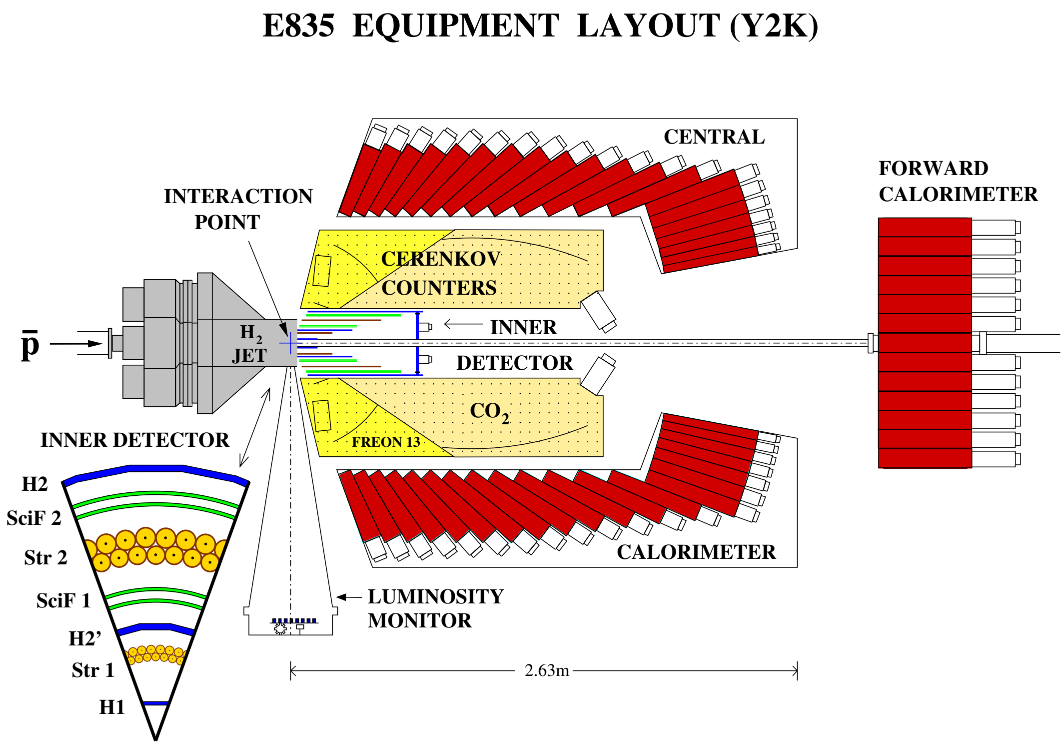

Figure 2.7: Side view of the E835 spectrometer.

Specific publications exist for most of the single detectors. In addition, a complete and detailed description of the experiment has been submitted to N.I.M.A. on April 2003 [45]. Hence, the following sections only summarize the main features of each detector. More space is given to the description of CCAL, which is the most relevant piece of the spectrometer for neutral analyses. A description of the trigger system and the data acquisition is also provided.

2.3.1 The Inner Detectors

The tracking system (see a wedge of its cross section in Figure 2.7) is made of a system of three scintillation counters (hodoscopes), named H1, H2′ and H2; a pair of straw chambers, Str1 and Str2; and two scintillating fiber trackers, SciF1 and SciF2. A fourth hodoscope, the Forward Veto (FV), covers the forward region to prevent leakage of charge particles. All of these detectors are contained in a cylindrical region of radius 17 cm and length 60 cm. The total thickness seen by particles emitted at $\theta = 90^\circ$ is 7% of a radiation length, X_0.

The hodoscopes

Each one of the hodoscopes, H1, H2′, H2, and FV, is segmented in several independent counters placed close to each other. Every independent counter is made of a plastic scintillator connected, by means of a light guide[5], to a phototube. The scintillators are made with a plastic material with index of refraction 1.58 and density 1.03 g/cm^3.

The hodoscopes H1, H2′ and H2 have the shape of a cylindrical shell with the $\bar{p}$-beam as symmetry axis, segmented by $\phi =$ constant planes. Their features are the followings:

H1 It is segmented in 8 elements. The distance from the beam axis is 2.2 cm. The coverage is complete in the azimuthal angle ϕ and from 9° and 65° in the polar angle θ. The thickness of the scintillator is 2 mm and provides from 10 to 20 photoelectrons for a minimum ionizing particle.

H2′ It is segmented in 24 elements, with cracks (that is the separation between its elements) not aligned with the cracks of H1 to reduce the leakage of particles. The distance from the beam axis is 7 cm. It provides complete coverage in ϕ and from 9° and 65° in θ. The tickness of the scintillator is 4 mm.

H2 It is segmented in 32 elements, with cracks aligned with the cracks of H1 (1 element of H1 covers 4 elements of H2). The distance from the beam axis is 16 cm. The coverage is complete in ϕ and from 12° and 65° in θ. The tickness of the scintillator is 4 mm and provides from 50 to 100 photoelectrons for a minimum ionizing particle.

The Forward Veto, instead, has the shape of a holed disk placed in the forward region around, and perpendicularly to, the beam pipe. Its features are the followings:

[5]With the exception of the Forward Veto, where the phototubes are directly attached to the scintillators.

FV It is segmented in 8 elements. It provides complete coverage in ϕ and from 2° and 12° in θ. The tickness of the scintillator is 2 mm.

These counters, because of their fast response, are used to for trigger purposes. As an example, the coincidence between H1 and H2 generates a first-level trigger for charged events. The coincidence among H1, H2$'$ and FV generates a veto signal for neutral events. The signals from H1, H2$'$ and H2 are also used, offline, to measure the energy loss per unit length in order to distinguish single particles from multiple overlapping particles.

The Straw Chambers

Purpose of the two chambers (not used for the $\pi^0\pi^0$, $\eta\eta$ and $\pi^0\eta$ analyses) is to determine the azimuthal angle ϕ of charge particles. They provide full coverage in ϕ and from 15° and 60° in θ. Each chamber is made of two layers (staggered to resolve left-right ambiguity) of 64 straws, arranged along a cylindrical shell about the $\bar{p}$-beam axis. The radius of the cylindrical shell is $\sim$54 mm for the inner chamber, STR1, and $\sim$120 mm for the outer chamber, STR2.

Each straw has a gold-plated tungsten wire pulled along the straw axis. The wire (anode) is kept at a high positive voltage, while the aluminized inner surface of the straw (cathode) is connected to ground. The straw is filled with a gas mixture of $\mathrm{Ar} : \mathrm{C_4H_{10}} : \mathrm{(OCH_3)_2CH_2} = 82 : 15 : 3$. The drift velocity, at the operating voltages, is $\sim 40\mu$m/ns. Part of the readout electronics, as well as the high voltage distribution boards, are installed on the downstream end of the chambers. Surface Mounting Devices (SMD) are employed. The straw chamber signals are analyzed by Time-to-Digital Converter (TDC).

The double pulse resolution is $\sim$25 ns. The particle-detection efficiency of a straw goes from $\sim$100%, in the proximity of the wire, to $\sim$80%, close to the straw surface. The angular resolution for a track, using both chambers, is about 9 mrad.

The straw chamber detector is fully described in a dedicated publication [46] and in [47].

The Scintillating Fiber Trackers

The two scintillating fiber trackers (not used for the $\pi^0\pi^0$, $\eta\eta$ and $\pi^0\eta$ analyses) provide a measurement of the polar angle θ for charge particles. They cover the full range in ϕ. The coverage in θ is from 15° and 55° for the inner tracker, SciF1, and from 15° and 65° for the outer tracker, SciF2. Each one of the two trackers is made of two layers of fibers (240 fibers per layer in SciF1 and 430 in SciF2). The four layers are wound (along planes perpendicular to the beam axis) around cylindrical supports of radii 85 and 92 mm for SciF1, and 144 and 150.6 mm for SciF2.

Each one of the fibers is connected, by means of a clear fiber, to a Visible Light Photon Counter (VLPC) kept at temperature of 6.5 K in a cryostat. The VLPC are solid state photosensitive devices with a quantum efficiency of 70% for 550 nm photons. The signals are sent to Analog-To-Digital Converters (ADCs), Time-To-Digital Converters (TDCs) and, also, used for trigger purposes.

The detection efficiency is greater than 95% and the intrinsic resolution is (0.7 ± 0.1) mrad.

More detailed descriptions of the inner tracker can be found in [48, 49].

2.3.2 The Čerenkov Counter

The duty of the Čerenkov counter (not used for the $\pi^0\pi^0$, $\eta\eta$ and $\pi^0\eta$ analyses) consists in identifying electrons and positrons among the exceedingly more copious hadrons. It exploits the principle that Čerenkov light is emitted when a charge particle passes through a medium with a velocity, β, greater than $1/n$, where n is the index of refraction of the medium. In other terms, light is emitted when the energy of the particle exceeds a threshold, $\frac{m}{\sqrt{1-1/n^2}}$, that depends on the mass of the particle. Since electrons are (much) lighter than any hadron, it is possible to choose a medium, a gas in our case, such that $e^+e^-$are above threshold and hadrons below.

The structure of the detector is a sealed chamber with the shape of a cylindrical shell. The inner and outer radii of 17 and 59 cm, respectively, and the coverage in θ is from 15° and 65°. A septum divide the structure in an upstream $(34° < \theta < 65°)$

and a downstream ($15° < \theta < 38°$) cell. The upstream cell is filled with CO_2, which has an index of refraction of 1.00041, corresponding to an energy threshold for $\pi^{\pm}$, the lightest charged hadrons, of 4.875 GeV. The downstream cell is filled with CF_2Cl_2 (Freon 12), which has an index of refraction of 1.00072, corresponding to an energy threshold for $\pi^{\pm}$ of 3.005 GeV. Each cell is optically separated in 8 wedges by $\phi = \text{constant}$ planes. The light generated in each wedge of the upstream (downstream) cell is reflected by a spherical and a plane (a single ellipsoidal) mirror into a photomultiplier, as shown in Figure 2.8.

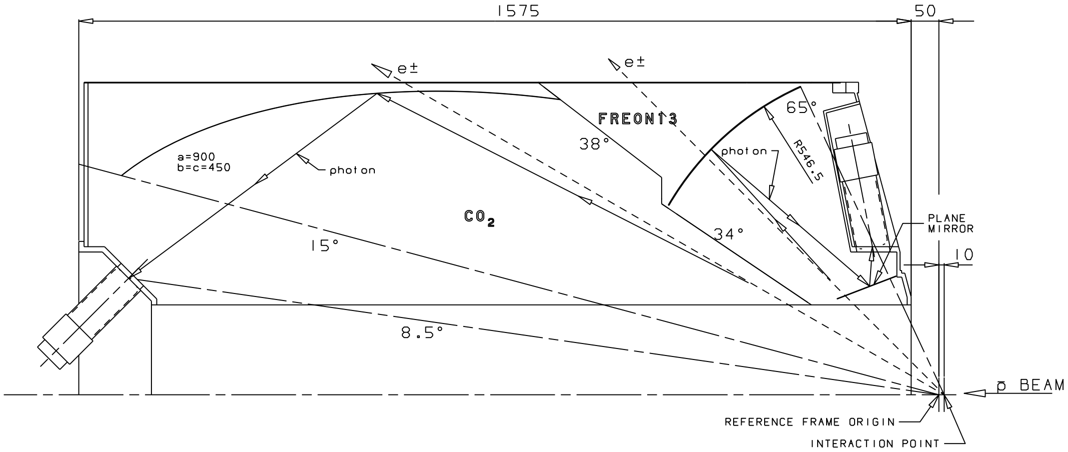

Figure 2.8: Side view of one of the wedges of the Čerenkov counter. The septum at 34°/38° divides the chamber in two cells. The spherical, plane and ellipsoidal mirrors are shown. Dimensions are reported in millimeters. Do not be confused by the fact that in this view the $\bar{p}$-beam travels from right to left, as opposite to the view in Figure 2.7.

The signals of the 16 channels of the Čerenkov counter are sent to ADCs, TDCs and charged trigger logic. The efficiency of electron and positron detection is (98.1±0.5)%.

A comprehensive description of the Čerenkov counter can be found in [50, 51].

2.3.3 The Central Calorimeter

It is the most important detector for the analyses of this dissertation. It measures energy and position of photons, electrons and positrons in the polar angle range $10.6^\circ < \theta < 70.0^\circ$, providing full coverage in the azimuthal angle ϕ.

The main features of the detector are described below; more details can be found in [52, 53, 54, 55] and, more recently, in [56, 57].

The central calorimeter (CCAL) is an electromagnetic shower detector made of 1280 lead glass blocks, which are shaped and oriented according to a projective geometry pointing toward the $p\bar{p}$ interaction region. As depicted in Figure 2.9, a ring of CCAL is defined by 64 blocks positioned at the same value of θ, while a wedge is defined by 20 blocks positioned at the same value of ϕ.

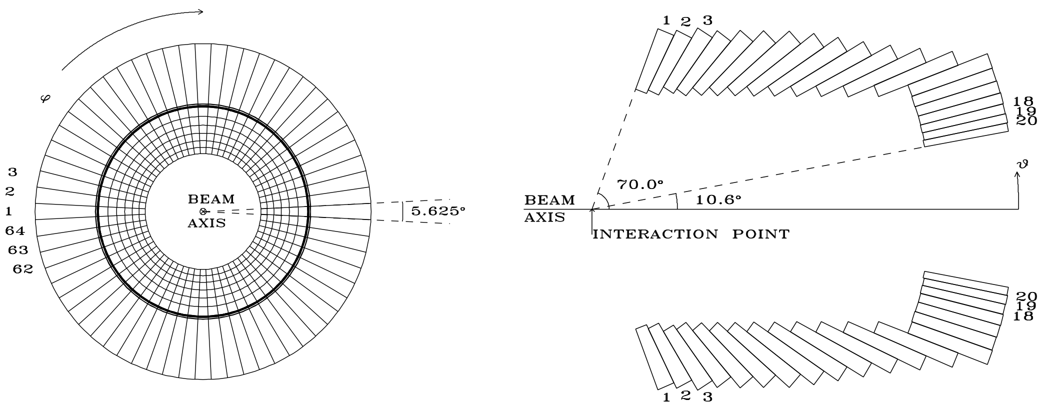

Figure 2.9: View of a ring (left) and two opposite wedges (right) of the central calorimeter.

The blocks are made of a Schott F2 type lead glass. The index of refraction (at 404.7 nm) is equal to 1.651, the density is 3.61 g/cm^3, and the radiation length is 3.141 cm. More details about dimensions and position of the blocks are given in Table 2.2. The frame that supports the blocks is made of stainless steel. The tickness of the inactive material is 1.47 mm in between wedges and 0.254 mm in between rings.

Ring	Length (cm)	Central θ (degree)	$\Delta\theta$ (degree)	Distance from Interaction Region (cm)
1	37.80	67.387	5.226	72.44
2	38.65	62.259	5.031	75.87
3	39.88	57.342	4.803	80.07
4	41.50	52.664	4.552	85.08
5	43.54	48.246	4.284	90.96
6	46.06	44.101	4.007	97.79
7	48.98	40.234	3.728	105.62
8	50.00	36.644	3.451	114.54
9	50.00	33.327	3.183	124.66
10	50.00	30.273	2.925	136.07
11	50.00	27.472	2.679	148.89
12	50.00	24.908	2.449	163.26
13	50.00	22.567	2.233	179.34
14	50.00	20.434	2.033	197.28
15	50.00	18.493	1.848	197.29
16	50.00	16.730	1.678	197.29
17	50.00	15.130	1.552	197.30
18	50.00	13.679	1.380	197.30
19	50.00	12.364	1.250	197.30
20	50.00	11.174	1.131	197.30

Table 2.2: Geometrical characteristics of the CCAL blocks. The 64 blocks contained in a ring share the same features.

An Hammamatsu photomultiplier is glued to each block to collect the Čerenkov light produced by the electromagnetic showers. The photomultipliers come in four different sizes to adjust to the varying size of the blocks and maximize the efficiency of collection of the light. A small fraction, 5%, of the signal of each one of the 1280 photomultipliers is sent a CCAL summer circuit for trigger purpose. The large remaining part of the signal goes over a 300 ns coaxial cable, which allows the trigger electronics the time to make a decision, to an electronic board that reshapes the signal to make it fit into a 100 ns gate for ADC integration. A fraction of the reshaped signal is sent to a discriminator followed by a TDC. The short ADC gate and the TDC time information are necessary to reduce the event contamination due to pileup.

To monitor the performance of each channel of the detector, it is used a system with a nitrogen laser, a scintillator and an optic fiber network. Pulses of a 430 nm light are sent into each block through their back faces. The amount of light delivered is measured by photodiodes, while the counter response is measured through the electronic chain described above. The monitorage system runs at a 0.1 Hz frequency throughout the data taking.

The Clusterizer

It is called clusterizer the software procedure that groups neighboring blocks hit by an electromagnetic shower to determine the energy and position of the particle that generated it. The group of neighboring blocks is called cluster.

First, cluster seeds are searched for. A seed is defined as a block with an energy deposit larger than in any of the eight neighbors of a 3×3 grid centered on it. Further requirement is that the energy of the block exceeds a certain seed threshold.

The sum of the deposits in all the nine blocks of the grid is called cluster energy. It is imposed a minimum energy threshold that the cluster has to exceed to be considered as such.

Generally the seed and cluster thresholds are set to 25 and 50 MeV, respectively; this is the case for the analyses presented in this dissertation. For analyses particularly dependent on the detection of low energy photons, those values are lowered to 5 and 20 MeV, respectively; this is the case for analyses involving the detection of 2 photons only, where the background due to undetected photons from the $\pi^0\pi^0$ and $\pi^0\gamma$ channels is copious.

Clusters are defined according to three categories: isolated, shared and split; which are described as follows. More detailed explanations are given in the quoted references, in particular [56, 57].

Isolated Clusters. An isolated cluster do not have a second seed in a 5×5 grid around its own seed. As a first approximation, the position of a cluster is assigned as the energy-weighted average of the centers of the blocks in the 3×3 grid. Then, since energy is lost in the cracks between blocks, a correction on both position and energy of the cluster is made. The shower profile is parameterized by a function, describing the core and the tail of the shower, which depends on parameters that have been measured with a test beam at Brookhaven National Laboratory [52]. The parameterization allows an estimate of the energy lost in each crack, which is used to re-determine the position and the energy of the cluster. The effectiveness of the energy correction is evident from Figure 2.10.

Shared Clusters. When a second seed is found in a 5×5 grid centered on a first one, it is assumed that two particles have impacted nearby, and a cluster is built around each one of the two seeds. The energy of those blocks that belong to both the 3×3 grids centered on each seed is shared between the two clusters. It is an iterative process which includes a method for correcting the position and the energy of the clusters. The method is derived by the one used for isolated clusters and is adapted to the situation of overlapping showers.

Split Clusters. Finally, a cluster may not have a second seed close by, but still present a feature indicating that it has likely been formed by two different showers so close to each other not to be resolved. That happens in particular when a π^0 decays in two photons of approximately equal energies in the laboratory frame[6], which

[6] Such a decay is generally referred to as symmetric decay.

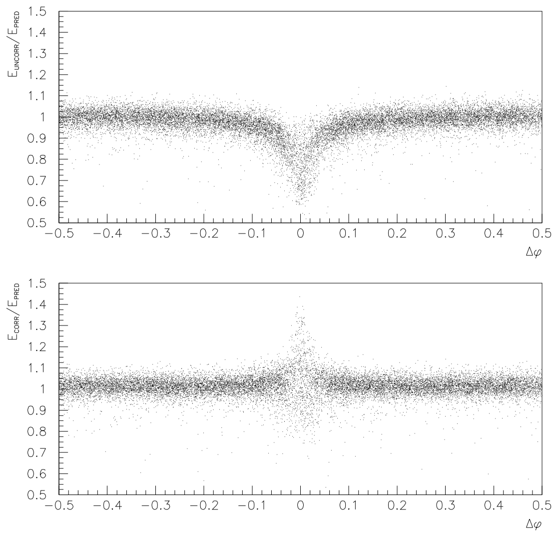

Figure 2.10: Events $J/\psi \rightarrow e^+e^-$ (real data). Ratio between the measured energy of the cluster and the energy predicted by the 2 body kinematics, before (top) and after (bottom) energy correction, as a function of the distance from the crack.

implies that the opening angle between them is at its minimum. The minimum opening angle, at the highest energies that E835 has run at, corresponds to a distance between the centers of the two showers as low as $\sim$1.5 block widths: often not enough to generate two seeds. The mentioned feature regards the cluster mass, defined as

$$M_{cl} \equiv \sqrt{\Big(\sum_{i=1}^{25} E_i\Big)^2 - \Big(\sum_{i=1}^{25} \vec{p_i}\Big)^2}\ , \tag{2.11}$$

where the sum runs over the 25 blocks of the 5×5 grid around the seed, E_i is the energy deposited in the i-th block, and $\vec{p_i}$ is equal to $E_i\hat{r}_i$, $\hat{r}_i$ being the unit vector from the interaction region to to the center of the i-th block. Electron and positron showers from $J/\psi \rightarrow e^+e^-$ decays show that the cluster mass of a single-particle shower does not exceed $\sim$ 100 MeV (see the e^+ and e^- cluster mass distribution in

Figure 2.11). Single-photon showers cannot deviate markedly from that distribution.

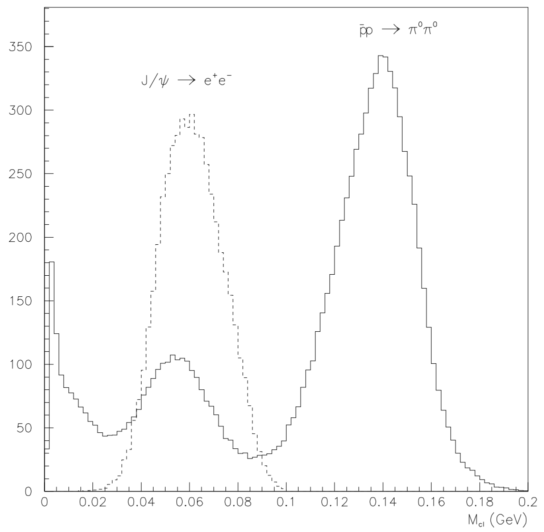

Figure 2.11: Real data distribution of the cluster mass for electrons and positrons from J/ψ decays (dashed), and for photons from a $\pi^0\pi^0$ sample (solid). The large peak at $M_{cl} > 100$ MeV is interpreted as due to coalesced photons from a symmetric decay of a π^0.

Therefore, the large peak at values higher than $\sim$ 100 MeV evident in the cluster mass distribution of photons from a $\pi^0\pi^0$ sample (see again Figure 2.11) must be due to pairs of coalesced photons: the CCAL segmentation is not fine enough to distinguish two seeds, but the energy deposit reveals its true origin thank to its suspiciously large spread. Each of these energy deposits, then, is split into two clusters following the procedure outlined a few lines below. The smaller peak in the $\pi^0\pi^0$ cluster mass distribution is made of isolated clusters. Shared clusters, which are the majority in the $\pi^0\pi^0$ sample, have been removed from the plot to better show the difference between isolated and split clusters.

According to the above understanding, the clusterizer checks the cluster mass of every energy deposit. If it finds that M_{cl} is grater than 100 MeV, called split threshold, it defines a second seed, chosen as the block with the largest deposit among the four blocks at the corners of the original seed. Two clusters, called split clusters, are then built around the two seeds. Following a procedure similar to the one adopted for shared clusters, the total energy is shared, and the positions and energies are corrected for losses in the cracks.

Figure 2.12 shows the necessity and the effectiveness of the split cluster proce-

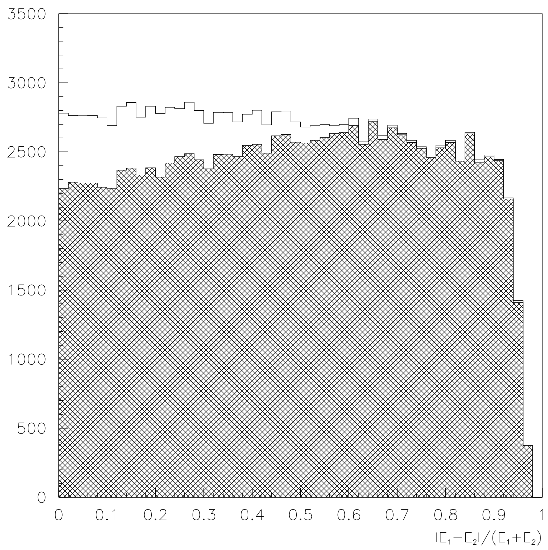

Figure 2.12: Distribution of the π^0 asymmetry (real data), defined as $(E_1 - E_2)/(E_1 + E_2)$, where E_1 and E_2 are the energies of the two photons. Open histogram: without split clusters; Shaded histogram: with split clusters.

dure: the expected uniformity of the π^0 asymmetry is recovered by including the split clusters.

CCAL performances

The angular resolution, measured for E760, is $\sigma_\theta \simeq 6$ mrad in the polar angle and $\sigma_\phi \simeq 11$ mrad in the azimuthal angle [52]. By using a $J/\psi \rightarrow e^+e^-$ sample selected by the hodoscopes and the Čerenkov counter, it has been checked that those values are unchanged for E835.

The method used to perform the energy calibration is described a few lines below by using $\pi^0\pi^0$ events. The energy resolution is determined by comparing the measured energy deposited by the electron, or the positron, with the energy calculated using the measured polar angle of the cluster[7]. The energy resolution, σ_E, is approximately described by the formula

$$\frac{\sigma_E(E)}{E} = \frac{6\%}{\sqrt{E(\mathrm{GeV})}} + 1.4\% \ . \tag{2.12}$$

Energy Calibration. The gain constant, g_i, of each one of the 1280 CCAL channels is defined as the ratio between the energy deposited in the block and the value recorded by the ADC. The gain constants are determined on a stack by stack basis by using the copious $\pi^0\pi^0 \rightarrow \gamma\gamma\,\gamma\gamma$ sample of the stack.

The measured energy, M_j , of each one of the two π^0 's is given by the sum of the energy deposited in all the blocks belonging to the clusters of the two decay photons:

$$M_j = \sum_{i=1}^{n} g_i \ A_{ij} \ , \tag{2.13}$$

where j is the index of one of the two pions, i runs over the blocks of the j-th pion, and A_{ij} is the ADC value recorded for every involved block. Naming E_j the energy calculated by using the measured polar angle of the pion, a χ^2 is defined as

$$\chi^2 = \sum_{j=1}^{N} \frac{(M_j - E_j)^2}{\sigma_j^2} \ , \tag{2.14}$$

where N is the number of π^0's and σ_j the estimated uncertainty on E_j. The values of the gain constant that minimize the χ^2, calculated analytically, are inserted back in Equation 2.14. The procedure is iterated until convergence is reached. The

[7]For a two-body final channel, the knowledge of the polar angle of one body is enough to determine all of the kinematic variables.

thin, marginal ring 20 cannot be calibrated with the $\pi^0\pi^0$sample; a punch-through[8] method is used, instead.

Once the above CCAL calibration is completed, the measured mass of the η is compared with the actual mass. A scale correction, typically 1-2%, is then applied to all gain constants so that measured and actual value matches.

Timing Algorithm. A timing information is added to every CCAL cluster by considering the TDC channels of the two block of the cluster with the highest ADC counts. If neither TDC channels have recorded a hit, the cluster is classified as undetermined. If either has recorded an in-time hit (that is within 10 ns from the mean event time), the cluster is classified as in-time. Out-of-time clusters are those for which none of the above apply.

The timing algorithm is tested with a $\pi^0\pi^0$ sample from which split clusters have been excluded. The reconstruction of these events is made with a cluster threshold set to 20 MeV, rather than 50 MeV, to see the algorithm response also at low energy. The number of clusters with time information rises sharply as the cluster energy varies from 20 to 50 MeV. The reason is that the higher the cluster energy the more likely the TDC hit threshold is exceeded. The algorithm marks as in-time over 99.5% of the clusters with energy above 50 MeV. The root mean square deviation for in-time clusters is 1.3 ns.

2.3.4 The Forward Calorimeter

A second electromagnetic shower calorimeter, FCAL, covers the forward region around the beam pipe. It covers the range in θ from 3.3° to 11°, complementary to the coverage of the central calorimeter.

The forward calorimeter is composed by an array of 144 blocks[9] with the shape of a parallelepiped arranged as shown in Figure 2.13. The block are made of SF2 lead glass, which has an index of refraction equal to 1.673 and a radiation length of

[8]Minimum ionizing particles that do not shower and release Čerenkov light in a single block, proportionally to the block length.

[9]The available blocks came in three different sizes.

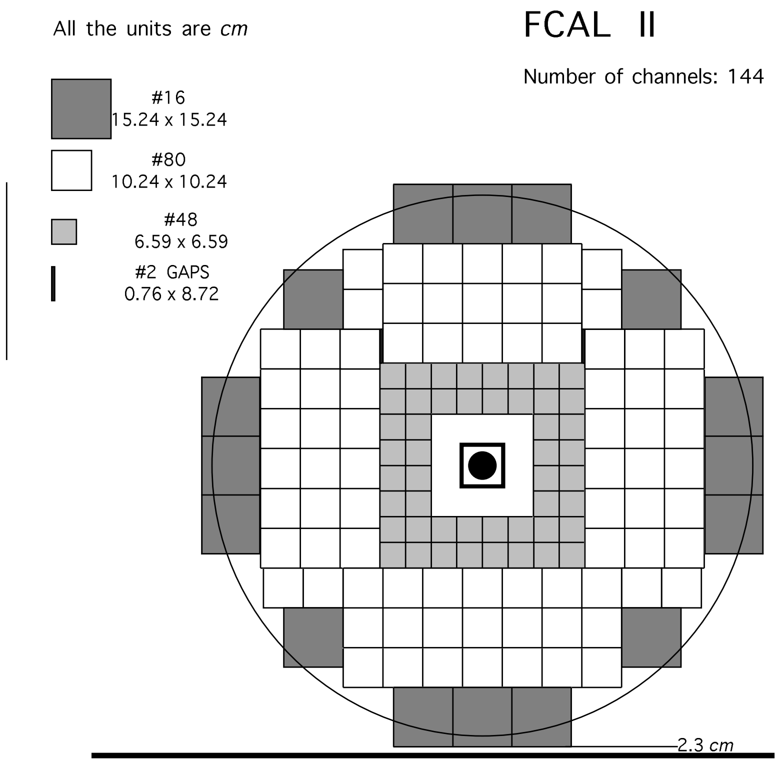

Figure 2.13: Front face (perpendicular to the beam axis) of the forward calorimeter.

2.76 cm. Every block is glued to a photomultiplier, connected to electronic shaper boards similar to the ones used for CCAL. The FCAL signals are sent to ADCs and TDCs.

The spatial resolution of FCAL is approximately 2 cm. The energy calibration is performed using a sample of $3\pi^0 \to 6\gamma$ events, requiring that 5 of the photons are detected by CCAL. The energy resolution, $\sigma_E(E)$, for a photon of energy E follows the Equation

$$\frac{\sigma_E(E)}{E} = \frac{0.06}{\sqrt{E(\mathrm{GeV})}} + 0.04\ . \qquad (2.15)$$

Several internal notes exist to describe FCAL more in details, in particular [58, 59].

2.3.5 The Luminosity Monitor

An accurate measurement of the luminosity is particularly important for an experiment, such as E835, that determines excitation curves of resonances.

The Luminosity Monitor is made of three solid state detectors placed beneath the $p\bar{p}$ interaction region (see Figure 2.7) and along a line corresponding to a value of θ just a few degree less than 90°. The central one of the three detectors is movable in the direction of the $\bar{p}$-beam. Three detectors allow a more reliable measurement of the luminosity and a check on the horizontal position of the $\bar{p}$-beam.

In that region of θ, the $p\bar{p}$ cross section is dominated by elastically scattered protons. The number of protons, N, passing through each one of the detector is given by

$$N = \mathcal{L} \int_{\Delta\Omega} \frac{d\sigma}{d\Omega} d\Omega \ , \tag{2.16}$$

where $\mathcal{L}$ is the luminosity and $\Delta\Omega$ is the solid angle of acceptance. The detectors' silicon surface barriers are sufficiently tick (500 μm) to stop completely the protons, which have an energy of just a few MeV.

The differential cross section, $d\sigma/d|t|$, versus squared momentum transfer, $|t|$, was measured by E760 [60], using the movable detector, for six values of the $\bar{p}$-beam momentum. It is shown in Figure 2.14 along with fits to the data.

For every energy point of the data taking, the luminosity is determined by counting the number of protons N and by using the fits to the cross section $d\sigma/d|t|$. A typical spectrum recorded by the detectors is shown in Figure 2.15. N is determined by subtracting the exponential background. A measurement is carried out every 2 minutes, so that a 60-second average of the instantaneous luminosity is also available throughout the data taking.

The estimate of the luminosity is obtained with a systematic error of less than 3% and a statistical error of about 0.3% for a 100 nb^{-1}. The luminosity monitor is described in an earlier publication [61].

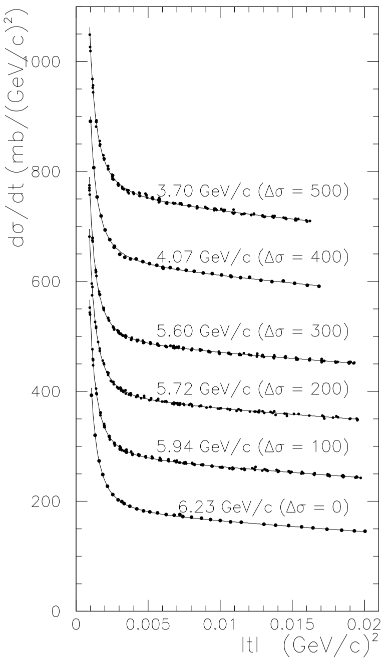

Figure 2.14: Measured $p\bar{p}$ differential cross section, $d\sigma/dt$, versus squared momentum transfer, $|t|$, at six values of the $\bar{p}$-beam momentum (shifted upward of an amount $\Delta\sigma$ to distinguish them). Fits to the data are shown.

2.3.6 The Trigger System

Independent triggers are formed for charged and neutral final states. The charged trigger [62] is mainly designed to identify an e^+e^- pair from the electromagnetic decay of the J/ψ or ψ', allowing the study of reactions such as $p\bar{p} \rightarrow J/\psi$ (and ψ') $\rightarrow e^+e^-$ and $p\bar{p} \rightarrow \chi_{c0}$ (χ_{c1} and χ_{c2}) $\rightarrow e^+e^-\gamma$. A specific trigger for the completely hadronic reaction $\bar{p}p \rightarrow \bar{c}c \rightarrow \phi\phi \rightarrow K^+K^-K^+K^-$ is implemented, as well. Multiple photon final states are identified by the neutral trigger. Since the reaction $\bar{p}p \rightarrow \pi^0\pi^0 \rightarrow \gamma\gamma\gamma\gamma$ belongs to this last category, the neutral trigger is described in the next section.

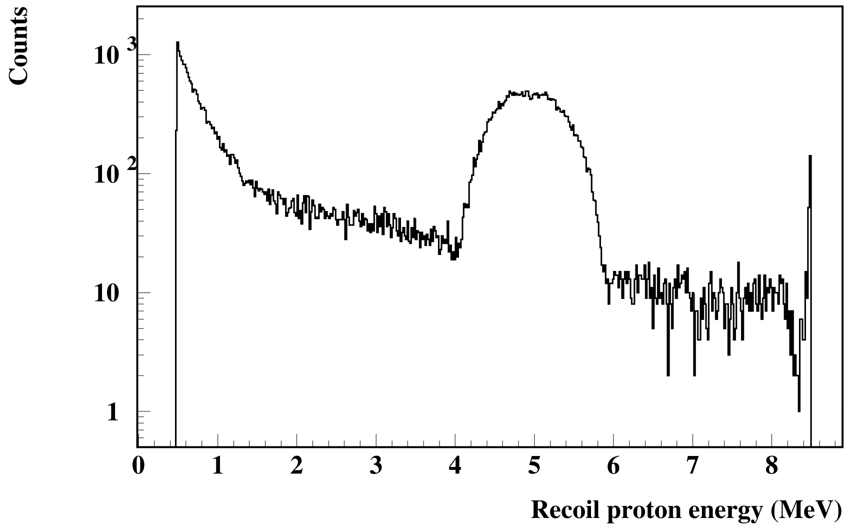

Figure 2.15: Typical spectrum recorded by one of the three solid state detectors of the luminosity monitor.

In addition to the above, several monitoring and efficiency study triggers are used. In particular, a random trigger (named Random Gate, or RG) is run at a frequency of 10 Hz to study accidentals and event pileup. The use of the RG trigger is discussed in section 3.8.

The Neutral Trigger

The main features of the neutral trigger are presented here, more details can be found in [63, 64] and at pp. 74-86 of [65].

It is formed by using the central calorimeter, complemented by the hodoscopes to detect the presence of charged tracks. Two distinct event categories are selected. The first one is characterized by two large deposits of energy in CCAL at opposite or almost opposite positions in azimuthal coordinate. The second one is characterized by a large fraction of the energy in the center of mass deposited in CCAL. The triggers PBG1 and PBG3 (from the acronym of Pb Glass) belong to the first category, while ETOT-HI and ETOT-LO (from TOTal Energy HIgh and LOw) belong to the second category.

The large number (1280) of CCAL channels is reduced, for trigger purposes, to 40 signals by associating neighbor blocks into superblocks. Each superblock consists of eight wedges and five rings[10] as shown in Figure 2.16. The 40 superblocks overlap

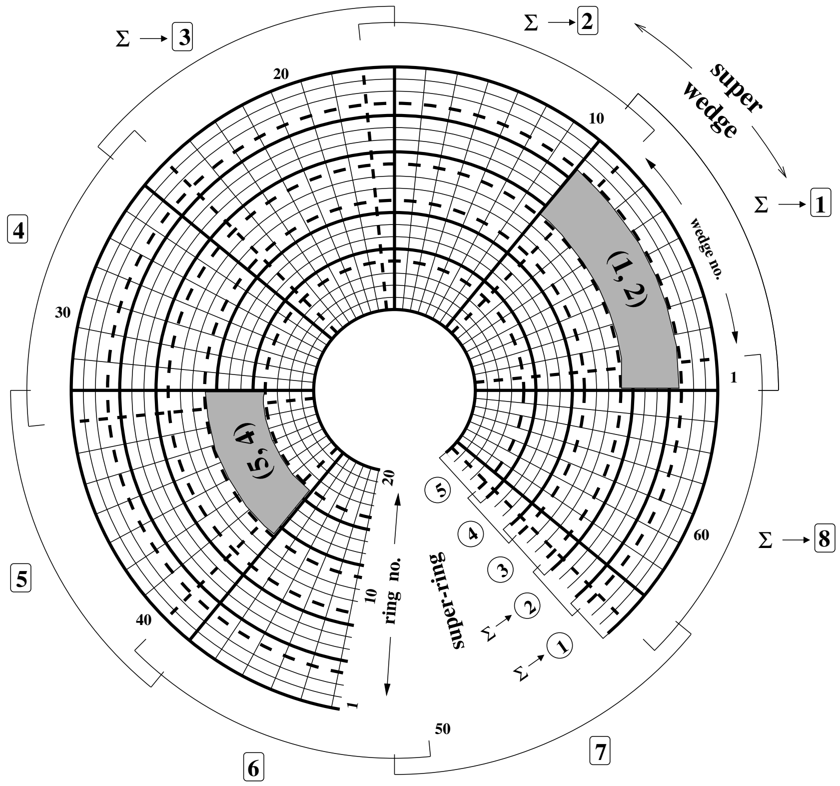

Figure 2.16: View of CCAL from the interaction region. The superblocks, delimited by tick lines (solid and dashed, alternatively), overlap each other to prevent inefficiencies when a shower hits the borders of the superblocks.

each other and divide the full CCAL in eight parts in ϕ and five parts in θ. The signals[11] from all the blocks of a superblock are summed to form the superblock

[10]With the exception of the 8 superblocks at high θ, which spans four rings.

[11]More precisely, only a small fraction of the signal of every block is devoted to the trigger, as mentioned in section 2.3.3.

signal. The 40 superblock signals are used as inputs of discriminator modules.

The CCAL triggers named above are defined as follows.

PBG1. It requires a signal in two superblocks whose position is consistent with two-body kinematics. It is designed for selecting $\gamma\gamma$ and e^+e^- final states. Events $\pi^0\pi^0 \rightarrow \gamma\gamma\gamma\gamma$ are also very efficiently selected through PBG1 because of the small opening angle between the two photons from the π^0 decay.

PBG3. It has similar requirements to PBG1 with a looser requirement on the coplanarity: the two hit superblocks do not need to be exactly opposite to each other in ϕ; rather, the superblock positions adjacent to the opposite position are also allowed. PBG3 selects events such as $J/\psi\,\gamma \rightarrow e^+e^-\gamma$.

ETOT-HI. It requires that 80% of the energy in the center of mass is deposited in the central calorimeter. It is designed to select multiple photon events.

ETOT-LO. It requires that 70% of the energy in the center of mass is deposited in the central calorimeter.

In order to establish whether an event is neutral or not, the signals of the hodoscopes are used to define the following logics:

FV-OR is defined as the "OR" between the eight elements of the Forward Veto.

H1×H2′ is defined as the "AND" between an element of the hodoscope H1 and one of the four[12] corresponding channels of H2′. If more than one of such cases occur, H1×H2′ is still on.

H2≥2 indicates that two or more elements of H2 are hit.

[12]Since the cracks are not aligned (see page 50), four elements of H2′ cover completely an element of H1.

CV, the Charged Veto, is defined as the "OR" between FV-OR and H1×H2′; its negation, $\overline{\mathrm{CV}} = \overline{\mathrm{H1} \times \mathrm{H2}'} \times \overline{\mathrm{FV-OR}}$, is used to declare an event as neutral[13].

Once the PBG1, PBG3, ETOT-HI or ETOT-LO triggers are formed, they are associated with the hodoscopes logics to make four final triggers:

Neutral-PBG1 $\equiv$ $\mathrm{PBG1} \times \overline{\mathrm{H1} \times \mathrm{H2}'} \times \overline{\mathrm{FV-OR}}$

Neutral-ETOT $\equiv$ $\mathrm{ETOT\text{-}HI} \times \overline{\mathrm{H1} \times \mathrm{H2}'} \times \overline{\mathrm{FV-OR}}$

ETOT-NoVeto $\equiv$ $\mathrm{ETOT\text{-}HI} \times \overline{\mathrm{H2} \geq 2}$

Neutral-ETOT-LO $\equiv$ $\mathrm{ETOT\text{-}LO} \times \overline{\mathrm{H1} \times \mathrm{H2}'} \times \overline{\mathrm{FV-OR}}$.

The Neutral-PBG1 and Neutral-ETOT triggers are used to select events from the reactions $\bar{p}p \rightarrow \pi^0\pi^0$ ($\pi^0\eta$, and $\eta\eta$) $\rightarrow \gamma\gamma\,\gamma\gamma$ with high efficiency, as discussed in section 2.3.6. The ETOT-NoVeto and Neutral-ETOT-LO triggers are mostly used for monitoring and efficiency purposes.

The selected events are then further processed by the software trigger PRUDE (Program Rejecting Un-wanted Data Events) for online reconstruction, filtering, sorting and logging.

2.3.7 The Data Acquisition System

E835 acquires and records data from four independent data acquisition streams running in parallel: the event data stream, which is described in some detail below; the data stream for the parameters of the antiproton beam; the data stream for the luminosity monitor; and the scaler data stream to monitor the rate of selected counters and trigger logics.

The event data stream is based on the DART [66] data acquisition, which is a system developed by a collaboration between the Fermilab Online System Department and the experiments that used it in the 1996/97 and 2000 fixed target runs.

[13]The symbols "×" is the operator "AND", and the overline is the operator "NOT".

It provides a common system of hardware and software, which has been configured and extended to meet the specific E835 requirements.

The beam parameter information data stream is received from the FNAL Beam Division via Ethernet.

The last two streams, luminosity monitor data and scaler data, are input and received via standard CAMAC backplane.

Three Silicon Graphics (SGI) computers are used to coordinate, process, filter, log and monitor the data streams. An SGI Indy, the run-control computer, coordinates the independent data streams, communicates with the CAMAC branches and performs the slow data acquisition functions. The event data acquisition, which consists of event building, filtering and logging, is performed by an SGI Challenge-L with 12 processors. Finally, the monitor-display computer is an SGI Indigo, which allows detector monitoring and event displaying.

The Event Data Acquisition

The layout of the event data acquisition is illustrated in Figure 2.17. The readout electronics consists of 195 ADC (LRS4300) and 114 TDC (LRS3377) organized in 17 CAMAC crates. They are arranged in 3 CAMAC branches, two parallel and one serial, and addressed by the run-control computer through two SCSI 411 Jorway Interfaces.

Data from the detectors are read out by the ADC and TDC modules, and transferred through their front-end ECL ports to the DART-developed Damn Yankee Controller (DYC) modules. The DYC is an intermediate data buffer which stores the 16-bit input data in a 32-bit wide FIFO. The DYC adds a header word including a word count, an error bit in the case of event overflow, and 4 bits of event synchronization. Data is sent out to two pairs of Access Dynamics DC2/DM115 modules[2] over two RS-485 cables.

Each ADC or TDC CAMAC crate is served by a DYC. The DYC responds to the request from the readout electronic modules it serves, which are connected in a daisy-chain, by issuing a readout enable to the first module, starting the data

[2]Access Dynamics, Inc - 3823 Hawkins St. NE - Albuquerque, NM 87109 - USA

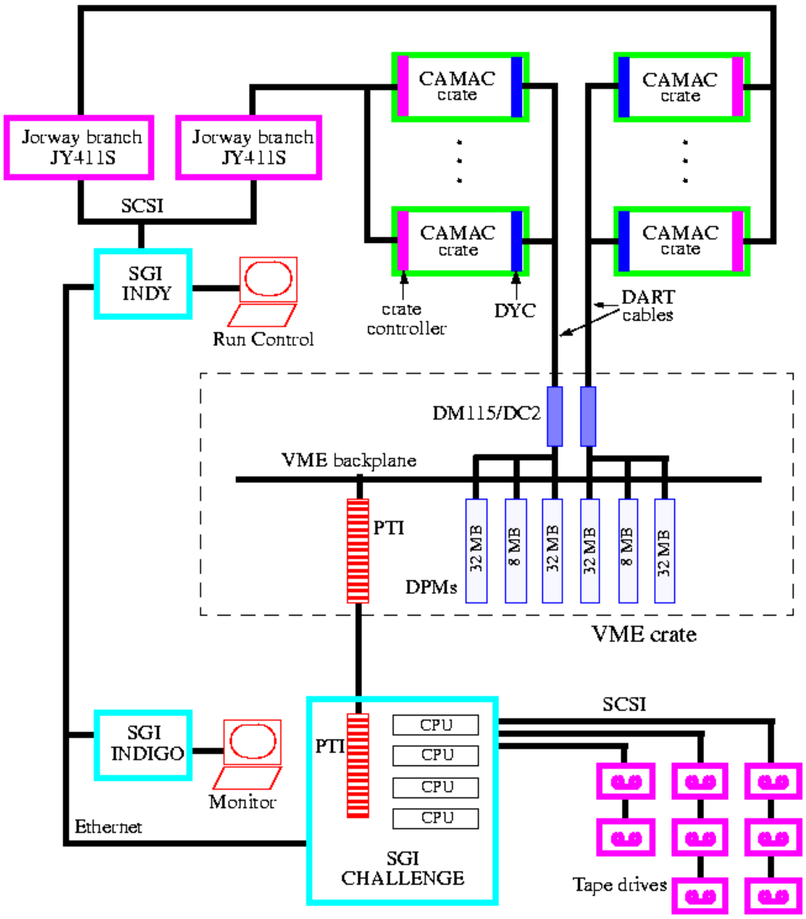

Figure 2.17: Layout of the hardware of the event data acquisition.

transfer. When the first readout electronic module has finished sending data, it enables the following module in the chain by sending a pass signal. The end of the data transfer is signified by the receipt of the pass signal from the last module.

While receiving data, the DYC modules issue a busy signal. The “OR” of the busy signals from all the DYC modules is sent to the trigger logic to inhibit triggers during the data reception.

The DYCs are connected in a daisy-chain via two RS-485 cables (labelled as DART cables in Figure 2.17) in two groups, each of them connected to one of the DC2/DM115 pairs. Data transmission to DC2/DM115 pairs is controlled by a wait signal, established by the destination buffer, and a permit token. On receipt of a permit token and in absence of a wait signal, the DYC transmits the header word and one event data over the RS-485 cable. When the DYC has completed its transmission, it passes the permit token to the following DYC in the daisy-chain. The DYC module is able to simultaneously perform the data reception from the readout electronic modules and the data transmission to the DC2/DM115.

Each DC2 is connected, via the VSBus of the VME crate, to two 32 MB and one 8 MB Dual Ported Memory (DPM) MM-6390[4]. The DC2 fills the two 32 MB DPMs with the data it receives from the DYCs using a “ping-pong” algorithm. According to this algorithm the DC2 writes the “ping” DPM with exactly N (the number is set in the configuration database) events before it switches to the “pong” DPM.

A process running on the Challenge, called gateway, reads data from the ping DPM via PTI (PT-VME64)[5] while the DC2 writes to the pong DPM. When all the data from the ping DPM are read, gateway allows the DC2 to write to the ping DPM and turns to read out the pong DPM. Both the DC2 and gateway poll to see if the other has finished using a DPM. The communication between the DC2 and gateway is done using the 8 MB DPM as a mailbox. Neither the DC2 nor gateway interrupt a data transfer while polling.

Gateway writes the two DC2 sets of data, which comprise N events, to two buffers in a reserved part of the memory of the Challenge-L, which has been designated as

[4]Micro Memory, Inc - 9540 Vassar Ave. - Chatsworth, CA 91311 - USA
[5]Performance Technologies - http://www.pt.com

memory to be shared among processes. When finished writing a buffer, gateway releases it to a filter queue before writing the other buffer in the shared memory. An online filter process runs on each CPU of the Challenge-L. Each filter queues for a gateway buffer. When one is available, an online filter processes the N events. First, the events are built taking data from both of the two DC2 data sets. Then, synchronization numbers of the DPMs and the DYCs are checked and the data integrity is verified for 0.1% of the events processed. Finally, an event header is added which includes a unique event number, date and time of processing and pointers to each DYC header word for later use by the offline. Some basic event trigger classification and online analysis bit flags are included.

The trigger information is decoded to classify the event. Such a classification determines which online filter analyses to perform, if any, and which logging stream the event, if not rejected, is sent to.

The following online analyses are performed: a simplified CCAL determination of energies and angles for electromagnetic showers and formation of invariant mass pairs to identify π^0, η and $\bar{c}c$ candidates; simple charged track reconstruction with electron identification and association with CCAL energy deposits for identifying events that fit exclusive e^+e^- final state or $J/\psi + X \to e^+e^- + X$ decay; and identification of four tracks in the charged detectors which loosely comply with the kinematics of $\bar{p}p \to \Phi\Phi \to 4K^{\pm}$.

The online filters set analysis bit flags in the event header word and write summary event information which is added to the end of the event. The analysis bit flags are compared to a list of trigger masks to determine acceptance or rejection of the event.

Accepted events are copied to logging buffers reserved in the shared memory for eventual recording to tape and transfer to the monitor-display computer. There are three logging streams; which stream an event is written to is based upon the event trigger classification and analysis bit flags. Events for which the filter determines a large invariant mass and those to be used for calibration purpose are written to other logging buffers. When the logging buffers are full, they are released to the appropriate logging queues and to the monitor-display computer. There are ten logging processes, each one with its own queue and tape drive. Every logging process receives buffers from all of the filter processes. Generally, five tape drivers record data in parallel to 8-mm EXABYTE tapes with a 5.0 GByte capacity, while the other five drivers are ready for a quick start as soon as one of the tapes in the first five drivers becomes full. The switching of the tape drivers signifies the end of a run of data taking and the beginning of a new one. Two of the five simultaneously running tape drivers are dedicated to neutral events, hence every run generates two neutral tapes. Other two of the five are dedicated to charged events, and one to efficiency study events.

For a characteristic instantaneous luminosity of $2.5 \times 10^{31}\ cm^{-2}s^{-1}$, the trigger rate is ~4 KHz. The typical event size from the readout electronics is ~1.2 KBytes. Therefore, the two daisy chains and gateway typically transfer ~4.8 MBytes/s to the set of online filters. The filters reduce the output event rate to ~1.2 KHz, which corresponds to writing ~1.4 MBytes/s to the logging streams. Each tape drive is capable of 1000 KBytes/s; the tape drives typically record data at a rate of 350, 300 and 250 KBytes/s for the neutral, charged and efficiency study events, respectively. The resulting lifetime of the data acquisition as a whole is typically 93%, at the above instantaneous luminosity. The inefficiency comes from inhibiting the triggers during the ADC conversion time and data transfer to the DYC modules.

Chapter 3

The Analysis of the $\pi^0\pi^0$ Channel

The first section of this chapter presents an overview of the kinematic features of the $p\bar{p} \to \pi^0\pi^0 \to \gamma\gamma\,\gamma\gamma$ reaction. Then, the analyzed E835-2000 data sample is described, the performed analysis discussed in detail, and the measured cross section presented. Finally, the cross section is fitted with the theoretical angular distribution and the resonance parameters are extracted.

3.1 Kinematics of the Reaction

An example of the reaction $p\bar{p} \to \pi^0\pi^0 \to \gamma\gamma\,\gamma\gamma$ is sketched, in the center of mass frame, in Figure 3.1.

Throughout this chapter, the definitions and notations below are used.

- an asterisk is added to a quantity expressed in the c.m. frame[1];
- a π^0 may be referred to as forward (π^0_{fw}) or backward (π^0_{bw}) according to its direction, in the c.m. frame, with respect to the $\bar{p}$ direction;
- θ^* is the angle, in the c.m. frame, between the π^0 and the $\bar{p}$ beam axis;
- E_{π^0}, $\vec{p}_{\pi^0}$ and p_{π^0} are the energy, momentum vector and its magnitude of a π^0 in the laboratory frame;

[1]Unless otherwise labelled, quantities are defined in the laboratory frame.

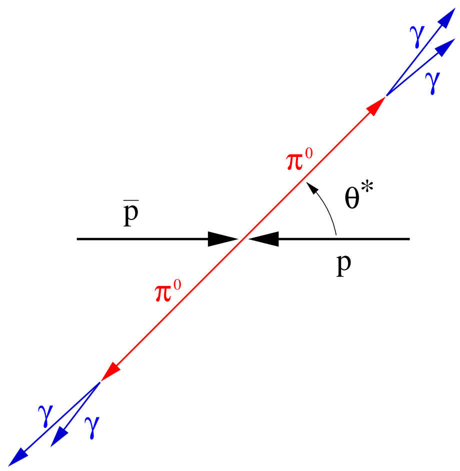

Figure 3.1: The $p\bar{p} \to \pi^0\pi^0 \to \gamma\gamma\,\gamma\gamma$ in the center of mass frame. Vectors represent the particles' momenta. The mean decay length of the π^0 in the C.M. frame is $\sim 300\ \mu$m.

- E_γ, $\vec{p}_\gamma$ and p_γ: as above but for a photon;
- $m_{\gamma\gamma} \equiv \sqrt{(E_{\gamma_1}, \vec{p}_{\gamma_1}) \cdot (E_{\gamma_2}, \vec{p}_{\gamma_2})}$ is the invariant mass between the two photons of a π^0 decay; $m^{fw}_{\gamma\gamma}$ and $m^{bw}_{\gamma\gamma}$ indicates the forward and backward $m_{\gamma\gamma}$, respectively;
- α is the opening angle between the two photons of a π^0 decay;
- $\vec{\beta}_{\pi^0} = (\vec{p}_{\pi^0}\, c)/E_{\pi^0}$, $\beta_{\pi^0} = |\vec{\beta}_{\pi^0}|$, and $\gamma_{\pi^0} = E_{\pi^0}/(m_{\pi^0}\, c^2)$ are the beta vector, its magnitude, and the gamma factor of a π^0 in the laboratory frame;
- $\vec{\beta}_{cm} \equiv (\vec{p}_{\bar{p}}\, c)/E_{cm}$ is the beta vector of the c.m. frame seen from the laboratory frame ($\vec{p}_{\bar{p}}$ is the antiproton momentum), $\beta_{cm} \equiv |\vec{\beta}_{cm}|$;
- $\gamma_{cm} \equiv E_{lab}/E_{cm}$ is the gamma factor of the c.m. frame seen from the laboratory frame.

In addition, it is convenient to define the angular variable

$$z \equiv \cos\theta^* \ . \tag{3.1}$$

The high value, $(98.798 \pm 0.032)\%$, of its branching ratio into two photons makes the $\gamma\gamma$ a very effective channel to detect a π^0. Its short lifetime, $\tau_{\pi^0} = (8.4 \pm 0.6) \times 10^{-17}$ s , makes the decay of the π^0 almost point-like. In the center of mass frame the mean decay length is ~ 0.3 μm and even in the laboratory frame, with favorable boost, it does not exceed 1 μm.

The opening angle, α, of the two photons from an in-flight π^0 decay, which is isotropic in the π^0 rest frame, has a probability distribution, $P(\alpha)$, given by

$$P(\alpha) = N \times \frac{\sin\alpha}{\sin^3\left(\frac{\alpha}{2}\right)} \times \frac{1}{\sin^2\left(\frac{\alpha}{2}\right) - \sin^2\left(\frac{\alpha_{min}}{2}\right)} , \tag{3.2}$$

where N is the normalization constant. The minimum opening angle,

$$\alpha_{min} = 2 \ \arcsin \frac{1}{\gamma_{\pi^0}} , \tag{3.3}$$

is reached when the π^0 decays symmetrically, that is when the two photons share the available energy equally.

To develop a feeling for the magnitude of the kinematic quantities involved, it is convenient to focus on the case where $\theta^* = 90°$ $(z = 0)$, that is the two π^0's share equally the energy and point toward the very central region (in polar angle) of the central calorimeter. At the χ_{c0} resonance, the energy of each π^0 is $E_{\pi^0}(z = 0) = E_{lab}/2 = 3.108$ GeV, determining a $\gamma_{\pi^0}(z = 0) = 23.03$. The corresponding minimum angle between the photons is $\alpha_{min}(z = 0) = 0.087$ rad $\simeq 5°$.

With this small value for α_{min} in mind, the plot in Figure 3.2 indicates that for the great majority of the π^0 decays the two photon's trajectories diverge slightly from each other. That makes it virtually impossible to incorrectly pair the four photons to form the two π^0's; on the other hand, it often makes the electromagnetic showers of two photons overlap in CCAL[2].

The energy, E_γ, of each photon follows a probability distribution, $P(E_\gamma)$, which is uniform and limited between a minimum, $E_{\gamma,min} = \frac{1-\beta_{\pi^0}}{2} E_{\pi^0}$, and a maximum,

[2]The remedy to this inconvenience is described in the discussion of the shared and split clusters on page 57 and followings.

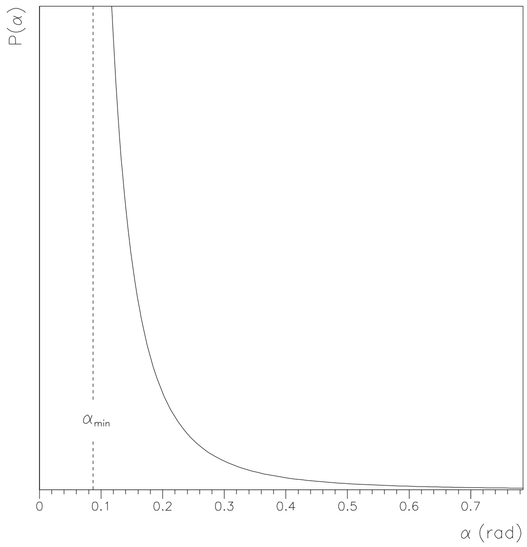

Figure 3.2: The probability distribution, $P(\alpha)$, of the opening angle, α, between the two photons of a in-flight π^0 decay. The indicated minimum opening angle, $\alpha_{min} = 0.087$ rad $\simeq 5°$, is relative to a π^0 emitted at $\theta^* = 90°$ in a $\bar{p}p \to \pi^0\pi^0$ reaction at the χ_{c0} energy.

$E_{\gamma,max} = \frac{1+\beta_{\pi^0}}{2} E_{\pi^0}$. The minimum is reached when the photon is emitted in the direction opposite to the π^0 direction, and the faster the π^0 is the slower the photon. In the $z = 0$ case, the minimum is $E_{\gamma,min} \simeq 1.5$ MeV while the maximum, $E_{\gamma,max} \simeq 3.1065$ GeV, almost coincides with the π^0 energy. Only a small fraction of photons, about 1.6% for a π^0 at $z = 0$, should in principle end up below the CCAL cluster threshold of 50 MeV (see page 56).

Table 3.1 completes the discussion with the values of the above kinematic variable at the borders of the acceptance of CCAL (which covers, at the E_{cm} of interest, from $z_{\pi^0} \simeq -0.6$ and $z_{\pi^0} \simeq +0.6$).

z_{π^0}	E_{π^0} (GeV)	γ_{π^0}	α_{min} (rad)	$E_{\gamma,min}$ (MeV)	$E_{\gamma,max}$ (GeV)	photons below threshold
-0.6	1.249	9.3	0.22	3.7	1.2454	3.7%
0	3.108	23.0	0.087	1.4	3.1065	1.6%
+0.6	4.966	36.8	0.054	0.9	4.9651	1.0%

Table 3.1: Values of the kinematic variables of the process $\bar{p}p \to \pi^0\pi^0$ and subsequent decays $\pi^0 \to \gamma\gamma$, for three possible directions of the π^0's: toward the backward boundary ($z_{\pi^0} \simeq -0.6$), the central part ($z_{\pi^0} \simeq 0$), and the forward boundary ($z_{\pi^0} \simeq +0.6$) of CCAL. The energy of the π^0 is given by $E_{\pi^0} = \gamma_{cm}(E^*_{\pi^0} + \vec{\beta}_{cm} \cdot \vec{p}^{\,*}_{\pi^0})$. See text for the formulas of the other variables. The last column indicates the percentage of photons, $(50 \text{ MeV} - E_{\gamma,min})/(E_{\gamma,max} - E_{\gamma,min})$, with energy below the 50-MeV CCAL cluster threshold.

3.2 The Data Sample

From January through November 2000, E835 collected a total amount of 113 pb^{-1} of Integrated Luminosity at Charmonium energies. Out of that amount, 32.8 pb^{-1} were taken at the χ_{c0} and are shared in 17 energy points ranging from $E_{cm} = 3340$ MeV to $E_{cm} = 3370$ MeV. Eight of these were collected between April the 7th and May the 2nd, six between June the 18 and July the 6th, one on August the 3rd, and the remaining two on August the 19th and 20th.

Each energy point, called stack, is made of of several runs[3] (from a minimum of 4 to a maximum of 15 runs), which are analyzed as a whole to extract the number of events of the reaction under study. Table 3.2 lists the energies of the 17 points and other relevant quantities. The spread of the E_{cm} distribution[4], discussed at page 42 and named $\sigma_{E_{cm}}$, is negligible compared to the total width of the χ_{c0} , which is 9.8 MeV (see Section 3.12). The luminosity, $\mathcal{L}$, of an energy point is the sum of the luminosities of the runs that constitute it. The mean instantaneous luminosity, $\langle d\mathcal{L}/dt\rangle$, is determined as the average of the instantaneous luminosities of its runs

[3]See page 74 for the definition of a run.

[4]Not to be confused with the uncertainty on the measurement of E_{cm}, which is contained within 200 keV (see page 40).

weighted on their $\mathcal{L}$.

E_{cm} (MeV)	$\sigma_{E_{cm}}$ (keV)	$\mathcal{L}$ (nb^{-1})	$\langle d\mathcal{L}/dt \rangle$ ($10^{31}\mathrm{s}^{-1}\mathrm{cm}^{-2}$)	E_{lab} (MeV)
3339.5	599	629.4	2.791	5943.0
3365.0	459	1423.7	2.435	6034.1
3384.4	396	1521.6	2.506	6103.9
3384.8	497	3370.4	2.431	6105.3
3392.0	340	1431.1	2.572	6131.3
3400.1	346	1482.8	2.049	6160.6
3406.1	427	2680.5	2.404	6182.4
3409.1	339	1134.5	1.707	6193.3
3410.3	498	1596.6	2.446	6197.6
3413.8	627	1953.9	2.878	6210.4
3415.0	356	2352.1	2.300	6214.7
3415.9	522	2466.5	2.636	6218.0
3418.0	348	1215.4	1.815	6225.7
3422.1	413	2152.3	2.461	6240.6
3426.0	391	1800.1	2.488	6254.8
3430.1	482	1438.2	3.029	6269.8
3469.9	340	2512.6	2.141	6416.2

Table 3.2: The 17 energy points (stacks) collected at the χ_{c0} energy: the energy in the center of mass, E_{cm}; the spread of its distribution, $\sigma_{E_{cm}}$; the luminosity, $\mathcal{L}$; the average instantaneous luminosity, $\langle d\mathcal{L}/dt \rangle$; and the energy in the laboratory frame, E_{lab} .

From the entire χ_{c0}-energy data sample, 486,122 events pass the selection for $\bar{p}p \rightarrow \pi^0\pi^0 \rightarrow \gamma\gamma\,\gamma\gamma$ (of which only $\sim 2\%$ are background from other processes). Online, they were identified through the Neutral-PBG1 and Neutral-ETOT triggers and, after passing through the chain described in Section 2.3.7, recorded on tape. PBG1, the two body trigger, is by itself almost 100% efficient for these events, due to the small opening angle between the photons of the π^0 decays. The few events missed by PBG1 are often caught by ETOT. The trigger efficiency is calculated in Section 3.10.

3.3 The Neutral Data Summary Tapes

The events that were classified online as neutral, were recorded on tapes labelled accordingly. Almost 900 neutral tapes were produced by E835-2000, 280 of them for the χ_{c0} data sample. Two neutral tapes were produced in parallel for each run of data taking.

After the end of the E835-2000 data taking, the neutral tapes were processed and reduced to a more manageable number of Neutral Data Summary Tapes (NDSTs) [67, 68]. The events were also sorted according to the number of in-time or undetermined (i.o.u) clusters (see page 62) in CCAL[5], to further reduce the size of the sample for performing a specific analysis. For example, the $\pi^0\pi^0$ analysis is run only on the sample with 4 i.o.u. CCAL clusters.

The event selection performed during the NDST production aimed to a rejection of those events with poor four-momentum conservation, according to what is measured by CCAL.

The NDST cuts[6] are:

NDST Cut 1. 2-9 in-time or undetermined clusters in CCAL,

NDST Cut 2. $|P_z - P_{\bar{p}}| < 0.15 \times P_{\bar{p}}$,

NDST Cut 3. $\sqrt{P_x^2 + P_y^2} < 350\ MeV$,

where $\vec{P} = (P_x, P_y, P_z)$ is the sum of the measured momentum of the i.o.u clusters in CCAL and $P_{\bar{p}}$ is the antiproton momentum.

The NDST production has reduced the neutral event sample of about 40%. The efficiency of the NDST selection for events $\bar{p}p \to \pi^0\pi^0 \to \gamma\gamma\gamma\gamma$ is discussed in Section 3.10.

---

[5]A second set of NDST was produced with a sorting based on the sum of the number of i.o.u clusters in CCAL and FCAL, but it is not described here since the analyses of this dissertation are performed on the first set.

[6]A "cut" is the requirement that the events have to satisfy in order to pass the selection.

3.4 Selection of Four Photon Events

Before focusing on the specific reaction $\bar{p}p \to \pi^0\pi^0 \to \gamma\gamma\,\gamma\gamma$, a preselection is applied in order to individuate those events with the more general characteristics of the reaction $\bar{p}p \to \gamma\gamma\gamma\gamma$.

The NDST sample with four in-time or undetermined CCAL clusters is used. A four constraint fit (4C-fit) to the hypothesis $\bar{p}p \to \gamma\gamma\gamma\gamma$ is performed using SQUAW [69] and a preliminary cut is made requesting that the Confidence Level (C.L.) is greater than 10^{-5}.

Figure 3.3 shows the C.L. of the fit for the 2,272,476 events with C.L.> 10^{-5}, which are about 89% of the original NDST sample with four i.o.u CCAL clusters.

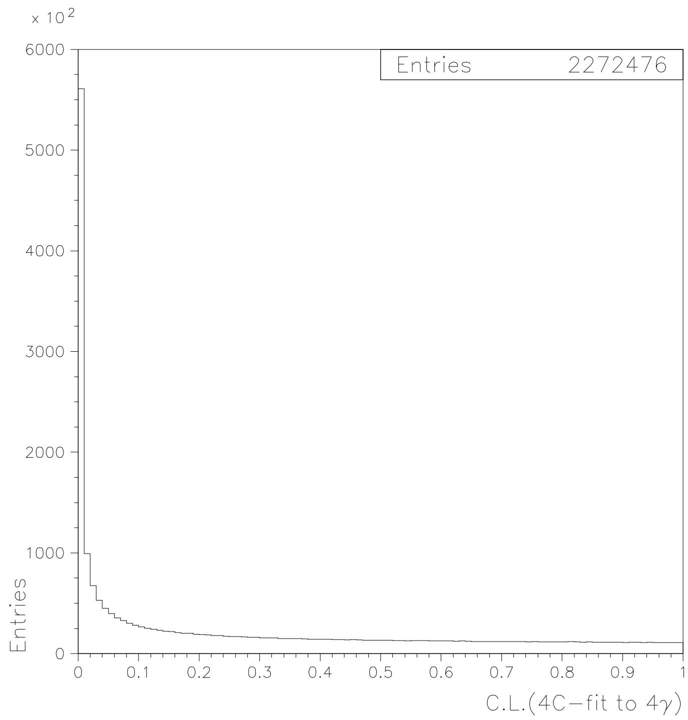

Figure 3.3: Confidence Level (C.L.) distribution of a 4C-fit to $\bar{p}p \to \gamma\gamma\gamma\gamma$.

At this point, the following selection is made:

Cut 1. 4 in-time clusters in CCAL,

Cut 2. the coordinate θ of each one of the four clusters has to be within CCAL rings 2 and 18 inclusive,

Cut 3. the energy of each one of the four clusters has to be greater than 100 MeV,

Cut 4. the Confidence Level (C.L.) of a four constraint fit (4C-fit) to the hypothesis $\bar{p}p \to \gamma\gamma\,\gamma\gamma$ has to be greater than 5%.

Cut 1 removes events where one or more of the four clusters are time-undetermined, because such clusters may be residual tails of a previous $p\bar{p}$ interaction. Cut 2, the fiducial volume cut, ensures that the electromagnetic showers are fully contained in the CCAL blocks and reduces the importance of ring 20, which cannot be calibrated with the $\pi^0\pi^0$ sample. Cut 3 rejects cluster for which the CCAL relative resolution is not optimal, see Equation 2.12. Finally, cut 4 tightens the requests on energy and momentum conservation imposed during the NDST production, with the purpose of reducing the probability that events from other reactions are misidentified as four photon events. The number of events surviving cuts 1 through 4 is 1,034,559.

With the goal of singling out those four-photon events that come from a two-body reaction, the photons are paired in the three possible ways (I will often refer to them as combinations) to form two invariant masses. The LEGO plot of the forward ($m_{\gamma\gamma}^{fw}$) versus the backward ($m_{\gamma\gamma}^{bw}$) invariant masses is shown in figure 3.4 in the region $m_{\gamma\gamma}^{fw}, m_{\gamma\gamma}^{bw} < 1.2$ GeV. A negligible number of events has more than one combination falling in the region of the $\pi^0\pi^0$, $\pi^0\eta$ and $\eta\eta$ peaks ($< 0.1\%$ of those events that populate the region of these peaks; see also Section 3.5).

Evident are the accumulation spots where both invariant masses have value $\simeq 135$ MeV, filled by $\pi^0\pi^0$ events, and $\simeq 550$ MeV, filled by $\eta\eta$ events. Events $\pi^0\eta$ fall on the locations where one $m_{\gamma\gamma}$ is $\simeq 135$ MeV and the other one is $\simeq 550$ MeV.

The two marked "berms" that stretch along the lines at forward- or backward-$m_{\gamma\gamma} \simeq 135$ MeV are produced by $\pi^0 X$ events, where X can be made by one or more particles that may partially escape detection. The two lighter berms due to ηX events are also clearly visible.

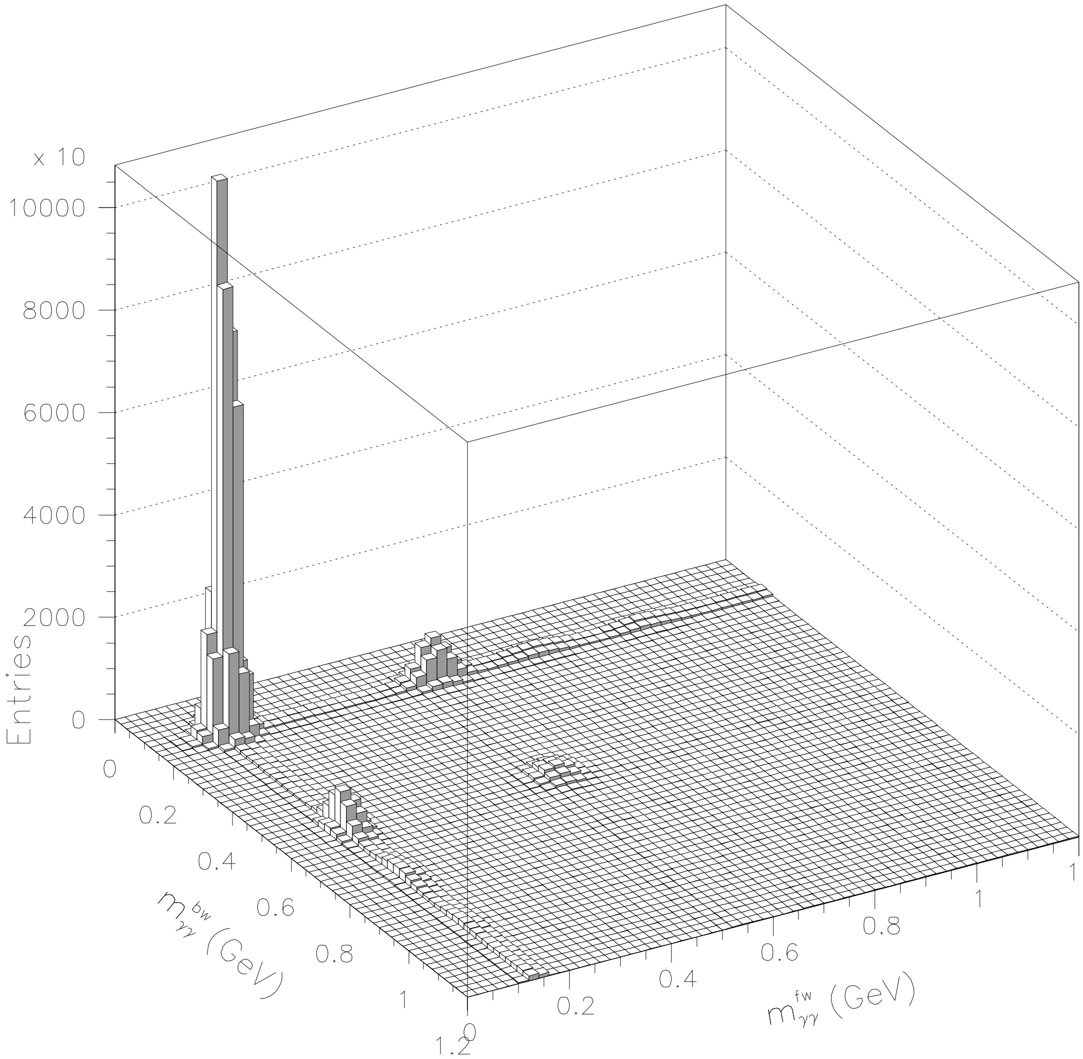

Figure 3.4: LEGO plot of the forward versus the backward invariant mass. Cuts 1 through 4 are applied. Although all three possible ways to pair the four photons are considered, a negligible number of events has more than one combination that falls within the region of the $\pi^0\pi^0$, $\pi^0\eta$ and $\eta\eta$ peaks. Events from all 17 energy points are merged in this plot.

The vertical $\pi^0 X$ berm is investigated in figure 3.5 by plotting $m_{\gamma\gamma}^{fw}$ after requesting that $m_{\gamma\gamma}^{bw}$ is within a π^0 mass window of [100-185] MeV. Even though the plot is

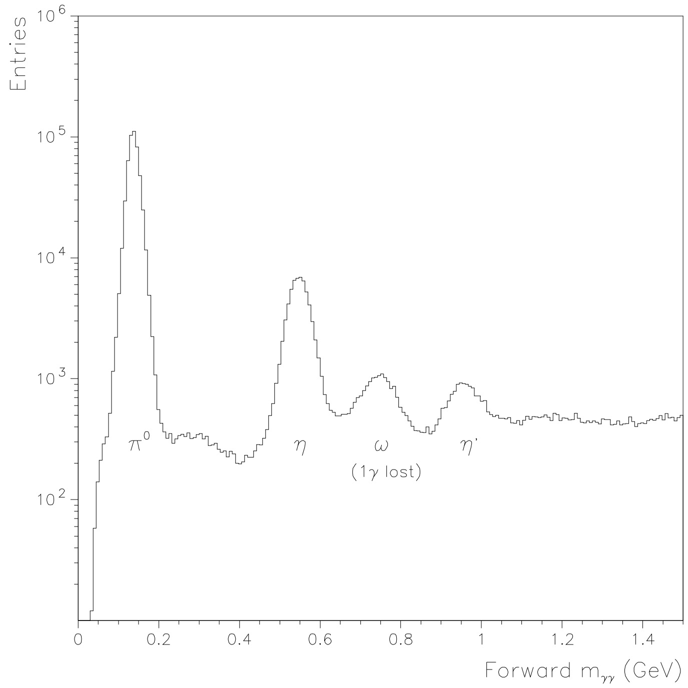

Figure 3.5: The forward $m_{\gamma\gamma}$ after requesting that the backward $m_{\gamma\gamma}$ falls within the π^0-mass window. Evident are the π^0, η, ω (one γ is lost), and η' peaks. All 17 energy points are merged in this plot.

made considering all three combinations of the four photons, the events contribute to it with only one combination, except 0.3% cases where a second combination place another $m_{\gamma\gamma}^{fw}$ at a value $\gtrsim$ 1 GeV.

A very pronounced peak at $m_{\gamma\gamma} \simeq 135$ MeV, standing out on top of a very small background, clearly indicates that the selection of an almost pure $\pi^0\pi^0$ sample is a fairly simple matter. The peak due to $\pi^0\eta$ events is also pronounced. The accumulation due to $\omega\pi^0$ events occurs through the ω decay in $\pi^0\gamma$ and subsequent π^0 decay in two photons; if the π^0 decays very asymmetrically, a quasi $\omega \to \gamma\gamma$ event appears in the plot. A peak due to $\pi^0\eta'$ events is also apparent.

As a reminder, our current knowledge of the main attributes of the particles involved is shown in Table 3.3. The relevant branching ratios are also reported, even if those are not the only factors determining the relative peak heights.

Particle	$I^G(J^{PC})$	Mass (MeV/c^2)	Full Width	Branching Ratios (%)
π^0	$1^-(0^{-+})$	134.9766±0.0006	(7.86±0.56) eV/c^2	$B(\gamma\gamma)$=98.798±0.032
η	$0^+(0^{-+})$	547.30±0.12	(1.18±0.11) keV/c^2	$B(\gamma\gamma)$=39.33±0.25
ω	$0^-(1^{--})$	782.57±0.12	(8.44±0.09) MeV/c^2	$B(\pi^0\gamma)$=8.5±0.5
η'	$0^+(0^{-+})$	957.78±0.14	(202±16 keV/c^2	$B(\gamma\gamma)$=2.12±0.14

Table 3.3: Attributes of the particles involved in the analyses. For each of them, the most relevant branching ratio is reported [39].

3.5 The $\pi^0\pi^0$ Event Topology

In order to determine which are the photons that are daughter of the same π^0, a six constraint fit (6C-fit) to the hypothesis $\bar{p}p \to \pi^0\pi^0 \to \gamma\gamma\gamma\gamma$ (simply referred to as the $\pi^0\pi^0$ fit) is performed on each one of the three ways (combinations) to pair them. The combination with the highest C.L. is chosen as the event topology[7].

The two scatter plots in Figure 3.6 indicate that only one combination, if any, is a credible candidate for the hypothesis. In fact, no events in the entire χ_{c0}-energy sample have more than one combination that satisfies Cuts 1 through 4 and the features of the $\pi^0\pi^0$ kinematics (Cuts 5 through 8 in next Section 3.6).

Notice that no events are rejected upon the C.L. of the $\pi^0\pi^0$ fit in order not to invalidate the estimate of the background performed in Section 3.9.

[7]For those events in which the fit is unsuccessful for all three combinations, a nominal topology is still defined by choosing the combination with lowest $\Delta m \equiv \sqrt{(m^{fw}_{\gamma\gamma} - m_{\pi^0})^2 + (m^{bw}_{\gamma\gamma} - m_{\pi^0})^2}$.

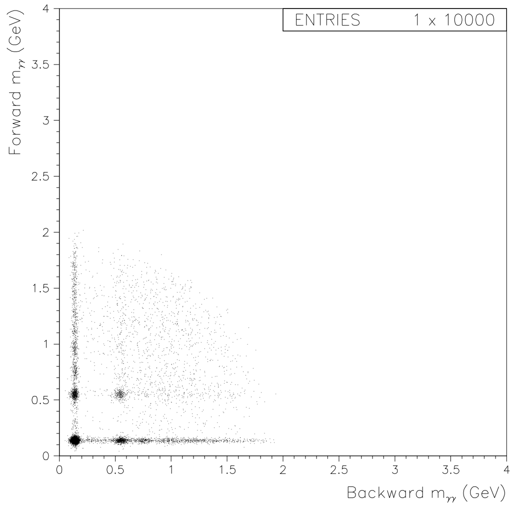

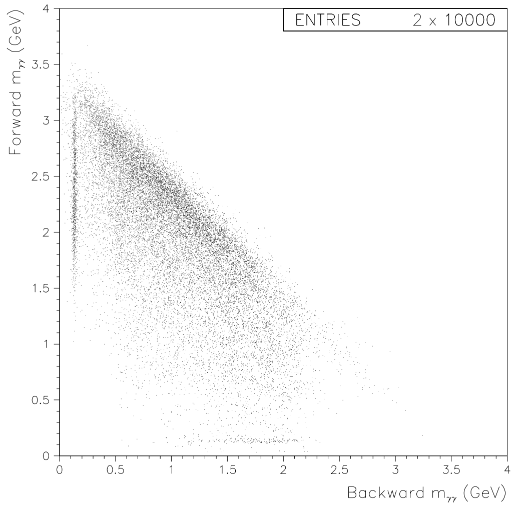

Figure 3.6: As in Figure 3.4 with the difference that the entry for the combination with the highest C.L. of a 6C-fit to $\bar{p}p \to \pi^0\pi^0 \to \gamma\gamma\,\gamma\gamma$ is plotted separately (left plot) from the other two entries (right plot). To avoid saturation in the accumulation spots, only 10,000 of the 1,034,559 events are plotted.

3.6 Selection of $\pi^0\pi^0$ Events

Once the $\pi^0\pi^0$ event topology is determined as the combination with the highest C.L. of the $\pi^0\pi^0$ fit, the following cuts are applied to that combination in order to select those events with the characteristics of the $\pi^0\pi^0$ reaction:

Cut 5. 100 MeV$< m_{\gamma\gamma}^{fw} <$ 185 MeV ,

Cut 6. 100 MeV$< m_{\gamma\gamma}^{bw} <$ 185 MeV ,

Cut 7. Akinematics $(\Delta\theta) <$ 12 mrad ,

Cut 8. Acoplanarity $(\Delta\phi) <$ 30 mrad ,

Cut 9. No invariant masses for which $|m_{\gamma\gamma} - m_{\pi^0}| <$ 45 MeV in the two combinations not chosen as the event topology ,

Cut 10. No successful fit (C.L.$< 10^{-5}$) to $\pi^0\eta \to \gamma\gamma\gamma\gamma$ or $\eta\eta \to \gamma\gamma\gamma\gamma$ in any of the 3 combinations.

According to cuts 5 and 6 an event is accepted if the two invariant masses fall within a $\sim 2.5\,\sigma$ range about the π^0 mass[8]. This is a rather "loose" requirement, allowed by the fact that the background in the vicinity of the π^0 peak is very little[9]. Hence, an enlargement of the selection acceptance, which improves its efficiency, does not deteriorate the cleanness of the sample. The slight asymmetry of the invariant mass cuts (a 10 MeV larger acceptance on the high-mass side of the π^0 mass) compensates for the slightly larger value of the reconstructed invariant mass for split clusters[10]. The split clusters are described on page 57; the slight overestimation of their $m_{\gamma\gamma}$ is well reproduced by the Monte Carlo simulation for determining the selection efficiency, as shown in the invariant mass plots in Figure 3.7.

Cuts 7 and 8 require that the 2-body kinematics of a $\pi^0\pi^0$ reaction are respected. The variable named "akinematics" is defined as

$$\Delta\theta \equiv \theta^{fw}_{\pi^0,meas} - \theta^{fw}_{\pi^0,calc}\,, \tag{3.4}$$

where $\theta^{fw}_{\pi^0,meas}$ is the measured azimuthal angle of the forward π^0, while $\theta^{fw}_{\pi^0,calc}$ is the value of the same quantity calculated by assuming $\pi^0\pi^0$ kinematics and using the measured azimuthal angle of the backward π^0. The "acoplanarity" is defined as π minus the difference between the measured polar angles of the two π^0's:

$$\Delta\phi \equiv \pi - (\phi^{fw}_{\pi^0,meas} - \theta^{bw}_{\pi^0,meas})\,. \tag{3.5}$$

Since the most copious background channels have at least a π^0 produced, cut 9 ensures that no π^0's are found in the combination that is not chosen as the event

[8] The root mean square (r.m.s.) of the π^0 peak is about 15 MeV, with a small variation as a function of z.

[9] As it is already apparent from, for instance, figure 3.5.

[10] As an alternative, one might have simply used symmetric cuts and, in addition, accepted the cluster pairs that are flagged as split clusters, since it is established that they are produced by symmetric $\pi^0 \to \gamma\gamma$ decays. However, this choice is not made since it would have posed an additional complication when performing the background subtraction described in section 3.9.

topology. Cut 10 might be, at this point, redundant but it is easily applied since the fits to the $\pi^0\eta$ and $\eta\eta$ hypotheses are performed to pursue those analyses and hence are available. Cut 9 and 10 have little effect once all the previous cuts are applied. The number of events surviving the full $\pi^0\pi^0$ selection (cuts 1 through 10) is 486,122 .

Figures 3.7 and 3.8 show the variables involved in the most relevant cuts for data and MC simulation at one, $E_{cm} = 3415$ MeV, of the 17 energy point. The arrows indicates the boundaries of acceptance of the cuts. Each variable is shown after applying all cuts with the exception of the cut involving the variable itself.

Figure 3.9 shows the C.L. of the 6-C fit to $\bar{p}p \rightarrow \pi^0\pi^0 \rightarrow \gamma\gamma\gamma\gamma$ for those events that have passed the selection. This C.L. is used to determine the event topology only, as described in section 3.5; no cuts are applied on this variable, so that the instrumental background can be estimated and subtracted using the technique described in section 3.9.

Figure 3.10 shows the region of the $\pi^0\pi^0$ peak in the invariant mass scatter plot after all cuts are applied except the ones on the invariant masses.

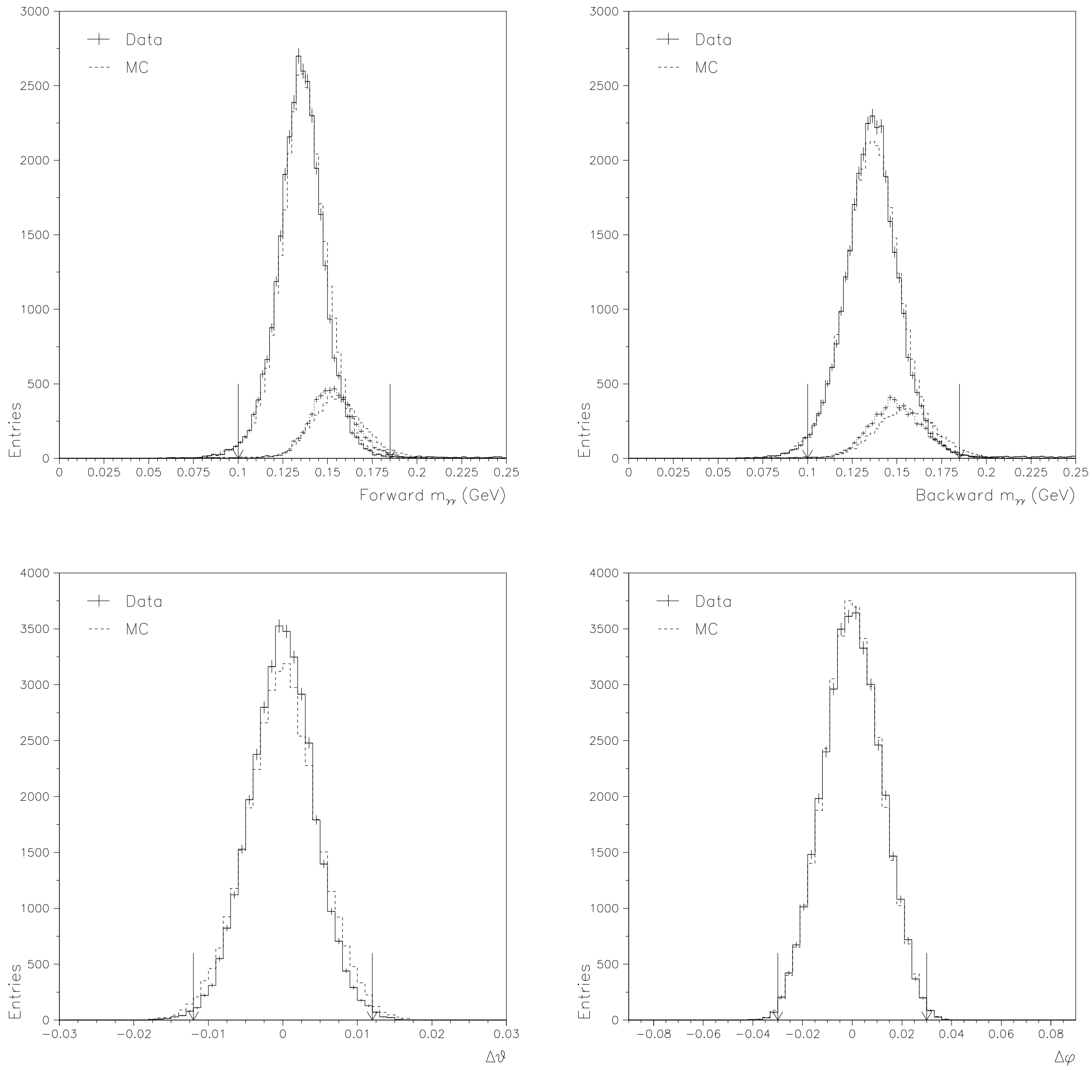

Figure 3.7: Variables involved in the $\pi^0\pi^0$ selection. Arrows indicate where the cuts are applied. Each variable is plotted after applying all of the other cuts. $E_{cm} = 3415$ MeV. Top left: the forward invariant mass (Cut 5), where the smaller peak is made by the split clusters (for which the CCAL clusterizer slightly overestimate the invariant mass); top right: the backward invariant mass (Cut 6); bottom left: the akinematics (Cut 7); bottom right: the acoplanarity (Cut 8).

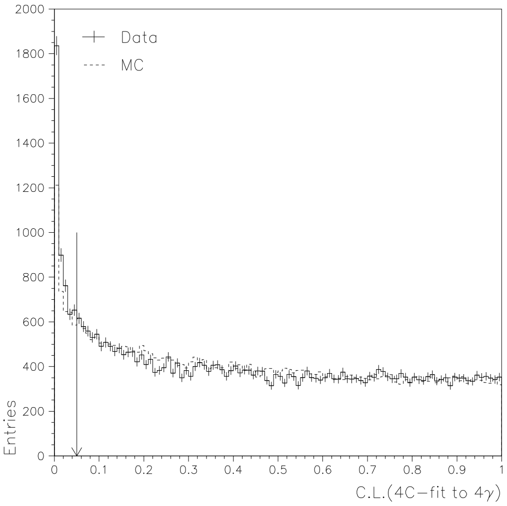

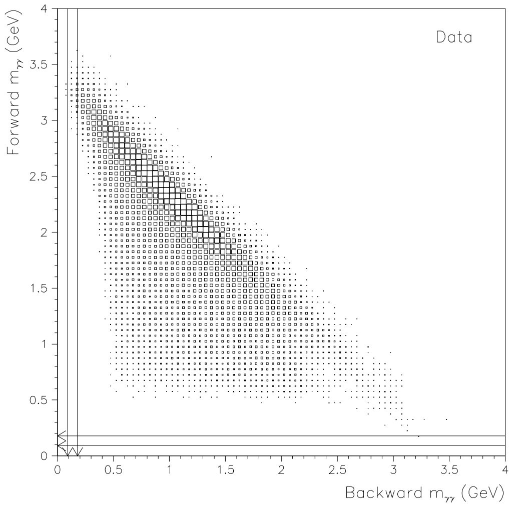

Figure 3.8: Variables involved in the $\pi^0\pi^0$ selection. Arrows indicate where the cuts are applied. Each variable is plotted after applying all of the other cuts. $E_{cm} = 3415$ MeV. Left: Confidence Level of the 4C-fit to $\bar{p}p \to \gamma\gamma\,\gamma\gamma$ (Cut 4); right: scatter plot of the invariant masses of the two combinations not chosen as the event topology (Cut 9).

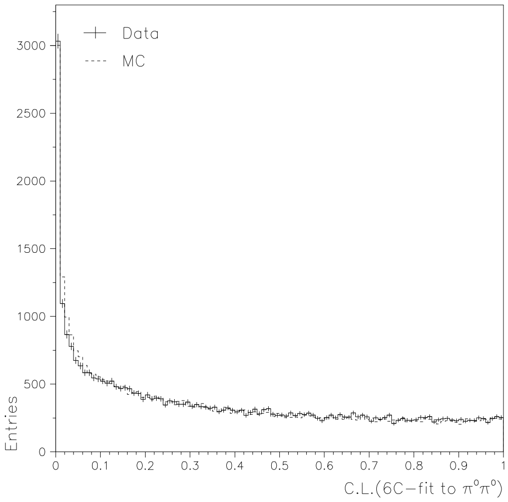

Figure 3.9: Confidence Level of the 6C-fit to $\bar{p}p \to \pi^0\pi^0 \to \gamma\gamma\,\gamma\gamma$; no cuts are applied to this variable. $E_{cm} = 3415$ MeV.

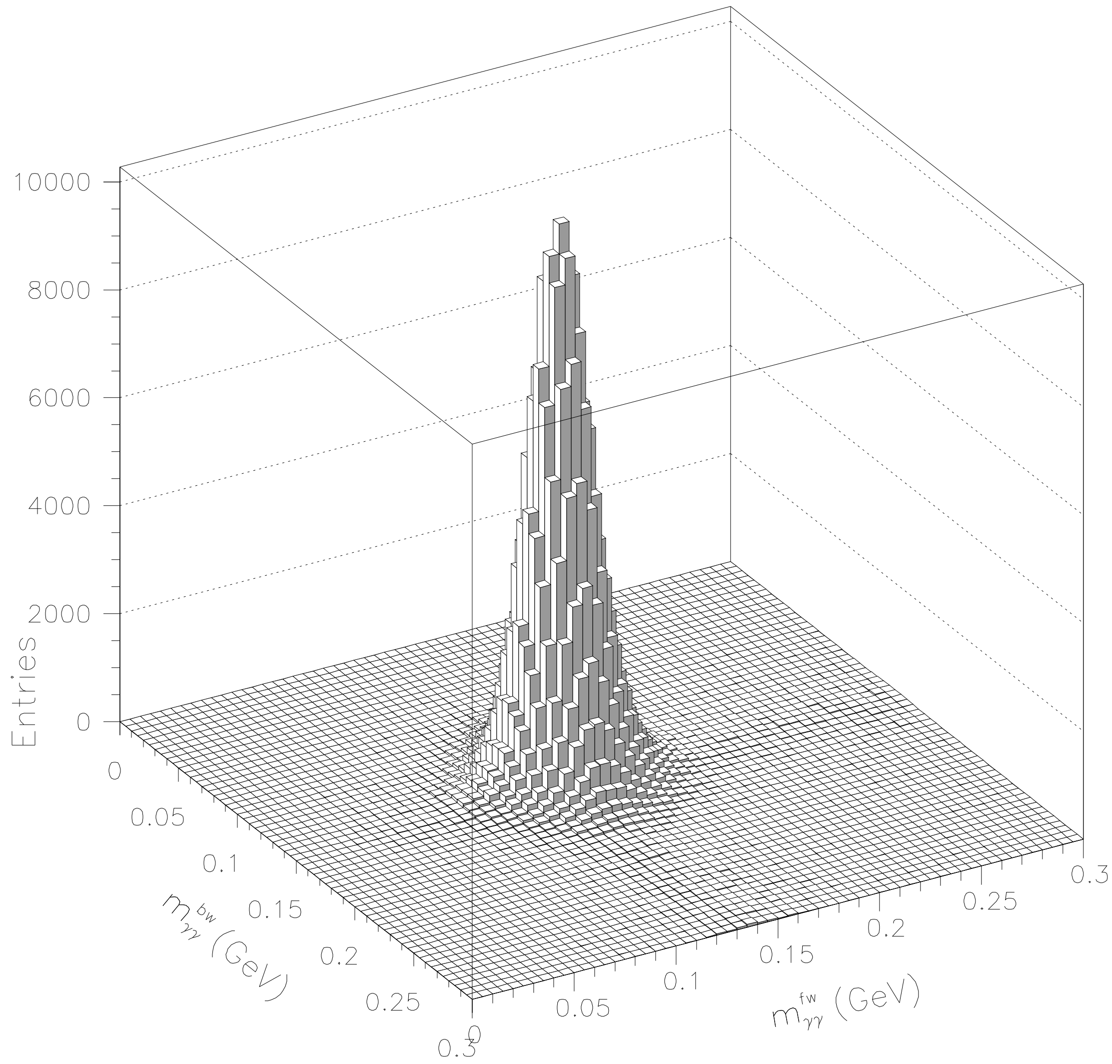

Figure 3.10: The region of the $\pi^0\pi^0$ peak in the LEGO plot of the forward versus the backward invariant masses for the combination chosen as the event topology; all $\pi^0\pi^0$ cuts are applied except the ones on the invariant masses themselves (Cuts 5 and 6). The events from all 17 energy points are merged in this plot.

3.7 Detector Acceptance and Selection Efficiency

The efficiency of the selection is determined simultaneously to the detector acceptance by generating and reconstructing Monte Carlo events $\bar{p}p \to \pi^0\pi^0 \to \gamma\gamma\,\gamma\gamma$. The MC reproductions of the real data distributions are shown in figures 3.7, 3.8 and 3.9.

Since it is necessary to know the selection efficiency as a function of $z \equiv |\cos\theta^*|$ to later determine the $\pi^0\pi^0$ differential cross section, the full z range $[0,1]$ is segmented in 40 bins of value $\Delta z = 0.025$. Events are generated isotropically. The product of the acceptance and efficiency, $a \times \epsilon$, of a certain bin of z is determined as the number of events passing the $\pi^0\pi^0$ selection and reconstructed in that bin divided by the number of events generated in that bin.

Figure 3.11 shows $a \times \epsilon$ for the several cuts as a function of the bins in z.

Correction for the limited polar angle resolution. Events generated in a certain bin of z may be reconstructed (or migrate) in a different bin because of the limited detector resolution. Since here MC events are generated isotropically, while the so-far-unknown angular distribution of the real data is not isotropic, the event migration takes place in different ways for the two cases. Appendix B describes how such an effect is estimated and how $a \times \epsilon$ can be determined by using a migration-corrected estimate of the angular distribution. However, in the case of the $\pi^0\pi^0$ channel the effect of the migration is very small for every bin (contained in a half a percent).

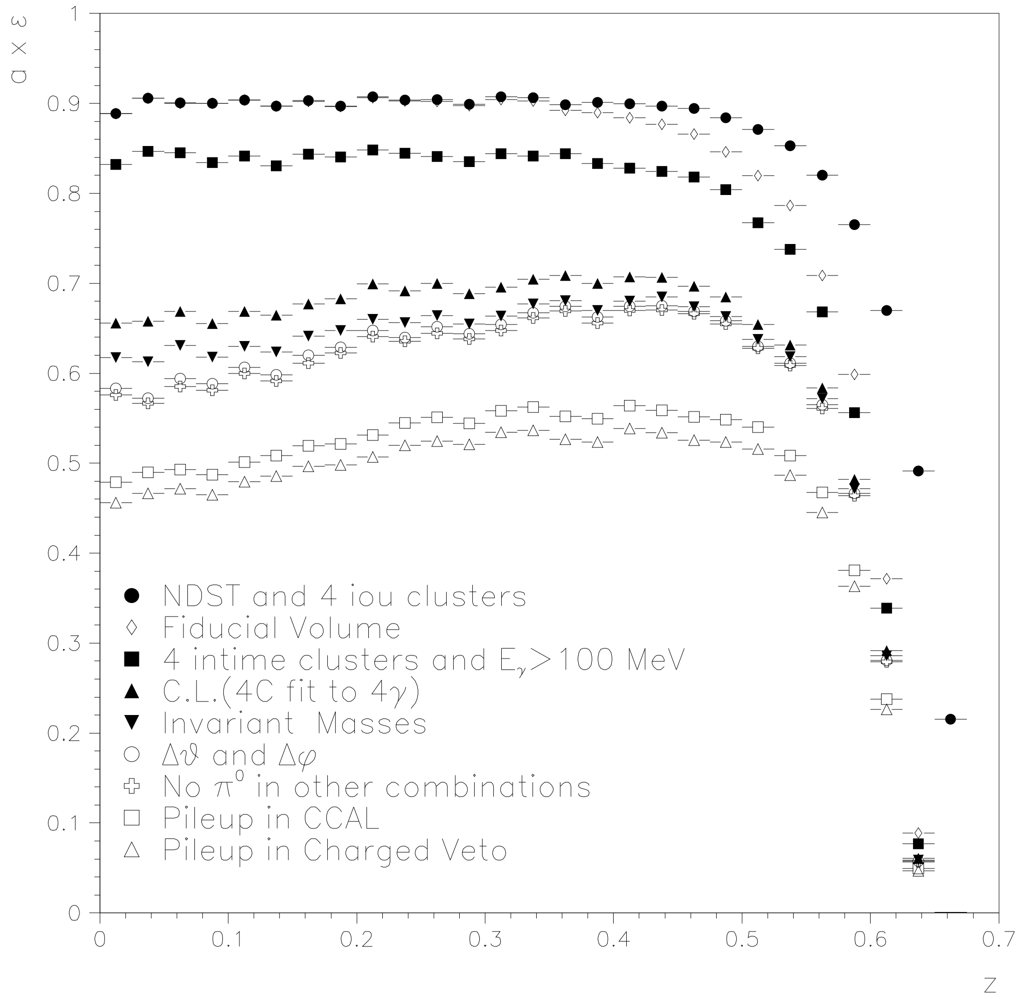

Figure 3.11: The product of the detector acceptance and selection efficiency, $a \times \epsilon$, for $\pi^0\pi^0$ events as a function of $z \equiv |\cos\theta^*|$ at $E_{cm} = 3415$ MeV. Here, the MC events are generated with a uniform angular distribution. Each cut shown, or group of cuts, is applied on top of the ones previously indicated. "NDST and 4 iou clusters" is the selection of the initial data sample: four in-time or undetermined clusters (iou) and the NDST cuts (page 81). "Fiducial volume": Cut 2 (page 82). "4 in-time clusters and $E_\gamma > 100$ MeV": Cut 1 and 3. "C.L.(4C fit to 4γ)": Cut 4. "Invariant Masses": Cut 5 and 6 (page 87). "$\Delta\theta$ and $\Delta\phi$": Cut 7 and 8. "No π^0 in other combinations": Cut 9. The two lower-most symbols represent the estimated fraction of $\pi^0\pi^0$ events surviving the contamination due to event pileup (see Section 3.8).

3.8 The Event Pileup

Because of the high instantaneous luminosity at which the experiment is run, one of the main sources of inefficiency is due to the pileup of different events. An event such as a $\pi^0\pi^0 \to \gamma\gamma\gamma\gamma$ may be rejected because of two reasons, which may occur individually or together:

1. an almost simultaneous charged event fires the Charged Veto, causing the failure of the neutral trigger logics;

2. an almost simultaneous CCAL energy deposit, possibly due to the tails of the signals from an earlier event, contaminates the $\pi^0\pi^0$ event with additional i.o.u. CCAL clusters or disrupts the $\pi^0\pi^0$ kinematics.

The event pileup is particularly insidious because it varies substantially with the instantaneous luminosity, which, despite the efforts made to limit its fluctuations during the data taking, is considerably different from energy point to energy point (see Table 3.2). Thus, when performing an energy scan of a resonance, it is critically important to estimate precisely the amount of the pileup contamination and correct for it.

The method used works as follows.

1. During the data taking, a Random Gate (RG) trigger is run at a frequency of 10 Hz with priority on the physical triggers. The gate of the data acquisition is opened and the signals of all channels of CCAL, FCAL and Charged Veto are recorded to later use.

2. During the MC simulation for the determination of the detector acceptance times the selection efficiency ($a \times \epsilon$), a RG event is overlapped to every generated MC event. This is done before the CCAL clusterizer is run. More precisely, the MC content of each ADC and TDC channel of the detectors is summed to the RG content of the same channel; thus, reproducing the actual data taking conditions. After that, the clusterization and the event selection is performed on the composite MC+RG event to determine $a \times \epsilon$.

The histogram marked by the symbol "Pileup in CCAL" in Figure 3.11 is determined by using MC+RG events, considering only the CCAL content of the RG event. The histogram marked by "Pileup in Charged Veto" is determined by using MC+RG events, considering the CCAL as well as the Charged Veto content of the RG event.

Generally speaking, the higher the instantaneous luminosity during the data taking, the higher is the probability that a $\pi^0\pi^0$ event is contaminated because of the pileup. However, higher is also the number of RG events in which it is recorded an accidental that, when the MC simulation is run, contaminates the MC $\pi^0\pi^0$ events determining its rejection. Thus, the loss of events during the data taking is compensated by a decrease of the efficiency times acceptance.

It has been previously pointed out that different energy points have different instantaneous luminosities. Not only that, even the several runs within the same energy point are generally collected at different instantaneous luminosities. In Figure 3.12, for each one of the 134 runs of the 17 energy points, the probability that a $\pi^0\pi^0$ event survives to the pileup contamination is plotted versus the instantaneous luminosity of the run. Such a probability is given by $a \times \epsilon$ determined with MC+RG (including both CCAL and Charged Veto) divided by $a \times \epsilon$ determined with pure MC.

The overall acceptance times efficiency of each energy point is determined by averaging the Random Gate acceptance times efficiency of its runs, $(a \times \epsilon)_{run}$, weighting on their (integrated) luminosity $\mathcal{L}_{run}$:

$$a \times \epsilon = \frac{1}{\sum_{run} \mathcal{L}_{run}} \times \sum_{run} \mathcal{L}_{run} \times (a \times \epsilon)_{run} \ . \tag{3.6}$$

The uncertainty on $a \times \epsilon$ is

$$\sigma_{a\times\epsilon} = \frac{1}{\sum_{run} \mathcal{L}_{run}} \times \sqrt{\sum_{run} \left[\mathcal{L}_{run} \times \sigma_{(a\times\epsilon)_{run}}\right]^2} \ . \tag{3.7}$$

The so-determined acceptance times efficiency, after the very small correction applied to take into account the limited polar angle resolution (see page 93), is used to calculate the $\pi^0\pi^0$ cross section. It should be pointed out than the pileup

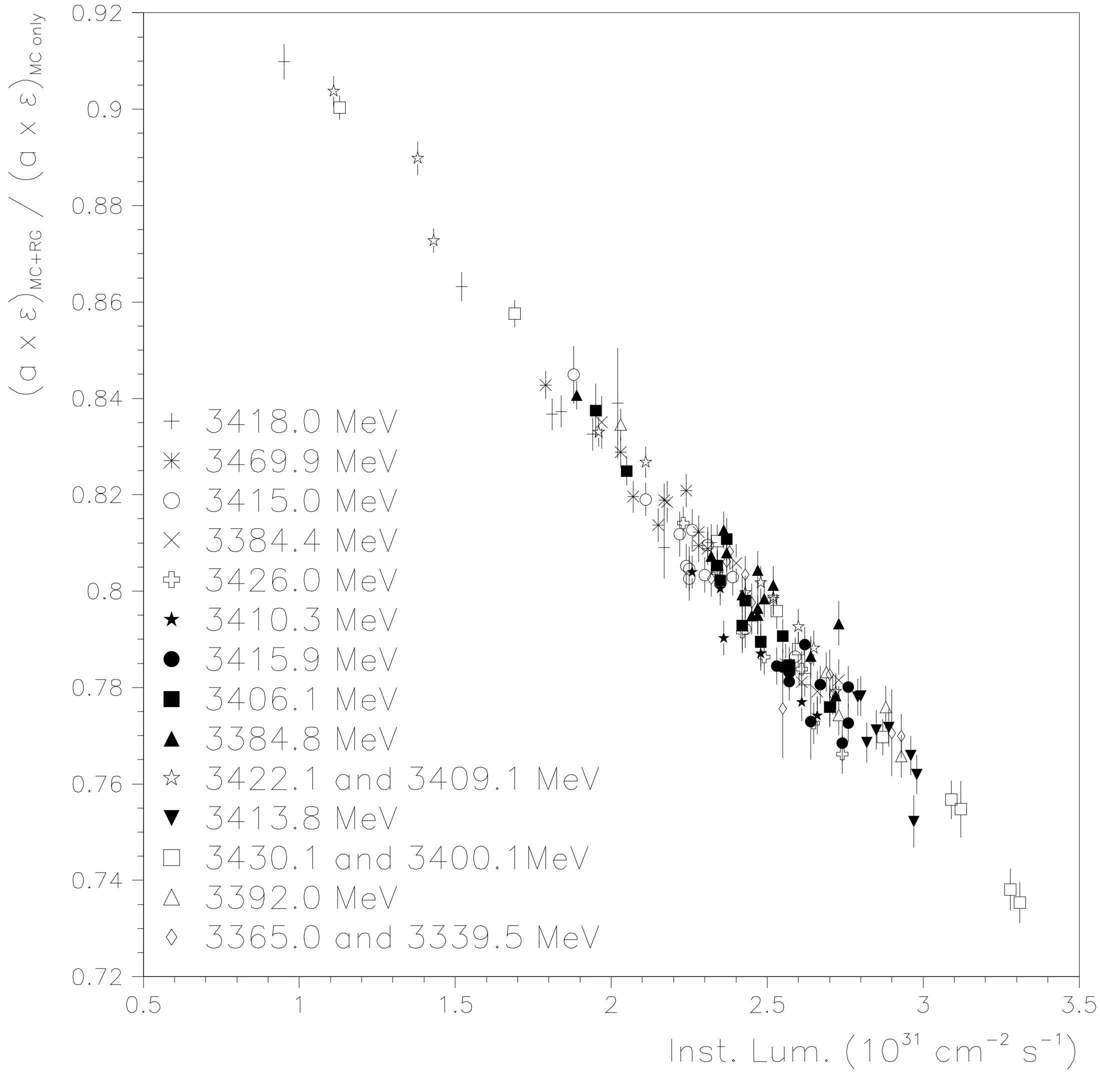

Figure 3.12: The probability that a $\pi^0\pi^0$ event survives to the pileup contamination versus the instantaneous luminosity, on a run by run basis. Different symbols are used for runs belonging to different stacks (a stack may include one or two energy points) and the "keys" are listed according to the chronological order of data collection. Vertical errors are determined by the size of the RG sample.

correction, even though it is determined on a bin (of z) by bin basis, does not show any dependence on z.

The impact of the pileup on the cross section is considerable. It affects the absolute scale and varies substantially from an energy point to another. The importance of the pileup correction is displayed in Figure 3.13 where the measured $\bar{p}p \to \pi^0\pi^0$ cross section[11] integrated from $z = 0$ to $z = 0.4$ is shown with and without correcting for the pileup contamination. The probability that a $\pi^0\pi^0$ event is lost due to the pileup is on average 80.3%, with fluctuations from energy point to energy point from 77.0% to 86.1% .

[11] The cross section is shown here a little bit prematurely. The next few sections and, in particular, Section 3.11 describes the remaining steps needed to calculate it.

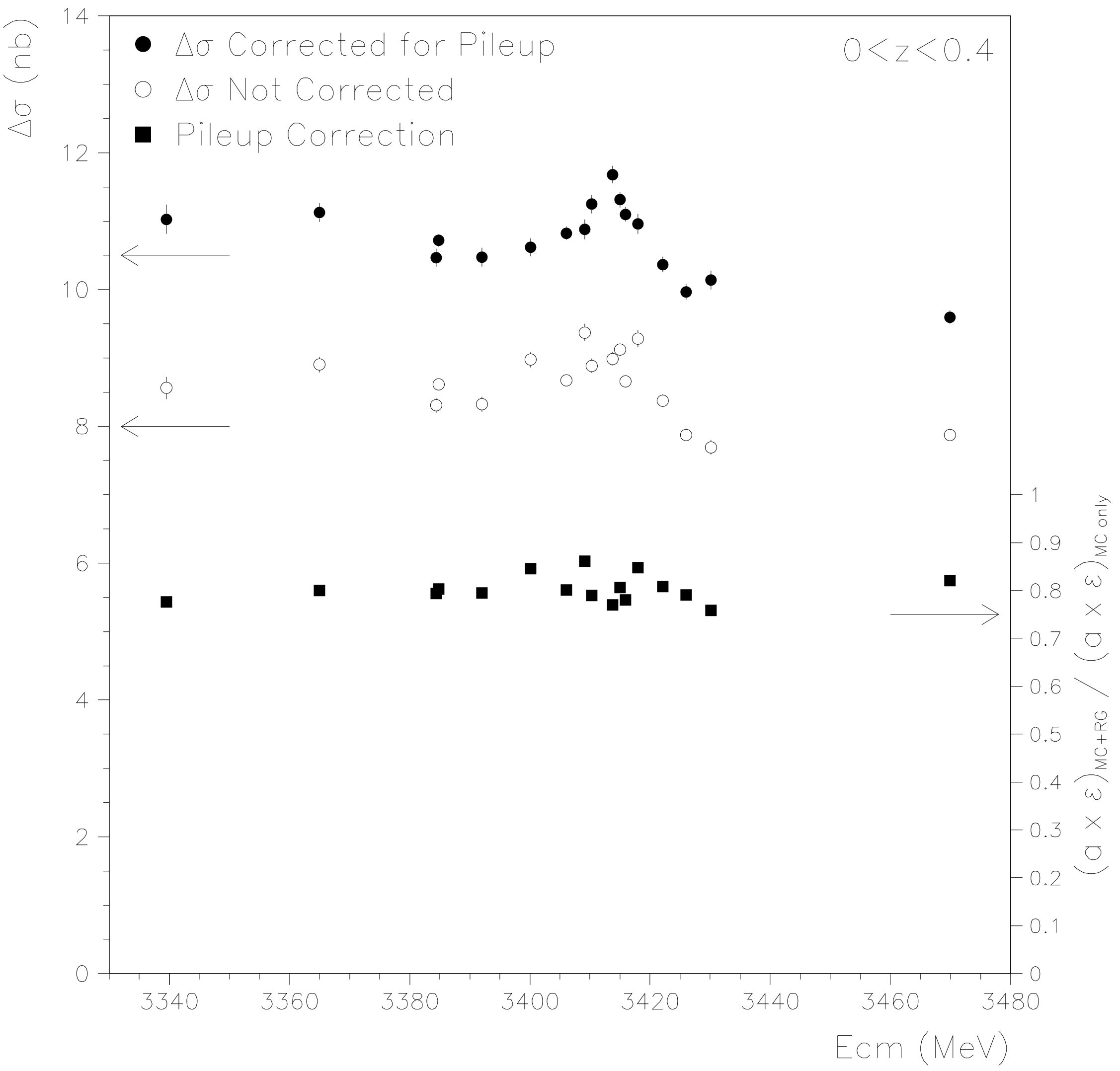

Figure 3.13: The importance of the pileup correction. The measured $\bar{p}p \to \pi^0\pi^0$ cross section (integrated from $z = 0$ to $z = 0.4$ and plotted versus E_{cm}) is shown before and after correcting for the pileup contamination. The probability that a $\pi^0\pi^0$ event is lost due to the pileup is shown with vertical axis on the right.

3.9 The Background

The amount of instrumental background, that is events produced by other processes that are misidentified as $\pi^0\pi^0$, can be inferred by observing the region around the $\pi^0\pi^0$ peak in the scatter plot of the two invariant masses in Figure 3.10.

The background takes the form of two berms, along the lines $m_{\gamma\gamma}^{fw} = m_{\pi^0}$ and $m_{\gamma\gamma}^{bw} = m_{\pi^0}$, and a less copious, more or less uniform substrate. Processes where no π^0's are formed contribute to the substrate, and do not have any accumulation or depletion under the $\pi^0\pi^0$ peak. Events from processes where a single π^0 is formed accumulate in the two berms. Single π^0 berms add up incoherently at their intersect, thus generating a background mound underlying the $\pi^0\pi^0$ peak. Processes where two or more π^0's are formed contribute to the berms and may also generated an accumulation at the berm intersect.

The level of background is determined independently for each bin in z. The scatter plot of the two invariant masses[12] is fitted to

$$f(m_{\gamma\gamma}^x, m_{\gamma\gamma}^y) = \underbrace{\frac{A}{\sigma^2}\, exp\Big[-\frac{(m_{\gamma\gamma}^x - m_{\pi^0})^2 + (m_{\gamma\gamma}^y - m_{\pi^0})^2}{2\sigma^2}\Big]}_{\pi^0\pi^0-signal} +$$
$$\underbrace{+\underbrace{B\left\{\frac{1}{\sigma}\, exp\Big[-\frac{(m_{\gamma\gamma}^x - m_{\pi^0})^2}{2\sigma^2}\Big] + \frac{1}{\sigma}\, exp\Big[-\frac{(m_{\gamma\gamma}^y - m_{\pi^0})^2}{2\sigma^2}\Big]\right\}}_{Berms} + \underbrace{C + D\,(m_{\gamma\gamma}^x + m_{\gamma\gamma}^y)}_{Plane}}_{background} \tag{3.8}$$

by minimizing a negative-log-likelihood where A, B, C, D and σ are free parameters. The area where the fit is performed is chosen as the one defined by 50 MeV< $m_{\gamma\gamma}^x$ <300 MeV and 50 MeV< $m_{\gamma\gamma}^y$ <300 MeV, so that the event-depleted area at low invariant masses is avoided or, at least, its importance in the fit very much reduced[13].

[12]The scatter plot is symmetrized by plotting $m_{\gamma\gamma}^{fw}$ alternatively on the x- and y-axis, where it takes the names $m_{\gamma\gamma}^x$ and $m_{\gamma\gamma}^y$, respectively.

[13]This depletion does not affect the region of the $\pi^0\pi^0$ peak, as the symmetry about m_{π^0} of the invariant mass distributions of the non-split clusters (see Figure 3.7) indicates. Such a

Figure 3.14 shows the entries in the scatter plot at $E_{cm} = 3415$ MeV, the function $f(m^x_{\gamma\gamma}, m^y_{\gamma\gamma})$ as resulted from the fit, and their magnified versions. In the magnified plot of the fit, the underlying contribution of the berms and the plane is also represented. The integral of the berms and the plane over the region selected by the invariant mass cuts (cuts 5 and 6 in section 3.6) is taken as an estimate of the background in the bin.

Table 3.4 reports the values of the fit parameters for the bins of the energy point $E_{cm} = 3415$ MeV, along with the associated background estimate and the total number of entries at the $\pi^0\pi^0$ peak.

To bind the overall background information, the background estimates of all bins of an energy point are then fitted with a six-degree polynomial as a function of z, as shown in Figure 3.15. The value of the resulting polynomial at the center of each bin is assumed to be the background of the bin and, then, subtracted from the $\pi^0\pi^0$ peak to obtain the bin content of $\pi^0\pi^0$ events. The uncertainty on the number of $\pi^0\pi^0$ events in the bin is conservatively taken as the square root of the entries in the peak before subtracting the background.

The procedure is then repeated for all energy points. On average, the background constitutes $2 - 2.5\%$ of the $\pi^0\pi^0$ peak for $z < 0.3$ and $1.5 - 2\%$ for $0.3 < z < 0.6$. Appendix C.5 provides a plot (Figure C.9) where the estimated background is shown versus the energy in the center of mass.

It has to be pointed out that the technique here described requires that the berms and, more generally, the region around the $\pi^0\pi^0$ peak in the invariant mass scatter plot are left intact by the event selection. In this way, the true amount of background underlying the $\pi^0\pi^0$ peak can be estimated without a bias. This is the reason why the C.L. of the 6C-fit to $\bar{p}p \to \pi^0\pi^0 \to \gamma\gamma\,\gamma\gamma$ is not used in the event selection, but only to determine the event topology.

---

symmetry has also been checked by means of a Gaussian fit. The depletion region, however, does prevent the usage of the elegant method employed in [65] for determining the background of the $\bar{p}p \to \omega\omega \to \pi^0\gamma\,\pi^0\gamma \to \gamma\gamma\gamma\,\gamma\gamma\gamma$. In such a method the coherent summation of the two berms is naturally obtained by means of a 45°-rotation of the axes of the scatter plot and a projection on one of the new axis. But, unfortunately, the method necessitates the selection of a 45°-rotated square area around the signal peak in the scatter plot. Two corners of that area, in the $\pi^0\pi^0$ case, would largely get into the event-depleted region and determine an underestimation of the background.

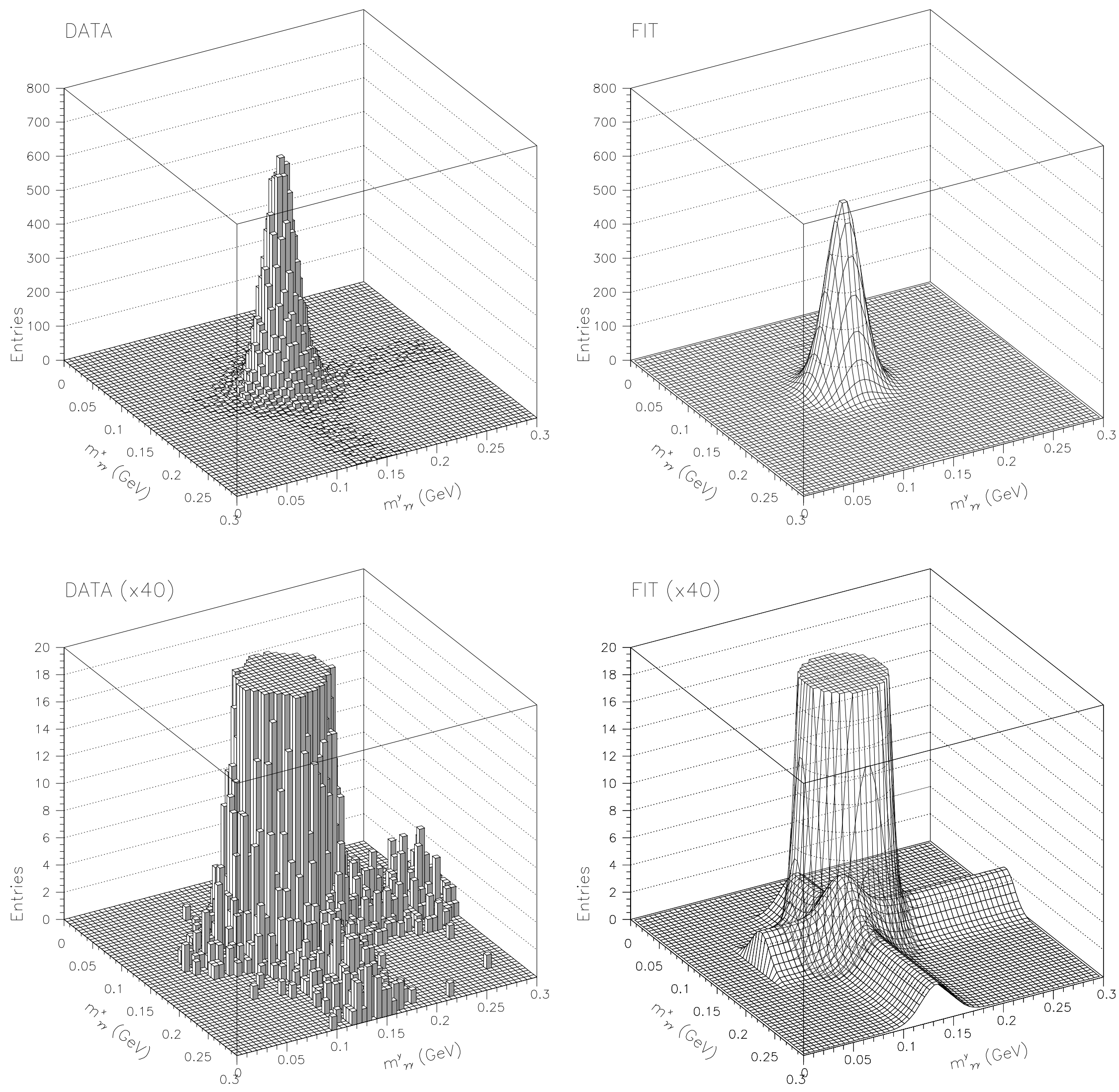

Figure 3.14: Top left: the (symmetrized) LEGO plot of the two $\gamma\gamma$ invariant masses at $E_{cm} = 3415$ MeV. All $\pi^0\pi^0$ cuts are applied except the ones on the invariant masses themselves. Top right: the fit parameterization of the top left plot. Bottom left: magnification of top left plot. Bottom right: magnification of top right plot, where the underlying background contribution (berms+plane) is made visible.

z	A/σ^2 $\left(\frac{\text{Events}}{25\ \text{MeV}^2}\right)$	B/σ $\left(\frac{\text{Events}}{25\ \text{MeV}^2}\right)$	σ (MeV)	Bkg Unbound/Bound (Events)	Peak (Events)
0.0125	9.47±0.48	0.102±0.016	18.37±0.37	30.8±7.4 / 21.0±4.6	819±29
0.0375	9.41±0.47	0.062±0.012	18.62±0.35	19.1±5.7 / 21.2±4.6	816±29
0.0625	9.72±0.48	0.066±0.012	18.73±0.35	20.3±5.9 / 21.4±4.6	849±29
0.0875	9.43±0.50	0.080±0.014	18.14±0.38	23.9±6.5 / 21.4±4.6	778±28
0.1125	9.87±0.53	0.069±0.014	17.60±0.37	20.1±6.0 / 21.0±4.6	770±28
0.1375	9.55±0.58	0.050±0.012	17.56±0.39	14.7±5.2 / 20.1±4.5	734±27
0.1625	8.76±0.47	0.059±0.012	18.31±0.38	17.7±5.5 / 18.9±4.3	733±27
0.1875	8.36±0.47	0.052±0.011	17.80±0.38	15.3±5.2 / 17.3±4.2	661±26
0.2125	8.03±0.47	0.072±0.013	17.13±0.39	20.6±5.9 / 15.6±3.9	596±24
0.2375	7.59±0.46	0.047±0.011	17.14±0.40	13.4±4.8 / 13.9±3.7	557±24
0.2625	7.67±0.45	0.042±0.010	17.92±0.41	12.4±4.7 / 12.5±3.5	616±25
0.2875	8.76±0.49	0.046±0.010	16.60±0.36	12.6±4.6 / 11.7±3.4	612±25
0.3125	10.29±0.60	0.062±0.013	15.87±0.36	16.9±5.4 / 11.8±3.4	656±26
0.3375	10.69±0.56	0.050±0.012	16.82±0.35	14.1±5.0 / 13.0±3.6	752±27
0.3625	13.98±0.67	0.060±0.013	15.91±0.29	16.5±5.5 / 15.4±3.9	889±30
0.3875	17.88±0.80	0.059±0.013	15.04±0.26	15.5±5.2 / 19.3±4.4	1019±32
0.4125	22.65±0.91	0.071±0.014	15.27±0.23	18.4±5.7 / 24.5±5.0	1324±36
0.4375	28.99±1.06	0.143±0.020	15.06±0.22	36.2±7.9 / 31.0±5.6	1661±41
0.4625	36.03±1.20	0.145±0.020	14.50±0.19	35.5±7.7 / 38.2±6.2	1914±44
0.4875	46.59±1.41	0.203±0.024	14.12±0.17	48.5±9.0 / 45.6±6.8	2354±49
0.5125	57.07±1.56	0.229±0.025	14.19±0.15	55.5±9.7 / 52.2±7.2	2907±54
0.5375	66.82±1.72	0.241±0.027	13.91±0.14	57.8±9.9 / 56.7±7.5	3262±57
0.5625	77.51±1.85	0.255±0.027	13.76±0.13	59.±10. / 57.4±7.6	3698±61
0.5875	78.38±1.82	0.213±0.025	14.24±0.13	51.3±9.4 / 52.0±7.2	3974±63

Table 3.4: Fit estimates for the parameters A, B, and σ (C and D, the coefficients of the plane, add a negligible contribution to the background and are omitted in the table) of Equation 3.8 for the bins in z at E_{cm} = 3415 MeV. The last two column report the estimated background under the $\pi^0\pi^0$ peak (before and after binding the background values by means of the six-degree polynomial fit, as described in the text) and the total entries in the peak.

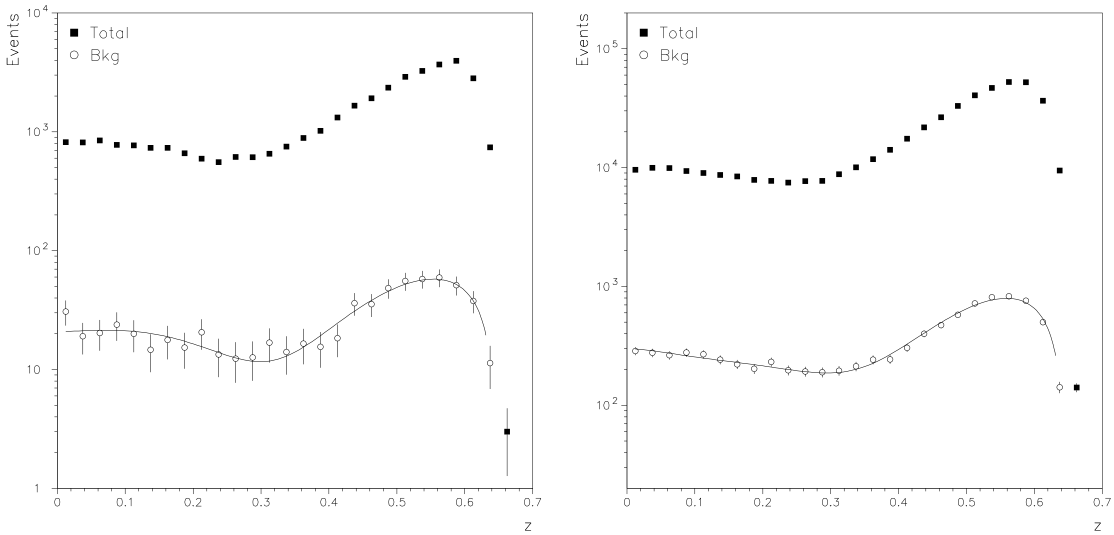

Figure 3.15: Left: At $E_{cm} = 3415$ MeV, the number of $\pi^0\pi^0$ candidate events (indicated as Total) and the estimated instrumental background events (Bkg) as a function of z. A six-degree polynomial fit is used to reduce the fluctuations. Right: As in left plot, but merging all 17 energy points to give an overview of the entire data sample. (The fall in the number of events at $z \gtrsim 0.6$ is an effect of the acceptance, since here the data are not acceptance-corrected.)

The effectiveness of the procedure for estimating the background is checked with a MC simulation. Events from the $\pi^0\omega$, $\omega\omega$ and $\pi^0\pi^0$ channels are generated, passed through the $\pi^0\pi^0$ selection, and overlapped. The quantity of events generated for each channel is such that the event distribution of the scatter plot in Figure 3.14 is approximately reproduced. The background subtraction procedure is then run on these MC events, and the resulting background estimate is confronted with the number of generated $\pi^0\omega$ and $\omega\omega$ events that actually pass the selection. The estimated and the actual number are found to be in agreement with each other.

3.10 NDST and Trigger Efficiencies

The efficiency of the NDST production is quite high for the events that pass the $\pi^0\pi^0$ selection. This is mostly due to cut 4 of Section 3.4 which tightens the requests imposed during the NDST production (see Section 3.3). The NDST efficiency of an energy point is determined by running the $\pi^0\pi^0$ selection on one original neutral tape (that is half of a run) of the energy point and on the part of the NDST sample that was produced from that original. The ratio between the numbers of events that pass the selection from the original tape and the NDST is taken as the NDST efficiency. The procedure is repeated for every energy point and the efficiency is found to be greater than 99% for each of them, as reported in Table 3.5.

The most of the selected $\pi^0\pi^0$ events have been simultaneously identified by Neutral-PBG1 and Neutral-ETOT triggers (see the Section 2.3.6), specifically 477,468 events (98.22% of the whole sample). A smaller fraction, 8,296 events (1.71%), triggered Neutral-PBG1 only and even fewer, 358 events (0.07%), triggered Neutral-ETOT only. For every energy point, the efficiencies of the PBG1 and ETOT triggers, (ϵ_{PBG1} and ϵ_{ETOT}, respectively) is determined as

$$\epsilon_{PBG1} = \frac{N_{PBG1}}{N_{TOT}} \tag{3.9}$$

and

$$\epsilon_{ETOT} = \frac{N_{ETOT}}{N_{TOT}} \ , \tag{3.10}$$

where N_{TOT} is the number of $\pi^0\pi^0$ events of the considered energy point, while N_{PBG1} and N_{ETOT} are the numbers of events that triggered PBG1 and ETOT, respectively. Such efficiencies are reported in Table 3.5. The trigger inefficiency due to the spurious firing of the Charged Veto is determined in Section 3.8. However, other components of the trigger system play a non-negligible role. Each one of two study triggers remove 1% of the events from the ETOT stream. In addition, the software filter PRUDE removes from the sample, again for study purposes, another 1% of the events that pass PBG1 and 1% of the events that pass ETOT-HI.

Energy (MeV)	ϵ_{NDST} (%)	ϵ_{PBG1} (%)	ϵ_{ETOT} (%)	ϵ_{trig} (%)
3339.5	99.20±0.19	99.904±0.029	97.11 ±0.16	96.088±0.029
3365.0	99.47±0.15	99.897±0.020	97.69 ±0.09	96.087±0.020
3384.4	99.45±0.17	99.927±0.017	98.55 ±0.08	96.074±0.017
3384.8	99.51±0.13	99.878±0.015	98.85 ±0.04	96.072±0.015
3392.0	99.72±0.11	99.908±0.020	98.00 ±0.09	96.080±0.020
3400.1	99.24±0.18	99.911±0.019	97.37 ±0.10	96.086±0.019
3406.1	99.83±0.08	99.931±0.013	98.61 ±0.06	96.073±0.013
3409.1	99.49±0.14	99.963±0.014	97.50 ±0.11	96.084±0.014
3410.3	99.74±0.11	99.921±0.018	98.44 ±0.08	96.076±0.018
3413.8	99.30±0.19	99.925±0.016	97.42 ±0.09	96.086±0.016
3415.0	99.24±0.20	99.940±0.013	98.81 ±0.06	96.072±0.013
3415.9	99.45±0.17	99.950±0.012	98.63 ±0.06	96.076±0.012
3418.0	99.41±0.16	99.964±0.013	99.09 ±0.07	96.068±0.013
3422.1	99.03±0.21	99.944±0.013	97.75 ±0.08	96.082±0.013
3426.0	99.62±0.14	99.950±0.014	98.61 ±0.07	96.073±0.014
3430.1	99.12±0.21	99.914±0.021	97.37 ±0.11	96.081±0.021
3469.9	99.51±0.16	99.948±0.012	98.99 ±0.05	96.070±0.012

Table 3.5: The NDST efficiency (ϵ_{NDST}), along with the Neutral-PBG1 (ϵ_{PBG1}) and the Neutral-ETOT (ϵ_{ETOT}) trigger efficiency of each energy point. The overall trigger efficiency (ϵ_{trig}) is decreased by those events that are re-directed toward study triggers.

Neglecting second order effects, the overall trigger efficiency, ϵ_{trig}, is calculated by

$$\epsilon_{trig} \simeq (0.99)^3 \Big[\epsilon_{PBG1}\, f_{PBG1\cap\overline{ETOT}} + \epsilon_{ETOT}\, f_{\overline{PBG1}\cap ETOT} + 0.99\,\epsilon_{PBG1}\, f_{PBG1\cap ETOT}\Big], \tag{3.11}$$

where $f_{PBG1\cap\overline{ETOT}}$, $f_{\overline{PBG1}\cap ETOT}$, and $f_{PBG1\cap ETOT}$ are the fraction of events that pass PBG1 only, PBG1 and ETOT, and ETOT only, respectively. The overall trigger efficiency is written in the last column of Table 3.5.

3.10.1 Photon Conversion Probability

The probability, P_γ, that a photon undergoes an e^+e^- pair production when traversing the inner detector materials[14] is calculated in [70]. In order for the event to be rejected from the neutral sample, the e^+e^- pair has to be detected by the charged trigger. The product of P_γ and the charged trigger efficiency for e^+e^- pairs, $\epsilon_{e^+e^-}$, is again calculated in [70]:

$$P_\gamma \times \epsilon_{e^+e^-} = (1.16 \pm 0.04_{stat} \pm 0.02_{syst})\% \ . \tag{3.12}$$

The rejection probability, P_{reject}, for events with four photons is

$$P_{reject} = (1 - P_\gamma \times \epsilon_{e^+e^-})^4 = 0.9375 \pm 0.0015_{stat} \pm 0.0008_{syst} \ . \tag{3.13}$$

3.11 The $\pi^0\pi^0$ Cross Section

The $\bar{p}p \to \pi^0\pi^0$ differential cross section, $d\sigma/dz$, is calculated in every bin of z as

$$\frac{d\sigma}{dz} = \frac{N_{\pi^0\pi^0}}{\mathcal{L} \times \ a \times \epsilon \ \times \epsilon_{trig} \times P_{reject} \times [B(\pi^0 \to \gamma\gamma)]^2 \times \Delta z} \ , \tag{3.14}$$

where $N_{\pi^0\pi^0}$ is the number of events passing the $\pi^0\pi^0$ selection and falling in the bin minus the estimated number of instrumental background events in that bin, $\mathcal{L}$ is the luminosity of the energy point (see Table 3.2), $a \times \epsilon$ is the product of the acceptance and efficiency (see Section 3.7) corrected for polar angle resolution and pileup (see Section 3.8), ϵ_{trig} is the overall trigger efficiency (see Table 3.5), P_{reject} is the probability of event rejection due to photon conversions into e^+e^- pair (see Equation 3.13), $B(\pi^0 \to \gamma\gamma) = (98.798 \pm 0.032)\%$ is the branching ratio of the π^0 in two photons, and $\Delta z = 0.025$ is the bin width.

Table 3.6 reports, for one of the 17 energy points, the bin-dependent quantities necessary to calculate the differential cross section. The complete series of tables, one for every energy point, is located in Appendix F.

[14]This effect is not implemented in the Monte Carlo simulation.

z	$\frac{d\sigma}{dz}$ (nb)	N_{tot} (events)	N_{bkg} (events)	$N_{\pi^0\pi^0}$ (events)	$a \times \epsilon$
0.0125	34.6 ± 1.3	819 ± 29	21.0 ± 4.6	798 ± 29	0.4492 ± 0.0042
0.0375	33.7 ± 1.3	816 ± 29	21.2 ± 4.6	795 ± 29	0.4599 ± 0.0042
0.0625	33.1 ± 1.2	849 ± 29	21.4 ± 4.6	828 ± 29	0.4867 ± 0.0044
0.0875	31.9 ± 1.2	778 ± 28	21.4 ± 4.6	757 ± 28	0.4625 ± 0.0043
0.1125	31.1 ± 1.2	770 ± 28	21.0 ± 4.6	749 ± 28	0.4694 ± 0.0043
0.1375	28.9 ± 1.1	734 ± 27	20.1 ± 4.5	714 ± 27	0.4818 ± 0.0043
0.1625	27.2 ± 1.1	733 ± 27	18.9 ± 4.3	714 ± 27	0.5114 ± 0.0045
0.1875	25.3 ± 1.0	661 ± 26	17.3 ± 4.2	644 ± 26	0.4966 ± 0.0044
0.2125	22.7 ± 1.0	596 ± 24	15.6 ± 3.9	580 ± 24	0.4985 ± 0.0044
0.2375	20.5 ± 0.9	557 ± 24	13.9 ± 3.7	543 ± 24	0.5169 ± 0.0045
0.2625	21.4 ± 0.9	616 ± 25	12.5 ± 3.5	603 ± 25	0.5489 ± 0.0046
0.2875	22.6 ± 1.0	612 ± 25	11.7 ± 3.4	600 ± 25	0.5167 ± 0.0045
0.3125	24.0 ± 1.0	656 ± 26	11.8 ± 3.4	644 ± 26	0.5242 ± 0.0045
0.3375	26.4 ± 1.0	752 ± 27	13.0 ± 3.6	739 ± 27	0.5448 ± 0.0046
0.3625	31.3 ± 1.1	889 ± 30	15.4 ± 3.9	874 ± 30	0.5438 ± 0.0046
0.3875	37.7 ± 1.3	1019 ± 32	19.3 ± 4.4	1000 ± 32	0.5162 ± 0.0045
0.4125	48.2 ± 1.4	1324 ± 36	24.5 ± 5.0	1299 ± 36	0.5259 ± 0.0045
0.4375	57.2 ± 1.5	1661 ± 41	31.0 ± 5.6	1630 ± 41	0.5553 ± 0.0047
0.4625	70.6 ± 1.8	1914 ± 44	38.2 ± 6.2	1876 ± 44	0.5175 ± 0.0045
0.4875	86.3 ± 2.0	2354 ± 49	45.6 ± 6.8	2308 ± 49	0.5214 ± 0.0045
0.5125	105.6 ± 2.2	2907 ± 54	52.2 ± 7.2	2855 ± 54	0.5271 ± 0.0046
0.5375	129.8 ± 2.6	3262 ± 57	56.7 ± 7.5	3205 ± 57	0.4813 ± 0.0044
0.5625	160.1 ± 3.1	3698 ± 61	57.4 ± 7.6	3641 ± 61	0.4432 ± 0.0042
0.5875	208.6 ± 4.0	3974 ± 63	52.0 ± 7.2	3922 ± 63	0.3666 ± 0.0038

Table 3.6: The bin-dependent quantities for the energy point E_{cm} = 3415 MeV: the center of the bin (z), the $\bar{p}p \to \pi^0\pi^0$ differential cross section ($\frac{d\sigma}{dz}$), the total number of events (N_{tot}) passing the $\pi^0\pi^0$ selection, the estimated number of instrumental background events (N_{bkg}), the number of $\pi^0\pi^0$ events ($N_{\pi^0\pi^0} \equiv N_{tot} - N_{bkg}$, with uncertainty conservatively taken as $\sqrt{N_{tot}}$), and the product of the acceptance and efficiency ($a \times \epsilon$) corrected for polar angle resolution and pileup (the uncertainty on $a \times \epsilon$ is determined by the number of RG events available).

Figure 3.16 shows the $\bar{p}p \to \pi^0\pi^0$ differential cross section for the energy point $E_{cm} = 3415$ MeV. The complete series of smaller-scale plots with the differential cross section of all 17 energy points is reported in Figures 3.17 and 3.18.

The cross section, $\Delta\sigma$, integrated over a certain range of z is obtained by summing $(d\sigma/dz) \times \Delta z$ of the bins included by the range. Figures 3.19 and 3.20 show the $\bar{p}p \to \pi^0\pi^0$ cross section integrated from $z = 0$ to increasing upper values z_{max}, while Figure 3.21 shows the integration over subsequent z-ranges as wide as 0.1 .

At off-resonance energies, the cross section is solely non-resonant continuum $\bar{p}p \to \pi^0\pi^0$ with a smooth dependence on the energy. A resonance signal is evident nearby the mass of the χ_{c0}. As a consequence of the interference between the resonance and the non resonant helicity-0 continuum, the peak is shifted a couple of MeV toward low energies with respect to the value of the χ_{c0} mass (which is precisely determined by the analysis of the reaction $\bar{p}p \to \chi_{c0} \to J/\psi\,\gamma$, $J/\psi \to e^+e^-$; as reported in Ref. [1] and in Section 3.12). As discussed in Section 3.9, the instrumental background is very small and has been subtracted.

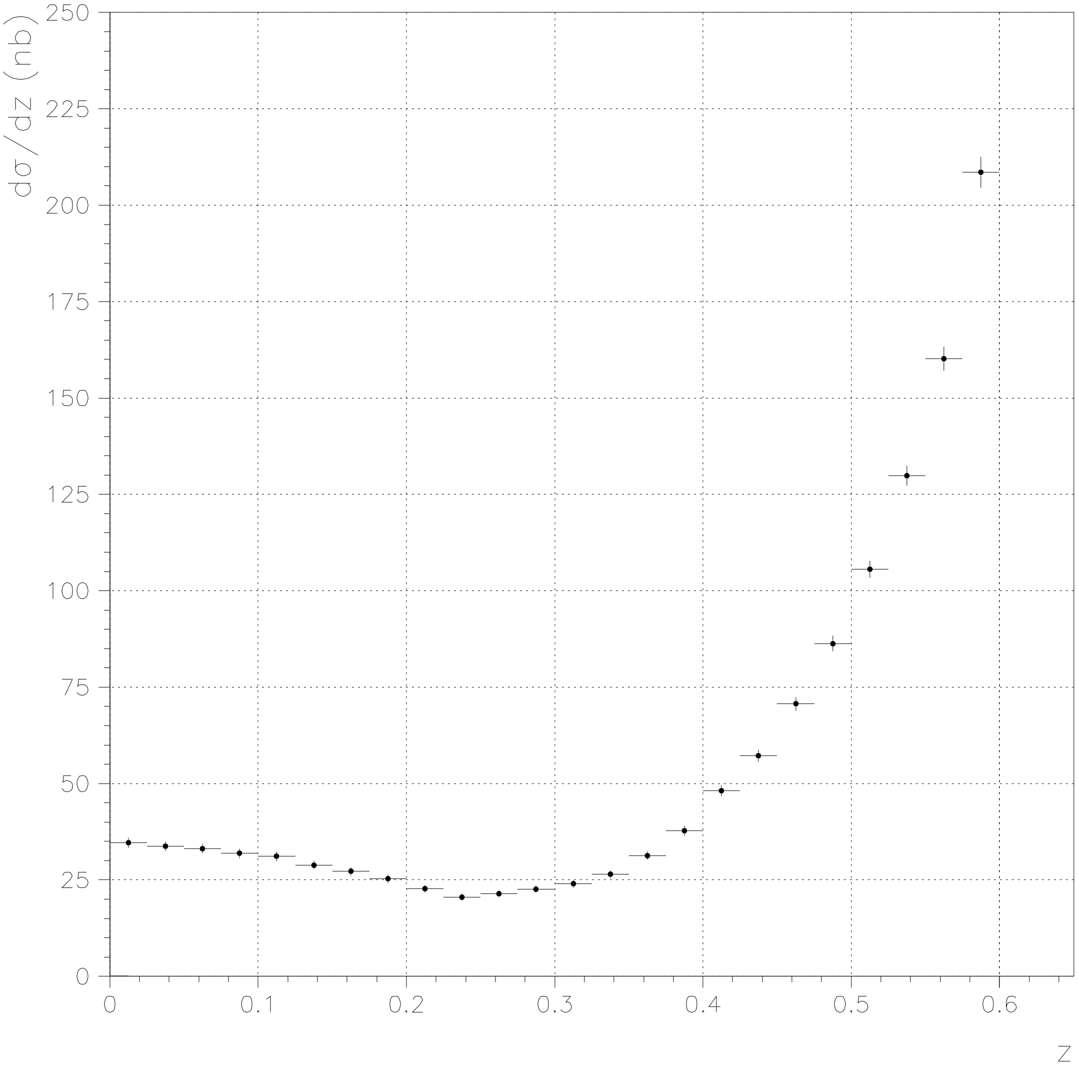

Figure 3.16: The measured $\bar{p}p \rightarrow \pi^0\pi^0$ differential cross section plotted versus z at $E_{cm} = 3415$ MeV.

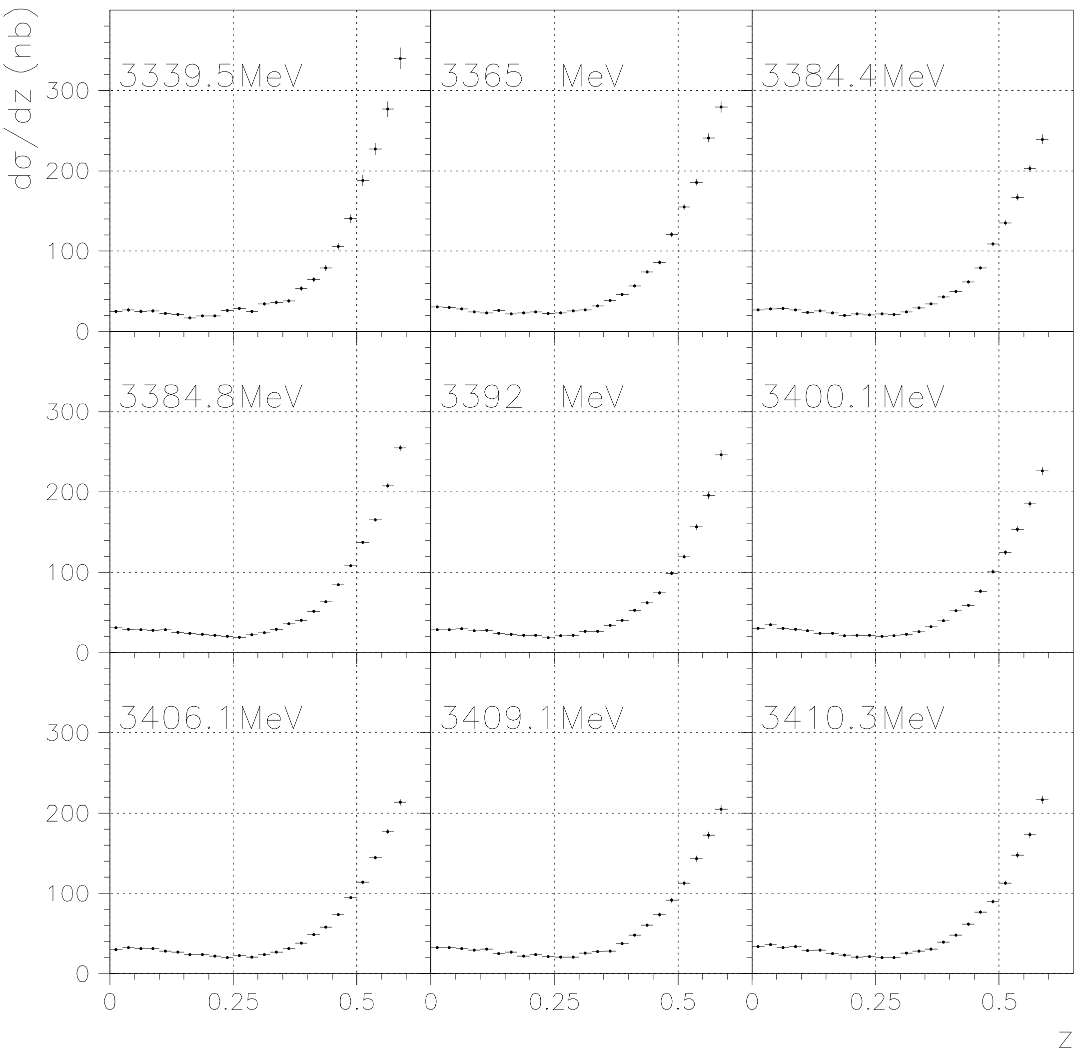

Figure 3.17: The measured $\bar{p}p \to \pi^0\pi^0$ differential cross section plotted versus z at the E_{cm} indicated in each plot.

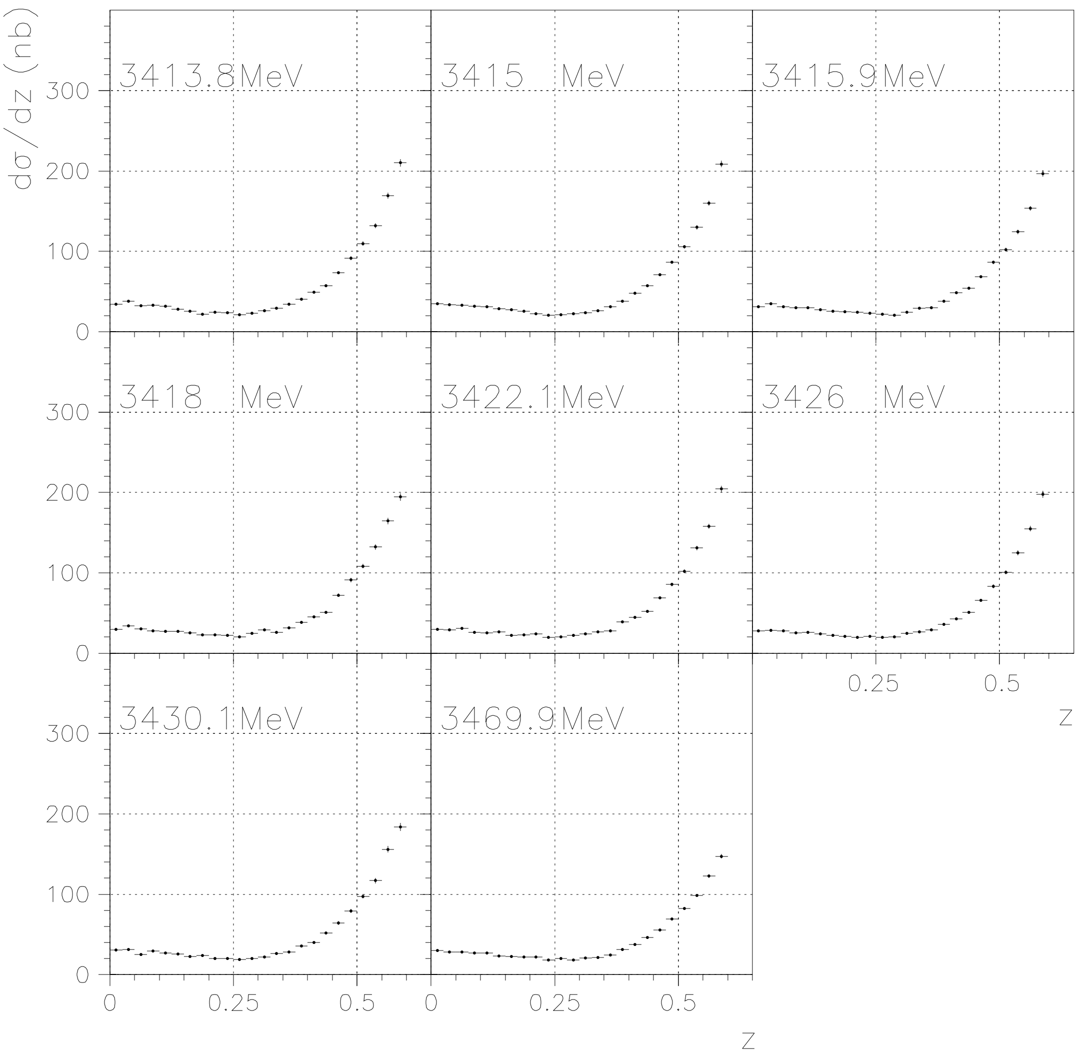

Figure 3.18: The measured $\bar{p}p \to \pi^0\pi^0$ differential cross section plotted versus z at the E_{cm} indicated in each plot.

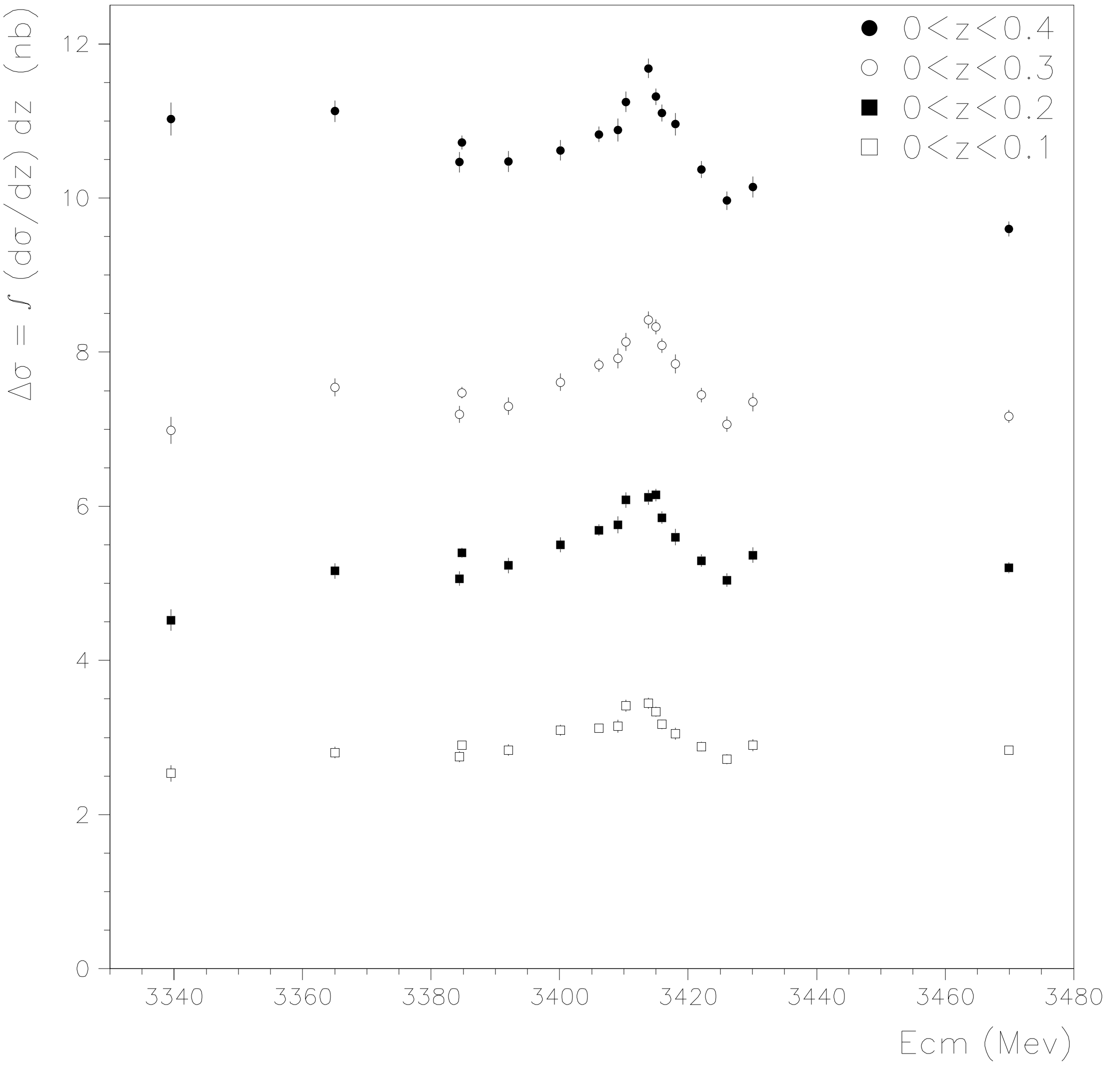

Figure 3.19: The measured $\bar{p}p \rightarrow \pi^0\pi^0$ cross section integrated over $0 < z < z_{max}$ plotted versus E_{cm} .

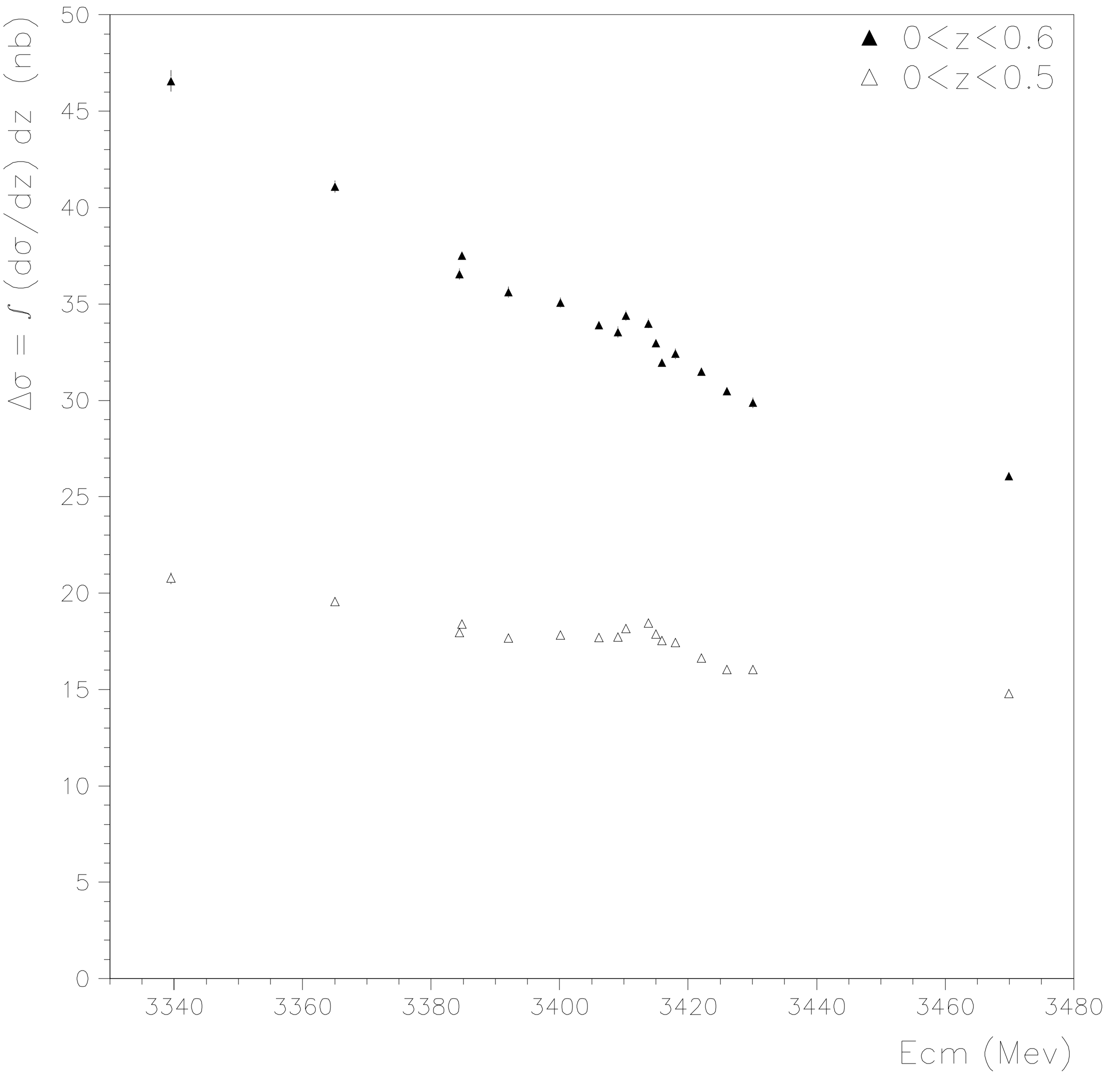

Figure 3.20: The measured $\bar{p}p \to \pi^0\pi^0$ cross section integrated over $0 < z < z_{max}$ plotted versus E_{cm} .

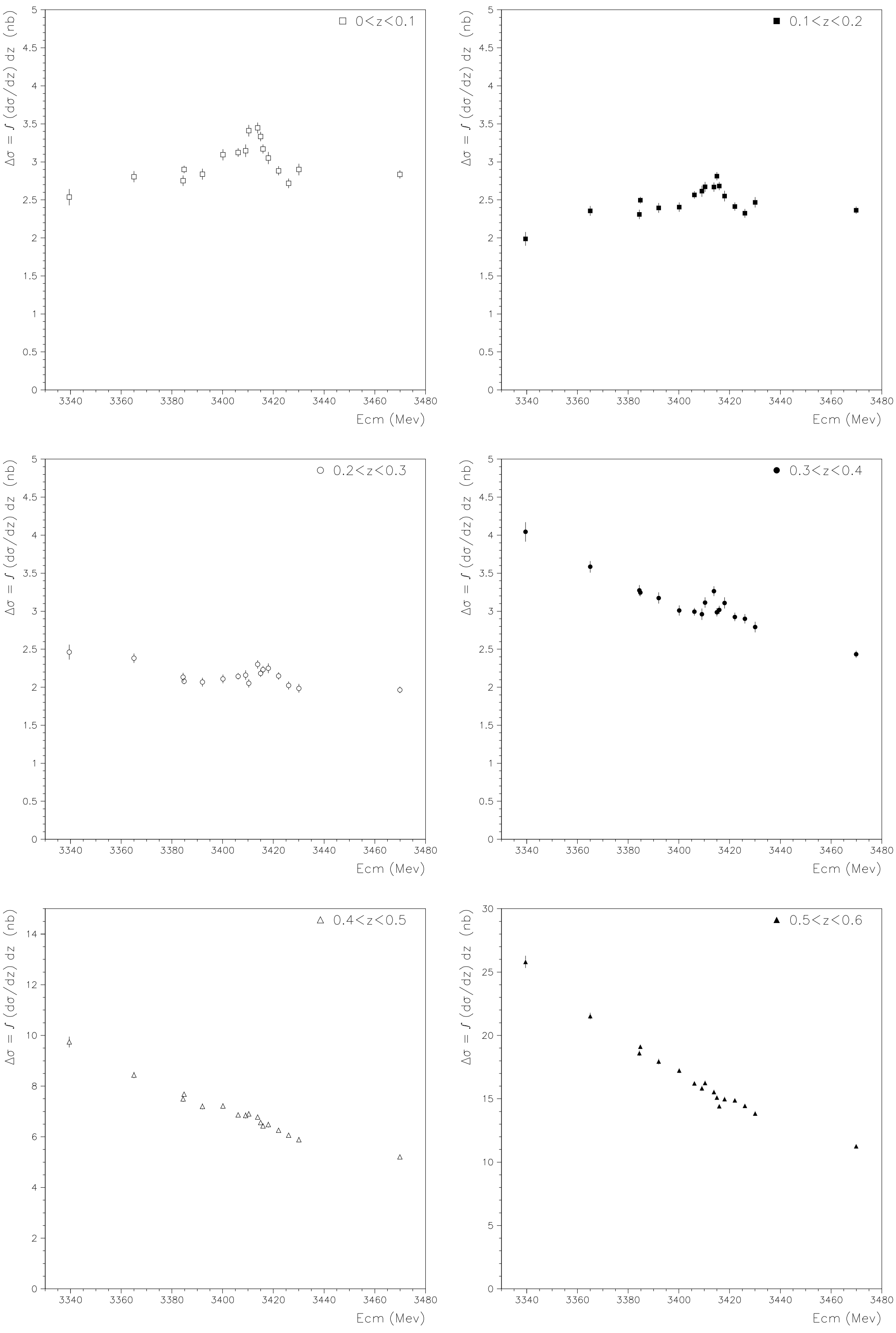

Figure 3.21: The measured $\bar{p}p \to \pi^0\pi^0$ cross section integrated over $z_{min} < z < z_{max}$ plotted versus E_{cm} .

3.12 The Reaction $\bar{p}p \to \chi_{c0} \to J/\psi\,\gamma$, $J/\psi \to e^+e^-$

Before proceeding with the analysis of the $\bar{p}p \to \chi_{c0} \to \pi^0\pi^0$ reaction, it is necessary to summarize what is already known about the χ_{c0} resonance.

The $\bar{p}p \to \pi^0\pi^0 \to \gamma\gamma\gamma\gamma$ data sample analyzed here was collected through the Neutral Trigger logic. Simultaneously, a Charged Trigger logic collected events from the reaction $\bar{p}p \to J/\psi\,\gamma$, $J/\psi \to e^+e^-$. These events have been already analyzed and the results published [1]. The measured cross section is reproduced in Figure 3.22 along with a fit to a Breit Wigner resonance plus a constant instrumental background.

This channel has a virtually zero instrumental background and non-resonant continuum. These conditions allow a precise extraction of the resonance parameters. The results for the mass and width of the χ_{c0}, as well as for the product of the branching ratios involved, are reported below:

$$M_{\chi_{c0}} = 3415.4 \pm 0.4 \pm 0.2\ \mathrm{MeV/c^2} \tag{3.15}$$

$$\Gamma_{\chi_{c0}} = 9.8 \pm 1.0 \pm 0.1\ \mathrm{MeV/c^2} \tag{3.16}$$

$$B(\chi_{c0} \to \bar{p}p) \times B(\chi_{c0} \to J/\psi\ \gamma) \times B(J/\psi \to e^+e^-) = (1.61 \pm 0.11 \pm 0.08) \times 10^{-7}. \tag{3.17}$$

By removing the well measured $B(\chi_{c0} \to e^+e^-) = (5.93 \pm 0.10)\%$ [39], it follows

$$B(\chi_{c0} \to \bar{p}p) \times B(\chi_{c0} \to J/\psi\ \gamma) = (27.2 \pm 1.9 \pm 1.3) \times 10^{-7}. \tag{3.18}$$

These values for the χ_{c0} mass and width will be used when fitting the cross section of the $\pi^0\pi^0$ channel.

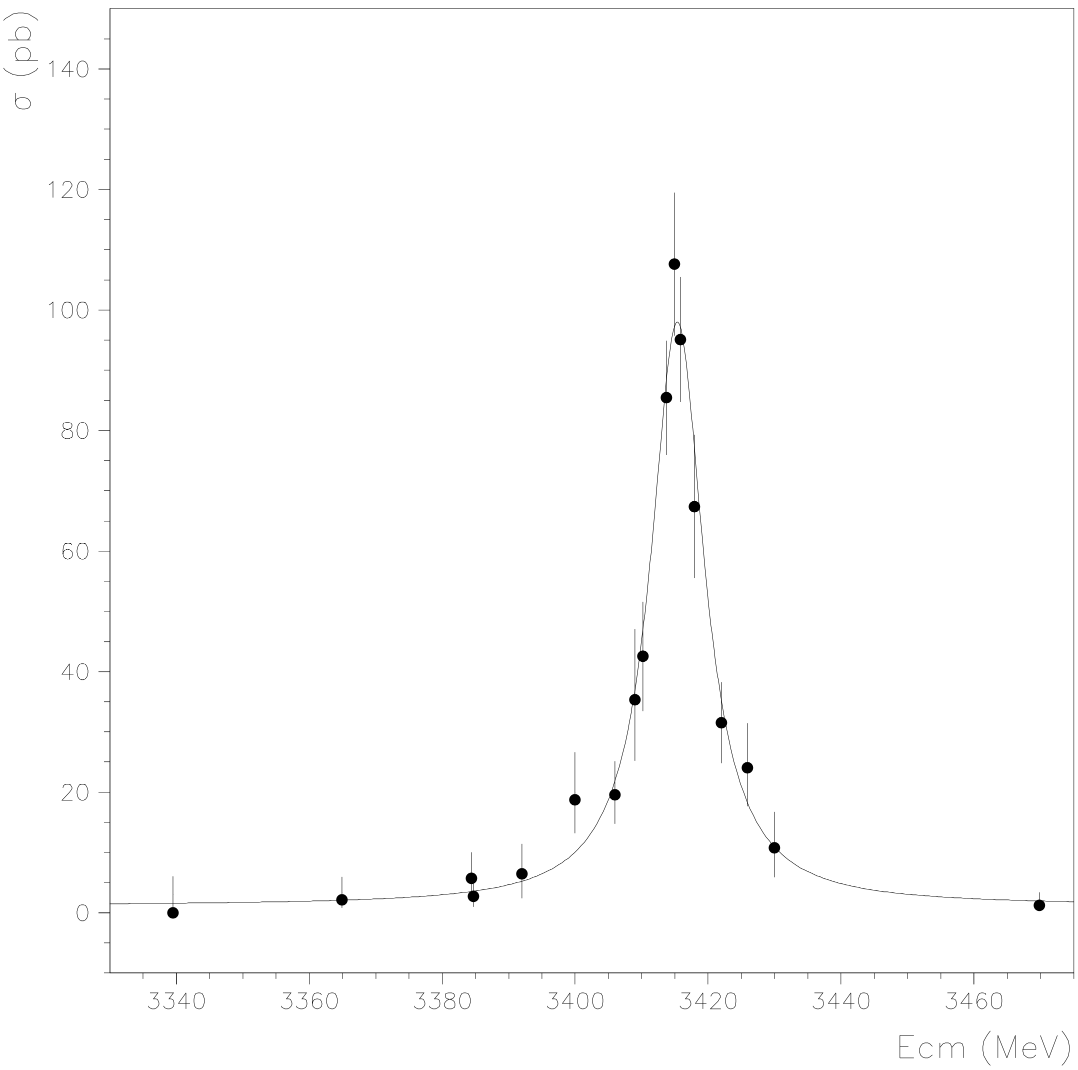

Figure 3.22: The Measured Cross Section $\bar{p}p \to J/\psi\ \gamma$, $J/\psi \to e^+e^-$.

3.13 Fit to the $\pi^0\pi^0$ Cross Section

A binned maximum likelihood fit[15] to the $\bar{p}p \rightarrow \pi^0\pi^0$ differential cross section is performed simultaneously on all of the 17 energy points of the data sample. The parameterization of Equation 1.16 is used with the definitions of Equations 1.14 and 1.15 , setting $J_{max} = 4$. These equations are rewritten here as follows:

$$\frac{d\sigma}{dz} = \left| -\frac{A_R}{x+i} + A\ e^{i\delta_A} \right|^2 + \left| B\ e^{i\delta_B} \right|^2, \tag{3.19}$$

with

$$A\ e^{i\delta_A} \equiv \sum_{J=0,2,4,\ldots}^{J_{max}=4} (2J+1)\ C_J(x)\ e^{i\delta_J(x)}\ P_J(z), \tag{3.20}$$

and

$$B\ e^{i\delta_B} \equiv \sum_{J=2,4,\ldots}^{J_{max}=4} \frac{2J+1}{\sqrt{J(J+1)}}\ C_J^1(x)\ e^{i\delta_J^1(x)}\ P_J^1(z), \tag{3.21}$$

where the coefficients A, B, C_J, and C_J^1 are real and positive, and the phases δ_A, δ_B, δ_J and δ_J^1 are real. The mass and with of the χ_{c0}, implicit in the definition of equation 1.13 of x, are constrained to the values of equations 3.15 and 3.16 determined by means of the $J/\psi\,\gamma$ channel [1].

The fit is performed on an angular range limited to $0 < z < 0.6$, since the acceptance times efficiency ($a \times \epsilon$, see Section 3.7) quickly drops to zero for $z \gtrsim 0.6$. Limiting the range to $0 < z < 0.6$ guarantees that $a \times \epsilon$ is $\gtrsim 20\%$ at all energy points. Within this range, the data sample consists of 431,625 $\pi^0\pi^0$ events (instrumental background already subtracted).

The result of the fit for $d\sigma(x, z)/dz$ is shown in Figure 3.23 at the energy point $E_{cm} = 3415$ MeV. The single components of the fit are also plotted. The line A^2+B^2 shows the sum of the two contributions to the non-resonant cross section. The effect of the resonance, amplified by the interference, is seen in the separation (evident at small z) between $d\sigma/dz$ and $A^2 + B^2$ and is almost entirely due to the interference-term of Equation 1.17 . The separation decreases as z increases, following the trend

[15] The CERN program MINUIT [71] is used.

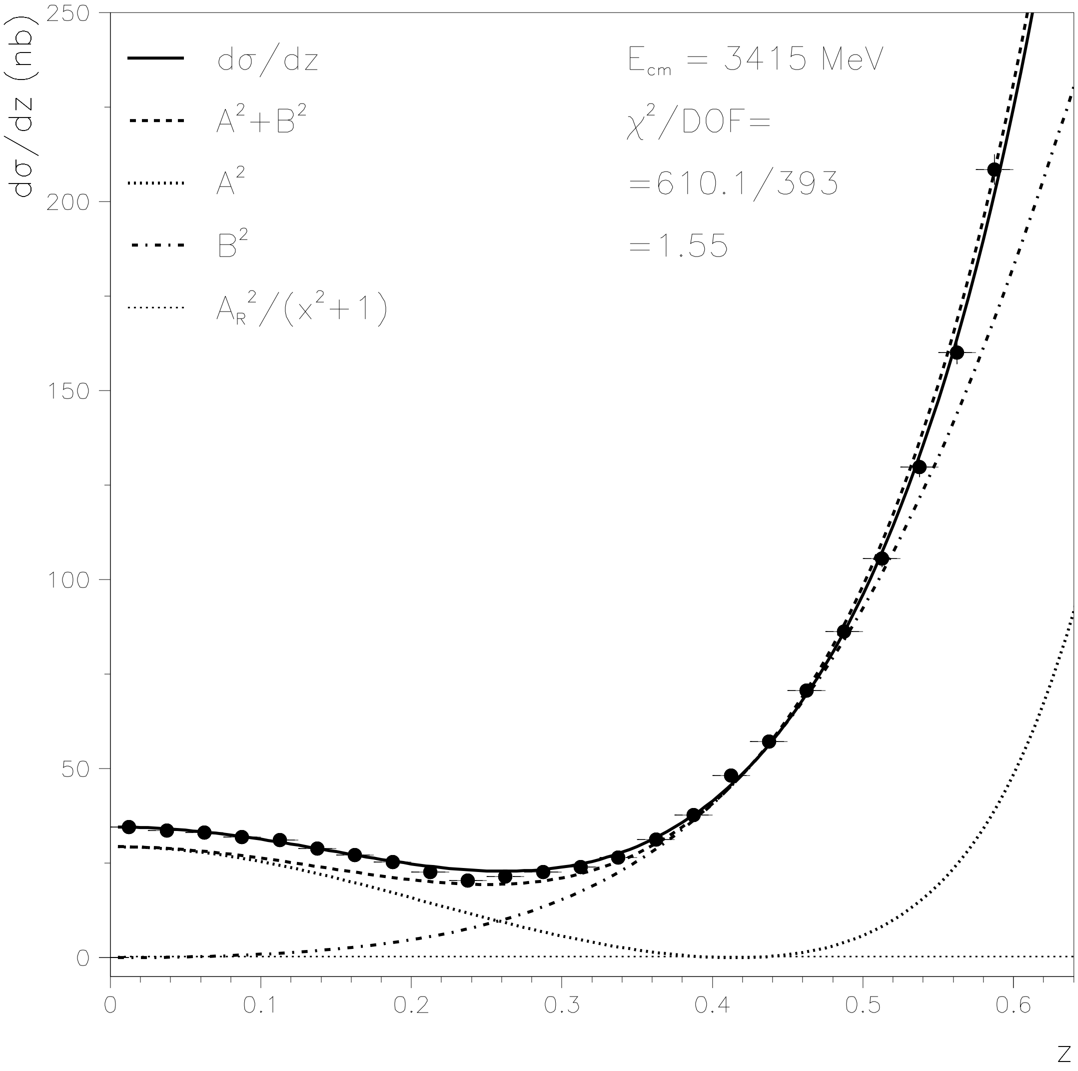

Figure 3.23: The $\bar{p}p \to \pi^0\pi^0$ differential cross section versus z at $E_{CM} = 3415$ MeV. The fit of Equations 3.19 , 3.20 and 3.21 and its components are also shown.

of A. The term B^2 is small at small values of z due to a factor z present in all the associate functions $P_J^1(z)$, as discussed in Section 1.4.2. The net suppression factor of B^2 with respect to A^2 is z^2 at small z. The contribution of the "pure" resonance, $A_R^2/(x^2+1)$, is relatively negligible and not discernible from zero.

The agreement of the fit with the data is shown at all 17 energy points in Appendix C.1 (Figures C.1 and C.2). In the same Appendix (Figures C.3 and C.4) the fit and the cross section are also shown integrated over different angular ranges and plotted versus E_{cm} .

The fit has 408 bins: 17 energy points times 24 bins in z (each one of $\Delta z = 0.025$). The number of free parameters is 15: the resonance amplitude, A_R; the coefficients $C_{J=0,2,4}$ and $C^1_{J=2,4}$, each of them is given a linear energy dependence (which results to be small); and the phases $\delta_{J=0,2,4}$ and[16] $(\delta_4^1 - \delta_2^1)$. The fit does not improve significantly by allowing the phases to vary with the energy. It should be noticed that the χ_{c0} region encompasses a narrow energy window on the scale of the non-resonant continuum. Table 3.7 reproduces the fit results for coefficients and phases.

J	C_J [nb$^{1/2}$]	C_J^1 [nb$^{1/2}$]
0	$C_0 = (12.8 \pm 0.7) - (0.19 \pm 0.02)\, x$	–
2	$C_2 = (8.3 \pm 0.4) - (0.055 \pm 0.010)\, x$	$C_2^1 = (5.19 \pm 0.13) - (0.063 \pm 0.005)\, x$
4	$C_4 = (2.5 \pm 0.2) + (0.022 \pm 0.003)\, x$	$C_4^1 = (1.52 \pm 0.09) - (0.021 \pm 0.003)\, x$
J	δ_J [degree]	δ_J^1 [degree]
0	$\delta_0 = -36.1 \pm 1.8$	–
2	$\delta_2 = -43.0 \pm 1.0$	–
4	$\delta_4 = -15.1 \pm 1.2$	$\delta_4^1 - \delta_2^1 = -0.7 \pm 0.2$

Table 3.7: Fit results for the coefficients (with a linear energy dependence) and phases of the partial wave expansion of Equations 3.20 and 3.21 . The quoted errors are statistical; systematic errors due to the limited available angular range ($z \leq 0.6$) should be dominant.

The partial wave summations of equations 3.20 and 3.21 are truncated at $J_{max} = 4$. A fit performed with $J = 0$ and $J = 2$ alone gives already a fairly adequate

[16] Only the difference between δ_4^1 and δ_2^1 is measurable.

description of the differential cross section in the available range of z (which is shown in Figure 3.24). The addition of a relatively small $J = 4$ amplitude is

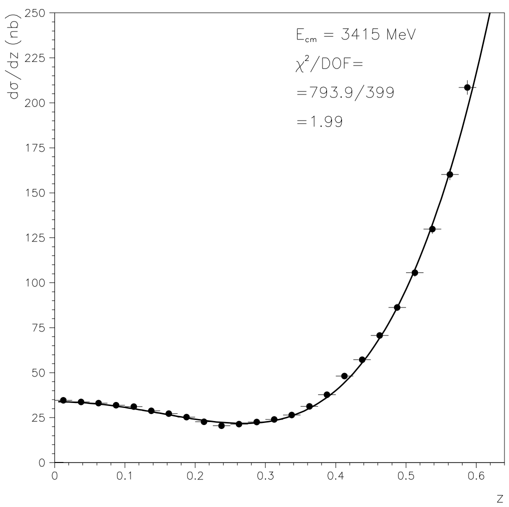

Figure 3.24: The fit of Equation 3.19 limiting to $J_{max} = 2$ the partial wave expansion in Equations 3.20 and 3.21 .

already "fine tuning"[17], as indicated by the relative amounts, at $x = 0$, of the coefficients $C_0 : (C_2, C_2^1) : (C_4, C_4^1) \simeq 1 : (0.65, 0.41) : (0.20, 0.12)$. The more complex structure of higher partial waves does not appear in our data, although the statistical resolution would be high enough to resolve it.

Physical considerations support this conclusion. In the c.m. frame, the $\bar{p}p$ impact parameter b correlates with the orbital angular momentum $L_{\bar{p}p}$ through the relation $\hbar\, L_{\bar{p}p} \simeq b\, p_i$ (wave mechanically smeared), where p_i is the momentum of the proton (or antiproton).

The formation of the χ_{c0} certainly requires the annihilation of all three valence

[17]The fit parameterization with $J_{max} = 4$ is able to describe quite well the general structure of the angular distribution and energy dependence, as Figures 3.23, C.1 and C.2 indicate. The somewhat high value of $\chi^2/DOF = 610.1/(408 - 15) = 1.55 \pm 0.07$ is mostly a consequence of the abundance of data: the resulting statistical errors are small and put in evidence the systematic fluctuations affecting the reconstructed cross section between contiguous bins in z, and between nearby energy points recorded at far times and different experimental conditions.

quark-antiquark pairs of the initial state (class 3, according to the classification on page 22) The non-resonant $\pi^0\pi^0$ final state can be produced by three, two, or one pair annihilations (class 3, 2 and 1, respectively). The high degree of required valence $\bar{q}q$ annihilation of class 3 and 2 heavily weights toward small b and hence small $L_{\bar{p}p}$. In class 1, a single $\bar{q}q$ pair annihilates. However, the formation of the $\pi^0\pi^0$ final state requires a large momentum transfer for a spectator quark to match the direction of a spectator antiquark (or vice versa). This unlikely occurs for peripheral impacts, where the spectators tend to retain most of the original large longitudinal component of their momentum. Therefore, $\pi^0\pi^0$ production is weighted toward small $L_{\bar{p}p}$ no matter if occurring in class 1, 2 or 3.

As Table 1.3 indicates, the $\pi^0\pi^0$ final states with $J = 0$ and $J = 2$ are both fed by the $L_{\bar{p}p} = 1$ initial state ($J = 2$ draws also from $L_{\bar{p}p} = 3$) and, as confirmed by our fit, should provide comparable amounts. $J = 4$ is fed by $L_{\bar{p}p} = 3$ and 5, and its contribution is already reduced. $J = 6$ is fed by $L_{\bar{p}p} = 5$ and 7, and should have little contribution, if any.

The fit presented in this section demonstrates the general structure of the $\bar{p}p \to \pi^0\pi^0$ angular distribution and estimates the number and amount of the contributing partial waves. However, the detector acceptance is limited to the angular range $0 < z < 0.6$ and the systematic errors on the coefficients $C_J^{|\lambda_i|}$ and phases $\delta_J^{|\lambda_i|}$ should dominate over the statistical errors reported in Table 3.7.

In addition, this fit proved to be little sensitive to the value of the resonant amplitude A_R. The reason is that the size of the (interference-enhanced) resonant signal is significant only at small values of z, while the fit is dominated by the high statistics of the non-resonant forward peak. The next section describes how the extraction of A_R is carried out[18].

3.14 Extraction of the Resonant Amplitude A_R

In order to extract the coupling of the χ_{c0} to the entrance and exit channels, it is critical to accurately determine the size of the magnification effect due to the

[18]See also the last paragraph of Section 3.14.2 on page 132.

interference between the resonance and the non-resonant continuum. As discussed in Section 1.4.2, only one component of the continuum interferes, specifically the component $Ae^{i\delta_A}$, which is produced by the helicity-0 initial $\bar{p}p$ state.

The other component of the continuum, the helicity-1 amplitude $Be^{i\delta_B}$, vanishes at $z = 0$ because of a factor z present in its constituent associate Legendre polynomials $P_J^1(z)$ (see Table 1.4). At small z, the z^2 suppression factor of B^2 with respect to A^2 greatly reduces the uncertainty on the relative size of the two components of the continuum and, as a consequence of that, on the knowledge of the amplification factor of the interference. Thus, the natural region to exploit in order to obtain a model-insensitive measurement of the resonance amplitude A_R is the region at small values of z.

3.14.1 Determination of the Cut on z

To investigate at which values of z the non interfering continuum starts to play a significant role, it is appropriate to perform a series of independent fits on each bin Δz. Every fit uses the parameterization of Equation 3.19 , where $Be^{i\delta_B}$ is set equal to zero. Specifically,

$$\Delta\sigma = \frac{d\sigma}{dz}\,\Delta z = \left| -\frac{A_R}{x+i} + A\ e^{i\delta_A}\right|^2 \Delta z. \tag{3.22}$$

The parameterization used for the helicity-0 component of the continuum is

$$A^2 \equiv a_0 + a_1 x + a_2 x^2\,, \tag{3.23}$$

which allows an energy dependence as the cross section of Figures 3.19, 3.20 and 3.21 calls for. The mass and width of the χ_{c0} are constrained to the values in equations 3.15 and 3.16 .

The purpose of setting B to zero is to single out at which value of z the helicity-1 contribution is no longer negligible. In fact, the growth with z of the helicity-1 component, not being accounted for in these fits, will have the effect of causing a decrease with z of the fit estimate of A_R, which - on the contrary - is known to be a constant (the decay $\chi_{c0} \to \pi^0\pi^0$ is isotropic).

Figure 3.25 shows the fits to the cross section versus E_{cm} in every bin Δz up to[19] $z = 0.3$. The fit results for the parameters of Equations 3.22 and 3.23 are shown in Figure 3.26. The observed drop at $z \gtrsim 0.15$ (top-left plot in Figure 3.26) of the fit estimate of A_R signifies that the helicity-1 component has grown significantly. Selecting the region

$$z \leq z_{cut} \equiv 0.125 \tag{3.24}$$

is then a good way to guarantee that the estimate of A_R is model-insensitive, although at an expense of the size of the data sample.

As stated, the fits in this section are performed on each single bin Δz independently from the fits in the other bins. This is useful to investigate the behavior of the several parameters of the fit as a function of z. Alternatively, a single fit can be performed on more bins merged, from $z = 0$ to $z = z_{max}$. This would bind the information from different bins in order to limit the fluctuations of the parameters. This is done in Appendix C.2 and the indication is still that the helicity-1 continuum starts playing a significative role at $z \gtrsim 0.15$.

In Appendix C.3, fits are performed on merged bins from $z = 0$ to $z = z_{max}$ setting the helicity-1 continuum B^2 to the estimate obtained from the partial wave expansion fit of Section 3.13. As the top-left plot in Figure C.7 shows, the decrease of A_R for $z \gtrsim 0.15$ is reduced but not canceled. As discussed in that appendix, this support the conservative choice of selecting the region $z \leq 0.125$ to extract A_R. This choice increases the statistical uncertainty on A_R, but limits the effects on A_R of the unknown systematic uncertainties that may affect B^2 (since B^2 is estimated by a partial wave expansion fit performed over an incomplete angular range $0 < z < 0.6$).

The Estimated Size of B^2 in the Region Selected by the Cut on z

Although the partial wave expansion fit (described in Section 3.13) is performed on the incomplete range $0 < z < 0.6$, it still provides an estimate on the size of B^2.

[19] These fits are not performed in the region $z \geq 0.3$ since their purpose is to determined the growth of the helicity-1 component in the small z region, and because these fits are not significant in the forward region where the resonant signal is too small relative to the continuum.

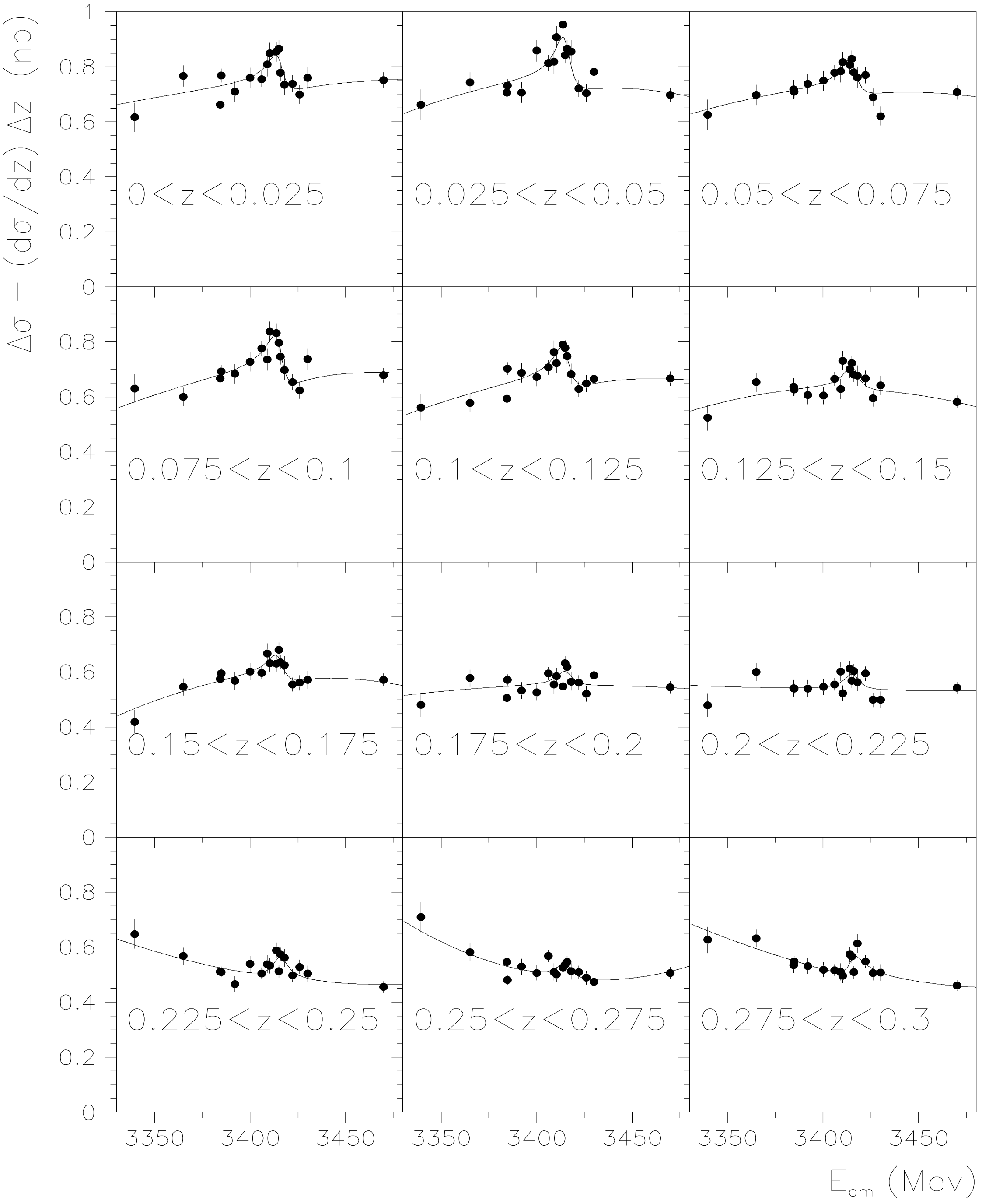

Figure 3.25: Fits to the $\bar{p}p \to \pi^0\pi^0$ cross section versus E_{cm}. Each fit is performed in a bin of size $\Delta z = 0.025$ using Equations 3.22 and 3.23 (the helicity-1 continuum $|B\ e^{i\delta_B}|^2 = 0$ is fixed to zero), independently from the fits in the other bins. The bins included here cover the region $z \leq 0.3$.

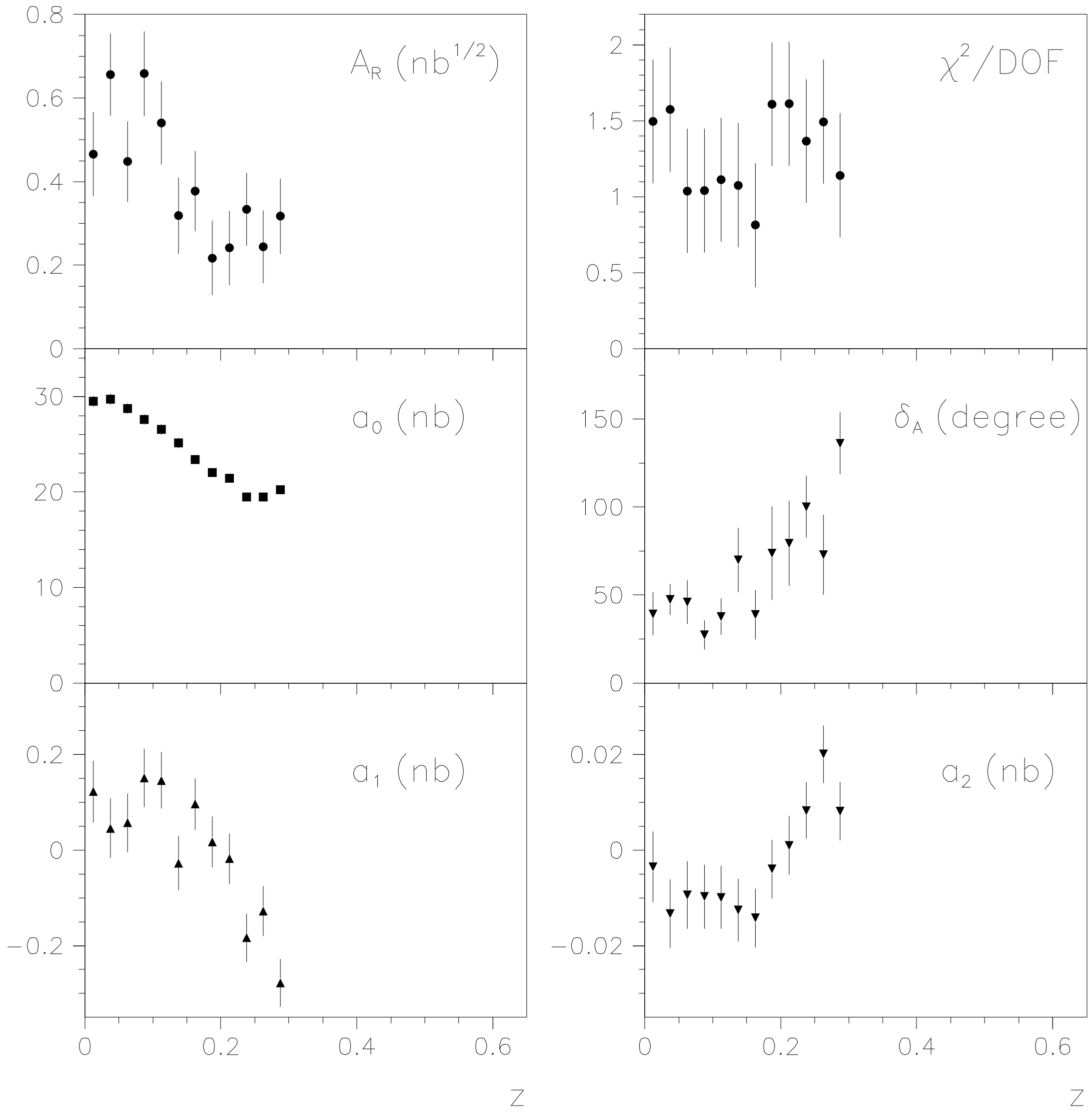

Figure 3.26: The parameters of Equations 3.22 and 3.23 as determined by the 12 independent fits of Figure 3.25.

Such a fit indicates that the ratio between the helicity-1 continuum and the total continuum as a function of z has the behavior plotted in Figure 3.27. The cut of

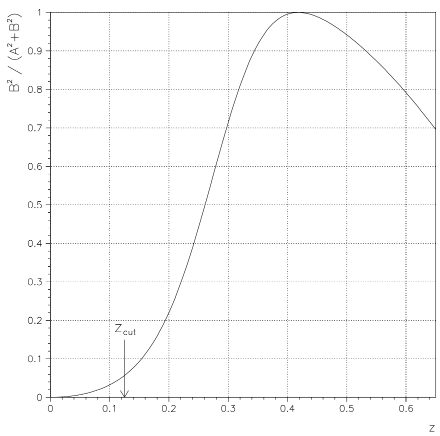

Figure 3.27: The ratio $\frac{B^2}{A^2+B^2}$ between the size of the helicity-1 non-resonant continuum and the total non-resonant continuum. The cut of Equation 3.24 is indicated.

Equation 3.24 prevents the contribution of the helicity-1 non-resonant continuum from growing above $\sim 5\%$ of the total non-resonant continuum. This limits the uncertainty on the magnitude of the enhancement of the resonant signal provided by the interference with the helicity-0 non-resonant continuum.

3.14.2 Determination of A_R

According to the understanding of the previous Section 3.14.1, the resonant amplitude A_R can be determined by restricting the angular range to $0 < z < z_{cut} \equiv 0.125$. A fit to the cross section using the full equation 3.19 can be performed simultaneously on the five bins included in the above angular range, so that the information from every bin is bound together.

Specifically, the parameterization used is

$$\Delta\sigma = \int_0^{z_{cut}} \left[\left| -\frac{A_R}{x+i} + A\, e^{i\delta_A} \right|^2 + \left| B\, e^{i\delta_B} \right|^2 \right] dz, \tag{3.25}$$

where z_{cut} is set to the value of equation 3.24 , which guarantees a model-insensitive estimate of A_R. (See Appendix C.3 for similar fits performed on different angular ranges.)

The magnitude of the helicity-0 continuum is parameterized as in Equation 3.23 with the addition of a z^2 dependence:

$$A^2 \equiv a_0 + a_1 x + a_2 x^2 + a_3 z^2. \tag{3.26}$$

Notice that, given the small range of z, a simple polynomial expansion on z about $z = 0$ is used as an adequate alternative to the partial wave expansion employed in the fit of Section 3.13. This reduces the number of free parameters that the fit necessitates, and then avoids the assumption on the number of partial waves involved. As usual, the mass and with of the χ_{c0}, implicit in the definition of x of equation 1.13 , are constrained to the values of equations 3.15 and 3.16 determined by studying the $J/\psi\,\gamma$ channel [1].

Even though in Section 3.14.1 it has been established that the helicity-1 continuum is very small within this reduced angular range, $|B\ e^{i\delta_B}|^2$ can still be taken into account since an estimate of it is available. This estimate comes from the fit over the full available angular range ($0 \leq z \leq 0.6$) described in Section 3.13, which is dominated by the forward peak of the helicity-1 non-resonant continuum. Explicitly, $B\ e^{i\delta_B}$ is given by Equation 3.21 with the values for C_J^1 and δ_J^1 from Table 3.7.

The result of the fit is shown in Figures 3.28, 3.29 and 3.30. There are 6 free parameters (A_R, a_0, a_1, a_2, a_3, and δ_A) for 85 bins: 17 energy points times 5 bins in z, from 0 to 0.125 . The resulting χ^2 is 90.5 for 79 degrees of freedom (DOF), giving $\chi^2/DOF = 1.15 \pm 0.16$. Table 3.8 reproduces the values of the parameters as determined by the fit.

As evident from Figures 3.28, 3.29, and 3.30, a_0 is the dominant term of the helicity-0 continuum, while a_1 and a_2 provide a small slope and curvature as a function of x, similarly to what is done in Equation 3.23. An indication that a_1 and a_2 can be treated as constants in the range $0 < z < 0.125$ comes from the two bottom plots in Figure 3.26. The middle-left plot in Figure 3.26 indicates that

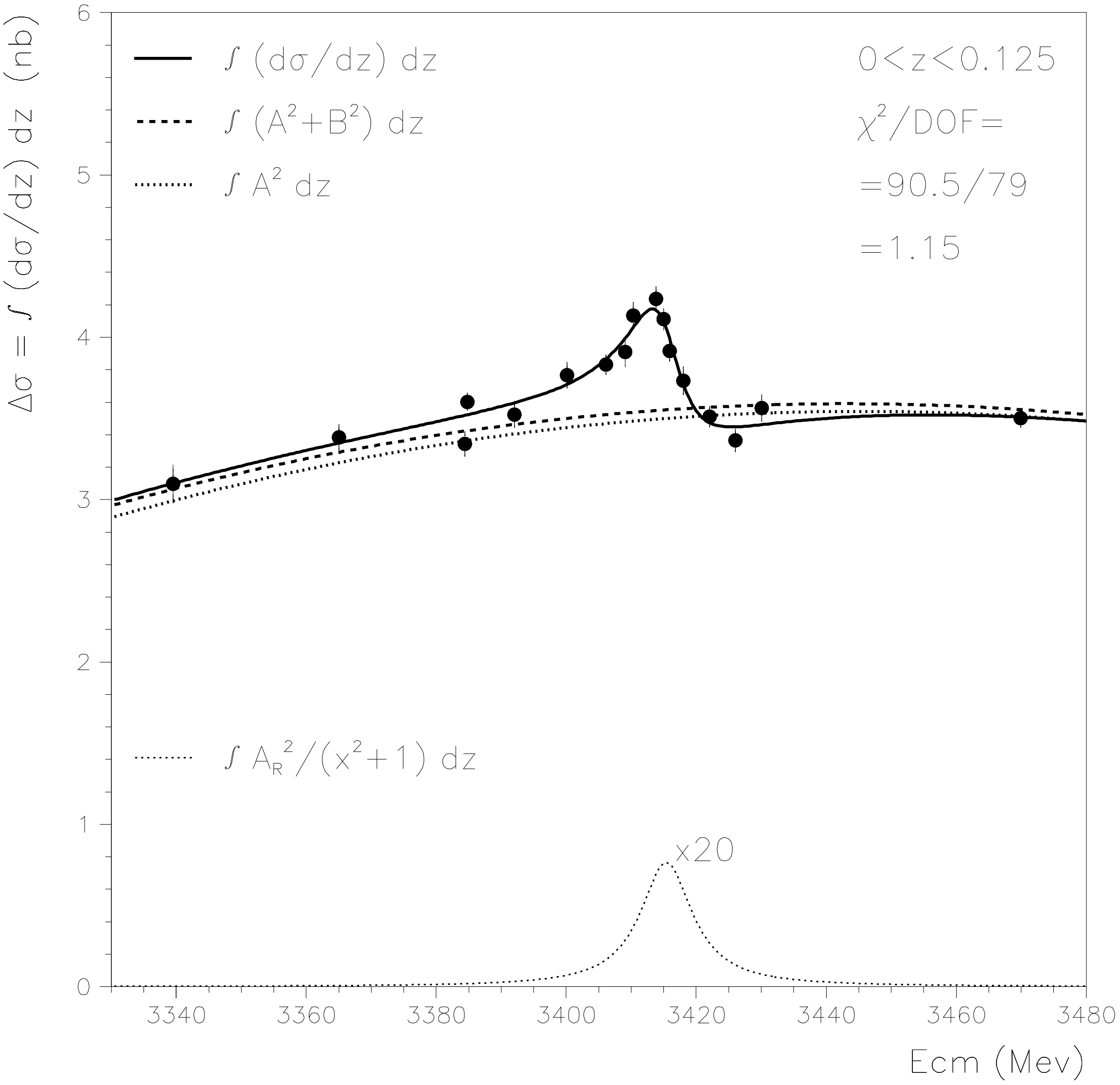

Figure 3.28: The $\bar{p}p \to \pi^0\pi^0$ cross section integrated over $0 < z < 0.125$ plotted versus E_{cm} . The fit of Equations 3.25 and 3.26 is shown along with its components. In the fit, the small contribution of $|B\ e^{i\delta_B}|^2$ is constrained to the estimate obtained in Section 3.13, and its integration corresponds to the separation between the curves $\int (A^2 + B^2)\, dz$ and $\int A^2\, dz$. The "pure" Breit Wigner curve, $\int \frac{A_R^2}{x^2+1}\, dz$, is shown multiplied by a factor 20 to make it comparable to the reshaped signal that is actually detected.

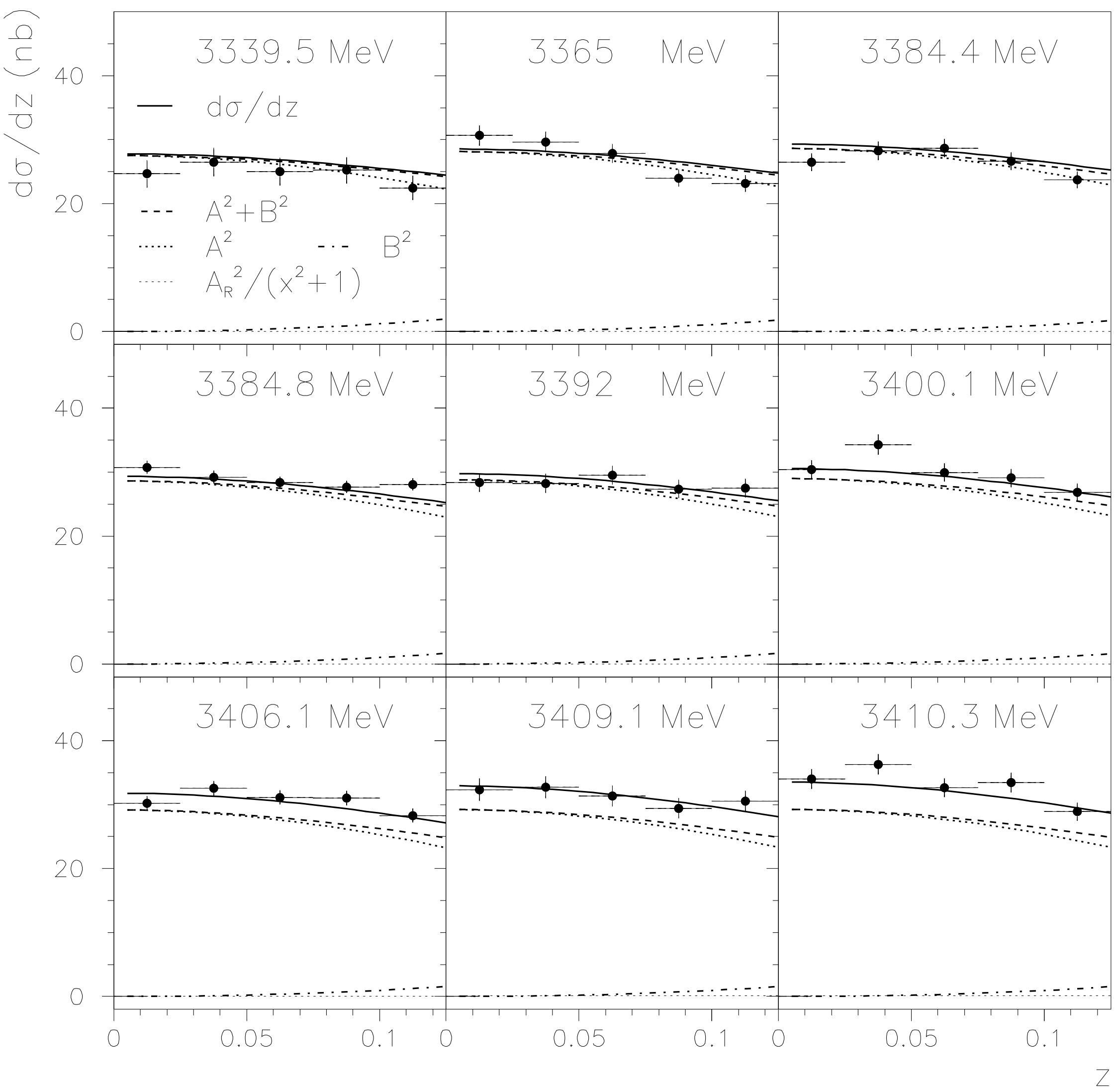

Figure 3.29: The $\bar{p}p \to \pi^0\pi^0$ differential cross section as a function of z (in the range $0 < z < 0.125$) at the E_{cm} indicated in each plot. The fit of Equations 3.25 and 3.26 is shown along with its components. In the fit, the small contribution of $|B\ e^{i\delta_B}|^2$ is constrained to the estimate obtained in Section 3.13 and corresponds to the separation between the curves A^2+B^2 and A^2. The contribution of the "pure" Breit Wigner, $\frac{A_R^2}{x^2+1}$, is relatively negligible. The difference between $d\sigma/dz$ and A^2+B^2, which is due to the interference signal, is maximum at the resonance energies.

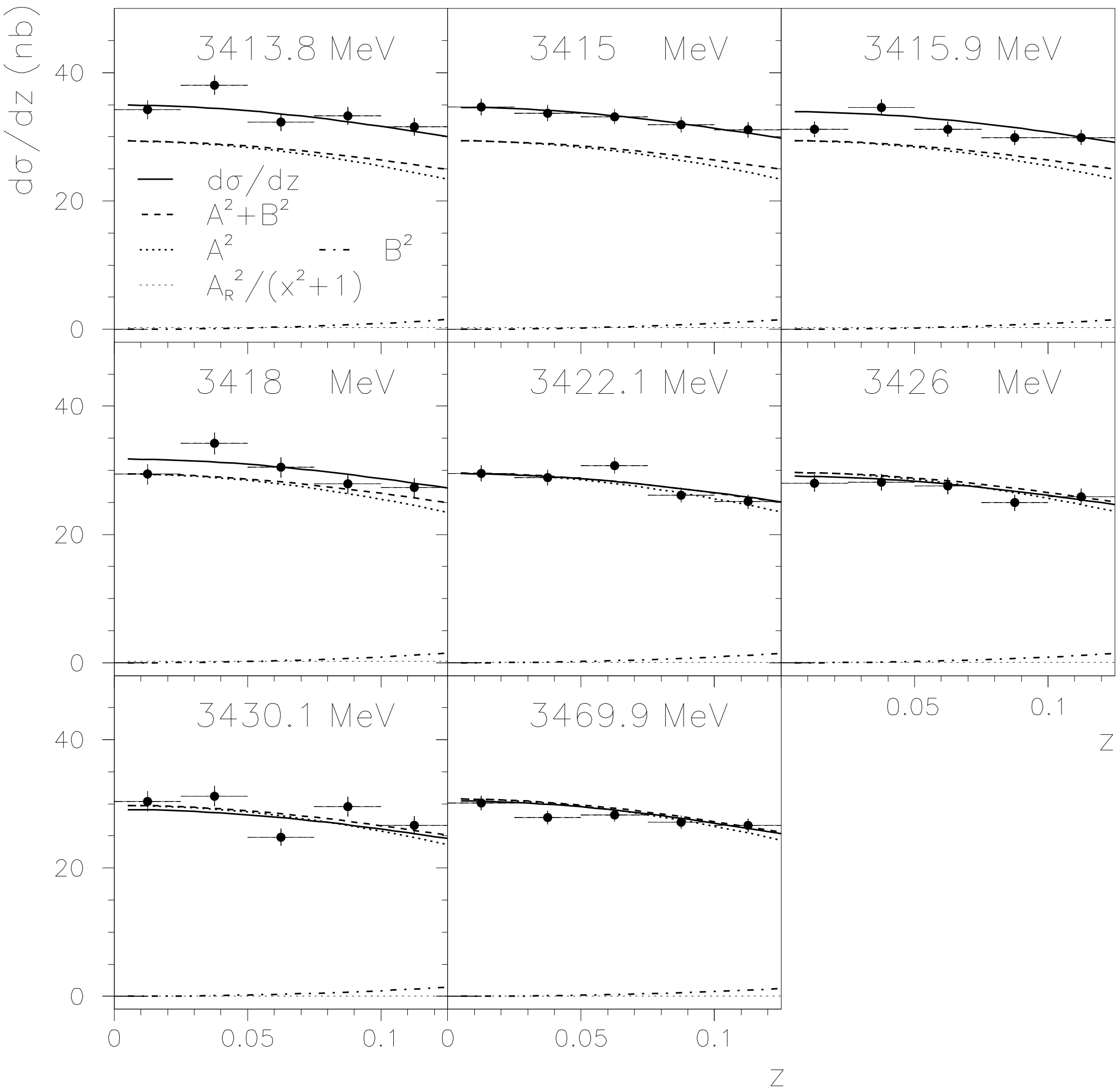

Figure 3.30: As in Figure 3.29, but at the remaining energies.

Parameter	Fit Result
A_R (nb$^{1/2}$)	0.553 ± 0.045
δ_A (degree)	39.2 ± 4.6
a_0 (nb)	29.88 ± 0.30
a_1 (nb)	0.115 ± 0.028
a_2 (nb)	-0.0095 ± 0.0031
a_3 (nb)	-365 ± 29

Table 3.8: Result from the fit to the $\bar{p}p \to \pi^0\pi^0$ cross section of Equation 3.25 and 3.26, with $|B\ e^{i\delta_B}|^2$ constrained to the estimate obtained in Section 3.13. Errors are statistical and determined by the MINOS function of the CERN package MINUIT [71].

there is a z^2 dependence in the reduced region $z \leq z_{cut} \equiv 0.125$; that dependence is accommodated by a_3.

By searching for improvements in the χ^2, it is found that the phase δ_A does not exhibit any dependence on z in this small z-range (as also indicated by the middle-right plot in Figure 3.26) nor on the energy, and that A^2 does not require additional powers of x and z, nor mixed terms such as xz^2 and x^2z^2.

It has to be stressed that the "pure" Breit-Wigner curve (the fictional cross section $\int \frac{A_R^2}{x^2+1}\,dz$ that would result if the non-resonant amplitudes could be turned off) is very small. In Figure 3.28 it is shown multiplied by a factor 20 to make its size comparable to the interference-enhanced and reshaped signal that is actually detected.

The plot of Figure 3.28 is the summation of five bins in z. The summation of the contributions of every single bin, along with the fit curves for $\Delta\sigma$, is shown in Figure 3.31.

A note on the fit of Section 3.13 . With the value of A_R determined in this section, it is now possible to perform a check on the partial wave expansion fit carried out over the range $0 < z < 0.6$ and described in Section 3.13. By re-performing that fit with A_R constrained to the value of Table 3.8, all of the other parameters do not move significantly from the values reproduced in Table 3.7.

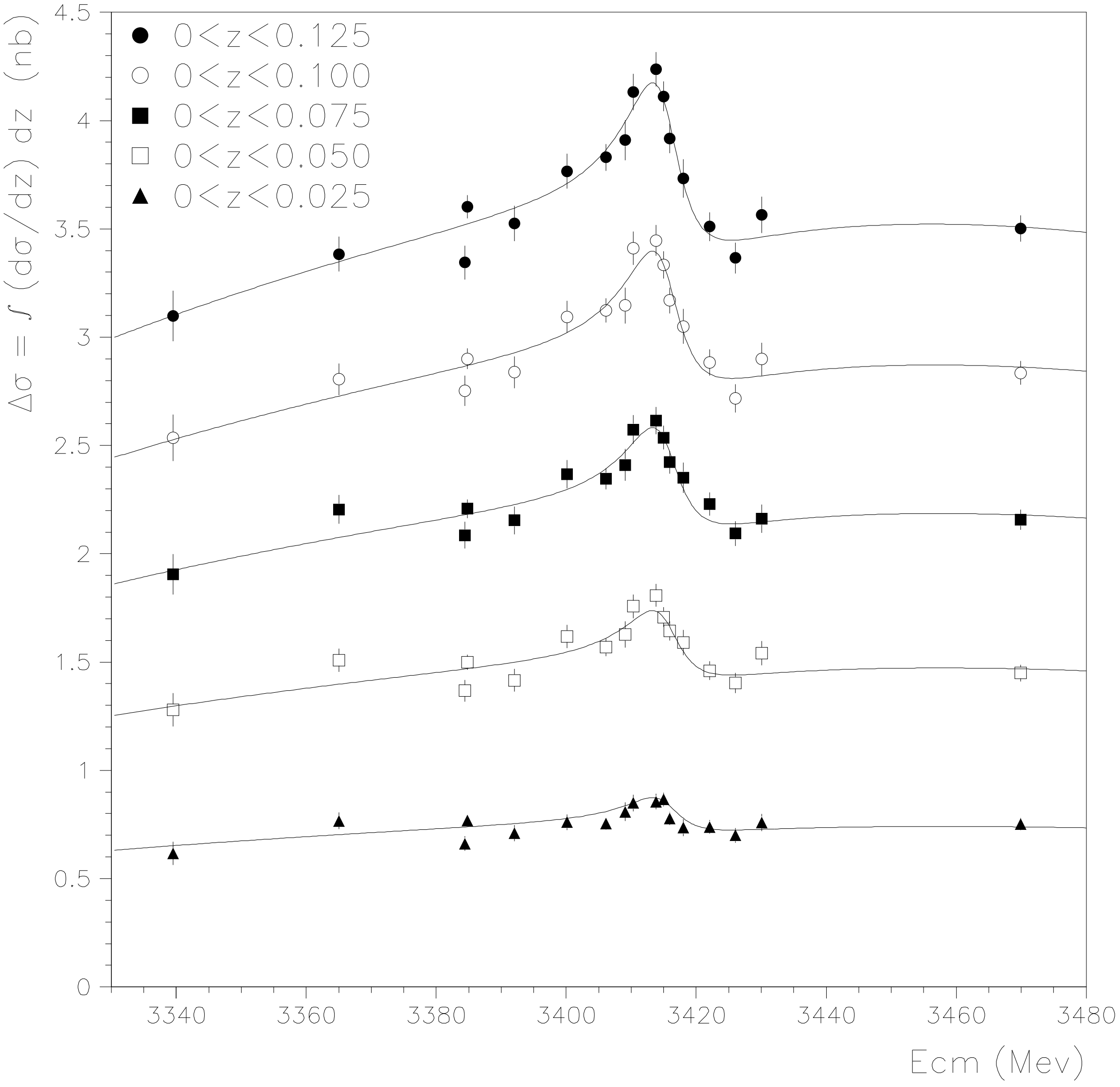

Figure 3.31: The $\bar{p}p \rightarrow \pi^0\pi^0$ cross section integrated over $0 < z < 0.125$ seen as a summation of the five bins Δz included in the range. The fit curves for $\Delta\sigma$ are also shown. The top-most points and curve coincide with the points and solid curve of Figure 3.28.

3.14.3 Result for the Product of the Branching Ratios

The value of A_R in Table 3.8 is related to the "pure" Breit-Wigner resonant cross section ($\sigma_{\bar{p}p\to\chi_{c0}\to\pi^0\pi^0}$) at $x = 0$ by

$$\left[\sigma_{\bar{p}p\to\chi_{c0}\to\pi^0\pi^0}\right]_{x=0} = \int_0^1 A_R^2\ dz = A_R^2 = (0.306 \pm 0.049_{stat})\ \text{nb}\ . \tag{3.27}$$

However, it has to be remembered that this cross section is fictitious since it cannot be measured separately from the non-resonant cross section. Only the cross section resulting from the interference between resonant and non-resonant amplitudes can be observed.

The relation between $\sigma_{\bar{p}p\to\chi_{c0}\to\pi^0\pi^0}$ and the product of the χ_{c0} input and output branching ratios is

$$\left[\sigma_{\bar{p}p\to\chi_{c0}\to\pi^0\pi^0}\right]_{x=0} = \pi\lambda\!\!\!^{-2} \times B(\chi_{c0} \to \bar{p}p) \times B(\chi_{c0} \to \pi^0\pi^0)\ , \tag{3.28}$$

where $\lambda\!\!\!^{-}$ is the center of mass De Broglie wavelength in the initial state:

$$\lambda\!\!\!^{-} = \frac{\hbar c}{\sqrt{(M_{\chi_{c0}}c^2/2)^2 - m_p^2 c^4}} \simeq 0.1383\ \text{fm}\ . \tag{3.29}$$

By combining equation 3.27 with equation 3.28 it follows

$$B(\chi_{c0} \to \bar{p}p) \times B(\chi_{c0} \to \pi^0\pi^0) = (5.09 \pm 0.81_{stat}) \times 10^{-7}\ . \tag{3.30}$$

The error is statistical. A study of the systematic errors is presented in Section 3.15.

3.15 Study of the Systematic Errors

The sources of the systematic errors affecting the product of the branching ratios $B(\chi_{c0} \to \bar{p}p) \times B(\chi_{c0} \to \pi^0\pi^0)$ are listed in Table 3.9, ordered according to sequence they enter into the data analysis.

The listed amounts are determined by modifying the measured cross section as

Source	Amount (%)
Background Subtraction	1.3
Luminosity	3
Seed Threshold	1
Cluster Threshold	1
Split Threshold	1
Event Selection	1
$\lvert B\ e^{i\delta_B}\rvert^2$	1.2
Additional terms in A^2	0.5
$M_{\chi_{c0}}$	2.5
$\Gamma_{\chi_{c0}}$	1
Total	4.9

Table 3.9: The sources of systematic uncertainty affecting $B(\chi_{c0} \to \bar{p}p) \times B(\chi_{c0} \to \pi^0\pi^0)$.

the considered source impacts it. Then, the fit of Section 3.14.2 is performed again. Finally, the new value of $B(\chi_{c0} \to \bar{p}p) \times B(\chi_{c0} \to \pi^0\pi^0)$ is compared with the one in Equation 3.30.

It has to be noticed that different sources of systematics may affect the measured cross section in different ways, such as raising or lowering it of a constant amount, and increasing or decreasing it proportionally to its value. Observing Equation 1.17 , one can realize that the impact on A_R^2, and consequently on $B(\chi_{c0} \to \bar{p}p) \times B(\chi_{c0} \to \pi^0\pi^0)$, depends on the specific way $\frac{d\sigma}{dz}$ is affected. For example, in this case where A^2 is dominant, an overestimate of $d\sigma/dz$ by a constant amount as large as 1% of a A^2 (A^2 is almost constant) produces an underestimate of A_R^2 of $\sim 1\%$. On the other hand, an overestimate of $d\sigma/dz$ by 1% of the size of $d\sigma/dz$ itself, produces an overestimate of A_R^2 of $\sim 1\%$.

The uncertainties due to the seed, cluster and split thresholds (see Section 2.3.3) are determined by varying separately each one of those thresholds by 10% of its value. Both the data selection and Monte Carlo (MC) simulation are run again, the cross section re-determined, and the fit of Section 3.14.2 re-performed.

Similar steps are applied for the uncertainty due to the event selection. Each one of the selection cuts is separately varied by 10% and applied to both MC events and real data. The cross section is then re-determined. The resulting systematics on the cross section from all cuts are summed in quadrature and the fit of Section 3.14.2 is run again.

The estimate of the uncertainty due to the imperfect knowledge of $|B\ e^{i\delta_B}|^2$ is described in Appendix C.4.

The systematics due to possible additional terms in the parameterization of equation 3.26 of A^2 is determined by adding parameters that multiply x^3, z^4, xz^2 and x^2z^2 (which, however, do not improve significantly the fit in the restricted angular range $0 < z < 0.125$) and running the fit again. The term with x^3 is basically the only responsible for the 0.5% uncertainty in Table 3.9.

The uncertainty on the knowledge of the mass and width of the χ_{c0} also affect $B(\chi_{c0} \to \bar{p}p) \times B(\chi_{c0} \to \pi^0\pi^0)$. The fit of Section 3.14.2 is re-performed with the value of the χ_{c0} mass constrained to $M_{\chi_{c0}} \pm \Delta M$, where $M_{\chi_{c0}}$ is the central value of Equation 3.15 and ΔM is the sum in quadrature of the statistical and systematic errors (the former dominates). The new values for the product of the branching ratios is compared with equation 3.30 . The same procedure is applied for the χ_{c0} width of Equation 3.16 . Even though the statistical error dominates on the systematic error in both measurements of equations 3.15 and 3.16 , the consequent uncertainty on $B(\chi_{c0} \to \bar{p}p) \times B(\chi_{c0} \to \pi^0\pi^0)$ is listed as systematic, since $M_{\chi_{c0}}$ and $\Gamma_{\chi_{c0}}$ are inputs for this analysis. This is done in compliance with the experiment tradition.

The sum in quadrature of the systematics errors listed in Table 3.9 is $\sim 4.9\%$, which corresponds to a systematic error on the product of the branching ratios of 0.25×10^{-7}.

Each time the fit is re-run to determine the above systematics on $B(\chi_{c0} \to \bar{p}p) \times B(\chi_{c0} \to \pi^0\pi^0)$, even the new value of the phase δ_A of the parameterization of equation 3.25 is compared with the one in Table 3.7. The total systematic error on δ_A is 6 degree.

3.16 Results from the $\pi^0\pi^0$ channel

The complete measurement of the product of the χ_{c0} input and output branching ratios for the $\pi^0\pi^0$ final state is

$$B(\chi_{c0} \to \bar{p}p) \times B(\chi_{c0} \to \pi^0\pi^0) = (5.09 \pm 0.81_{stat} \pm 0.25_{syst}) \times 10^{-7} \ . \qquad (3.31)$$

The measurement of the difference of phase, in the small z region (see Equation 3.25), between the helicity-0 non-resonant amplitude A and the resonant amplitude A_R is

$$\delta_A(z \simeq 0) = (39 \pm 5_{stat} \pm 6_{syst}) \text{ degree.} \qquad (3.32)$$

The above results are in agreement with another E835 data analysis of the $\pi^0\pi^0$ channel [72].

Notice that the reported value of δ_A is determined in the restricted angular region $0 < z < 0.125$, from which the notation $\delta_A(z \simeq 0)$. There are not a priori reasons for δ_A to be a constant. In fact, δ_A is the phase of a complex number defined as the summation of several terms (see Equation 1.14). Each one of these terms is itself a complex number depending on z (through the Legendre polynomials) and on x (through the coefficients $C_J(x)$ and phases $\delta_J(x)$, even though the partial wave expansion fit does not call for energy-dependence in the phases). What is experimentally observed is simply that δ_A does not exhibit a z nor x dependence in the restricted region $0 < z < 0.125$.

The phase δ_A is responsible for the interference pattern seen in the $\bar{p}p \to \pi^0\pi^0$ cross section. However, its value is probably not particularly significant from the theoretical point of view, since it is determined by the particular and local combination of the value and orientation of the several $C_J(x)\, e^{i\delta_J(x)}$ involved. The values of the single phases δ_0, δ_2, and δ_4 (reported in Table 3.7) may be more relevant. Notably, the phase δ_0 is the difference between the non-resonant ($\bar{p}p \to \pi^0\pi^0$) and resonant ($\bar{p}p \to \chi_{c0} \to \pi^0\pi^0$) processes with the same quantum number J. It may be also noticed that δ_0, δ_2, and δ_4 are not drastically different from each other.

3.16.1 Estimate of $M_{\chi_{c0}}$ and $\Gamma_{\chi_{c0}}$ Using the $\pi^0\pi^0$ Data Alone.

The measurements presented so far have been obtained with the χ_{c0} mass ($M_{\chi_{c0}}$) and width ($\Gamma_{\chi_{c0}}$) constrained to the high precision values coming from the analysis of the channel $\bar{p}p \to \chi_{c0} \to J/\psi\,\gamma,\ J/\psi \to e^+e^-$ (reported in Section 3.12).

It is worth checking the capability of the interference technique in determining $M_{\chi_{c0}}$ and $\Gamma_{\chi_{c0}}$, in addition to $B(\chi_{c0} \to \bar{p}p) \times B(\chi_{c0} \to \pi^0\pi^0)$. The fit described in Section 3.14.2 is re-performed here with $M_{\chi_{c0}}$ and $\Gamma_{\chi_{c0}}$ (embedded in the definition of x) left as free parameters [20]. The result of the new fit is shown in Figure 3.32.

The results for mass and width are

$$M_{\chi_{c0}} = 3414.7^{+0.7}_{-0.6} \pm 0.2 \text{ MeV/c}^2 \tag{3.33}$$

$$\Gamma_{\chi_{c0}} = 8.6^{+1.7}_{-1.3} \pm 0.1 \text{ MeV/c}^2 \ . \tag{3.34}$$

The product of the branching ratio becomes [21]

$$B(\chi_{c0} \to \bar{p}p) \times B(\chi_{c0} \to \pi^0\pi^0) = (5.42^{+0.91}_{-0.96} \pm 0.22) \times 10^{-7} \ . \tag{3.35}$$

The phase varies just slightly: $\delta_A = (47 \pm 10 \pm 6)$ degrees. The other fit parameters (a_0, a_1, a_2, and a_3) do not vary significantly from the values in Table 3.8.

This fit should be considered as a consistency check and is not intended to challenge the values of $M_{\chi_{c0}}$ and $\Gamma_{\chi_{c0}}$ determined using the channel $\bar{p}p \to \chi_{c0} \to J/\psi\,\gamma$, nor the value of $B(\chi_{c0} \to \bar{p}p) \times B(\chi_{c0} \to \pi^0\pi^0)$ in Equation 3.31. However, the results from this section prove that the interferometric technique developed in this dissertation is able to determine the resonance parameters without relying on external inputs. The uncertainties on $M_{\chi_{c0}}$ and $\Gamma_{\chi_{c0}}$ from the analysis of the $\pi^0\pi^0$ channel alone are larger but still comparable to those from the analysis of the

[20] The small contribution of $|B\ e^{i\delta_B}|^2$ is constrained to an estimate obtained using the partial wave expansion fit described in Section 3.13 with the difference that, again, $M_{\chi_{c0}}$ and $\Gamma_{\chi_{c0}}$ are left free to fluctuate. However, the results for the parameters of the partial wave expansion fit are basically unaltered from the case where $M_{\chi_{c0}}$ and $\Gamma_{\chi_{c0}}$ are constrained.

[21] The systematic error in equation 3.35 is slightly smaller than in equation 3.31, since the systematic errors due to $M_{\chi_{c0}}$ and $\Gamma_{\chi_{c0}}$ in Table 3.9 are no longer applicable. Of course, this decrease is more than compensated by the increased statistical error.

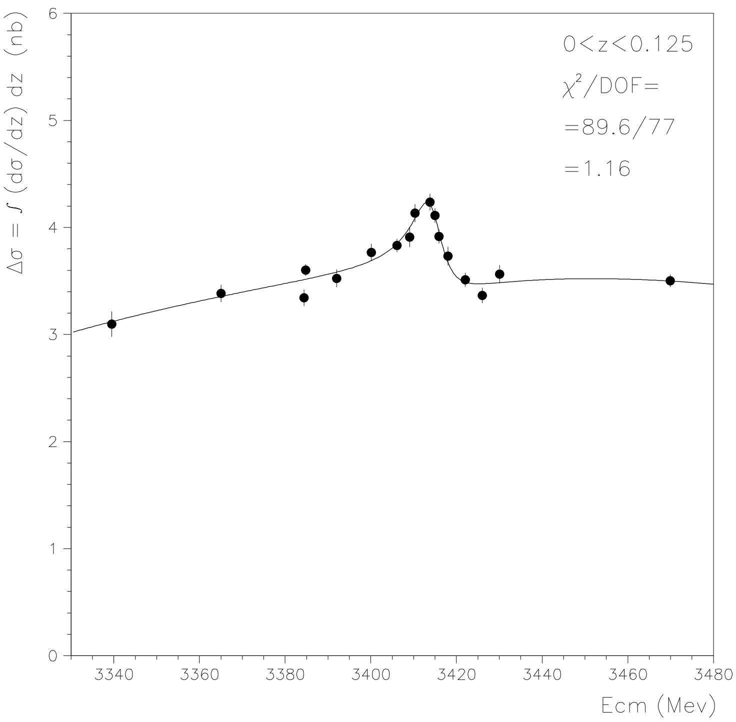

Figure 3.32: The $\bar{p}p \to \pi^0\pi^0$ cross section integrated over $0 < z < 0.125$ plotted versus E_{cm} . The fit of Equations 3.25 and 3.26 is performed with $M_{\chi_{c0}}$ and $\Gamma_{\chi_{c0}}$ as free parameters.

$J/\psi\,\gamma$ channel.

Chapter 4

The Analysis of the $\pi^0\eta$ Channel

Any charmonium state has isospin (I) equal to zero. Hence, the χ_{c0} cannot decay into the $I = 1$ channel $\pi^0\eta$ unless through an isospin violating process.

The study of the reaction $\bar{p}p \to \pi^0\eta$ is therefore useful for more reasons. First, because it provides further information on the $\bar{p}p$ interaction. Second, because the cross section should not present evidence of the χ_{c0} resonance and, consequently, serves as a control measurement for the systematics of the experiment and the data analyses. Finally, it provides a test for the correctness of the determination of the acceptance for π^0's η's, as discussed on page 162.

The characteristics of the reaction $\bar{p}p \to \pi^0\eta$ are very similar to the ones of the reaction $\bar{p}p \to \pi^0\pi^0$, and the analysis presented in this chapter is carried out following the steps described in Chapter 3 with just a few differences. Hence, the $\pi^0\eta$ analysis is presented here in a more schematic way, with frequent references to the sections of that chapter. When the differences between the two analyses are more substantial, more details are given.

4.1 Kinematics of the Reaction

The sketch in Figure 3.1 holds for the reaction $\bar{p}p \to \pi^0\eta$, as well, with an η in place of one of the two π^0s. The notations and definitions used in this chapter are similar to those used in Section 3.1, with obvious modifications when necessary. A main difference is due to the fact that here the two final state particles are distinguishable, then it is useful to define z as:

$$z \equiv \cos\theta^*_{\pi^0} \ , \tag{4.1}$$

where $\theta^*_{\pi^0}$ is the angle, in the c.m. frame, between the π^0 and the $\bar{p}$ beam axis. Hence, z is negative when the π^0 is emitted backward, in the c.m., with respect to the $\bar{p}$ beam direction.

The branching ratio of the η into $\gamma\gamma$ is $(39.43 \pm 0.26)\%$. Even though this is smaller than the one of the π^0, it still makes the η efficiently detectable. The mean decay length of the η is even shorter than the one of the π^0, making the η decay virtually point-like.

At the χ_{c0} energy, the momentum of either η or π^0 in the center of mass frame is $p^*_f \simeq 1661$ MeV (as compared to ~ 1702.4 MeV for the $\pi^0\pi^0$ case). Let us consider the case where the final state particles are emitted perpendicularly, in the c.m. frame, to the beam axis (to be compared with the middle raw in Table 3.1). The energy of the η in the laboratory frame is $E_\eta \simeq 3183$ MeV, which is slightly more than $E_{lab}/2$ given that $m_\eta > m_{\pi^0}$. The corresponding γ_η is about 5.8 which gives, using Equation 3.3, $\alpha_{min} \simeq 0.35$ rad $\simeq 20°$. A first effect of this larger opening angle, compared to the π^0 case, is that for the decay $\eta \to \gamma\gamma$ no clusters need to be split offline by the CCAL clusterizer. A second effect is that the minimum energy of the emitted photons is $E_{\gamma,min} \simeq 24$ MeV and consequently the number of photons below CCAL cluster threshold decreases to about 0.8%.

4.2 The $\pi^0\eta$ Event Topology

The data sample from which the $\pi^0\eta$ events are extracted from is the same that provides the $\pi^0\pi^0$ events (see Sections 3.2 and 3.3). Even the selection of events with four photons coincides (see Section 3.4). The accumulation of $\pi^0\eta$ events can be seen in Figure 3.4 or, enhanced by the logarithmic scale, in Figure 5.1.

The $\pi^0\eta$ event topology is determined by calculating the two two-photon invariant masses for each one of the three ways (combinations) to pair the four photons.

For each combination, a six constrain fit (6C-fit) to the hypothesis $\bar{p}p \to \pi^0\eta \to \gamma\gamma\,\gamma\gamma$ (referred to as the $\pi^0\eta$ fit) is performed associating the π^0 with the smaller invariant mass ($m_{\gamma\gamma}^{sm}$) and the η with the larger ($m_{\gamma\gamma}^{gt}$). The combination with the highest confidence level C.L. is chosen as the event topology[1].

Even in the $\pi^0\eta$ case, as in the $\pi^0\pi^0$, there is no doubt about choosing the candidate combination for the hypothesis. Only one event in the entire χ_{c0}-energy sample have two combinations that both satisfy Cuts 1 through 4 of Section 3.4 and the features of the $\pi^0\eta$ kinematics (Cuts 5 through 8 in next Section 4.3).

4.3 Selection of $\pi^0\eta$ Events

Once the $\pi^0\eta$ event topology is determined as the combination with the highest C.L. of the $\pi^0\eta$ fit, the following cuts are applied to that combination in order to select those events with the characteristics of the $\pi^0\eta$ reaction:

Cut 5. 100 MeV$< m_{\gamma\gamma}^{sm} < 185$ MeV,

Cut 6. $|m_{\gamma\gamma}^{gt} - 547.3| < 70$ MeV,

Cut 7. Akinematics $(\Delta\theta) < 14$ mrad,

Cut 8. Acoplanarity $(\Delta\phi) < 38$ mrad,

Cut 9. No invariant masses for which $|m_{\gamma\gamma} - m_{\pi^0}| < 45$ MeV in the two combinations not chosen as the event topology,

Cut 10. No successful fit (C.L.$< 10^{-5}$) to $\pi^0\pi^0 \to \gamma\gamma\,\gamma\gamma$ or $\eta\eta \to \gamma\gamma\,\gamma\gamma$ in any of the 3 combinations,

Cut 11. the event triggered the Neutral-ETOT logic.

[1]For those events in which the fit is unsuccessful for all three combinations, a nominal topology is still defined by choosing the combination with lowest $\Delta m \equiv \sqrt{(m_{\gamma\gamma}^{sm} - m_{\pi^0})^2 + (\frac{m_{\gamma\gamma}^{gt} - m_\eta}{2.5})^2}$, where $m_{\gamma\gamma}^{sm} < m_{\gamma\gamma}^{gt}$.

The above cuts are analogous to those used for the $\pi^0\pi^0$ event selection, described in Section 3.6, with a few differences explained as follows.

Cut 6 is symmetric about the mass of the η. The asymmetry about the π^0 mass introduced[2] in cut 5 is not necessary for the $\eta \to \gamma\gamma$ decay. The η mass is larger and makes the directions of the two photons sufficiently divergent for CCAL to be always able to separate them.

In cut 7, the variable named "akinematics" is defined as

$$\Delta\theta \equiv \theta_{\pi^0,meas} - \theta_{\pi^0,calc}\,, \tag{4.2}$$

where $\theta_{\pi^0,meas}$ is the measured azimuthal angle of the π^0, while $\theta_{\pi^0,calc}$ is the value of the same quantity calculated by assuming $\pi^0\eta$ kinematics and using the measured azimuthal angle of the η. In cut 8, the "acoplanarity" is defined as π minus the difference between the measured polar angles of the π^0 and η:

$$\Delta\phi \equiv \pi - (\phi_{\pi^0,meas} - \phi_{\eta,meas})\,. \tag{4.3}$$

Cut 11 restricts the data sample to those events that satisfied the Neutral-ETOT trigger (see Section 4.6).

The number of events surviving the $\pi^0\eta$ event selection (cuts 1 through 11) is 113,061 .

Figures 4.1 and 4.2 show the variables involved in the most relevant cuts for data and MC simulation at one, $E_{cm} = 3415.9$ MeV, of the 17 energy point. The arrows indicates the boundaries of acceptance of the cuts. Each variable is shown after applying all cuts with the exception of the cut involving the variable itself.

Figure 4.3 shows the C.L. of the 6-C fit to $\bar{p}p \to \pi^0\eta \to \gamma\gamma\,\gamma\gamma$ for those events that have passed the selection. This C.L. is only used to determine the event topology, as described in section 4.2; no cuts are applied on it, so that the instrumental background can be estimated and subtracted using the technique described

[2]When the two photons from a π^0 decay are too close to each other to be resolved, they are split offline by the CCAL clusterizer. In that process, a slight over-estimation of the invariant mass occurs (see Section 3.6 and page 57 for more details.)

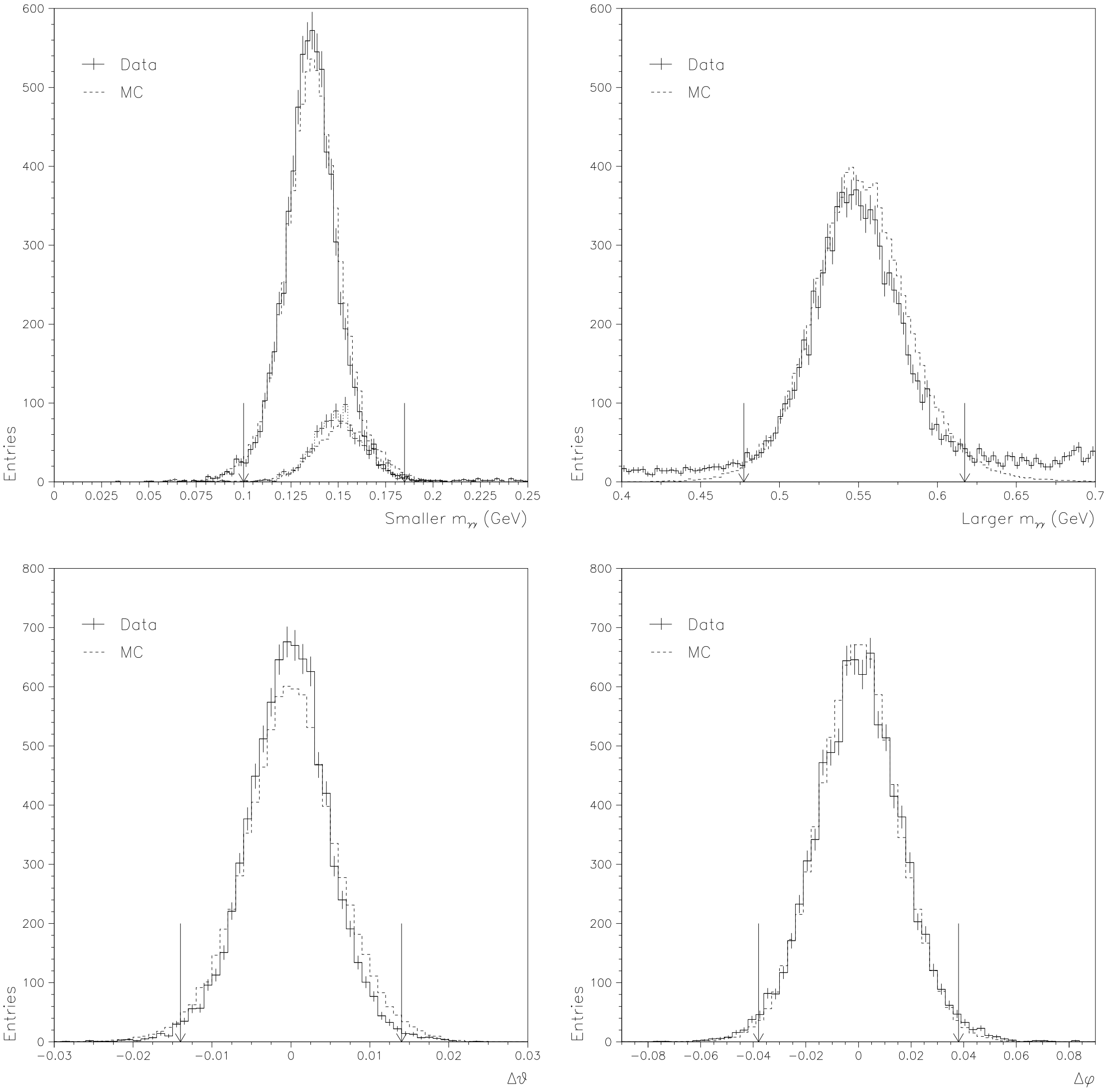

Figure 4.1: Variables involved in the $\pi^0\eta$ selection. Arrows indicate where the cuts are applied. Each variable is plotted after applying all of the other cuts. $E_{cm} = 3415.9$ MeV. Top left: the smaller invariant mass (Cut 5), where the smaller peak is made by the split clusters (for which the CCAL clusterizer slightly overestimate the invariant mass); top right: the larger invariant mass (Cut 6), the two photons from the η are always resolved and no clusters need to be split offline; bottom left: the akinematics (Cut 7); bottom right: the acoplanarity (Cut 8).

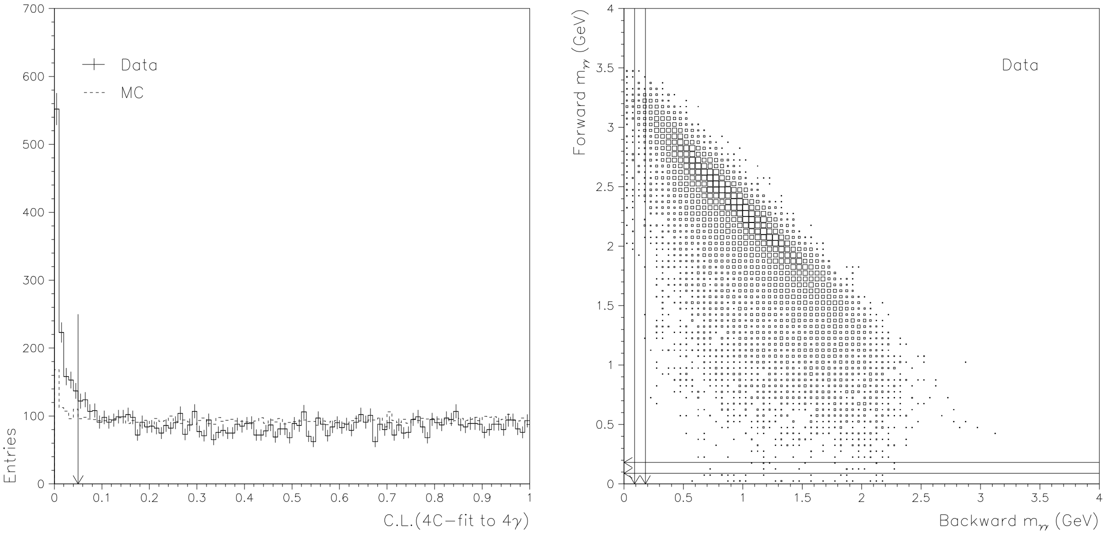

Figure 4.2: Variables involved in the $\pi^0\eta$ selection. Arrows indicate where the cuts are applied. Each variable is plotted after applying all of the other cuts. $E_{cm} = 3415.9$ MeV. Left: Confidence Level of the 4C-fit to $\bar{p}p \to \gamma\gamma\,\gamma\gamma$ (Cut 4); right: scatter plot of the invariant masses of the two combinations not chosen as the event topology (Cut 9).

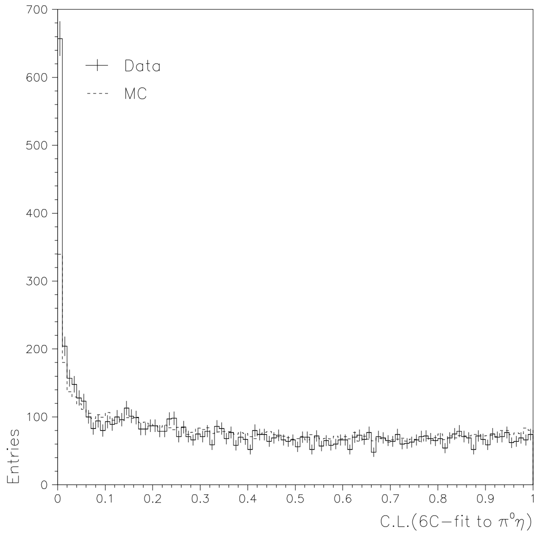

Figure 4.3: Confidence Level of the 6C-fit to $\bar{p}p \to \pi^0\eta \to \gamma\gamma\,\gamma\gamma$; no cuts are applied to this variable. $E_{cm} = 3415.9$ MeV.

in Section 4.5.

Figure 4.4 shows the region of the $\pi^0\eta$ peak in the invariant mass LEGO plot after all cuts are applied except the ones on the invariant masses.

4.4 Detector Acceptance and Selection Efficiency

The acceptance of the detector and efficiency of the $\pi^0\eta$ selection are determined analogously to the way described in Section 3.7 for the $\pi^0\pi^0$ analysis.

Figure 4.5 shows the product of the acceptance and efficiency, $a \times \epsilon$, for the several cuts as a function of the bins in z.

Given that the two final state particle are distinguishable, it is useful to discriminate between the case when the π^0 is emitted in the forward or the backward direction with respect (in the c.m. frame) to the $\bar{p}$ beam. The variable z is defined by Equation 4.1 with this purpose.

Correction for the limited polar angle resolution. It will be shown in Section 4.7 that the $\pi^0\eta$ channel has a differential cross section with more pronounced structures (in the E835 acceptance range) than the $\pi^0\pi^0$ channel. This makes the effect of the limited polar angle resolution more significant for $\pi^0\eta$ events (such an effect is referred to as event migration from a bin in z to another). The event migration is discussed in Appendix B.

The Event Pileup. The event pileup is discussed in detail in Section 3.8 for the $\pi^0\pi^0$ channel. The pileup corrections to the efficiency for the $\pi^0\eta$ channel are determined following the same procedure thereby described. Such rate-dependent corrections are almost independent on the particular final state. The probability that a $\pi^0\eta$ event is lost due to the pileup is on average 80.3%, with fluctuations from energy point to energy point from 76.2% to 86.4%.

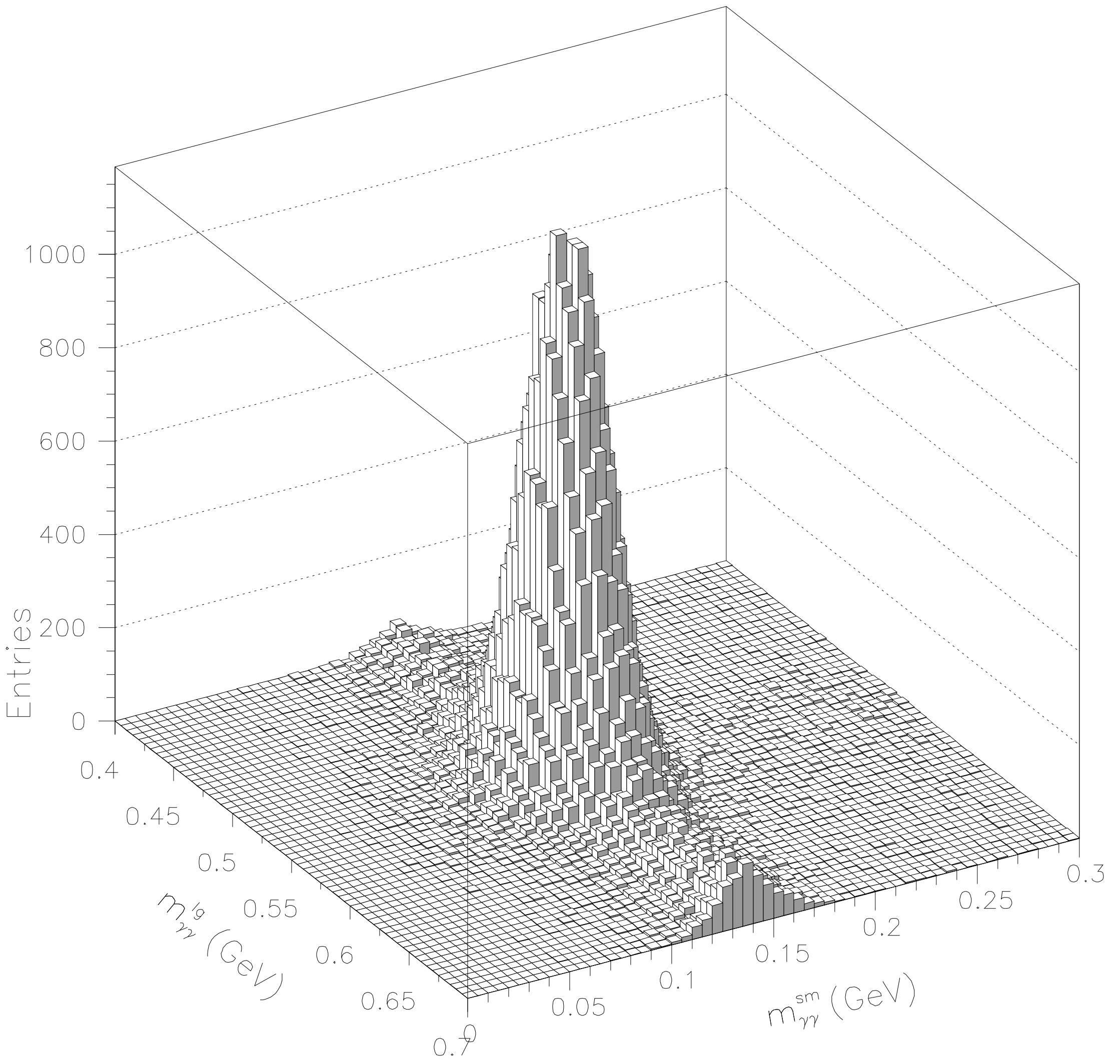

Figure 4.4: The region of the $\pi^0\eta$ peak in the LEGO plot of the smaller versus the larger invariant mass for the combination chosen as the event topology; all $\pi^0\eta$ cuts are applied except the ones on the invariant masses themselves (Cuts 5 and 6). The events from all 17 energy points are merged in this plot.

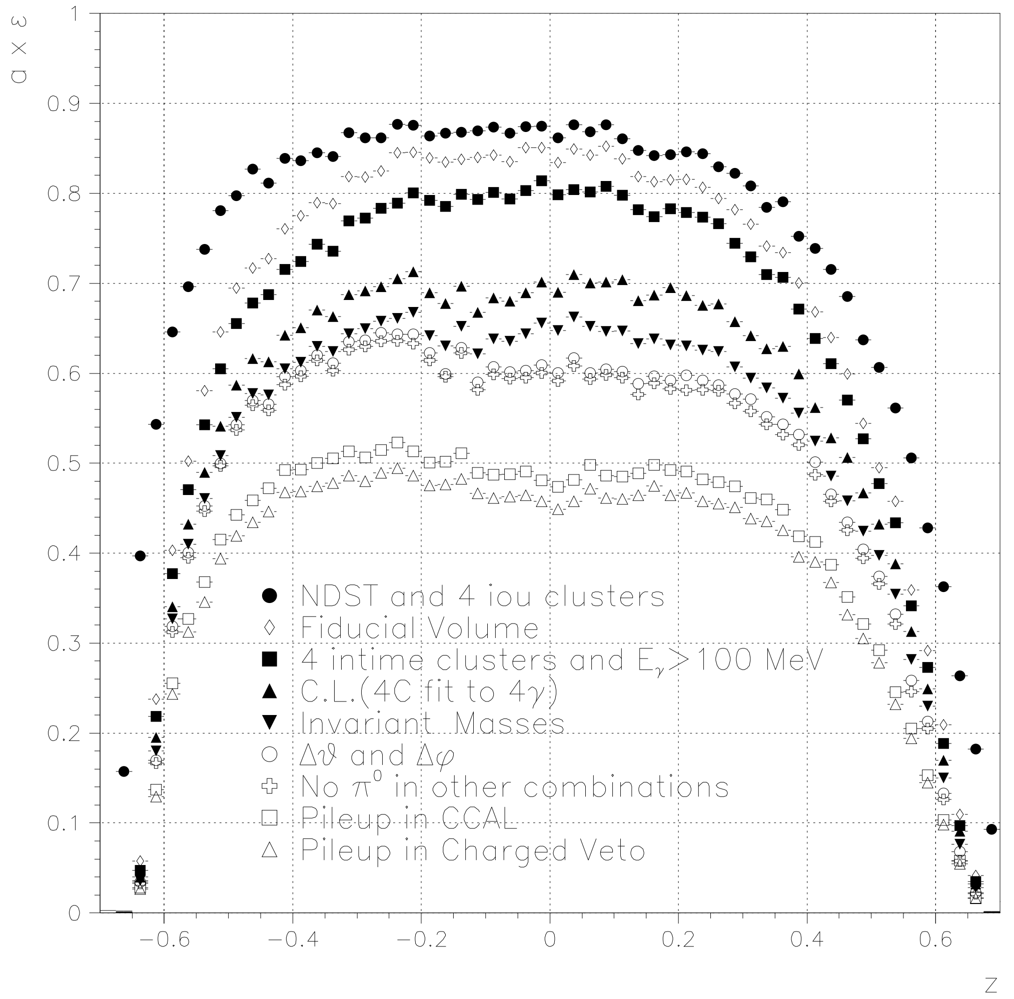

Figure 4.5: The product of the detector acceptance and selection efficiency, $a \times \epsilon$, for $\pi^0\eta$ events as a function of $z \equiv \cos\theta^*_{\pi^0}$ at $E_{cm} = 3415.9$ MeV. Here, the MC events are generated with a uniform angular distribution. Each cut shown, or group of cuts, is applied on top of the ones previously indicated. "NDST and 4 iou clusters" is the selection of the initial data sample: four in-time or undetermined clusters (iou) and the NDST cuts (page 81). "Fiducial volume": Cut 2 (page 82). "4 in-time clusters and $E_\gamma > 100$ MeV": Cut 1 and 3. "C.L.(4C fit to 4γ)": Cut 4. "Invariant Masses": Cut 5 and 6 (page 142). "$\Delta\theta$ and $\Delta\phi$": Cut 7 and 8. "No π^0 in other combinations": Cut 9. The two lower-most symbols represent the estimated fraction of $\pi^0\eta$ events surviving the contamination due to event pileup (see page 146).

4.5 The Background

The background is determined by fitting the scatter plot of the two invariant masses in the region of the $\pi^0\eta$ accumulation (see Figure 4.4) analogously to the way described in Section 3.9.

Even here, as in the $\pi^0\pi^0$ case, the background takes the form of two berms. The berm along the line $m^{sm}_{\gamma\gamma} = m_{\pi^0}$ is more copious than the berm along $m^{lg}_{\gamma\gamma} = m_\eta$. An even less copious, more or less uniform substrate is also present.

The amount of background is determined independently for each bin of z. The function used in the negative-log-likelihood fit of the scatter plot is:

$$f(m^{lg}_{\gamma\gamma}, m^{sm}_{\gamma\gamma}) = \underbrace{\frac{A}{\sigma_{\pi^0}\,\sigma_\eta}\; exp\Big[-\frac{(m^{lg}_{\gamma\gamma}-m_\eta)^2}{2\sigma^2_\eta} - \frac{(m^{sm}_{\gamma\gamma}-m_{\pi^0})^2}{2\sigma^2_{\pi^0}}\Big]}_{\pi^0\eta-signal} +$$

$$\underbrace{+\underbrace{\frac{B}{\sigma_\eta}\; exp\Big[-\frac{(m^{lg}_{\gamma\gamma}-m_\eta)^2}{2\sigma^2_\eta}\Big] + \frac{C}{\sigma_{\pi^0}}\; exp\Big[-\frac{(m^{sm}_{\gamma\gamma}-m_{\pi^0})^2}{2\sigma^2_{\pi^0}}\Big]}_{Berms} + \underbrace{D}_{Plane}}_{background} \tag{4.4}$$

where A, B, C and D are free parameters, while σ_{π^0} and σ_η are fixed to 15 and 30 MeV. The fit is performed over the area defined by $|m^{lg}_{\gamma\gamma} - m_\eta|$ <140 MeV and 50 MeV< $m^{sm}_{\gamma\gamma}$ <300 MeV.

Figure 4.6 shows the entries in the scatter plot at E_{cm} = 3415.9 MeV, the function $f(m^{lg}_{\gamma\gamma}, m^{sm}_{\gamma\gamma})$ as resulted from the fit, and their magnified versions. In the magnified plot of the fit, the underlying contribution of the berms and the plane is also represented. The integral of the berms and the plane over the region selected by the invariant mass cuts (cuts 5 and 6 in section 4.3) is taken as an estimate of the background in the bin.

Table 4.1 reports the values of the fit parameters (A, B, and C; while the contribute from the plane is very small and D is omitted from the table) for the bins of the energy point E_{cm} = 3415.9 MeV. The associated background (in the column "Unbound Bkg") and the total number of entries at the $\pi^0\eta$ peak are also

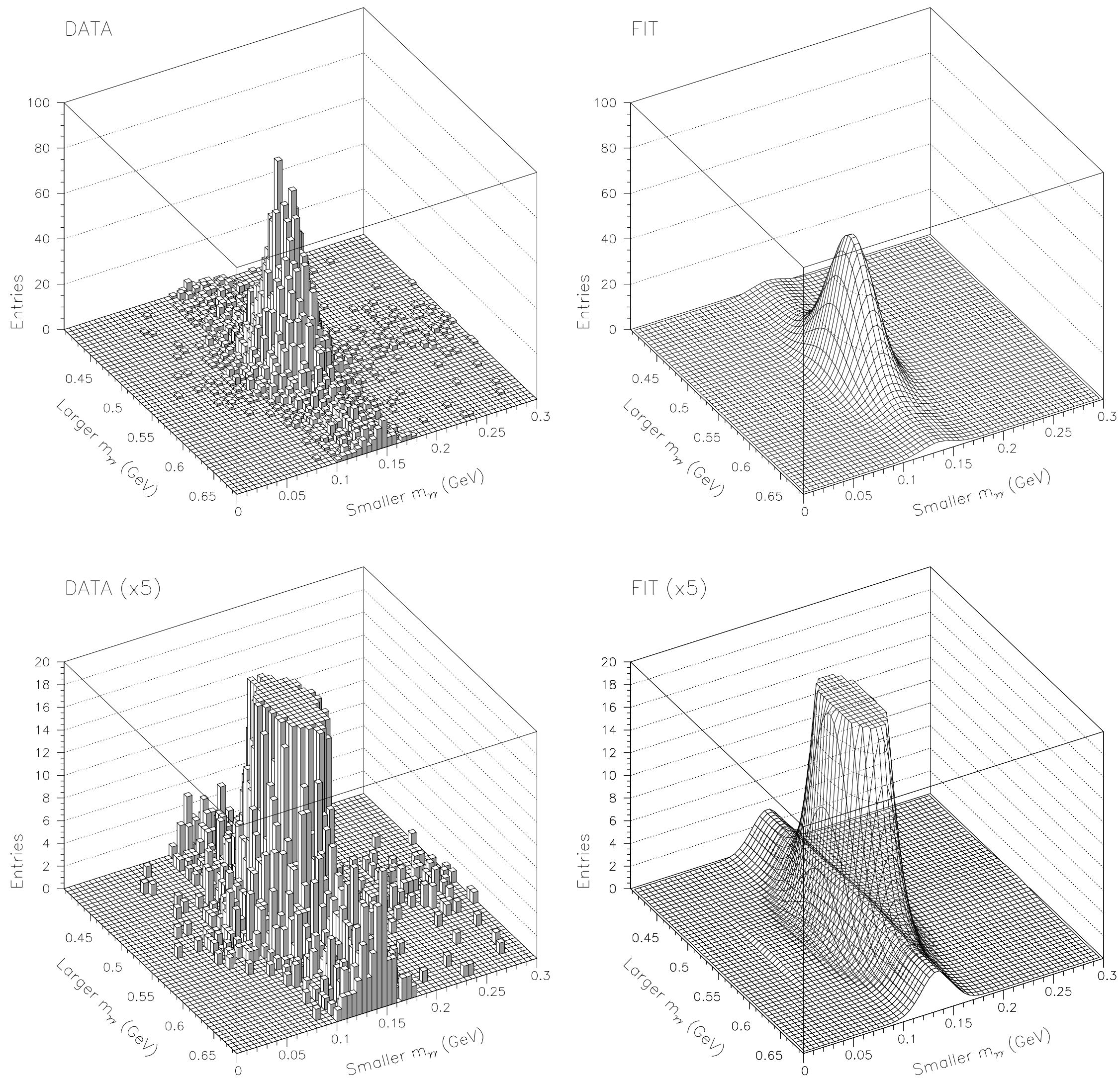

Figure 4.6: Top left: the LEGO plot of the smaller versus the larger invariant mass at $E_{cm} = 3415.9$ MeV. All $\pi^0\eta$ cuts are applied except those on the invariant masses themselves. Top right: the fit parameterization of the top left plot. Bottom left: magnification of top left plot. Bottom right: magnification of top right plot, where the underlying background contribution (berms+plane) is made visible.

given.

To bind the overall background information, the background estimates of all bins of an energy point are then fitted with an eight-degree polynomial as a function of z, as shown in Figure 4.7. The value of the resulting polynomial at the center of

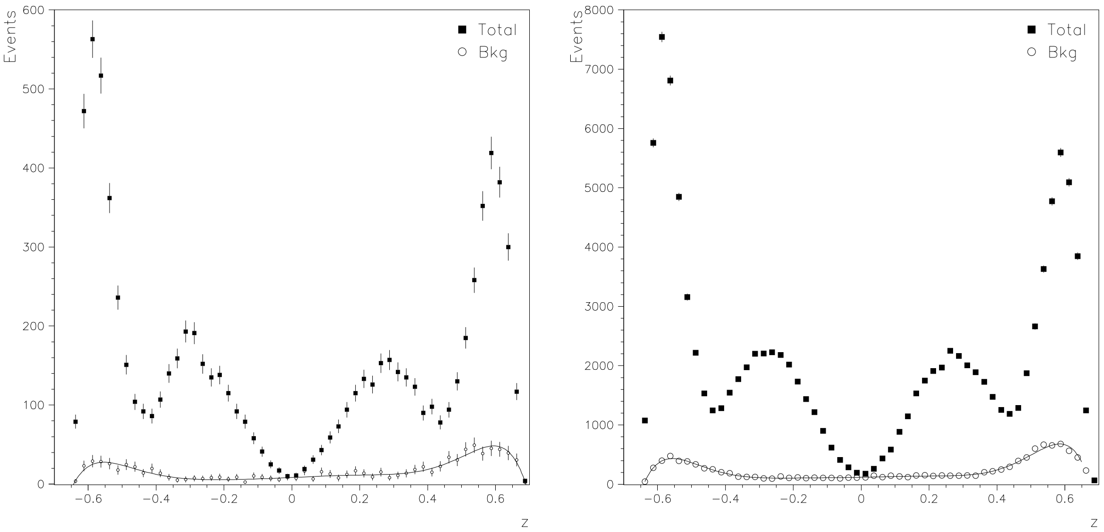

Figure 4.7: Left: At $E_{cm} = 3415.9$ MeV, the number of $\pi^0\eta$ candidate events (indicated as Total) and the estimated instrumental background events (Bkg) as a function of z. An eight-degree polynomial fit is used to reduce the fluctuations. Right: As in left plot, but merging all 17 energy points to give an overview of the entire data sample. (The fall in the number of events at $|z| \gtrsim 0.6$ is an effect of the acceptance, since here the data are not acceptance-corrected.)

each bin is assumed to be the background of the bin and and is reported in column "Bound Bkg" in the table. Then, this background is subtracted from the total entries in the $\pi^0\eta$ peak to obtain the bin content of $\pi^0\eta$ events. The uncertainty on the number of $\pi^0\eta$ events in the bin is conservatively taken as the square root of the entries in the peak before subtracting the background.

In the range $-0.6 < z < 0.6$ at $E_{cm} = 3415.9$ MeV, the background constitutes $\sim 11\%$ of the $\pi^0\eta$ candidate events. Appendix D.2 provides a plot (Figure D.6)

z	$A/(\sigma_\eta\sigma_{\pi^0})$ $\left(\frac{\text{Evts}}{25\ \text{MeV}^2}\right)$	$10^3 \cdot B/\sigma_\eta$ $\left(\frac{\text{Evts}}{25\ \text{MeV}^2}\right)$	C/σ_{π^0} $\left(\frac{\text{Evts}}{25\ \text{MeV}^2}\right)$	Unbound/Bound Bkg (Evts)	Peak (Evts)
-0.5875	4.90±0.22	12.2±5.8	0.125±0.026	29.1±7.8 / 25.4±7.8	563±24
-0.5625	4.49±0.21	12.9±5.6	0.121±0.025	28.4±7.6 / 27.8±7.6	517±23
-0.5375	3.08±0.18	12.2±5.8	0.109±0.023	25.9±7.2 / 27.4±7.2	362±19
-0.5125	2.02±0.14	5.8±4.8	0.076±0.020	17.8±6.0 / 25.2±6.0	236±15
-0.4875	1.18±0.12	5.2±3.6	0.111±0.022	24.5±6.8 / 22.2±6.8	151±12
-0.4625	0.74±0.10	10.0±4.3	0.093±0.020	21.9±6.4 / 19.0±6.4	104±10
-0.4375	0.72±0.09	14.7±5.2	0.049±0.016	13.9±5.2 / 16.0±5.2	92±10
-0.4125	0.63±0.09	4.3±3.0	0.089±0.020	19.7±6.1 / 13.3±6.1	86± 9
-0.3875	0.86±0.10	9.3±4.9	0.055±0.016	13.8±5.1 / 11.0±5.1	107±10
-0.3625	1.21±0.11	0.0±0.0	0.039±0.014	8.5±4.2 / 9.3±4.2	140±12
-0.3375	1.38±0.11	1.9±3.4	0.019±0.010	4.9±3.2 / 8.0±3.2	159±13
-0.3125	1.68±0.13	6.5±5.8	0.017±0.012	6.0±3.8 / 7.0±3.8	193±14
-0.2875	1.67±0.13	1.0±2.1	0.034±0.013	7.3±3.8 / 6.4±3.8	191±14
-0.2625	1.30±0.11	6.3±3.9	0.025±0.011	6.8±3.6 / 6.0±3.6	152±12
-0.2375	1.16±0.11	3.8±4.3	0.032±0.013	8.1±4.1 / 5.8±4.1	135±12
-0.2125	1.16±0.11	14.5±7.5	0.024±0.012	8.8±4.3 / 5.7±4.3	138±12
-0.1875	1.00±0.10	6.5±4.2	0.022±0.010	6.1±3.4 / 5.7±3.4	115±11
-0.1625	0.76±0.09	8.5±4.5	0.031±0.011	8.8±4.0 / 5.8±4.0	92±10
-0.1375	0.69±0.08	7.2±4.3	0.004±0.005	2.5±2.1 / 6.0±2.1	79± 9
-0.1125	0.42±0.07	11.2±5.8	0.034±0.012	10.3±4.4 / 6.3±4.4	58± 8
-0.0875	0.32±0.06	9.6±4.2	0.030±0.012	8.7±4.0 / 6.6±4.0	41± 6
-0.0625	0.16±0.05	4.1±3.8	0.027±0.012	7.1±3.7 / 7.0±3.7	25± 5
-0.0375	0.09±0.04	7.4±3.8	0.019±0.009	5.7±3.2 / 7.5±3.2	17± 4
-0.0125	0.02±0.03	8.8±4.4	0.030±0.011	8.4±3.8 / 8.0±3.8	10± 3
0.0125	0.04±0.03	0.0±0.0	0.036±0.012	7.4±3.7 / 8.5±3.7	11± 3
0.0375	0.02±0.04	6.2±3.9	0.071±0.017	16.6±5.4 / 9.0±5.4	19± 4
0.0625	0.22±0.05	0.0±0.0	0.028±0.012	6.4±3.6 / 9.6±3.6	31± 6
0.0875	0.25±0.07	8.8±4.5	0.064±0.016	15.5±5.3 / 10.1±5.3	43± 7
0.1125	0.42±0.07	1.8±1.8	0.059±0.017	12.8±5.0 / 10.6±5.0	59± 8
0.1375	0.59±0.08	1.0±3.9	0.029±0.015	7.7±4.2 / 11.0±4.2	73± 9
0.1625	0.73±0.09	11.8±5.5	0.045±0.014	12.3±4.8 / 11.3±4.8	94±10
0.1875	0.88±0.10	10.7±5.8	0.068±0.018	16.8±5.7 / 11.5±5.7	115±11
0.2125	1.07±0.11	8.3±4.8	0.054±0.016	13.6±5.2 / 11.6±5.2	133±12
0.2375	1.08±0.11	0.9±2.6	0.040±0.015	9.0±4.3 / 11.7±4.3	126±11
0.2625	1.27±0.12	16.2±6.6	0.053±0.016	15.2±5.4 / 11.9±5.4	153±12
0.2875	1.34±0.12	7.7±4.9	0.029±0.012	8.2±4.0 / 12.1±4.0	157±13
0.3125	1.19±0.11	1.9±2.6	0.051±0.016	11.0±4.7 / 12.6±4.7	142±12
0.3375	1.08±0.11	9.3±5.2	0.054±0.016	13.6±5.1 / 13.5±5.1	135±12
0.3625	0.95±0.11	3.3±4.2	0.083±0.019	18.4±6.0 / 14.8±6.0	123±11
0.3875	0.63±0.09	5.4±3.4	0.099±0.021	22.0±6.5 / 16.9±6.5	90± 9
0.4125	0.76±0.10	2.2±2.1	0.070±0.018	15.1±5.4 / 19.6±5.4	98±10
0.4375	0.53±0.09	2.9±3.6	0.101±0.021	22.5±6.6 / 23.2±6.6	78± 9
0.4625	0.55±0.09	8.1±4.0	0.153±0.025	34.0±7.9 / 27.5±7.9	94±10
0.4875	0.92±0.11	7.7±4.8	0.133±0.025	30.5±7.7 / 32.5±7.7	130±11
0.5125	1.30±0.13	8.3±4.0	0.201±0.030	44.0±9.1 / 37.9±9.1	185±14
0.5375	1.93±0.15	1.3±2.2	0.233±0.033	49.2±9.8 / 43.0±9.8	258±16
0.5625	2.88±0.18	3.5±3.7	0.177±0.030	38.5±8.8 / 46.9±8.8	352±19
0.5875	3.44±0.20	0.0±0.0	0.216±0.033	45.1±9.7 / 48.4±9.7	419±20

Table 4.1: Results from the fit to the scatter plot in each bin Δz (see text).

where the estimated background is plotted versus the energy in the center of mass.

4.6 NDST and Trigger Efficiencies

The Neutral Data Summary Tape efficiency for $\pi^0\eta$ events is determined using the same procedure described in Section 3.10 for $\pi^0\pi^0$, and is reported in Table 4.2. Even for the $\pi^0\eta$ channel, the NDST efficiency is always larger than 99%.

Energy (MeV)	ϵ_{NDST} (%)	ϵ_{ETOT} (%)	ϵ_{trig} (%)
3339.5	99.14±0.38	98.68 ±0.22	94.87 ±0.22
3365.0	99.30±0.35	98.37 ±0.17	94.56 ±0.16
3384.4	99.76±0.24	98.75 ±0.15	94.91 ±0.15
3384.8	99.42±0.29	99.38 ±0.07	95.52 ±0.07
3392.0	99.82±0.18	98.43 ±0.17	94.61 ±0.17
3400.1	99.61±0.27	98.09 ±0.18	94.29 ±0.18
3406.1	99.63±0.26	98.85 ±0.11	95.01 ±0.11
3409.1	99.33±0.33	98.55 ±0.18	94.72 ±0.18
3410.3	99.32±0.39	98.67 ±0.15	94.84 ±0.15
3413.8	99.33±0.39	98.21 ±0.17	94.39 ±0.17
3415.0	99.75±0.25	98.92 ±0.12	95.07 ±0.12
3415.9	100.00−0.23	98.93 ±0.11	95.09 ±0.11
3418.0	99.39±0.35	99.11 ±0.14	95.25 ±0.14
3422.1	99.42±0.33	97.81 ±0.17	94.01 ±0.17
3426.0	99.78±0.22	98.88 ±0.14	95.03 ±0.14
3430.1	99.17±0.41	97.88 ±0.22	94.07 ±0.22
3469.9	100.00−0.28	99.05 ±0.11	95.18 ±0.11

Table 4.2: The NDST efficiency (ϵ_{NDST}), along with the Neutral-ETOT (ϵ_{ETOT}) trigger efficiency of each energy point. The overall trigger efficiency (ϵ_{trig}) is decreased by those events that are re-directed toward study triggers.

Given the larger opening angle of the two photons from an η (as compared to those from a π^0), the two-body trigger Neutral-PBG1 is less efficacious and reliable in detecting $\pi^0\eta$ than $\pi^0\pi^0$ events. Its efficiency, ϵ_{PBG1}, is decreased to an average of 94.4% as compared to the efficiency in Table 3.5 for $\pi^0\pi^0$ events. On the other hand, the efficiency of Neutral-ETOT is slightly increased. In the entire sample of events that passed cuts 1 through 4 on page 82 and the $\pi^0\eta$ cuts 5 through 10 on page 4.3, only 1,417 events (1.2%) have triggered Neutral-PBG1 alone; 6,400 events (5.6%) have triggered Neutral-ETOT alone; and 106,661 events (93.2%) have triggered both. Consequently, the simplifying choice of using only the sample that triggered Neutral-ETOT (or both) is made (cut 11 on page 142).

The efficiency of Neutral-ETOT, ϵ_{ETOT}, is determined as done for the $\pi^0\pi^0$ case. Considering the fraction of events redirected toward study triggers, the overall trigger efficiency is

$$\epsilon_{trig} \simeq (0.99)^3\, \epsilon_{ETOT} \left[f_{\overline{PBG1}\cap ETOT} + 0.99\, f_{PBG1\cap ETOT} \right], \tag{4.5}$$

where the involved quantities are described in Section 3.10. The efficiencies ϵ_{ETOT} and ϵ_{trig} for every energy point are reported in Table 4.2.

Photon Conversion Probability. The probability that one or more photon conversions into e^+e^- cause the loss of a 4-photon event is described in Section 3.10.1.

4.7 The $\pi^0\eta$ Cross Section

The $\bar{p}p \to \pi^0\eta$ differential cross section, $d\sigma/dz$, is calculated in every bin of z as

$$\frac{d\sigma}{dz} = \frac{N_{\pi^0\eta}}{\mathcal{L}\times\ a\times\epsilon\ \times\epsilon_{trig}\times P_{reject}\times B(\pi^0\to\gamma\gamma)\times B(\eta\to\gamma\gamma)\times\Delta z}\ , \tag{4.6}$$

where $N_{\pi^0\eta}$ is the number of events passing the $\pi^0\eta$ selection and falling in the bin minus the estimated number of instrumental background events in that bin, $\mathcal{L}$ is the luminosity of the energy point (see Table 3.2), $a\times\epsilon$ is the product of the acceptance and efficiency (see Section 4.4) corrected for polar angle resolution and pileup (see page 146), ϵ_{trig} is the overall trigger efficiency (see Table 4.2), P_{reject} is the probability of event rejection due to photon conversions into e^+e^- pair (see Equation 3.13), $B(\pi^0\to\gamma\gamma) = (98.798\pm0.032)\%$, $B(\eta\to\gamma\gamma) = (39.43\pm0.26)\%$, and $\Delta z = 0.025$ is the bin width.

The series of tables, one for every energy point, with the bin-dependent quantities necessary to calculate the differential cross section is located in Appendix G.

Figure 4.8 shows the $\bar{p}p \to \pi^0\eta$ differential cross section for the energy point at $E_{cm} = 3415.9$ MeV. The complete series of smaller-scale plots with the differential cross section of all 17 energy points is reported in Figures 4.9 and 4.10.

The cross section, $\Delta\sigma$, integrated over a certain range of z is obtained by summing $(d\sigma/dz) \times \Delta z$ of the bins included by the range. Figures 4.11 and 4.12 show the $\bar{p}p \to \pi^0\eta$ cross section integrated from $z = -z_{max}$ to $z = -z_{max}$, while Figure 4.13 shows the integration over subsequent ranges $z_{min} < |z| < z_{max}$ as wide as 0.1 .

The continuum cross section $\bar{p}p \to \pi^0\eta$ has a smooth variation with the energy. In addition to the statistical fluctuations, some systematics irregularities seem to be present. They are likely to be due to the more structured angular distribution, as compared to $\pi^0\pi^0$. In the presence of marked variations in the angular distribution, possible systematics in the determination of acceptance and efficiency may result in higher fluctuations in the reconstructed cross section. However, no clear signal from the χ_{c0} is present. This is expected since the decay of the χ_{c0} (as every charmonium state) into $\pi^0\eta$ is suppressed by isospin conservation.

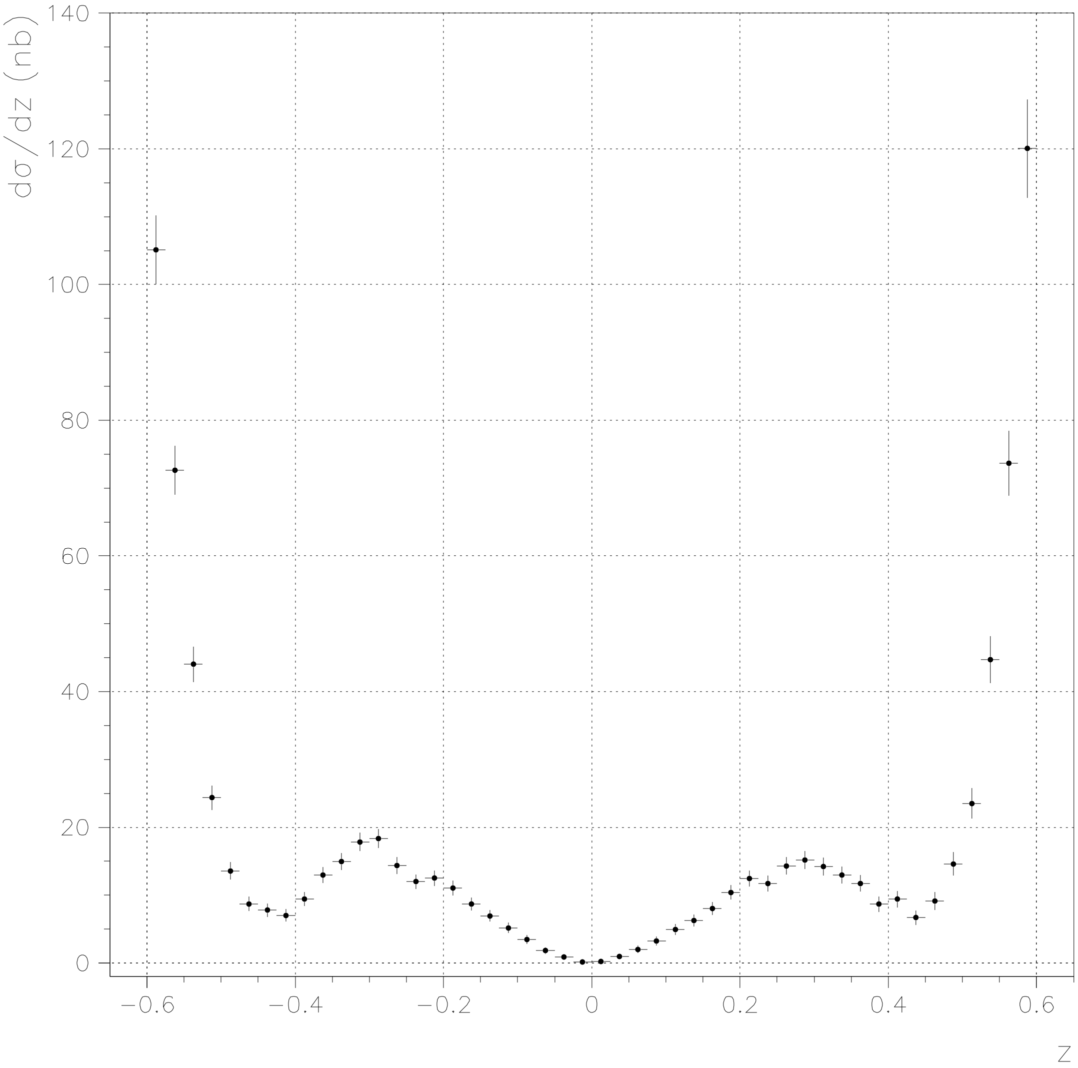

Figure 4.8: The measured $\bar{p}p \rightarrow \pi^0\eta$ differential cross section plotted versus z at $E_{cm} =$ 3415.9 MeV.

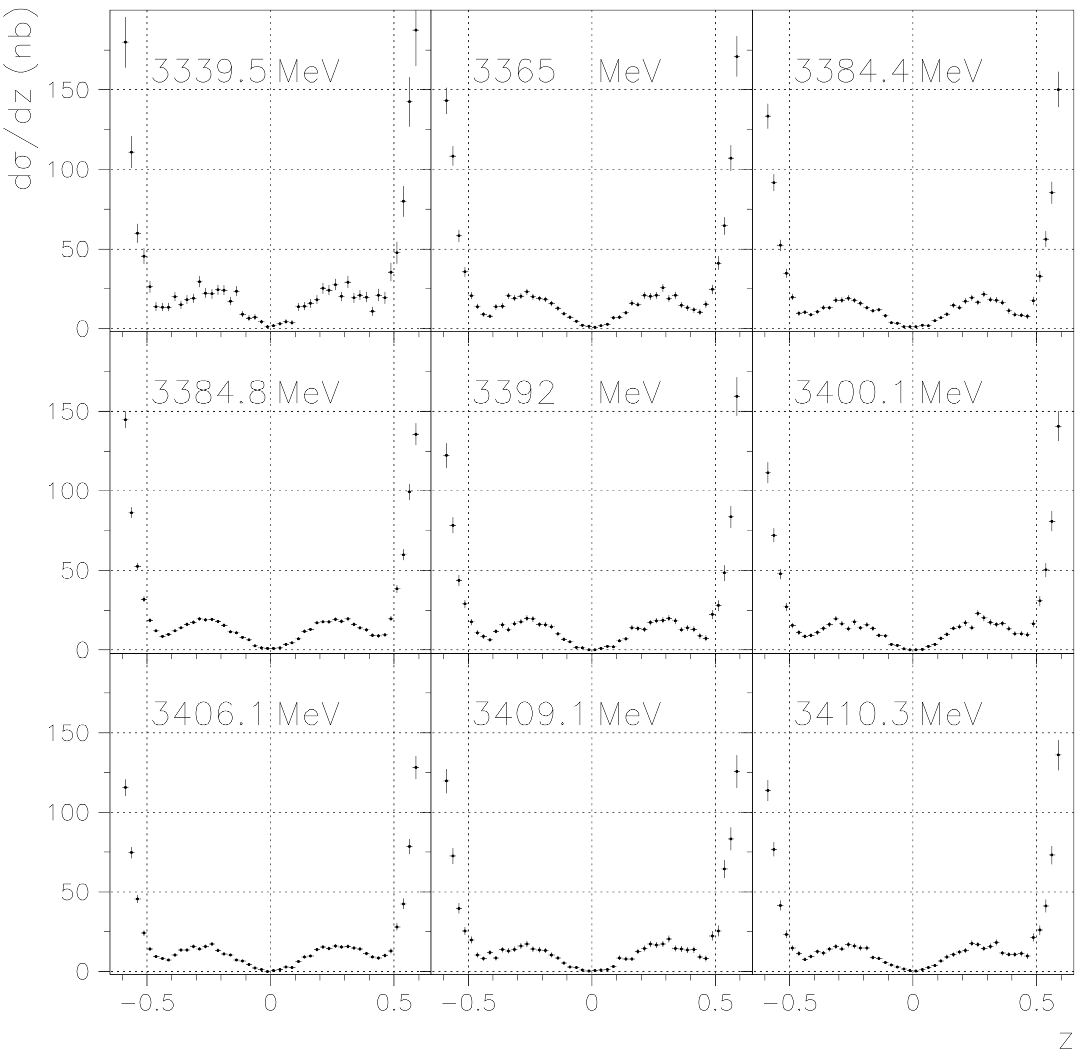

Figure 4.9: The measured $\bar{p}p \rightarrow \pi^0\eta$ differential cross section plotted versus z at the E_{cm} indicated in each plot.

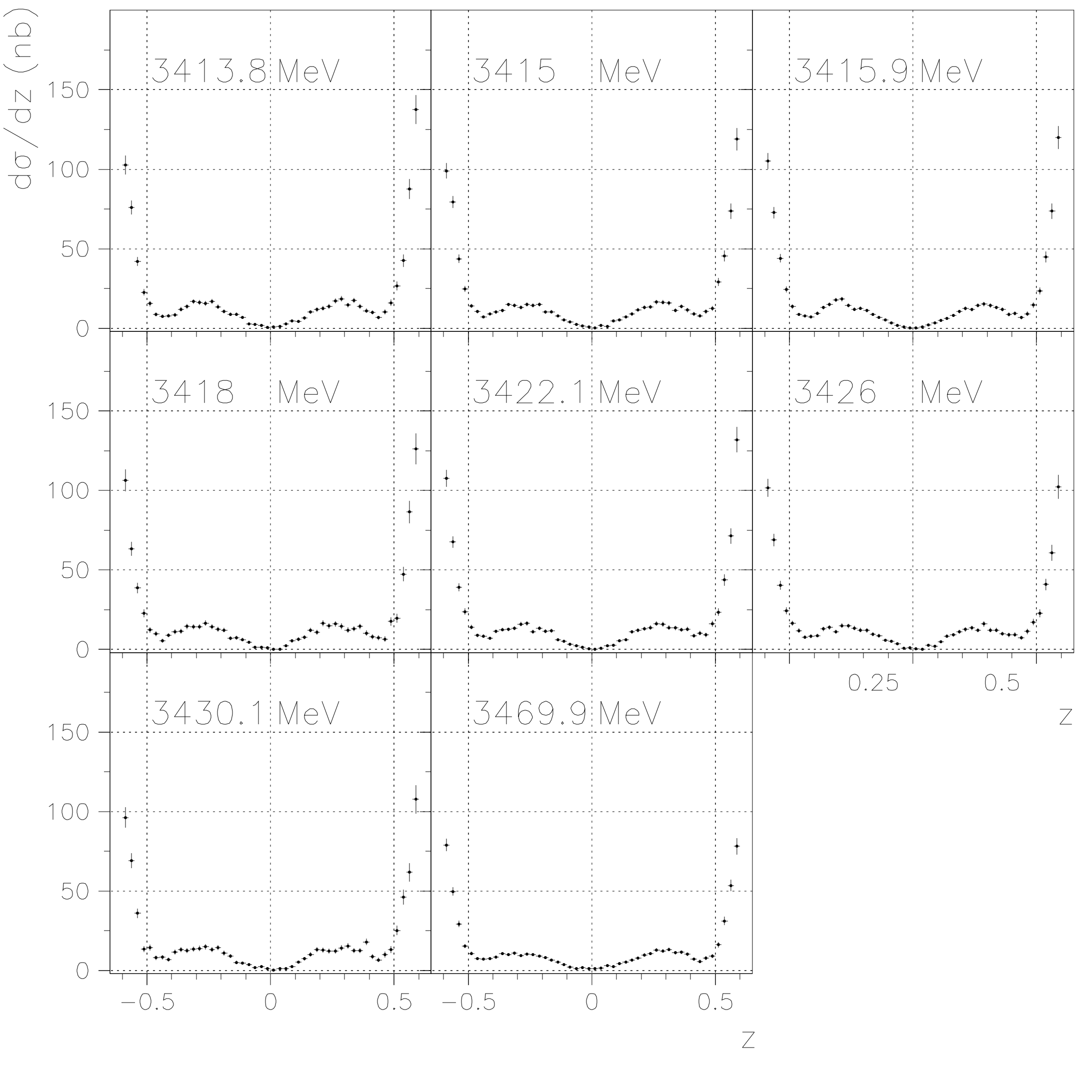

Figure 4.10: The measured $\bar{p}p \to \pi^0\eta$ differential cross section plotted versus z at the E_{cm} indicated in each plot.

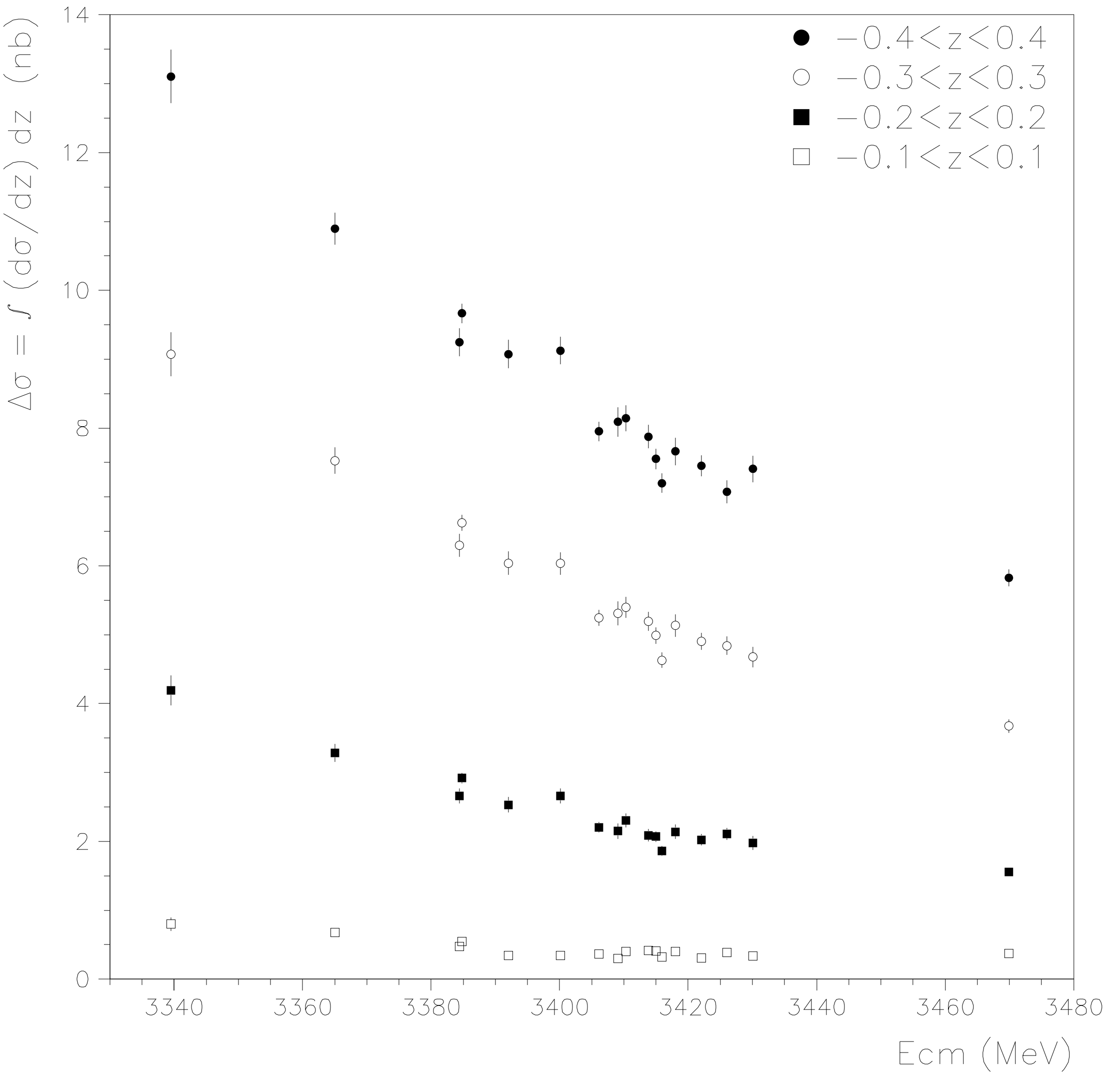

Figure 4.11: The measured $\bar{p}p \rightarrow \pi^0\eta$ cross section integrated over $-z_{max} < z < z_{max}$ plotted versus E_{cm} .

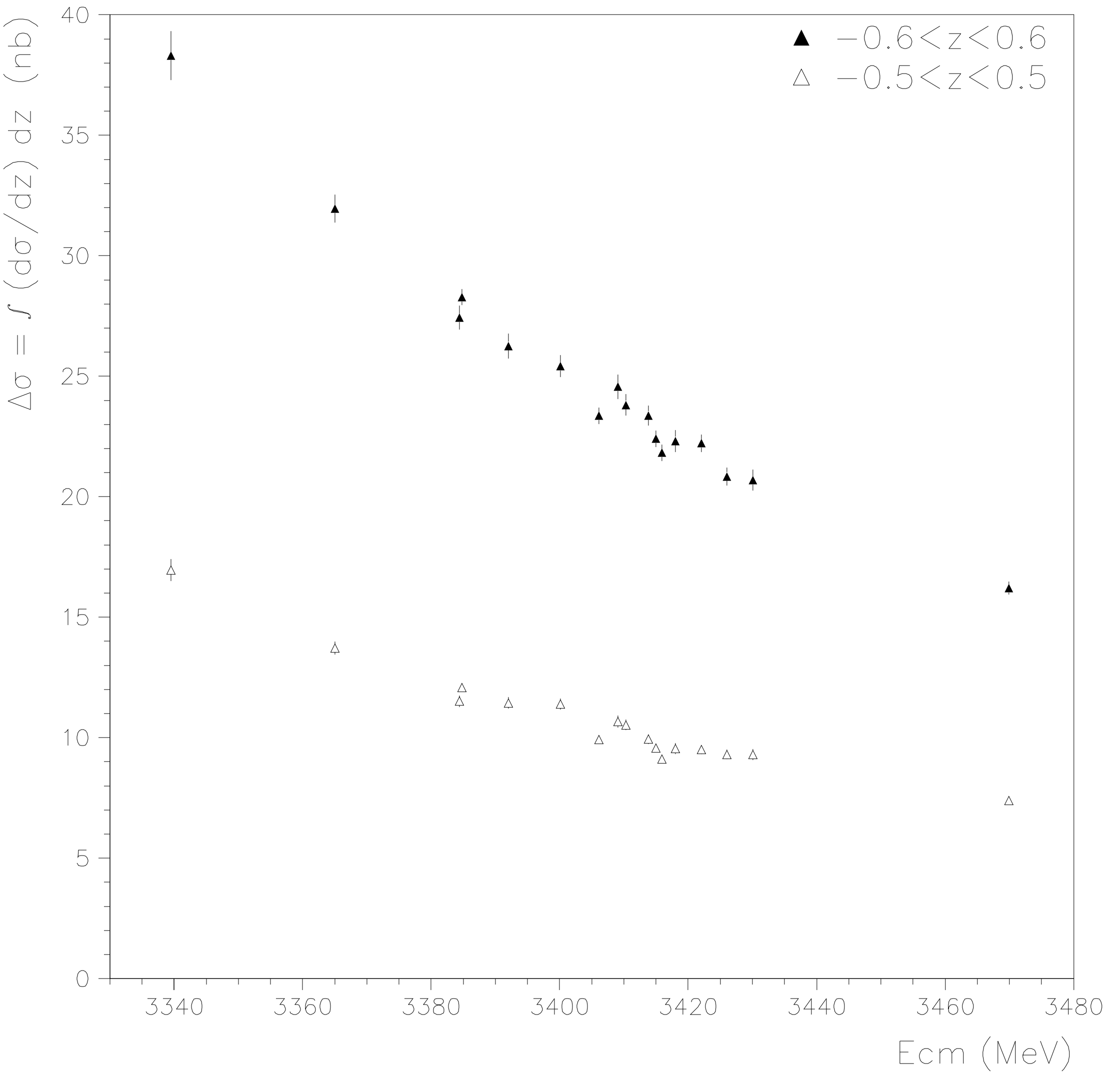

Figure 4.12: The measured $\bar{p}p \to \pi^0\eta$ cross section integrated over $-z_{max} < z < z_{max}$ plotted versus E_{cm} .

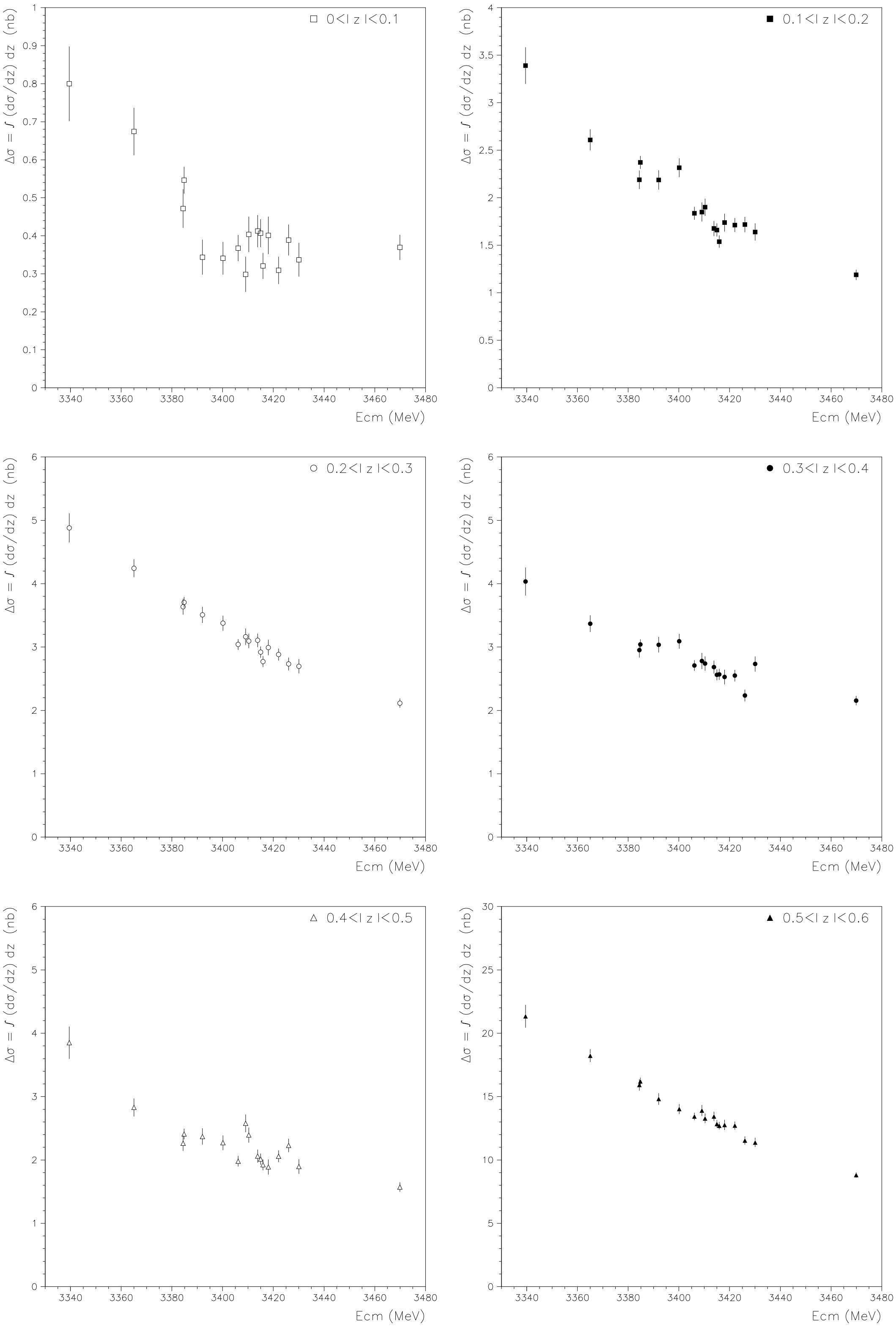

Figure 4.13: The measured $\bar{p}p \to \pi^0\eta$ cross section integrated over $z_{min} < |z| < z_{max}$ plotted versus E_{cm} .

4.8 Fit to the $\pi^0\eta$ Cross Section

A binned maximum likelihood fit[3] to the $\bar{p}p \to \pi^0\eta$ differential cross section is performed simultaneously at all 17 energy points of the data sample. Equation 1.16 is used with the definitions in Equations 1.14 and 1.15. As in the $\pi^0\pi^0$ case, J_{max} is set equal to 4. For the moment, the parameter A_R is set to zero.

The result of the fit for $d\sigma(x,z)/dz$ is shown in Figure 4.14 at the energy point $E_{cm} = 3415.9$ MeV. The agreement of the partial wave expansion fit with the data is shown at all 17 energy points in Appendix D.1 (Figures D.1 and D.2).

Since the initial state ($\bar{p}p$) is an ensemble of C-eigenstates, the final $\pi^0\eta$ must be symmetric in the c.m. polar angle and hence in z (see also Equation A.24). But the $\eta \to \gamma\gamma$ opening angles are much larger than those of the π^0's. The acceptance and efficiency ($a\times\epsilon$) for these two distinguishable pseudoscalars are different, particularly near the central calorimeter boundaries. Figures 4.5 shows that the calculated $a \times \epsilon$ is different for the cases where the π^0 or the η are produced forward. When the η is slower because of being emitted backward, the $\eta \to \gamma\gamma$ opening angle is even larger and the chance of loosing a photon increases. This is confirmed by Figure 4.7, which shows that the acceptance-uncorrected data are not symmetric for $|z| \gtrsim 0.5$. As can be seen from Figures 4.14, D.1 and D.2, the corrected data display excellent agreement for forward/backward symmetry. This important diagnostic test brings confidence that even in the $\pi^0\pi^0$ and $\eta\eta$ analyses, where the test is not available, the acceptance times efficiency is correctly determined.

In Appendix D.1, the fit and the cross section are also shown integrated over different angular ranges and plotted versus E_{cm} (Figures D.3, D.4 and D.5).

The angular range used for the fit is $-0.6 < z < 0.6$, since for $|z| \gtrsim 0.6$ the product of acceptance and efficiency becomes too small ($a \times \epsilon \lesssim 10\%$ for $z \gtrsim 0.6$ and $a \times \epsilon \lesssim 20\%$ for $z \lesssim -0.6$, see Figure 4.5) and the $a\times\epsilon$-corrected data begin to lose the forward/backward symmetry. The total number of $\pi^0\eta$ events within this range and after subtracting the background is 85,751. The fit has 816 bins: 17 energy points times 48 bins in z (each one of $\Delta z = 0.025$). The number

[3]The CERN program MINUIT [71] is used.

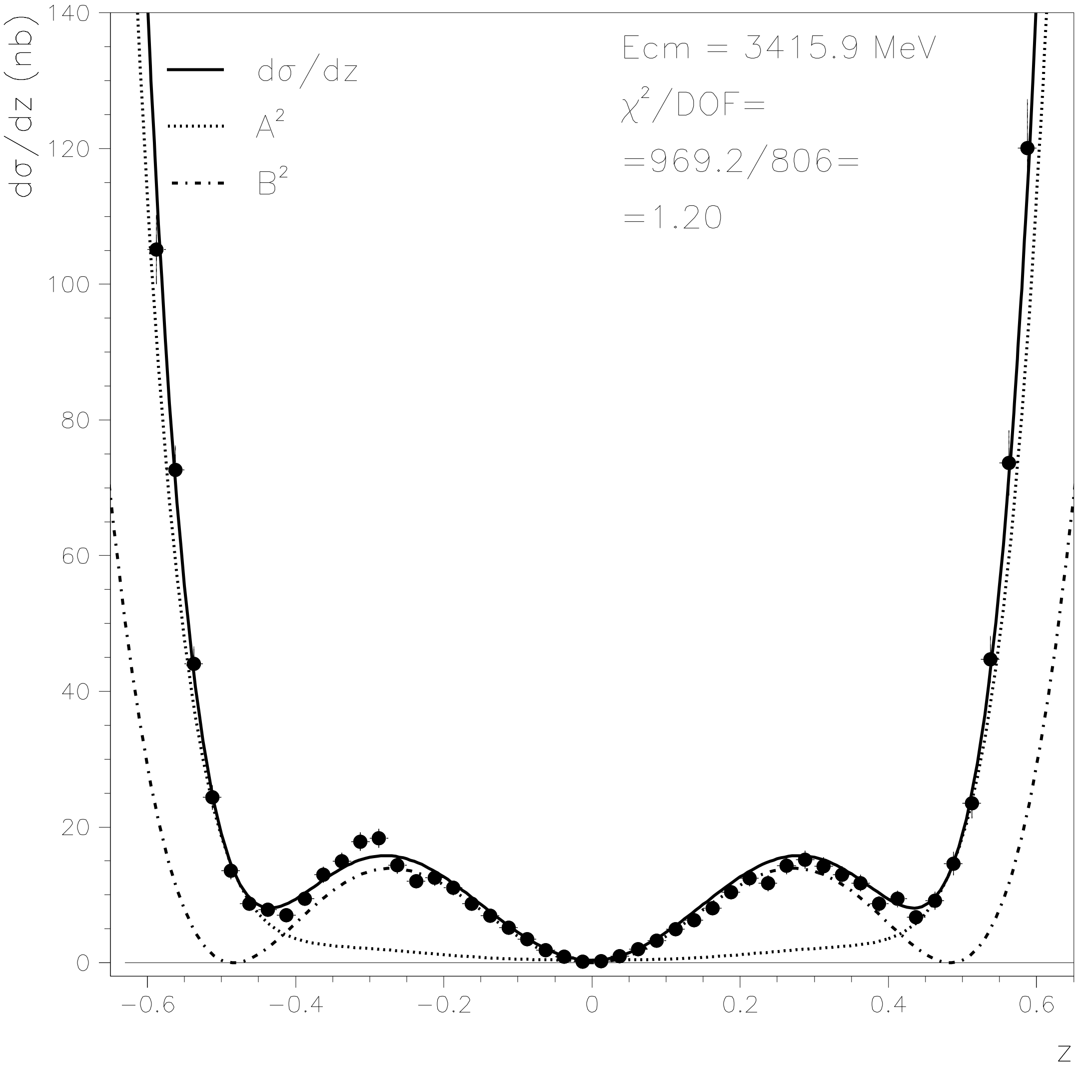

Figure 4.14: The $\bar{p}p \to \pi^0\eta$ differential cross section versus z at $E_{CM} = 3415.9$ MeV. The fit of Equations 1.16 (with $A_R = 0$), 1.14 and 1.15 (solid line) and its components (dotted and dashed-dotted curves) are also shown.

of free parameters is 10: the coefficients $C_{J=0,2,4}$ and $C^1_{J=2,4}$ (where C_0, C^1_2 and C^1_4 necessitate a small linear energy dependence, while C_2 and C_4 do not); and the phases[4] $(\delta_2 - \delta_0)$ and $(\delta_2 - \delta_0)$. Even in this case, as in the $\pi^0\pi^0$, the fit does not improve significantly by allowing the phases to vary with the energy. The phase $(\delta^1_4 - \delta^1_2)$ results have a value consistent with zero and is therefore set equal to zero. The values of the fit parameters are reproduced in Table 4.3.

J	C_J [nb$^{1/2}$]	C^1_J [nb$^{1/2}$]
0	$C_0 = (19.7 \pm 0.3) - (0.076 \pm 0.003)\, x$	–
2	$C_2 = (12.2 \pm 0.2)$	$C^1_2 = (2.8 \pm 0.2) - (0.129 \pm 0.008)\, x$
4	$C_4 = (3.21 \pm 0.09)$	$C^1_4 = (2.54 \pm 0.09) - (0.087 \pm 0.004)\, x$
J	δ_J [degree]	δ^1_J [degree]
0	–	–
2	$\delta_2 - \delta_0 = 4.5 \pm 0.8$	–
4	$\delta_4 - \delta_0 = 9 \pm 2$	$\delta^1_4 - \delta^1_2 = 0$

Table 4.3: Fit results for the coefficients (with a linear energy dependence when found necessary) and phases of the partial wave expansion of Equations 1.14 and 1.15 . The quoted errors are statistical; systematic errors due to the limited available angular range $(-0.6 < z < 0.6)$ should be dominant.

It should be mentioned that in the $\pi^0\eta$ angular distribution at the analyzed energies, the necessity of the $J = 4$ amplitude is more evident than in the $\pi^0\pi^0$. In fact, a fit with $J_{max} = 2$ cannot reproduce the multiple minima at $z = 0$ and $|z| \simeq 0.45$.

4.9 Upper Limit for the Product of the Branching Ratios

The decay of any charmonium state into $\pi^0\eta$ is suppressed by isospin conservation. The measured cross section $\bar{p}p \rightarrow \pi^0\eta$ does not show evidence of a χ_{c0} induced

[4]Only the phase differences are measurable.

signal. An upper limit for the resonant process can be determined.

The partial wave expansion fit over the full available range $-0.6 < z < 0.6$, which in Section 4.8 is performed with $A_R = 0$, proves to be little sensitive to the introduction of a small free parameter A_R. It is necessary to reduce the angular range to extract information on a possible resonant signal.

As in the $\pi^0\pi^0$ case, the non-interfering helicity-1 continuum (of magnitude B^2) vanishes at $z = 0$ because so do the Legendre functions $P^1_J(z)$. In the $\pi^0\eta$ case, even the interfering helicity-0 continuum (of magnitude A^2) is very small at $z \simeq 0$ [5]. According to the partial wave expansion fit, the dominance at small z of the helicity-0 over the helicity-1 is already lost at $|z| \gtrsim 0.025$ (see in particular Figure D.5). The advantage of selecting the very small region $|z| < 0.025$ to reduce the uncertainty on the relative amount of A^2 and B^2 is attempted but compromised by the small data sample.

Subsequent fits over increasing ranges $|z| < z_{max}$ are performed with the same methodology described in Section 3.14.2. The magnitude B^2 of the helicity-1 continuum is fixed to the estimate from the partial wave expansion fit, while A^2 is parameterized as in Equation 3.26. The more stringent limit to A_R obtained from the small z region comes from the fit over $0 < |z| < z_{max} = 0.15$. For larger values of z_{max} up to ~ 0.4, the contribution of B^2 becomes much larger than A^2 (see Figure 4.8). Any resonant signal that is not large enough to induce an interference-enhanced pattern at smaller z would be completely hidden at $0.15 \lesssim |z| \lesssim 0.4$.

The result of the fit over $0 < |z| < z_{max} = 0.15$ is shown in Figure 4.15. The result for the resonant amplitude would be $A_R = (0.095^{+0.082}_{-0.078})$ nb$^{1/2}$. This would determine[6] a value for the product of the branching ratios $B(\chi_{c0} \to \bar{p}p) \times B(\chi_{c0} \to \pi^0\eta) = 0.30^{+0.74}_{-0.30} \times 10^{-7}$, which is consistent with zero but with an upper limit at 90% of confidence level only ~ 4 times smaller than $B(\chi_{c0} \to \bar{p}p) \times B(\chi_{c0} \to \pi^0\pi^0)$.

[5] This dip must be due to an accidental cancellation of the involved partial waves, mostly $C_0\, e^{i\delta_0}$ and $C_2\, e^{i\delta_2}$, and is not present at different energies [33].

[6] The resonance amplitude A_R is related to the fictitious cross section $\sigma_{\bar{p}p\to\chi_{c0}\to\pi^0\pi^0}$ at $x = 0$ by

$$\sigma_{\bar{p}p\to\chi_{c0}\to\pi^0\eta} = \int_{-1}^{1} A_R^2\, dz = 2 \times A_R^2. \tag{4.7}$$

With respect to Equation 3.27, a factor 2 arises from the different definitions of z in Equations 3.1

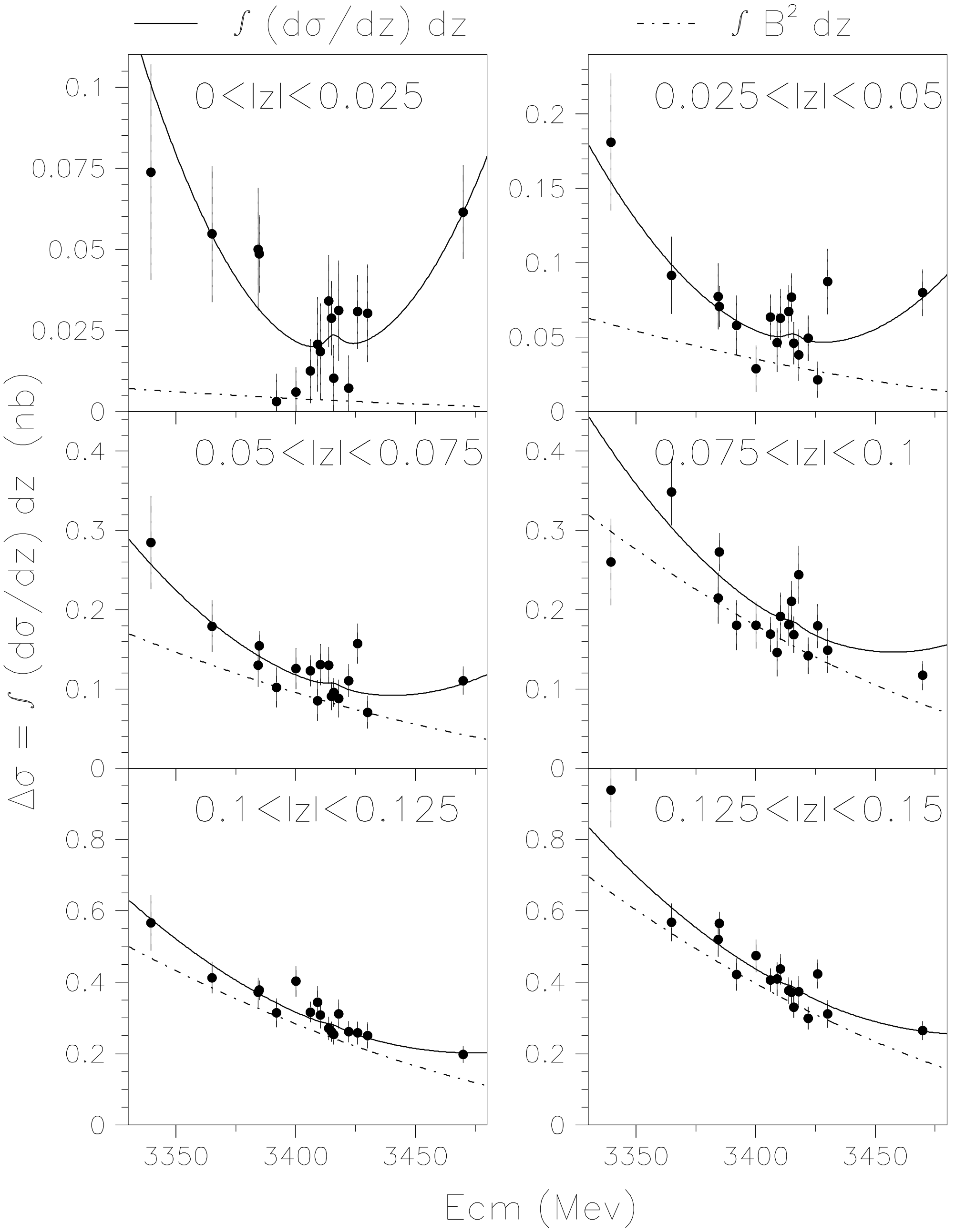

Figure 4.15: Fit and measured $\bar{p}p \rightarrow \pi^0\eta$ cross section integrated over $z_{min} < |z| < z_{max}$ plotted versus E_{cm}. The fit is performed over the range $0 < |z| < 0.15$ using Equations 3.25 (with A_R free) and 3.26. The contribution of $B^2 = |B\ e^{i\delta_B}|^2$ is constrained to the estimate obtained in Section 4.8 and is indicated by the dashed-dotted curve.

The reason for such a non-restrictive upper limit is a consequence of the pronounced minimum at small $|z|$ that the $\pi^0\eta$ cross section presents at these energies. This minimum is caused by a large local cancellation of the partial waves of the helicity-0 continuum (the helicity-1 is certainly equal to zero at $z = 0$ because of the factor z present in the associate Legendre Polynomials $P_J^1(z)$). Consequently, the enhancement of a possible interference signal provided by the helicity-0 continuum is small compared to that observed in the $\pi^0\pi^0$ case, and would not be enough to make visible a small resonance signal (even considering that the amount of $\pi^0\eta$ continuum to overcome is smaller than the $\pi^0\pi^0$ continuum).

A more restrictive upper limit can be determined from the region $0.4 < z < 0.6$ by relying on the result of the partial wave expansion fit. In fact, Figure 4.14 indicates that the helicity-0 continuum dominates again for $z \gtrsim 0.4$. As a consequence of this, the interference term of Equation 1.17 would more clearly reveal the presence of the resonance at $z \gtrsim 0.4$. Accordingly, a fit is performed over the range $0.4 < |z| < 0.6$ using Equations 3.25 (with A_R free) and 3.26 [7]. Again, the contribution of $B^2 = |B\ e^{i\delta_B}|^2$ is constrained to the estimate obtained in Section 4.8. Since no interference pattern is evident, the phase δ_A in Equation 3.25 must be constrained. Different values with steps of 45° are attempted. All of them give comparable upper limits for A_R (remember that the size of the interference pattern is independent on δ_A when A_R^2 is much smaller than A^2).

The least constraining result comes from the fit with $\delta_A = -135°$, which is shown in Figure 4.16, and provides the upper limit at 90% confidence level

$$B(\chi_{c0} \to \bar{p}p) \times B(\chi_{c0} \to \pi^0\eta) < 4 \times 10^{-8}\ . \tag{4.9}$$

The above includes the uncertainty on the estimate of B^2 (determined using a

and 4.1. The relation with the product of the branching ratios is the usual

$$\sigma_{\bar{p}p\to\chi_{c0}\to\pi^0\pi^0} = \pi\lambda\!\!\!^{-2} \times B(\chi_{c0} \to \bar{p}p) \times B(\chi_{c0} \to \pi^0\eta)\ . \tag{4.8}$$

[7] Two additional terms, a_4z^4 and a_5xz^2, are necessary to describe the steep rise of $d\sigma/dz$ at $0.4 < |z| < 0.6$ and its energy dependence.

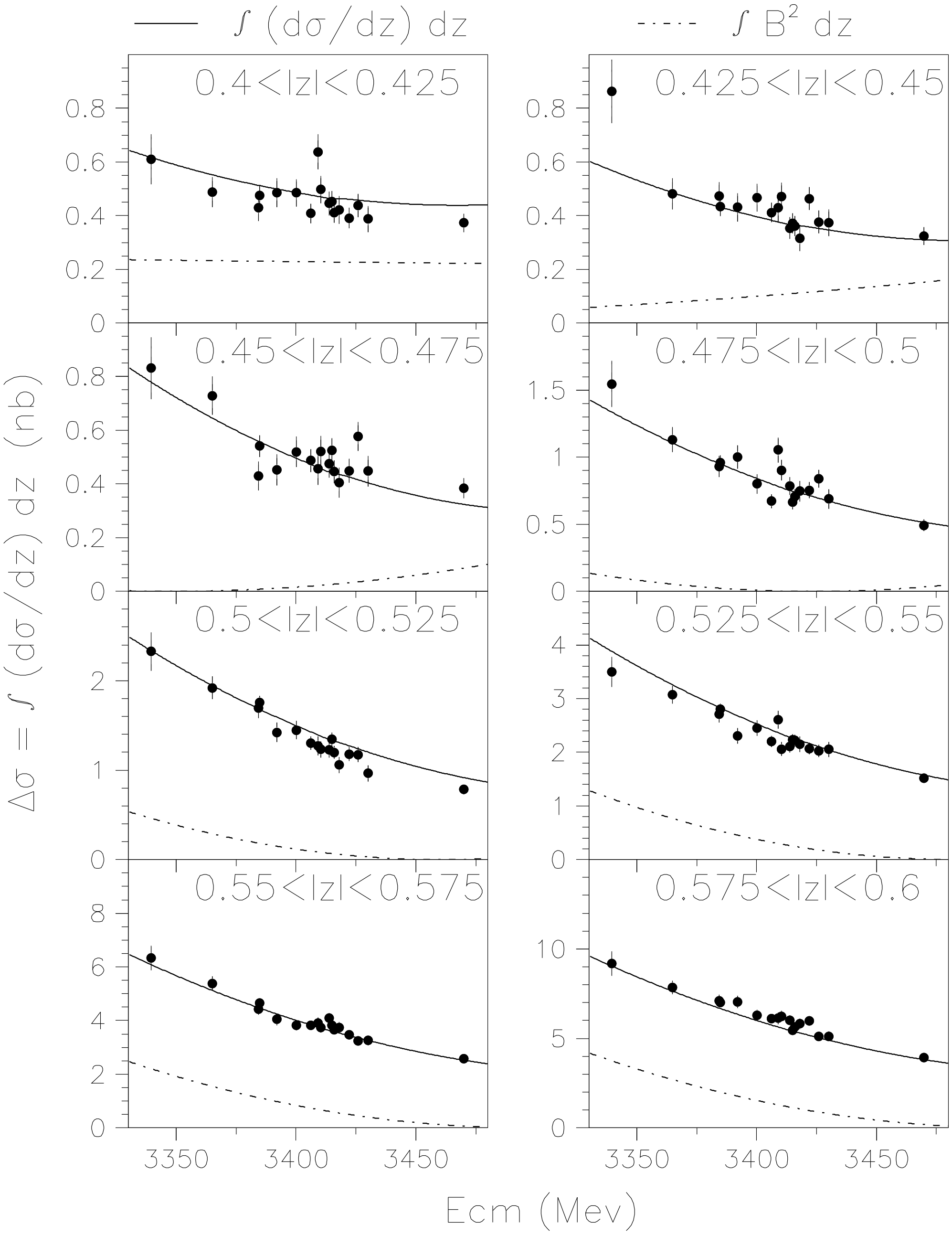

Figure 4.16: Fit and measured $\bar{p}p \rightarrow \pi^0\eta$ cross section integrated over $z_{min} < |z| < z_{max}$ plotted versus E_{cm}. The fit is performed over the range $0.4 < |z| < 0.6$ using Equations 3.25 (with A_R free) and 3.26. The contribution of $B^2 = |B\ e^{i\delta_B}|^2$ is constrained to the estimate obtained in Section 4.8 and is indicated by the dashed-dotted curve.

method analogous to that described in Section C.4) and a $\sim 15\%$ systematic error[8].

The upper limit of Equation 4.9 is about 13 times smaller than the measured $B(\chi_{c0} \to \bar{p}p) \times B(\chi_{c0} \to \pi^0\pi^0)$ of Equation 3.31.

[8]The systematic error is simply set to 3 times the percentage systematic error determined for the product of the branching ratios of the $\pi^0\pi^0$ analysis.

Chapter 5

The analysis of the $\eta\eta$ channel

The final state $\eta\eta$ has isospin equal to zero and, as the $\pi^0\pi^0$, can be produced through the resonant process $p\bar{p} \to \chi_{c0} \to \eta\eta$. Conditions similar to those of the $\pi^0\pi^0$ channel are expected and found, with a dominant non-resonant production of the final state. However, a much lower number of events is available. This is due to a factor $\sim 1/6$ resulting from the lower branching ratio $B(\eta \to \gamma\gamma)$ as compared to $B(\pi^0 \to \gamma\gamma)$, but is also due to a lower value of the $p\bar{p} \to \eta\eta$ differential cross sections in the region of the detector acceptance. The analysis of the reaction $\bar{p}p \to \eta\eta$ is very similar to the two previous analyses and is presented schematically with frequent references to Chapter 3 or Chapter 4. More details are given when substantial differences exist.

5.1 Kinematics of the Reaction

The sketch in Figure 3.1 holds for the reaction $\bar{p}p \to \eta\eta$ by replacing π^0's by η's. The same is true for the notations in Section 3.1.

A variable z is again defined by

$$z \equiv |\cos\theta^*| \, , \tag{5.1}$$

where θ^* is the angle, in the c.m. frame, between the η-production axis and the

$\bar{p}$-beam axis.

The branching ratio $B(\eta \to \gamma\gamma) = (39.43 \pm 0.26)\%$ makes the η still efficiently detectable, but impacts the size of the $\eta\eta$ sample when compared to the $\pi^0\pi^0$. The η decays are virtually point-like. The momentum of every η in the c.m. frame is $p^*_f \simeq 1617.6$ MeV (as compared to ~ 1661 MeV and ~ 1702.4 MeV for the $\pi^0\eta$ and $\pi^0\pi^0$ cases, respectively). In the case where the η's are emitted perpendicularly, in the c.m. frame, to the beam axis the value of γ_η is about 5.7. This is not much different from the value of γ_η in the $\pi^0\eta$ case, and the consequences on α_{min}, split clusters and $E_{\gamma,min}$ are similar to those written at the end of Section 4.1.

5.2 Selection of Four Photon Events

The $\eta\eta$ events are extracted from the same sample that provides the $\pi^0\pi^0$ and $\pi^0\eta$ events (see Sections 3.2 and 3.3). The selection of events with four photons coincides (see Section 3.4). The $\eta\eta$ peak in the LEGO plot of Figure 3.4 can be enhanced by using a logarithmic scale for the vertical axis: see Figure 5.1.

An ηX berm of Figure 5.1 (where X can be made of one or more particles that may partially escape detection) is investigated in figure 5.2 by plotting $m^{fw}_{\gamma\gamma}$ after requesting that $m^{bw}_{\gamma\gamma}$ is within 70 MeV from the mass of the η. The pronounced peak at $m_{\gamma\gamma} \simeq 135$ MeV is due to the already analyzed $\eta\pi^0$ events. The still pronounced peak at $m_{\gamma\gamma} \simeq 550$ MeV is due to $\eta\eta$ events and constitutes the sample of the analysis of this chapter. The accumulations due to $\eta\omega$ events (where a photon is lost from the decay $\omega \to \pi^0\gamma \to \gamma\gamma\,\gamma$) and $\eta\eta'$ events are also visible.

5.3 The $\eta\eta$ Event Topology

The $\eta\eta$ event topology is determined by calculating the two two-photon invariant masses for each one of the three ways (combinations) to pair the four photons. For each combination, a six constrain fit (6C-fit) to the hypothesis $\bar{p}p \to \eta\eta \to \gamma\gamma\,\gamma\gamma$ is performed. The combination with the highest confidence level (C.L.) is chosen as

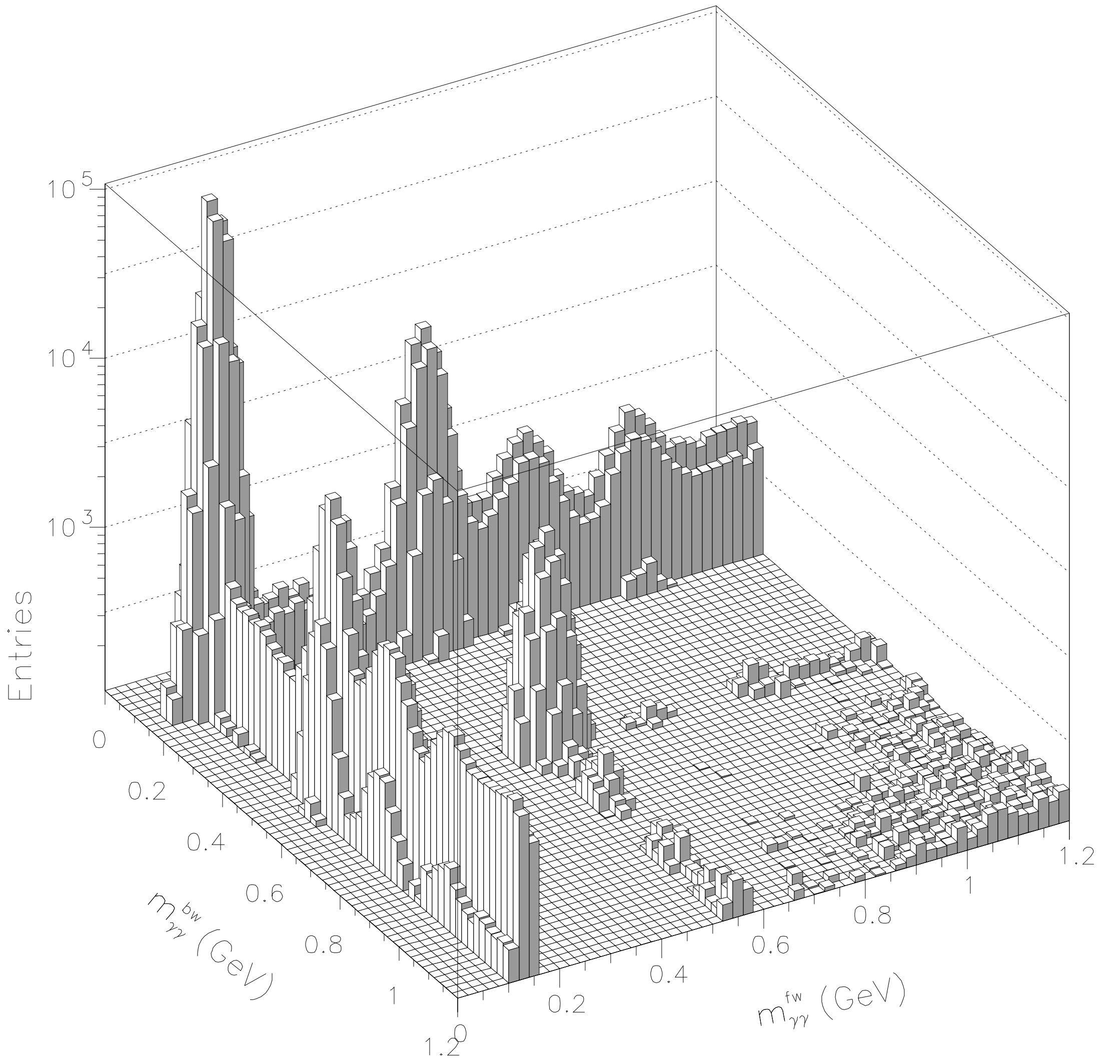

Figure 5.1: The LEGO plot of Figure 3.4 with logarithmic scale on the vertical axis ($m_{\gamma\gamma}^{fw}$ is the forward and $m_{\gamma\gamma}^{bw}$ is the backward two-photon invariant mass). The $\eta\eta$ peak is visible in the center.

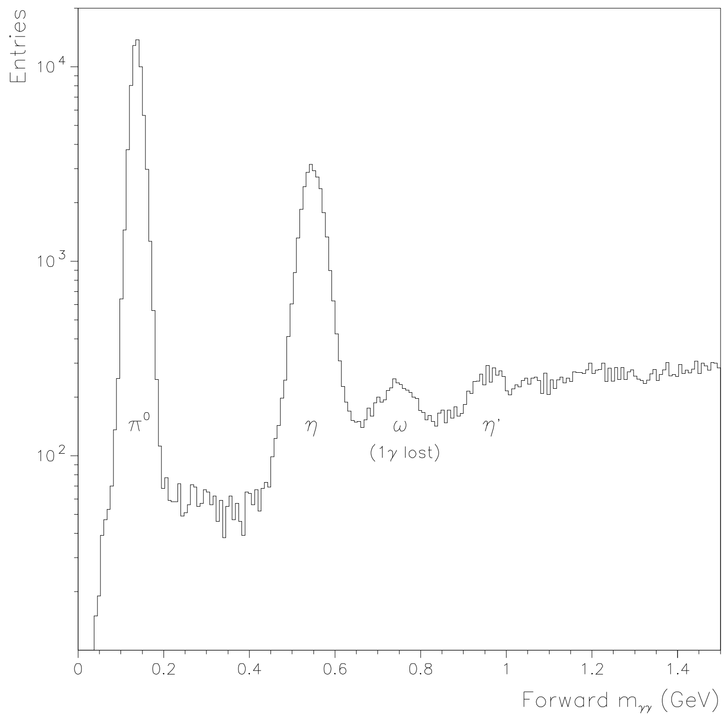

Figure 5.2: The forward $m_{\gamma\gamma}$ after requesting that the backward $m_{\gamma\gamma}$ falls within the η-mass window. Evident are the π^0, η, ω (one γ is lost), and η' peaks. All 17 energy points are merged in this plot.

the event topology[1].

Little doubt arises about determining the candidate topology for $\eta\eta$ events. In the entire χ_{c0}-energy sample, only 31 events ($\sim 0.13\%$) have two combinations that both satisfy the general four-photon selection (Cuts 1 through 4 of Section 3.4) and the features of the $\eta\eta$ kinematics (Cuts 5 through 8 in next Section 5.4).

[1]For those events in which the fit is unsuccessful for all three combinations, a nominal topology is still defined by choosing the combination with lowest $\Delta m \equiv \sqrt{(m_{\gamma\gamma}^{fw} - m_\eta)^2 + (m_{\gamma\gamma}^{bw} - m_\eta)^2}$, where $m_{\gamma\gamma}^{fw}$ and $m_{\gamma\gamma}^{bw}$ are the forward and backward (according to their directions, in the c.m. frame, with respect to the $\bar{p}$ direction) invariant masses.

5.4 Selection of $\eta\eta$ Events

Once the $\eta\eta$ event topology is determined as the combination with the highest C.L. of the $\eta\eta$ fit, the following cuts are applied to that combination in order to select those events with the characteristics of the $\eta\eta$ reaction:

Cut 5. $|m_{\gamma\gamma}^{fw} - 547.3| < 70$ MeV ,

Cut 6. $|m_{\gamma\gamma}^{bw} - 547.3| < 70$ MeV ,

Cut 7. Akinematics $(\Delta\theta) < 15$ mrad ,

Cut 8. Acoplanarity $(\Delta\phi) < 45$ mrad ,

Cut 9. No invariant masses for which $|m_{\gamma\gamma} - m_\eta| < 45$ MeV in the two combinations not chosen as the event topology ,

Cut 10. No successful fit (C.L.$< 10^{-5}$) to $\pi^0\pi^0 \to \gamma\gamma\,\gamma\gamma$ or $\pi^0\eta \to \gamma\gamma\,\gamma\gamma$ in any of the 3 combinations,

Cut 11. the event triggered the Neutral-ETOT logic.

The above cuts are analogous to those used for the $\pi^0\pi^0$ and $\pi^0\eta$ event selection, described in Sections 3.6 and 4.3.

Cuts 7 and 8 require that the 2-body kinematics of the $\eta\eta$ reaction are respected. The variable named "akinematics" is defined as

$$\Delta\theta \equiv \theta_{\eta,meas}^{fw} - \theta_{\eta,calc}^{fw} \,, \tag{5.2}$$

where $\theta_{\eta,meas}^{fw}$ is the measured azimuthal angle of the forward η, while $\theta_{\eta,calc}^{fw}$ is the value of the same quantity calculated by assuming $\eta\eta$ kinematics and using the measured azimuthal angle of the backward η. The "acoplanarity" is defined as π minus the difference between the measured polar angles of the two η's:

$$\Delta\phi \equiv \pi - (\phi_{\eta,meas}^{fw} - \theta_{\eta,meas}^{bw}) \,. \tag{5.3}$$

As in the $\pi^0\eta$ analysis, Cut 11 restricts the sample to those events that were selected by the Neutral-ETOT trigger (see Section 5.7).

The number of events surviving the $\eta\eta$ event selection (cuts 1 through 4 on page 82, and cuts 5 through 11 here) is 23,788 . The $\eta\eta$ sample is much smaller than the $\pi^0\pi^0$ and $\pi^0\eta$ samples.

Figures 5.3 and 5.4 show the variables involved in the most relevant cuts for data and MC simulation at one, $E_{cm} = 3415$ MeV, of the 17 energy point. The arrows indicates the boundaries of acceptance of the cuts. Each variable is shown after applying all cuts with the exception of the cut involving the variable itself.

Figure 5.5 shows the C.L. of the 6-C fit to $\bar{p}p \to \eta\eta \to \gamma\gamma\gamma\gamma$ for those events that have passed the selection. This C.L. is only used to determine the event topology, as described in section 5.3; no cuts are applied on it, so that the instrumental background can be estimated and subtracted using the technique described in Section 5.6.

Figure 5.6 shows the region of the $\eta\eta$ peak in the invariant mass LEGO plot after all cuts are applied except the ones on the invariant masses themselves.

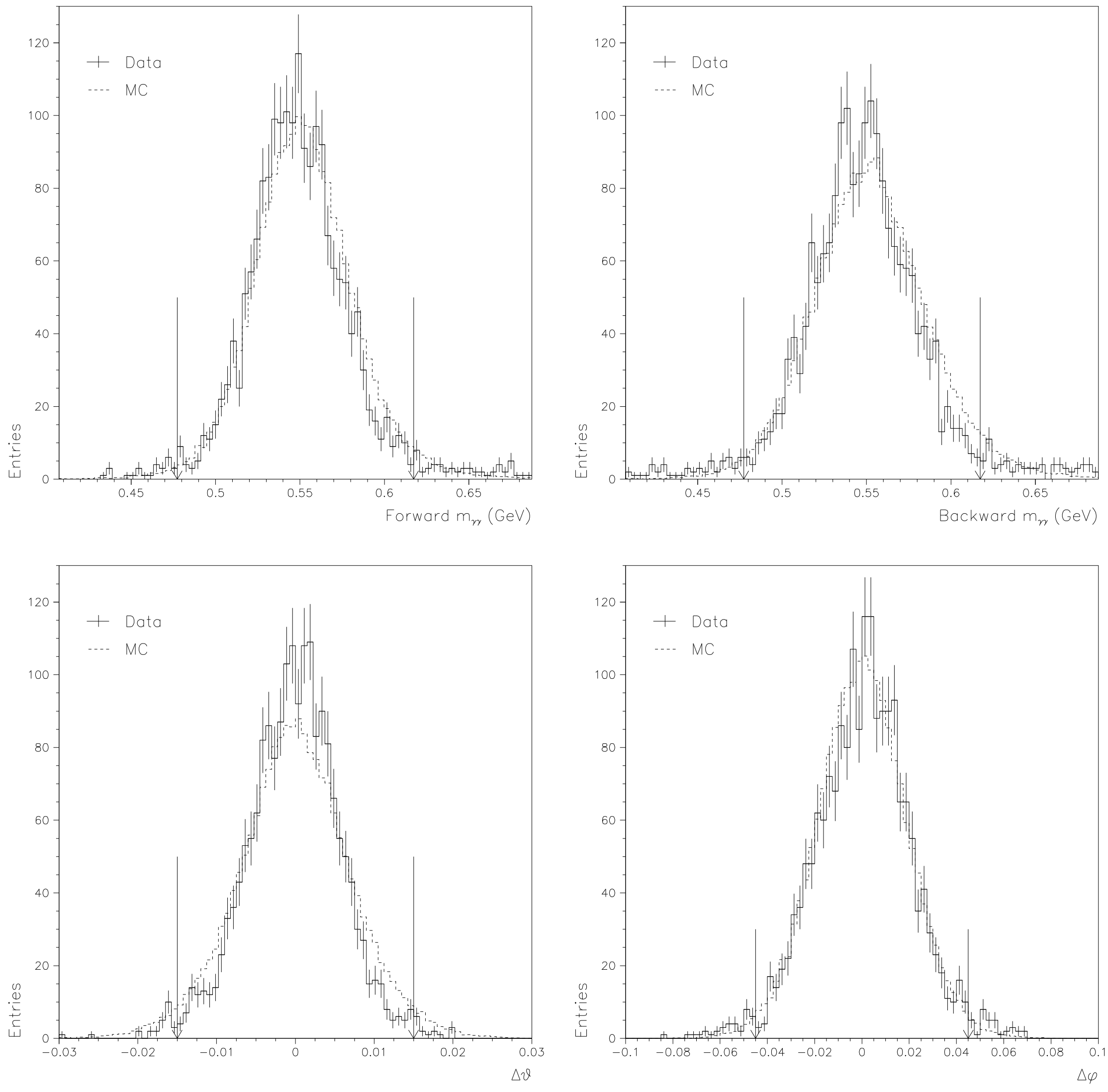

Figure 5.3: Variables involved in the $\eta\eta$ selection. Arrows indicate where the cuts are applied. Each variable is plotted after applying all of the other cuts. $E_{cm} = 3415$ MeV. Top left: the forward invariant mass (Cut 5); top right: the backward invariant mass (Cut 6); bottom left: the akinematics (Cut 7); bottom right: the acoplanarity (Cut 8).

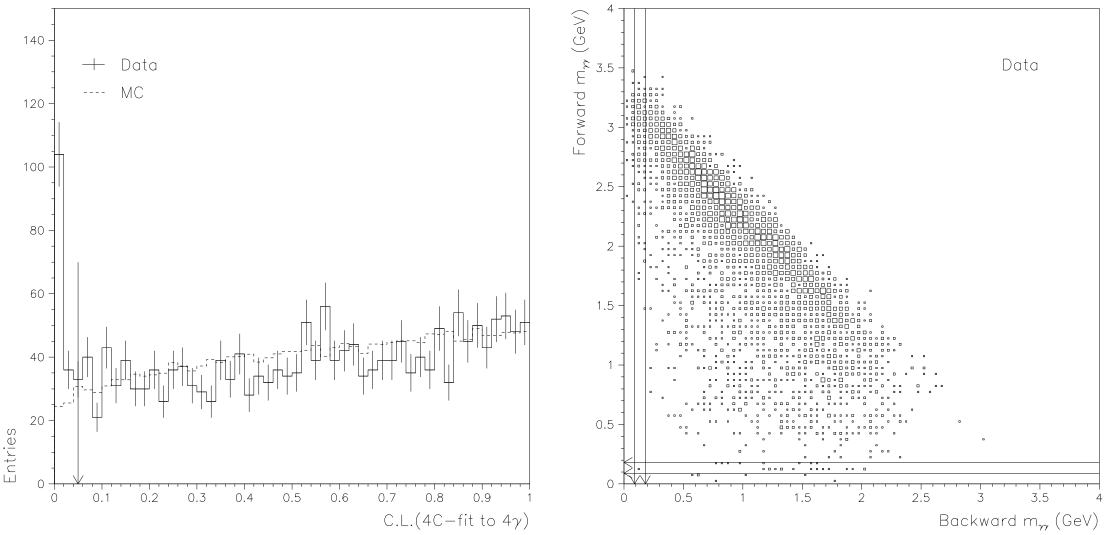

Figure 5.4: Variables involved in the $\eta\eta$ selection. Arrows indicate where the cuts are applied. Each variable is plotted after applying all of the other cuts. $E_{cm} = 3415$ MeV. Left: Confidence Level of the 4C-fit to $\bar{p}p \to \gamma\gamma\,\gamma\gamma$ (Cut 4); right: scatter plot of the invariant masses of the two combinations not chosen as the event topology (Cut 9).

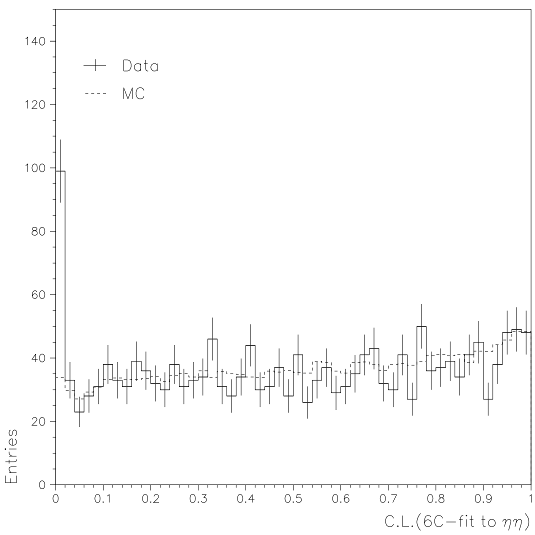

Figure 5.5: Confidence Level of the 6C-fit to $\bar{p}p \to \eta\eta \to \gamma\gamma\,\gamma\gamma$; no cuts are applied to this variable. $E_{cm} = 3415$ MeV.

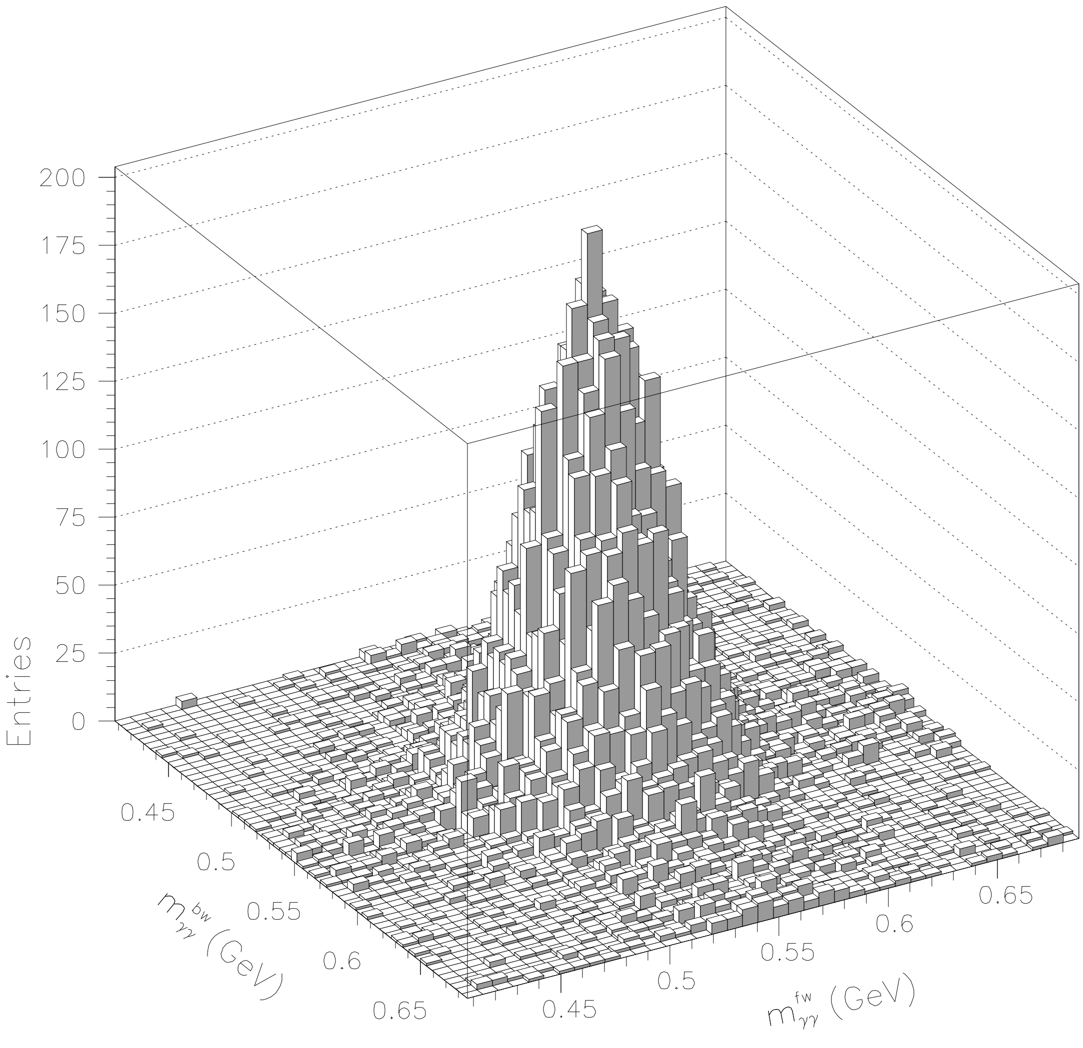

Figure 5.6: The region of the $\eta\eta$ peak in the LEGO plot of the forward versus the backward invariant mass for the combination chosen as the event topology; all $\eta\eta$ cuts are applied except the ones on the invariant masses themselves (Cuts 5 and 6). The events from all 17 energy points are merged in this plot.

5.5 Detector Acceptance and Selection Efficiency

The acceptance of the detector and efficiency of the $\eta\eta$ selection are determined with the same method described in Section 3.7.

Figure 5.7 shows the product of the acceptance and efficiency, $a \times \epsilon$, for the several cuts as a function of the bins in z.

Correction for the limited polar angle resolution. It will be shown in Section 4.7 that the differential cross section of the $\eta\eta$ channel has structures that are more pronounced than the $\pi^0\pi^0$ channel but less than the $\pi^0\eta$ channel. Consequently, the impact of the limited polar angle resolution for $\eta\eta$ is somewhat in between what observed for the other two channels (see Appendix B).

The Event Pileup. The event pileup is discussed in detail in Section 3.8 for the $\pi^0\pi^0$ channel. The pileup corrections to the efficiency for the $\eta\eta$ channel are determined following the same procedure thereby described. Such rate-dependent corrections are almost independent on the particular final state. The probability that a $\eta\eta$ event is lost due to the pileup is on average 80.3%, with fluctuations from energy point to energy point from 76.1% to 86.4%.

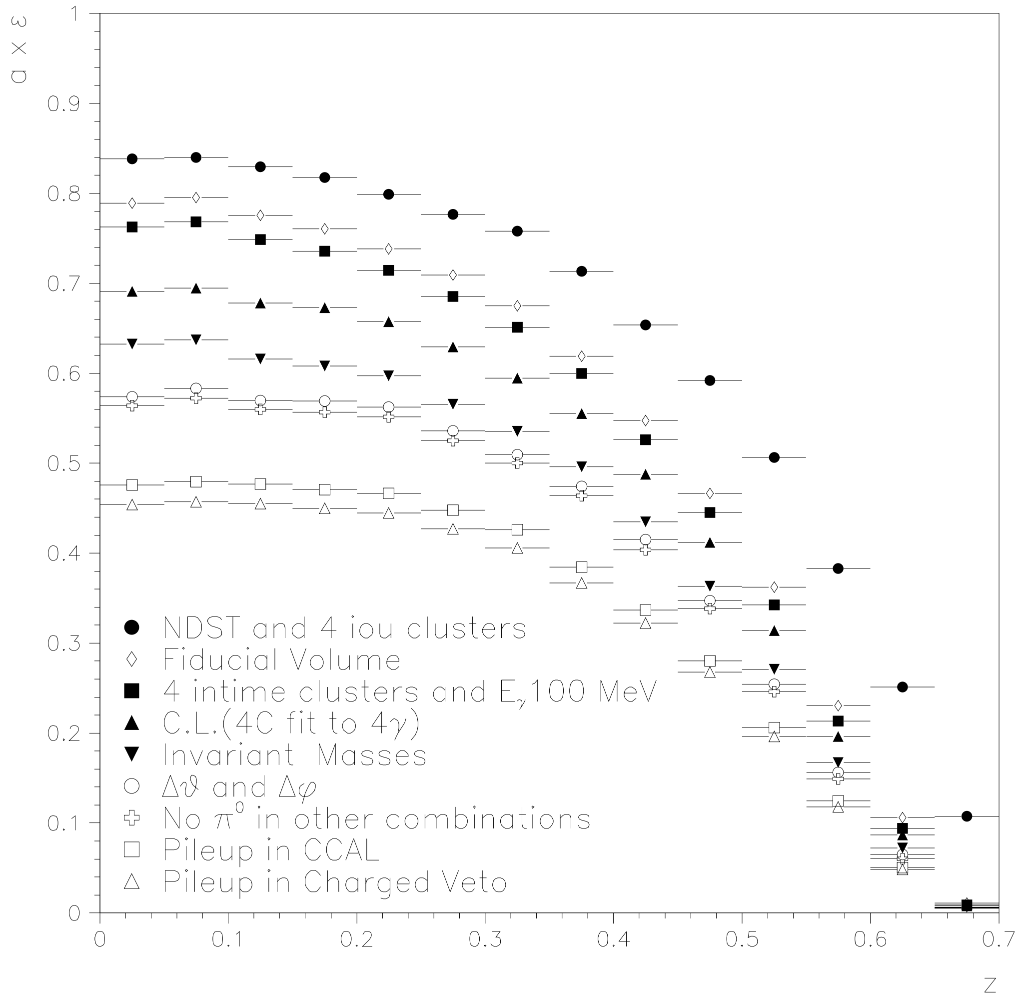

Figure 5.7: The product of the detector acceptance and selection efficiency, $a \times \epsilon$, for $\eta\eta$ events as a function of $z \equiv |\cos\theta^*|$ at $E_{cm} = 3415$ MeV. Here, the MC events are generated with a uniform angular distribution. Each cut shown, or group of cuts, is applied on top of the ones previously indicated. "NDST and 4 iou clusters" is the selection of the initial data sample: four in-time or undetermined clusters (iou) and the NDST cuts (page 81). "Fiducial volume": Cut 2 (page 82). "4 in-time clusters and $E_\gamma > 100$ MeV": Cut 1 and 3. "C.L.(4C fit to 4γ)": Cut 4. "Invariant Masses": Cut 5 and 6 (page 174). "$\Delta\theta$ and $\Delta\phi$": Cut 7 and 8. "No π^0 in other combinations": Cut 9. The two lower-most symbols represent the estimated fraction of $\eta\eta$ events surviving the contamination due to event pileup (see page 179).

5.6 The Background

As in the previous two analyses, the background in the $\eta\eta$ channel is studied by observing the region around the $\eta\eta$ peak in the scatter plot of the two two-photon invariant masses (see Figure 5.6). Even in this case, there are two background berms (along the $m^{fw}_{\gamma\gamma} = m_\eta$ and $m^{bw}_{\gamma\gamma} = m_\eta$ axes) and a less copious scattered background. Background events from final channels where a single η is produced accumulate in the two berms that add up incoherently at the intersect and generates a mound underlying the peak of real $\eta\eta$ events. Background events where two or more η's are produced contribute to the berms and might also generate an accumulation at the berm intersect. Events where no η's are produced contribute to the scattered background, and do not have any particular structure under the $\eta\eta$ peak.

The amount of background is determined by fitting the scatter plot of every energy point by minimizing a negative-log-likelihood [2]. The function used is:

$$f(m^x_{\gamma\gamma}, m^y_{\gamma\gamma}) = \underbrace{\frac{A}{\sigma^2}\ exp\Big[-\frac{(m^x_{\gamma\gamma}-m_\eta)^2+(m^y_{\gamma\gamma}-m_\eta)^2}{2\sigma^2}\Big]}_{\eta\eta-signal} +$$

$$\underbrace{+\underbrace{B\ \Big\{\frac{1}{\sigma}\ exp\Big[-\frac{(m^x_{\gamma\gamma}-m_\eta)^2}{2\sigma^2}\Big]+\ \frac{1}{\sigma}\ exp\Big[-\frac{(m^y_{\gamma\gamma}-m_\eta)^2}{2\sigma^2}\Big]\Big\}}_{Berms}+\underbrace{C+D\ (m^x_{\gamma\gamma}+m^y_{\gamma\gamma})}_{Plane}}_{background} \tag{5.4}$$

where A, B, C, D and σ are free parameters. The area where the fit is performed is chosen as the one defined by $|m^x_{\gamma\gamma} - m_\eta| <$140 MeV and $|m^y_{\gamma\gamma} - m_\eta| <$140 MeV.

The size, Δz, of the bins in z is chosen as 0.05 (twice the size of the bins for the $\pi^0\pi^0$ and $\pi^0\eta$ analyses) to guarantee a sufficient number of $\eta\eta$ candidates in each bin. However, that does not guarantee a sufficient number of background entries to populate the berms and the surrounding of the $\eta\eta$ peak to perform the the scatter plot fit on single Δz bins. Hence, what is fitted is the scatter plot with the events

[2]The scatter plot is symmetrized by plotting $m^{fw}_{\gamma\gamma}$ alternatively on the x- and y-axis, where it takes the names $m^x_{\gamma\gamma}$ and $m^y_{\gamma\gamma}$, respectively.

of the entire z-range of an energy point.

Figure 5.8 shows the entries (over the full range of z) in the scatter plot for the energy point at $E_{cm} = 3415$ MeV, the function $f(m^x_{\gamma\gamma}, m^y_{\gamma\gamma})$ as determined by the fit, and their magnified versions. In the magnified plot of the fit, the underlying contribution of the berms and the plane is also represented. The integral of the berms and the plane over the region selected by the invariant mass cuts (cuts 5 and 6 in section 5.4) is taken as an estimate of the background over the full range of z of the energy point $E_{cm} = 3415$ MeV. For this energy point, the parameters of Equation 5.4 determined by the fit to the plot in Figure 5.8 are:

- $A/\sigma^2 = 19.11 \pm 0.70$ Events/(49 MeV^2)
- $B/\sigma = 0.392 \pm 0.043$ Events/(49 MeV^2)
- $\sigma = 26.26 \pm 0.40$ MeV
- $C/\sigma = 0.0 \pm 1.5 \times 10^{-5}$ Events/(49 MeV^2)
- $D/\sigma = 24.3 \pm 7.2 \times 10^{-3}$ Events/(49 MeV^3).

This parameters determine a number of background events over the full range of z of ~ 157, to be compared to a number of $\eta\eta$ candidates of 1,836 .

The above procedure is repeated for all the 17 energy points, so that for each of them the background events in the full z-range is determined.

At this point, since we are interested in the $\eta\eta$ differential cross-section, we need to determine the background in each bin of z. In order to do that, it is necessary to determine the background angular distribution. A sufficient number of entries to populate the berms and scattered background in each single z-bin can be obtained only by merging all 17 energy points.

Before doing that, we need to check that the background angular distribution is not significantly different from energies off-resonance and at-resonance. By merging the energy points at resonance (the nine points between $E_{cm} = 3406.1$ and 3426 MeV), selecting the events that fall around the $\eta\eta$ peak by applying the cuts:

- $|m^x_{\gamma\gamma} - m_\eta| < 140$ MeV

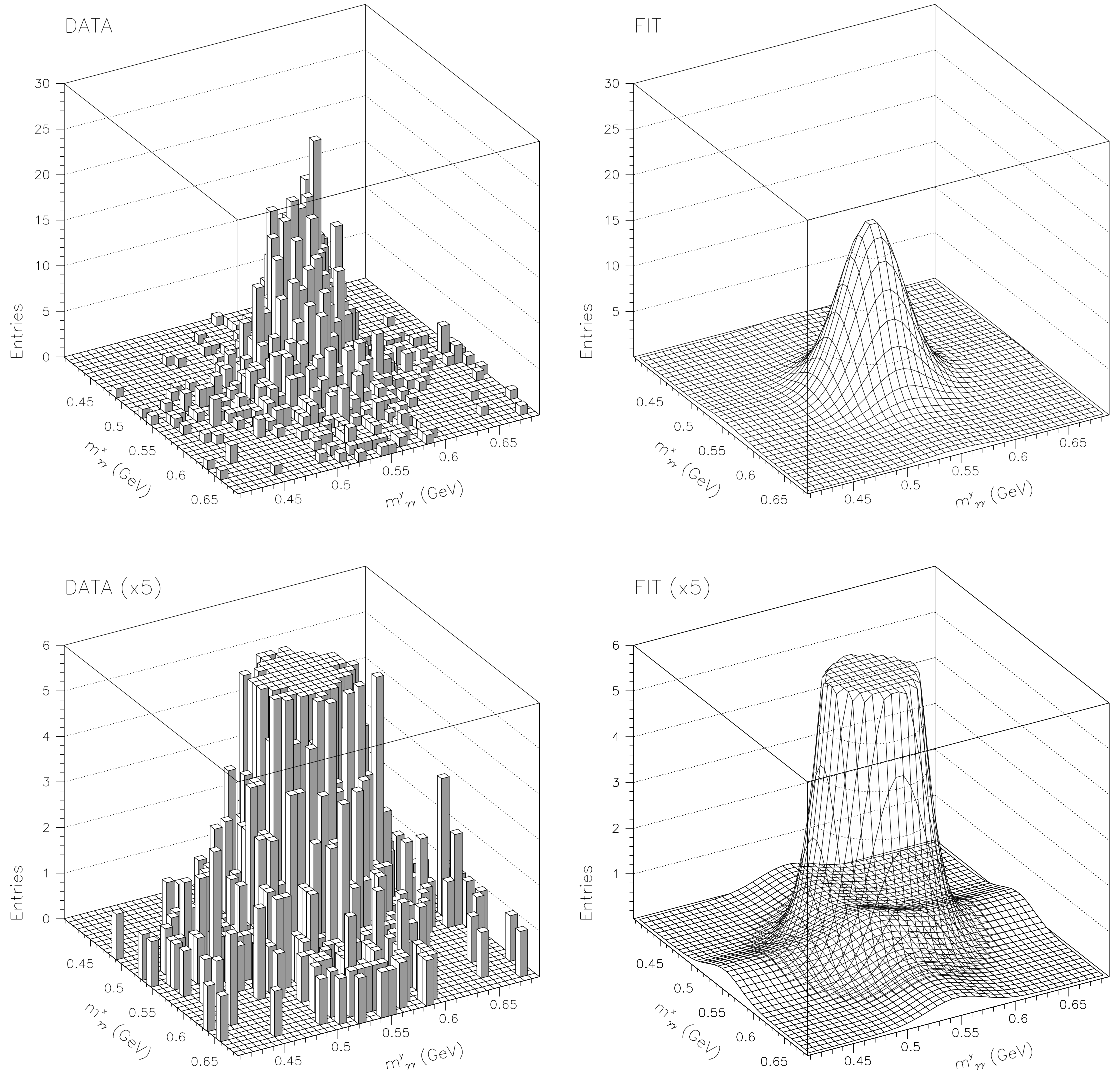

Figure 5.8: Top left: the (symmetrized) LEGO plot of the two $\gamma\gamma$ invariant masses at $E_{cm} = 3415$ MeV. All $\eta\eta$ cuts are applied except the ones on the invariant masses themselves. Top right: the fit parameterization of the top left plot. Bottom left: magnification of top left plot. Bottom right: magnification of top right plot, where the underlying background contribution (berms+plane) is made visible.

- $|m^y_{\gamma\gamma} - m_\eta| < 140$ MeV
- $\sqrt{(m^x_{\gamma\gamma} - m_\eta)^2 + (m^y_{\gamma\gamma} - m_\eta)^2} > 90$ MeV ,

and plotting them versus z, we obtain the at-resonance background distribution of Figure 5.9. Repeating the same procedure for the remaining eight energy points, we obtain the off-resonance background distribution (shown in the same figure).

The at-resonance and off-resonance background angular distributions are not significantly different. We are then allowed to merge the two distributions and perform a 5-degree polynomial fit that gives us a function for the background angular distribution valid at all 17 energies. The fit curve is also shown in Figure 5.9.

Now, for each single energy point, the previously determined background entries in the full z-range can be multiplied by the polynomial fit of Figure 5.9 to obtain the estimate of the background events in each single bin of z. Figure 5.10 shows the number of events that pass the $\eta\eta$ selection and the number of events attributed to the background in every bin of the energy point $E_{cm} = 3415$ MeV. For each bin in z, the estimate background is subtracted from the total number of selected events.

On average, the background constitutes $\sim 8\%$ of the $\eta\eta$ candidates. Appendix E.2 provides a plot (Figure E.5) where the estimated background is shown versus the energy in the center of mass.

5.7 NDST and Trigger Efficiencies

The $\eta\eta$ sample is not large enough to determine with sufficient precision the Neutral Data Summary Tape efficiency for this channel [3]. However, the NDST selection (Section 3.3) has little in it that may impact $\bar{p}p \to \eta\eta \to \gamma\gamma\,\gamma\gamma$ differently than $\bar{p}p \to \pi^0\eta$ (or $\pi^0\pi^0$) $\to \gamma\gamma\,\gamma\gamma$. In addition, the 5%-cut on the confidence level of the fit to $\bar{p}p \to \gamma\gamma\gamma\gamma$, applied in all three analyses, tightens the NDST cuts. Therefore, it is sensible to set the NDST efficiency for $\eta\eta$ events equal to that determined for $\pi^0\eta$ events, which is rewritten in Table 5.1.

[3] The method to determine the NDST efficiency uses only one of the original neutral tapes for each energy point (see Section 3.3).

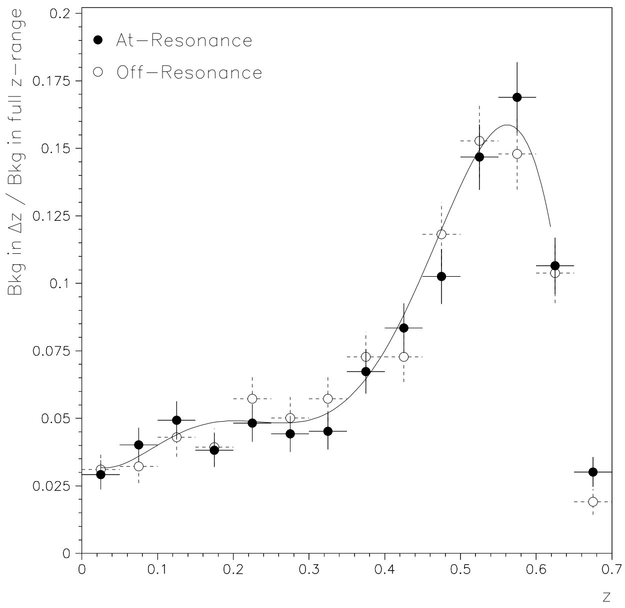

Figure 5.9: Background angular distribution for at-resonance and off-resonance energies. A 5-degree polynomial fit (solid line) is performed on the two merged distributions.

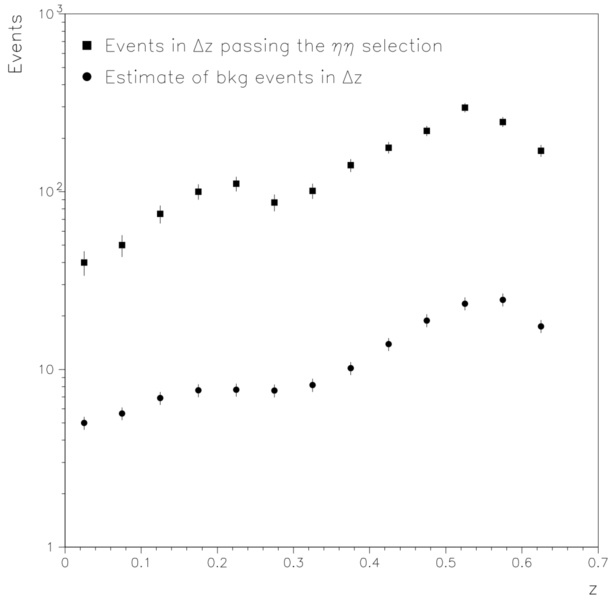

Figure 5.10: Selected $\eta\eta$ and background events in each bin Δz at $E_{cm} = 3415$ MeV. (The fall in the number of events at $z \gtrsim 0.6$ is an effect of the acceptance, since here the data are not acceptance-corrected.)

Energy (MeV)	ϵ_{NDST} (%)	ϵ_{ETOT} (%)	ϵ_{trig} (%)
3339.5	99.14±0.38	97.53±0.68	93.83±0.67
3365.0	99.30±0.35	98.11±0.41	94.37±0.41
3384.4	99.76±0.24	98.57±0.37	94.78±0.37
3384.8	99.42±0.29	99.33±0.16	95.53±0.16
3392.0	99.82±0.18	98.43±0.39	94.66±0.39
3400.1	99.61±0.27	97.54±0.47	93.81±0.47
3406.1	99.63±0.26	98.89±0.25	95.08±0.25
3409.1	99.33±0.33	97.87±0.51	94.12±0.51
3410.3	99.32±0.39	98.57±0.36	94.78±0.36
3413.8	99.33±0.39	97.54±0.42	93.79±0.42
3415.0	99.75±0.25	99.28±0.21	95.46±0.21
3415.9	100.00−0.23	99.05±0.24	95.22±0.24
3418.0	99.39±0.35	99.78±0.15	95.94±0.15
3422.1	99.42±0.33	98.09±0.36	94.32±0.36
3426.0	99.78±0.22	98.18±0.39	94.39±0.39
3430.1	99.17±0.41	97.76±0.49	94.00±0.49
3469.9	100.00−0.28	99.44±0.20	95.59±0.20

Table 5.1: The NDST efficiency (ϵ_{NDST}), along with the Neutral-ETOT (ϵ_{ETOT}) trigger efficiency of each energy point. The overall trigger efficiency (ϵ_{trig}) is decreased by those events that are re-directed toward study triggers.

The simplifying choice of using only events selected by the trigger logic Neutral-ETOT is made (cut 11 on page 174). The motivations for this choice are those explained in Section 4.6 for the $\pi^0\eta$ channel. Such motivations apply even more to the $\eta\eta$ case. In fact, the efficiency of the Neutral-PBG1 trigger, ϵ_{PBG1}, falls to an average of 89.9%, while the one of Neutral-ETOT, ϵ_{ETOT}, is unaltered. In the entire sample of events that passes cuts 1 through 4 on page 82 and the $\eta\eta$ cuts 5 through 10 on page 174, only 303 events (1.3%) have triggered Neutral-PBG1 alone; 2,424 events (10.0%) have triggered Neutral-ETOT alone; and 21,364 events (88.7%) have triggered both.

The efficiency of Neutral-ETOT, ϵ_{ETOT}, is determined as done for the $\pi^0\pi^0$ and $\pi^0\eta$ cases. Equation 4.5 is used to calculate the overall trigger efficiency. The efficiencies ϵ_{ETOT} and ϵ_{trig} for every energy point are reported in Table 5.1.

Photon Conversion Probability. The probability that one or more photon conversions into e^+e^- cause the loss of a 4-photon event is described in Section 3.10.1.

5.8 The $\eta\eta$ Cross Section

The $\bar{p}p \to \eta\eta$ differential cross section, $d\sigma/dz$, is calculated in every bin of z as

$$\frac{d\sigma}{dz} = \frac{N_{\eta\eta}}{\mathcal{L}\times\ a\times\epsilon\ \times\epsilon_{trig}\times P_{reject}\times[B(\eta\to\gamma\gamma)]^2\times\Delta z}\ , \tag{5.5}$$

where $N_{\eta\eta}$ is the number of events passing the $\eta\eta$ selection and falling in the bin minus the estimated number of instrumental background events in that bin, $\mathcal{L}$ is the luminosity of the energy point (see Table 3.2), $a\times\epsilon$ is the product of the acceptance and efficiency (see Section 5.5) corrected for polar angle resolution and pileup (see page 179), ϵ_{trig} is the overall trigger efficiency (see Table 5.1), P_{reject} is the probability of event rejection due to photon conversions into e^+e^- pair (see Equation 3.13), $B(\eta\to\gamma\gamma) = (39.43\pm 0.26)\%$, and $\Delta z = 0.05$ is the bin width[4].

[4]The bin width is chosen twice as large as the bin size of the previous two analyses to allow a sufficient number of $\eta\eta$ candidates in every bin.

Table 5.2 reports, for one of the 17 energy points, the bin-dependent quantities necessary to calculate the differential cross section. The complete series of tables, one for every energy point, is located in Appendix H.

z	$d\sigma/dz$ (nb)	N_{tot}	N_{bkg}	$N_{\eta\eta}$	$a \times \epsilon$
0.0250	4.6 ± 0.8	40 ± 6.3	5.0 ± 2.2	35.0 ± 6.3	$0.450\ (0.465) \pm 0.003$
0.0750	5.9 ± 0.9	50 ± 7.1	5.7 ± 2.4	44.4 ± 7.1	$0.459\ (0.464) \pm 0.003$
0.1250	9.3 ± 1.2	75 ± 8.7	6.9 ± 2.6	68.1 ± 8.7	$0.453\ (0.451) \pm 0.003$
0.1750	12.7 ± 1.4	100 ± 10.0	7.6 ± 2.8	92.4 ± 10.0	$0.450\ (0.446) \pm 0.003$
0.2250	14.4 ± 1.5	111 ± 10.5	7.7 ± 2.8	103.3 ± 10.5	$0.444\ (0.441) \pm 0.003$
0.2750	11.5 ± 1.4	87 ± 9.3	7.6 ± 2.8	79.4 ± 9.3	$0.424\ (0.426) \pm 0.003$
0.3250	13.9 ± 1.5	101 ± 10.1	8.2 ± 2.9	92.8 ± 10.1	$0.406\ (0.412) \pm 0.003$
0.3750	21.5 ± 2.0	141 ± 11.9	10.2 ± 3.2	130.8 ± 11.9	$0.367\ (0.374) \pm 0.003$
0.4250	30.7 ± 2.5	177 ± 13.3	13.9 ± 3.7	163.1 ± 13.3	$0.324\ (0.327) \pm 0.003$
0.4750	46.2 ± 3.4	220 ± 14.8	18.8 ± 4.3	201.2 ± 14.8	$0.267\ (0.268) \pm 0.002$
0.5250	86.7 ± 5.5	297 ± 17.2	23.5 ± 4.8	273.5 ± 17.2	$0.196\ (0.194) \pm 0.002$
0.5750	116.5 ± 8.4	247 ± 15.7	24.7 ± 5.0	222.3 ± 15.7	$0.119\ (0.117) \pm 0.002$

Table 5.2: The bin-dependent quantities for the energy point E_{cm} = 3415 MeV: the center of the bin (z), the $\bar{p}p \to \eta\eta$ differential cross section ($\frac{d\sigma}{dz}$), the total number of events (N_{tot}) passing the $\eta\eta$ selection, the estimated number of instrumental background events (N_{bkg}), the number of $\eta\eta$ events ($N_{\eta\eta} \equiv N_{tot} - N_{bkg}$, with uncertainty conservatively taken as $\sqrt{N_{tot}}$). The last column reproduces the product of the acceptance and efficiency ($a \times \epsilon$) corrected for pileup; the uncertainty on $a \times \epsilon$ is determined by the number of Random Gate events available. The value of $a \times \epsilon$ given outside the brackets is determined by using a uniform $\pi^0\eta$ angular distribution. The value given inside the brackets is determined by using the estimate of the angular distribution corrected for the limited polar angle resolution, as described in Appendix B.

Figure 5.11 shows the $\bar{p}p \to \eta\eta$ differential cross section for the energy point E_{cm} = 3415 MeV. The complete series of smaller-scale plots with the differential cross section of all 17 energy points is reported in Figures 5.12 and 5.13.

The cross section, $\Delta\sigma$, integrated over a certain range of z is obtained by summing $(d\sigma/dz) \times \Delta z$ of the bins included in the range. Figures 5.14 and 5.15 show the $\bar{p}p \to \eta\eta$ cross section integrated from $z = 0$ to increasing upper values z_{max} ,

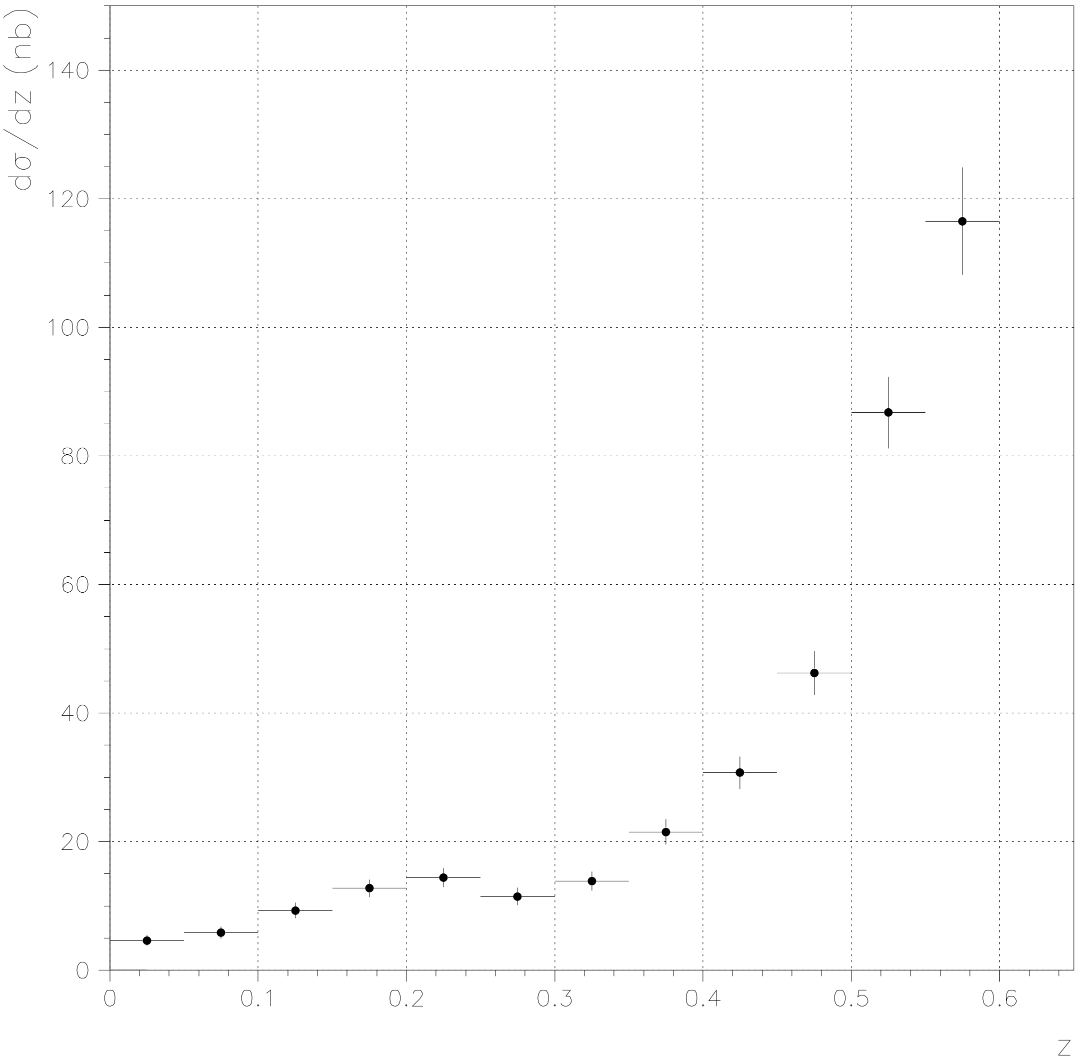

Figure 5.11: The measured $\bar{p}p \to \eta\eta$ differential cross section plotted versus z at $E_{cm} = 3415$ MeV.

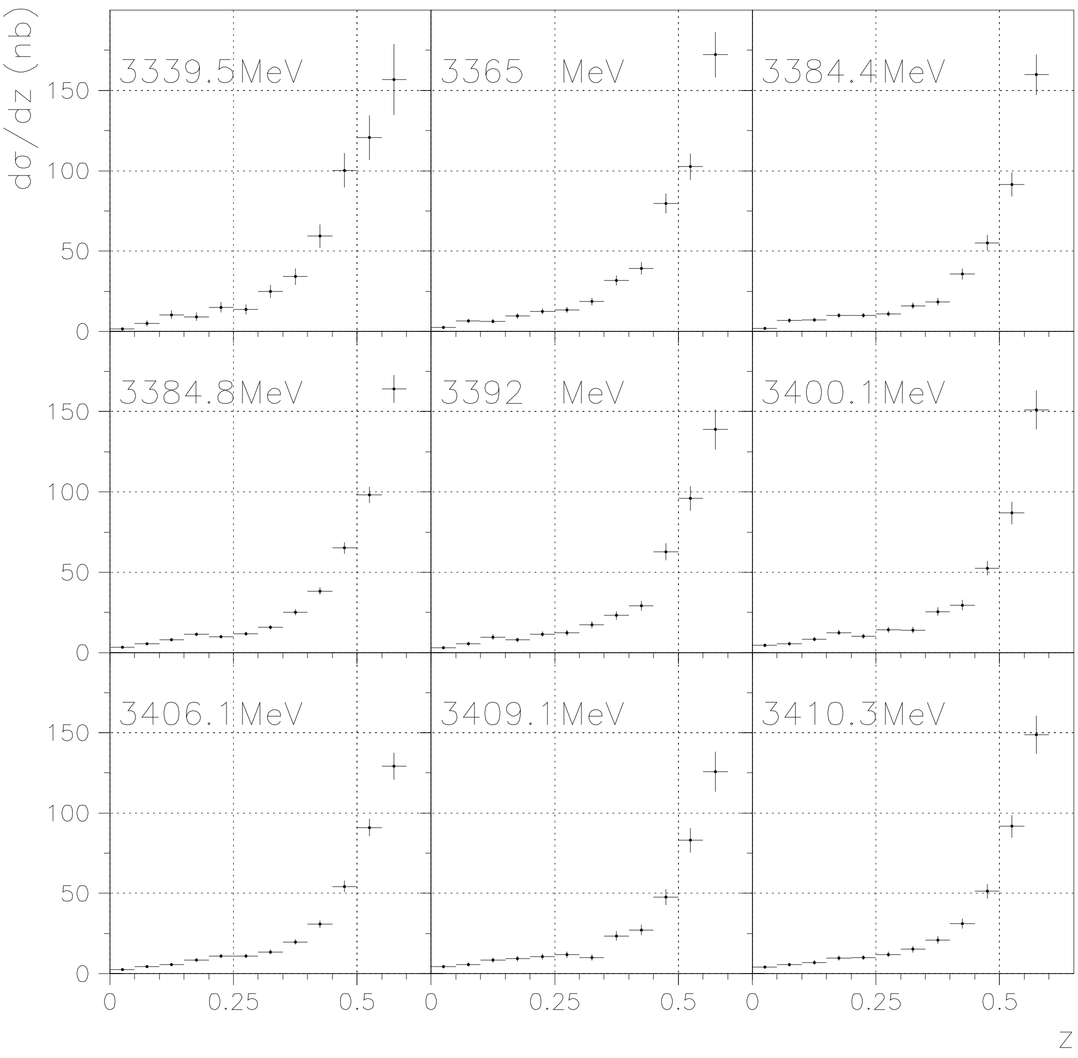

Figure 5.12: The measured $\bar{p}p \rightarrow \eta\eta$ differential cross section plotted versus z at the E_{cm} indicated in each plot.

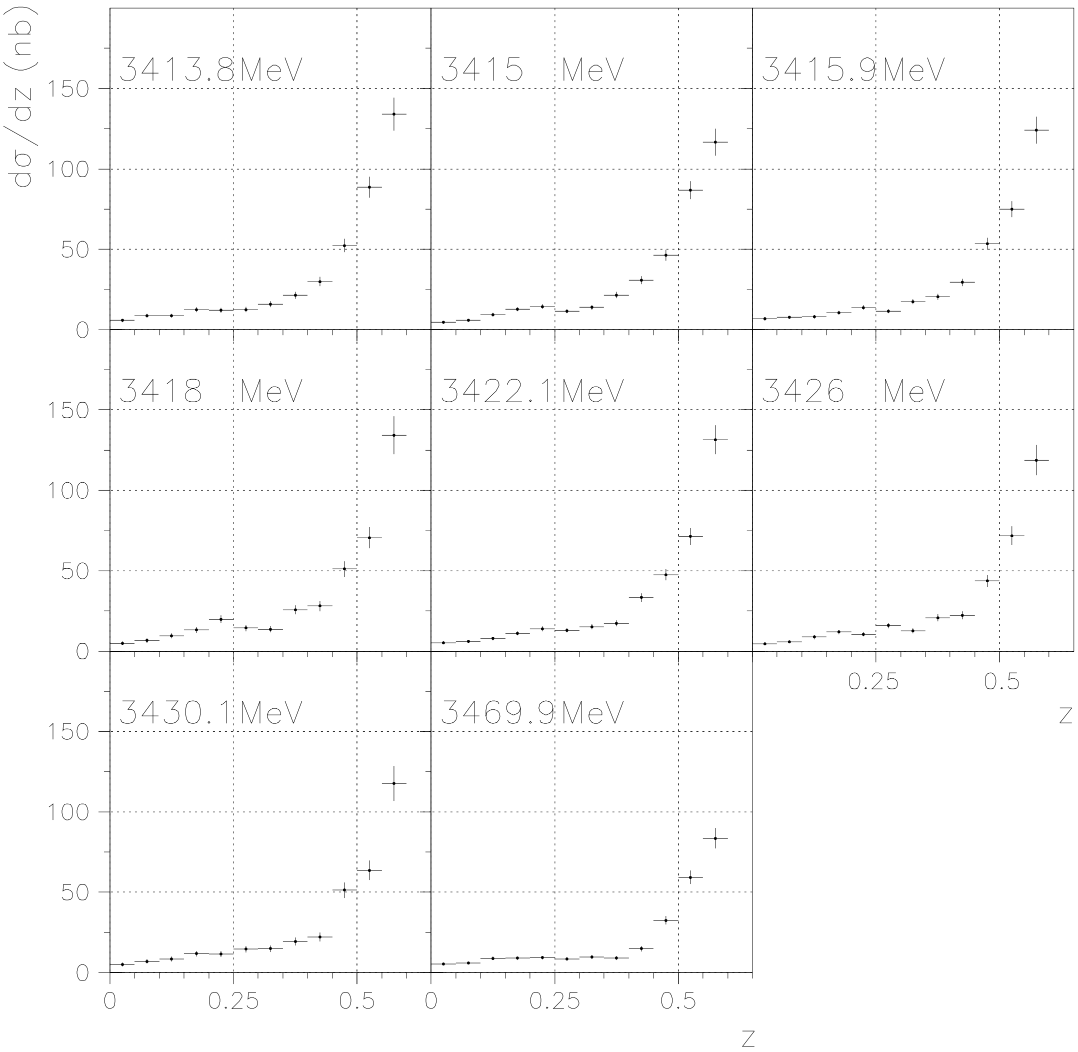

Figure 5.13: The measured $\bar{p}p \to \eta\eta$ differential cross section plotted versus z at the E_{cm} indicated in each plot.

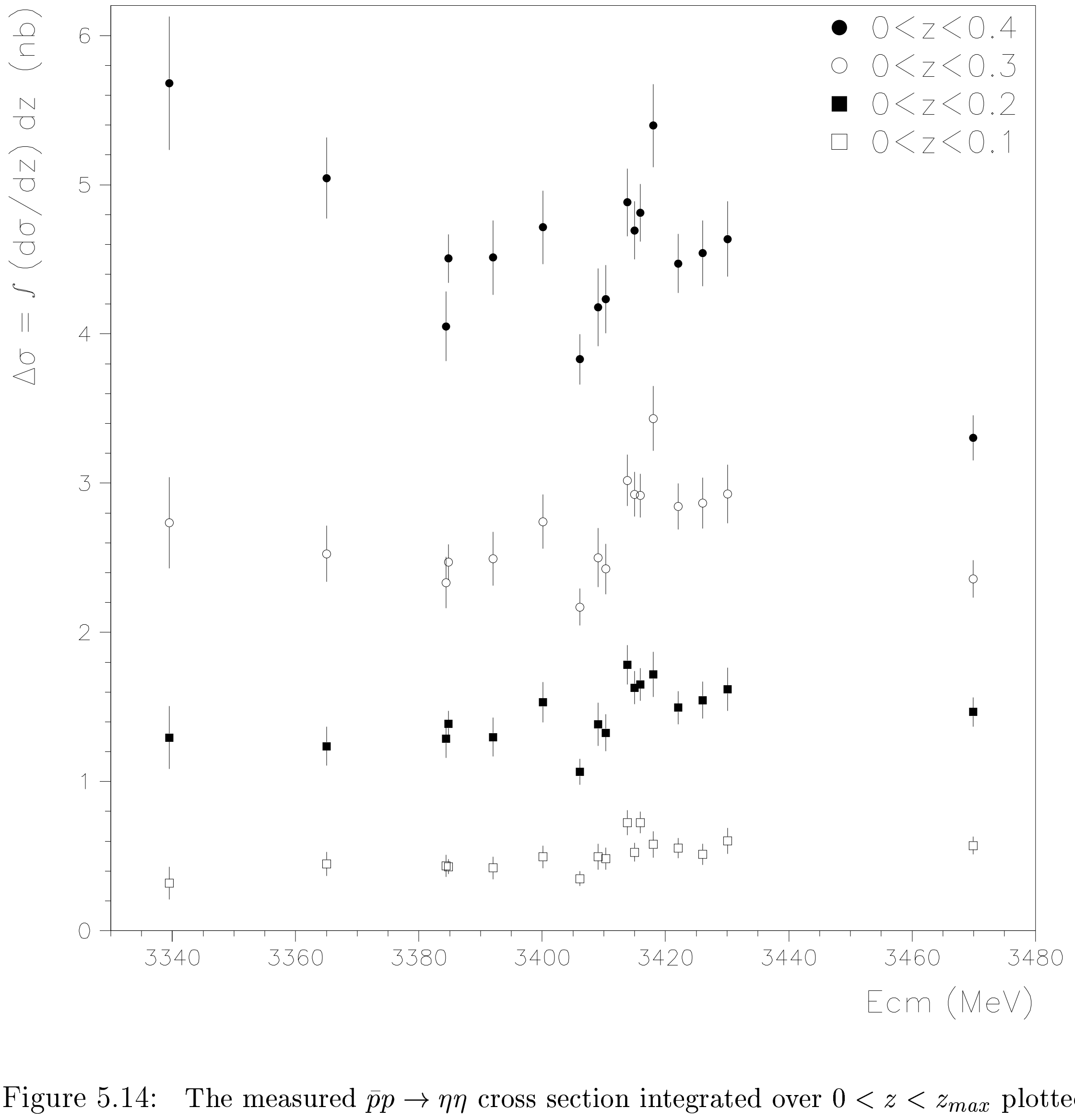

Figure 5.14: The measured $\bar{p}p \to \eta\eta$ cross section integrated over $0 < z < z_{max}$ plotted versus E_{cm} .

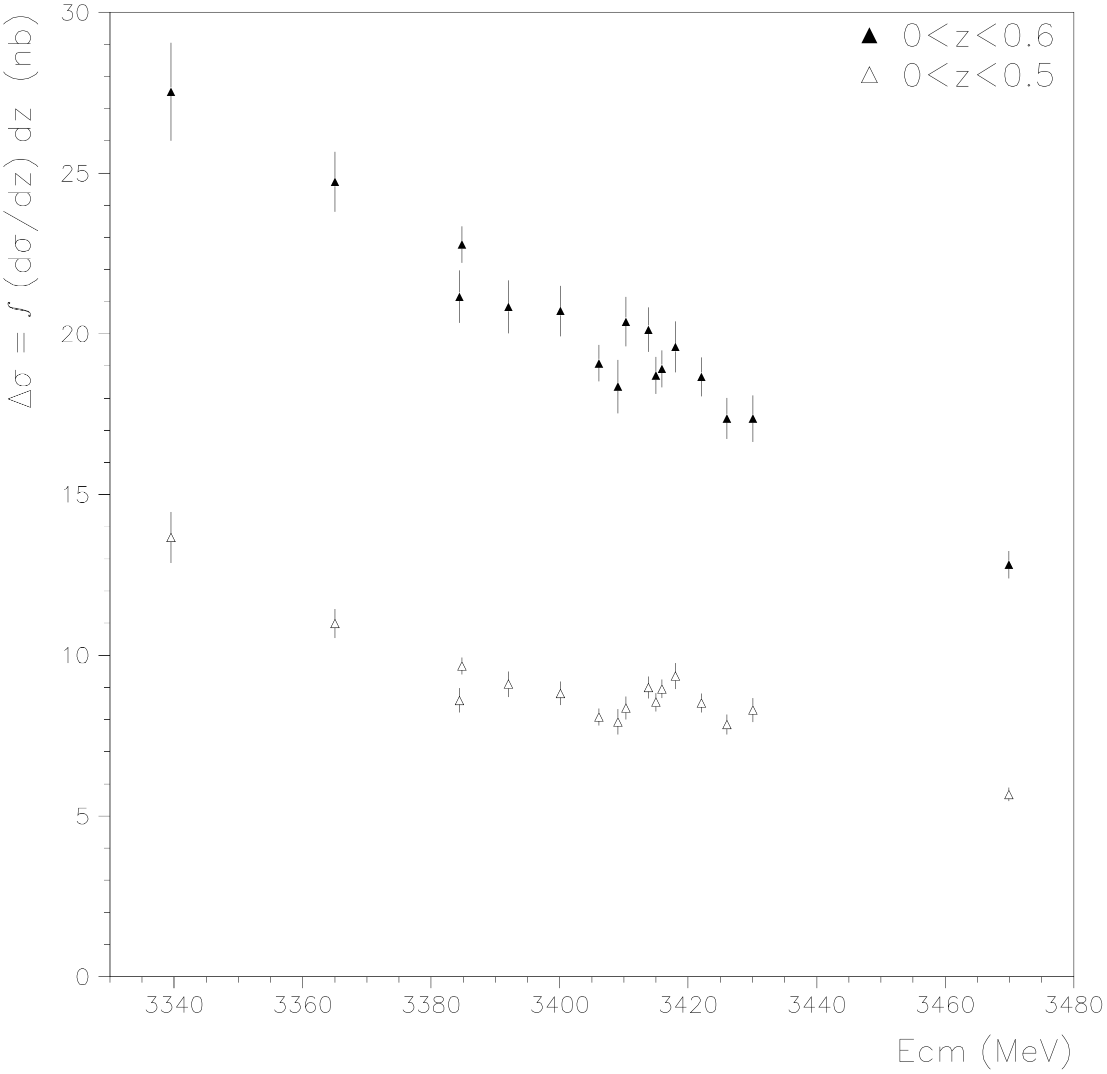

Figure 5.15: The measured $\bar{p}p \to \eta\eta$ cross section integrated over $0 < z < z_{max}$ plotted versus E_{cm} .

while Figure 5.16 shows the integration over subsequent z-ranges as wide as 0.1 .

As in the $\pi^0\pi^0$ case, the cross section is dominated by the non-resonant continuum $\bar{p}p \rightarrow \eta\eta$, which has a smooth dependence on the energy. Even in the $\eta\eta$ channel, a resonance signal is visible nearby the mass of the χ_{c0} . The interference pattern appears different from the one observed in the $\pi^0\pi^0$ channel. There is destructive interference on the low energy side of the resonance, and constructive on the high side. The maximum of the pattern is shifted toward the high side of the χ_{c0} mass [1].

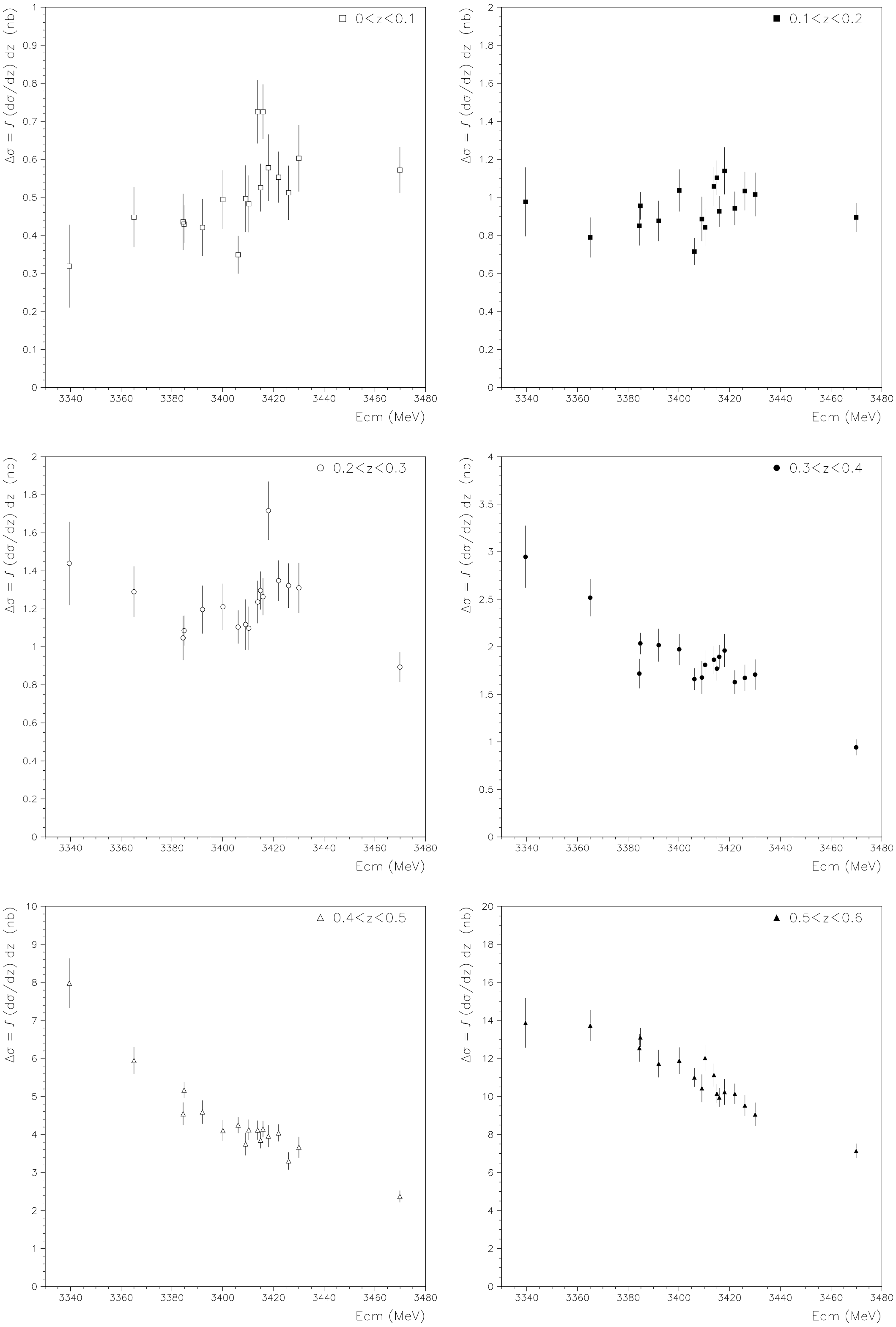

Figure 5.16: The measured $\bar{p}p \to \eta\eta$ cross section integrated over $z_{min} < z < z_{max}$ plotted versus E_{cm} .

5.9 Fit to the $\eta\eta$ Cross Section

Following the procedure adopted in the $\pi^0\pi^0$ analysis, a binned maximum likelihood fit to the $\bar{p}p \to \eta\eta$ differential cross section is performed simultaneously on all of the 17 energy points of the data sample. The parameterization used is given in Equation 3.19, with the partial wave expansion of Equations 3.20 and 3.21. The mass and with of the χ_{c0}, implicit in the definition of x of equation 1.13, are constrained to the values of equations 3.15 and 3.16 determined by means of the $J/\psi\,\gamma$ channel [1]. The fit is performed on an angular range limited to $0 < z < 0.6$. Within this range, the data sample consists of 19,675 $\eta\eta$ events (instrumental background already subtracted).

The result of the fit for $d\sigma(x,z)/dz$ is shown in Figure 5.17, where the energy points closer to the resonance are merged. The discussion of the single components of the fit, which are also shown in the figure, follows closely the one provided in Section 3.13 for the $\pi^0\pi^0$ fit. Even here, the contribution of the "pure" resonance, $A_R^2/(x^2+1)$, is not discernible from zero. The non-interfering helicity-1 continuum, of magnitude B^2, vanishes at $z = 0$ due to the factor z present in all associate functions $P_J^1(z)$. B^2 dominates at larger z, but its growth begins at a larger value of z, as compared to the $\pi^0\pi^0$ case. The interfering helicity-0 continuum, of magnitude A^2, dominates for a large part of the angular range ($0 < z \lesssim 0.5$) and provides the amplification for the interference-enhanced resonance signal seen in the separation between $d\sigma/dz$ and $A^2 + B^2$. This separation is almost entirely due to the interference-term of Equation 1.17.

The agreement of the fit with the data is shown at all 17 energy points in Appendix E.1 (Figures E.1 and E.2). In the same Appendix (Figures E.3 and E.4) the fit and the cross section are shown integrated over different angular ranges and plotted versus E_{cm}.

Since the number of events available in the $\eta\eta$ channel is limited (about 20 and 4 times less than the $\pi^0\pi^0$ and $\pi^0\eta$ channels, respectively), the shape of the angular distribution within the available range in z is not as resolved as in the other channels. With respect to the $\pi^0\pi^0$ and $\pi^0\eta$, the $\eta\eta$ channel requires a minor number

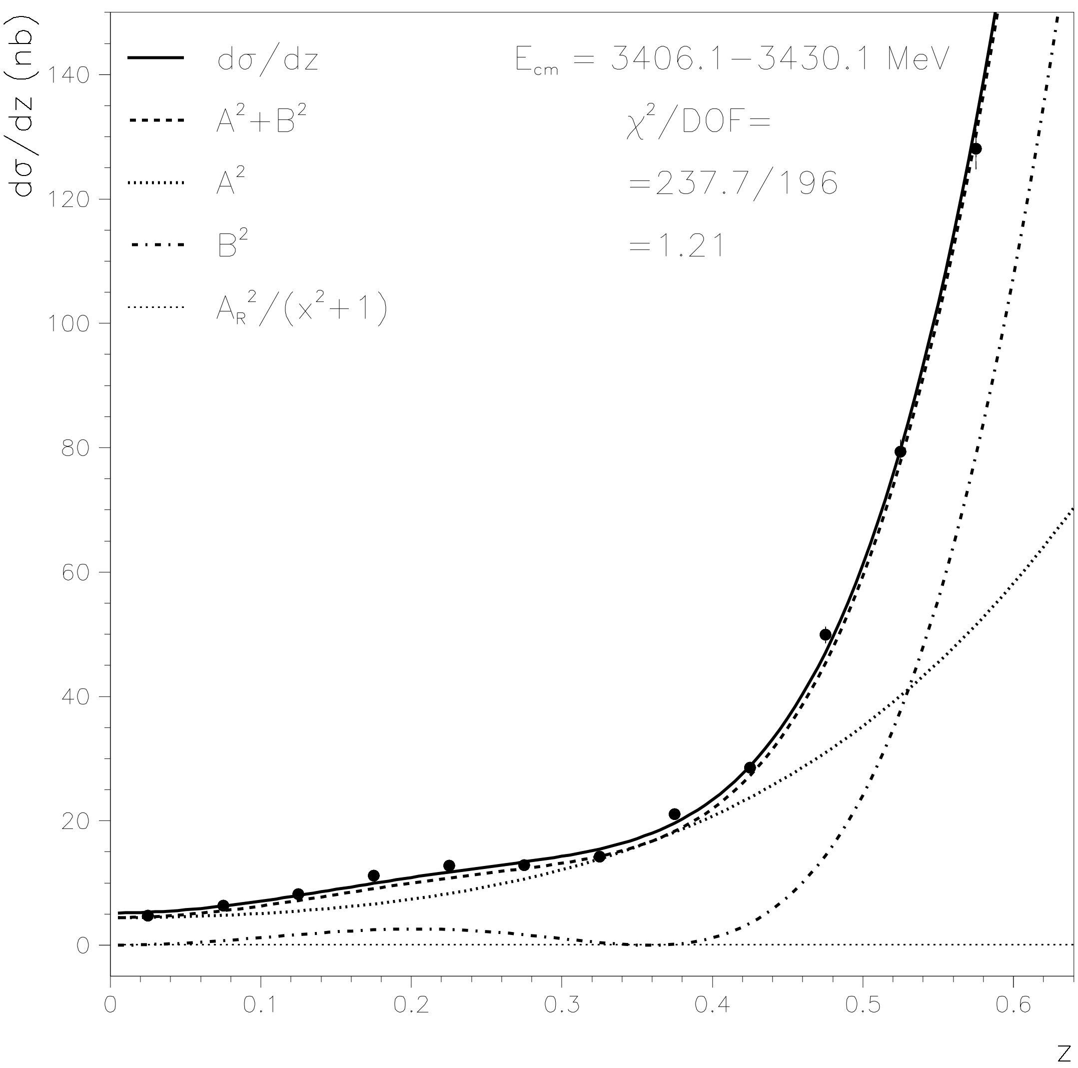

Figure 5.17: The $\bar{p}p \to \eta\eta$ differential cross section versus z at $E_{cm} = 3406.1 - 3430.1$ MeV (the energies closer to the χ_{c0} resonance are merged in this plot to reduce fluctuations). The fit of Equations 3.19, 3.20 and 3.21 and its components are also shown.

of parameters to obtain a fit that cannot be significantly improved (the F-test is used to see if the addition of further parameters is justified). In the best fit C_0 and C_2 have a linear energy dependence; C_4 vanishes and is subsequently constrained to zero; and C_{21} and C_{41} do not require an energy dependence. The phases δ_0, δ_2 and δ_4 are equal to each other, different from zero [5] and constant in energy. The phases of the helicity-1 continuum[6] also are not significantly different from each other and do not exhibit an energy dependence. Notice that even in the $\pi^0\pi^0$ and $\pi^0\eta$ cases the phases of the non-resonant amplitudes (with equal helicity) are very similar to each other. Table 5.3 reproduces the fit results for coefficients and phases.

J	C_J [nb$^{1/2}$]	C_J^1 [nb$^{1/2}$]
0	$C_0 = (7.27 \pm 0.11) - (0.269 \pm 0.012)\,x$	–
2	$C_2 = (2.07 \pm 0.06) - (0.116 \pm 0.006)\,x$	$C_2^1 = (4.56 \pm 0.07)$
4	$C_4 = 0$	$C_4^1 = (2.65 \pm 0.05)$
J	δ_J [degree]	δ_J^1 [degree]
0	$\delta_0 = 138.2 \pm 2.9$	–
2	$\delta_2 = 138.2 \pm 2.9$	–
4	$\delta_4 = 138.2 \pm 2.9$	$\delta_4^1 - \delta_2^1 = 0$

Table 5.3: Fit results for the coefficients (with a linear energy dependence when found necessary) and phases of the partial wave expansion of Equations 3.20 and 3.21. The quoted errors are statistical; systematic errors due to the limited available angular range ($z \leq 0.6$) should be dominant.

5.10 Extraction of the Resonant Amplitude A_R

To determine the product of the branching ratios of the χ_{c0} to the entrance and exit channels, it is critical to know the size of the magnification effect due to the interference between the resonance and the non-resonant continuum. Only the helicity-0

[5] This means that the phase of the resonance amplitude is different from the phases of the non-resonant amplitudes, but the phases of the non-resonant amplitudes do not exhibit a significant difference among themselves.

[6] Only the difference between δ_4^1 and δ_2^1 is measurable.

component of the continuum interferes and hence it is necessary to determine accurately the relative contributions of the helicity-0 and the helicity-1 continuum.

5.10.1 Fits on single bins Δz with $|B\ e^{i\delta_B}|^2 = 0$.

The helicity-1 amplitude, $Be^{i\delta_B}$, vanishes at $z = 0$ because of a factor z present in the associate Legendre polynomials, $P^1_J(z)$, that constitute it (see Table 1.4).

As done in Section 3.14.1 for the $\pi^0\pi^0$ analysis, the growth of the non-interfering continuum can be investigated by performing a series of independent fits on each bin[7] Δz. Each one of these fit uses the parameterization of Equation 3.19 eith $Be^{i\delta_B}$ set equal to zero. Specifically,

$$\Delta\sigma = \frac{d\sigma}{dz}\ \Delta z = \left| -\frac{A_R}{x+i} + A\ e^{i\delta_A} \right|^2\ \Delta z. \tag{5.6}$$

The parameterization used for the helicity-0 component of the continuum is

$$A^2 \equiv a_0 + a_1 x \tag{5.7}$$

to allow a linear energy dependence. The mass and width of the χ_{c0} are constrained to the values of equations 3.15 and 3.16 .

The helicity-1 component is constrained to zero to determine at which value of z its contribution is no longer negligible. In fact , a drop for increasing z in the fit estimate of A_R (A_R is known to be a constant) would signify that the helicity-1 component, which is not accounted for in these fits, has grown significantly.

Figure 5.18 shows the fits to the cross section versus E_{cm} in every bin Δz up to[8] $z = 0.4$. The fit results for the parameters of Equations 5.6 and 5.7 are shown in Figure 5.19.

The top-left plot in Figure 5.19 shows that no drop of A_R is apparent in the

[7]For these fits, bins with a width $\Delta z = 0.1$ (twice the width generally used in the $\eta\eta$ analysis) are used to reduce the statistical fluctuations.

[8]These fits are not performed in the region $z \geq 0.4$ since their purpose is to determined the growth of the helicity-1 component in the small z region, and because these fits are not significant in the forward region where the interference-enhanced resonant signal is too small relatively to the continuum.

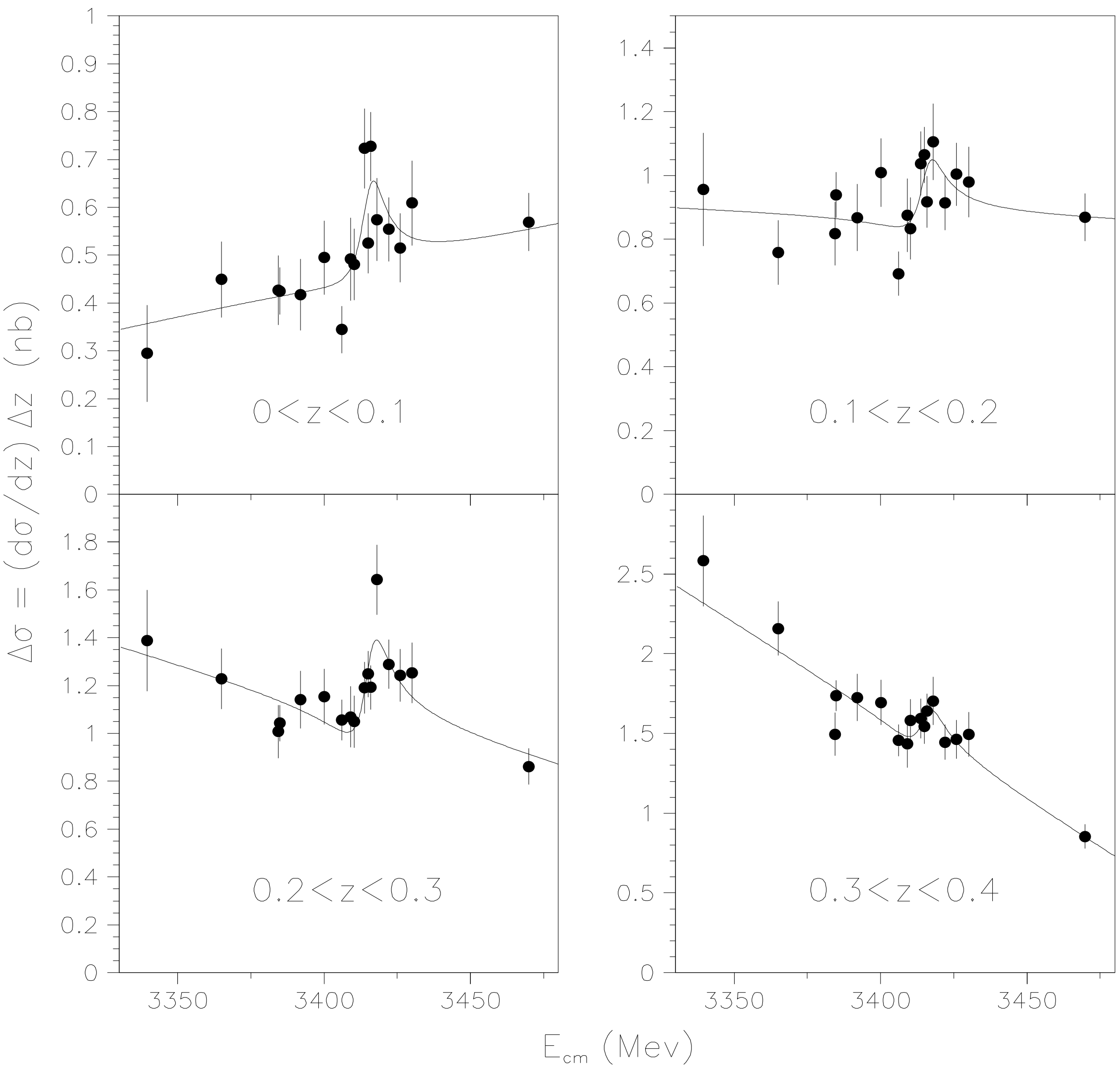

Figure 5.18: Fits to the $\bar{p}p \to \eta\eta$ cross section versus E_{cm}. Each fit is performed in a bin of size $\Delta z = 0.1$ independently from the fits in the other bins using Equations 5.6 and 5.7 (the helicity-1 continuum $|B\ e^{i\delta_B}|^2$ is fixed to zero). The bins included here cover the region $z \leq 0.4$.

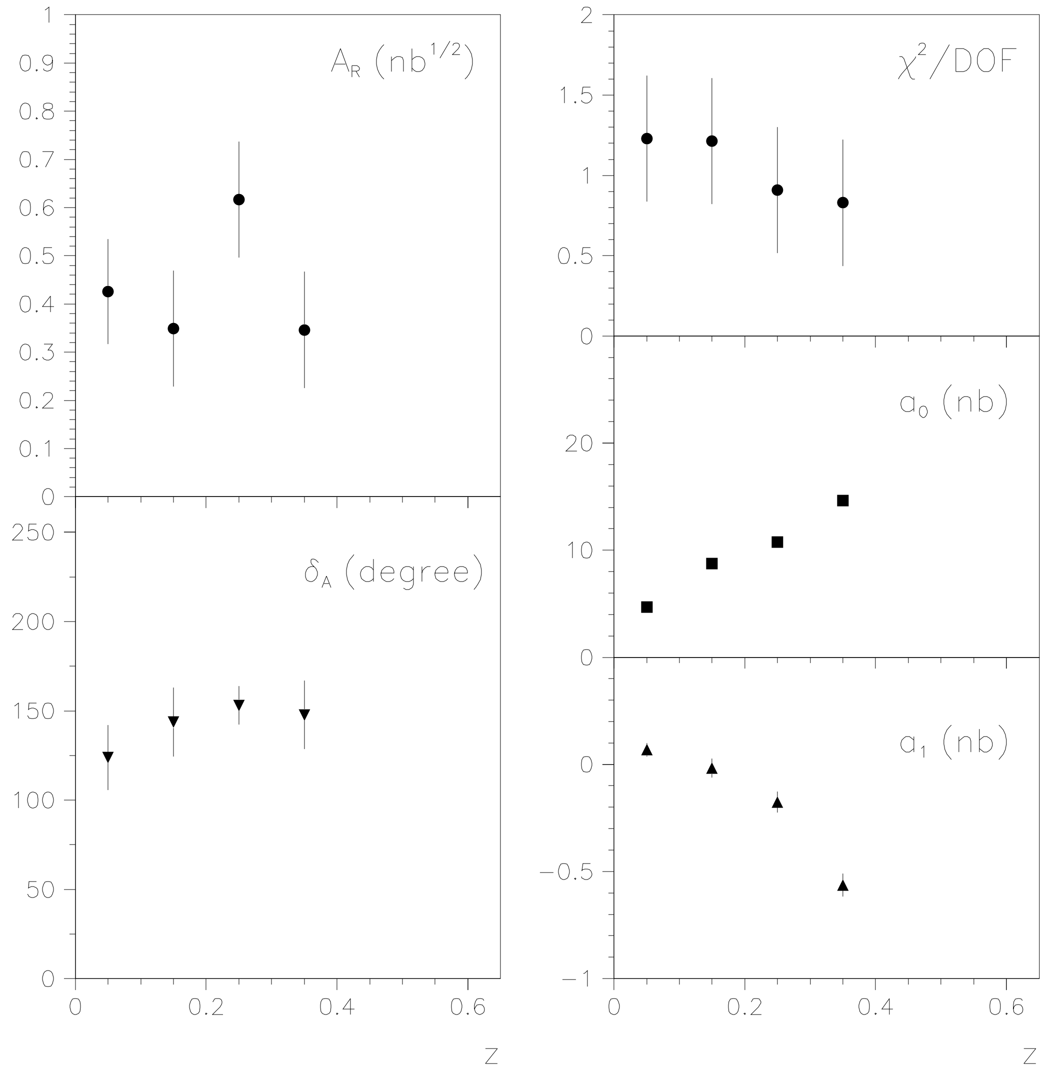

Figure 5.19: The parameters of Equations 5.6 and 5.7 as determined by the 4 independent fits of Figure 5.18.

region $0 < z < 0.4$. That is an indication that the rise of B^2 occurs at larger z than in the $\pi^0\pi^0$ case[9], or such a rise is not so significant to be resolved with the available data sample. The fit in Figure 5.17 also indicates that B^2 does not take over until $z \gtrsim 0.4$. This is helpful, since in order to see a clear signal in the plot of the $\eta\eta$ cross section versus E_{CM}, it is necessary to accumulate events and integrate over a larger z-range than in the $\pi^0\pi^0$ analysis[10].

Of course, incorporating a larger z-range in the fit that is used to estimate A_R (described in the next Sections 5.10.2 and 5.10.3, where the helicity-1 continuum is inserted in the fit relying on its estimate from Section 5.9) introduces a larger uncertainty on the relative contributions of A^2 and B^2 (at $z = 0$ this uncertainty is zero, since $B^2_{(z=0)} = 0$), and consequently on A_R itself [11]. On the other hand, the smaller is B^2 the smaller is the impact that our unperfect knowledge of it has on the estimate of A_R. The above indications that B^2 is contained relatively to A^2 in the range $0 < z \lesssim 0.4$ reduces the concerns about using a larger angular region to determine A_R.

5.10.2 Fits over $0 < z < z_{max}$ Setting $|B\ e^{i\delta_B}|^2$ to the Estimate from Section 5.9

Analogously to what is done in Appendix C.3 for the $\pi^0\pi^0$ analysis, the information from the different bins can be merged by performing new fits integrating over ranges $0 < z < z_{max}$ with increasing[12] z_{max}. The parameterization used is

$$\Delta\sigma = \int_0^{z_{max}} \left[\left| -\frac{A_R}{x+i} + A\ e^{i\delta_A} \right|^2 + \left| B\ e^{i\delta_B} \right|^2 \right] dz. \tag{5.8}$$

[9] In the $\pi^0\pi^0$ channel, the drop occurs at ~ 0.15 (see top-left plot in Figure 3.25)

[10] With the 20 times larger sample of $\pi^0\pi^0$ events, it is possible to resolve a very clear resonant signal integrating over a short z-range. That enables us to restrict to $0 < z < 0.125$ the integration range for the extraction of A_R, severely reducing the uncertainty on the helicity-1 continuum.

[11] Compare the systematic errors due to the B^2 in Tables 5.5 and 3.9 for the $\eta\eta$ and $\pi^0\pi^0$ cases, respectively.

[12] The used steps for the increment of z_{max} are $\Delta z = 0.05$, that is bin width generally used during the $\eta\eta$ analysis

The contribution of the helicity-1 continuum is inserted by constraining it to the estimate from the partial wave expansion fit of Section 5.9. The parameterization of the magnitude of the helicity-0 continuum is

$$A^2 \equiv a_0 + a_1 x + a_2 z^2 + a_3 z^2 x + a_4 z^4 \ , \tag{5.9}$$

where the necessary parameters are added, with increasing z_{max}, by searching for improvements in the χ^2 of the fit (using the F-test).

The fact that an energy/polar-angle mixing term ($a_3 z^2 x$) is required is already indicated by the parameter a_1 in Figure 5.19, and it becomes necessary for $z_{max} \geq 0.2$ The parameters a_3 and a_4 need to be inserted for $z_{max} \geq 0.1$ and $z_{max} \geq 0.25$, respectively (see parameter a_0 in Figure 5.19 or the shape of the differential cross section in Figures 5.11, 5.12 and 5.13). The phase δ_A does not require any significant dependence in x nor in z (in this reduced z-range), as already suggested by Figure 5.19.

The results for the resonant amplitude A_R as a function of z_{max} are shown in Figure 5.20 along with the reduced χ^2 of the fits.

5.10.3 Determination of A_R

Figure 5.20 shows that the estimate of A_R from the the fits in the previous Section 5.10.2 stabilizes for $z_{max} > 0.2$. The value of A_R is extracted from the fit performed over the angular range $0 < z < 0.35$ by setting

$$z_{max} = 0.35\,. \tag{5.10}$$

The result of this fit is shown in Figures 5.21 and 5.22.

Table 5.4 reproduces the values of the parameters as determined by the fit.

Figure 5.21 shows that even in the process $\bar{p}p \to \eta\eta$, as in the $\pi^0\pi^0$, a small resonant production $\bar{p}p \to \chi_{c0} \to \eta\eta$ interferes with the helicity-0 continuum production of the final state (of magnitude A^2) and generates an enhanced interference pattern. The selected angular region of integration is larger than in the $\pi^0\pi^0$ analysis, but

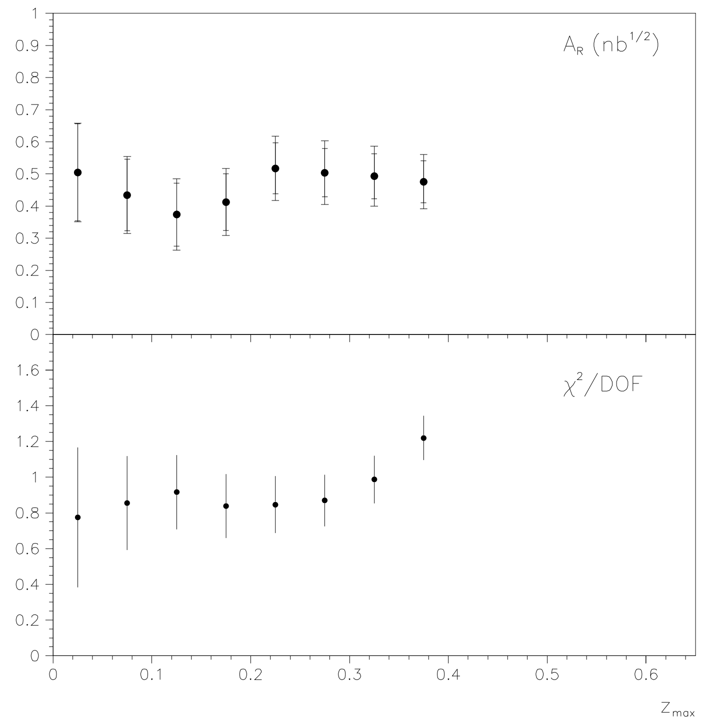

Figure 5.20: The resonance amplitude and the reduced χ^2 of the fits of Equations 5.8 and 5.9 (with $|B\ e^{i\delta_B}|^2$ set to the estimate obtained in Section 5.9) plotted as a function of z_{max}. The inner error bars of A_R are statistical and the outer systematic due to the uncertainty on B^2 (determined with the same procedure described for $\pi^0\pi^0$ in Appendix C.4).

still guarantees that the non-interfering helicity-1 continuum (B^2) is relatively small. The size of the interference pattern is about 10 times larger than the peak (A_R^2) of the "pure" Breit-Wigner cross section. This amplification factor is smaller than the one in the $\pi^0\pi^0$ process because of the different size of differential cross section (what matters is the helicity-0 component) for the two processes in the respective integration ranges (see Figures 3.29, 3.30 and 5.22). The helicity-0 continuum A^2 in the $\eta\eta$ channel has a smaller size and provides a smaller enhancement to the interference signal than in the $\pi^0\pi^0$ case.

Since the plot of Figure 5.21 is the summation of seven bins in z of width $\Delta z =$

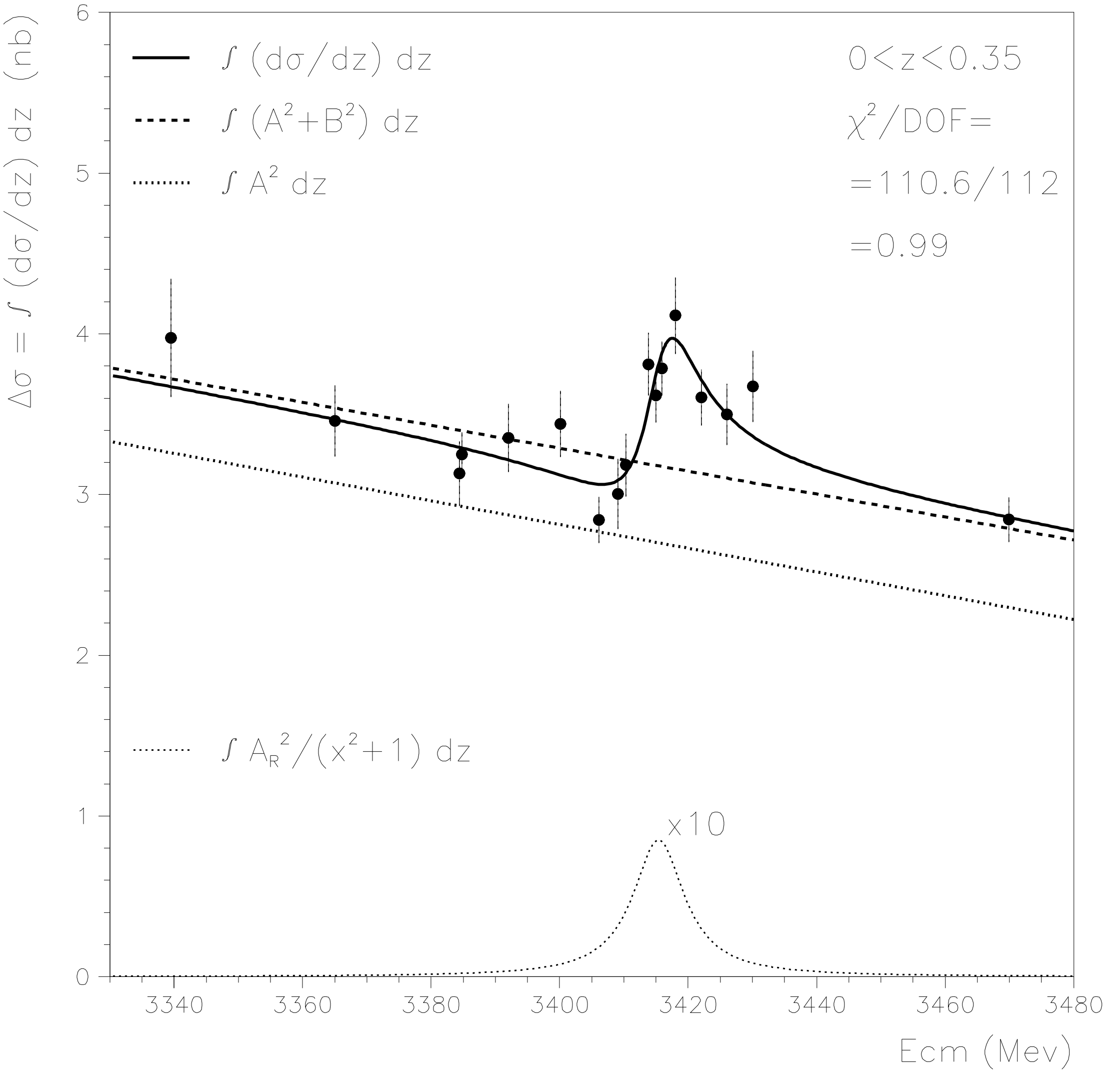

Figure 5.21: The $\bar{p}p \to \eta\eta$ cross section integrated over $0 < z < 0.35$ plotted versus E_{cm} . The fit of Equation 5.8 and 5.9 over the range $z_{max} = 0.35$ is shown along with its components. In the fit, the contribution of $|B\ e^{i\delta_B}|^2$ is constrained to the estimate obtained in Section 5.9, and its integration corresponds to the separation between the curves $\int (A^2 + B^2)\, dz$ and $\int A^2\, dz$. The "pure" Breit Wigner curve, $\int \frac{A_R^2}{x^2+1}\, dz$, is shown multiplied by a factor 10 to make it comparable to the reshaped signal that is actually detected.

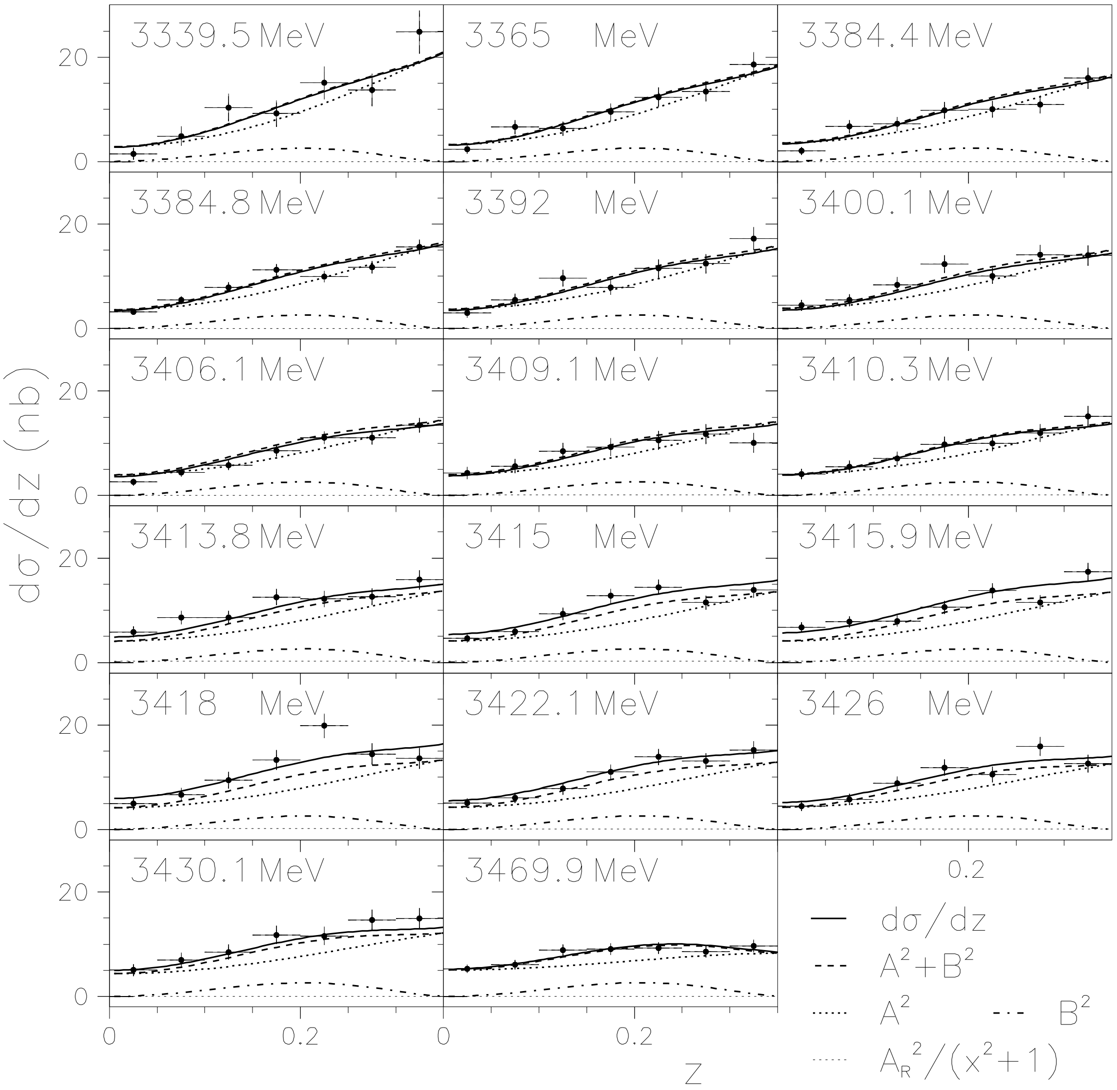

Figure 5.22: The $\bar{p}p \to \eta\eta$ differential cross section as a function of z (in the range $0 < z < 0.35$) at the E_{cm} indicated in each plot. The fit of Equation 5.8 and 5.9 over the range $z_{max} = 0.35$ is shown along with its components. In the fit, the contribution of $|B\ e^{i\delta_B}|^2$ is constrained to the estimate obtained in Section 5.9 and corresponds to the separation between the curves $A^2 + B^2$ and A^2. The contribution of the "pure" Breit Wigner, $\frac{A_R^2}{x^2+1}$, is relatively negligible.

Parameter	Fit Result
A_R (nb$^{1/2}$)	0.493 ± 0.070
δ_A (degree)	144 ± 8
a_0 (nb)	4.10 ± 0.20
a_1 (nb)	0.085 ± 0.028
a_2 (nb)	105 ± 12
a_3 (nb)	-4.61 ± 0.63
a_4 (nb)	-230 ± 120

Table 5.4: Result from the fit to the $\bar{p}p \to \eta\eta$ cross section of Equation 5.8 and 5.9 over the range $z_{max} = 0.35$, with $|B\ e^{i\delta_B}|^2$ constrained to the estimate obtained in Section 5.9. Errors are statistical and determined by the MINOS function of the CERN package MINUIT [71].

0.05, the summation of the contributions of every single bin is shown in Figure 5.23 along with the fit curves for $\Delta\sigma$.

A note on the fit of Section 5.9 . As done in the $\pi^0\pi^0$ analysis, even for $\eta\eta$ it is possible to check the consistency of the value of A_R determined in this section with the partial wave expansion fit carried out over the range $0 < z < 0.6$ in Section 5.9. By re-performing the partial wave expansion fit with A_R constrained to the value of Table 5.4, all of the other parameters of the fit do not move significantly from the values reproduced in Table 5.3.

5.10.4 Result for the Product of the Branching Ratios

The value of A_R in Table 5.4 is related to the fictional[13] "pure" Breit-Wigner resonant cross section ($\sigma_{\bar{p}p\to\chi_{c0}\to\eta\eta}$) at $x = 0$ by

$$\left[\sigma_{\bar{p}p\to\chi_{c0}\to\eta\eta}\right]_{x=0} = \int_0^1 A_R^2\ dz = A_R^2 = (0.243 \pm 0.069_{stat})\ \text{nb}\ . \tag{5.11}$$

[13]This cross section cannot be measured separately from the non-resonant cross section. Only the cross section resulting from the interference between resonant and non-resonant amplitudes is observable.

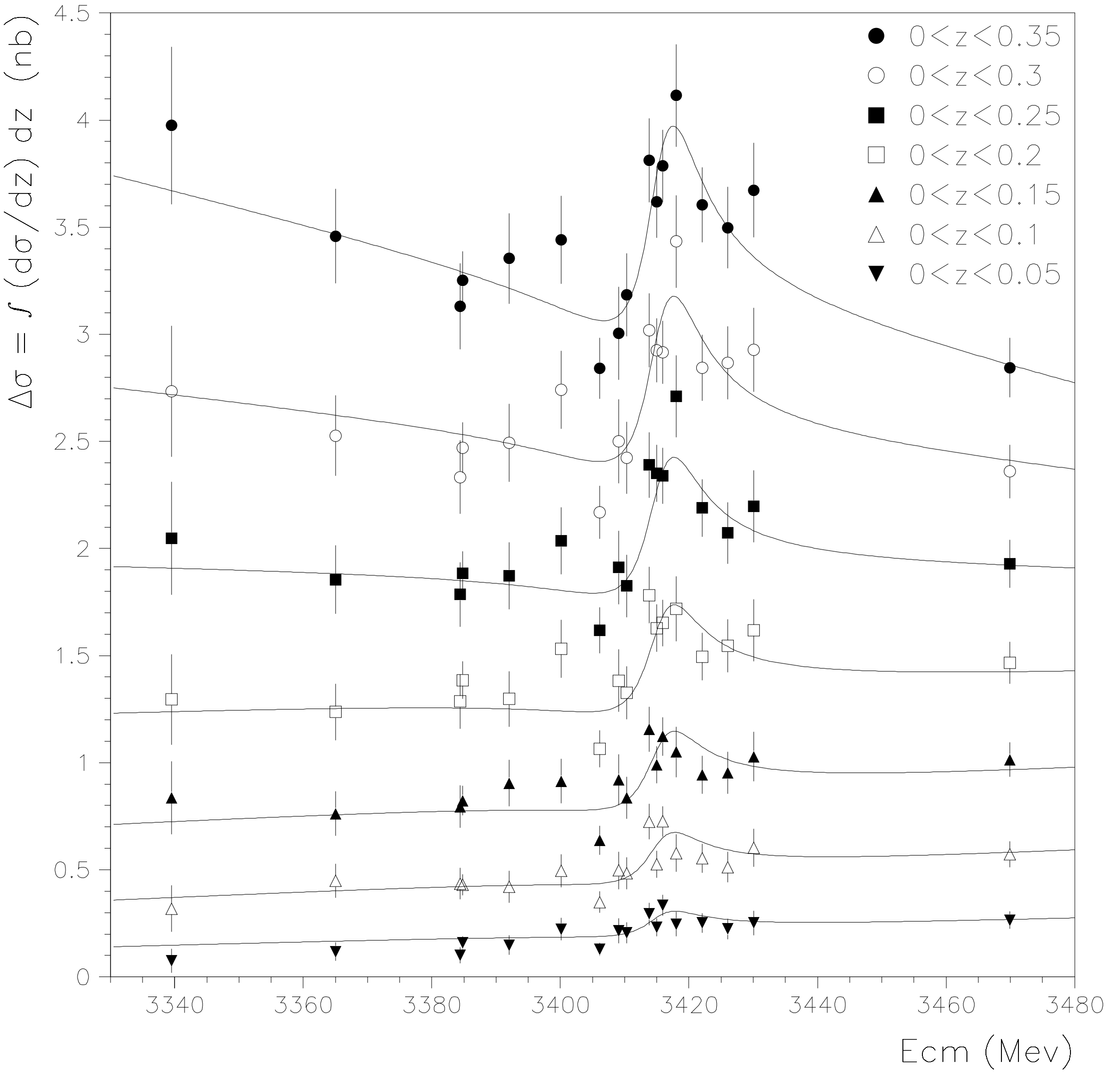

Figure 5.23: The $\bar{p}p \to \eta\eta$ cross section integrated over $0 < z < 0.35$ seen as a summation of the seven bins Δz included in the range. The fit curves for $\Delta\sigma$ are also shown. The top-most points and curve coincides with the points and solid curve of Figure 5.21.

The relation with the product of the χ_{c0} input and output branching ratios is the analogue of Equation 3.28, with the value of the center of mass De Broglie wavelength in the initial state given in Equation 3.29. The result is:

$$B(\chi_{c0} \to \bar{p}p) \times B(\chi_{c0} \to \eta\eta) = (4.0 \pm 1.2_{stat}) \times 10^{-7} \ . \tag{5.12}$$

The error is statistical. The systematic errors is discussed in Section 5.11.

5.11 Study of the Systematic Errors

Table 5.5 lists the sources and the amounts of the systematic errors affecting the product of the branching ratios $B(\chi_{c0} \to \bar{p}p) \times B(\chi_{c0} \to \pi^0\pi^0)$. They are determined as described in Section 3.15.

Source	Amount (%)
Background Subtraction	2
Luminosity	3
Seed/Cluster/Split Threshold	2
Event Selection	1.5
$\lvert B\ e^{i\delta_B}\rvert^2$	$\{^{+9.6}_{-4.8}$
Additional terms in A^2	$\{^{+3.1}_{-1.0}$
$M_{\chi_{c0}}$	1
$\Gamma_{\chi_{c0}}$	1.2
Total	$\{^{+0.44}_{-0.25}$

Table 5.5: The sources of systematic uncertainty affecting $B(\chi_{c0} \to \bar{p}p) \times B(\chi_{c0} \to \eta\eta)$.

As expected, the larger systematic error comes from the uncertainty on the size of the helicity-1 continuum $B^2 = |B\ e^{i\delta_B}|^2$. The sum in quadrature of the amounts in the table gives an overall systematic error on the product of the branching ratios of $(^{+0.44}_{-0.25}) \times 10^{-7}$ which will be taken as $(^{+0.5}_{-0.3}) \times 10^{-7}$.

Regarding the phase δ_A between the amplitude of the resonance and the amplitude of the helicity-0 continuum, the total systematic error is 6 degree.

5.12 Results from the $\eta\eta$ channel

Summarizing, the complete measurement of the product of the χ_{c0} input and output branching ratios for the $\eta\eta$ final state is

$$B(\chi_{c0} \to \bar{p}p) \times B(\chi_{c0} \to \eta\eta) = (4.0 \pm 1.2_{stat}\ {}^{+0.5}_{-0.3\,syst}) \times 10^{-7}\ . \tag{5.13}$$

The measurement of the difference of phase in the considered angular region (see Equation 5.10) between the helicity-0 non-resonant amplitude A and the resonant amplitude A_R (see Equation 5.8) is [14]

$$\delta_A(0 < z < 0.35) = (144 \pm 8_{stat} \pm 6_{syst}) \text{ degree.} \tag{5.14}$$

The phase δ_A is responsible for the shape of the interference pattern seen in the measured cross section. It is different from the corresponding phase observed in the $\pi^0\pi^0$ channel (Equation 3.32). In the $\eta\eta$ channel, the interference is destructive on the low energy side of the resonance and constructive on the high side.

5.12.1 Estimate of $M_{\chi_{c0}}$ and $\Gamma_{\chi_{c0}}$ Using the $\eta\eta$ Data Alone.

As done in Section 3.16.1 for the $\pi^0\pi^0$ analysis, it is possible to attempt the determination of $M_{\chi_{c0}}$ and $\Gamma_{\chi_{c0}}$ without relying on the measurements from the analysis of the channel $\bar{p}p \to \chi_{c0} \to J/\psi\,\gamma$, $J/\psi \to e^+e^-$. To this purpose, the fit described in Section 5.10.3 is re-performed with $M_{\chi_{c0}}$ and $\Gamma_{\chi_{c0}}$ left as free parameters. The result of the fit is shown in Figure 5.24.

The fit results for mass and width are

$$M_{\chi_{c0}} = 3412.2^{+2.1}_{-1.8} \pm 0.2 \text{ MeV/c}^2 \tag{5.15}$$

$$\Gamma_{\chi_{c0}} = 10.3^{+3.0}_{-3.1} \pm 0.1 \text{ MeV/c}^2\ . \tag{5.16}$$

[14] Although there are no a priori reasons for δ_A to be constant, no dependence on x or z is resolvable in the considered region ($0 < z < 0.35$).

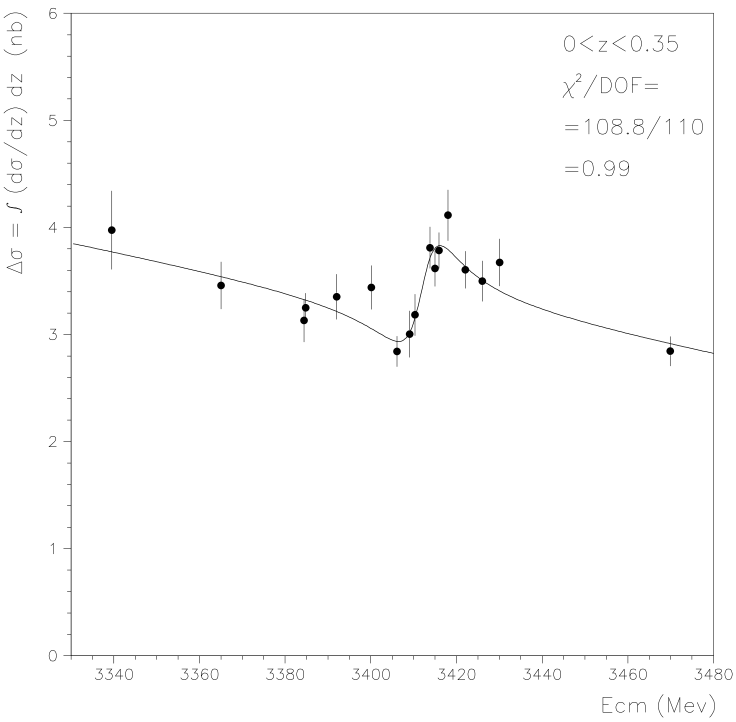

Figure 5.24: The $\bar{p}p \to \eta\eta$ cross section integrated over $0 < z < 0.35$ plotted versus E_{cm} . The fit of Equation 5.8 and 5.9 over the range $z_{max} = 0.35$ is performed with $M_{\chi_{c0}}$ and $\Gamma_{\chi_{c0}}$ as free parameters.

The product of the branching ratio is almost unaltered:

$$B(\chi_{c0} \to \bar{p}p) \times B(\chi_{c0} \to \pi^0\pi^0) = (4.1^{+1.2}_{-1.1}{}^{+0.5}_{-0.3}) \times 10^{-7} \ . \tag{5.17}$$

The new value of the phase is $\delta_A = (173^{+17}_{-19} \pm 6)$ degrees, while the other parameters of the fit (a_0, a_1, a_2, a_3, and a_4) are not significantly different from the values in Table 5.4.

Chapter 6

Discussion of the Results and Conclusions

6.1 Results for the χ_{c0} state of Charmonium

The χ_{c0} measurements presented in the chapters of the $\pi^0\pi^0$ and $\eta\eta$ analyses are summarized in Table 6.1, along with the results from the already published analysis $\bar{p}p \to J/\psi\,\gamma$, $J/\psi \to e^+e^-$ [1][1].

The header of the table indicates the input channel ($\bar{p}p$), which is common to the three analyses, and the output channels ($J/\psi\,\gamma$, $\pi^0\pi^0$, and $\eta\eta$). The well-known branching ratios for the detection of the short-lived particles in the output channels, that is $B(J/\psi \to e^+e^-) = (5.93 \pm 0.10)\%$, $B(\pi^0 \to \gamma\gamma) = (98.798 \pm 0.032)\%$ and $B(\eta \to \gamma\gamma) = (39.43 \pm 0.26)\%$ [39], have been already accounted for and removed from the scene.

The middle part of the table reproduces the results for $M_{\chi_{c0}}$, $\Gamma_{\chi_{c0}}$, and $B_{in} \times B_{out}$ (and, for $\pi^0\pi^0$ and $\eta\eta$, for the phase δ_A at small z between the helicity-0 non-resonant and resonant amplitudes) as determined by each one of the three analyses independently from the other two (see Section 3.12 for $J/\psi\,\gamma$, Section 3.16.1 for $\pi^0\pi^0$, and Section 5.12.1 for $\eta\eta$). There is good agreement on the measurements

[1] The analysis of the process $\bar{p}p \to J/\psi\,\gamma$, $J/\psi \to e^+e^-$ is summarized in Section 3.12 but not performed for this dissertation.

$B_{in} \equiv$	Common channel $B(\chi_{c0} \to \bar{p}p)$		
$B_{out} \equiv$	$B(\chi_{c0} \to J/\psi\,\gamma)$	$B(\chi_{c0} \to \pi^0\pi^0)$	$B(\chi_{c0} \to \eta\eta)$
With $M_{\chi_{c0}}$, $\Gamma_{\chi_{c0}}$, and $B_{in} \times B_{out}$ as free parameters			
$M_{\chi_{c0}}$ (MeV/c^2)	$3415.4 \pm 0.4 \pm 0.2$ (^{a})	$3414.7^{+0.7}_{-0.6} \pm 0.2$	$3412.2^{+2.1}_{-1.8} \pm 0.2$
$\Gamma_{\chi_{c0}}$ (MeV)	$9.8 \pm 1.0 \pm 0.1$ (^{a})	$8.6^{+1.7}_{-1.3} \pm 0.1$	$10.3^{+3.0}_{-3.1} \pm 0.1$
$B_{in} \times B_{out}$ (10^{-7})	$27.2 \pm 1.9 \pm 1.3$	$5.42^{+0.91}_{-0.96} \pm 0.22$	$4.1^{+1.2\,+0.5}_{-1.1\,-0.3}$
δ_A (degree)	–	$47 \pm 10 \pm 6$	$173^{+17}_{-19} \pm 6$
With $M_{\chi_{c0}}$ and $\Gamma_{\chi_{c0}}$ constrained to values (^{a}), and $B_{in} \times B_{out}$ as free parameter			
Final result for $B_{in} \times B_{out}$ (10^{-7})		$5.09 \pm 0.81 \pm 0.25$	$4.0 \pm 1.2^{+0.5}_{-0.3}$
and phase δ_A (degree)		$39 \pm 5 \pm 6$	$144 \pm 8 \pm 6$

Table 6.1: E835 Results for the χ_{c0} .

of $M_{\chi_{c0}}$ and $\Gamma_{\chi_{c0}}$ from the $J/\psi\,\gamma$ and $\pi^0\pi^0$ channels. The limited-size sample of $\eta\eta$ events gives lower-precision measurements; the width estimate is in agreement with the other two channels, while the mass is slightly underestimated (correlated with a probable slight overestimation of the phase δ_A). The results from the $J/\psi\,\gamma$ channel are more precise and presumably more accurate, as it is understandable by confronting Figures 3.22, 3.32, and 5.24. The background (mistakenly identified events from different final states) does not play a significant role in any of the three channels; it is very small for both $J/\psi\,\gamma \to e^+e^-\,\gamma$ and $\pi^0\pi^0 \to \gamma\gamma\,\gamma\gamma$, and not a real issue for $\eta\eta \to \gamma\gamma\,\gamma\gamma$. What is important is that the absence of non-resonant production in the $J/\psi\,\gamma \to e^+e^-\,\gamma$ channel permits a fit with a limited number of parameters. On the other hand, the large non-resonant continuum in the $\pi^0\pi^0$ and $\eta\eta$ channels, although useful as provider of the amplification for the interference pattern, introduces additional variables. In particular, the phase δ_A and the size of the interfering continuum increase the coupling among the enlarged number of fit parameters. Consequently, the statistical uncertainties are somewhat larger than in the $J/\psi\,\gamma$ channel (but, in the $\pi^0\pi^0$ case, still comparable).

These results demonstrate that the technique developed during the execution of the $\pi^0\pi^0$ and $\eta\eta$ analyses is an effective tool to correctly extract the parameters of a resonance in an environment dominated by the non-resonant production of the selected final state.

The bottom part of the Table 6.1 reproduces the results for $B_{in} \times B_{out}$ and the phase δ_A as determined by constraining $M_{\chi_{c0}}$ and $\Gamma_{\chi_{c0}}$ to the higher-precision measurements from the $J/\psi\,\gamma$ channel (see Sections 3.14.2 and 3.14.3 for $\pi^0\pi^0$, and Sections 5.10.3 and 5.10.4 for $\eta\eta$). It should be remembered that the $J/\psi\,\gamma$ data sample was collected simultaneously to the $\pi^0\pi^0$ and $\eta\eta$ samples, just by a different trigger. The energy and luminosity determinations are the same for the three channels. By using the better-measured values of $M_{\chi_{c0}}$ and $\Gamma_{\chi_{c0}}$ from the $J/\psi\,\gamma$ analysis, the values of $B_{in} \times B_{out}$ and δ_A in the $\pi^0\pi^0$ channel are determined with higher accuracy and precision [2]. The values in the bottom part of Table 6.1 are intended to be the final results for $B_{in} \times B_{out}$ and δ_A.

The value of the phase δ_A between the helicity-0 non-resonant and resonant amplitudes is determined in a restricted angular region at small z ($0 < z < 0.125$ for $\pi^0\pi^0$ and $0 < z < 0.35$ for $\eta\eta$). No appreciable changes of its value are seen within the considered regions. The phase δ_A is responsible for the shape of the interference pattern seen in the cross section and is reasonably well measured. Its specific value is determined by the local combination of several partial waves (see Equation 1.14), which largely cancel each other. It may be more relevant to examine the values of the phase differences δ_0, δ_2, and δ_4 between the single non-resonant partial wave amplitudes and the resonant amplitude (see Tables 3.7 and 5.3). In particular, δ_0 is the difference of phase between the non-resonant and resonant amplitudes with the same quantum number J. However, it should be said that the values of these single partial wave phases may be affected by significant systematics, since the partial

[2]In the limited-size $\eta\eta$ channel, by preventing the underestimation of $M_{\chi_{c0}}$ to occur, an improvement on the accuracy and precision of δ_A is obtained.

wave expansion fits are performed over an incomplete angular range $0 < z < 0.6$ (limited by the detector acceptance).

For later use, the ratio between $B_{in} \times B_{out}$ of the two channels $J/\psi\,\gamma$ and $\pi^0\pi^0$ is determined and, since the common B_{in} cancels in the ratio, provides [3]

$$\frac{B(\chi_{c0} \to J/\psi\,\gamma)}{B(\chi_{c0} \to \pi^0\pi^0)} = 5.34 \pm 0.93 \pm 0.34 \ . \tag{6.1}$$

Similarly, the ratio between $B_{in} \times B_{out}$ of the two channels $\pi^0\pi^0$ and $\eta\eta$ gives

$$\frac{B(\chi_{c0} \to \eta\eta)}{B(\chi_{c0} \to \pi^0\pi^0)} = 0.79 \pm 0.27^{+0.10}_{-0.06} \ . \tag{6.2}$$

Concerning the analysis of the channel $\pi^0\eta$, no resonant signal is detected. This is expected since the χ_{c0}, as any charmonium state, cannot decay into this isospin-1 final state unless violating isospin conservation. A 90% confidence level upper limit is established by Equation 4.9, which is reproduced here:

$$B(\chi_{c0} \to \bar{p}p) \times B(\chi_{c0} \to \pi^0\eta) < 4 \times 10^{-8} \ . \tag{6.3}$$

The excellent forward/backward symmetry displayed by the $\pi^0\eta$ cross section (see Figure 4.14) provides an important diagnostic on the ability to correctly determine the acceptance and efficiency for π^0 and η particles, as discussed on page 162.

All of the results presented so far are obtained from the E835 run 2000 data sample alone, with the exception of the well-known branching ratios $B(J/\psi \to e^+e^-)$, $B(\pi^0 \to \gamma\gamma)$ and $B(\eta \to \gamma\gamma)$ [39] (reported on page 212). In order to deconstruct the branching ratios of the entrance and exit channels, we must use data from the literature.

Regarding the $\bar{p}p \to \pi^0\pi^0$ channel, the branching ratio $B(\chi_{c0} \to \pi^0\pi^0)$ is more than an order of magnitude larger (and consequently better measured) than $B(\chi_{c0} \to p\bar{p}$. A measurement $B(\chi_{c0} \to \pi^0\pi^0) = (2.79 \pm 0.32 \pm 0.57) \times 10^{-3}$ has been recently

[3]Some of the systematic errors cancel out (for example the one due to the luminosity and E_{cm} determinations) and some other have to be determined by re-running both fits in Sections 3.14.2 and 3.12.

reported by the experiment BES [73], which agrees with a 1985 measurement from Crystal Ball [39, 74]. However, a consistent and more precise determination of it is computed by using isospin symmetry:

$$B(\chi_{c0} \to \pi^0\pi^0) = \frac{1}{2}B(\chi_{c0} \to \pi^+\pi^-) = (2.5 \pm 0.35) \times 10^{-3}\ , \tag{6.4}$$

where $B(\chi_{c0} \to \pi^+\pi^-) = (5.0 \pm 0.7) \times 10^{-3}$ is taken from [39]. By using our measurement for $B(\chi_{c0} \to \bar{p}p) \times B(\chi_{c0} \to \pi^0\pi^0)$, and the above Equation 6.4, we then obtain

$$B(\chi_{c0} \to \bar{p}p) = (2.04 \pm 0.32_{stat} \pm 0.10_{sys} \pm 0.28_{PDG}) \times 10^{-4}\ , \tag{6.5}$$

where the subscript PDG labels the uncertainty derived from the PDG [39] measurement. The above value is in agreement with $B(\chi_{c0} \to \bar{p}p) = (2.2 \pm 0.5) \times 10^{-4}$ from [39].

Considering the $\eta\eta$ channel, by using the E835 measurement of Equation 6.2 and again Equation 6.4, we obtain:

$$B(\chi_{c0} \to \eta\eta) = (1.98 \pm 0.68_{stat}\ {}^{+0.25}_{-0.15}{}_{sys} \pm 0.28_{PDG}) \times 10^{-3}\ , \tag{6.6}$$

This is in agreement with a measurement $B(\chi_{c0} \to \eta\eta) = (2.02 \pm 0.84 \pm 0.59) \times 10^{-3}$ reported by BES [73], again in agreement with a 1985 measurement from Crystal Ball [39, 74].

6.2 The Radiative Transitions of the χ_{cJ} States.

It is interesting to compare the E1 radiative transition of all three χ_{cJ} states. By neglecting the presumably small differences among the radial wave functions of the three χ_{cJ} states, the theory of the electric dipole transition predicts that the partial widths $\Gamma_{\chi_{cJ} \to J/\psi\,\gamma}$ should be proportional to the third power of the momentum q_J of the emitted photon.

The above Equation 6.4 and the E835 measurement of Equation 6.1 give:

$$B(\chi_{c0} \to J/\psi\,\gamma) = (1.34 \pm 0.23_{stat} \pm 0.09_{syst} \pm 0.19_{PDG})\,\%. \tag{6.7}$$

By using the E835 value for the χ_{c0} mass of Equation 3.16, then it follows:

$$\Gamma_{\chi_{c0}\to J/\psi\,\gamma} = (131 \pm 26_{stat} \pm 8_{syst} \pm 18_{PDG})\ \mathrm{keV}. \tag{6.8}$$

For approximately 20 years the χ_{c0} transition rate had been anomalously low [4]. The energy independent adjusted quantities $\Gamma(\chi_{cJ} \to J/\psi\,\gamma)/(q_J/q_0)^3$ now are in excellent agreement, as indicated in Table 6.2 (where the uncertainties are summed in quadrature).

$c\bar{c}$	$B(\chi_{cJ} \to J/\psi\ \gamma)$ (%)	$\Gamma_{\chi_{cJ}}$ (MeV)	$\Gamma_{\chi_{cJ}\to J/\psi\gamma}$ (keV)	q_J (MeV)	$(\frac{q_J}{q_0})^3$	$\frac{\Gamma_{\chi_{cJ}\to J/\psi\gamma}}{(q_J/q_{\chi_0})^3}$ (keV)
χ_{c0}	1.33 ± 0.31	$9.8 \pm 1.0 \pm 0.1$	131 ± 33	303	1	131 ± 33
χ_{c1}	31.6 ± 3.2	0.92 ± 0.13	290 ± 50	389	2.10	138 ± 24
χ_{c2}	18.7 ± 2.0	2.08 ± 0.17	389 ± 52	430	2.86	136 ± 18

Table 6.2: Comparison among the E1 radiative transitions of the three χ_{cJ} states into J/ψ . The reported quantities are: the branching ratio $B(\chi_{cJ} \to J/\psi\ \gamma)$, the full width $\Gamma_{\chi_{cJ}}$, the partial width $\Gamma_{\chi_{cJ}\to J/\psi\,\gamma}$, the energy q of the photon emitted in the transition, the ratio $(q/q_0)^3$ where q_0 is the energy of the photon from the χ_{c0} , and the scaled partial width $\Gamma(\chi_{cJ} \to J/\psi\,\gamma)/(q_J/q_0)^3$.

6.3 The $\bar{p}p$ Annihilation into a Pseudoscalar Meson Pair

Aside from the charmonium results, this work provides the measurements of the cross sections for three pseudoscalar-pseudoscalar meson final states in proton-antiproton annihilations in the energy range 3340 − 3470 MeV. The differential cross sections as a function of the production angle of the meson pair are shown in Figures 3.17 and 3.18 for the $\pi^0\pi^0$ final state, 4.9 and 4.10 for the $\pi^0\eta$, and 5.12 and 5.13 for $\eta\eta$. The numerical values are reproduced in the list of tables in Appendices F, G and H.

The study of the differential cross section of the final channels $\pi^0\pi^0$ and $\pi^0\eta$ provides information on the dynamics of the proton-antiproton annihilation into a pseudoscalar meson pair at the examined energies [4].

The partial wave expansion fits described in Sections 3.13 ($\pi^0\pi^0$) and 4.8 ($\pi^0\eta$) indicate that the size of the angular momentum contributions decreases rapidly with J and only $J = 0$, 2 and 4 are necessary to describe the angular distributions. By simply using the commonly accepted size of the proton in applying the wave mechanically smeared relation $\hbar L_{\bar{p}p} \simeq b\, p_i$ (where $L_{\bar{p}p}$ is the orbital angular momentum of the $\bar{p}p$ system, b is the impact parameter, and p_i is the initial state center of mass momentum), it could be inferred that a larger number of partial waves would participate in the interaction. This is probably true for different final states and is certainly true for elastic $\bar{p}p$ scattering. However, the pseudoscalar-pseudoscalar meson final states selected here are unlikely to be produced in peripheral impacts, as discussed on page 122; some of those considerations are repeated as follows.

The production of the $\pi^0\pi^0$ final state can occur via the annihilation of one, two or three valence $\bar{q}q$ pairs of the $\bar{p}p$ initial state (classes 1, 2 and 3 according to the definitions on page 22) [5]. The required high degree of annihilation of classes 2 and 3 naturally weights their occurrence toward central impacts. Class 1 requires the annihilation of only one $\bar{q}q$ pair. However, it additionally requires that the remaining partons of the proton (qq) and antiproton ($\bar{q}\bar{q}$) separate and rearrange themselves into $q\bar{q} + q\bar{q}$. This is unlikely to happen for large impact parameters, where the partons tend to retain their original large longitudinal component of

[4] The $\eta\eta$ channels has a smaller number of events and the cross section is not as well resolved as in the $\pi^0\pi^0$ and $\pi^0\eta$ channels. Consequently, the information from $\pi^0\pi^0$ and $\pi^0\eta$ has provided guidance in the $\eta\eta$ analysis. However, what is determined in the $\pi^0\pi^0$ and $\pi^0\eta$ channels finds support in what is observed in the $\eta\eta$.

[5] The $\pi^0\eta$ cannot be produced in class 3, since total valence quark annihilation implies that an isospin-0 intermediate state is produced (gluons do not carry isospin). Such an intermediate state cannot generate the isospin-1 final state $\pi^0\eta$.

momentum. Consequently, no matter whether the process occurs through class 1, 2 or 3, the production of a pseudoscalar-pseudoscalar final state is heavily weighted toward central $\bar{p}p$ impacts and, hence, toward small values of the orbital angular momentum $L_{\bar{p}p}$ of the $\bar{p}p$ system. Table 1.3 indicates that only odd values of $L_{\bar{p}p}$ can produce the $J^{PC} = \text{even}^{++}$ of a pseudoscalar meson pair, and each $L_{\bar{p}p}$ feeds both $J = L_{\bar{p}p} \pm 1$. It is then reasonable to expect larger contributions from the partial waves with $J = 0$ and 2 as compared to those from $J = 4$. This is observed in the $\pi^0\pi^0$ channel (see Table 3.7), in the $\pi^0\eta$ (Table 4.3) [6], and $\eta\eta$ (Table 5.3). It may also be noticed that the estimated differences of phase between amplitudes with the same helicity are relatively small.

6.4 Conclusions

This dissertation has studied charmonium formation, specifically the χ_{c0} state, in proton-antiproton annihilation and its subsequent decay into pseudoscalar-pseudoscalar meson final states.

The original intent for pursuing this study was the search for alternative means of discovering and measuring charmonium states and, particularly, possible hadromolecular states [75]. The $J^{PC} = 0^{++}$ states $a_0(980)$, with isospin $I = 1$, and $f_0(980)$, with $I = 0$, are hadromolecular state candidates with masses right below the mass of a pair of K mesons. Analogous hadromolecular states at charmonium energies would be $c\bar{c}q\bar{q}$ bound states, where q represents a light quark. These should definitely decay into a pseudoscalar meson pair with the corresponding isospin:

- $I = 1$: $c\bar{c}q\bar{q} \rightarrow \pi^0\eta$
- $I = 0$: $c\bar{c}q\bar{q} \rightarrow \pi^0\pi^0$ and $\eta\eta$.

A search for these hadromolecular state could be initiated in the vicinity of (and below) the mass of a pair of D mesons, that is $2m_D \simeq 3740$ MeV. The physics interpretation of such states would be greatly facilitated in the uncongested charmonium

[6] With the exception, in $\pi^0\eta$, of the helicity-1 component, where C_2^1 and C_4^1 have comparable sizes.

energy region with respect to the overpopulated light quark region. The discovery of $c\bar{c}q\bar{q}$ states would be quite significant for the understanding of the spectroscopy of light quark mesons.

The choice of performing this study on the χ_{c0} resonance is a consequence of the $J^{PC} = 0^{++}$ quantum numbers of the χ_{c0}, which allows it to decay into a pseudoscalar meson pair. A large luminosity was collected in the χ_{c0} region in the year 2000 run of E835. The primary goal, successfully achieved (see Section 3.12 or Reference [1]), was the determination of the resonance parameters through the study of the process $\bar{p}p \to J/\psi\,\gamma$, $J/\psi \to e^+e^-$ to complete the program of studying the χ_{cJ} triplet initiated by E760. The execution of a scan of the χ_{c0} was facilitated by the work of the Fermilab Beams Division that increased the antiproton accumulator transition energy (see footnote on page 17). During the E760 and E835-1996/97 runs, such transition energy was at $E_{cm} \simeq 3400$ MeV, very close to the χ_{c0} mass, and it was extremely awkward to scan this resonance.

The presence of a large non-resonant continuum production of the final states, as compared to the resonant production through a charmonium intermediary state, was known at the outset. However, the awareness that the interfering mechanism would produce an enhanced interference pattern in the cross section, hopefully large enough to be detected, was a strong motivation to pursue the analysis. This perception was not common knowledge and was regarded with suspicion. Of course, the physics behind the interference mechanism was well known prior to this work, and the performed calculation of the angular distribution was straightforward. What is innovative is the exploitation of such mechanism to detect and measure a resonant signal that would be, if the interference could be turned off, two orders of magnitude smaller than the non-resonant cross section. Several other measurements of interference patterns exist in particle physics and many in nuclear physics; but the general case presents a larger resonance reshaped by a smaller interfering continuum. In addition, a specific analysis that manages the two different components of the continuum (one interfering and the other non-interfering with the resonance) and extract the resonance parameters has been developed. The effectiveness of this analysis has been demonstrated.

Now that confidence has been gained that measurements of resonances can be accomplished in hadronic decay channels in presence of a larger non-resonant production of the final state, new strategies can be considered. For example, other than the above discussed search for hadromolecules, the search for the poorly known charmonium singlet states could be performed by investigating hadronic final states, relying on the enhancement provided by the interference. Particular consideration could be given to the final channel made of a pair of ϕ mesons, detected through the decays $\phi \to K^+K^-$. The $\phi\phi$ final state shares with charmonium the fact that it does not have valence quark overlap with the initial $\bar{p}p$ state. The process $\bar{p}p \to \phi\phi$ may then occur only with the annihilation of all the valence quarks and antiquarks of the $\bar{p}p$. In other words, only class 3 (according to the classification on page 22) contributes to the non-resonant production of the final state, as is certainly the case for the resonant $\bar{c}c$ production. As a consequence, the disparity between the size of the continuum and the resonance should be less intense than in the cases analyzed in this dissertation. The singlet states η_c and η_c' may be searched for in the channel $\bar{p}p \to \phi\phi \to K^+K^-\ K^+K^-$, while the singlet state h_c in the channel $\bar{p}p \to \gamma\phi\phi \to \gamma\, K^+K^-\ K^+K^-$. Of course, the detection of these channels would definitely be facilitated by providing momentum analysis.

Appendix A

The Angular Distribution

The helicity formalism of M. Jacob and G. C. Wick [35] is used in this appendix to calculate the angular distribution for the processes $\bar{p}p \to \pi^0\pi^0$, $\bar{p}p \to \eta\eta$ and $\bar{p}p \to \pi^0\eta$. References to some equations of [76] are also made during the following calculation. The helicity, λ, of a particle is defined as the projection of its spin, $\vec{S}$, along the direction of its motion:

$$\lambda \equiv \frac{\vec{S} \cdot \vec{p}}{|\vec{p}\,|}, \tag{A.1}$$

where $\vec{p}$ is the momentum of the particle. For massive particle, the sign of the helicity depends on the considered frame. We define λ_p and $\lambda_{\bar{p}}$ as the helicity of the colliding proton and antiproton in the center of mass (c.m.) frame. A two-particle plane-wave helicity state in the center of mass may be expressed as (see Equation 3.13 of [76])

$$|p\theta\phi\lambda_1\lambda_2\rangle = (2\pi)^3 \left(\frac{4E_{cm}}{p}\right)^{1/2} |\theta\phi\lambda_1\lambda_2\rangle|\widetilde{P}\rangle \tag{A.2}$$

where p, θ and ϕ are the magnitude, the polar angle and azimuthal angle of the momentum vector; λ_1 and λ_2 are the helicities of the two particles; and $\widetilde{P}$ is the four-momentum normalized as $\langle\widetilde{P}'|\widetilde{P}\rangle = \delta^4(\widetilde{P}' - \widetilde{P})$.

A.1 Amplitude for $|i\rangle \rightarrow |JM\rangle$

In the case of a $p\bar{p}$ initial state, $|i\rangle$, the notations of Equation A.2 become

$$|i\rangle \equiv |p_i\theta_i\phi_i\lambda_p\lambda_{\bar{p}}\rangle = (2\pi)^3\Big(\frac{4E_{cm}}{p_i}\Big)^{1/2}|\theta_i\phi_i\lambda_p\lambda_{\bar{p}}\rangle|\widetilde{P}_i\rangle, \tag{A.3}$$

where the subscript i signifies initial state.

To later exploit the conservation of the total angular momentum, an expansion of the initial state in the two-particle spherical helicity basis is performed by inserting the unity operator $\sum_{J_iM_i}|J_iM_i\lambda_p\lambda_{\bar{p}}\rangle\langle J_iM_i\lambda_p\lambda_{\bar{p}}|$:

$$|i\rangle = (2\pi)^3\Big(\frac{4E_{cm}}{p_i}\Big)^{1/2}\sum_{J_iM_i}|J_iM_i\lambda_p\lambda_{\bar{p}}\rangle \underbrace{\langle J_iM_i\lambda_p\lambda_{\bar{p}}|\theta_i\phi_i\lambda_p\lambda_{\bar{p}}\rangle}_{=\sqrt{\frac{2J_i+1}{4\pi}}D^{J_i}_{M_i,\lambda_i}(\phi_i,\theta_i,-\phi_i)}|\widetilde{P}_i\rangle =$$

$$= (2\pi)^3\Big(\frac{4E_{cm}}{p_i}\Big)^{1/2}\sum_{J_iM_i}\sqrt{\frac{2J_i+1}{4\pi}}\,D^{J_i}_{M_i,\lambda_i}(\phi_i,\theta_i,-\phi_i)\,|J_iM_i\lambda_p\lambda_{\bar{p}}\rangle|\widetilde{P}_i\rangle \tag{A.4}$$

where it is introduced the D-function $D^J_{M,\lambda_i}(\phi_i,\theta_i,-\phi_i)$, see Equation (4.15) of Ref. [76], and the initial state helicity $\lambda_i \equiv \lambda_p - \lambda_{\bar{p}}$. The D-functions are defined as

$$D^j_{m',m}(\alpha,\beta,\gamma) = e^{-i\alpha m'}\,d^j_{m',m}(\beta)\,e^{-i\gamma m}. \tag{A.5}$$

where

$$d^j_{m',m}(\beta) \equiv \sum_n \frac{(-1)^n[(j+m)(j-m)(j+m')(j-m')]^{1/2}}{(j-m-n)(j+m-n)(n+m'-m)n}\times$$
$$\times\Big(\cos\frac{\beta}{2}\Big)^{2j+m-m'-2n}\times\Big(-\sin\frac{\beta}{2}\Big)^{m'-m+2n} \tag{A.6}$$

In our case, the simplest choice for θ_i and ϕ_i is to define the beam axis as the quantization axis, which means $\theta_i = 0$ and allows to set the no-longer-meaningful $\phi_i = 0$. This implies

$$D^{J_i}_{M_i,\lambda_i}(\phi_i=0,\theta_i=0,-\phi_i=0) = d^{J_i}_{M_i,\lambda_i}(\theta_i=0) = \delta_{M_i,\lambda_i}, \tag{A.7}$$

and therefore,

$$|i\rangle = (2\pi)^3 \Big(\frac{4E_{cm}}{p_i}\Big)^{1/2} \sum_{J_i M_i} \sqrt{\frac{2J_i+1}{4\pi}} \delta_{M_i,\lambda_i} |J_i M_i \lambda_p \lambda_{\bar{p}}\rangle |\widetilde{P}_i\rangle. \tag{A.8}$$

The presence of δ_{M_i,λ_i} is due to the fact that the the projection of the $\bar{p}p$ orbital angular momentum on the chosen quantization axis is equal to zero. As a consequence, the only contribute to the third component M_i of the total angular momentum comes from the spin of the particles, which implies $M_i = \lambda_i$.

The amplitude for the formation of an intermediate states $|JM\rangle$ with total angular momentum J and third component M is

$$A(i \to JM) = \langle JM|U|i\rangle =$$

$$= (2\pi)^3 \Big(\frac{4E_{cm}}{p_i}\Big)^{1/2} \sum_{J_i M_i} \sqrt{\frac{2J_i+1}{4\pi}} \delta_{M_i,\lambda_i} \underbrace{\langle JM|U|J_i M_i \lambda_p \lambda_{\bar{p}}\rangle}_{=\delta_{J,J_i}\delta_{M,M_i}A_{J_i\lambda_p\lambda_{\bar{p}}}} =$$

$$= (2\pi)^3 \Big(\frac{4E_{cm}}{p_i}\Big)^{1/2} \sqrt{\frac{2J+1}{4\pi}} A_{J\lambda_p\lambda_{\bar{p}}} \delta_{M,\lambda_i}, \tag{A.9}$$

where $\delta(\widetilde{P}_i - \widetilde{P}_{JM})$ has been dropped ($\widetilde{P}_{JM}$ is the four-momentum of the intermediate state). It has been introduced the energy dependent matrix element, $A_{J\lambda_p\lambda_{\bar{p}}}$, for the $p\bar{p}$ state with total angular momentum J and helicities $\lambda_p\lambda_{\bar{p}}$ to form the intermediate $|JM\rangle$ state. $A_{J\lambda_p\lambda_{\bar{p}}}$ is independent on M because of rotational invariance.

A.2 Amplitude for $|JM\rangle \to |f\rangle$

In a similar way, the final $\pi^0\pi^0$ (or $\pi^0\eta$ or $\eta\eta$) state is written as

$$|f\rangle \equiv |p_f \theta_f \phi_f \lambda_{\pi_1^0} \lambda_{\pi_2^0}\rangle = (2\pi)^3 \Big(\frac{4E_{cm}}{p_f}\Big)^{1/2} |\theta_f \phi_f \lambda_{\pi_1^0} \lambda_{\pi_2^0}\rangle |\widetilde{P}_f\rangle, \tag{A.10}$$

where the subscript f signifies final state. Specifically, p_f, θ_f and ϕ_f are the magnitude, polar angle and azimuthal angle of the final state momentum vector. The

π^0 helicity, even though equal to zero (as the one of the η), is written for completeness.

The expansion in the two-particle spherical helicity basis gives

$$|f\rangle = (2\pi)^3\Big(\frac{4E_{cm}}{p_f}\Big)^{1/2}\sum_{J_f M_f}|J_f M_f \lambda_{\pi_1^0}\lambda_{\pi_2^0}\rangle \underbrace{\langle J_f M_f \lambda_{\pi_1^0}\lambda_{\pi_2^0}|\theta_f \phi_f \lambda_{\pi_1^0}\lambda_{\pi_2^0}\rangle}_{=\sqrt{\frac{2J_f+1}{4\pi}}D^{J_f}_{M_f,\lambda_f}(\phi_f,\theta_f,-\phi_f)}|\widetilde{P}_f\rangle =$$

$$= (2\pi)^3\Big(\frac{4E_{cm}}{p_f}\Big)^{1/2}\sum_{J_f M_f}\sqrt{\frac{2J_f+1}{4\pi}}\,D^{J_f}_{M_f,\lambda_f}(\phi_f,\theta_f,-\phi_f)\,|J_f M_f \lambda_{\pi_1^0}\lambda_{\pi_2^0}\rangle|\widetilde{P}_f\rangle \quad \text{(A.11)}$$

where $\lambda_f \equiv \lambda_{\pi_1^0} - \lambda_{\pi_2^0} = 0$ is the final state helicity. The definition of the D-function, Equation A.5 , and $\lambda_f = 0$ give

$$D^{J_f}_{M_f,\lambda_f=0}(\phi_f,\theta_f,-\phi_f) = e^{-i\phi_f M_f}\,d^{J_f}_{M_f,0}(\theta_f) = e^{-i\phi_f M_f}\sqrt{\frac{(J_f-M_f)!}{(J_f+M_f)!}}P_J^{M_f}(\cos\theta_f), \quad \text{(A.12)}$$

where $P_J^{M_f}(\cos\theta_f)$ are the associated Legendre polynomials. Thus,

$$|f\rangle =$$

$$(2\pi)^3\Big(\frac{4E_{cm}}{p_f}\Big)^{1/2}\sum_{J_f M_f}\sqrt{\frac{2J_f+1}{4\pi}\cdot\frac{(J_f-M_f)!}{(J_f+M_f)!}}e^{-i\phi_f M_f}P_J^{M_f}(\cos\theta_f)\,|J_f M_f\rangle|\widetilde{P}_f\rangle, \quad \text{(A.13)}$$

where $\lambda_{\pi_1^0} = \lambda_{\pi_2^0} = 0$ have been dropped.

The amplitude for the decay of the intermediate $|JM\rangle$ state into a $\pi^0\pi^0$ final state is

$$A(JM \to f) = \langle f|U|JM\rangle =$$

$$= (2\pi)^3\Big(\frac{4E_{cm}}{p_f}\Big)^{1/2}\sum_{J_f M_f}\sqrt{\frac{2J_f+1}{4\pi}\cdot\frac{(J_f-M_f)!}{(J_f+M_f)!}}e^{-i\phi_f M_f}P_{J_f}^{M_f}(\cos\theta_f)\,\underbrace{\langle J_f M_f|U|JM\rangle}_{=\delta_{J,J_f}\delta_{M,M_f}B^*_{J_f}} =$$

$$= (2\pi)^3\Big(\frac{4E_{cm}}{p_f}\Big)^{1/2}\sqrt{\frac{2J+1}{4\pi}\cdot\frac{(J-M)!}{(J+M)!}}B^*_J e^{-i\phi_f M}P_J^M(\cos\theta_f) \quad \text{(A.14)}$$

where $\delta(\widetilde{P}_f - \widetilde{P}_{JM})$ has been dropped, and B_J^* is the energy dependent matrix element for the intermediate $|JM\rangle$ state to form the final $\pi^0\pi^0$ state (with equal JM). As in the case of $A_{J\lambda_p\lambda_{\bar{p}}}$, even B_J^* is independent on M because of rotational invariance.

A.3 Differential Cross Section

The amplitude for the complete process $|i\rangle \to |JM\rangle \to |f\rangle$ is the product of Equation A.9 and Equation A.14:

$$A(i \to JM \to f) = A(i \to JM) \times A(JM \to f) =$$

$$= (2\pi)^6 \frac{4E_{cm}}{\sqrt{p_i p_f}} \frac{2J+1}{4\pi} \sqrt{\frac{(J-M)!}{(J+M)!}}\; F_J^{\lambda_i}\; \delta_{M,\lambda_i}\; e^{-i\phi_f M} P_J^M(\cos\theta_f)\,, \tag{A.15}$$

where we have defined $F_J^{\lambda_i} \equiv A_{J\lambda_p\lambda_{\bar{p}}}\; B_J^*$. The index λ_i is used rather than $\lambda_p\lambda_{\bar{p}}$ since $A_{J\lambda_p\lambda_{\bar{p}}}$ depends (apart from J) only on the relative orientation of λ_p and $\lambda_{\bar{p}}$.

The angular distribution, or differential cross section, is given by the coherent sum of the amplitudes for the formation and decay of all possible $|JM\rangle$ intermediate states, averaged[1] on the four possible helicity orientations of the proton and antiproton:

$$\frac{d\sigma}{d\Omega_f}(\theta_f, \phi_f) = \frac{1}{4} \sum_{\lambda_p} \sum_{\lambda_{\bar{p}}} \Big| \sum_J \sum_M A(i \to JM \to f) \Big|^2 .$$

The insertion of Equation A.15 gives

$$\frac{d\sigma}{d\Omega_f}(\theta_f, \phi_f) =$$

[1]The protons and antiprotons are not polarized.

$$= (2\pi)^{10} \frac{{E_{cm}}^2}{p_i p_f} \sum_{\lambda_p} \sum_{\lambda_{\bar{p}}} \Big| \sum_J \sum_M (2J+1) \sqrt{\frac{(J-M)!}{(J+M)!}} \, F_J^{\lambda_i} \, \delta_{M,\lambda_i} \, e^{-i\phi_f M} P_J^M(\cos\theta_f) \Big|^2. \tag{A.16}$$

Again, the presence of δ_{M,λ_i} signifies that the only contribution to the third component M of the total angular momentum comes from the helicity λ_i of the initial state. As a consequence, the sum over M is removed, leaving $M = \lambda_i$, and the term $e^{-i\phi_f M} = e^{-i\phi_f \lambda_i}$ can therefore be factorized and dropped, since $|e^{-i\phi_f \lambda_i}|^2$. This shows that the cross section is independent on the azimuthal angle ϕ_f of the π^0 axis, as natural given the cylindrical symmetry about the chosen quantization axis. It is then appropriate to integrate over the 2π azimuthal range:

$$\frac{d\sigma}{d\cos\theta_f}(\theta_f) =$$

$$= (2\pi)^{11} \frac{{E_{cm}}^2}{p_i p_f} \sum_{\lambda_p} \sum_{\lambda_{\bar{p}}} \Big| \sum_J (2J+1) \sqrt{\frac{(J-\lambda_i)!}{(J+\lambda_i)!}} \, F_J^{\lambda_i} P_J^{\lambda_i}(\cos\theta_f) \Big|^2. \tag{A.17}$$

The two sums over $\lambda_p = \pm\frac{1}{2}$ and $\lambda_{\bar{p}} = \pm\frac{1}{2}$ correspond to a single sum over $\lambda_i = -1$, 0 (twice), and $+1$. Furthermore, since Equation (43) of Reference [35] shows that

$$F_J^{-\lambda_i} = \frac{P_{\pi^0} P_{\pi^0}}{P_p P_{\bar{p}}} (-1)^{s_{\pi^0} + s_{\pi^0} - s_p - s_{\bar{p}}} F_J^{\lambda_i} = F_J^{\lambda_i}, \tag{A.18}$$

where $P_{\pi^0} = -1$, $P_p = +1$, $P_{\bar{p}} = -1$, $s_{\pi^0} = 0$, $s_p = \frac{1}{2}$, and $s_{\bar{p}} = \frac{1}{2}$ are the parities and spins of the π^0, proton, and antiproton; and it holds

$$\sqrt{\frac{(J-(-\lambda_i))!}{(J+(-\lambda_i))!}} \, P_J^{-\lambda_i}(\cos\theta_f) = \sqrt{\frac{(J+\lambda_i)!}{(J-\lambda_i)!}} \, (-1)^{\lambda_i} \frac{(J-\lambda_i)!}{(J+\lambda_i)!} \, P_J^{\lambda_i}(\cos\theta_f) =$$

$$= (-1)^{\lambda_i} \sqrt{\frac{(J-\lambda_i)!}{(J+\lambda_i)!}} \, P_J^{\lambda_i}(\cos\theta_f); \tag{A.19}$$

it follows that the contribution of the term with $\lambda_i = -1$ in Equation A.17 is equal to the contribution of the term with $\lambda_i = +1$. Therefore, the two sums over λ_p and

$\lambda_{\bar{p}}$ can finally be replaced by a single sum over $|\lambda_i| = 0, 1$ times a factor 2:

$$\frac{d\sigma}{d\cos\theta_f}(\theta_f) =$$

$$= (2\pi)^{11}\frac{2E_{cm}{}^2}{p_i p_f}\sum_{|\lambda_i|=0,1}\left|\sum_J (2J+1)\sqrt{\frac{(J-|\lambda_i|)!}{(J+|\lambda_i|)!}}\,F_J^{|\lambda_i|}P_J^{|\lambda_i|}(\cos\theta_f)\right|^2. \qquad \text{(A.20)}$$

In the next section it is investigated which are the values of J that have a non-zero contribute to the partial wave expansion of the above equation.

A.4 The J^{PC} States that Access the Final Channel

In order to establish which ones of the possible J^{PC} values of the initial $\bar{p}p$ state can access the final $\pi^0\pi^0$ state (or the $\pi^0\eta$ and $\eta\eta$ states), it is useful to review, with the help of Table A.1, the quantum numbers of the particles involved.

Particle	J^{PC}	$I\,(I_3)$
p	$\frac{1}{2}^+$	$\frac{1}{2}\,(\frac{1}{2})$
$\bar{p}$	$\frac{1}{2}^-$	$\frac{1}{2}\,(-\frac{1}{2})$
π^0	0^{-+}	$1\,(0)$
η	0^{-+}	$0\,(0)$

Table A.1: Spin (J), parity (P), charge conjugation (C), isospin (I) and its third component (I_3), of the relevant particles.

These quantum numbers, in turn, dictate that the quantum numbers of the particle pairs relevant to us are the ones in Table A.2.

The J^{PC} column of Table A.2 indicates that only the J^{PC} = even^{++} contributions to the initial $\bar{p}p$ state can access the final states[2] ($\pi^0\pi^0$, $\pi^0\eta$, and $\eta\eta$ have equal

[2]On the other hand, not all of the possible J^{PC} numbers of the final states can be produced in $\bar{p}p$ collisions.

Particle	P	C	J^{PC}	$I\,(I_3)$
$\bar{p}p$	$(-1)^{L+1}$	$(-1)^{L+S}$	$0^{(-+,++)};\ 1^{(--,+-,++)};\ 2^{(--,-+,++)};$ $3^{(--,+-,++)};\ 4^{(--,-+,++)};\ ...$	$1\,(0);\ 0\,(0)$
$\pi^0\pi^0$	$(-1)^L$	$+$	$0^{++};\ 1^{-+};\ 2^{++}; 3^{-+};\ 4^{++};\ ...$	$2\,(0);\ 0\,(0)$
$\pi^0\eta$	$(-1)^L$	$+$	$0^{++};\ 1^{-+};\ 2^{++}; 3^{-+};\ 4^{++};\ ...$	$1\,(0)$
$\eta\eta$	$(-1)^L$	$+$	$0^{++};\ 1^{-+};\ 2^{++}; 3^{-+};\ 4^{++};\ ...$	$0\,(0)$

Table A.2: Parity (P), charge conjugation (C), total angular momentum (J), isospin (I) and its third component (I_3), of the relevant particle pairs. L is the orbital angular momentum between the two particles, and S their combined spin.

possible J^{PC} numbers).

The fact that only even values of J access the final state affects the sum over J in equation A.20, which is then rewritten as

$$\frac{d\sigma}{dz}(z) = \sum_{|\lambda_i|=0,1} \left| \sum_{J=0,2,4,\,...}^{J_{max}} (2J+1) \sqrt{\frac{(J-|\lambda_i|)!}{(J+|\lambda_i|)!}}\; C_J^{|\lambda_i|}\; e^{i\delta_J^{|\lambda_i|}} P_J^{|\lambda_i|}(z) \right|^2 . \tag{A.21}$$

In the above equation the common factor $\frac{(2\pi)^{11} 2 E_{cm}{}^2}{p_i p_f}$ and the complex quantities $F_J^{|\lambda_i|}$ are merged as

$$C_J^{|\lambda_i|}\; e^{i\delta_J^{|\lambda_i|}} \equiv \frac{(2\pi)^{11} 2 E_{cm}{}^2}{p_i p_f}\; F_J^{|\lambda_i|}\;, \tag{A.22}$$

where the coefficients $C_J^{|\lambda_i|}$ are positive real numbers and the phases $\lambda_J^{|\lambda_i|}$ are real. In addition, it is convenient to define[3]

$$z \equiv |\cos\theta_f|\;. \tag{A.23}$$

Finally, the sum over J is limited to a certain value J_{max} because of the limited range of the interaction.

[3]The definition $z \equiv |\cos\theta_f|$ is made for $\pi^0\pi^0$ and $\eta\eta$ final states. For $\pi^0\eta$ final states, where it is possible to distinguish the two final state particles, z is defined as the cosine of the polar angle of the pion. Hence, z is positive or negative if the π^0 or the η is emitted in the forward direction, respectively. However, notice that $d\sigma/dz$ is still forward-backward symmetric.

By expanding the sum over $|\lambda_i|$, the differential cross section for the processes $\bar{p}p \to \pi^0\pi^0$, $\bar{p}p \to \eta\eta$ or $\bar{p}p \to \pi^0\eta$ becomes:

$$\frac{d\sigma}{dz}(z) =$$

$$= \Big| \sum_{J=0,2,4,\ldots}^{J_{max}} (2J+1)\; C_J \; e^{i\delta_J} \; P_J(z) \Big|^2 + \Big| \sum_{J=2,4,\ldots}^{J_{max}} \frac{2J+1}{\sqrt{J(J+1)}} \; C_J^1 \; e^{i\delta_J^1} \; P_J^1(z) \Big|^2, \quad \text{(A.24)}$$

where the first and second terms are generated by the initial $\bar{p}p$ state with $\lambda_i = 0$ (helicity-0) and $|\lambda_i| = 1$ (helicity-1), respectively[4].

[4]The superscript 0 is dropped in the coefficients C_J^0 and phases δ_J^0 .

Appendix B

Correction for Limited Polar Angle Resolution

For a fraction of the events, it happens that the two final state particles are generated within a certain bin of z (defined in Equations 3.1 and 4.1) but, after the detection and CCAL clusterization take place, the reconstructed value of z ends up within a different bin. Such an effect is here called event migration. The net event gain or loss of a bin depends on the local shape of the angular distribution, the detector resolution and the width of the bins. Since the MC events are generated isotropically while the (at this point still unknown) differential cross section of the real events is not isotropic, the event migration occurring during the simulation is different from the one occurring for real data.

In order to correct for it, the event migration is estimated by recording, during the MC simulation, both the bin where an event is generated and the bin where the event is reconstructed. A matrix with the number of events, N_{ij}, generated in a bin j and reconstructed a bin i is then built. An efficiency-migration matrix[1] M, with elements M_{ij}, is calculated by dividing the content of each matrix element N_{ij} by

[1] The matrix incorporates, other than the migration information, the selection efficiency information, because the MC events considered are the ones that pass the $\pi^0\pi^0$ selection.

the total number of events generated in the bin i:

$$M_{ij} \equiv \frac{N_{ij}}{\sum_{j=1}^{40} N_{ij}} \ . \tag{B.1}$$

Considering now real data and calling R_i the number of events surviving the $\pi^0\pi^0$ selection and reconstructed in the bin i, the estimate of the number of event, G_j, for which the two final state particles are actually generated in the bin j is given by

$$G_j = \sum_{i=1}^{40} (M^{-1})_{ij} \times R_i, \tag{B.2}$$

where M^{-1} is the inverse of the matrix M. A 10-degree polynomial fit, with even powers only, is then performed on the elements G_j as a function of z. The resulting polynomial, $P(z)$, gives the migration-corrected estimate of the $\pi^0\pi^0$ (or $\pi^0\eta$ or $\eta\eta$) angular distribution. $P(z)$ could now be used to generate MC events with the correct angular distribution and redetermine the product of the acceptance and efficiency, the vector $a \times \epsilon$, as the number of events reconstructed in a bin divided by the number of events generated in the same bin. But it is not necessary to run again the MC simulation, since sufficient information is already available in the matrix M. It is enough to say that the events generated in a bin j are $P_j = P(z_j)$, where z_j is the center of the bin, and the events reconstructed in the same bin are $\sum_{j=1}^{40} M_{ij} \times P_j$. The so-redetermined vector $a \times \epsilon$, since it is determined by using the migration-corrected estimate of the angular distribution, is affected by the same event migration that affects the real data[2].

Figure B.1 gives an insight on the magnitude of the event migration. For $\pi^0\pi^0$ events, the distribution of the sum between $\cos\theta_{\pi^0_{fw}}$ and $\cos\theta_{\pi^0_{bw}}$ is plotted, where $\theta_{\pi^0_{fw}}$ and $\theta_{\pi^0_{bw}}$ are the polar angles (in the c.m. frame) of the forward and

[2] The reader may wonder why one does not just use the estimates G_j to continue the analysis toward the determination of the $\pi^0\pi^0$ differential cross section. The reason is that the differential cross section is obtained by performing a log-likelihood fit and that requires to work with the actually measured events R_i along with the vector $a \times \epsilon$. It is also true that one could use the matrix M^{-1} along with R_i. But dealing with a matrix would add an undesired complication to the already complex log-likelihood fit, which is performed simultaneously on the 17 energy points times 24 bins in z (see Section 3.13).

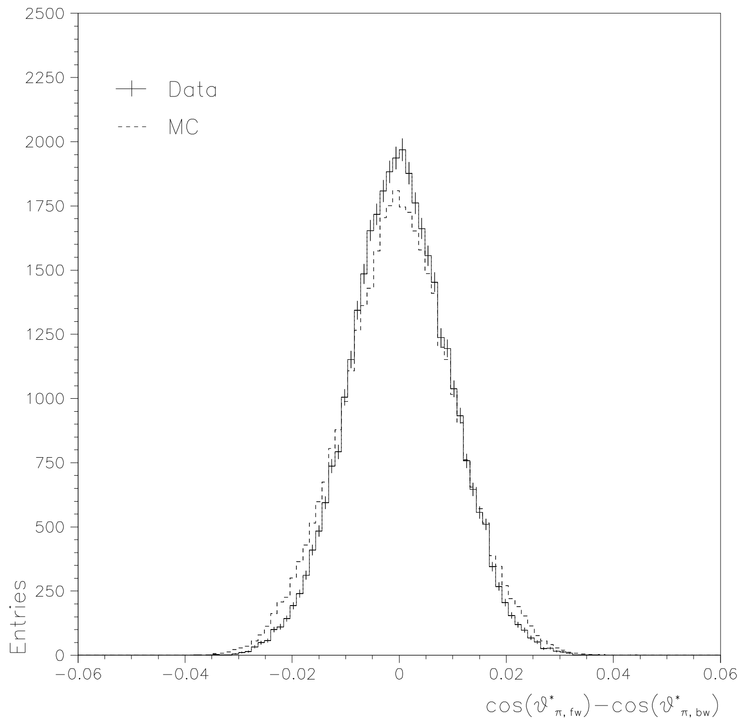

Figure B.1: The distribution of $\cos(\theta_{\pi^0_{fw}}) + \cos(\theta_{\pi^0_{bw}})$ for $\pi^0\pi^0$ events. The $\pi^0\pi^0$ event selection is applied with the exception of cut 7 on page 87.

backward pions[3]. The dispersion of such a quantity, which would be a constant with a perfect polar angle resolution, indicates that the resolution on z is comparable to the size $\Delta z = 0.025$ of the bins. However, even if it is substantial the number of events that migrate from their original bin to a different destination bin (up to $\sim 25\%$), the gain and loss of each bin tend to compensate to each other, making the net gain or loss very much contained.

For the three analyses $\pi^0\pi^0$, $\pi^0\eta$ and $\eta\eta$, Figure B.2 reproduces the ratio between $a \times \epsilon$ determined by using the estimated angular distribution and $a \times \epsilon$ determined

[3]The plot is produced by applying all $\pi^0\pi^0$ cuts with the exception of cut 7 on page 87. No restriction on the polar angles are applied in the plot, the variation of the distribution as a function of the polar angle is contained. Also, notice that the $\pi^0\pi^0$ final state has a very small background (see section 3.9).

by using a uniform angular distribution. This ratio is greater than 1 whenever the

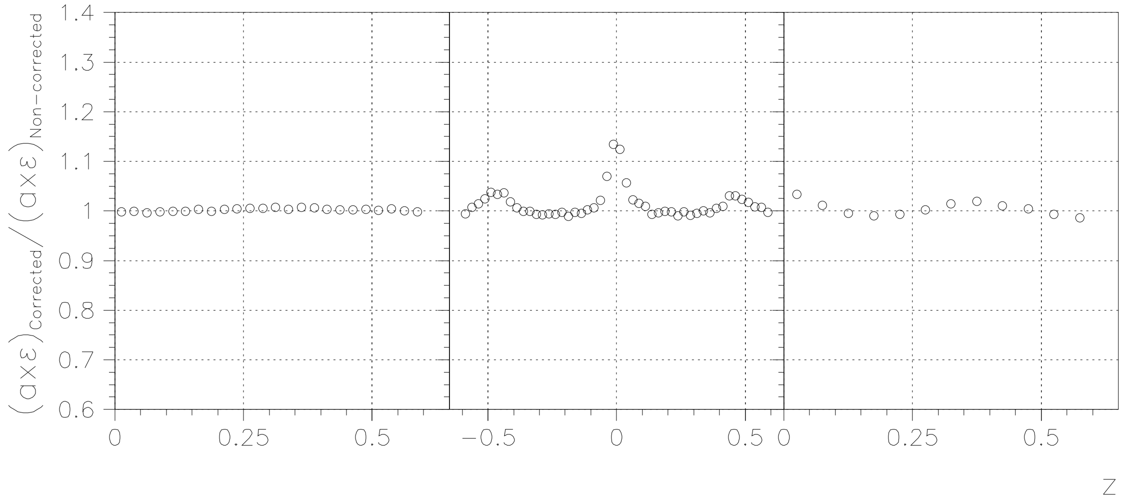

Figure B.2: The product acceptance $\times$ efficiency ($a \times \epsilon$) determined by using the estimated angular distribution divided by $a \times \epsilon$ determined by using a uniform angular distribution. Left: $\pi^0\pi^0$ channel. Center: $\pi^0\eta$ channel. Right: $\eta\eta$ channel.

accumulation of events from neighbor bins exceeds the loss due to events migrated toward those neighbors. This happens in a significant way at the minima of $\frac{d\sigma}{dz}$.

Event Migration in the $\pi^0\pi^0$ channel

In the case of the $\pi^0\pi^0$ final channel, the shape of the differential cross section does not present sharp structures as function of z. Therefore, the net gain and loss of the bins is very much contained, as the left plot in Figure B.2 indicates. The correction the the product of the acceptance and efficiency, $a \times \epsilon$, is within a half of a percent for every bin.

Event Migration in the $\pi^0\eta$ channel

The differential cross section $\bar{p}p \to \pi^0\eta$ in the χ_{c0} region has a structure with pronounced minima, as it is shown in Section 4.7. In particular, the minimum at $z = 0$ is almost a zero. As a consequence, the net gain in the number of events in the bins at small z may be a significant fraction of the events that where actually produced at small z. Hence, the value of $a \times \epsilon$ at small z may be "artificially" raised (see middle plot in Figure B.2).

Event Migration in the $\eta\eta$ channel

The structure of the differential cross section in the channel $\bar{p}p \to \eta\eta$ is somewhat in between those of the two previous channels. It has a minimum at $z = 0$, but not as sharp as in the $\pi^0\eta$ channel. Consequently the size of the event migration is less important than for $\pi^0\eta$ events, but not as small as for $\pi^0\pi^0$ events (see right plot in Figure B.2). Notice also that the bins used for the $\eta\eta$ analysis are twice as large as those for $\pi^0\pi^0$ and $\pi^0\eta$.

Appendix C

Supplement to the Analysis $\pi^0\pi^0$

This appendix includes additional plots and studies that, although important when performing the $\pi^0\pi^0$ analysis, are not included in the body of Chapter 3 to avoid overloading it.

C.1 Fit to the Differential Cross Section over $0 < z < 0.6$ at all Energy Points

The partial wave expansion fit of Equations 3.19 , 3.20 and 3.21 is compared to the data in the following Figures C.1 and C.2.

In Figures C.4 and C.3 the fitted and the measured $d\sigma(x,z)/dz$ are integrated over different ranges of z plotted versus E_{cm} .

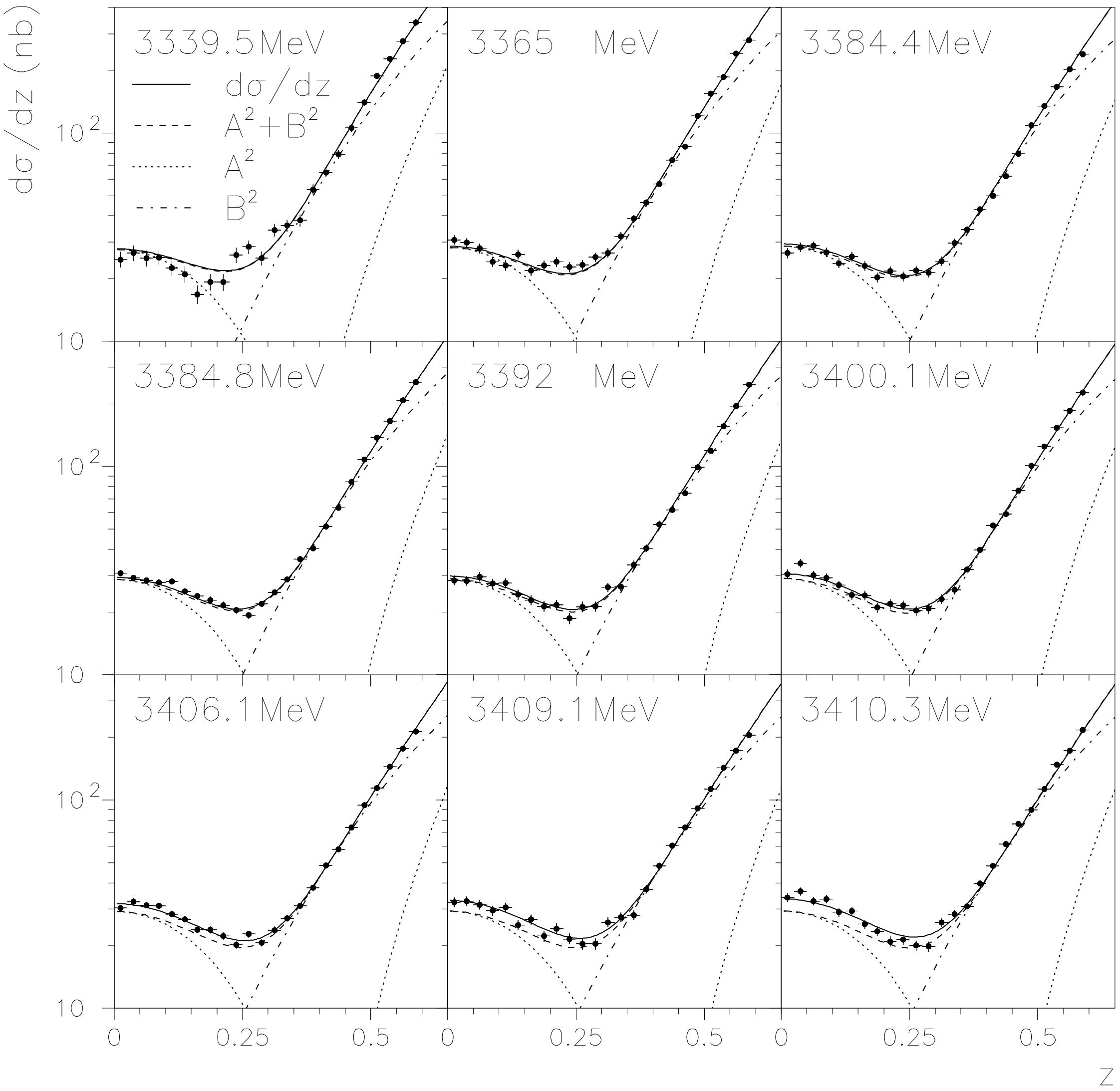

Figure C.1: The measured $\bar{p}p \rightarrow \pi^0\pi^0$ differential cross section (logarithmic scale) plotted versus z at the E_{cm} indicated in each plot. The fit of Equations 3.19 , 3.20 and 3.21 and its components are also shown.

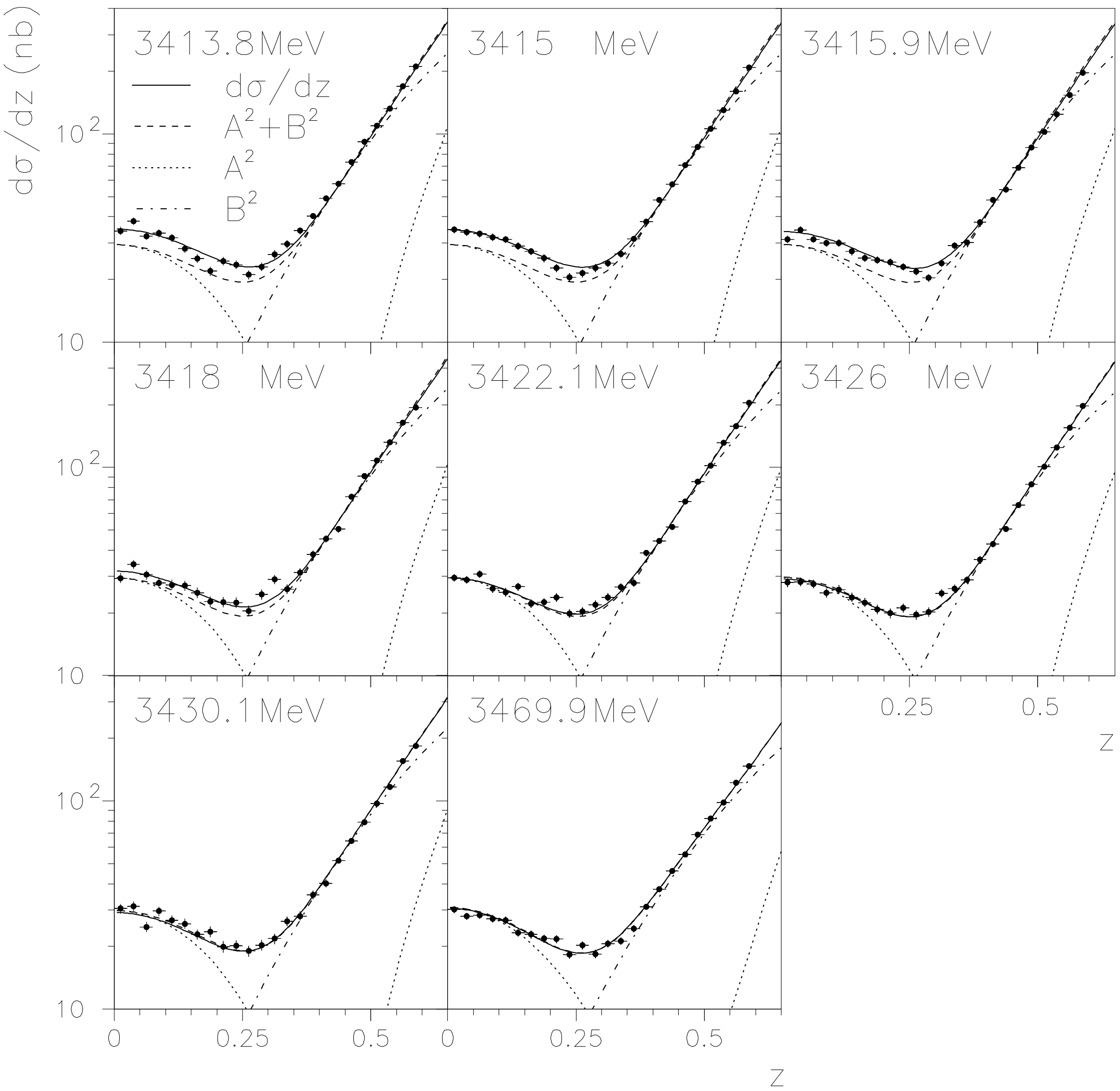

Figure C.2: As Figure C.1, at the remaining energies.

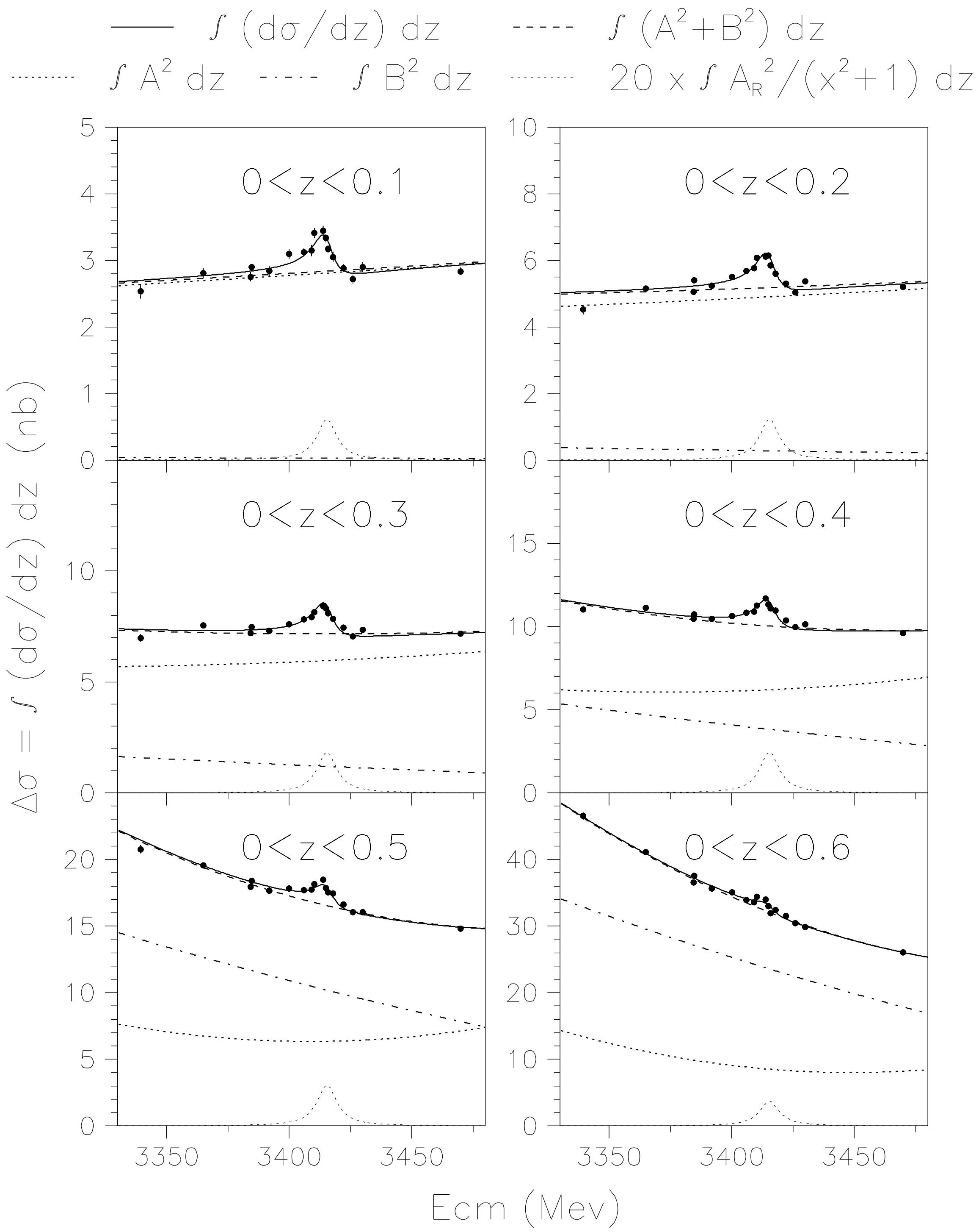

Figure C.3: The measured $\bar{p}p \rightarrow \pi^0\pi^0$ cross section integrated over $0 < z < z_{max}$ plotted versus E_{cm} . The fit of Equations 3.19 , 3.20 and 3.21 and its components are also shown.

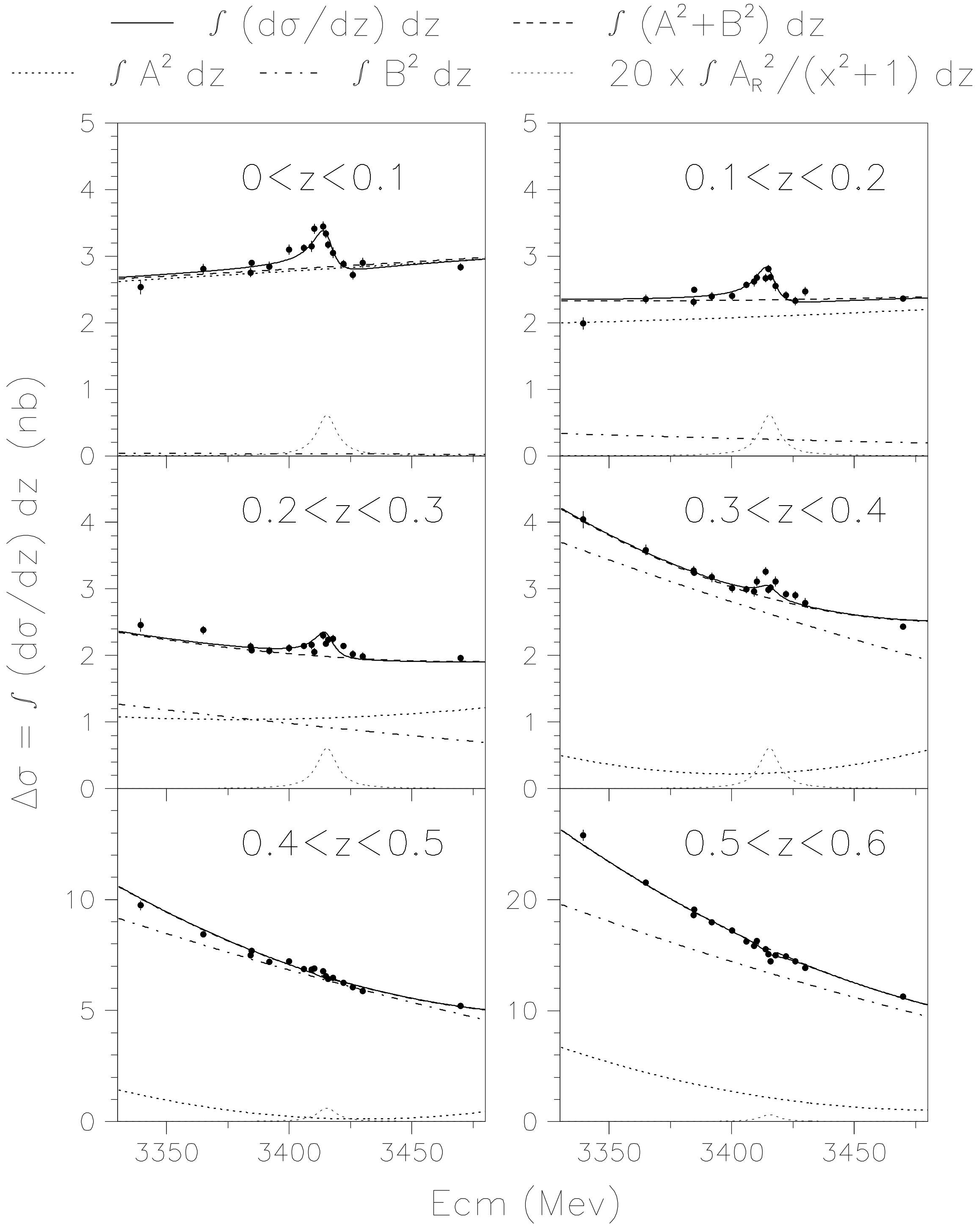

Figure C.4: The measured $\bar{p}p \to \pi^0\pi^0$ cross section integrated over $z_{min} < z < z_{max}$ plotted versus E_{cm} . The fit of Equations 3.19 , 3.20 and 3.21 and its components are also shown.

C.2 Fits over $0 < z < z_{max}$ Setting $|B\ e^{i\delta_B}|^2 = 0$

The fits to the $\bar{p}p \to \pi^0\pi^0$ cross section described in Section 3.14.1 can be performed on several merged bins, from $z = 0$ to different values of $z = z_{max}$, to bind the information from the several bins and limit the fluctuations of the fit parameters.

The parameterization of the fits is similar to the one of Equation 3.22 , with the difference that an integration is performed over $0 < z < z_{max}$:

$$\Delta\sigma = \int_0^{z_{max}} \left| -\frac{A_R}{x+i} + A\ e^{i\delta_A} \right|^2 dz\ , \tag{C.1}$$

and it is necessary to add a dependence on z to equation 3.23 :

$$A^2 \equiv a_0 + a_1 x + a_2 x^2 + a_3 z^2 + a_4 z^4\ . \tag{C.2}$$

The terms $a_3 z^2$ and $a_4 z^4$ are actually called for in the fit only for $z_{max} \geq 0.1$ and $z_{max} \geq 0.225$, respectively . The helicity-1 continuum $|B\ e^{i\delta_B}|^2$ is constrained to zero.

Figure C.5 shows the integrated cross section for increasing values of z_{max} and the fit results. Figure C.6 shows the fit parameters as a function of z_{max}.

The fluctuation of the parameters are reduced, as compared to Figure 3.26, by the fact that the bins in z are bound to each other by the integration over z. A decrease of the resonant amplitude A_R still begins at $z \gtrsim 0.15$, putting in evidence the growth of the helicity-1 continuum which is not accounted for in these fits. As observed in Section 3.14.1, this support the choice of restricting the angular range to $z \leq z_{cut} \equiv 0.125$ when determining A_R. In addition, the growth of the χ^2/DOF indicates that for larger z_{max} the parameterizations of equations C.1 and C.2 are no longer sufficient to describe the structure of the cross section.

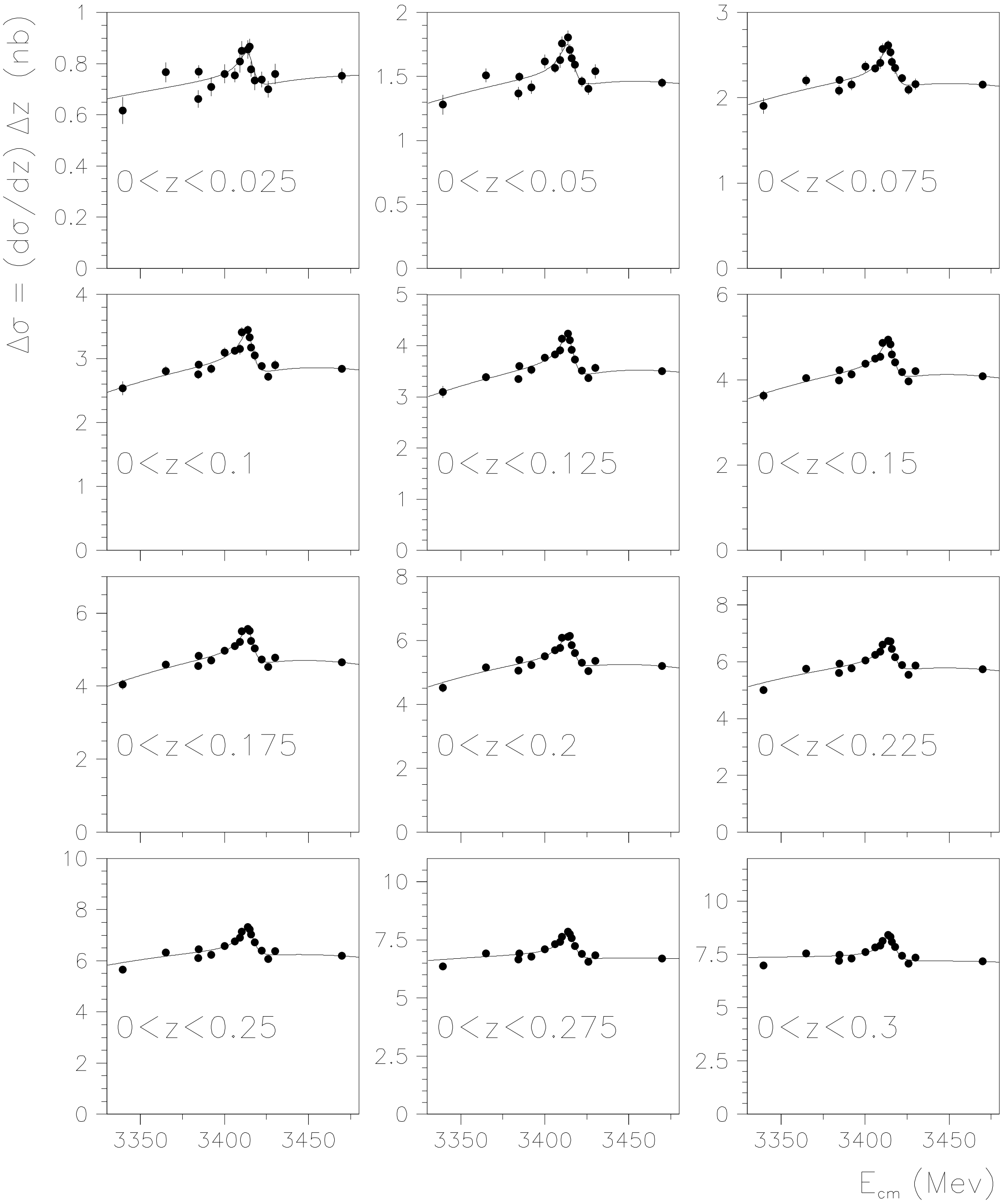

Figure C.5: Fits to the $\bar{p}p \to \pi^0\pi^0$ cross section integrated over $0 < z < z_{max}$, for increasing values of z_{max} , versus E_{cm}. The parameterization used is equations C.1 and C.2 (the helicity-1 continuum $|B\ e^{i\delta_B}|^2$ is fixed to zero).

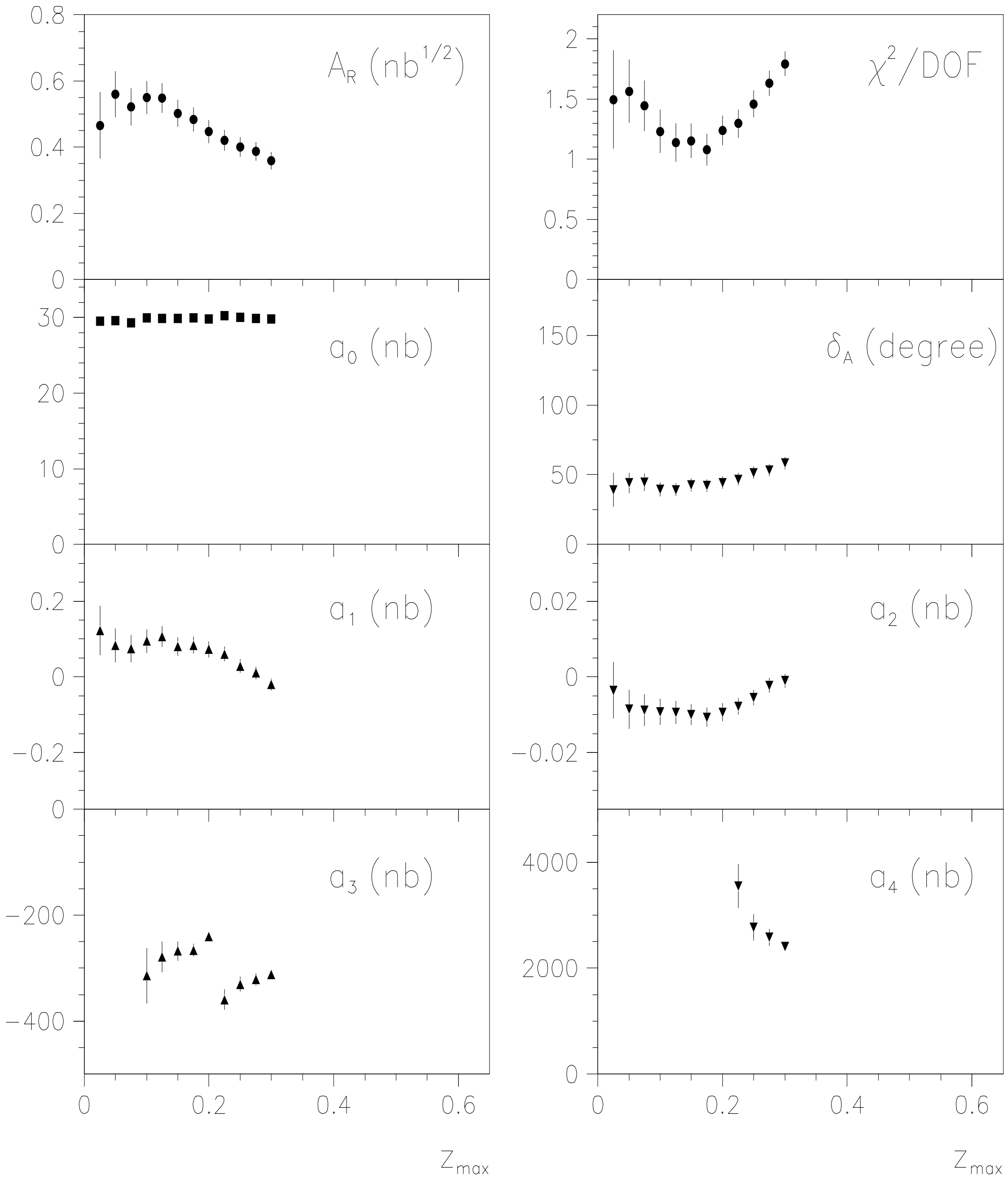

Figure C.6: The parameters of Equations C.1 and C.2 (the helicity-1 continuum $|B\ e^{i\delta_B}|^2$ is fixed to zero) plotted as a function of z_{max}. The parameters a_3 and a_4 are necessary only for $z_{max} \geq 0.1$ and $z_{max} \geq 0.225$, respectively.

C.3 Fits over $0 < z < z_{max}$ Setting $|B\ e^{i\delta_B}|^2$ to the Estimate from Section 3.13

Fits [1] to the $\bar{p}p \to \pi^0\pi^0$ cross section can be performed with the equation:

$$\Delta\sigma = \int_0^{z_{max}} \left[\left| -\frac{A_R}{x+i} + A\ e^{i\delta_A} \right|^2 + \left| B\ e^{i\delta_B} \right|^2 \right] dz. \tag{C.3}$$

The parameterization of the magnitude of the helicity-0 continuum is equal to the one used in Appendix C.2:

$$A^2 \equiv a_0 + a_1 x + a_2 x^2 + a_3 z^2 + a_4 z^4\ , \tag{C.4}$$

while the helicity-1 continuum $|B\ e^{i\delta_B}|^2$ is constrained to the estimate obtained in Section 3.13.

The curves of these fits are not appreciably different from the ones in Figure C.5 and thus are not reproduced here. The behavior of the parameters as a function of z_{max} is, instead, shown in Figure C.7.

The decrease of A_R (top-left plot in Figure C.7) for increasing z is reduced, with respect to the top-left plot in Figure C.6, by the fact that the estimate of $|B\ e^{i\delta_B}|^2$ is introduced in the parameterization of the present fits. Nonetheless, a moderate but steady decrease still persists. Such a decrease may be caused by the fact that the polynomial expansion of equation C.4 is no longer adequate for larger z (see the growth of χ^2/DOF in top-right plot of Figure C.7). Otherwise, it may be an indication that the estimate of the helicity-1 component $|B\ e^{i\delta_B}|^2$ of the continuum may be affected by significant systematics. That would not be surprising. In fact, it should be recalled that $|B\ e^{i\delta_B}|^2$ is estimated by a fit performed on the incomplete angular range $0 < z < 0.6$.

This supports the choice of extracting the value of the resonant amplitude A_R from a restricted angular range $0 < z < 0.125$ (as described in Section 3.14.2) to

[1] The fits described in this appendix include the fit performed in Section 3.14.2, where z_{max} is set equal to $z_{cut} \equiv 0.125$.

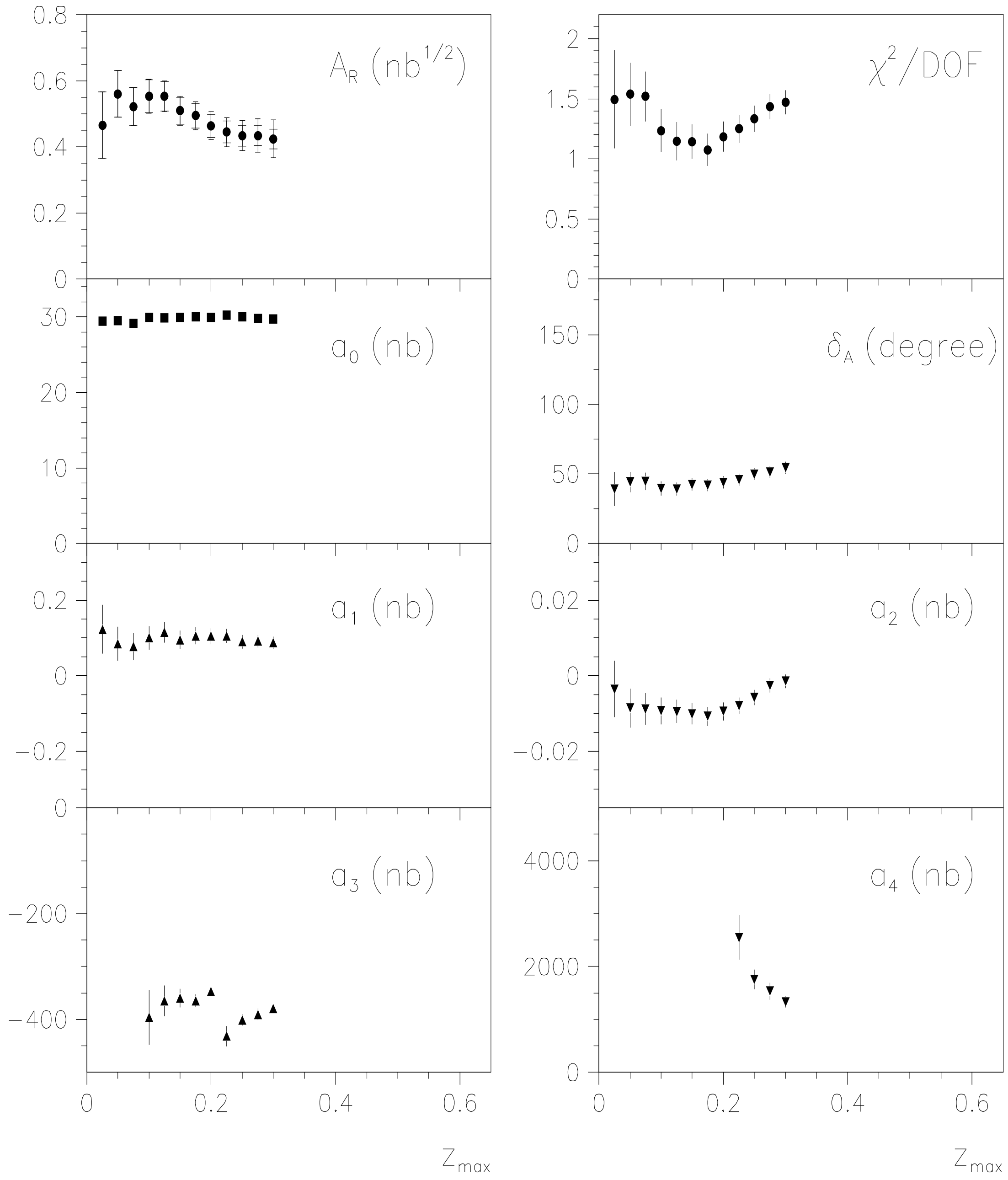

Figure C.7: The parameters of Equations C.3 and C.4 (with $|B\ e^{i\delta_B}|^2$ set to the estimate obtained in Section 3.13) plotted as a function of z_{max}. In the top-left plot, the inner error bars of A_R are statistical and the outer systematic (determined as described in Appendix C.4). The parameters a_3 and a_4 are necessary only for $z_{max} \geq 0.1$ and $z_{max} \geq 0.225$, respectively.

guarantee that the contribution of $|B\ e^{i\delta_B}|^2$ is sufficiently small not to impact the estimate of A_R.

C.4 Systematic Errors from the Estimate of $|B\ e^{i\delta_B}|^2$

The uncertainty on the amplitude of the helicity-1 continuum,

$$B\ e^{i\delta_B} \equiv \sum_{J=2,4,\dots}^{J_{max}=4} \frac{2J+1}{\sqrt{J(J+1)}}\ C_J^1\ e^{i\delta_J^1}\ P_J^1(z), \tag{C.5}$$

produces an additional uncertainty on the resonant amplitude A_R.

The involved parameters (C_2^1, C_4^1 and $\delta_4^1 - \delta_2^1$) have been estimated in Section 3.13 and come with the values and uncertainties of Table 3.7. The corresponding uncertainty on the helicity-1 cross section, $|B\ e^{i\delta_B}|^2 = B^2$, is established by varying simultaneously all parameters within their uncertainties ($\pm 1\sigma$) and recording those values that produce the maximum and the minimum of the integral of $|B\ e^{i\delta_B}|^2$ over the considered angular range. Figure C.8 shows the upper (B^2_{max}) and the lower (B^2_{min}) boundaries of B^2, along with B^2 itself, as a function of z at $E_{cm} = 3415$ MeV.

The systematic error on the resonant amplitude A_R is determined by re-performing the fit of Section 3.14.2 constraining the parameters C_2^1, C_4^1 and $\delta_4^1 - \delta_2^1$ to the values corresponding to B^2_{max} and B^2_{min}. For each one of the two cases, the new estimate of A_R is compared to the estimate in Table 3.8.

The outer error bars in the top-left plot in Figure C.7 indicate the systematic uncertainties of A_R determined as described here and by considering every range $0 < z < z_{max}$ up to $z_{max} = 0.3$. The systematic error quoted in Table 3.9 is the one obtained with $z_{max} = z_{cut} \equiv 0.125$.

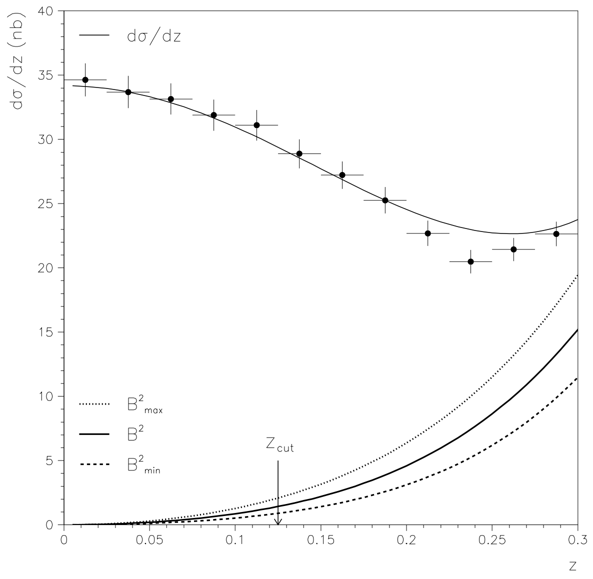

Figure C.8: The upper (B^2_{max}) and lower (B^2_{min}) boundaries of the helicity-1 cross section B^2 as a function of z at $E_{cm} = 3415$ MeV. The arrow indicates the angular range cut of equation 3.24 . The experimental points and the fit to $\frac{d\sigma}{dz}$ are also shown.

C.5 The Background Versus E_{cm}

Figure C.9 reproduces the amount of cross section due to background events simulating the $\pi^0\pi^0$ final state (as estimated with the procedure of Section 3.9) plotted versus the energy in the center of mass. The considered angular region ($0 < z < 0.125$) is the one used in Section 3.14.2 to extract the resonance amplitude. For comparison, the $\pi^0\pi^0$ cross section is also plotted, along with the cross section that would result without performing the subtraction of the background.

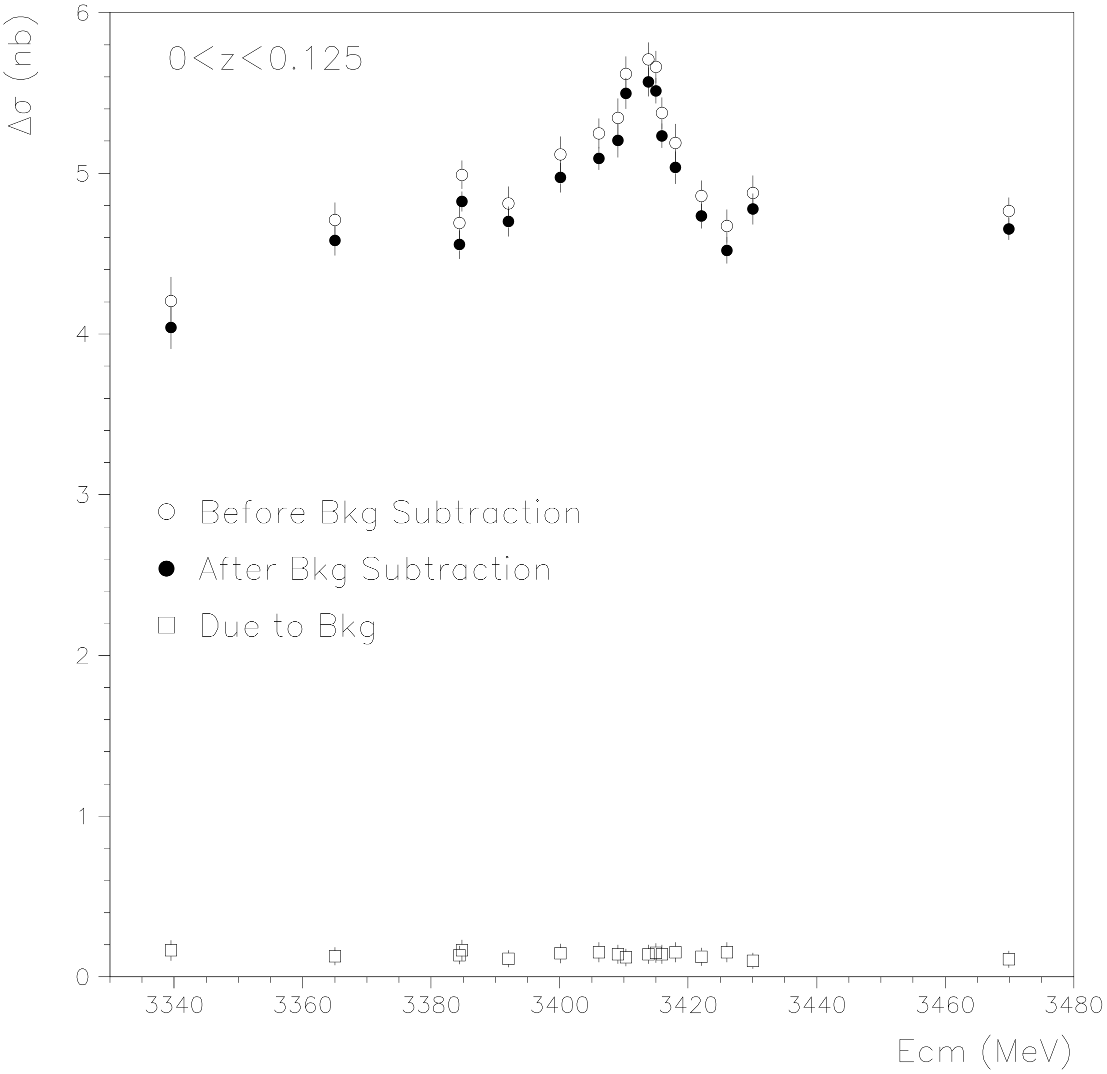

Figure C.9: The effect of the background subtraction on the $\pi^0\pi^0$ cross section $\Delta\sigma$ integrated over the angular region ($0 < z < 0.125$) used to extract the resonance amplitude. The amount of cross section due to background events simulating the $\pi^0\pi^0$ final state is at the level of $\sim 2.5\%$ and lies at the bottom of the plot. The $\pi^0\pi^0$ cross section is also shown, along with the cross section that would result without performing the subtraction of the background.

Appendix D

Supplement to the Analysis $\pi^0\eta$

This appendix includes additional plots that are not included in the body of Chapter 5.

D.1 Fit to the Differential Cross Section over $-0.6 < z < 0.6$ at all Energy Points

The fit of equations 1.16 with A_R set equal to zero, and with the partial wave expansions Equations 1.14 and 1.15 (with $J_{max} = 4$), is compared to the data in the following Figures D.1 and D.2.

In Figures D.4 and D.3 the fitted and the measured $d\sigma(x,z)/dz$ are integrated over different ranges of z plotted versus E_{cm} .

It is also interesting to investigate the small z region in greater detail, because of the presence of a dip in $d\sigma/dz$ at $z = 0$. This is done in Figure D.5

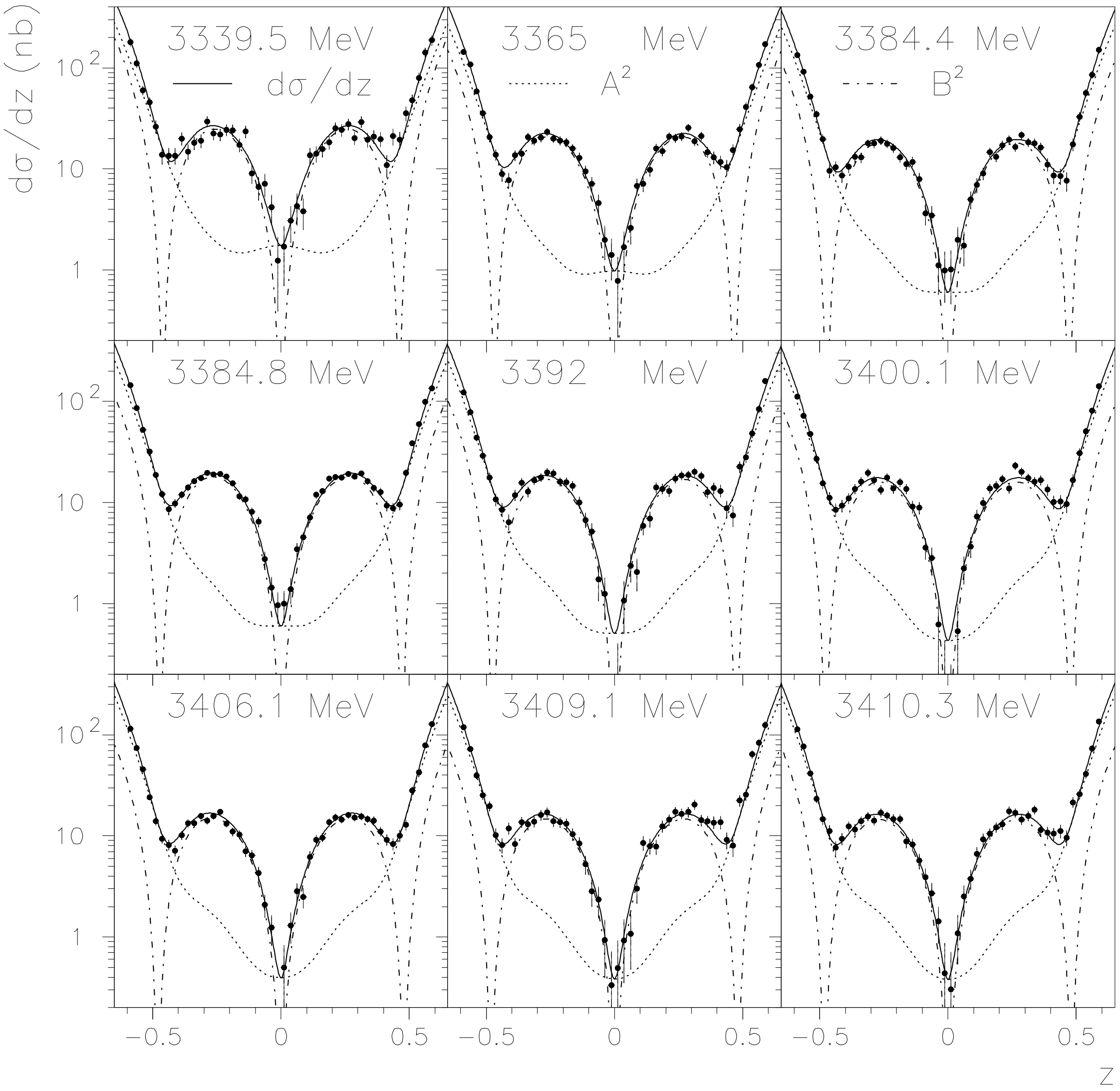

Figure D.1: The measured $\bar{p}p \to \pi^0\eta$ differential cross section (logarithmic scale) plotted versus z at the E_{cm} indicated in each plot. The fit of Equations 1.16 (with $A_R = 0$), 1.14 and 1.15 (with $J_{max} = 4$) and its components are also shown.

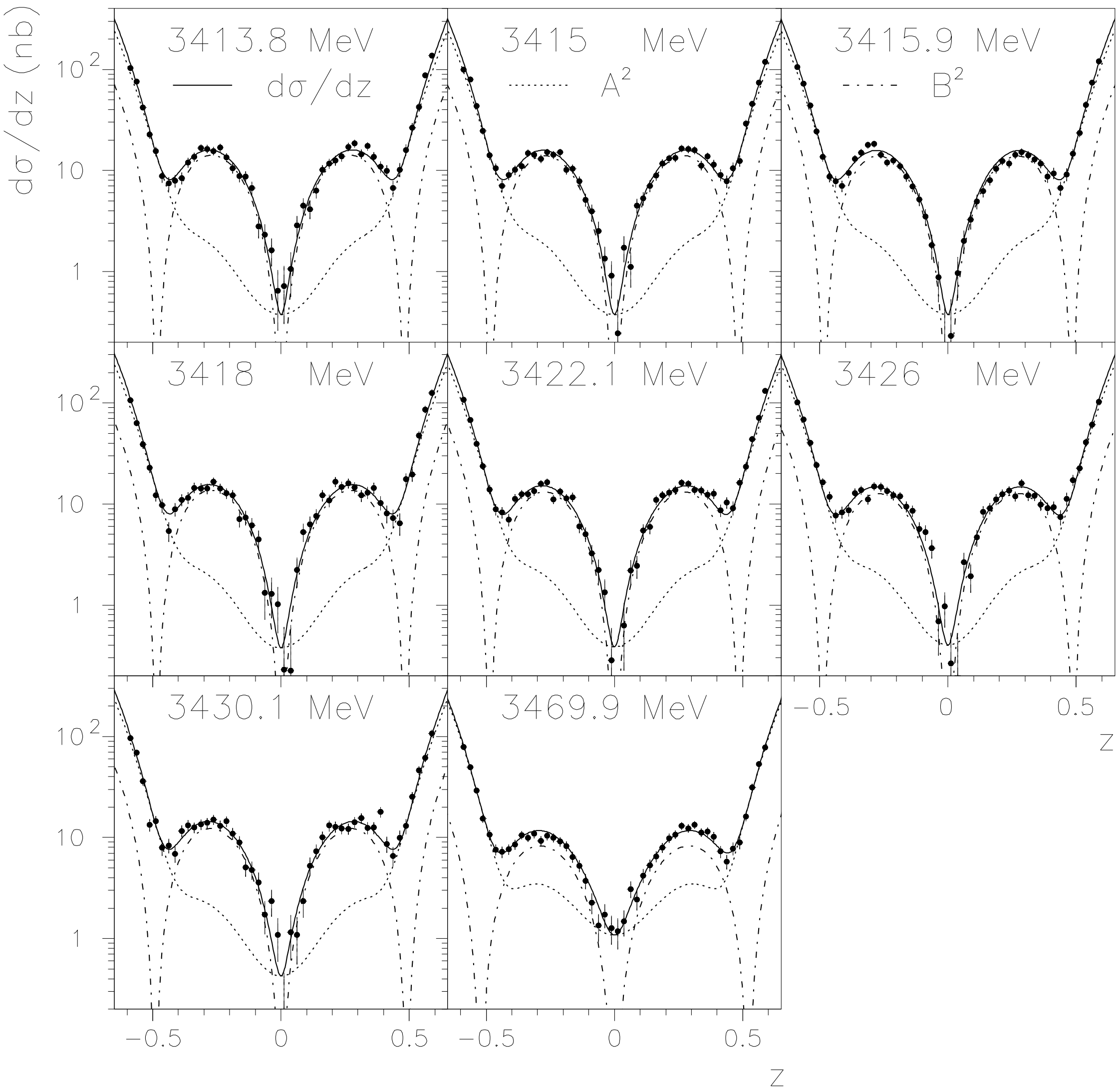

Figure D.2: As Figure D.1, at the remaining energies.

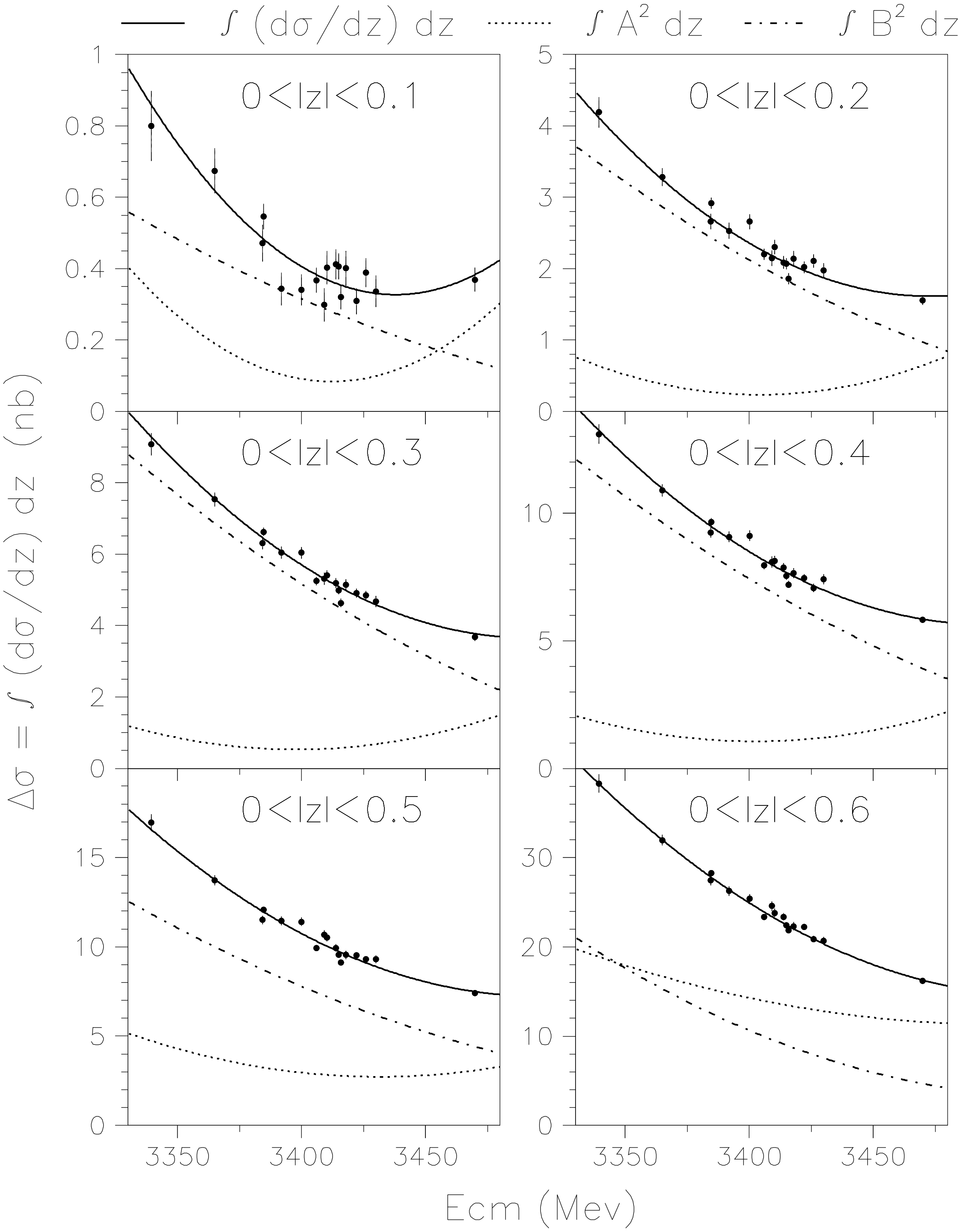

Figure D.3: The measured $\bar{p}p \to \pi^0\eta$ cross section integrated over $0 < |z| < z_{max}$ plotted versus E_{cm} . The fit of Equations 1.16 (with $A_R = 0$), 1.14 and 1.15 (with $J_{max} = 4$) and its components are also shown.

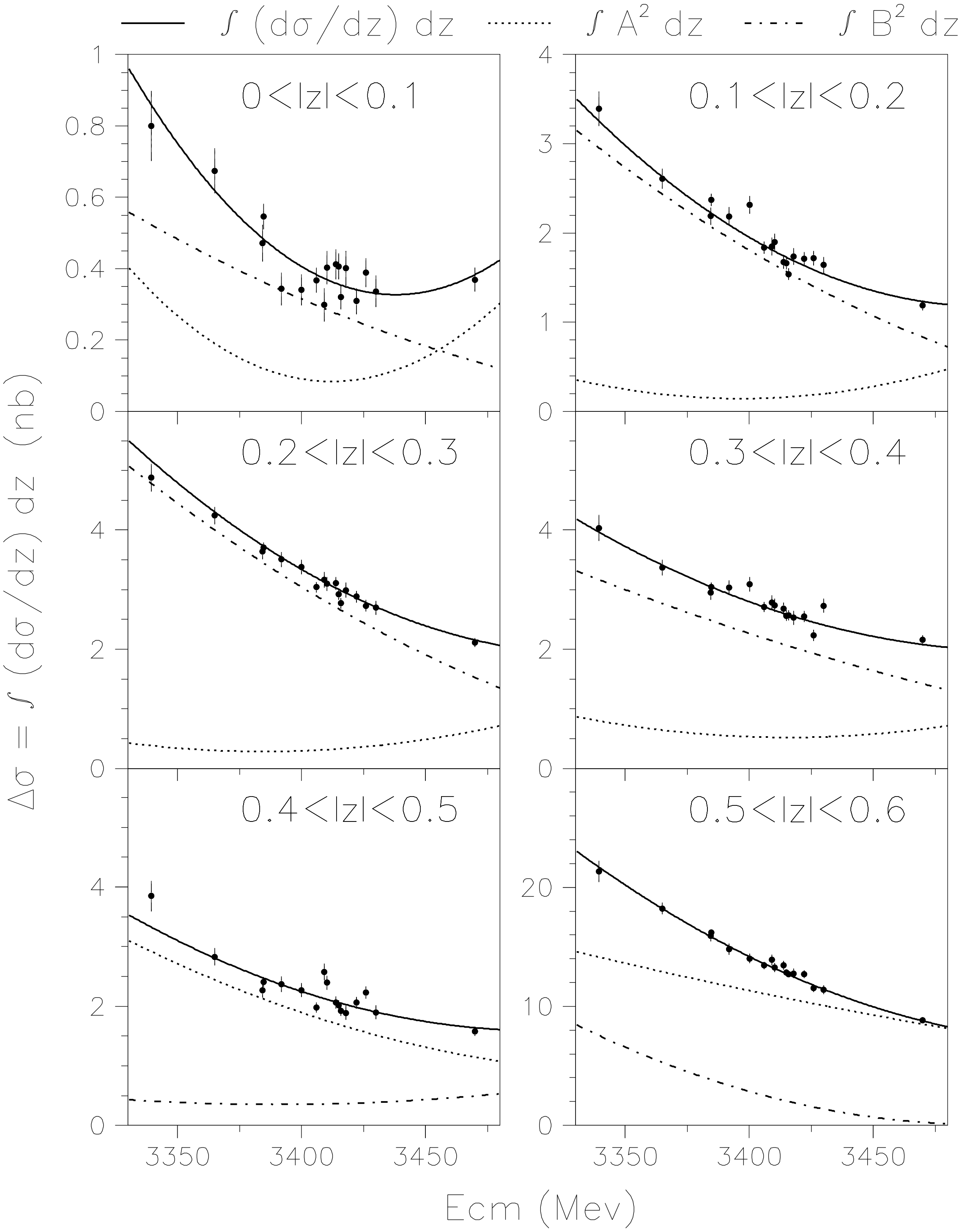

Figure D.4: The measured $\bar{p}p \to \pi^0\eta$ cross section integrated over $z_{min} < |z| < z_{max}$ plotted versus E_{cm}. The fit of Equations 1.16 (with $A_R = 0$), 1.14 and 1.15 (with $J_{max} = 4$) and its components are also shown.

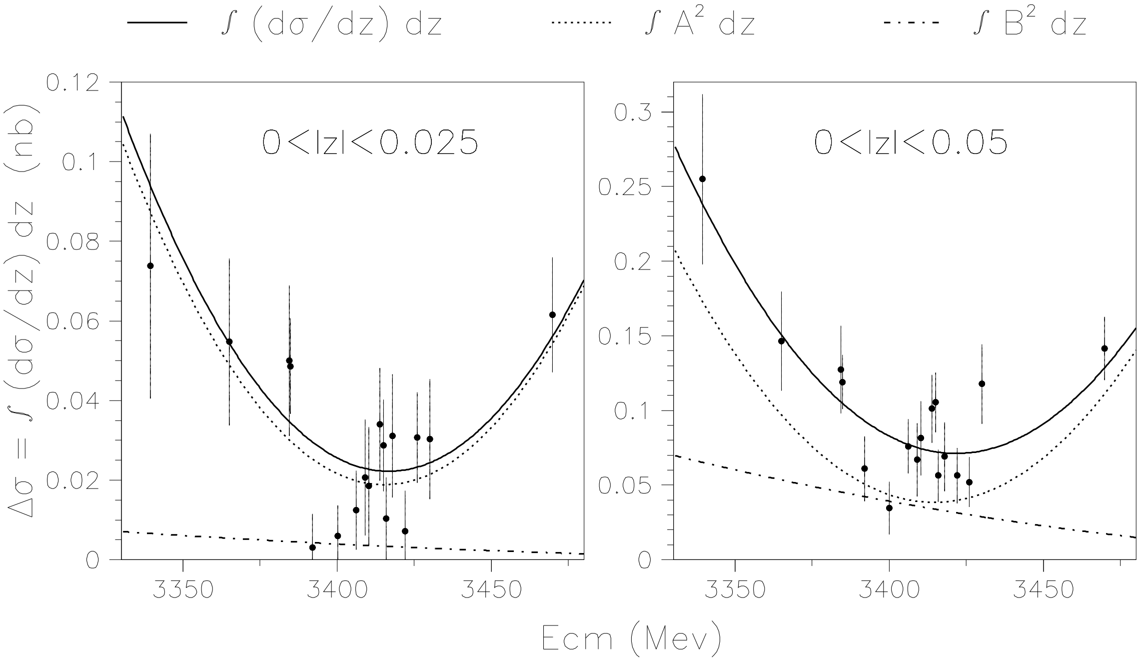

Figure D.5: The measured $\bar{p}p \to \pi^0\eta$ cross section integrated over $0 < |z| < 0.025$ (left) and $0 < |z| < 0.05$ (right) plotted versus E_{cm}. The fit of Equations 1.16 (with $A_R = 0$), 1.14 and 1.15 (with $J_{max} = 4$) and its components are also shown.

D.2 The Background Versus E_{cm}

Figure D.6 reproduces the amount of cross section due to background events simulating the $\pi^0\eta$ final state (as estimated with the procedure of Section 4.5), integrated over the angular region $-0.6 < z < 0.6$ and plotted versus the energy in the center of mass. For comparison, the $\pi^0\eta$ cross section is also plotted, along with the cross section that would appear without subtracting the background.

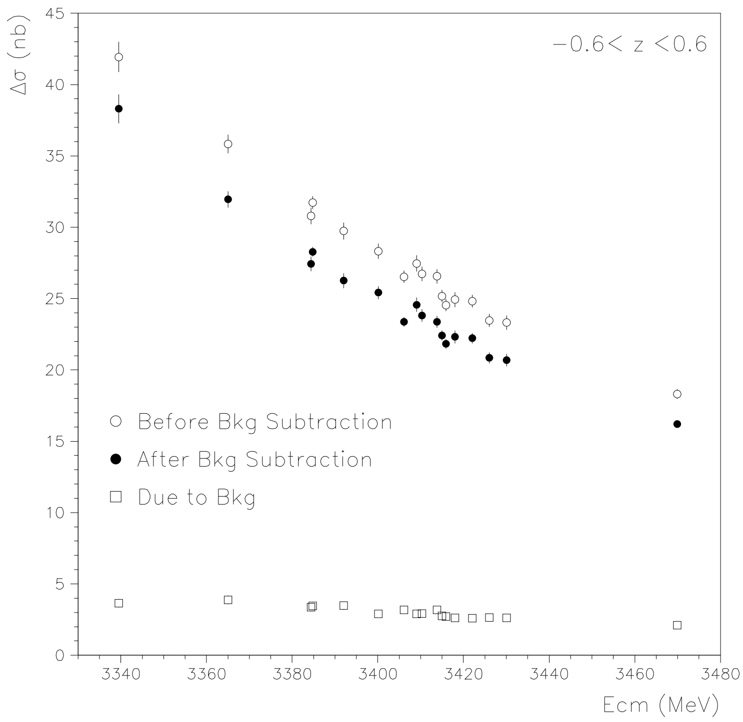

Figure D.6: The effect of the background subtraction on the $\pi^0\eta$ cross section $\Delta\sigma$ integrated over the angular region $-0.6 < z < 0.6$. The amount of cross section due to background events simulating the $\pi^0\eta$ final state is at the level of $\sim 12.8\%$ (on average over the 17 energy points) and lies at the bottom of the plot. The $\pi^0\eta$ cross section is also shown, along with the cross section that would appear without subtracting the background.

Appendix E

Supplement to the Analysis $\eta\eta$

This appendix includes additional plots and studies that are not included in the body of Chapter 5 to avoid overloading it.

E.1 Fit to the Differential Cross Section over $0 < z < 0.6$ at all Energy Points

The partial wave expansion fit of Equations 3.19 , 3.20 and 3.21 is compared to the data in the following Figures E.1 and E.2.

In Figures E.4 and E.3 the fitted and the measured $d\sigma(x, z)/dz$ are integrated over different ranges of z plotted versus E_{cm} .

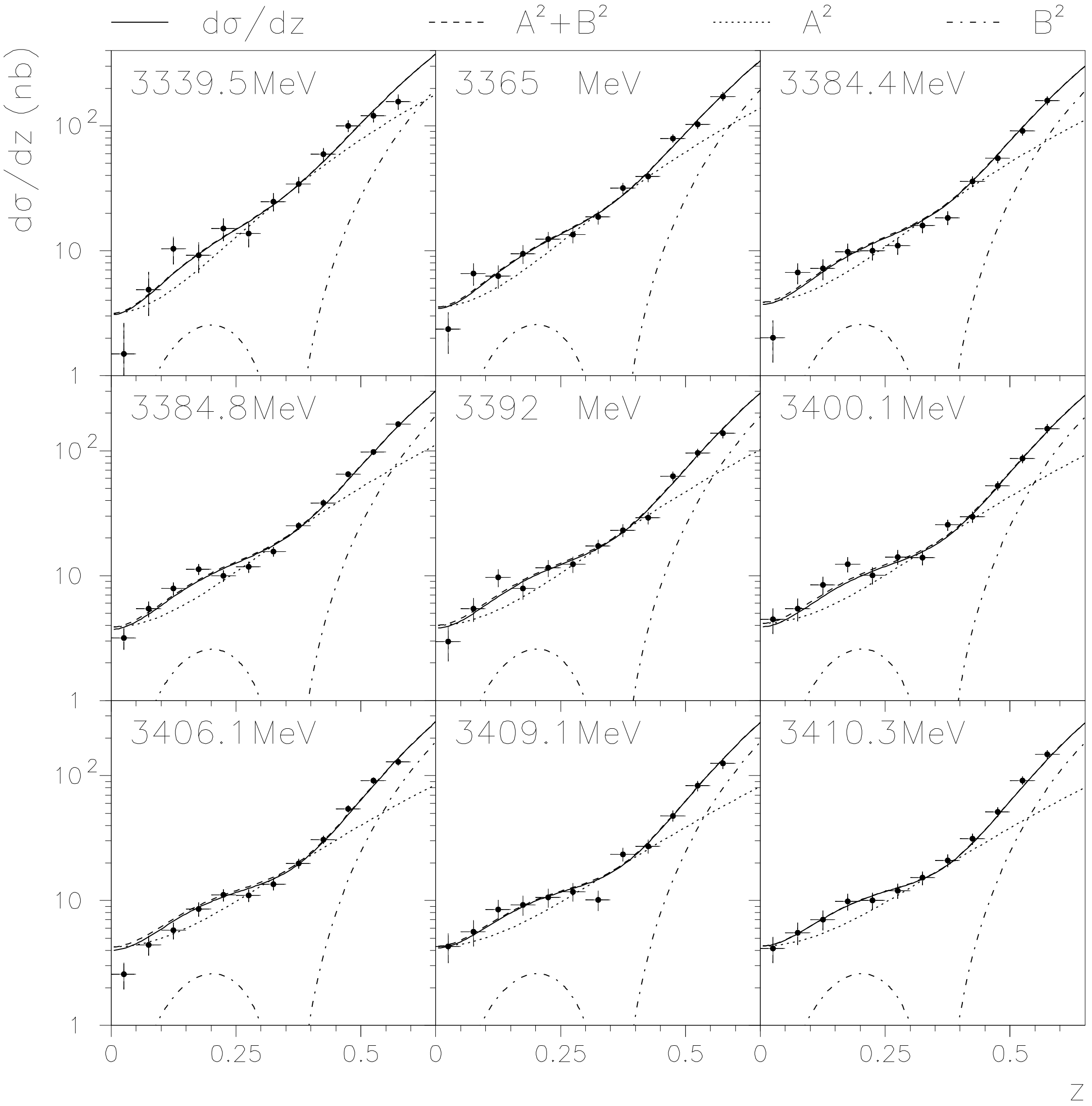

Figure E.1: The measured $\bar{p}p \to \eta\eta$ differential cross section (logarithmic scale) plotted versus z at the E_{cm} indicated in each plot. The fit of Equations 3.19 , 3.20 and 3.21 and its components are also shown.

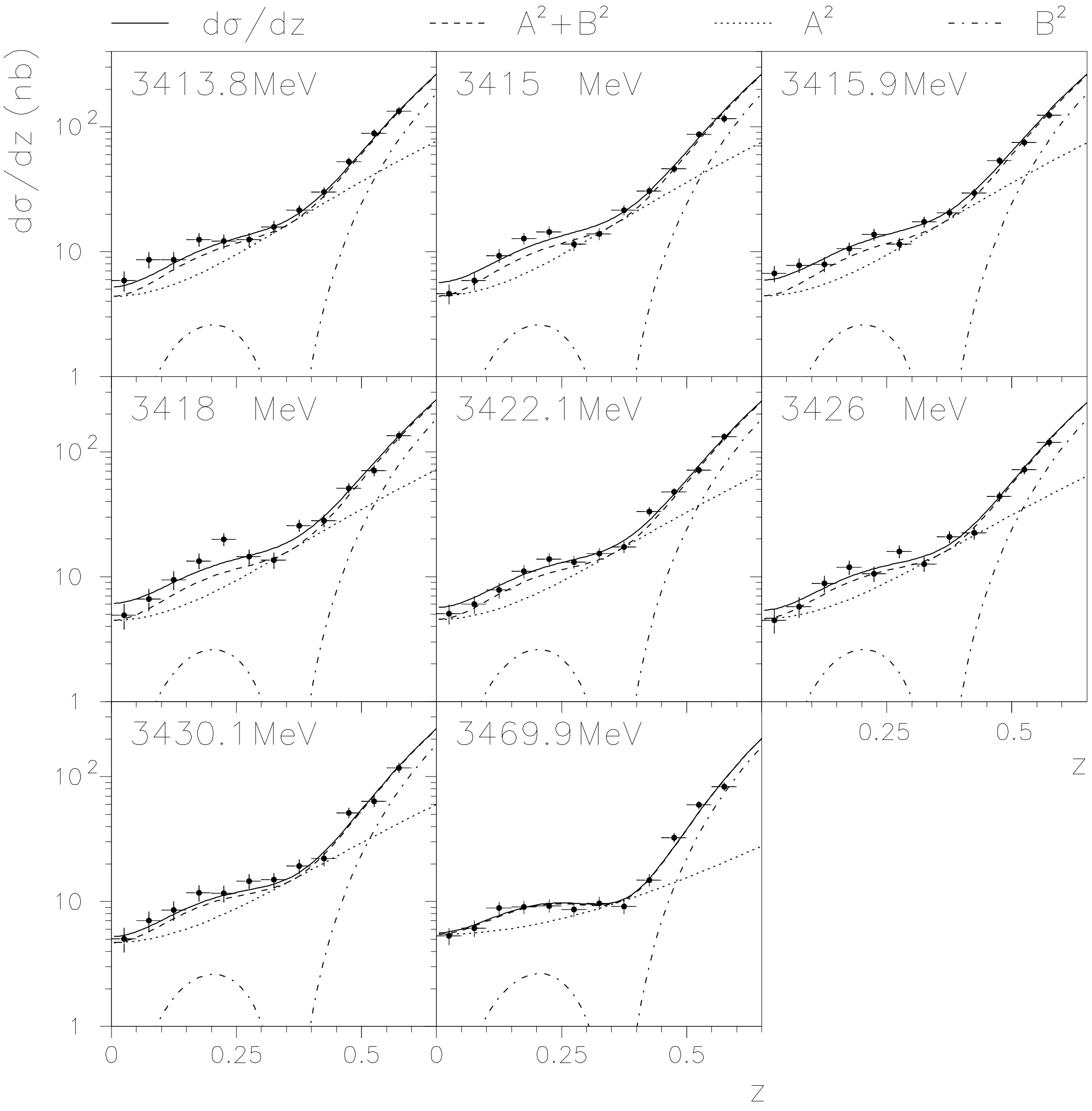

Figure E.2: As Figure E.1, at the remaining energies.

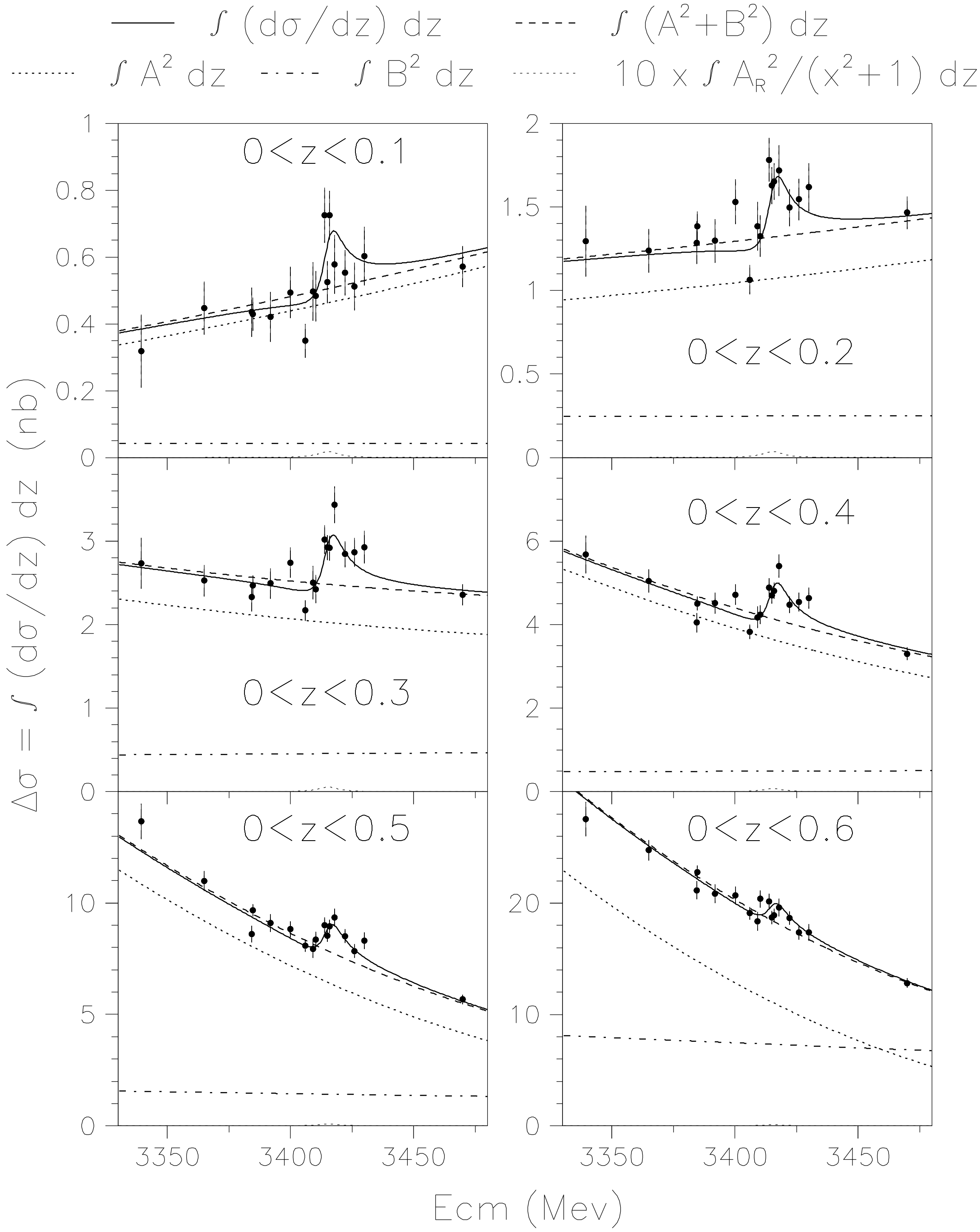

Figure E.3: The measured $\bar{p}p \to \eta\eta$ cross section integrated over $0 < z < z_{max}$ plotted versus E_{cm} . The fit of Equations 3.19 , 3.20 and 3.21 and its components are also shown.

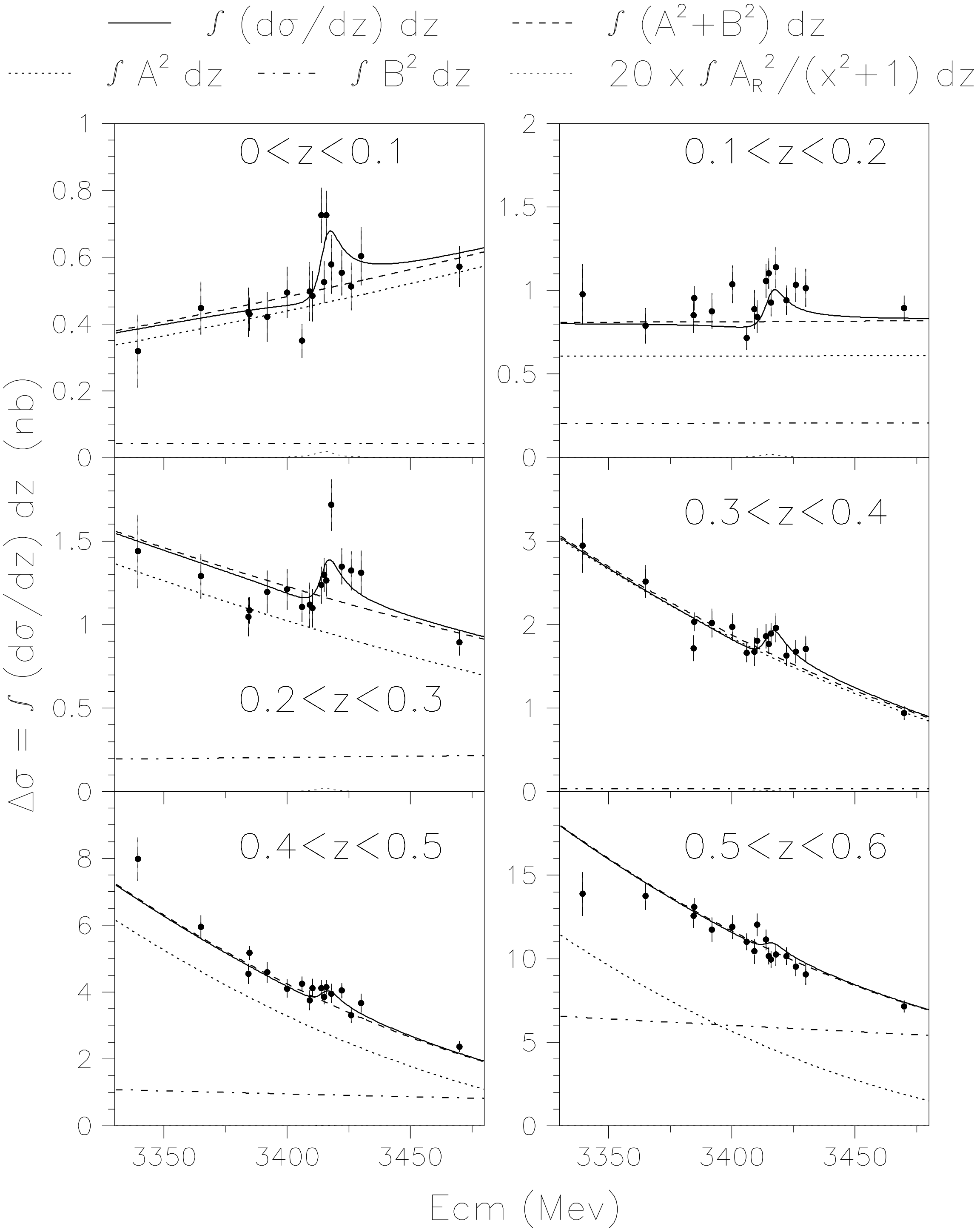

Figure E.4: The measured $\bar{p}p \to \eta\eta$ cross section integrated over $z_{min} < z < z_{max}$ plotted versus E_{cm}. The fit of Equations 3.19 , 3.20 and 3.21 and its components are also shown.

E.2 The Background versus E_{cm}

Figure E.5 shows the amount of cross section due to background events that simulate the $\eta\eta$ final state (as estimated with the procedure of Section 5.6) plotted versus the energy in the center of mass. The considered angular region ($0 < z < 0.35$) is the one used in Section 5.10.3 to extract the resonance amplitude. For comparison, the $\eta\eta$ cross section is also plotted, along with the cross section that would appear without subtracting the background.

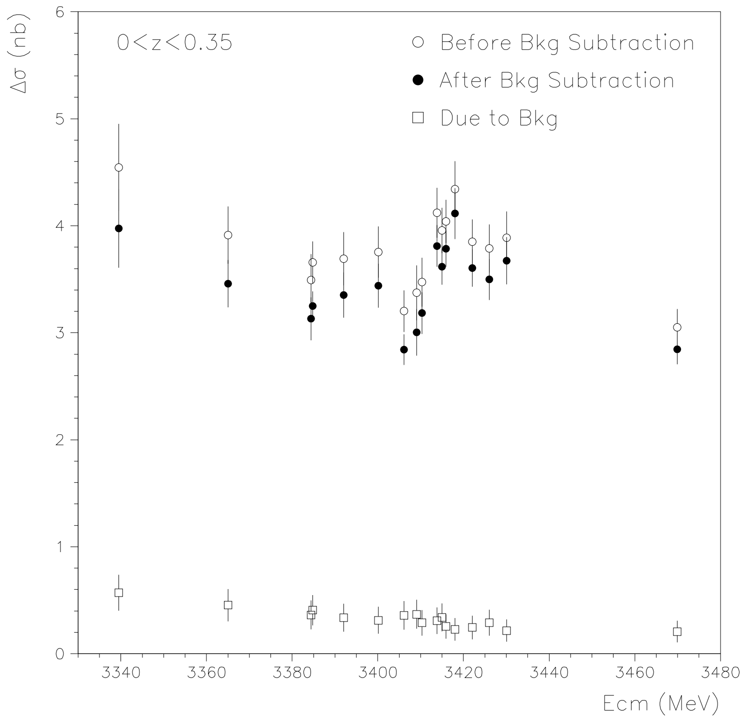

Figure E.5: The effect of the background subtraction on the $\eta\eta$ cross section $\Delta\sigma$ integrated over the angular region ($0 < z < 0.35$) used to extract the resonance amplitude. The amount of cross section due to background events simulating the $\eta\eta$ final state is at the level of $\sim 8.5\%$ and lies at the bottom of the plot. The $\eta\eta$ cross section is also shown, along with the cross section that would result without performing the subtraction of the background.

Appendix F

The $\bar{p}p \to \pi^0\pi^0$ Cross Section Tables

The following list of tables reproduce the measured $\bar{p}p \to \pi^0\pi^0$ cross section (and the z-dependent quantities used to calculate it) at every energy point of the χ_{c0} sample. In particular: the z value of the center of the bin, the $\bar{p}p \to \pi^0\pi^0$ differential cross section ($\frac{d\sigma}{dz}$), the total number of events (N_{tot}) passing the $\pi^0\pi^0$ selection, the estimated number of instrumental background events (N_{bkg}), the number of $\pi^0\pi^0$ events ($N_{\pi^0\pi^0} \equiv N_{tot} - N_{bkg}$, with uncertainty conservatively taken as $\sqrt{N_{tot}}$), and the product of the acceptance and efficiency ($a \times \epsilon$) corrected for polar angle resolution and pileup (the uncertainty on $a \times \epsilon$ is determined by the number of Random Gate events available).

$\bar{p}p \to \pi^0\pi^0$ at $E_{cm} = 3339.5$ MeV ($\mathcal{L} = 629.4\ 10^{31}\mathrm{s}^{-1}\mathrm{cm}^{-2}$)					
z	$\frac{d\sigma}{dz}$ (nb)	N_{tot} (events)	N_{bkg} (events)	$N_{\pi^0\pi^0}$ (events)	$a \times \epsilon$
0.0125	24.7 ± 2.1	154 ± 12	6.2 ± 2.5	148 ± 12	0.4362 ± 0.0086
0.0375	26.5 ± 2.2	163 ± 13	6.2 ± 2.5	157 ± 13	0.4311 ± 0.0086
0.0625	25.0 ± 2.2	154 ± 12	6.2 ± 2.5	148 ± 12	0.4303 ± 0.0085
0.0875	25.2 ± 2.0	173 ± 13	6.0 ± 2.5	167 ± 13	0.4820 ± 0.0090
0.1125	22.5 ± 1.9	156 ± 12	5.8 ± 2.4	150 ± 12	0.4870 ± 0.0091
0.1375	21.0 ± 1.9	138 ± 12	5.5 ± 2.3	133 ± 12	0.4603 ± 0.0089
0.1625	16.8 ± 1.7	112 ± 11	5.1 ± 2.3	107 ± 11	0.4642 ± 0.0089
0.1875	19.3 ± 1.7	138 ± 12	4.7 ± 2.2	133 ± 12	0.5044 ± 0.0093
0.2125	19.2 ± 1.7	138 ± 12	4.4 ± 2.1	134 ± 12	0.5073 ± 0.0093
0.2375	25.9 ± 2.1	169 ± 13	4.1 ± 2.0	165 ± 13	0.4638 ± 0.0090
0.2625	28.3 ± 2.2	190 ± 14	4.0 ± 2.0	186 ± 14	0.4782 ± 0.0091
0.2875	25.0 ± 1.9	188 ± 14	4.2 ± 2.0	184 ± 14	0.5349 ± 0.0095
0.3125	34.2 ± 2.3	243 ± 16	4.6 ± 2.1	238 ± 16	0.5075 ± 0.0093
0.3375	35.9 ± 2.4	248 ± 16	5.3 ± 2.3	243 ± 16	0.4919 ± 0.0092
0.3625	38.0 ± 2.5	272 ± 16	6.4 ± 2.5	266 ± 16	0.5090 ± 0.0094
0.3875	53.5 ± 2.9	395 ± 20	7.9 ± 2.8	387 ± 20	0.5269 ± 0.0096
0.4125	64.7 ± 3.3	452 ± 21	9.7 ± 3.1	442 ± 21	0.4982 ± 0.0092
0.4375	78.9 ± 3.7	556 ± 24	11.7 ± 3.4	544 ± 24	0.5024 ± 0.0093
0.4625	105.6 ± 4.4	766 ± 28	13.8 ± 3.7	752 ± 28	0.5191 ± 0.0096
0.4875	140.4 ± 5.4	950 ± 31	15.8 ± 4.0	934 ± 31	0.4846 ± 0.0092
0.5125	188.0 ± 6.6	1192 ± 35	17.4 ± 4.2	1175 ± 35	0.4552 ± 0.0089
0.5375	227.3 ± 7.6	1418 ± 38	18.1 ± 4.3	1400 ± 38	0.4487 ± 0.0088
0.5625	276.8 ± 9.6	1429 ± 38	17.5 ± 4.2	1412 ± 38	0.3715 ± 0.0080
0.5875	340.0 ± 13.2	1206 ± 35	14.9 ± 3.9	1191 ± 35	0.2552 ± 0.0065

Table F.1: This and the following tables: the cross section $\bar{p}p \to \pi^0\pi^0$.

$\bar{p}p \to \pi^0\pi^0$ at $E_{cm} = 3365.0$ MeV ($\mathcal{L} = 1423.7\ 10^{31}\mathrm{s}^{-1}\mathrm{cm}^{-2}$)					
z	$\frac{d\sigma}{dz}$ (nb)	N_{tot} (events)	N_{bkg} (events)	$N_{\pi^0\pi^0}$ (events)	$a \times \epsilon$
0.0125	30.6 ± 1.5	440 ± 21	10.0 ± 3.2	430 ± 21	0.4506 ± 0.0055
0.0375	29.7 ± 1.5	415 ± 20	10.3 ± 3.2	405 ± 20	0.4381 ± 0.0054
0.0625	27.9 ± 1.5	408 ± 20	10.6 ± 3.3	397 ± 20	0.4578 ± 0.0055
0.0875	24.0 ± 1.3	370 ± 19	10.9 ± 3.3	359 ± 19	0.4806 ± 0.0057
0.1125	23.1 ± 1.3	357 ± 19	11.0 ± 3.3	346 ± 19	0.4807 ± 0.0057
0.1375	26.1 ± 1.4	389 ± 20	10.8 ± 3.3	378 ± 20	0.4651 ± 0.0056
0.1625	21.8 ± 1.2	345 ± 19	10.4 ± 3.2	335 ± 19	0.4920 ± 0.0058
0.1875	23.1 ± 1.2	382 ± 20	9.9 ± 3.1	372 ± 20	0.5175 ± 0.0059
0.2125	24.0 ± 1.3	389 ± 20	9.3 ± 3.0	380 ± 20	0.5078 ± 0.0059
0.2375	22.7 ± 1.2	367 ± 19	8.7 ± 3.0	358 ± 19	0.5067 ± 0.0059
0.2625	23.3 ± 1.3	380 ± 19	8.4 ± 2.9	372 ± 19	0.5131 ± 0.0059
0.2875	25.3 ± 1.3	434 ± 21	8.4 ± 2.9	426 ± 21	0.5407 ± 0.0061
0.3125	26.6 ± 1.3	442 ± 21	9.0 ± 3.0	433 ± 21	0.5238 ± 0.0060
0.3375	32.0 ± 1.5	519 ± 23	10.3 ± 3.2	509 ± 23	0.5113 ± 0.0059
0.3625	38.6 ± 1.6	658 ± 26	12.4 ± 3.5	646 ± 26	0.5366 ± 0.0060
0.3875	46.2 ± 1.8	794 ± 28	15.4 ± 3.9	779 ± 28	0.5413 ± 0.0061
0.4125	56.9 ± 2.0	931 ± 31	19.1 ± 4.4	912 ± 31	0.5148 ± 0.0059
0.4375	74.1 ± 2.3	1233 ± 35	23.6 ± 4.9	1209 ± 35	0.5240 ± 0.0059
0.4625	85.8 ± 2.5	1449 ± 38	28.3 ± 5.3	1421 ± 38	0.5317 ± 0.0060
0.4875	120.6 ± 3.2	1897 ± 44	33.0 ± 5.7	1864 ± 44	0.4964 ± 0.0058
0.5125	154.9 ± 3.7	2422 ± 49	36.9 ± 6.1	2385 ± 49	0.4945 ± 0.0058
0.5375	185.6 ± 4.2	2809 ± 53	39.1 ± 6.3	2770 ± 53	0.4793 ± 0.0057
0.5625	241.1 ± 5.4	3126 ± 56	38.3 ± 6.2	3088 ± 56	0.4114 ± 0.0053
0.5875	279.4 ± 6.8	2730 ± 52	33.1 ± 5.8	2697 ± 52	0.3100 ± 0.0045

$\bar{p}p \to \pi^0\pi^0$ at $E_{cm} = 3384.4$ MeV ($\mathcal{L} = 1521.6\ 10^{31}\mathrm{s}^{-1}\mathrm{cm}^{-2}$)					
z	$\frac{d\sigma}{dz}$ (nb)	N_{tot} (events)	N_{bkg} (events)	$N_{\pi^0\pi^0}$ (events)	$a \times \epsilon$
0.0125	26.5 ± 1.4	403 ± 20	11.6 ± 3.4	391 ± 20	0.4443 ± 0.0053
0.0375	28.2 ± 1.4	427 ± 21	11.9 ± 3.4	415 ± 21	0.4420 ± 0.0053
0.0625	28.7 ± 1.4	450 ± 21	12.2 ± 3.5	438 ± 21	0.4587 ± 0.0054
0.0875	26.7 ± 1.4	432 ± 21	12.4 ± 3.5	420 ± 21	0.4734 ± 0.0055
0.1125	23.7 ± 1.3	379 ± 19	12.3 ± 3.5	367 ± 19	0.4653 ± 0.0054
0.1375	25.5 ± 1.3	411 ± 20	11.9 ± 3.5	399 ± 20	0.4714 ± 0.0055
0.1625	23.0 ± 1.2	388 ± 20	11.2 ± 3.4	377 ± 20	0.4924 ± 0.0056
0.1875	20.2 ± 1.1	351 ± 19	10.3 ± 3.2	341 ± 19	0.5070 ± 0.0057
0.2125	21.7 ± 1.2	364 ± 19	9.2 ± 3.0	355 ± 19	0.4925 ± 0.0056
0.2375	20.4 ± 1.1	348 ± 19	8.1 ± 2.9	340 ± 19	0.4998 ± 0.0056
0.2625	21.8 ± 1.2	377 ± 19	7.3 ± 2.7	370 ± 19	0.5093 ± 0.0056
0.2875	21.3 ± 1.1	383 ± 20	6.8 ± 2.6	376 ± 20	0.5299 ± 0.0058
0.3125	24.2 ± 1.2	417 ± 20	7.0 ± 2.6	410 ± 20	0.5090 ± 0.0057
0.3375	29.5 ± 1.4	502 ± 22	8.0 ± 2.8	494 ± 22	0.5033 ± 0.0057
0.3625	34.3 ± 1.4	629 ± 25	9.9 ± 3.1	619 ± 25	0.5432 ± 0.0059
0.3875	42.9 ± 1.7	757 ± 28	12.8 ± 3.6	744 ± 28	0.5215 ± 0.0058
0.4125	49.9 ± 1.8	875 ± 30	16.8 ± 4.1	858 ± 30	0.5175 ± 0.0057
0.4375	61.9 ± 2.0	1121 ± 33	21.6 ± 4.6	1099 ± 33	0.5342 ± 0.0058
0.4625	79.3 ± 2.3	1433 ± 38	26.9 ± 5.2	1406 ± 38	0.5332 ± 0.0058
0.4875	108.8 ± 2.9	1852 ± 43	32.3 ± 5.7	1820 ± 43	0.5029 ± 0.0057
0.5125	134.9 ± 3.3	2292 ± 48	36.9 ± 6.1	2255 ± 48	0.5026 ± 0.0056
0.5375	167.0 ± 3.9	2643 ± 51	39.8 ± 6.3	2603 ± 51	0.4687 ± 0.0055
0.5625	202.9 ± 4.6	2835 ± 53	39.6 ± 6.3	2795 ± 53	0.4143 ± 0.0051
0.5875	239.2 ± 5.8	2627 ± 51	34.6 ± 5.9	2592 ± 51	0.3259 ± 0.0045

$\bar{p}p \to \pi^0\pi^0$ at $E_{cm} = 3384.8$ MeV ($\mathcal{L} = 3370.4\ 10^{31}\mathrm{s}^{-1}\mathrm{cm}^{-2}$)					
z	$\frac{d\sigma}{dz}$ (nb)	N_{tot} (events)	N_{bkg} (events)	$N_{\pi^0\pi^0}$ (events)	$a \times \epsilon$
0.0125	30.7 ± 1.0	1052 ± 32	32.3 ± 5.7	1020 ± 32	0.4501 ± 0.0036
0.0375	29.2 ± 1.0	989 ± 31	32.8 ± 5.7	956 ± 31	0.4440 ± 0.0035
0.0625	28.4 ± 0.9	1015 ± 32	33.3 ± 5.8	982 ± 32	0.4695 ± 0.0037
0.0875	27.7 ± 0.9	998 ± 32	33.6 ± 5.8	964 ± 32	0.4724 ± 0.0037
0.1125	28.1 ± 0.9	1012 ± 32	33.3 ± 5.8	979 ± 32	0.4727 ± 0.0037
0.1375	25.1 ± 0.9	909 ± 30	32.5 ± 5.7	876 ± 30	0.4740 ± 0.0037
0.1625	23.8 ± 0.8	901 ± 30	31.2 ± 5.6	870 ± 30	0.4960 ± 0.0038
0.1875	22.8 ± 0.8	892 ± 30	29.4 ± 5.4	863 ± 30	0.5122 ± 0.0038
0.2125	21.6 ± 0.8	828 ± 29	27.4 ± 5.2	801 ± 29	0.5040 ± 0.0038
0.2375	20.4 ± 0.8	776 ± 28	25.4 ± 5.0	751 ± 28	0.4997 ± 0.0038
0.2625	19.2 ± 0.7	774 ± 28	23.9 ± 4.9	750 ± 28	0.5288 ± 0.0039
0.2875	21.9 ± 0.8	878 ± 30	23.1 ± 4.8	855 ± 30	0.5288 ± 0.0039
0.3125	24.8 ± 0.8	971 ± 31	23.5 ± 4.8	948 ± 31	0.5177 ± 0.0038
0.3375	28.7 ± 0.9	1118 ± 33	25.4 ± 5.0	1093 ± 33	0.5164 ± 0.0038
0.3625	35.8 ± 1.0	1481 ± 38	29.1 ± 5.4	1452 ± 38	0.5502 ± 0.0040
0.3875	40.4 ± 1.1	1625 ± 40	34.6 ± 5.9	1590 ± 40	0.5334 ± 0.0039
0.4125	51.6 ± 1.2	2040 ± 45	42.1 ± 6.5	1998 ± 45	0.5253 ± 0.0039
0.4375	63.5 ± 1.4	2573 ± 51	51.1 ± 7.2	2522 ± 51	0.5390 ± 0.0039
0.4625	84.3 ± 1.6	3353 ± 58	61.2 ± 7.8	3292 ± 58	0.5296 ± 0.0039
0.4875	107.8 ± 1.9	4108 ± 64	71.5 ± 8.5	4037 ± 64	0.5080 ± 0.0038
0.5125	137.1 ± 2.2	5138 ± 72	80.4 ± 9.0	5058 ± 72	0.5004 ± 0.0038
0.5375	165.3 ± 2.6	5934 ± 77	86.3 ± 9.3	5848 ± 77	0.4798 ± 0.0037
0.5625	207.6 ± 3.1	6595 ± 81	86.6 ± 9.3	6508 ± 81	0.4253 ± 0.0035
0.5875	254.7 ± 4.0	6317 ± 79	78.2 ± 8.8	6239 ± 79	0.3323 ± 0.0031

$\bar{p}p \to \pi^0\pi^0$ at $E_{cm} = 3392.0$ MeV ($\mathcal{L} = 1431.1\ 10^{31}\mathrm{s}^{-1}\mathrm{cm}^{-2}$)					
z	$\frac{d\sigma}{dz}$ (nb)	N_{tot} (events)	N_{bkg} (events)	$N_{\pi^0\pi^0}$ (events)	$a \times \epsilon$
0.0125	28.4 ± 1.5	412 ± 20	8.9 ± 3.0	403 ± 20	0.4527 ± 0.0056
0.0375	28.3 ± 1.5	400 ± 20	9.1 ± 3.0	391 ± 20	0.4410 ± 0.0056
0.0625	29.5 ± 1.5	436 ± 21	9.4 ± 3.1	427 ± 21	0.4606 ± 0.0057
0.0875	27.3 ± 1.4	412 ± 20	9.7 ± 3.1	402 ± 20	0.4690 ± 0.0057
0.1125	27.5 ± 1.4	409 ± 20	9.7 ± 3.1	399 ± 20	0.4630 ± 0.0057
0.1375	24.2 ± 1.3	367 ± 19	9.6 ± 3.1	357 ± 19	0.4700 ± 0.0057
0.1625	22.7 ± 1.3	363 ± 19	9.1 ± 3.0	354 ± 19	0.4963 ± 0.0059
0.1875	21.3 ± 1.2	339 ± 18	8.5 ± 2.9	330 ± 18	0.4947 ± 0.0059
0.2125	21.6 ± 1.2	339 ± 18	7.8 ± 2.8	331 ± 18	0.4885 ± 0.0059
0.2375	18.6 ± 1.1	298 ± 17	7.2 ± 2.7	291 ± 17	0.4974 ± 0.0060
0.2625	21.2 ± 1.2	352 ± 19	6.7 ± 2.6	345 ± 19	0.5201 ± 0.0061
0.2875	21.3 ± 1.2	354 ± 19	6.6 ± 2.6	347 ± 19	0.5208 ± 0.0061
0.3125	26.3 ± 1.3	426 ± 21	7.0 ± 2.6	419 ± 21	0.5084 ± 0.0060
0.3375	26.5 ± 1.3	433 ± 21	8.1 ± 2.8	425 ± 21	0.5111 ± 0.0060
0.3625	33.7 ± 1.5	581 ± 24	9.9 ± 3.1	571 ± 24	0.5406 ± 0.0062
0.3875	40.5 ± 1.7	681 ± 26	12.6 ± 3.5	668 ± 26	0.5262 ± 0.0061
0.4125	52.8 ± 1.9	868 ± 29	16.1 ± 4.0	852 ± 29	0.5139 ± 0.0060
0.4375	61.7 ± 2.1	1063 ± 33	20.3 ± 4.5	1043 ± 33	0.5383 ± 0.0062
0.4625	74.4 ± 2.3	1255 ± 35	24.9 ± 5.0	1230 ± 35	0.5268 ± 0.0062
0.4875	98.9 ± 2.8	1602 ± 40	29.6 ± 5.4	1572 ± 40	0.5070 ± 0.0060
0.5125	119.3 ± 3.1	1947 ± 44	33.7 ± 5.8	1913 ± 44	0.5111 ± 0.0060
0.5375	156.4 ± 3.8	2399 ± 49	36.3 ± 6.0	2363 ± 49	0.4816 ± 0.0059
0.5625	195.6 ± 4.7	2571 ± 51	36.3 ± 6.0	2535 ± 51	0.4131 ± 0.0054
0.5875	246.4 ± 6.1	2573 ± 51	32.4 ± 5.7	2541 ± 51	0.3287 ± 0.0048

$\bar{p}p \to \pi^0\pi^0$ at $E_{cm} = 3400.1$ MeV ($\mathcal{L} = 1482.8\ 10^{31}\mathrm{s}^{-1}\mathrm{cm}^{-2}$)					
z	$\frac{d\sigma}{dz}$ (nb)	N_{tot} (events)	N_{bkg} (events)	$N_{\pi^0\pi^0}$ (events)	$a \times \epsilon$
0.0125	30.4 ± 1.5	474 ± 22	12.9 ± 3.6	461 ± 22	0.4685 ± 0.0050
0.0375	34.3 ± 1.6	530 ± 23	13.1 ± 3.6	517 ± 23	0.4656 ± 0.0050
0.0625	29.9 ± 1.4	489 ± 22	13.4 ± 3.7	476 ± 22	0.4910 ± 0.0051
0.0875	29.1 ± 1.4	468 ± 22	13.5 ± 3.7	455 ± 22	0.4831 ± 0.0051
0.1125	26.9 ± 1.4	434 ± 21	13.3 ± 3.7	421 ± 21	0.4837 ± 0.0051
0.1375	24.2 ± 1.3	400 ± 20	12.9 ± 3.6	387 ± 20	0.4946 ± 0.0052
0.1625	24.1 ± 1.2	415 ± 20	12.3 ± 3.5	403 ± 20	0.5174 ± 0.0053
0.1875	21.0 ± 1.2	365 ± 19	11.4 ± 3.4	354 ± 19	0.5195 ± 0.0053
0.2125	21.8 ± 1.2	369 ± 19	10.4 ± 3.2	359 ± 19	0.5079 ± 0.0052
0.2375	21.6 ± 1.2	379 ± 19	9.4 ± 3.1	370 ± 19	0.5300 ± 0.0054
0.2625	20.3 ± 1.1	370 ± 19	8.6 ± 2.9	361 ± 19	0.5515 ± 0.0055
0.2875	20.7 ± 1.1	369 ± 19	8.1 ± 2.9	361 ± 19	0.5379 ± 0.0054
0.3125	23.0 ± 1.2	412 ± 20	8.2 ± 2.9	404 ± 20	0.5416 ± 0.0054
0.3375	25.6 ± 1.2	458 ± 21	9.0 ± 3.0	449 ± 21	0.5426 ± 0.0054
0.3625	32.0 ± 1.4	594 ± 24	10.7 ± 3.3	583 ± 24	0.5640 ± 0.0055
0.3875	39.8 ± 1.6	721 ± 27	13.2 ± 3.6	708 ± 27	0.5497 ± 0.0054
0.4125	52.2 ± 1.8	927 ± 30	16.5 ± 4.1	910 ± 30	0.5391 ± 0.0054
0.4375	59.0 ± 1.9	1115 ± 33	20.7 ± 4.5	1094 ± 33	0.5732 ± 0.0056
0.4625	76.6 ± 2.2	1376 ± 37	25.2 ± 5.0	1351 ± 37	0.5453 ± 0.0054
0.4875	100.8 ± 2.7	1762 ± 42	29.9 ± 5.5	1732 ± 42	0.5311 ± 0.0054
0.5125	124.6 ± 3.0	2168 ± 47	33.9 ± 5.8	2134 ± 47	0.5295 ± 0.0054
0.5375	153.7 ± 3.5	2492 ± 50	36.5 ± 6.0	2456 ± 50	0.4940 ± 0.0052
0.5625	185.0 ± 4.1	2743 ± 52	36.4 ± 6.0	2707 ± 52	0.4524 ± 0.0049
0.5875	226.1 ± 5.2	2690 ± 52	32.2 ± 5.7	2658 ± 52	0.3634 ± 0.0044

$\bar{p}p \to \pi^0\pi^0$ at $E_{cm} = 3406.1$ MeV ($\mathcal{L} = 2680.5\ 10^{31}\mathrm{s}^{-1}\mathrm{cm}^{-2}$)					
z	$\frac{d\sigma}{dz}$ (nb)	N_{tot} (events)	N_{bkg} (events)	$N_{\pi^0\pi^0}$ (events)	$a \times \epsilon$
0.0125	30.2 ± 1.1	818 ± 29	24.3 ± 4.9	794 ± 29	0.4467 ± 0.0040
0.0375	32.5 ± 1.2	884 ± 30	24.7 ± 5.0	859 ± 30	0.4491 ± 0.0040
0.0625	31.1 ± 1.1	905 ± 30	25.1 ± 5.0	880 ± 30	0.4804 ± 0.0042
0.0875	31.0 ± 1.1	881 ± 30	25.2 ± 5.0	856 ± 30	0.4688 ± 0.0041
0.1125	28.3 ± 1.1	801 ± 28	24.9 ± 5.0	776 ± 28	0.4661 ± 0.0041
0.1375	26.6 ± 1.0	780 ± 28	24.0 ± 4.9	756 ± 28	0.4825 ± 0.0042
0.1625	23.9 ± 0.9	734 ± 27	22.6 ± 4.7	711 ± 27	0.5068 ± 0.0043
0.1875	23.8 ± 0.9	717 ± 27	20.6 ± 4.5	696 ± 27	0.4970 ± 0.0042
0.2125	22.2 ± 0.9	670 ± 26	18.5 ± 4.3	652 ± 26	0.4990 ± 0.0042
0.2375	20.2 ± 0.8	622 ± 25	16.3 ± 4.0	606 ± 25	0.5102 ± 0.0043
0.2625	22.7 ± 0.9	732 ± 27	14.4 ± 3.8	718 ± 27	0.5372 ± 0.0044
0.2875	20.7 ± 0.8	644 ± 25	13.2 ± 3.6	631 ± 25	0.5193 ± 0.0043
0.3125	23.7 ± 0.9	736 ± 27	13.0 ± 3.6	723 ± 27	0.5184 ± 0.0043
0.3375	27.1 ± 1.0	860 ± 29	14.1 ± 3.7	846 ± 29	0.5317 ± 0.0044
0.3625	31.0 ± 1.0	1006 ± 32	16.7 ± 4.1	989 ± 32	0.5428 ± 0.0044
0.3875	38.0 ± 1.2	1191 ± 35	21.1 ± 4.6	1170 ± 35	0.5241 ± 0.0044
0.4125	48.5 ± 1.3	1537 ± 39	27.3 ± 5.2	1510 ± 39	0.5294 ± 0.0044
0.4375	57.9 ± 1.4	1916 ± 44	34.9 ± 5.9	1881 ± 44	0.5528 ± 0.0045
0.4625	73.7 ± 1.7	2325 ± 48	43.6 ± 6.6	2281 ± 48	0.5261 ± 0.0044
0.4875	94.6 ± 2.0	2884 ± 54	52.5 ± 7.2	2831 ± 54	0.5088 ± 0.0043
0.5125	114.0 ± 2.2	3521 ± 59	60.6 ± 7.8	3460 ± 59	0.5161 ± 0.0043
0.5375	144.4 ± 2.6	4160 ± 64	66.2 ± 8.1	4094 ± 64	0.4821 ± 0.0042
0.5625	177.0 ± 3.1	4592 ± 68	67.1 ± 8.2	4525 ± 68	0.4347 ± 0.0040
0.5875	213.3 ± 3.9	4498 ± 67	60.6 ± 7.8	4437 ± 67	0.3537 ± 0.0036

$\bar{p}p \to \pi^0\pi^0$ at $E_{cm} = 3409.1$ MeV ($\mathcal{L} = 1134.5\ 10^{31}\mathrm{s}^{-1}\mathrm{cm}^{-2}$)					
z	$\frac{d\sigma}{dz}$ (nb)	N_{tot} (events)	N_{bkg} (events)	$N_{\pi^0\pi^0}$ (events)	$a \times \epsilon$
0.0125	32.4 ± 1.7	395 ± 20	10.6 ± 3.3	384 ± 20	0.4788 ± 0.0053
0.0375	32.7 ± 1.7	405 ± 20	10.6 ± 3.3	394 ± 20	0.4857 ± 0.0053
0.0625	31.3 ± 1.6	407 ± 20	10.5 ± 3.2	396 ± 20	0.5099 ± 0.0055
0.0875	29.4 ± 1.6	378 ± 19	10.2 ± 3.2	368 ± 19	0.5034 ± 0.0055
0.1125	30.5 ± 1.6	384 ± 20	9.8 ± 3.1	374 ± 20	0.4941 ± 0.0054
0.1375	25.1 ± 1.5	323 ± 18	9.1 ± 3.0	314 ± 18	0.5035 ± 0.0054
0.1625	26.7 ± 1.5	361 ± 19	8.2 ± 2.9	353 ± 19	0.5323 ± 0.0056
0.1875	22.2 ± 1.3	301 ± 17	7.3 ± 2.7	294 ± 17	0.5331 ± 0.0056
0.2125	24.1 ± 1.4	325 ± 18	6.4 ± 2.5	319 ± 18	0.5333 ± 0.0056
0.2375	21.5 ± 1.3	295 ± 17	5.6 ± 2.4	289 ± 17	0.5419 ± 0.0057
0.2625	20.4 ± 1.2	293 ± 17	5.0 ± 2.2	288 ± 17	0.5690 ± 0.0058
0.2875	20.4 ± 1.2	284 ± 17	4.8 ± 2.2	279 ± 17	0.5521 ± 0.0057
0.3125	25.8 ± 1.4	359 ± 19	5.1 ± 2.2	354 ± 19	0.5520 ± 0.0057
0.3375	27.3 ± 1.4	392 ± 20	6.0 ± 2.4	386 ± 20	0.5691 ± 0.0058
0.3625	28.0 ± 1.4	418 ± 20	7.5 ± 2.7	410 ± 20	0.5917 ± 0.0059
0.3875	37.2 ± 1.7	530 ± 23	9.9 ± 3.1	520 ± 23	0.5629 ± 0.0058
0.4125	48.1 ± 1.9	682 ± 26	12.9 ± 3.6	669 ± 26	0.5606 ± 0.0058
0.4375	60.4 ± 2.2	886 ± 30	16.4 ± 4.1	870 ± 30	0.5803 ± 0.0059
0.4625	73.8 ± 2.5	1042 ± 32	20.4 ± 4.5	1022 ± 32	0.5582 ± 0.0058
0.4875	91.4 ± 2.8	1263 ± 36	24.3 ± 4.9	1239 ± 36	0.5464 ± 0.0057
0.5125	112.7 ± 3.1	1589 ± 40	27.8 ± 5.3	1561 ± 40	0.5582 ± 0.0057
0.5375	143.0 ± 3.7	1879 ± 43	30.2 ± 5.5	1849 ± 43	0.5209 ± 0.0055
0.5625	172.3 ± 4.4	2026 ± 45	30.6 ± 5.5	1995 ± 45	0.4668 ± 0.0053
0.5875	205.0 ± 5.3	2019 ± 45	27.8 ± 5.3	1991 ± 45	0.3915 ± 0.0048

$\bar{p}p \to \pi^0\pi^0$ at $E_{cm} = 3410.3$ MeV ($\mathcal{L} = 1596.6\ 10^{31}\mathrm{s}^{-1}\mathrm{cm}^{-2}$)					
z	$\frac{d\sigma}{dz}$ (nb)	N_{tot} (events)	N_{bkg} (events)	$N_{\pi^0\pi^0}$ (events)	$a \times \epsilon$
0.0125	34.0 ± 1.5	538 ± 23	8.9 ± 3.0	529 ± 23	0.4448 ± 0.0052
0.0375	36.3 ± 1.6	581 ± 24	9.6 ± 3.1	571 ± 24	0.4495 ± 0.0052
0.0625	32.7 ± 1.5	555 ± 24	10.6 ± 3.2	544 ± 24	0.4763 ± 0.0054
0.0875	33.5 ± 1.5	545 ± 23	11.6 ± 3.4	533 ± 23	0.4555 ± 0.0053
0.1125	28.9 ± 1.4	479 ± 22	12.4 ± 3.5	467 ± 22	0.4613 ± 0.0053
0.1375	29.3 ± 1.4	496 ± 22	12.9 ± 3.6	483 ± 22	0.4715 ± 0.0054
0.1625	25.3 ± 1.3	455 ± 21	13.1 ± 3.6	442 ± 21	0.4990 ± 0.0055
0.1875	23.4 ± 1.2	419 ± 20	12.8 ± 3.6	406 ± 20	0.4961 ± 0.0055
0.2125	20.9 ± 1.1	372 ± 19	12.2 ± 3.5	360 ± 19	0.4916 ± 0.0055
0.2375	21.3 ± 1.1	387 ± 20	11.5 ± 3.4	376 ± 20	0.5029 ± 0.0056
0.2625	20.0 ± 1.1	384 ± 20	10.6 ± 3.3	373 ± 20	0.5330 ± 0.0057
0.2875	19.8 ± 1.1	364 ± 19	10.0 ± 3.2	354 ± 19	0.5103 ± 0.0056
0.3125	25.8 ± 1.3	468 ± 22	9.8 ± 3.1	458 ± 22	0.5068 ± 0.0056
0.3375	28.3 ± 1.3	534 ± 23	10.1 ± 3.2	524 ± 23	0.5291 ± 0.0057
0.3625	30.8 ± 1.3	586 ± 24	11.3 ± 3.4	575 ± 24	0.5326 ± 0.0057
0.3875	39.6 ± 1.6	725 ± 27	13.4 ± 3.7	712 ± 27	0.5134 ± 0.0056
0.4125	48.3 ± 1.7	901 ± 30	16.5 ± 4.1	884 ± 30	0.5237 ± 0.0057
0.4375	61.4 ± 1.9	1179 ± 34	20.5 ± 4.5	1158 ± 34	0.5387 ± 0.0057
0.4625	77.0 ± 2.2	1417 ± 38	25.2 ± 5.0	1392 ± 38	0.5165 ± 0.0056
0.4875	89.5 ± 2.5	1607 ± 40	30.3 ± 5.5	1577 ± 40	0.5032 ± 0.0055
0.5125	112.8 ± 2.8	2075 ± 46	34.9 ± 5.9	2040 ± 46	0.5167 ± 0.0056
0.5375	147.7 ± 3.5	2480 ± 50	38.4 ± 6.2	2442 ± 50	0.4721 ± 0.0054
0.5625	173.0 ± 4.0	2650 ± 51	39.2 ± 6.3	2611 ± 51	0.4311 ± 0.0051
0.5875	216.7 ± 5.1	2709 ± 52	36.0 ± 6.0	2673 ± 52	0.3525 ± 0.0046

$\bar{p}p \to \pi^0\pi^0$ at $E_{cm} = 3413.8$ MeV ($\mathcal{L} = 1953.9\ 10^{31}\text{s}^{-1}\text{cm}^{-2}$)					
z	$\frac{d\sigma}{dz}$ (nb)	N_{tot} (events)	N_{bkg} (events)	$N_{\pi^0\pi^0}$ (events)	$a \times \epsilon$
0.0125	34.2 ± 1.4	638 ± 25	13.5 ± 3.7	625 ± 25	0.4278 ± 0.0050
0.0375	38.1 ± 1.5	719 ± 27	14.1 ± 3.8	705 ± 27	0.4341 ± 0.0050
0.0625	32.3 ± 1.3	651 ± 26	15.0 ± 3.9	636 ± 26	0.4620 ± 0.0052
0.0875	33.3 ± 1.4	638 ± 25	15.8 ± 4.0	622 ± 25	0.4383 ± 0.0050
0.1125	31.6 ± 1.4	615 ± 25	16.3 ± 4.0	599 ± 25	0.4443 ± 0.0051
0.1375	28.0 ± 1.3	562 ± 24	16.4 ± 4.0	546 ± 24	0.4561 ± 0.0052
0.1625	25.2 ± 1.2	538 ± 23	15.9 ± 4.0	522 ± 23	0.4850 ± 0.0053
0.1875	21.9 ± 1.1	455 ± 21	15.0 ± 3.9	440 ± 21	0.4714 ± 0.0053
0.2125	24.5 ± 1.2	496 ± 22	13.7 ± 3.7	482 ± 22	0.4622 ± 0.0052
0.2375	23.5 ± 1.1	498 ± 22	12.2 ± 3.5	486 ± 22	0.4840 ± 0.0053
0.2625	21.0 ± 1.0	458 ± 21	10.8 ± 3.3	447 ± 21	0.4984 ± 0.0054
0.2875	23.0 ± 1.1	490 ± 22	9.6 ± 3.1	480 ± 22	0.4903 ± 0.0054
0.3125	26.4 ± 1.2	559 ± 24	9.0 ± 3.0	550 ± 24	0.4887 ± 0.0054
0.3375	29.5 ± 1.2	652 ± 26	9.3 ± 3.1	643 ± 26	0.5106 ± 0.0055
0.3625	34.3 ± 1.3	769 ± 28	10.7 ± 3.3	758 ± 28	0.5183 ± 0.0055
0.3875	40.3 ± 1.5	877 ± 30	13.4 ± 3.7	864 ± 30	0.5020 ± 0.0054
0.4125	48.9 ± 1.6	1050 ± 32	17.3 ± 4.2	1033 ± 32	0.4953 ± 0.0054
0.4375	57.4 ± 1.7	1320 ± 36	22.5 ± 4.7	1297 ± 36	0.5300 ± 0.0056
0.4625	73.5 ± 2.0	1589 ± 40	28.6 ± 5.4	1560 ± 40	0.4980 ± 0.0054
0.4875	91.4 ± 2.4	1899 ± 44	35.2 ± 5.9	1864 ± 44	0.4781 ± 0.0053
0.5125	109.7 ± 2.6	2310 ± 48	41.3 ± 6.4	2269 ± 48	0.4847 ± 0.0054
0.5375	132.1 ± 3.1	2563 ± 51	45.8 ± 6.8	2517 ± 51	0.4466 ± 0.0051
0.5625	169.2 ± 3.7	3024 ± 55	47.3 ± 6.9	2977 ± 55	0.4125 ± 0.0049
0.5875	210.2 ± 4.8	3070 ± 55	43.5 ± 6.6	3026 ± 55	0.3375 ± 0.0044

$\bar{p}p \to \pi^0\pi^0$ at $E_{cm} = 3415.0$ MeV ($\mathcal{L} = 2352.1\ 10^{31}\mathrm{s}^{-1}\mathrm{cm}^{-2}$)					
z	$\frac{d\sigma}{dz}$ (nb)	N_{tot} (events)	N_{bkg} (events)	$N_{\pi^0\pi^0}$ (events)	$a \times \epsilon$
0.0125	34.6 ± 1.3	819 ± 29	21.0 ± 4.6	798 ± 29	0.4492 ± 0.0042
0.0375	33.7 ± 1.3	816 ± 29	21.2 ± 4.6	795 ± 29	0.4599 ± 0.0042
0.0625	33.1 ± 1.2	849 ± 29	21.4 ± 4.6	828 ± 29	0.4867 ± 0.0044
0.0875	31.9 ± 1.2	778 ± 28	21.4 ± 4.6	757 ± 28	0.4625 ± 0.0043
0.1125	31.1 ± 1.2	770 ± 28	21.0 ± 4.6	749 ± 28	0.4694 ± 0.0043
0.1375	28.9 ± 1.1	734 ± 27	20.1 ± 4.5	714 ± 27	0.4818 ± 0.0043
0.1625	27.2 ± 1.1	733 ± 27	18.9 ± 4.3	714 ± 27	0.5114 ± 0.0045
0.1875	25.3 ± 1.0	661 ± 26	17.3 ± 4.2	644 ± 26	0.4966 ± 0.0044
0.2125	22.7 ± 1.0	596 ± 24	15.6 ± 3.9	580 ± 24	0.4985 ± 0.0044
0.2375	20.5 ± 0.9	557 ± 24	13.9 ± 3.7	543 ± 24	0.5169 ± 0.0045
0.2625	21.4 ± 0.9	616 ± 25	12.5 ± 3.5	603 ± 25	0.5489 ± 0.0046
0.2875	22.6 ± 1.0	612 ± 25	11.7 ± 3.4	600 ± 25	0.5167 ± 0.0045
0.3125	24.0 ± 1.0	656 ± 26	11.8 ± 3.4	644 ± 26	0.5242 ± 0.0045
0.3375	26.4 ± 1.0	752 ± 27	13.0 ± 3.6	739 ± 27	0.5448 ± 0.0046
0.3625	31.3 ± 1.1	889 ± 30	15.4 ± 3.9	874 ± 30	0.5438 ± 0.0046
0.3875	37.7 ± 1.3	1019 ± 32	19.3 ± 4.4	1000 ± 32	0.5162 ± 0.0045
0.4125	48.2 ± 1.4	1324 ± 36	24.5 ± 5.0	1299 ± 36	0.5259 ± 0.0045
0.4375	57.2 ± 1.5	1661 ± 41	31.0 ± 5.6	1630 ± 41	0.5553 ± 0.0047
0.4625	70.6 ± 1.8	1914 ± 44	38.2 ± 6.2	1876 ± 44	0.5175 ± 0.0045
0.4875	86.3 ± 2.0	2354 ± 49	45.6 ± 6.8	2308 ± 49	0.5214 ± 0.0045
0.5125	105.6 ± 2.2	2907 ± 54	52.2 ± 7.2	2855 ± 54	0.5271 ± 0.0046
0.5375	129.8 ± 2.6	3262 ± 57	56.7 ± 7.5	3205 ± 57	0.4813 ± 0.0044
0.5625	160.1 ± 3.1	3698 ± 61	57.4 ± 7.6	3641 ± 61	0.4432 ± 0.0042
0.5875	208.6 ± 4.0	3974 ± 63	52.0 ± 7.2	3922 ± 63	0.3666 ± 0.0038

$\bar{p}p \to \pi^0\pi^0$ at $E_{cm} = 3415.9$ MeV ($\mathcal{L} = 2466.5\ 10^{31}\mathrm{s}^{-1}\mathrm{cm}^{-2}$)					
z	$\frac{d\sigma}{dz}$ (nb)	N_{tot} (events)	N_{bkg} (events)	$N_{\pi^0\pi^0}$ (events)	$a \times \epsilon$
0.0125	31.1 ± 1.2	756 ± 28	20.3 ± 4.5	736 ± 28	0.4382 ± 0.0044
0.0375	34.6 ± 1.3	842 ± 29	20.5 ± 4.5	822 ± 29	0.4404 ± 0.0044
0.0625	31.2 ± 1.2	811 ± 28	20.6 ± 4.5	790 ± 28	0.4701 ± 0.0046
0.0875	29.9 ± 1.2	754 ± 27	20.5 ± 4.5	734 ± 27	0.4556 ± 0.0045
0.1125	29.9 ± 1.2	740 ± 27	20.1 ± 4.5	720 ± 27	0.4465 ± 0.0045
0.1375	27.2 ± 1.1	702 ± 26	19.3 ± 4.4	683 ± 26	0.4651 ± 0.0045
0.1625	25.4 ± 1.0	692 ± 26	18.2 ± 4.3	674 ± 26	0.4921 ± 0.0047
0.1875	24.8 ± 1.0	660 ± 26	16.9 ± 4.1	643 ± 26	0.4820 ± 0.0046
0.2125	24.1 ± 1.0	648 ± 25	15.4 ± 3.9	633 ± 25	0.4862 ± 0.0047
0.2375	23.0 ± 1.0	635 ± 25	14.2 ± 3.8	621 ± 25	0.5012 ± 0.0047
0.2625	21.8 ± 0.9	623 ± 25	13.2 ± 3.6	610 ± 25	0.5182 ± 0.0048
0.2875	20.3 ± 0.9	558 ± 24	12.9 ± 3.6	545 ± 24	0.4969 ± 0.0047
0.3125	24.0 ± 1.0	656 ± 26	13.4 ± 3.7	643 ± 26	0.4974 ± 0.0047
0.3375	29.0 ± 1.1	837 ± 29	14.9 ± 3.9	822 ± 29	0.5258 ± 0.0048
0.3625	30.1 ± 1.1	872 ± 30	17.7 ± 4.2	854 ± 30	0.5270 ± 0.0048
0.3875	37.7 ± 1.2	1070 ± 33	21.7 ± 4.7	1048 ± 33	0.5162 ± 0.0048
0.4125	48.3 ± 1.4	1363 ± 37	26.9 ± 5.2	1336 ± 37	0.5135 ± 0.0048
0.4375	54.1 ± 1.5	1613 ± 40	33.1 ± 5.8	1580 ± 40	0.5415 ± 0.0049
0.4625	68.6 ± 1.7	1917 ± 44	40.0 ± 6.3	1877 ± 44	0.5075 ± 0.0048
0.4875	86.2 ± 2.0	2385 ± 49	46.9 ± 6.8	2338 ± 49	0.5030 ± 0.0047
0.5125	102.3 ± 2.2	2865 ± 54	52.8 ± 7.3	2812 ± 54	0.5099 ± 0.0048
0.5375	124.2 ± 2.6	3205 ± 57	56.6 ± 7.5	3148 ± 57	0.4702 ± 0.0046
0.5625	153.4 ± 3.0	3659 ± 60	56.7 ± 7.5	3602 ± 60	0.4355 ± 0.0044
0.5875	196.8 ± 3.9	3822 ± 62	50.9 ± 7.1	3771 ± 62	0.3554 ± 0.0040

$\bar{p}p \to \pi^0\pi^0$ at $E_{cm} = 3418.0$ MeV ($\mathcal{L} = 1215.4\ 10^{31}\mathrm{s}^{-1}\mathrm{cm}^{-2}$)					
z	$\frac{d\sigma}{dz}$ (nb)	N_{tot} (events)	N_{bkg} (events)	$N_{\pi^0\pi^0}$ (events)	$a \times \epsilon$
0.0125	29.4 ± 1.6	383 ± 20	11.2 ± 3.3	372 ± 20	0.4760 ± 0.0050
0.0375	34.2 ± 1.7	445 ± 21	11.4 ± 3.4	434 ± 21	0.4773 ± 0.0050
0.0625	30.5 ± 1.6	423 ± 21	11.8 ± 3.4	411 ± 21	0.5084 ± 0.0052
0.0875	27.9 ± 1.5	372 ± 19	12.0 ± 3.5	360 ± 19	0.4856 ± 0.0051
0.1125	27.3 ± 1.5	369 ± 19	12.0 ± 3.5	357 ± 19	0.4924 ± 0.0051
0.1375	27.1 ± 1.5	372 ± 19	11.7 ± 3.4	360 ± 19	0.5011 ± 0.0051
0.1625	25.0 ± 1.4	368 ± 19	11.1 ± 3.3	357 ± 19	0.5374 ± 0.0054
0.1875	22.6 ± 1.3	322 ± 18	10.2 ± 3.2	312 ± 18	0.5194 ± 0.0053
0.2125	22.5 ± 1.3	324 ± 18	9.2 ± 3.0	315 ± 18	0.5262 ± 0.0053
0.2375	22.4 ± 1.3	333 ± 18	8.0 ± 2.8	325 ± 18	0.5458 ± 0.0054
0.2625	20.5 ± 1.2	311 ± 18	7.0 ± 2.6	304 ± 18	0.5591 ± 0.0055
0.2875	24.5 ± 1.3	360 ± 19	6.2 ± 2.5	354 ± 19	0.5434 ± 0.0054
0.3125	29.0 ± 1.5	414 ± 20	5.9 ± 2.4	408 ± 20	0.5304 ± 0.0053
0.3375	26.0 ± 1.3	401 ± 20	6.2 ± 2.5	395 ± 20	0.5717 ± 0.0055
0.3625	31.3 ± 1.5	477 ± 22	7.2 ± 2.7	470 ± 22	0.5661 ± 0.0055
0.3875	38.1 ± 1.7	572 ± 24	9.1 ± 3.0	563 ± 24	0.5561 ± 0.0055
0.4125	45.4 ± 1.8	688 ± 26	11.8 ± 3.4	676 ± 26	0.5612 ± 0.0055
0.4375	50.6 ± 1.9	801 ± 28	15.2 ± 3.9	786 ± 28	0.5843 ± 0.0056
0.4625	72.1 ± 2.4	1064 ± 33	19.3 ± 4.4	1045 ± 33	0.5453 ± 0.0054
0.4875	91.1 ± 2.7	1320 ± 36	23.6 ± 4.9	1296 ± 36	0.5361 ± 0.0054
0.5125	108.2 ± 3.0	1605 ± 40	27.5 ± 5.2	1577 ± 40	0.5490 ± 0.0054
0.5375	132.0 ± 3.5	1788 ± 42	30.4 ± 5.5	1758 ± 42	0.5014 ± 0.0052
0.5625	164.6 ± 4.1	2085 ± 46	31.2 ± 5.6	2054 ± 46	0.4699 ± 0.0050
0.5875	194.3 ± 4.9	2040 ± 45	28.6 ± 5.3	2011 ± 45	0.3899 ± 0.0046

$\bar{p}p \to \pi^0\pi^0$ at $E_{cm} = 3422.1$ MeV ($\mathcal{L} = 2152.3\ 10^{31}\mathrm{s}^{-1}\mathrm{cm}^{-2}$)					
z	$\frac{d\sigma}{dz}$ (nb)	N_{tot} (events)	N_{bkg} (events)	$N_{\pi^0\pi^0}$ (events)	$a \times \epsilon$
0.0125	29.6 ± 1.2	643 ± 25	14.4 ± 3.8	629 ± 25	0.4540 ± 0.0045
0.0375	28.8 ± 1.2	635 ± 25	14.9 ± 3.9	620 ± 25	0.4589 ± 0.0045
0.0625	30.8 ± 1.2	703 ± 27	15.7 ± 4.0	687 ± 27	0.4767 ± 0.0046
0.0875	26.1 ± 1.2	575 ± 24	16.4 ± 4.0	559 ± 24	0.4561 ± 0.0045
0.1125	25.1 ± 1.1	564 ± 24	16.7 ± 4.1	547 ± 24	0.4651 ± 0.0046
0.1375	26.7 ± 1.1	605 ± 25	16.6 ± 4.1	588 ± 25	0.4704 ± 0.0046
0.1625	22.2 ± 1.0	544 ± 23	16.1 ± 4.0	528 ± 23	0.5075 ± 0.0048
0.1875	22.5 ± 1.0	529 ± 23	15.1 ± 3.9	514 ± 23	0.4882 ± 0.0047
0.2125	23.8 ± 1.1	564 ± 24	13.8 ± 3.7	550 ± 24	0.4942 ± 0.0047
0.2375	19.9 ± 0.9	488 ± 22	12.4 ± 3.5	476 ± 22	0.5101 ± 0.0048
0.2625	20.3 ± 0.9	521 ± 23	11.2 ± 3.3	510 ± 23	0.5348 ± 0.0049
0.2875	21.9 ± 1.0	532 ± 23	10.3 ± 3.2	522 ± 23	0.5086 ± 0.0048
0.3125	23.8 ± 1.0	584 ± 24	10.2 ± 3.2	574 ± 24	0.5153 ± 0.0048
0.3375	26.6 ± 1.1	678 ± 26	11.0 ± 3.3	667 ± 26	0.5356 ± 0.0049
0.3625	27.9 ± 1.1	718 ± 27	13.0 ± 3.6	705 ± 27	0.5397 ± 0.0049
0.3875	38.8 ± 1.3	964 ± 31	16.4 ± 4.0	948 ± 31	0.5218 ± 0.0049
0.4125	44.3 ± 1.4	1119 ± 33	21.1 ± 4.6	1098 ± 33	0.5295 ± 0.0049
0.4375	51.8 ± 1.5	1376 ± 37	27.1 ± 5.2	1349 ± 37	0.5554 ± 0.0050
0.4625	68.7 ± 1.8	1704 ± 41	33.9 ± 5.8	1670 ± 41	0.5192 ± 0.0049
0.4875	85.4 ± 2.1	2099 ± 46	41.0 ± 6.4	2058 ± 46	0.5145 ± 0.0048
0.5125	102.1 ± 2.3	2568 ± 51	47.5 ± 6.9	2521 ± 51	0.5269 ± 0.0049
0.5375	130.9 ± 2.8	3031 ± 55	52.0 ± 7.2	2979 ± 55	0.4856 ± 0.0047
0.5625	157.7 ± 3.2	3387 ± 58	52.9 ± 7.3	3334 ± 58	0.4512 ± 0.0045
0.5875	204.4 ± 4.2	3606 ± 60	48.0 ± 6.9	3558 ± 60	0.3716 ± 0.0041

$\bar{p}p \to \pi^0\pi^0$ at $E_{cm} = 3426.0$ MeV ($\mathcal{L} = 1800.1\ 10^{31}\mathrm{s}^{-1}\mathrm{cm}^{-2}$)					
z	$\frac{d\sigma}{dz}$ (nb)	N_{tot} (events)	N_{bkg} (events)	$N_{\pi^0\pi^0}$ (events)	$a \times \epsilon$
0.0125	28.0 ± 1.3	506 ± 22	16.4 ± 4.0	490 ± 22	0.4437 ± 0.0049
0.0375	28.2 ± 1.3	525 ± 23	16.5 ± 4.1	508 ± 23	0.4580 ± 0.0050
0.0625	27.6 ± 1.3	525 ± 23	16.6 ± 4.1	508 ± 23	0.4678 ± 0.0051
0.0875	25.0 ± 1.2	470 ± 22	16.5 ± 4.1	454 ± 22	0.4610 ± 0.0051
0.1125	25.9 ± 1.3	481 ± 22	16.0 ± 4.0	465 ± 22	0.4552 ± 0.0050
0.1375	23.8 ± 1.2	459 ± 21	15.3 ± 3.9	444 ± 21	0.4733 ± 0.0051
0.1625	22.4 ± 1.1	461 ± 21	14.3 ± 3.8	447 ± 21	0.5052 ± 0.0053
0.1875	20.8 ± 1.1	406 ± 20	13.0 ± 3.6	393 ± 20	0.4790 ± 0.0051
0.2125	19.9 ± 1.1	394 ± 20	11.6 ± 3.4	382 ± 20	0.4865 ± 0.0052
0.2375	21.1 ± 1.1	435 ± 21	10.3 ± 3.2	425 ± 21	0.5097 ± 0.0053
0.2625	19.6 ± 1.0	414 ± 20	9.1 ± 3.0	405 ± 20	0.5246 ± 0.0054
0.2875	20.2 ± 1.0	412 ± 20	8.4 ± 2.9	404 ± 20	0.5062 ± 0.0053
0.3125	24.9 ± 1.2	499 ± 22	8.3 ± 2.9	491 ± 22	0.5003 ± 0.0053
0.3375	26.2 ± 1.2	562 ± 24	9.0 ± 3.0	553 ± 24	0.5351 ± 0.0055
0.3625	28.9 ± 1.2	624 ± 25	10.6 ± 3.3	613 ± 25	0.5388 ± 0.0055
0.3875	36.0 ± 1.4	737 ± 27	13.3 ± 3.6	724 ± 27	0.5094 ± 0.0053
0.4125	42.9 ± 1.5	908 ± 30	16.9 ± 4.1	891 ± 30	0.5269 ± 0.0054
0.4375	50.6 ± 1.6	1106 ± 33	21.4 ± 4.6	1085 ± 33	0.5438 ± 0.0055
0.4625	65.9 ± 1.9	1361 ± 37	26.6 ± 5.2	1334 ± 37	0.5141 ± 0.0053
0.4875	83.1 ± 2.2	1696 ± 41	31.9 ± 5.7	1664 ± 41	0.5081 ± 0.0053
0.5125	100.5 ± 2.5	2080 ± 46	36.8 ± 6.1	2043 ± 46	0.5156 ± 0.0053
0.5375	124.7 ± 2.9	2381 ± 49	40.4 ± 6.4	2341 ± 49	0.4762 ± 0.0051
0.5625	154.9 ± 3.5	2784 ± 53	41.4 ± 6.4	2743 ± 53	0.4492 ± 0.0050
0.5875	197.7 ± 4.4	2988 ± 55	38.3 ± 6.2	2950 ± 55	0.3786 ± 0.0046

$\bar{p}p \to \pi^0\pi^0$ at $E_{cm} = 3430.1$ MeV ($\mathcal{L} = 1438.2\ 10^{31}\mathrm{s}^{-1}\mathrm{cm}^{-2}$)					
z	$\frac{d\sigma}{dz}$ (nb)	N_{tot} (events)	N_{bkg} (events)	$N_{\pi^0\pi^0}$ (events)	$a \times \epsilon$
0.0125	30.4 ± 1.6	409 ± 20	5.3 ± 2.3	404 ± 20	0.4239 ± 0.0059
0.0375	31.2 ± 1.6	430 ± 21	6.0 ± 2.4	424 ± 21	0.4334 ± 0.0060
0.0625	24.8 ± 1.4	368 ± 19	7.1 ± 2.7	361 ± 19	0.4640 ± 0.0062
0.0875	29.5 ± 1.5	414 ± 20	8.3 ± 2.9	406 ± 20	0.4385 ± 0.0060
0.1125	26.6 ± 1.5	369 ± 19	9.3 ± 3.0	360 ± 19	0.4310 ± 0.0060
0.1375	25.7 ± 1.4	377 ± 19	9.9 ± 3.2	367 ± 19	0.4559 ± 0.0061
0.1625	22.8 ± 1.3	359 ± 19	10.2 ± 3.2	349 ± 19	0.4876 ± 0.0063
0.1875	23.5 ± 1.3	348 ± 19	10.0 ± 3.2	338 ± 19	0.4586 ± 0.0062
0.2125	20.0 ± 1.2	301 ± 17	9.5 ± 3.1	291 ± 17	0.4660 ± 0.0062
0.2375	20.2 ± 1.2	326 ± 18	8.8 ± 3.0	317 ± 18	0.5021 ± 0.0064
0.2625	19.0 ± 1.1	306 ± 17	7.9 ± 2.8	298 ± 17	0.5010 ± 0.0064
0.2875	20.3 ± 1.2	318 ± 18	7.3 ± 2.7	311 ± 18	0.4883 ± 0.0064
0.3125	21.8 ± 1.2	342 ± 18	7.0 ± 2.6	335 ± 18	0.4906 ± 0.0064
0.3375	26.4 ± 1.4	424 ± 21	7.2 ± 2.7	417 ± 21	0.5039 ± 0.0065
0.3625	28.0 ± 1.4	460 ± 21	8.3 ± 2.9	452 ± 21	0.5144 ± 0.0066
0.3875	35.4 ± 1.6	549 ± 23	10.3 ± 3.2	539 ± 23	0.4857 ± 0.0064
0.4125	40.2 ± 1.7	652 ± 26	13.2 ± 3.6	639 ± 26	0.5065 ± 0.0065
0.4375	51.7 ± 1.9	856 ± 29	17.2 ± 4.1	839 ± 29	0.5177 ± 0.0065
0.4625	64.2 ± 2.2	1013 ± 32	21.8 ± 4.7	991 ± 32	0.4924 ± 0.0064
0.4875	79.2 ± 2.5	1264 ± 36	26.8 ± 5.2	1237 ± 36	0.4987 ± 0.0065
0.5125	97.4 ± 2.8	1550 ± 39	31.4 ± 5.6	1519 ± 39	0.4975 ± 0.0064
0.5375	116.8 ± 3.3	1743 ± 42	34.9 ± 5.9	1708 ± 42	0.4665 ± 0.0062
0.5625	155.9 ± 4.1	2116 ± 46	35.9 ± 6.0	2080 ± 46	0.4259 ± 0.0060
0.5875	183.6 ± 4.9	2114 ± 46	33.0 ± 5.7	2081 ± 46	0.3617 ± 0.0055

$\bar{p}p \to \pi^0\pi^0$ at $E_{cm} = 3469.9$ MeV ($\mathcal{L} = 2512.6\ 10^{31}\mathrm{s}^{-1}\mathrm{cm}^{-2}$)					
z	$\frac{d\sigma}{dz}$ (nb)	N_{tot} (events)	N_{bkg} (events)	$N_{\pi^0\pi^0}$ (events)	$a \times \epsilon$
0.0125	30.1 ± 1.1	779 ± 28	15.5 ± 3.9	764 ± 28	0.4617 ± 0.0040
0.0375	27.9 ± 1.1	767 ± 28	15.9 ± 4.0	751 ± 28	0.4900 ± 0.0041
0.0625	28.3 ± 1.1	777 ± 28	16.5 ± 4.1	760 ± 28	0.4896 ± 0.0041
0.0875	27.1 ± 1.1	712 ± 27	17.1 ± 4.1	695 ± 27	0.4658 ± 0.0040
0.1125	26.7 ± 1.1	706 ± 27	17.4 ± 4.2	689 ± 27	0.4699 ± 0.0040
0.1375	23.3 ± 1.0	661 ± 26	17.4 ± 4.2	644 ± 26	0.5033 ± 0.0041
0.1625	22.8 ± 0.9	652 ± 26	17.1 ± 4.1	635 ± 26	0.5061 ± 0.0041
0.1875	21.8 ± 0.9	600 ± 24	16.4 ± 4.0	584 ± 24	0.4869 ± 0.0041
0.2125	21.7 ± 0.9	615 ± 25	15.4 ± 3.9	600 ± 25	0.5028 ± 0.0041
0.2375	18.2 ± 0.8	561 ± 24	14.3 ± 3.8	547 ± 24	0.5454 ± 0.0043
0.2625	20.2 ± 0.9	605 ± 25	13.3 ± 3.6	592 ± 25	0.5318 ± 0.0042
0.2875	18.4 ± 0.8	547 ± 23	12.5 ± 3.5	534 ± 23	0.5282 ± 0.0042
0.3125	20.7 ± 0.9	611 ± 25	12.2 ± 3.5	599 ± 25	0.5276 ± 0.0042
0.3375	21.3 ± 0.8	680 ± 26	12.6 ± 3.6	667 ± 26	0.5707 ± 0.0044
0.3625	24.4 ± 0.9	733 ± 27	13.9 ± 3.7	719 ± 27	0.5366 ± 0.0043
0.3875	31.0 ± 1.1	918 ± 30	16.3 ± 4.0	902 ± 30	0.5296 ± 0.0042
0.4125	37.6 ± 1.2	1187 ± 34	19.7 ± 4.4	1167 ± 34	0.5644 ± 0.0044
0.4375	46.0 ± 1.3	1415 ± 38	24.1 ± 4.9	1391 ± 38	0.5503 ± 0.0043
0.4625	55.5 ± 1.5	1632 ± 40	29.5 ± 5.4	1603 ± 40	0.5253 ± 0.0042
0.4875	69.0 ± 1.6	2099 ± 46	35.2 ± 5.9	2064 ± 46	0.5444 ± 0.0043
0.5125	82.3 ± 1.8	2447 ± 49	40.9 ± 6.4	2406 ± 49	0.5318 ± 0.0043
0.5375	98.4 ± 2.1	2767 ± 53	45.6 ± 6.8	2721 ± 53	0.5033 ± 0.0042
0.5625	122.5 ± 2.4	3318 ± 58	48.1 ± 6.9	3270 ± 58	0.4858 ± 0.0041
0.5875	147.3 ± 2.9	3457 ± 59	47.1 ± 6.9	3410 ± 59	0.4214 ± 0.0038

Appendix G

The $\bar{p}p \to \pi^0\eta$ Cross Section Tables

The following list of tables reproduces the measured $\bar{p}p \to \pi^0\eta$ cross section (and the z-dependent quantities used to calculate it) at every energy point of the χ_{c0} sample. In particular: the value of the center of the z-bin (where z is defined as $z \equiv \cos\theta^*_{\pi^0}$); the $\bar{p}p \to \pi^0\eta$ differential cross section ($\frac{d\sigma}{dz}$); the total number of events (N_{tot}) passing the $\pi^0\eta$ selection; the estimated number of instrumental background events (N_{bkg}); and the number of $\pi^0\eta$ events ($N_{\pi^0\eta} \equiv N_{tot} - N_{bkg}$, with uncertainty conservatively taken as $\sqrt{N_{tot}}$). The last column reproduces the product of the acceptance and efficiency ($a \times \epsilon$) corrected for pileup; the uncertainty on $a \times \epsilon$ is determined by the number of Random Gate events available. The value of $a \times \epsilon$ given outside the brackets is determined by using a uniform $\pi^0\eta$ angular distribution. The value given inside the brackets is determined by using the estimate of the angular distribution corrected for the limited polar angle resolution, as described in Appendix B.

Where $\frac{d\sigma}{dz}$ is very small (at $z \simeq 0$) and a particularly low fluctuation of N_{tot} occurs, the estimated background events N_{bkg} may exceed N_{tot}. In those cases $N_{\pi^0\eta}$ is set equal to zero. That happens in 3 bins out of 816.

At $E_{cm} \simeq 3400$ MeV and $z \simeq 0$, there is a virtual zero in $\frac{d\sigma}{dz}$. The estimate of the number of events migrating in the central bins as a consequence of the limited polar angle resolution is then a large fraction of the events actually generated at $z \simeq 0$. Consequently, the correction applied to compensate for the migration may result in an artificially high value of the bracketed $a \times \epsilon$.

$\bar{p}p \to \pi^0\eta$ at $E_{cm} = 3339.5$ MeV ($\mathcal{L} = 629.4\ 10^{31}\mathrm{s}^{-1}\mathrm{cm}^{-2}$)					
z	$d\sigma/dz$ (nb)	N_{tot}	N_{bkg}	$N_{\pi^0\pi^0}$	$a \times \epsilon$
-0.5875	179.9 ± 15.8	181 ± 13.4	5.2 ± 2.3	175.8 ± 13.4	$0.182\ (0.181) \pm 0.008$
-0.5625	110.8 ± 10.0	160 ± 12.7	7.4 ± 2.7	152.6 ± 12.7	$0.258\ (0.256) \pm 0.009$
-0.5375	60.0 ± 6.1	124 ± 11.1	8.3 ± 2.9	115.7 ± 11.1	$0.351\ (0.358) \pm 0.011$
-0.5125	45.4 ± 5.0	104 ± 10.2	8.5 ± 2.9	95.5 ± 10.2	$0.384\ (0.390) \pm 0.012$
-0.4875	26.3 ± 3.8	65 ± 8.1	8.1 ± 2.8	56.9 ± 8.1	$0.388\ (0.401) \pm 0.012$
-0.4625	13.7 ± 2.7	40 ± 6.3	7.4 ± 2.7	32.6 ± 6.3	$0.426\ (0.440) \pm 0.012$
-0.4375	13.5 ± 2.6	39 ± 6.2	6.5 ± 2.5	32.5 ± 6.2	$0.434\ (0.448) \pm 0.012$
-0.4125	13.5 ± 2.6	39 ± 6.2	5.5 ± 2.3	33.5 ± 6.2	$0.446\ (0.459) \pm 0.012$
-0.3875	20.0 ± 3.0	56 ± 7.5	4.5 ± 2.1	51.5 ± 7.5	$0.473\ (0.477) \pm 0.013$
-0.3625	14.9 ± 2.6	41 ± 6.4	3.6 ± 1.9	37.4 ± 6.4	$0.467\ (0.465) \pm 0.013$
-0.3375	18.2 ± 2.8	50 ± 7.1	2.8 ± 1.7	47.2 ± 7.1	$0.479\ (0.482) \pm 0.013$
-0.3125	19.0 ± 2.8	51 ± 7.1	2.2 ± 1.5	48.8 ± 7.1	$0.486\ (0.476) \pm 0.013$
-0.2875	29.5 ± 3.5	78 ± 8.8	1.6 ± 1.3	76.4 ± 8.8	$0.479\ (0.481) \pm 0.013$
-0.2625	22.3 ± 3.1	58 ± 7.6	1.2 ± 1.1	56.8 ± 7.6	$0.474\ (0.472) \pm 0.013$
-0.2375	21.8 ± 3.0	55 ± 7.4	0.9 ± 1.0	54.1 ± 7.4	$0.467\ (0.461) \pm 0.013$
-0.2125	24.3 ± 3.2	63 ± 7.9	0.8 ± 0.9	62.2 ± 7.9	$0.476\ (0.474) \pm 0.013$
-0.1875	24.2 ± 3.2	62 ± 7.9	0.7 ± 0.8	61.3 ± 7.9	$0.472\ (0.471) \pm 0.013$
-0.1625	17.3 ± 2.7	44 ± 6.6	0.7 ± 0.8	43.3 ± 6.6	$0.466\ (0.465) \pm 0.013$
-0.1375	23.4 ± 3.3	55 ± 7.4	0.8 ± 0.9	54.2 ± 7.4	$0.433\ (0.429) \pm 0.012$
-0.1125	9.0 ± 1.9	24 ± 4.9	1.0 ± 1.0	23.0 ± 4.9	$0.466\ (0.473) \pm 0.013$
-0.0875	6.6 ± 1.7	17 ± 4.1	1.1 ± 1.1	15.9 ± 4.1	$0.442\ (0.445) \pm 0.012$
-0.0625	7.1 ± 1.8	18 ± 4.2	1.4 ± 1.2	16.6 ± 4.2	$0.431\ (0.433) \pm 0.012$
-0.0375	4.2 ± 1.4	12 ± 3.5	1.6 ± 1.2	10.4 ± 3.5	$0.447\ (0.464) \pm 0.012$
-0.0125	1.2 ± 0.9	5 ± 2.2	1.7 ± 1.3	3.3 ± 2.2	$0.454\ (0.488) \pm 0.012$
0.0125	1.7 ± 1.0	6 ± 2.5	1.9 ± 1.4	4.1 ± 2.5	$0.413\ (0.445) \pm 0.012$
0.0375	3.1 ± 1.2	10 ± 3.2	2.0 ± 1.4	8.0 ± 3.2	$0.465\ (0.484) \pm 0.013$
0.0625	4.3 ± 1.5	12 ± 3.5	2.0 ± 1.4	9.9 ± 3.5	$0.426\ (0.433) \pm 0.012$
0.0875	3.8 ± 1.3	12 ± 3.5	2.0 ± 1.4	9.9 ± 3.5	$0.479\ (0.485) \pm 0.013$
0.1125	13.6 ± 2.4	36 ± 6.0	2.0 ± 1.4	34.0 ± 6.0	$0.463\ (0.464) \pm 0.013$
0.1375	14.1 ± 2.6	34 ± 5.8	1.9 ± 1.4	32.1 ± 5.8	$0.420\ (0.423) \pm 0.012$
0.1625	15.8 ± 2.7	38 ± 6.2	1.8 ± 1.3	36.2 ± 6.2	$0.427\ (0.426) \pm 0.012$
0.1875	18.2 ± 2.8	48 ± 6.9	1.6 ± 1.3	46.4 ± 6.9	$0.475\ (0.472) \pm 0.013$
0.2125	25.3 ± 3.4	61 ± 7.8	1.5 ± 1.2	59.5 ± 7.8	$0.439\ (0.437) \pm 0.012$
0.2375	24.2 ± 3.4	57 ± 7.5	1.4 ± 1.2	55.6 ± 7.5	$0.427\ (0.425) \pm 0.012$
0.2625	27.6 ± 3.6	65 ± 8.1	1.4 ± 1.2	63.5 ± 8.1	$0.429\ (0.427) \pm 0.012$
0.2875	20.2 ± 3.0	51 ± 7.1	1.6 ± 1.3	49.4 ± 7.1	$0.460\ (0.453) \pm 0.013$
0.3125	29.3 ± 3.8	65 ± 8.1	2.0 ± 1.4	63.0 ± 8.1	$0.397\ (0.400) \pm 0.011$
0.3375	19.4 ± 3.2	44 ± 6.6	2.5 ± 1.6	41.5 ± 6.6	$0.398\ (0.395) \pm 0.012$
0.3625	20.9 ± 3.2	50 ± 7.1	3.4 ± 1.8	46.6 ± 7.1	$0.412\ (0.414) \pm 0.012$
0.3875	19.7 ± 3.3	45 ± 6.7	4.6 ± 2.1	40.4 ± 6.7	$0.378\ (0.380) \pm 0.011$
0.4125	10.9 ± 2.7	27 ± 5.2	6.0 ± 2.5	21.0 ± 5.2	$0.350\ (0.357) \pm 0.011$
0.4375	21.0 ± 3.9	44 ± 6.6	7.8 ± 2.8	36.2 ± 6.6	$0.313\ (0.320) \pm 0.010$
0.4625	19.5 ± 3.8	45 ± 6.7	9.7 ± 3.1	35.3 ± 6.7	$0.327\ (0.336) \pm 0.011$
0.4875	35.5 ± 5.7	62 ± 7.9	11.7 ± 3.4	50.4 ± 7.9	$0.259\ (0.263) \pm 0.009$
0.5125	47.7 ± 7.0	75 ± 8.7	13.5 ± 3.7	61.5 ± 8.7	$0.236\ (0.239) \pm 0.009$
0.5375	79.9 ± 9.5	107 ± 10.3	14.9 ± 3.9	92.1 ± 10.3	$0.215\ (0.214) \pm 0.009$
0.5625	142.5 ± 15.5	133 ± 11.5	15.4 ± 3.9	117.6 ± 11.5	$0.154\ (0.153) \pm 0.007$
0.5875	187.5 ± 22.6	118 ± 10.9	14.5 ± 3.8	103.5 ± 10.9	$0.103\ (0.102) \pm 0.006$

Table G.1: This and the following tables: the cross section $\bar{p}p \to \pi^0\eta$.

$\bar{p}p \to \pi^0\eta$ at $E_{cm} = 3365.0$ MeV ($\mathcal{L} = 1423.7\ 10^{31}\mathrm{s}^{-1}\mathrm{cm}^{-2}$)					
z	$d\sigma/dz$ (nb)	N_{tot}	N_{bkg}	$N_{\pi^0\pi^0}$	$a \times \epsilon$
-0.5875	143.1 ± 8.4	395 ± 19.9	18.9 ± 4.4	376.1 ± 19.9	$0.217\ (0.216) \pm 0.005$
-0.5625	108.5 ± 6.2	401 ± 20.0	22.1 ± 4.7	378.9 ± 20.0	$0.286\ (0.287) \pm 0.006$
-0.5375	58.3 ± 3.9	290 ± 17.0	23.0 ± 4.8	267.0 ± 17.0	$0.370\ (0.376) \pm 0.007$
-0.5125	35.6 ± 2.9	198 ± 14.1	22.3 ± 4.7	175.7 ± 14.1	$0.399\ (0.405) \pm 0.007$
-0.4875	20.6 ± 2.2	131 ± 11.4	20.7 ± 4.6	110.3 ± 11.4	$0.434\ (0.440) \pm 0.008$
-0.4625	13.8 ± 1.8	97 ± 9.8	18.7 ± 4.3	78.3 ± 9.8	$0.446\ (0.465) \pm 0.008$
-0.4375	8.9 ± 1.4	68 ± 8.2	16.5 ± 4.1	51.5 ± 8.2	$0.455\ (0.476) \pm 0.008$
-0.4125	7.7 ± 1.3	59 ± 7.7	14.3 ± 3.8	44.7 ± 7.7	$0.462\ (0.474) \pm 0.008$
-0.3875	13.6 ± 1.6	95 ± 9.8	12.3 ± 3.5	82.7 ± 9.8	$0.494\ (0.500) \pm 0.008$
-0.3625	14.2 ± 1.7	92 ± 9.6	10.6 ± 3.3	81.4 ± 9.6	$0.469\ (0.472) \pm 0.008$
-0.3375	20.6 ± 2.0	128 ± 11.3	9.1 ± 3.0	118.9 ± 11.3	$0.476\ (0.475) \pm 0.008$
-0.3125	19.0 ± 1.8	124 ± 11.1	7.8 ± 2.8	116.2 ± 11.1	$0.511\ (0.503) \pm 0.008$
-0.2875	20.3 ± 1.9	133 ± 11.5	6.8 ± 2.6	126.2 ± 11.5	$0.508\ (0.510) \pm 0.008$
-0.2625	23.1 ± 2.1	141 ± 11.9	6.1 ± 2.5	134.9 ± 11.9	$0.485\ (0.480) \pm 0.008$
-0.2375	19.9 ± 1.9	124 ± 11.1	5.6 ± 2.4	118.4 ± 11.1	$0.489\ (0.488) \pm 0.008$
-0.2125	19.0 ± 1.8	123 ± 11.1	5.3 ± 2.3	117.7 ± 11.1	$0.517\ (0.510) \pm 0.008$
-0.1875	18.3 ± 1.8	112 ± 10.6	5.1 ± 2.3	106.9 ± 10.6	$0.482\ (0.480) \pm 0.008$
-0.1625	15.9 ± 1.7	99 ± 9.9	5.1 ± 2.3	93.9 ± 9.9	$0.486\ (0.486) \pm 0.008$
-0.1375	12.9 ± 1.5	81 ± 9.0	5.2 ± 2.3	75.8 ± 9.0	$0.484\ (0.483) \pm 0.008$
-0.1125	9.4 ± 1.3	62 ± 7.9	5.5 ± 2.3	56.5 ± 7.9	$0.490\ (0.494) \pm 0.008$
-0.0875	7.1 ± 1.2	46 ± 6.8	5.8 ± 2.4	40.2 ± 6.8	$0.464\ (0.464) \pm 0.008$
-0.0625	4.6 ± 1.0	32 ± 5.7	6.1 ± 2.5	25.9 ± 5.7	$0.456\ (0.465) \pm 0.008$
-0.0375	2.0 ± 0.7	18 ± 4.2	6.5 ± 2.5	11.5 ± 4.2	$0.451\ (0.476) \pm 0.008$
-0.0125	1.4 ± 0.6	16 ± 4.0	6.9 ± 2.6	9.1 ± 4.0	$0.482\ (0.531) \pm 0.008$
0.0125	0.8 ± 0.6	12 ± 3.5	7.2 ± 2.7	4.8 ± 3.5	$0.460\ (0.503) \pm 0.008$
0.0375	1.7 ± 0.7	17 ± 4.1	7.5 ± 2.7	9.5 ± 4.1	$0.440\ (0.464) \pm 0.008$
0.0625	2.6 ± 0.8	23 ± 4.8	7.7 ± 2.8	15.3 ± 4.8	$0.472\ (0.483) \pm 0.008$
0.0875	6.8 ± 1.2	49 ± 7.0	7.8 ± 2.8	41.2 ± 7.0	$0.490\ (0.496) \pm 0.008$
0.1125	7.1 ± 1.2	49 ± 7.0	7.8 ± 2.8	41.2 ± 7.0	$0.470\ (0.476) \pm 0.008$
0.1375	9.8 ± 1.4	62 ± 7.9	7.6 ± 2.8	54.4 ± 7.9	$0.453\ (0.455) \pm 0.008$
0.1625	16.0 ± 1.8	98 ± 9.9	7.4 ± 2.7	90.6 ± 9.9	$0.469\ (0.466) \pm 0.008$
0.1875	15.0 ± 1.7	95 ± 9.8	7.0 ± 2.7	88.0 ± 9.8	$0.480\ (0.481) \pm 0.008$
0.2125	20.8 ± 2.0	124 ± 11.1	6.7 ± 2.6	117.3 ± 11.1	$0.466\ (0.463) \pm 0.008$
0.2375	20.2 ± 2.0	114 ± 10.7	6.4 ± 2.5	107.6 ± 10.7	$0.439\ (0.437) \pm 0.008$
0.2625	20.8 ± 2.0	122 ± 11.1	6.1 ± 2.5	115.9 ± 11.1	$0.459\ (0.456) \pm 0.008$
0.2875	25.5 ± 2.2	147 ± 12.1	6.2 ± 2.5	140.8 ± 12.1	$0.457\ (0.453) \pm 0.008$
0.3125	18.8 ± 2.0	101 ± 10.1	6.5 ± 2.5	94.5 ± 10.1	$0.415\ (0.412) \pm 0.008$
0.3375	21.0 ± 2.1	115 ± 10.7	7.3 ± 2.7	107.7 ± 10.7	$0.419\ (0.421) \pm 0.008$
0.3625	14.6 ± 1.8	84 ± 9.2	8.6 ± 2.9	75.4 ± 9.2	$0.424\ (0.424) \pm 0.008$
0.3875	13.0 ± 1.8	73 ± 8.5	10.6 ± 3.3	62.4 ± 8.5	$0.390\ (0.395) \pm 0.007$
0.4125	11.8 ± 1.8	67 ± 8.2	13.4 ± 3.7	53.6 ± 8.2	$0.366\ (0.375) \pm 0.007$
0.4375	10.4 ± 1.8	62 ± 7.9	16.8 ± 4.1	45.2 ± 7.9	$0.347\ (0.358) \pm 0.007$
0.4625	15.3 ± 2.2	84 ± 9.2	20.8 ± 4.6	63.2 ± 9.2	$0.328\ (0.339) \pm 0.007$
0.4875	24.6 ± 3.0	114 ± 10.7	25.1 ± 5.0	88.8 ± 10.7	$0.291\ (0.297) \pm 0.006$
0.5125	41.2 ± 4.2	154 ± 12.4	29.4 ± 5.4	124.5 ± 12.4	$0.247\ (0.249) \pm 0.006$
0.5375	64.5 ± 5.5	213 ± 14.6	33.0 ± 5.7	179.9 ± 14.6	$0.227\ (0.229) \pm 0.006$
0.5625	107.0 ± 8.2	263 ± 16.2	35.0 ± 5.9	228.0 ± 16.2	$0.175\ (0.175) \pm 0.005$
0.5875	171.0 ± 12.7	290 ± 17.0	34.0 ± 5.8	256.0 ± 17.0	$0.124\ (0.123) \pm 0.004$

$\bar{p}p \to \pi^0\eta$ at $E_{cm} = 3384.4$ MeV ($\mathcal{L} = 1521.6\ 10^{31}\mathrm{s}^{-1}\mathrm{cm}^{-2}$)					
z	$d\sigma/dz$ (nb)	N_{tot}	N_{bkg}	$N_{\pi^0\pi^0}$	$a \times \epsilon$
-0.5875	133.5 ± 7.7	400 ± 20.0	19.2 ± 4.4	380.8 ± 20.0	$0.219\ (0.217) \pm 0.005$
-0.5625	91.7 ± 5.3	385 ± 19.6	22.1 ± 4.7	362.9 ± 19.6	$0.301\ (0.302) \pm 0.006$
-0.5375	52.2 ± 3.5	282 ± 16.8	22.4 ± 4.7	259.6 ± 16.8	$0.372\ (0.379) \pm 0.007$
-0.5125	34.9 ± 2.8	200 ± 14.1	21.2 ± 4.6	178.8 ± 14.1	$0.386\ (0.391) \pm 0.007$
-0.4875	19.8 ± 2.0	134 ± 11.6	19.1 ± 4.4	114.9 ± 11.6	$0.428\ (0.443) \pm 0.007$
-0.4625	9.5 ± 1.4	74 ± 8.6	16.6 ± 4.1	57.4 ± 8.6	$0.440\ (0.459) \pm 0.007$
-0.4375	10.4 ± 1.5	77 ± 8.8	14.0 ± 3.7	63.0 ± 8.8	$0.444\ (0.463) \pm 0.007$
-0.4125	8.6 ± 1.3	67 ± 8.2	11.5 ± 3.4	55.5 ± 8.2	$0.478\ (0.494) \pm 0.008$
-0.3875	10.5 ± 1.4	76 ± 8.7	9.3 ± 3.1	66.7 ± 8.7	$0.484\ (0.486) \pm 0.008$
-0.3625	13.1 ± 1.5	90 ± 9.5	7.5 ± 2.7	82.5 ± 9.5	$0.479\ (0.480) \pm 0.008$
-0.3375	13.0 ± 1.5	88 ± 9.4	6.0 ± 2.4	82.0 ± 9.4	$0.484\ (0.481) \pm 0.008$
-0.3125	17.8 ± 1.7	121 ± 11.0	4.9 ± 2.2	116.1 ± 11.0	$0.499\ (0.496) \pm 0.008$
-0.2875	17.9 ± 1.7	117 ± 10.8	4.0 ± 2.0	113.0 ± 10.8	$0.482\ (0.480) \pm 0.008$
-0.2625	19.0 ± 1.8	124 ± 11.1	3.5 ± 1.9	120.5 ± 11.1	$0.485\ (0.482) \pm 0.008$
-0.2375	17.8 ± 1.7	117 ± 10.8	3.3 ± 1.8	113.7 ± 10.8	$0.491\ (0.487) \pm 0.008$
-0.2125	16.0 ± 1.6	111 ± 10.5	3.2 ± 1.8	107.8 ± 10.5	$0.517\ (0.513) \pm 0.008$
-0.1875	13.0 ± 1.5	86 ± 9.3	3.4 ± 1.8	82.7 ± 9.3	$0.488\ (0.485) \pm 0.008$
-0.1625	11.2 ± 1.4	71 ± 8.4	3.6 ± 1.9	67.4 ± 8.4	$0.463\ (0.460) \pm 0.008$
-0.1375	11.8 ± 1.4	77 ± 8.8	4.0 ± 2.0	73.0 ± 8.8	$0.469\ (0.473) \pm 0.008$
-0.1125	7.9 ± 1.2	54 ± 7.3	4.4 ± 2.1	49.6 ± 7.3	$0.476\ (0.477) \pm 0.008$
-0.0875	3.6 ± 0.8	27 ± 5.2	4.8 ± 2.2	22.2 ± 5.2	$0.461\ (0.467) \pm 0.008$
-0.0625	3.4 ± 0.8	26 ± 5.1	5.3 ± 2.3	20.7 ± 5.1	$0.448\ (0.459) \pm 0.008$
-0.0375	1.1 ± 0.6	13 ± 3.6	5.7 ± 2.4	7.3 ± 3.6	$0.462\ (0.497) \pm 0.008$
-0.0125	1.0 ± 0.5	13 ± 3.6	6.1 ± 2.5	6.9 ± 3.6	$0.465\ (0.531) \pm 0.008$
0.0125	1.0 ± 0.6	13 ± 3.6	6.4 ± 2.5	6.6 ± 3.6	$0.442\ (0.499) \pm 0.008$
0.0375	2.0 ± 0.7	19 ± 4.4	6.6 ± 2.6	12.4 ± 4.4	$0.445\ (0.477) \pm 0.007$
0.0625	1.7 ± 0.7	18 ± 4.2	6.7 ± 2.6	11.3 ± 4.2	$0.480\ (0.493) \pm 0.008$
0.0875	5.0 ± 1.0	39 ± 6.2	6.7 ± 2.6	32.3 ± 6.2	$0.490\ (0.496) \pm 0.008$
0.1125	6.9 ± 1.1	49 ± 7.0	6.6 ± 2.6	42.4 ± 7.0	$0.462\ (0.468) \pm 0.008$
0.1375	9.0 ± 1.3	62 ± 7.9	6.3 ± 2.5	55.6 ± 7.9	$0.469\ (0.469) \pm 0.008$
0.1625	14.6 ± 1.6	96 ± 9.8	6.0 ± 2.5	90.0 ± 9.8	$0.473\ (0.470) \pm 0.008$
0.1875	13.2 ± 1.5	89 ± 9.4	5.7 ± 2.4	83.3 ± 9.4	$0.482\ (0.482) \pm 0.008$
0.2125	17.2 ± 1.8	106 ± 10.3	5.3 ± 2.3	100.7 ± 10.3	$0.449\ (0.447) \pm 0.008$
0.2375	19.5 ± 1.9	118 ± 10.9	5.0 ± 2.2	113.0 ± 10.9	$0.446\ (0.443) \pm 0.008$
0.2625	16.5 ± 1.7	104 ± 10.2	4.9 ± 2.2	99.1 ± 10.2	$0.462\ (0.458) \pm 0.008$
0.2875	21.6 ± 2.0	133 ± 11.5	5.0 ± 2.2	128.0 ± 11.5	$0.453\ (0.452) \pm 0.008$
0.3125	18.3 ± 1.9	109 ± 10.4	5.5 ± 2.3	103.5 ± 10.4	$0.436\ (0.432) \pm 0.008$
0.3375	17.9 ± 1.9	105 ± 10.2	6.5 ± 2.5	98.5 ± 10.2	$0.420\ (0.419) \pm 0.007$
0.3625	16.4 ± 1.8	99 ± 9.9	8.0 ± 2.8	91.0 ± 9.9	$0.424\ (0.424) \pm 0.007$
0.3875	11.1 ± 1.6	67 ± 8.2	10.2 ± 3.2	56.8 ± 8.2	$0.387\ (0.391) \pm 0.007$
0.4125	8.6 ± 1.5	56 ± 7.5	13.2 ± 3.6	42.8 ± 7.5	$0.370\ (0.379) \pm 0.007$
0.4375	8.5 ± 1.6	59 ± 7.7	16.8 ± 4.1	42.2 ± 7.7	$0.365\ (0.377) \pm 0.007$
0.4625	7.6 ± 1.6	56 ± 7.5	21.0 ± 4.6	35.0 ± 7.5	$0.339\ (0.350) \pm 0.007$
0.4875	17.4 ± 2.5	95 ± 9.8	25.6 ± 5.1	69.4 ± 9.8	$0.298\ (0.303) \pm 0.006$
0.5125	32.9 ± 3.5	147 ± 12.1	30.1 ± 5.5	116.9 ± 12.1	$0.265\ (0.271) \pm 0.006$
0.5375	56.1 ± 5.0	196 ± 14.0	34.0 ± 5.8	162.0 ± 14.0	$0.218\ (0.220) \pm 0.005$
0.5625	85.4 ± 7.0	236 ± 15.4	36.3 ± 6.0	199.7 ± 15.4	$0.178\ (0.178) \pm 0.005$
0.5875	150.3 ± 11.1	292 ± 17.1	35.9 ± 6.0	256.1 ± 17.1	$0.132\ (0.130) \pm 0.004$

$\bar{p}p \to \pi^0\eta$ at $E_{cm} = 3384.8$ MeV ($\mathcal{L} = 3370.4\ 10^{31}\mathrm{s}^{-1}\mathrm{cm}^{-2}$)					
z	$d\sigma/dz$ (nb)	N_{tot}	N_{bkg}	$N_{\pi^0\pi^0}$	$a \times \epsilon$
-0.5875	144.6 ± 5.3	985 ± 31.4	41.0 ± 6.4	944.0 ± 31.4	$0.226\ (0.224) \pm 0.004$
-0.5625	86.3 ± 3.4	816 ± 28.6	47.1 ± 6.9	768.9 ± 28.6	$0.303\ (0.306) \pm 0.004$
-0.5375	52.5 ± 2.4	633 ± 25.2	47.9 ± 6.9	585.1 ± 25.2	$0.376\ (0.382) \pm 0.005$
-0.5125	31.8 ± 1.8	417 ± 20.4	45.5 ± 6.7	371.6 ± 20.4	$0.397\ (0.401) \pm 0.005$
-0.4875	18.7 ± 1.3	286 ± 16.9	41.2 ± 6.4	244.8 ± 16.9	$0.430\ (0.448) \pm 0.005$
-0.4625	12.1 ± 1.1	198 ± 14.1	36.2 ± 6.0	161.8 ± 14.1	$0.440\ (0.458) \pm 0.005$
-0.4375	8.6 ± 0.9	150 ± 12.2	31.1 ± 5.6	118.9 ± 12.2	$0.452\ (0.474) \pm 0.005$
-0.4125	9.8 ± 0.9	164 ± 12.8	26.4 ± 5.1	137.6 ± 12.8	$0.472\ (0.484) \pm 0.005$
-0.3875	12.0 ± 1.0	195 ± 14.0	22.2 ± 4.7	172.8 ± 14.0	$0.491\ (0.494) \pm 0.005$
-0.3625	14.0 ± 1.1	213 ± 14.6	18.8 ± 4.3	194.2 ± 14.6	$0.475\ (0.476) \pm 0.005$
-0.3375	16.2 ± 1.1	243 ± 15.6	16.0 ± 4.0	227.0 ± 15.6	$0.483\ (0.481) \pm 0.005$
-0.3125	17.4 ± 1.1	272 ± 16.5	13.9 ± 3.7	258.1 ± 16.5	$0.515\ (0.510) \pm 0.005$
-0.2875	19.6 ± 1.2	297 ± 17.2	12.4 ± 3.5	284.6 ± 17.2	$0.499\ (0.497) \pm 0.005$
-0.2625	18.9 ± 1.2	282 ± 16.8	11.3 ± 3.4	270.6 ± 16.8	$0.493\ (0.490) \pm 0.005$
-0.2375	19.2 ± 1.2	289 ± 17.0	10.7 ± 3.3	278.3 ± 17.0	$0.502\ (0.498) \pm 0.005$
-0.2125	17.9 ± 1.1	276 ± 16.6	10.3 ± 3.2	265.7 ± 16.6	$0.512\ (0.508) \pm 0.005$
-0.1875	15.5 ± 1.1	231 ± 15.2	10.1 ± 3.2	220.9 ± 15.2	$0.491\ (0.488) \pm 0.005$
-0.1625	11.5 ± 0.9	170 ± 13.0	10.1 ± 3.2	159.9 ± 13.0	$0.478\ (0.475) \pm 0.005$
-0.1375	10.7 ± 0.9	164 ± 12.8	10.2 ± 3.2	153.8 ± 12.8	$0.490\ (0.493) \pm 0.005$
-0.1125	8.0 ± 0.8	125 ± 11.2	10.3 ± 3.2	114.7 ± 11.2	$0.492\ (0.490) \pm 0.005$
-0.0875	6.4 ± 0.7	98 ± 9.9	10.5 ± 3.2	87.5 ± 9.9	$0.465\ (0.468) \pm 0.005$
-0.0625	2.7 ± 0.5	48 ± 6.9	10.7 ± 3.3	37.3 ± 6.9	$0.456\ (0.467) \pm 0.005$
-0.0375	1.4 ± 0.4	32 ± 5.7	11.0 ± 3.3	21.0 ± 5.7	$0.471\ (0.503) \pm 0.005$
-0.0125	1.0 ± 0.3	26 ± 5.1	11.2 ± 3.3	14.8 ± 5.1	$0.483\ (0.532) \pm 0.005$
0.0125	1.0 ± 0.3	26 ± 5.1	11.4 ± 3.4	14.6 ± 5.1	$0.460\ (0.505) \pm 0.005$
0.0375	1.4 ± 0.4	31 ± 5.6	11.7 ± 3.4	19.4 ± 5.6	$0.457\ (0.480) \pm 0.005$
0.0625	3.4 ± 0.5	61 ± 7.8	11.9 ± 3.4	49.1 ± 7.8	$0.481\ (0.490) \pm 0.005$
0.0875	4.5 ± 0.6	76 ± 8.7	12.1 ± 3.5	64.0 ± 8.7	$0.483\ (0.488) \pm 0.005$
0.1125	7.1 ± 0.8	109 ± 10.4	12.2 ± 3.5	96.8 ± 10.4	$0.465\ (0.470) \pm 0.005$
0.1375	11.9 ± 1.0	169 ± 13.0	12.4 ± 3.5	156.6 ± 13.0	$0.454\ (0.453) \pm 0.005$
0.1625	13.0 ± 1.0	193 ± 13.9	12.7 ± 3.6	180.3 ± 13.9	$0.478\ (0.477) \pm 0.005$
0.1875	17.2 ± 1.2	254 ± 15.9	13.0 ± 3.6	241.0 ± 15.9	$0.484\ (0.482) \pm 0.005$
0.2125	17.8 ± 1.2	251 ± 15.8	13.4 ± 3.7	237.6 ± 15.8	$0.460\ (0.458) \pm 0.005$
0.2375	17.6 ± 1.2	246 ± 15.7	14.1 ± 3.8	231.9 ± 15.7	$0.453\ (0.452) \pm 0.005$
0.2625	19.1 ± 1.2	275 ± 16.6	15.2 ± 3.9	259.8 ± 16.6	$0.469\ (0.466) \pm 0.005$
0.2875	18.0 ± 1.2	255 ± 16.0	16.7 ± 4.1	238.3 ± 16.0	$0.457\ (0.455) \pm 0.005$
0.3125	19.4 ± 1.3	259 ± 16.1	18.9 ± 4.3	240.1 ± 16.1	$0.427\ (0.424) \pm 0.005$
0.3375	16.2 ± 1.2	225 ± 15.0	21.9 ± 4.7	203.1 ± 15.0	$0.431\ (0.430) \pm 0.005$
0.3625	13.8 ± 1.1	201 ± 14.2	25.8 ± 5.1	175.2 ± 14.2	$0.433\ (0.434) \pm 0.005$
0.3875	12.7 ± 1.2	177 ± 13.3	30.7 ± 5.5	146.3 ± 13.3	$0.395\ (0.396) \pm 0.005$
0.4125	9.3 ± 1.1	141 ± 11.9	36.8 ± 6.1	104.2 ± 11.9	$0.379\ (0.387) \pm 0.005$
0.4375	8.8 ± 1.1	143 ± 12.0	43.9 ± 6.6	99.1 ± 12.0	$0.377\ (0.388) \pm 0.005$
0.4625	9.5 ± 1.2	148 ± 12.2	51.8 ± 7.2	96.2 ± 12.2	$0.336\ (0.346) \pm 0.004$
0.4875	19.6 ± 1.7	236 ± 15.4	60.3 ± 7.8	175.7 ± 15.4	$0.301\ (0.308) \pm 0.004$
0.5125	38.4 ± 2.5	374 ± 19.3	68.6 ± 8.3	305.4 ± 19.3	$0.269\ (0.273) \pm 0.004$
0.5375	59.8 ± 3.5	466 ± 21.6	75.7 ± 8.7	390.3 ± 21.6	$0.224\ (0.224) \pm 0.004$
0.5625	99.5 ± 5.0	600 ± 24.5	80.1 ± 8.9	519.9 ± 24.5	$0.179\ (0.179) \pm 0.003$
0.5875	135.4 ± 6.9	611 ± 24.7	79.7 ± 8.9	531.4 ± 24.7	$0.135\ (0.135) \pm 0.003$

$\bar{p}p \to \pi^0\eta$ at $E_{cm} = 3392.0$ MeV ($\mathcal{L} = 1431.1\ 10^{31}\mathrm{s}^{-1}\mathrm{cm}^{-2}$)					
z	$d\sigma/dz\,$(nb)	N_{tot}	N_{bkg}	$N_{\pi^0\pi^0}$	$a \times \epsilon$
-0.5875	122.2 ± 7.6	350 ± 18.7	20.8 ± 4.6	329.2 ± 18.7	$0.221\ (0.219) \pm 0.006$
-0.5625	78.3 ± 5.0	320 ± 17.9	22.9 ± 4.8	297.1 ± 17.9	$0.307\ (0.308) \pm 0.007$
-0.5375	43.8 ± 3.4	223 ± 14.9	22.3 ± 4.7	200.7 ± 14.9	$0.366\ (0.372) \pm 0.007$
-0.5125	29.0 ± 2.6	163 ± 12.8	20.1 ± 4.5	142.9 ± 12.8	$0.397\ (0.401) \pm 0.008$
-0.4875	17.6 ± 2.0	113 ± 10.6	17.1 ± 4.1	95.9 ± 10.6	$0.422\ (0.443) \pm 0.008$
-0.4625	10.7 ± 1.5	75 ± 8.7	14.0 ± 3.7	61.0 ± 8.7	$0.442\ (0.465) \pm 0.008$
-0.4375	8.5 ± 1.4	60 ± 7.8	11.0 ± 3.3	49.0 ± 7.8	$0.453\ (0.469) \pm 0.008$
-0.4125	6.4 ± 1.2	46 ± 6.8	8.4 ± 2.9	37.6 ± 6.8	$0.467\ (0.477) \pm 0.008$
-0.3875	11.8 ± 1.5	76 ± 8.7	6.2 ± 2.5	69.8 ± 8.7	$0.478\ (0.480) \pm 0.008$
-0.3625	15.7 ± 1.7	96 ± 9.8	4.5 ± 2.1	91.5 ± 9.8	$0.474\ (0.474) \pm 0.008$
-0.3375	12.7 ± 1.5	78 ± 8.8	3.3 ± 1.8	74.7 ± 8.8	$0.478\ (0.476) \pm 0.008$
-0.3125	16.5 ± 1.7	105 ± 10.2	2.5 ± 1.6	102.5 ± 10.2	$0.510\ (0.504) \pm 0.009$
-0.2875	17.7 ± 1.8	109 ± 10.4	2.0 ± 1.4	107.0 ± 10.4	$0.490\ (0.490) \pm 0.008$
-0.2625	19.9 ± 1.9	121 ± 11.0	1.8 ± 1.4	119.2 ± 11.0	$0.492\ (0.487) \pm 0.008$
-0.2375	19.4 ± 1.8	121 ± 11.0	1.9 ± 1.4	119.2 ± 11.0	$0.500\ (0.499) \pm 0.008$
-0.2125	16.0 ± 1.7	100 ± 10.0	2.0 ± 1.4	98.0 ± 10.0	$0.504\ (0.496) \pm 0.009$
-0.1875	15.9 ± 1.7	95 ± 9.8	2.3 ± 1.5	92.7 ± 9.8	$0.474\ (0.475) \pm 0.008$
-0.1625	14.5 ± 1.6	87 ± 9.3	2.6 ± 1.6	84.4 ± 9.3	$0.478\ (0.473) \pm 0.008$
-0.1375	10.0 ± 1.3	63 ± 7.9	3.0 ± 1.7	60.0 ± 7.9	$0.487\ (0.487) \pm 0.008$
-0.1125	6.7 ± 1.1	43 ± 6.6	3.5 ± 1.9	39.5 ± 6.6	$0.479\ (0.478) \pm 0.008$
-0.0875	5.2 ± 1.0	33 ± 5.7	4.0 ± 2.0	29.0 ± 5.7	$0.453\ (0.456) \pm 0.008$
-0.0625	1.7 ± 0.7	14 ± 3.7	4.5 ± 2.1	9.5 ± 3.7	$0.438\ (0.447) \pm 0.008$
-0.0375	1.2 ± 0.6	13 ± 3.6	5.0 ± 2.2	8.1 ± 3.6	$0.473\ (0.527) \pm 0.008$
-0.0125	0.0 ± 0.2	4 ± 2.0	4.0 ± 2.0	0.0 ± 2.0	$0.481\ (0.842) \pm 0.008$
0.0125	0.1 ± 0.3	7 ± 2.6	5.9 ± 2.4	1.1 ± 2.6	$0.436\ (0.765) \pm 0.008$
0.0375	1.1 ± 0.6	13 ± 3.6	6.2 ± 2.5	6.8 ± 3.6	$0.463\ (0.512) \pm 0.008$
0.0625	2.4 ± 0.7	21 ± 4.6	6.5 ± 2.6	14.4 ± 4.6	$0.482\ (0.498) \pm 0.008$
0.0875	2.0 ± 0.7	19 ± 4.4	6.8 ± 2.6	12.2 ± 4.4	$0.479\ (0.486) \pm 0.008$
0.1125	5.9 ± 1.1	39 ± 6.2	6.8 ± 2.6	32.1 ± 6.2	$0.442\ (0.445) \pm 0.008$
0.1375	6.9 ± 1.2	45 ± 6.7	6.8 ± 2.6	38.2 ± 6.7	$0.450\ (0.451) \pm 0.008$
0.1625	14.0 ± 1.6	89 ± 9.4	6.7 ± 2.6	82.3 ± 9.4	$0.477\ (0.477) \pm 0.008$
0.1875	13.6 ± 1.6	86 ± 9.3	6.4 ± 2.5	79.6 ± 9.3	$0.476\ (0.474) \pm 0.008$
0.2125	13.0 ± 1.6	77 ± 8.8	6.1 ± 2.5	70.9 ± 8.8	$0.442\ (0.443) \pm 0.008$
0.2375	17.2 ± 1.8	101 ± 10.1	5.8 ± 2.4	95.2 ± 10.1	$0.455\ (0.449) \pm 0.008$
0.2625	18.4 ± 1.8	115 ± 10.7	5.5 ± 2.4	109.5 ± 10.7	$0.484\ (0.483) \pm 0.008$
0.2875	18.6 ± 1.9	108 ± 10.4	5.5 ± 2.3	102.5 ± 10.4	$0.450\ (0.447) \pm 0.008$
0.3125	20.0 ± 2.1	107 ± 10.3	5.7 ± 2.4	101.3 ± 10.3	$0.414\ (0.412) \pm 0.008$
0.3375	18.2 ± 2.0	101 ± 10.1	6.3 ± 2.5	94.7 ± 10.1	$0.424\ (0.423) \pm 0.008$
0.3625	12.6 ± 1.6	75 ± 8.7	7.6 ± 2.8	67.4 ± 8.7	$0.434\ (0.433) \pm 0.008$
0.3875	13.9 ± 1.8	76 ± 8.7	9.5 ± 3.1	66.5 ± 8.7	$0.389\ (0.390) \pm 0.007$
0.4125	13.0 ± 1.8	73 ± 8.5	12.2 ± 3.5	60.8 ± 8.5	$0.374\ (0.379) \pm 0.007$
0.4375	8.8 ± 1.6	57 ± 7.5	15.8 ± 4.0	41.2 ± 7.5	$0.370\ (0.382) \pm 0.007$
0.4625	7.4 ± 1.7	51 ± 7.1	20.1 ± 4.5	30.9 ± 7.1	$0.327\ (0.337) \pm 0.007$
0.4875	22.5 ± 2.8	110 ± 10.5	25.0 ± 5.0	85.0 ± 10.5	$0.298\ (0.307) \pm 0.006$
0.5125	27.9 ± 3.4	125 ± 11.2	30.1 ± 5.5	94.9 ± 11.2	$0.271\ (0.276) \pm 0.006$
0.5375	48.3 ± 4.9	168 ± 13.0	34.8 ± 5.9	133.2 ± 13.0	$0.221\ (0.224) \pm 0.006$
0.5625	83.5 ± 7.2	222 ± 14.9	38.0 ± 6.2	184.0 ± 14.9	$0.177\ (0.179) \pm 0.005$
0.5875	159.4 ± 12.1	288 ± 17.0	38.4 ± 6.2	249.6 ± 17.0	$0.128\ (0.127) \pm 0.004$

$\bar{p}p \to \pi^0\eta$ at $E_{cm} = 3400.1$ MeV ($\mathcal{L} = 1482.8\ 10^{31}\text{s}^{-1}\text{cm}^{-2}$)					
z	$d\sigma/dz$ (nb)	N_{tot}	N_{bkg}	$N_{\pi^0\pi^0}$	$a \times \epsilon$
-0.5875	111.4 ± 6.6	364 ± 19.1	19.7 ± 4.4	344.3 ± 19.1	$0.246\ (0.244) \pm 0.005$
-0.5625	72.0 ± 4.4	329 ± 18.1	21.5 ± 4.6	307.5 ± 18.1	$0.333\ (0.337) \pm 0.006$
-0.5375	47.7 ± 3.3	258 ± 16.1	20.6 ± 4.5	237.4 ± 16.1	$0.384\ (0.392) \pm 0.006$
-0.5125	27.1 ± 2.4	164 ± 12.8	18.4 ± 4.3	145.6 ± 12.8	$0.415\ (0.424) \pm 0.007$
-0.4875	15.4 ± 1.8	106 ± 10.3	15.5 ± 3.9	90.5 ± 10.3	$0.449\ (0.463) \pm 0.007$
-0.4625	11.1 ± 1.5	80 ± 8.9	12.7 ± 3.6	67.3 ± 8.9	$0.459\ (0.476) \pm 0.007$
-0.4375	8.5 ± 1.3	62 ± 7.9	10.2 ± 3.2	51.8 ± 7.9	$0.469\ (0.480) \pm 0.007$
-0.4125	9.3 ± 1.3	67 ± 8.2	8.1 ± 2.9	58.9 ± 8.2	$0.488\ (0.500) \pm 0.007$
-0.3875	11.0 ± 1.4	78 ± 8.8	6.6 ± 2.6	71.4 ± 8.8	$0.510\ (0.511) \pm 0.007$
-0.3625	13.6 ± 1.5	92 ± 9.6	5.6 ± 2.4	86.4 ± 9.6	$0.501\ (0.502) \pm 0.007$
-0.3375	16.1 ± 1.6	108 ± 10.4	5.0 ± 2.2	103.0 ± 10.4	$0.504\ (0.505) \pm 0.007$
-0.3125	19.7 ± 1.8	136 ± 11.7	4.8 ± 2.2	131.2 ± 11.7	$0.531\ (0.526) \pm 0.008$
-0.2875	16.6 ± 1.7	112 ± 10.6	4.8 ± 2.2	107.2 ± 10.6	$0.514\ (0.510) \pm 0.007$
-0.2625	13.3 ± 1.5	92 ± 9.6	4.9 ± 2.2	87.1 ± 9.6	$0.517\ (0.515) \pm 0.007$
-0.2375	17.6 ± 1.7	122 ± 11.1	5.1 ± 2.3	116.9 ± 11.1	$0.527\ (0.524) \pm 0.007$
-0.2125	13.8 ± 1.5	98 ± 9.9	5.3 ± 2.3	92.7 ± 9.9	$0.537\ (0.531) \pm 0.008$
-0.1875	15.8 ± 1.6	109 ± 10.4	5.5 ± 2.4	103.5 ± 10.4	$0.522\ (0.517) \pm 0.008$
-0.1625	13.6 ± 1.5	92 ± 9.6	5.7 ± 2.4	86.3 ± 9.6	$0.504\ (0.502) \pm 0.007$
-0.1375	9.1 ± 1.2	65 ± 8.1	5.7 ± 2.4	59.3 ± 8.1	$0.514\ (0.515) \pm 0.007$
-0.1125	8.8 ± 1.2	62 ± 7.9	5.8 ± 2.4	56.2 ± 7.9	$0.502\ (0.502) \pm 0.007$
-0.0875	3.6 ± 0.8	28 ± 5.3	5.7 ± 2.4	22.3 ± 5.3	$0.484\ (0.492) \pm 0.007$
-0.0625	2.8 ± 0.8	23 ± 4.8	5.7 ± 2.4	17.3 ± 4.8	$0.477\ (0.487) \pm 0.007$
-0.0375	0.6 ± 0.4	10 ± 3.2	5.6 ± 2.4	4.4 ± 3.2	$0.492\ (0.557) \pm 0.007$
-0.0125	0.2 ± 0.2	8 ± 2.8	5.6 ± 2.4	2.4 ± 2.8	$0.488\ (0.979) \pm 0.007$
0.0125	0.0 ± 0.2	6 ± 2.5	5.5 ± 2.3	0.5 ± 2.5	$0.470\ (0.928) \pm 0.007$
0.0375	0.5 ± 0.4	9 ± 3.0	5.5 ± 2.3	3.5 ± 3.0	$0.478\ (0.527) \pm 0.007$
0.0625	2.2 ± 0.7	20 ± 4.5	5.4 ± 2.3	14.6 ± 4.5	$0.507\ (0.516) \pm 0.007$
0.0875	3.7 ± 0.8	29 ± 5.4	5.4 ± 2.3	23.6 ± 5.4	$0.500\ (0.509) \pm 0.007$
0.1125	7.3 ± 1.2	50 ± 7.1	5.3 ± 2.3	44.7 ± 7.1	$0.484\ (0.484) \pm 0.007$
0.1375	9.9 ± 1.3	65 ± 8.1	5.2 ± 2.3	59.8 ± 8.1	$0.476\ (0.476) \pm 0.007$
0.1625	13.7 ± 1.5	93 ± 9.6	5.1 ± 2.3	87.9 ± 9.6	$0.507\ (0.506) \pm 0.007$
0.1875	14.6 ± 1.6	98 ± 9.9	5.0 ± 2.2	93.0 ± 9.9	$0.506\ (0.504) \pm 0.007$
0.2125	16.9 ± 1.8	104 ± 10.2	4.8 ± 2.2	99.2 ± 10.2	$0.461\ (0.462) \pm 0.007$
0.2375	13.8 ± 1.6	88 ± 9.4	4.7 ± 2.2	83.3 ± 9.4	$0.481\ (0.476) \pm 0.007$
0.2625	23.0 ± 2.0	150 ± 12.2	4.7 ± 2.2	145.3 ± 12.2	$0.500\ (0.497) \pm 0.007$
0.2875	20.0 ± 1.9	123 ± 11.1	4.8 ± 2.2	118.2 ± 11.1	$0.467\ (0.465) \pm 0.007$
0.3125	17.3 ± 1.8	105 ± 10.2	5.2 ± 2.3	99.8 ± 10.2	$0.456\ (0.454) \pm 0.007$
0.3375	16.0 ± 1.8	97 ± 9.8	5.9 ± 2.4	91.1 ± 9.8	$0.450\ (0.448) \pm 0.007$
0.3625	16.6 ± 1.8	102 ± 10.1	7.1 ± 2.7	94.9 ± 10.1	$0.449\ (0.451) \pm 0.007$
0.3875	13.3 ± 1.7	79 ± 8.9	8.9 ± 3.0	70.1 ± 8.9	$0.413\ (0.414) \pm 0.007$
0.4125	10.1 ± 1.5	64 ± 8.0	11.3 ± 3.4	52.7 ± 8.0	$0.405\ (0.411) \pm 0.007$
0.4375	10.2 ± 1.6	66 ± 8.1	14.5 ± 3.8	51.5 ± 8.1	$0.391\ (0.399) \pm 0.006$
0.4625	9.6 ± 1.7	63 ± 7.9	18.3 ± 4.3	44.7 ± 7.9	$0.356\ (0.366) \pm 0.006$
0.4875	16.6 ± 2.3	91 ± 9.5	22.5 ± 4.7	68.5 ± 9.5	$0.319\ (0.326) \pm 0.006$
0.5125	30.8 ± 3.3	141 ± 11.9	26.9 ± 5.2	114.1 ± 11.9	$0.288\ (0.292) \pm 0.006$
0.5375	50.2 ± 4.6	181 ± 13.4	30.9 ± 5.6	150.2 ± 13.4	$0.234\ (0.236) \pm 0.005$
0.5625	80.9 ± 6.4	236 ± 15.4	33.4 ± 5.8	202.6 ± 15.4	$0.197\ (0.197) \pm 0.005$
0.5875	140.7 ± 9.7	310 ± 17.6	33.2 ± 5.8	276.8 ± 17.6	$0.156\ (0.155) \pm 0.004$

$\bar{p}p \to \pi^0\eta$ at E_{cm} = 3406.1 MeV ($\mathcal{L} = 2680.5\ 10^{31}\mathrm{s}^{-1}\mathrm{cm}^{-2}$)					
z	$d\sigma/dz$ (nb)	N_{tot}	N_{bkg}	$N_{\pi^0\pi^0}$	$a \times \epsilon$
-0.5875	115.5 ± 5.2	670 ± 25.9	39.0 ± 6.2	631.0 ± 25.9	$0.239\ (0.236) \pm 0.004$
-0.5625	74.6 ± 3.5	585 ± 24.2	41.5 ± 6.4	543.5 ± 24.2	$0.311\ (0.315) \pm 0.005$
-0.5375	45.6 ± 2.5	440 ± 21.0	39.4 ± 6.3	400.6 ± 21.0	$0.374\ (0.380) \pm 0.005$
-0.5125	24.1 ± 1.7	265 ± 16.3	35.0 ± 5.9	230.0 ± 16.3	$0.403\ (0.413) \pm 0.005$
-0.4875	14.0 ± 1.3	175 ± 13.2	29.6 ± 5.4	145.4 ± 13.2	$0.432\ (0.449) \pm 0.006$
-0.4625	9.4 ± 1.0	127 ± 11.3	24.3 ± 4.9	102.7 ± 11.3	$0.455\ (0.472) \pm 0.006$
-0.4375	8.1 ± 1.0	108 ± 10.4	19.6 ± 4.4	88.4 ± 10.4	$0.453\ (0.469) \pm 0.006$
-0.4125	7.2 ± 0.9	97 ± 9.8	15.8 ± 4.0	81.2 ± 9.8	$0.481\ (0.491) \pm 0.006$
-0.3875	10.2 ± 1.0	126 ± 11.2	12.8 ± 3.6	113.2 ± 11.2	$0.478\ (0.480) \pm 0.006$
-0.3625	13.3 ± 1.2	156 ± 12.5	10.8 ± 3.3	145.2 ± 12.5	$0.471\ (0.471) \pm 0.006$
-0.3375	13.3 ± 1.1	160 ± 12.7	9.4 ± 3.1	150.6 ± 12.7	$0.491\ (0.489) \pm 0.006$
-0.3125	15.7 ± 1.2	196 ± 14.0	8.7 ± 2.9	187.3 ± 14.0	$0.521\ (0.515) \pm 0.006$
-0.2875	14.2 ± 1.2	171 ± 13.1	8.3 ± 2.9	162.7 ± 13.1	$0.497\ (0.495) \pm 0.006$
-0.2625	15.8 ± 1.2	185 ± 13.6	8.2 ± 2.9	176.8 ± 13.6	$0.489\ (0.485) \pm 0.006$
-0.2375	17.3 ± 1.3	212 ± 14.6	8.3 ± 2.9	203.7 ± 14.6	$0.512\ (0.510) \pm 0.006$
-0.2125	13.2 ± 1.1	162 ± 12.7	8.5 ± 2.9	153.5 ± 12.7	$0.508\ (0.504) \pm 0.006$
-0.1875	11.0 ± 1.0	130 ± 11.4	8.7 ± 2.9	121.3 ± 11.4	$0.478\ (0.477) \pm 0.006$
-0.1625	10.3 ± 1.0	123 ± 11.1	8.8 ± 3.0	114.2 ± 11.1	$0.484\ (0.480) \pm 0.006$
-0.1375	7.0 ± 0.8	90 ± 9.5	9.0 ± 3.0	81.0 ± 9.5	$0.495\ (0.497) \pm 0.006$
-0.1125	6.5 ± 0.8	82 ± 9.1	9.2 ± 3.0	72.8 ± 9.1	$0.488\ (0.488) \pm 0.006$
-0.0875	4.3 ± 0.7	56 ± 7.5	9.5 ± 3.1	46.5 ± 7.5	$0.471\ (0.471) \pm 0.006$
-0.0625	2.1 ± 0.5	32 ± 5.7	9.7 ± 3.1	22.3 ± 5.7	$0.448\ (0.462) \pm 0.006$
-0.0375	1.2 ± 0.4	25 ± 5.0	10.1 ± 3.2	14.9 ± 5.0	$0.484\ (0.523) \pm 0.006$
-0.0125	0.0 ± 0.2	8 ± 2.8	8.0 ± 2.8	0.0 ± 2.8	$0.485\ (0.572) \pm 0.006$
0.0125	0.5 ± 0.3	17 ± 4.1	10.8 ± 3.3	6.2 ± 4.1	$0.458\ (0.538) \pm 0.006$
0.0375	1.3 ± 0.4	26 ± 5.1	11.2 ± 3.3	14.8 ± 5.1	$0.460\ (0.492) \pm 0.006$
0.0625	2.8 ± 0.6	44 ± 6.6	11.5 ± 3.4	32.5 ± 6.6	$0.493\ (0.498) \pm 0.006$
0.0875	2.5 ± 0.6	40 ± 6.3	11.7 ± 3.4	28.3 ± 6.3	$0.482\ (0.492) \pm 0.006$
0.1125	6.2 ± 0.8	78 ± 8.8	11.8 ± 3.4	66.2 ± 8.8	$0.457\ (0.462) \pm 0.006$
0.1375	9.2 ± 1.0	112 ± 10.6	11.7 ± 3.4	100.3 ± 10.6	$0.473\ (0.472) \pm 0.006$
0.1625	9.6 ± 1.0	122 ± 11.1	11.4 ± 3.4	110.6 ± 11.1	$0.497\ (0.496) \pm 0.006$
0.1875	13.6 ± 1.2	160 ± 12.7	10.9 ± 3.3	149.1 ± 12.7	$0.475\ (0.473) \pm 0.006$
0.2125	15.3 ± 1.2	173 ± 13.2	10.2 ± 3.2	162.8 ± 13.2	$0.463\ (0.462) \pm 0.006$
0.2375	14.5 ± 1.2	162 ± 12.7	9.5 ± 3.1	152.5 ± 12.7	$0.458\ (0.455) \pm 0.006$
0.2625	16.1 ± 1.3	187 ± 13.7	8.8 ± 3.0	178.2 ± 13.7	$0.482\ (0.479) \pm 0.006$
0.2875	15.3 ± 1.3	167 ± 12.9	8.4 ± 2.9	158.6 ± 12.9	$0.452\ (0.450) \pm 0.006$
0.3125	15.6 ± 1.3	164 ± 12.8	8.5 ± 2.9	155.5 ± 12.8	$0.434\ (0.431) \pm 0.006$
0.3375	14.7 ± 1.2	161 ± 12.7	9.4 ± 3.1	151.6 ± 12.7	$0.447\ (0.445) \pm 0.006$
0.3625	14.2 ± 1.3	152 ± 12.3	11.3 ± 3.4	140.7 ± 12.3	$0.428\ (0.428) \pm 0.006$
0.3875	11.1 ± 1.2	117 ± 10.8	14.6 ± 3.8	102.4 ± 10.8	$0.397\ (0.399) \pm 0.005$
0.4125	9.2 ± 1.1	101 ± 10.1	19.5 ± 4.4	81.5 ± 10.1	$0.378\ (0.384) \pm 0.005$
0.4375	8.3 ± 1.1	102 ± 10.1	26.0 ± 5.1	76.0 ± 10.1	$0.385\ (0.395) \pm 0.005$
0.4625	10.1 ± 1.3	116 ± 10.8	34.1 ± 5.8	81.9 ± 10.8	$0.341\ (0.352) \pm 0.005$
0.4875	12.9 ± 1.6	139 ± 11.8	43.3 ± 6.6	95.7 ± 11.8	$0.312\ (0.321) \pm 0.005$
0.5125	28.0 ± 2.4	238 ± 15.4	52.9 ± 7.3	185.1 ± 15.4	$0.280\ (0.286) \pm 0.004$
0.5375	42.5 ± 3.2	293 ± 17.1	61.5 ± 7.8	231.5 ± 17.1	$0.235\ (0.235) \pm 0.004$
0.5625	78.5 ± 4.7	430 ± 20.7	67.1 ± 8.2	362.9 ± 20.7	$0.198\ (0.200) \pm 0.004$
0.5875	128.2 ± 7.3	489 ± 22.1	66.6 ± 8.2	422.4 ± 22.1	$0.144\ (0.143) \pm 0.003$

$\bar{p}p \to \pi^0\eta$ at $E_{cm} = 3409.1$ MeV ($\mathcal{L} = 1134.5\ 10^{31}\mathrm{s}^{-1}\mathrm{cm}^{-2}$)					
z	$d\sigma/dz$ (nb)	N_{tot}	N_{bkg}	$N_{\pi^0\pi^0}$	$a \times \epsilon$
-0.5875	119.6 ± 7.7	307 ± 17.5	17.0 ± 4.1	290.0 ± 17.5	0.251 $(0.250) \pm 0.005$
-0.5625	72.6 ± 5.0	259 ± 16.1	17.6 ± 4.2	241.4 ± 16.1	0.338 $(0.342) \pm 0.006$
-0.5375	39.7 ± 3.4	176 ± 13.3	16.2 ± 4.0	159.8 ± 13.3	0.410 $(0.414) \pm 0.007$
-0.5125	25.4 ± 2.6	122 ± 11.1	13.9 ± 3.7	108.1 ± 11.1	0.430 $(0.438) \pm 0.007$
-0.4875	19.7 ± 2.2	102 ± 10.1	11.3 ± 3.4	90.7 ± 10.1	0.456 $(0.473) \pm 0.007$
-0.4625	10.2 ± 1.6	58 ± 7.6	8.8 ± 3.0	49.2 ± 7.6	0.474 $(0.495) \pm 0.007$
-0.4375	8.1 ± 1.4	46 ± 6.8	6.7 ± 2.6	39.3 ± 6.8	0.487 $(0.499) \pm 0.008$
-0.4125	11.9 ± 1.6	65 ± 8.1	5.1 ± 2.3	59.9 ± 8.1	0.509 $(0.520) \pm 0.008$
-0.3875	8.3 ± 1.3	46 ± 6.8	4.0 ± 2.0	42.0 ± 6.8	0.520 $(0.522) \pm 0.008$
-0.3625	13.7 ± 1.7	72 ± 8.5	3.3 ± 1.8	68.7 ± 8.5	0.514 $(0.517) \pm 0.008$
-0.3375	13.0 ± 1.6	70 ± 8.4	3.0 ± 1.7	67.0 ± 8.4	0.534 $(0.531) \pm 0.008$
-0.3125	13.9 ± 1.7	76 ± 8.7	2.9 ± 1.7	73.1 ± 8.7	0.545 $(0.542) \pm 0.008$
-0.2875	16.1 ± 1.8	83 ± 9.1	3.0 ± 1.7	80.0 ± 9.1	0.516 $(0.513) \pm 0.008$
-0.2625	17.2 ± 1.9	91 ± 9.5	3.2 ± 1.8	87.8 ± 9.5	0.529 $(0.526) \pm 0.008$
-0.2375	14.0 ± 1.7	77 ± 8.8	3.4 ± 1.8	73.6 ± 8.8	0.542 $(0.539) \pm 0.008$
-0.2125	13.6 ± 1.7	74 ± 8.6	3.6 ± 1.9	70.4 ± 8.6	0.536 $(0.532) \pm 0.008$
-0.1875	13.1 ± 1.6	72 ± 8.5	3.7 ± 1.9	68.3 ± 8.5	0.539 $(0.535) \pm 0.008$
-0.1625	10.4 ± 1.5	56 ± 7.5	3.8 ± 2.0	52.2 ± 7.5	0.516 $(0.516) \pm 0.008$
-0.1375	8.4 ± 1.3	48 ± 6.9	3.8 ± 2.0	44.2 ± 6.9	0.541 $(0.541) \pm 0.008$
-0.1125	5.2 ± 1.1	30 ± 5.5	3.8 ± 2.0	26.2 ± 5.5	0.515 $(0.515) \pm 0.008$
-0.0875	2.8 ± 0.9	18 ± 4.2	3.8 ± 2.0	14.2 ± 4.2	0.510 $(0.513) \pm 0.008$
-0.0625	2.3 ± 0.8	15 ± 3.9	3.8 ± 2.0	11.2 ± 3.9	0.477 $(0.492) \pm 0.008$
-0.0375	0.9 ± 0.5	9 ± 3.0	3.8 ± 2.0	5.2 ± 3.0	0.520 $(0.569) \pm 0.008$
-0.0125	0.3 ± 0.4	6 ± 2.5	3.9 ± 2.0	2.1 ± 2.5	0.495 $(0.649) \pm 0.008$
0.0125	0.5 ± 0.4	7 ± 2.6	4.0 ± 2.0	3.0 ± 2.6	0.490 $(0.627) \pm 0.007$
0.0375	0.9 ± 0.6	9 ± 3.0	4.2 ± 2.0	4.8 ± 3.0	0.497 $(0.541) \pm 0.008$
0.0625	1.1 ± 0.6	10 ± 3.2	4.4 ± 2.1	5.6 ± 3.2	0.520 $(0.537) \pm 0.008$
0.0875	3.0 ± 0.9	20 ± 4.5	4.6 ± 2.1	15.4 ± 4.5	0.523 $(0.529) \pm 0.008$
0.1125	8.5 ± 1.4	47 ± 6.9	4.8 ± 2.2	42.2 ± 6.9	0.499 $(0.508) \pm 0.008$
0.1375	8.0 ± 1.4	44 ± 6.6	5.0 ± 2.2	39.0 ± 6.6	0.503 $(0.504) \pm 0.008$
0.1625	7.8 ± 1.3	45 ± 6.7	5.2 ± 2.3	39.8 ± 6.7	0.523 $(0.523) \pm 0.008$
0.1875	12.5 ± 1.7	66 ± 8.1	5.3 ± 2.3	60.7 ± 8.1	0.502 $(0.500) \pm 0.008$
0.2125	14.5 ± 1.8	76 ± 8.7	5.3 ± 2.3	70.7 ± 8.7	0.503 $(0.503) \pm 0.008$
0.2375	17.3 ± 2.0	88 ± 9.4	5.3 ± 2.3	82.7 ± 9.4	0.497 $(0.492) \pm 0.008$
0.2625	16.6 ± 1.9	89 ± 9.4	5.3 ± 2.3	83.7 ± 9.4	0.518 $(0.518) \pm 0.008$
0.2875	17.2 ± 2.0	87 ± 9.3	5.4 ± 2.3	81.6 ± 9.3	0.493 $(0.487) \pm 0.008$
0.3125	20.5 ± 2.2	98 ± 9.9	5.5 ± 2.3	92.5 ± 9.9	0.465 $(0.465) \pm 0.007$
0.3375	14.3 ± 1.9	71 ± 8.4	5.8 ± 2.4	65.2 ± 8.4	0.470 $(0.469) \pm 0.007$
0.3625	14.0 ± 1.8	71 ± 8.4	6.5 ± 2.5	64.5 ± 8.4	0.472 $(0.474) \pm 0.007$
0.3875	13.6 ± 1.9	65 ± 8.1	7.6 ± 2.7	57.4 ± 8.1	0.433 $(0.435) \pm 0.007$
0.4125	13.7 ± 2.0	63 ± 7.9	9.1 ± 3.0	53.9 ± 7.9	0.400 $(0.406) \pm 0.007$
0.4375	9.1 ± 1.7	49 ± 7.0	11.2 ± 3.4	37.8 ± 7.0	0.415 $(0.426) \pm 0.007$
0.4625	8.0 ± 1.8	43 ± 6.6	13.9 ± 3.7	29.1 ± 6.6	0.361 $(0.371) \pm 0.006$
0.4875	22.4 ± 2.9	90 ± 9.5	17.1 ± 4.1	72.9 ± 9.5	0.330 $(0.335) \pm 0.006$
0.5125	25.5 ± 3.3	96 ± 9.8	20.5 ± 4.5	75.5 ± 9.8	0.299 $(0.305) \pm 0.006$
0.5375	64.4 ± 5.7	181 ± 13.4	23.8 ± 4.9	157.2 ± 13.4	0.249 $(0.251) \pm 0.005$
0.5625	83.2 ± 7.2	194 ± 13.9	26.2 ± 5.1	167.8 ± 13.9	0.207 $(0.208) \pm 0.005$
0.5875	125.6 ± 10.4	216 ± 14.7	26.7 ± 5.2	189.3 ± 14.7	0.157 $(0.155) \pm 0.004$

$\bar{p}p \to \pi^0\eta$ at $E_{cm} = 3410.3$ MeV ($\mathcal{L} = 1596.6\ 10^{31}\mathrm{s}^{-1}\mathrm{cm}^{-2}$)					
z	$d\sigma/dz$ (nb)	N_{tot}	N_{bkg}	$N_{\pi^0\pi^0}$	$a \times \epsilon$
-0.5875	113.6 ± 6.5	395 ± 19.9	18.6 ± 4.3	376.4 ± 19.9	$0.242\ (0.242) \pm 0.005$
-0.5625	76.8 ± 4.6	354 ± 18.8	21.2 ± 4.6	332.8 ± 18.8	$0.312\ (0.317) \pm 0.006$
-0.5375	41.4 ± 3.1	234 ± 15.3	21.3 ± 4.6	212.7 ± 15.3	$0.366\ (0.376) \pm 0.007$
-0.5125	23.4 ± 2.3	148 ± 12.2	19.9 ± 4.5	128.2 ± 12.2	$0.394\ (0.401) \pm 0.007$
-0.4875	14.7 ± 1.7	109 ± 10.4	17.7 ± 4.2	91.3 ± 10.4	$0.434\ (0.455) \pm 0.007$
-0.4625	11.2 ± 1.5	85 ± 9.2	15.2 ± 3.9	69.8 ± 9.2	$0.439\ (0.454) \pm 0.007$
-0.4375	7.6 ± 1.2	62 ± 7.9	12.8 ± 3.6	49.2 ± 7.9	$0.457\ (0.470) \pm 0.008$
-0.4125	9.4 ± 1.3	73 ± 8.5	10.6 ± 3.3	62.4 ± 8.5	$0.477\ (0.486) \pm 0.008$
-0.3875	12.5 ± 1.5	91 ± 9.5	8.8 ± 3.0	82.2 ± 9.5	$0.477\ (0.482) \pm 0.008$
-0.3625	11.6 ± 1.4	82 ± 9.1	7.4 ± 2.7	74.6 ± 9.1	$0.473\ (0.471) \pm 0.008$
-0.3375	14.0 ± 1.5	98 ± 9.9	6.4 ± 2.5	91.6 ± 9.9	$0.482\ (0.479) \pm 0.008$
-0.3125	15.5 ± 1.6	113 ± 10.6	5.7 ± 2.4	107.3 ± 10.6	$0.505\ (0.505) \pm 0.008$
-0.2875	14.2 ± 1.5	100 ± 10.0	5.2 ± 2.3	94.8 ± 10.0	$0.493\ (0.487) \pm 0.008$
-0.2625	16.8 ± 1.7	117 ± 10.8	5.0 ± 2.2	112.0 ± 10.8	$0.486\ (0.485) \pm 0.008$
-0.2375	15.9 ± 1.5	118 ± 10.9	5.0 ± 2.2	113.0 ± 10.9	$0.523\ (0.520) \pm 0.008$
-0.2125	14.8 ± 1.5	106 ± 10.3	5.1 ± 2.2	100.9 ± 10.3	$0.504\ (0.500) \pm 0.008$
-0.1875	14.7 ± 1.6	97 ± 9.8	5.2 ± 2.3	91.8 ± 9.8	$0.456\ (0.455) \pm 0.007$
-0.1625	8.8 ± 1.2	63 ± 7.9	5.3 ± 2.3	57.7 ± 7.9	$0.477\ (0.477) \pm 0.008$
-0.1375	8.2 ± 1.2	62 ± 7.9	5.5 ± 2.3	56.5 ± 7.9	$0.499\ (0.500) \pm 0.008$
-0.1125	5.7 ± 1.0	43 ± 6.6	5.6 ± 2.4	37.4 ± 6.6	$0.482\ (0.481) \pm 0.008$
-0.0875	3.9 ± 0.9	31 ± 5.6	5.8 ± 2.4	25.2 ± 5.6	$0.467\ (0.473) \pm 0.008$
-0.0625	2.7 ± 0.8	23 ± 4.8	5.8 ± 2.4	17.2 ± 4.8	$0.456\ (0.465) \pm 0.007$
-0.0375	1.4 ± 0.6	16 ± 4.0	5.9 ± 2.4	10.1 ± 4.0	$0.486\ (0.516) \pm 0.008$
-0.0125	0.4 ± 0.4	9 ± 3.0	5.9 ± 2.4	3.1 ± 3.0	$0.463\ (0.512) \pm 0.007$
0.0125	0.3 ± 0.4	8 ± 2.8	5.9 ± 2.4	2.1 ± 2.8	$0.452\ (0.502) \pm 0.007$
0.0375	1.1 ± 0.6	13 ± 3.6	5.9 ± 2.4	7.1 ± 3.6	$0.453\ (0.478) \pm 0.007$
0.0625	2.5 ± 0.7	23 ± 4.8	5.8 ± 2.4	17.2 ± 4.8	$0.485\ (0.496) \pm 0.008$
0.0875	3.8 ± 0.8	31 ± 5.6	5.7 ± 2.4	25.3 ± 5.6	$0.482\ (0.490) \pm 0.008$
0.1125	6.6 ± 1.1	49 ± 7.0	5.6 ± 2.4	43.4 ± 7.0	$0.471\ (0.477) \pm 0.008$
0.1375	9.2 ± 1.3	63 ± 7.9	5.5 ± 2.4	57.5 ± 7.9	$0.458\ (0.455) \pm 0.008$
0.1625	10.5 ± 1.3	75 ± 8.7	5.4 ± 2.3	69.6 ± 8.7	$0.485\ (0.483) \pm 0.008$
0.1875	12.2 ± 1.4	86 ± 9.3	5.3 ± 2.3	80.7 ± 9.3	$0.484\ (0.484) \pm 0.008$
0.2125	13.0 ± 1.5	85 ± 9.2	5.3 ± 2.3	79.7 ± 9.2	$0.447\ (0.446) \pm 0.007$
0.2375	17.6 ± 1.8	114 ± 10.7	5.4 ± 2.3	108.6 ± 10.7	$0.455\ (0.450) \pm 0.008$
0.2625	17.0 ± 1.7	117 ± 10.8	5.6 ± 2.4	111.4 ± 10.8	$0.480\ (0.479) \pm 0.008$
0.2875	14.5 ± 1.6	95 ± 9.8	6.0 ± 2.4	89.0 ± 9.8	$0.451\ (0.448) \pm 0.007$
0.3125	15.7 ± 1.7	98 ± 9.9	6.6 ± 2.6	91.4 ± 9.9	$0.426\ (0.425) \pm 0.007$
0.3375	18.1 ± 1.9	114 ± 10.7	7.6 ± 2.8	106.4 ± 10.7	$0.431\ (0.428) \pm 0.007$
0.3625	11.4 ± 1.5	78 ± 8.8	9.1 ± 3.0	68.9 ± 8.8	$0.439\ (0.440) \pm 0.007$
0.3875	10.8 ± 1.5	70 ± 8.4	10.9 ± 3.3	59.0 ± 8.4	$0.399\ (0.400) \pm 0.007$
0.4125	10.5 ± 1.5	72 ± 8.5	13.3 ± 3.7	58.7 ± 8.5	$0.401\ (0.407) \pm 0.007$
0.4375	11.2 ± 1.7	74 ± 8.6	16.2 ± 4.0	57.8 ± 8.6	$0.368\ (0.377) \pm 0.007$
0.4625	9.6 ± 1.7	66 ± 8.1	19.6 ± 4.4	46.4 ± 8.1	$0.342\ (0.352) \pm 0.007$
0.4875	21.5 ± 2.5	117 ± 10.8	23.2 ± 4.8	93.8 ± 10.8	$0.311\ (0.319) \pm 0.006$
0.5125	25.9 ± 2.9	131 ± 11.4	26.8 ± 5.2	104.2 ± 11.4	$0.289\ (0.293) \pm 0.006$
0.5375	41.1 ± 4.2	155 ± 12.4	30.0 ± 5.5	125.0 ± 12.4	$0.222\ (0.222) \pm 0.005$
0.5625	73.1 ± 5.9	233 ± 15.3	32.1 ± 5.7	200.9 ± 15.3	$0.199\ (0.201) \pm 0.005$
0.5875	136.0 ± 9.6	306 ± 17.5	32.3 ± 5.7	273.7 ± 17.5	$0.147\ (0.147) \pm 0.004$

$\bar{p}p \to \pi^0\eta$ at $E_{cm} = 3413.8$ MeV ($\mathcal{L} = 1953.9\ 10^{31}\mathrm{s}^{-1}\mathrm{cm}^{-2}$)					
z	$d\sigma/dz$ (nb)	N_{tot}	N_{bkg}	$N_{\pi^0\pi^0}$	$a \times \epsilon$
-0.5875	102.7 ± 6.0	407 ± 20.2	26.8 ± 5.2	380.2 ± 20.2	0.225 (0.222) $\pm$ 0.005
-0.5625	76.1 ± 4.4	399 ± 20.0	27.8 ± 5.3	371.2 ± 20.0	0.288 (0.293) $\pm$ 0.006
-0.5375	41.9 ± 2.9	272 ± 16.5	25.8 ± 5.1	246.2 ± 16.5	0.346 (0.352) $\pm$ 0.006
-0.5125	22.6 ± 2.1	168 ± 13.0	22.3 ± 4.7	145.7 ± 13.0	0.379 (0.386) $\pm$ 0.007
-0.4875	15.5 ± 1.6	129 ± 11.4	18.6 ± 4.3	110.4 ± 11.4	0.413 (0.428) $\pm$ 0.007
-0.4625	8.8 ± 1.2	78 ± 8.8	15.3 ± 3.9	62.7 ± 8.8	0.412 (0.428) $\pm$ 0.007
-0.4375	7.5 ± 1.1	68 ± 8.2	12.7 ± 3.6	55.3 ± 8.2	0.428 (0.444) $\pm$ 0.007
-0.4125	7.9 ± 1.1	73 ± 8.5	10.9 ± 3.3	62.1 ± 8.5	0.465 (0.472) $\pm$ 0.007
-0.3875	8.4 ± 1.1	73 ± 8.5	9.7 ± 3.1	63.3 ± 8.5	0.448 (0.451) $\pm$ 0.007
-0.3625	12.0 ± 1.3	101 ± 10.1	9.1 ± 3.0	91.9 ± 10.1	0.461 (0.461) $\pm$ 0.007
-0.3375	13.7 ± 1.4	116 ± 10.8	8.8 ± 3.0	107.2 ± 10.8	0.471 (0.470) $\pm$ 0.007
-0.3125	16.7 ± 1.5	146 ± 12.1	8.7 ± 3.0	137.3 ± 12.1	0.495 (0.492) $\pm$ 0.008
-0.2875	16.3 ± 1.5	136 ± 11.7	8.6 ± 2.9	127.4 ± 11.7	0.472 (0.469) $\pm$ 0.007
-0.2625	15.6 ± 1.5	129 ± 11.4	8.4 ± 2.9	120.5 ± 11.4	0.465 (0.463) $\pm$ 0.007
-0.2375	16.8 ± 1.5	145 ± 12.0	8.1 ± 2.9	136.9 ± 12.0	0.492 (0.488) $\pm$ 0.008
-0.2125	13.5 ± 1.4	114 ± 10.7	7.7 ± 2.8	106.3 ± 10.7	0.475 (0.473) $\pm$ 0.007
-0.1875	10.5 ± 1.2	87 ± 9.3	7.1 ± 2.7	79.9 ± 9.3	0.461 (0.455) $\pm$ 0.007
-0.1625	8.8 ± 1.1	74 ± 8.6	6.4 ± 2.5	67.6 ± 8.6	0.461 (0.462) $\pm$ 0.007
-0.1375	8.7 ± 1.1	74 ± 8.6	5.7 ± 2.4	68.3 ± 8.6	0.471 (0.470) $\pm$ 0.007
-0.1125	6.7 ± 1.0	55 ± 7.4	5.1 ± 2.2	49.9 ± 7.4	0.447 (0.445) $\pm$ 0.007
-0.0875	2.8 ± 0.7	26 ± 5.1	4.6 ± 2.1	21.4 ± 5.1	0.455 (0.460) $\pm$ 0.007
-0.0625	2.3 ± 0.6	22 ± 4.7	4.4 ± 2.1	17.6 ± 4.7	0.441 (0.454) $\pm$ 0.007
-0.0375	1.6 ± 0.5	18 ± 4.2	4.4 ± 2.1	13.6 ± 4.2	0.474 (0.501) $\pm$ 0.008
-0.0125	0.6 ± 0.4	10 ± 3.2	4.7 ± 2.2	5.3 ± 3.2	0.442 (0.493) $\pm$ 0.007
0.0125	0.7 ± 0.4	11 ± 3.3	5.3 ± 2.3	5.7 ± 3.3	0.435 (0.479) $\pm$ 0.007
0.0375	1.1 ± 0.5	14 ± 3.7	6.1 ± 2.5	7.9 ± 3.7	0.422 (0.449) $\pm$ 0.007
0.0625	2.9 ± 0.7	30 ± 5.5	7.0 ± 2.7	23.0 ± 5.5	0.473 (0.481) $\pm$ 0.007
0.0875	4.5 ± 0.9	42 ± 6.5	8.1 ± 2.8	33.9 ± 6.5	0.449 (0.456) $\pm$ 0.007
0.1125	4.1 ± 0.8	41 ± 6.4	9.1 ± 3.0	31.9 ± 6.4	0.456 (0.463) $\pm$ 0.007
0.1375	6.3 ± 1.0	57 ± 7.5	9.9 ± 3.1	47.1 ± 7.5	0.446 (0.445) $\pm$ 0.007
0.1625	10.1 ± 1.2	89 ± 9.4	10.5 ± 3.2	78.5 ± 9.4	0.464 (0.465) $\pm$ 0.007
0.1875	11.7 ± 1.3	99 ± 9.9	10.8 ± 3.3	88.2 ± 9.9	0.455 (0.452) $\pm$ 0.007
0.2125	12.6 ± 1.4	100 ± 10.0	10.7 ± 3.3	89.3 ± 10.0	0.423 (0.424) $\pm$ 0.007
0.2375	13.8 ± 1.5	110 ± 10.5	10.3 ± 3.2	99.7 ± 10.5	0.437 (0.434) $\pm$ 0.007
0.2625	17.1 ± 1.6	138 ± 11.8	9.6 ± 3.1	128.4 ± 11.8	0.452 (0.450) $\pm$ 0.007
0.2875	18.5 ± 1.7	137 ± 11.7	8.8 ± 3.0	128.2 ± 11.7	0.419 (0.415) $\pm$ 0.007
0.3125	14.5 ± 1.5	108 ± 10.4	8.0 ± 2.8	100.0 ± 10.4	0.413 (0.412) $\pm$ 0.007
0.3375	17.4 ± 1.7	129 ± 11.4	7.5 ± 2.7	121.5 ± 11.4	0.419 (0.418) $\pm$ 0.007
0.3625	13.7 ± 1.5	99 ± 9.9	7.7 ± 2.8	91.3 ± 9.9	0.400 (0.399) $\pm$ 0.007
0.3875	10.9 ± 1.4	77 ± 8.8	8.7 ± 3.0	68.3 ± 8.8	0.373 (0.375) $\pm$ 0.007
0.4125	9.9 ± 1.4	73 ± 8.5	11.0 ± 3.3	62.0 ± 8.5	0.369 (0.374) $\pm$ 0.007
0.4375	6.7 ± 1.2	57 ± 7.5	14.7 ± 3.8	42.4 ± 7.5	0.369 (0.379) $\pm$ 0.007
0.4625	10.2 ± 1.6	77 ± 8.8	19.8 ± 4.4	57.2 ± 8.8	0.326 (0.336) $\pm$ 0.006
0.4875	16.0 ± 2.1	106 ± 10.3	26.2 ± 5.1	79.8 ± 10.3	0.293 (0.299) $\pm$ 0.006
0.5125	26.5 ± 2.8	155 ± 12.4	33.3 ± 5.8	121.7 ± 12.4	0.272 (0.275) $\pm$ 0.006
0.5375	42.5 ± 3.9	200 ± 14.1	40.1 ± 6.3	159.9 ± 14.1	0.222 (0.225) $\pm$ 0.005
0.5625	87.5 ± 6.3	305 ± 17.5	44.9 ± 6.7	260.1 ± 17.5	0.177 (0.178) $\pm$ 0.005
0.5875	137.6 ± 9.2	360 ± 19.0	45.0 ± 6.7	315.0 ± 19.0	0.137 (0.137) $\pm$ 0.004

$\bar{p}p \to \pi^0\eta$ at $E_{cm} = 3415.0$ MeV ($\mathcal{L} = 2352.1\ 10^{31}\mathrm{s}^{-1}\mathrm{cm}^{-2}$)					
z	$d\sigma/dz$ (nb)	N_{tot}	N_{bkg}	$N_{\pi^0\pi^0}$	$a \times \epsilon$
-0.5875	99.0 ± 5.0	522 ± 22.9	32.3 ± 5.7	489.7 ± 22.9	$0.245\ (0.243) \pm 0.004$
-0.5625	79.4 ± 3.8	547 ± 23.4	34.2 ± 5.8	512.8 ± 23.4	$0.316\ (0.318) \pm 0.005$
-0.5375	43.7 ± 2.6	372 ± 19.3	32.1 ± 5.7	339.9 ± 19.3	$0.378\ (0.383) \pm 0.005$
-0.5125	24.6 ± 1.9	231 ± 15.2	28.0 ± 5.3	203.0 ± 15.2	$0.396\ (0.406) \pm 0.006$
-0.4875	14.1 ± 1.4	154 ± 12.4	23.3 ± 4.8	130.7 ± 12.4	$0.440\ (0.457) \pm 0.006$
-0.4625	10.5 ± 1.2	118 ± 10.9	18.7 ± 4.3	99.3 ± 10.9	$0.451\ (0.466) \pm 0.006$
-0.4375	7.1 ± 0.9	83 ± 9.1	14.7 ± 3.8	68.3 ± 9.1	$0.459\ (0.475) \pm 0.006$
-0.4125	9.1 ± 1.0	102 ± 10.1	11.6 ± 3.4	90.4 ± 10.1	$0.482\ (0.491) \pm 0.006$
-0.3875	10.1 ± 1.1	109 ± 10.4	9.4 ± 3.1	99.6 ± 10.4	$0.481\ (0.484) \pm 0.006$
-0.3625	11.1 ± 1.1	117 ± 10.8	7.9 ± 2.8	109.1 ± 10.8	$0.485\ (0.485) \pm 0.006$
-0.3375	14.8 ± 1.2	159 ± 12.6	7.1 ± 2.7	151.9 ± 12.6	$0.505\ (0.505) \pm 0.006$
-0.3125	14.3 ± 1.2	154 ± 12.4	6.7 ± 2.6	147.3 ± 12.4	$0.511\ (0.507) \pm 0.006$
-0.2875	13.1 ± 1.2	139 ± 11.8	6.6 ± 2.6	132.4 ± 11.8	$0.502\ (0.499) \pm 0.006$
-0.2625	15.1 ± 1.3	158 ± 12.6	6.7 ± 2.6	151.3 ± 12.6	$0.496\ (0.493) \pm 0.006$
-0.2375	14.3 ± 1.2	156 ± 12.5	6.8 ± 2.6	149.2 ± 12.5	$0.519\ (0.515) \pm 0.006$
-0.2125	15.1 ± 1.3	161 ± 12.7	6.8 ± 2.6	154.2 ± 12.7	$0.503\ (0.502) \pm 0.006$
-0.1875	10.2 ± 1.1	108 ± 10.4	6.8 ± 2.6	101.2 ± 10.4	$0.494\ (0.489) \pm 0.006$
-0.1625	10.4 ± 1.1	107 ± 10.3	6.6 ± 2.6	100.4 ± 10.3	$0.476\ (0.475) \pm 0.006$
-0.1375	7.8 ± 0.9	87 ± 9.3	6.4 ± 2.5	80.6 ± 9.3	$0.510\ (0.508) \pm 0.006$
-0.1125	5.1 ± 0.8	56 ± 7.5	6.2 ± 2.5	49.8 ± 7.5	$0.477\ (0.478) \pm 0.006$
-0.0875	3.9 ± 0.7	43 ± 6.6	6.0 ± 2.4	37.0 ± 6.6	$0.462\ (0.465) \pm 0.006$
-0.0625	2.5 ± 0.6	30 ± 5.5	5.9 ± 2.4	24.1 ± 5.5	$0.462\ (0.471) \pm 0.006$
-0.0375	1.3 ± 0.4	20 ± 4.5	5.9 ± 2.4	14.1 ± 4.5	$0.483\ (0.517) \pm 0.006$
-0.0125	0.9 ± 0.4	16 ± 4.0	6.0 ± 2.5	10.0 ± 4.0	$0.478\ (0.543) \pm 0.006$
0.0125	0.2 ± 0.3	9 ± 3.0	6.4 ± 2.5	2.6 ± 3.0	$0.469\ (0.527) \pm 0.006$
0.0375	1.7 ± 0.5	24 ± 4.9	6.9 ± 2.6	17.1 ± 4.9	$0.461\ (0.488) \pm 0.006$
0.0625	1.1 ± 0.4	19 ± 4.4	7.6 ± 2.8	11.4 ± 4.4	$0.492\ (0.503) \pm 0.006$
0.0875	4.5 ± 0.7	53 ± 7.3	8.4 ± 2.9	44.6 ± 7.3	$0.481\ (0.489) \pm 0.006$
0.1125	5.3 ± 0.8	61 ± 7.8	9.2 ± 3.0	51.8 ± 7.8	$0.475\ (0.480) \pm 0.006$
0.1375	7.1 ± 0.9	77 ± 8.8	10.1 ± 3.2	66.9 ± 8.8	$0.469\ (0.466) \pm 0.006$
0.1625	8.9 ± 1.0	101 ± 10.1	10.9 ± 3.3	90.1 ± 10.1	$0.501\ (0.499) \pm 0.006$
0.1875	11.6 ± 1.2	124 ± 11.1	11.6 ± 3.4	112.4 ± 11.1	$0.476\ (0.476) \pm 0.006$
0.2125	13.1 ± 1.2	138 ± 11.8	12.2 ± 3.5	125.8 ± 11.8	$0.472\ (0.471) \pm 0.006$
0.2375	13.4 ± 1.3	137 ± 11.7	12.6 ± 3.5	124.4 ± 11.7	$0.463\ (0.459) \pm 0.006$
0.2625	16.5 ± 1.4	177 ± 13.3	12.8 ± 3.6	164.2 ± 13.3	$0.492\ (0.491) \pm 0.006$
0.2875	16.3 ± 1.4	161 ± 12.7	13.1 ± 3.6	147.9 ± 12.7	$0.451\ (0.447) \pm 0.006$
0.3125	15.9 ± 1.4	151 ± 12.3	13.3 ± 3.6	137.7 ± 12.3	$0.429\ (0.427) \pm 0.006$
0.3375	11.2 ± 1.2	114 ± 10.7	13.7 ± 3.7	100.3 ± 10.7	$0.441\ (0.441) \pm 0.006$
0.3625	13.8 ± 1.3	139 ± 11.8	14.5 ± 3.8	124.5 ± 11.8	$0.447\ (0.446) \pm 0.006$
0.3875	11.4 ± 1.3	109 ± 10.4	15.8 ± 4.0	93.2 ± 10.4	$0.401\ (0.403) \pm 0.006$
0.4125	9.0 ± 1.2	90 ± 9.5	17.9 ± 4.2	72.1 ± 9.5	$0.389\ (0.393) \pm 0.006$
0.4375	7.8 ± 1.1	84 ± 9.2	20.9 ± 4.6	63.1 ± 9.2	$0.386\ (0.398) \pm 0.005$
0.4625	10.5 ± 1.4	100 ± 10.0	24.9 ± 5.0	75.1 ± 10.0	$0.340\ (0.351) \pm 0.005$
0.4875	12.4 ± 1.6	112 ± 10.6	29.8 ± 5.5	82.2 ± 10.6	$0.318\ (0.325) \pm 0.005$
0.5125	29.2 ± 2.5	208 ± 14.4	35.3 ± 5.9	172.7 ± 14.4	$0.287\ (0.291) \pm 0.005$
0.5375	45.4 ± 3.4	268 ± 16.4	41.0 ± 6.4	227.0 ± 16.4	$0.244\ (0.246) \pm 0.004$
0.5625	73.7 ± 4.9	337 ± 18.4	45.7 ± 6.8	291.3 ± 18.4	$0.193\ (0.195) \pm 0.004$
0.5875	118.9 ± 7.1	419 ± 20.5	47.9 ± 6.9	371.1 ± 20.5	$0.154\ (0.154) \pm 0.003$

$\bar{p}p \to \pi^0\eta$ at $E_{cm} = 3415.9$ MeV ($\mathcal{L} = 2466.5$ $10^{31}\mathrm{s}^{-1}\mathrm{cm}^{-2}$)					
z	$d\sigma/dz$ (nb)	N_{tot}	N_{bkg}	$N_{\pi^0\pi^0}$	$a \times \epsilon$
-0.5875	105.1 ± 5.1	563 ± 23.7	25.4 ± 5.0	537.6 ± 23.7	0.241 $(0.239) \pm 0.005$
-0.5625	72.7 ± 3.6	517 ± 22.7	27.8 ± 5.3	489.2 ± 22.7	0.311 $(0.315) \pm 0.005$
-0.5375	44.0 ± 2.6	362 ± 19.0	27.4 ± 5.2	334.6 ± 19.0	0.349 $(0.356) \pm 0.006$
-0.5125	24.4 ± 1.8	236 ± 15.4	25.2 ± 5.0	210.8 ± 15.4	0.397 $(0.405) \pm 0.006$
-0.4875	13.6 ± 1.3	151 ± 12.3	22.2 ± 4.7	128.8 ± 12.3	0.423 $(0.444) \pm 0.006$
-0.4625	8.7 ± 1.1	104 ± 10.2	19.0 ± 4.4	85.0 ± 10.2	0.438 $(0.457) \pm 0.006$
-0.4375	7.8 ± 1.0	92 ± 9.6	16.0 ± 4.0	76.0 ± 9.6	0.439 $(0.457) \pm 0.006$
-0.4125	7.0 ± 0.9	86 ± 9.3	13.3 ± 3.6	72.7 ± 9.3	0.475 $(0.484) \pm 0.006$
-0.3875	9.4 ± 1.0	107 ± 10.3	11.0 ± 3.3	96.0 ± 10.3	0.474 $(0.477) \pm 0.007$
-0.3625	13.0 ± 1.2	140 ± 11.8	9.3 ± 3.0	130.7 ± 11.8	0.471 $(0.471) \pm 0.006$
-0.3375	15.0 ± 1.3	159 ± 12.6	8.0 ± 2.8	151.1 ± 12.6	0.475 $(0.473) \pm 0.006$
-0.3125	17.8 ± 1.4	193 ± 13.9	7.0 ± 2.6	186.0 ± 13.9	0.493 $(0.488) \pm 0.007$
-0.2875	18.3 ± 1.4	191 ± 13.8	6.4 ± 2.5	184.6 ± 13.8	0.472 $(0.471) \pm 0.006$
-0.2625	14.4 ± 1.2	152 ± 12.3	6.0 ± 2.4	146.0 ± 12.3	0.482 $(0.476) \pm 0.007$
-0.2375	12.0 ± 1.1	135 ± 11.6	5.8 ± 2.4	129.2 ± 11.6	0.505 $(0.505) \pm 0.007$
-0.2125	12.5 ± 1.1	138 ± 11.8	5.7 ± 2.4	132.3 ± 11.8	0.500 $(0.495) \pm 0.007$
-0.1875	11.1 ± 1.1	115 ± 10.7	5.7 ± 2.4	109.3 ± 10.7	0.463 $(0.462) \pm 0.006$
-0.1625	8.7 ± 1.0	92 ± 9.6	5.8 ± 2.4	86.2 ± 9.6	0.468 $(0.465) \pm 0.006$
-0.1375	7.0 ± 0.9	79 ± 8.9	6.0 ± 2.5	73.0 ± 8.9	0.488 $(0.491) \pm 0.007$
-0.1125	5.2 ± 0.8	58 ± 7.6	6.3 ± 2.5	51.7 ± 7.6	0.467 $(0.467) \pm 0.006$
-0.0875	3.5 ± 0.7	41 ± 6.4	6.6 ± 2.6	34.4 ± 6.4	0.459 $(0.462) \pm 0.006$
-0.0625	1.8 ± 0.5	25 ± 5.0	7.0 ± 2.6	18.0 ± 5.0	0.451 $(0.464) \pm 0.006$
-0.0375	0.9 ± 0.4	17 ± 4.1	7.5 ± 2.7	9.6 ± 4.1	0.472 $(0.511) \pm 0.006$
-0.0125	0.2 ± 0.3	10 ± 3.2	8.0 ± 2.8	2.0 ± 3.2	0.464 $(0.531) \pm 0.006$
0.0125	0.2 ± 0.3	11 ± 3.3	8.5 ± 2.9	2.5 ± 3.3	0.444 $(0.509) \pm 0.006$
0.0375	1.0 ± 0.4	19 ± 4.4	9.0 ± 3.0	10.0 ± 4.4	0.453 $(0.482) \pm 0.006$
0.0625	2.0 ± 0.5	31 ± 5.6	9.6 ± 3.1	21.4 ± 5.6	0.482 $(0.496) \pm 0.007$
0.0875	3.3 ± 0.7	43 ± 6.6	10.1 ± 3.2	32.9 ± 6.6	0.466 $(0.473) \pm 0.006$
0.1125	4.9 ± 0.8	59 ± 7.7	10.6 ± 3.3	48.4 ± 7.7	0.452 $(0.459) \pm 0.006$
0.1375	6.3 ± 0.9	73 ± 8.5	11.0 ± 3.3	62.0 ± 8.5	0.467 $(0.464) \pm 0.007$
0.1625	8.1 ± 1.0	94 ± 9.7	11.3 ± 3.4	82.7 ± 9.7	0.480 $(0.481) \pm 0.007$
0.1875	10.4 ± 1.1	115 ± 10.7	11.5 ± 3.4	103.5 ± 10.7	0.466 $(0.465) \pm 0.006$
0.2125	12.5 ± 1.2	133 ± 11.5	11.6 ± 3.4	121.4 ± 11.5	0.458 $(0.456) \pm 0.006$
0.2375	11.7 ± 1.2	126 ± 11.2	11.7 ± 3.4	114.3 ± 11.2	0.459 $(0.456) \pm 0.006$
0.2625	14.3 ± 1.3	153 ± 12.4	11.9 ± 3.4	141.1 ± 12.4	0.465 $(0.462) \pm 0.006$
0.2875	15.2 ± 1.3	157 ± 12.5	12.1 ± 3.5	144.9 ± 12.5	0.448 $(0.447) \pm 0.006$
0.3125	14.2 ± 1.3	142 ± 11.9	12.6 ± 3.6	129.4 ± 11.9	0.429 $(0.427) \pm 0.006$
0.3375	12.9 ± 1.3	135 ± 11.6	13.5 ± 3.7	121.5 ± 11.6	0.442 $(0.440) \pm 0.006$
0.3625	11.7 ± 1.2	123 ± 11.1	14.8 ± 3.9	108.2 ± 11.1	0.431 $(0.432) \pm 0.006$
0.3875	8.7 ± 1.1	90 ± 9.5	16.9 ± 4.1	73.2 ± 9.5	0.394 $(0.394) \pm 0.006$
0.4125	9.4 ± 1.2	98 ± 9.9	19.6 ± 4.4	78.4 ± 9.9	0.385 $(0.391) \pm 0.006$
0.4375	6.7 ± 1.1	78 ± 8.8	23.2 ± 4.8	54.8 ± 8.8	0.371 $(0.385) \pm 0.006$
0.4625	9.1 ± 1.3	94 ± 9.7	27.5 ± 5.2	66.5 ± 9.7	0.330 $(0.341) \pm 0.005$
0.4875	14.6 ± 1.7	130 ± 11.4	32.5 ± 5.7	97.5 ± 11.4	0.305 $(0.312) \pm 0.005$
0.5125	23.5 ± 2.2	185 ± 13.6	37.9 ± 6.2	147.1 ± 13.6	0.287 $(0.293) \pm 0.005$
0.5375	44.7 ± 3.5	258 ± 16.1	43.0 ± 6.6	215.0 ± 16.1	0.224 $(0.225) \pm 0.004$
0.5625	73.7 ± 4.8	352 ± 18.8	46.9 ± 6.8	305.1 ± 18.8	0.194 $(0.194) \pm 0.004$
0.5875	120.0 ± 7.3	419 ± 20.5	48.4 ± 7.0	370.6 ± 20.5	0.146 $(0.145) \pm 0.004$

$\bar{p}p \to \pi^0\eta$ at $E_{cm} = 3418.0$ MeV ($\mathcal{L} = 1215.4\ 10^{31}\mathrm{s}^{-1}\mathrm{cm}^{-2}$)					
z	$d\sigma/dz$ (nb)	N_{tot}	N_{bkg}	$N_{\pi^0\pi^0}$	$a \times \epsilon$
-0.5875	106.5 ± 6.9	295 ± 17.2	15.4 ± 3.9	279.6 ± 17.2	$0.250\ (0.251) \pm 0.005$
-0.5625	63.3 ± 4.5	248 ± 15.8	17.7 ± 4.2	230.3 ± 15.8	$0.341\ (0.348) \pm 0.006$
-0.5375	38.7 ± 3.3	178 ± 13.3	17.7 ± 4.2	160.3 ± 13.3	$0.390\ (0.395) \pm 0.007$
-0.5125	22.7 ± 2.4	122 ± 11.1	16.4 ± 4.0	105.6 ± 11.1	$0.431\ (0.443) \pm 0.007$
-0.4875	12.3 ± 1.7	77 ± 8.8	14.4 ± 3.8	62.6 ± 8.8	$0.466\ (0.487) \pm 0.007$
-0.4625	9.7 ± 1.6	61 ± 7.8	12.1 ± 3.5	48.9 ± 7.8	$0.460\ (0.481) \pm 0.007$
-0.4375	5.4 ± 1.2	38 ± 6.2	9.9 ± 3.1	28.1 ± 6.2	$0.481\ (0.499) \pm 0.007$
-0.4125	8.9 ± 1.4	56 ± 7.5	7.8 ± 2.8	48.2 ± 7.5	$0.510\ (0.519) \pm 0.007$
-0.3875	11.0 ± 1.5	65 ± 8.1	6.1 ± 2.5	58.9 ± 8.1	$0.508\ (0.509) \pm 0.007$
-0.3625	11.5 ± 1.5	65 ± 8.1	4.7 ± 2.2	60.3 ± 8.1	$0.501\ (0.500) \pm 0.007$
-0.3375	14.5 ± 1.7	83 ± 9.1	3.7 ± 1.9	79.3 ± 9.1	$0.526\ (0.523) \pm 0.007$
-0.3125	14.3 ± 1.6	83 ± 9.1	2.9 ± 1.7	80.1 ± 9.1	$0.538\ (0.534) \pm 0.008$
-0.2875	14.2 ± 1.7	79 ± 8.9	2.5 ± 1.6	76.5 ± 8.9	$0.521\ (0.515) \pm 0.007$
-0.2625	16.6 ± 1.8	91 ± 9.5	2.2 ± 1.5	88.8 ± 9.5	$0.513\ (0.512) \pm 0.007$
-0.2375	14.3 ± 1.6	82 ± 9.1	2.1 ± 1.4	79.9 ± 9.1	$0.535\ (0.534) \pm 0.007$
-0.2125	12.8 ± 1.5	74 ± 8.6	2.1 ± 1.4	71.9 ± 8.6	$0.546\ (0.538) \pm 0.008$
-0.1875	12.1 ± 1.5	68 ± 8.2	2.2 ± 1.5	65.8 ± 8.2	$0.517\ (0.517) \pm 0.007$
-0.1625	7.0 ± 1.2	39 ± 6.2	2.3 ± 1.5	36.7 ± 6.2	$0.498\ (0.497) \pm 0.007$
-0.1375	7.3 ± 1.2	44 ± 6.6	2.5 ± 1.6	41.5 ± 6.6	$0.534\ (0.539) \pm 0.007$
-0.1125	6.1 ± 1.1	35 ± 5.9	2.7 ± 1.6	32.3 ± 5.9	$0.503\ (0.503) \pm 0.007$
-0.0875	4.5 ± 1.0	26 ± 5.1	2.9 ± 1.7	23.1 ± 5.1	$0.483\ (0.493) \pm 0.007$
-0.0625	1.3 ± 0.6	10 ± 3.2	3.1 ± 1.8	6.9 ± 3.2	$0.483\ (0.501) \pm 0.007$
-0.0375	1.3 ± 0.6	11 ± 3.3	3.3 ± 1.8	7.7 ± 3.3	$0.519\ (0.568) \pm 0.007$
-0.0125	1.0 ± 0.5	10 ± 3.2	3.5 ± 1.9	6.5 ± 3.2	$0.517\ (0.615) \pm 0.007$
0.0125	0.2 ± 0.4	5 ± 2.2	3.6 ± 1.9	1.4 ± 2.2	$0.486\ (0.568) \pm 0.007$
0.0375	0.2 ± 0.4	5 ± 2.2	3.8 ± 1.9	1.2 ± 2.2	$0.487\ (0.525) \pm 0.007$
0.0625	2.2 ± 0.7	16 ± 4.0	3.9 ± 2.0	12.1 ± 4.0	$0.510\ (0.523) \pm 0.007$
0.0875	5.3 ± 1.1	32 ± 5.7	4.0 ± 2.0	28.0 ± 5.7	$0.501\ (0.506) \pm 0.007$
0.1125	6.3 ± 1.2	37 ± 6.1	4.0 ± 2.0	33.0 ± 6.1	$0.493\ (0.498) \pm 0.007$
0.1375	7.6 ± 1.3	44 ± 6.6	4.0 ± 2.0	40.0 ± 6.6	$0.506\ (0.501) \pm 0.007$
0.1625	12.2 ± 1.5	71 ± 8.4	4.0 ± 2.0	67.0 ± 8.4	$0.525\ (0.525) \pm 0.008$
0.1875	10.8 ± 1.5	60 ± 7.8	4.0 ± 2.0	56.0 ± 7.8	$0.495\ (0.495) \pm 0.007$
0.2125	16.5 ± 1.9	88 ± 9.4	4.0 ± 2.0	84.0 ± 9.4	$0.487\ (0.484) \pm 0.007$
0.2375	14.8 ± 1.8	79 ± 8.9	4.1 ± 2.0	74.9 ± 8.9	$0.488\ (0.483) \pm 0.007$
0.2625	16.0 ± 1.8	90 ± 9.5	4.2 ± 2.0	85.8 ± 9.5	$0.512\ (0.511) \pm 0.007$
0.2875	14.6 ± 1.8	77 ± 8.8	4.4 ± 2.1	72.6 ± 8.8	$0.479\ (0.476) \pm 0.007$
0.3125	12.1 ± 1.7	63 ± 7.9	4.8 ± 2.2	58.1 ± 7.9	$0.458\ (0.457) \pm 0.007$
0.3375	13.0 ± 1.7	70 ± 8.4	5.5 ± 2.4	64.5 ± 8.4	$0.476\ (0.474) \pm 0.007$
0.3625	14.4 ± 1.8	77 ± 8.8	6.5 ± 2.6	70.5 ± 8.8	$0.467\ (0.468) \pm 0.007$
0.3875	10.3 ± 1.6	54 ± 7.3	7.9 ± 2.8	46.1 ± 7.3	$0.426\ (0.428) \pm 0.007$
0.4125	8.0 ± 1.6	44 ± 6.6	9.7 ± 3.1	34.3 ± 6.6	$0.402\ (0.408) \pm 0.007$
0.4375	7.2 ± 1.5	44 ± 6.6	11.9 ± 3.5	32.1 ± 6.6	$0.410\ (0.423) \pm 0.007$
0.4625	6.5 ± 1.6	40 ± 6.3	14.5 ± 3.8	25.5 ± 6.3	$0.361\ (0.375) \pm 0.006$
0.4875	17.6 ± 2.6	78 ± 8.8	17.4 ± 4.2	60.6 ± 8.8	$0.323\ (0.329) \pm 0.006$
0.5125	19.5 ± 2.8	84 ± 9.2	20.3 ± 4.5	63.7 ± 9.2	$0.308\ (0.312) \pm 0.006$
0.5375	47.4 ± 4.7	150 ± 12.2	22.8 ± 4.8	127.2 ± 12.2	$0.252\ (0.256) \pm 0.005$
0.5625	86.4 ± 7.0	214 ± 14.6	24.5 ± 5.0	189.5 ± 14.6	$0.208\ (0.209) \pm 0.005$
0.5875	126.0 ± 9.8	235 ± 15.3	24.6 ± 5.0	210.4 ± 15.3	$0.161\ (0.159) \pm 0.004$

$\bar{p}p \to \pi^0\eta$ at $E_{cm} = 3422.1$ MeV ($\mathcal{L} = 2152.3\ 10^{31}\mathrm{s}^{-1}\mathrm{cm}^{-2}$)					
z	$d\sigma/dz$ (nb)	N_{tot}	N_{bkg}	$N_{\pi^0\pi^0}$	$a \times \epsilon$
-0.5875	107.6 ± 5.5	506 ± 22.5	25.9 ± 5.1	480.1 ± 22.5	$0.243\ (0.244) \pm 0.005$
-0.5625	67.6 ± 3.7	430 ± 20.7	28.5 ± 5.3	401.5 ± 20.7	$0.320\ (0.324) \pm 0.005$
-0.5375	39.1 ± 2.6	298 ± 17.3	27.8 ± 5.3	270.2 ± 17.3	$0.372\ (0.377) \pm 0.006$
-0.5125	23.8 ± 2.0	200 ± 14.1	25.1 ± 5.0	174.9 ± 14.1	$0.392\ (0.402) \pm 0.006$
-0.4875	14.0 ± 1.4	138 ± 11.8	21.5 ± 4.6	116.5 ± 11.8	$0.440\ (0.455) \pm 0.006$
-0.4625	8.8 ± 1.1	95 ± 9.8	17.7 ± 4.2	77.3 ± 9.8	$0.463\ (0.478) \pm 0.007$
-0.4375	8.3 ± 1.1	84 ± 9.2	14.2 ± 3.8	69.8 ± 9.2	$0.443\ (0.461) \pm 0.006$
-0.4125	7.0 ± 1.0	75 ± 8.7	11.2 ± 3.3	63.8 ± 8.7	$0.491\ (0.498) \pm 0.007$
-0.3875	11.3 ± 1.2	108 ± 10.4	8.8 ± 3.0	99.2 ± 10.4	$0.477\ (0.481) \pm 0.007$
-0.3625	12.5 ± 1.2	117 ± 10.8	7.0 ± 2.6	110.0 ± 10.8	$0.482\ (0.481) \pm 0.007$
-0.3375	12.5 ± 1.2	121 ± 11.0	5.8 ± 2.4	115.2 ± 11.0	$0.504\ (0.502) \pm 0.007$
-0.3125	13.4 ± 1.2	128 ± 11.3	5.2 ± 2.3	122.8 ± 11.3	$0.505\ (0.502) \pm 0.007$
-0.2875	15.9 ± 1.4	148 ± 12.2	4.9 ± 2.2	143.1 ± 12.2	$0.494\ (0.492) \pm 0.007$
-0.2625	16.4 ± 1.4	152 ± 12.3	4.9 ± 2.2	147.1 ± 12.3	$0.493\ (0.490) \pm 0.007$
-0.2375	11.1 ± 1.1	110 ± 10.5	5.1 ± 2.3	104.9 ± 10.5	$0.520\ (0.516) \pm 0.007$
-0.2125	13.2 ± 1.2	127 ± 11.3	5.5 ± 2.3	121.5 ± 11.3	$0.506\ (0.503) \pm 0.007$
-0.1875	11.3 ± 1.2	104 ± 10.2	5.9 ± 2.4	98.1 ± 10.2	$0.475\ (0.473) \pm 0.007$
-0.1625	11.7 ± 1.2	109 ± 10.4	6.3 ± 2.5	102.7 ± 10.4	$0.482\ (0.480) \pm 0.007$
-0.1375	6.0 ± 0.9	62 ± 7.9	6.7 ± 2.6	55.4 ± 7.9	$0.498\ (0.500) \pm 0.007$
-0.1125	5.0 ± 0.8	51 ± 7.1	7.0 ± 2.6	44.0 ± 7.1	$0.477\ (0.477) \pm 0.007$
-0.0875	3.2 ± 0.7	35 ± 5.9	7.3 ± 2.7	27.7 ± 5.9	$0.463\ (0.468) \pm 0.006$
-0.0625	2.2 ± 0.6	27 ± 5.2	7.5 ± 2.7	19.5 ± 5.2	$0.460\ (0.479) \pm 0.006$
-0.0375	1.3 ± 0.5	21 ± 4.6	7.7 ± 2.8	13.3 ± 4.6	$0.495\ (0.541) \pm 0.007$
-0.0125	0.3 ± 0.3	11 ± 3.3	7.9 ± 2.8	3.1 ± 3.3	$0.470\ (0.595) \pm 0.006$
0.0125	0.0 ± 0.3	8 ± 2.8	8.0 ± 2.8	0.0 ± 2.8	$0.459\ (0.573) \pm 0.006$
0.0375	0.6 ± 0.4	14 ± 3.7	8.2 ± 2.9	5.8 ± 3.7	$0.464\ (0.502) \pm 0.006$
0.0625	2.2 ± 0.6	29 ± 5.4	8.4 ± 2.9	20.6 ± 5.4	$0.495\ (0.512) \pm 0.007$
0.0875	2.4 ± 0.6	30 ± 5.5	8.5 ± 2.9	21.5 ± 5.5	$0.472\ (0.480) \pm 0.007$
0.1125	5.4 ± 0.9	56 ± 7.5	8.7 ± 2.9	47.3 ± 7.5	$0.473\ (0.475) \pm 0.007$
0.1375	5.9 ± 0.9	59 ± 7.7	8.8 ± 3.0	50.2 ± 7.7	$0.462\ (0.461) \pm 0.006$
0.1625	10.9 ± 1.1	110 ± 10.5	8.9 ± 3.0	101.1 ± 10.5	$0.506\ (0.505) \pm 0.007$
0.1875	12.2 ± 1.2	115 ± 10.7	9.1 ± 3.0	105.9 ± 10.7	$0.473\ (0.476) \pm 0.006$
0.2125	13.0 ± 1.3	116 ± 10.8	9.2 ± 3.0	106.8 ± 10.8	$0.454\ (0.450) \pm 0.006$
0.2375	13.7 ± 1.3	127 ± 11.3	9.3 ± 3.1	117.7 ± 11.3	$0.469\ (0.467) \pm 0.007$
0.2625	16.2 ± 1.4	151 ± 12.3	9.5 ± 3.1	141.5 ± 12.3	$0.479\ (0.477) \pm 0.007$
0.2875	15.8 ± 1.5	137 ± 11.7	9.8 ± 3.1	127.2 ± 11.7	$0.443\ (0.439) \pm 0.006$
0.3125	13.7 ± 1.4	119 ± 10.9	10.3 ± 3.2	108.7 ± 10.9	$0.431\ (0.432) \pm 0.006$
0.3375	13.5 ± 1.4	122 ± 11.1	11.0 ± 3.3	111.0 ± 11.1	$0.452\ (0.449) \pm 0.006$
0.3625	12.4 ± 1.3	110 ± 10.5	12.1 ± 3.5	98.0 ± 10.5	$0.432\ (0.431) \pm 0.006$
0.3875	12.7 ± 1.4	107 ± 10.3	13.5 ± 3.7	93.5 ± 10.3	$0.400\ (0.403) \pm 0.006$
0.4125	8.7 ± 1.2	79 ± 8.9	15.5 ± 3.9	63.5 ± 8.9	$0.395\ (0.400) \pm 0.006$
0.4375	10.3 ± 1.3	93 ± 9.6	18.1 ± 4.2	74.9 ± 9.6	$0.387\ (0.398) \pm 0.006$
0.4625	9.1 ± 1.4	80 ± 8.9	21.2 ± 4.6	58.8 ± 8.9	$0.343\ (0.351) \pm 0.006$
0.4875	16.2 ± 1.9	119 ± 10.9	24.9 ± 5.0	94.1 ± 10.9	$0.310\ (0.317) \pm 0.005$
0.5125	23.4 ± 2.3	158 ± 12.6	29.1 ± 5.4	128.9 ± 12.6	$0.295\ (0.300) \pm 0.005$
0.5375	43.6 ± 3.5	227 ± 15.1	33.3 ± 5.8	193.7 ± 15.1	$0.240\ (0.242) \pm 0.005$
0.5625	71.4 ± 4.9	304 ± 17.4	37.2 ± 6.1	266.8 ± 17.4	$0.204\ (0.204) \pm 0.004$
0.5875	131.9 ± 8.1	392 ± 19.8	40.0 ± 6.3	352.1 ± 19.8	$0.147\ (0.146) \pm 0.004$

$\bar{p}p \to \pi^0\eta$ at $E_{cm} = 3426.0$ MeV ($\mathcal{L} = 1800.1\ 10^{31}\mathrm{s}^{-1}\mathrm{cm}^{-2}$)					
z	$d\sigma/dz$ (nb)	N_{tot}	N_{bkg}	$N_{\pi^0\pi^0}$	$a \times \epsilon$
-0.5875	101.6 ± 5.8	402 ± 20.1	21.5 ± 4.6	380.5 ± 20.1	$0.240\ (0.241) \pm 0.005$
-0.5625	68.8 ± 4.0	370 ± 19.2	22.8 ± 4.8	347.2 ± 19.2	$0.319\ (0.325) \pm 0.006$
-0.5375	40.3 ± 2.9	251 ± 15.8	21.4 ± 4.6	229.6 ± 15.8	$0.363\ (0.367) \pm 0.006$
-0.5125	24.3 ± 2.1	173 ± 13.2	18.8 ± 4.3	154.2 ± 13.2	$0.401\ (0.409) \pm 0.007$
-0.4875	16.4 ± 1.7	128 ± 11.3	15.8 ± 4.0	112.2 ± 11.3	$0.429\ (0.441) \pm 0.007$
-0.4625	11.8 ± 1.4	97 ± 9.8	12.9 ± 3.6	84.1 ± 9.8	$0.446\ (0.458) \pm 0.007$
-0.4375	7.7 ± 1.1	66 ± 8.1	10.5 ± 3.2	55.5 ± 8.1	$0.453\ (0.466) \pm 0.007$
-0.4125	8.3 ± 1.1	72 ± 8.5	8.7 ± 3.0	63.3 ± 8.5	$0.486\ (0.493) \pm 0.007$
-0.3875	8.7 ± 1.2	70 ± 8.4	7.5 ± 2.7	62.5 ± 8.4	$0.460\ (0.464) \pm 0.007$
-0.3625	12.8 ± 1.4	99 ± 9.9	6.8 ± 2.6	92.2 ± 9.9	$0.462\ (0.463) \pm 0.007$
-0.3375	13.8 ± 1.4	111 ± 10.5	6.4 ± 2.5	104.6 ± 10.5	$0.491\ (0.489) \pm 0.007$
-0.3125	11.0 ± 1.2	94 ± 9.7	6.2 ± 2.5	87.8 ± 9.7	$0.514\ (0.511) \pm 0.008$
-0.2875	15.0 ± 1.5	119 ± 10.9	6.2 ± 2.5	112.8 ± 10.9	$0.486\ (0.485) \pm 0.007$
-0.2625	14.8 ± 1.5	117 ± 10.8	6.2 ± 2.5	110.8 ± 10.8	$0.485\ (0.482) \pm 0.007$
-0.2375	13.4 ± 1.3	114 ± 10.7	6.2 ± 2.5	107.8 ± 10.7	$0.523\ (0.519) \pm 0.008$
-0.2125	12.2 ± 1.3	98 ± 9.9	6.1 ± 2.5	91.9 ± 9.9	$0.489\ (0.486) \pm 0.007$
-0.1875	11.9 ± 1.3	95 ± 9.8	5.9 ± 2.4	89.1 ± 9.8	$0.486\ (0.483) \pm 0.007$
-0.1625	9.5 ± 1.2	76 ± 8.7	5.6 ± 2.4	70.4 ± 8.7	$0.483\ (0.479) \pm 0.007$
-0.1375	8.6 ± 1.1	70 ± 8.4	5.2 ± 2.3	64.8 ± 8.4	$0.488\ (0.487) \pm 0.007$
-0.1125	5.7 ± 0.9	45 ± 6.7	4.9 ± 2.2	40.1 ± 6.7	$0.457\ (0.456) \pm 0.007$
-0.0875	5.3 ± 0.9	41 ± 6.4	4.5 ± 2.1	36.5 ± 6.4	$0.446\ (0.447) \pm 0.007$
-0.0625	3.6 ± 0.8	31 ± 5.6	4.3 ± 2.1	26.7 ± 5.6	$0.449\ (0.472) \pm 0.007$
-0.0375	0.7 ± 0.4	10 ± 3.2	4.2 ± 2.0	5.8 ± 3.2	$0.494\ (0.546) \pm 0.007$
-0.0125	1.0 ± 0.4	14 ± 3.7	4.2 ± 2.0	9.8 ± 3.7	$0.455\ (0.653) \pm 0.007$
0.0125	0.3 ± 0.3	7 ± 2.6	4.4 ± 2.1	2.6 ± 2.6	$0.460\ (0.640) \pm 0.007$
0.0375	0.2 ± 0.3	6 ± 2.5	4.7 ± 2.2	1.3 ± 2.5	$0.465\ (0.507) \pm 0.007$
0.0625	2.6 ± 0.6	26 ± 5.1	5.2 ± 2.3	20.9 ± 5.1	$0.492\ (0.507) \pm 0.007$
0.0875	1.9 ± 0.6	20 ± 4.5	5.7 ± 2.4	14.3 ± 4.5	$0.472\ (0.477) \pm 0.007$
0.1125	4.7 ± 0.9	40 ± 6.3	6.3 ± 2.5	33.7 ± 6.3	$0.461\ (0.466) \pm 0.007$
0.1375	8.4 ± 1.1	67 ± 8.2	6.8 ± 2.6	60.2 ± 8.2	$0.465\ (0.462) \pm 0.007$
0.1625	9.1 ± 1.1	77 ± 8.8	7.3 ± 2.7	69.7 ± 8.8	$0.498\ (0.494) \pm 0.007$
0.1875	11.1 ± 1.3	87 ± 9.3	7.7 ± 2.8	79.3 ± 9.3	$0.458\ (0.458) \pm 0.007$
0.2125	12.5 ± 1.4	98 ± 9.9	8.0 ± 2.8	90.0 ± 9.9	$0.463\ (0.461) \pm 0.007$
0.2375	13.5 ± 1.4	105 ± 10.2	8.1 ± 2.9	96.9 ± 10.2	$0.465\ (0.460) \pm 0.007$
0.2625	12.0 ± 1.4	96 ± 9.8	8.1 ± 2.9	87.9 ± 9.8	$0.473\ (0.472) \pm 0.007$
0.2875	16.0 ± 1.6	118 ± 10.9	8.1 ± 2.8	109.9 ± 10.9	$0.446\ (0.443) \pm 0.007$
0.3125	12.1 ± 1.4	90 ± 9.5	8.1 ± 2.8	81.9 ± 9.5	$0.435\ (0.434) \pm 0.007$
0.3375	12.1 ± 1.4	91 ± 9.5	8.3 ± 2.9	82.7 ± 9.5	$0.441\ (0.440) \pm 0.007$
0.3625	9.8 ± 1.3	74 ± 8.6	8.8 ± 3.0	65.2 ± 8.6	$0.424\ (0.427) \pm 0.007$
0.3875	9.0 ± 1.3	68 ± 8.2	9.8 ± 3.1	58.2 ± 8.2	$0.414\ (0.414) \pm 0.007$
0.4125	9.3 ± 1.4	68 ± 8.2	11.4 ± 3.4	56.6 ± 8.2	$0.386\ (0.393) \pm 0.007$
0.4375	7.4 ± 1.3	59 ± 7.7	13.9 ± 3.7	45.1 ± 7.7	$0.386\ (0.392) \pm 0.007$
0.4625	11.3 ± 1.6	79 ± 8.9	17.3 ± 4.2	61.7 ± 8.9	$0.345\ (0.353) \pm 0.006$
0.4875	17.2 ± 2.1	106 ± 10.3	21.6 ± 4.6	84.5 ± 10.3	$0.311\ (0.316) \pm 0.006$
0.5125	22.7 ± 2.6	127 ± 11.3	26.4 ± 5.1	100.5 ± 11.3	$0.282\ (0.285) \pm 0.006$
0.5375	40.8 ± 3.7	190 ± 13.8	31.6 ± 5.6	158.4 ± 13.8	$0.248\ (0.250) \pm 0.005$
0.5625	60.6 ± 5.0	224 ± 15.0	36.0 ± 6.0	188.0 ± 15.0	$0.200\ (0.199) \pm 0.005$
0.5875	102.2 ± 7.6	281 ± 16.8	38.6 ± 6.2	242.4 ± 16.8	$0.152\ (0.152) \pm 0.004$

$\bar{p}p \to \pi^0\eta$ at E_{cm} = 3430.1 MeV ($\mathcal{L}$ = 1438.2 10^{31}s^{-1}cm^{-2})					
z	$d\sigma/dz$ (nb)	N_{tot}	N_{bkg}	$N_{\pi^0\pi^0}$	$a \times \epsilon$
-0.5875	96.3 ± 6.4	296 ± 17.2	14.1 ± 3.8	281.9 ± 17.2	0.241 (0.240) $\pm$ 0.006
-0.5625	69.0 ± 4.7	280 ± 16.7	15.4 ± 3.9	264.6 ± 16.7	0.309 (0.314) $\pm$ 0.007
-0.5375	36.0 ± 3.1	178 ± 13.3	15.2 ± 3.9	162.8 ± 13.3	0.360 (0.370) $\pm$ 0.008
-0.5125	13.4 ± 1.9	79 ± 8.9	14.1 ± 3.8	64.9 ± 8.9	0.385 (0.397) $\pm$ 0.008
-0.4875	14.5 ± 1.8	89 ± 9.4	12.7 ± 3.6	76.3 ± 9.4	0.417 (0.432) $\pm$ 0.008
-0.4625	8.0 ± 1.4	53 ± 7.3	11.2 ± 3.3	41.8 ± 7.3	0.413 (0.429) $\pm$ 0.008
-0.4375	8.3 ± 1.4	55 ± 7.4	9.7 ± 3.1	45.3 ± 7.4	0.433 (0.444) $\pm$ 0.008
-0.4125	6.9 ± 1.2	48 ± 6.9	8.5 ± 2.9	39.5 ± 6.9	0.462 (0.470) $\pm$ 0.009
-0.3875	11.6 ± 1.5	74 ± 8.6	7.4 ± 2.7	66.6 ± 8.6	0.471 (0.469) $\pm$ 0.009
-0.3625	13.2 ± 1.6	79 ± 8.9	6.6 ± 2.6	72.4 ± 8.9	0.447 (0.450) $\pm$ 0.009
-0.3375	12.5 ± 1.5	79 ± 8.9	5.9 ± 2.4	73.1 ± 8.9	0.482 (0.477) $\pm$ 0.009
-0.3125	13.5 ± 1.6	85 ± 9.2	5.4 ± 2.3	79.6 ± 9.2	0.486 (0.482) $\pm$ 0.009
-0.2875	13.9 ± 1.6	84 ± 9.2	5.0 ± 2.2	79.0 ± 9.2	0.469 (0.464) $\pm$ 0.009
-0.2625	15.0 ± 1.7	90 ± 9.5	4.6 ± 2.1	85.4 ± 9.5	0.465 (0.467) $\pm$ 0.009
-0.2375	13.1 ± 1.5	83 ± 9.1	4.3 ± 2.1	78.7 ± 9.1	0.497 (0.493) $\pm$ 0.009
-0.2125	14.5 ± 1.7	87 ± 9.3	4.0 ± 2.0	83.0 ± 9.3	0.475 (0.469) $\pm$ 0.009
-0.1875	11.0 ± 1.5	65 ± 8.1	3.8 ± 2.0	61.2 ± 8.1	0.457 (0.456) $\pm$ 0.009
-0.1625	9.0 ± 1.3	55 ± 7.4	3.6 ± 1.9	51.4 ± 7.4	0.468 (0.470) $\pm$ 0.009
-0.1375	5.1 ± 1.0	33 ± 5.7	3.4 ± 1.8	29.6 ± 5.7	0.478 (0.475) $\pm$ 0.009
-0.1125	4.8 ± 1.0	30 ± 5.5	3.2 ± 1.8	26.8 ± 5.5	0.454 (0.458) $\pm$ 0.009
-0.0875	3.6 ± 0.9	23 ± 4.8	3.1 ± 1.8	19.9 ± 4.8	0.451 (0.451) $\pm$ 0.009
-0.0625	1.7 ± 0.6	13 ± 3.6	3.1 ± 1.8	9.9 ± 3.6	0.454 (0.469) $\pm$ 0.009
-0.0375	2.3 ± 0.7	17 ± 4.1	3.1 ± 1.8	13.9 ± 4.1	0.458 (0.488) $\pm$ 0.009
-0.0125	1.1 ± 0.5	10 ± 3.2	3.1 ± 1.8	6.9 ± 3.2	0.458 (0.517) $\pm$ 0.009
0.0125	0.1 ± 0.3	4 ± 2.0	3.2 ± 1.8	0.8 ± 2.0	0.440 (0.492) $\pm$ 0.009
0.0375	1.2 ± 0.6	10 ± 3.2	3.4 ± 1.8	6.6 ± 3.2	0.443 (0.467) $\pm$ 0.009
0.0625	1.1 ± 0.5	10 ± 3.2	3.6 ± 1.9	6.4 ± 3.2	0.474 (0.483) $\pm$ 0.009
0.0875	2.3 ± 0.7	17 ± 4.1	3.8 ± 1.9	13.2 ± 4.1	0.455 (0.463) $\pm$ 0.009
0.1125	5.3 ± 1.0	33 ± 5.7	4.0 ± 2.0	29.1 ± 5.7	0.448 (0.451) $\pm$ 0.009
0.1375	7.3 ± 1.2	46 ± 6.8	4.1 ± 2.0	41.9 ± 6.8	0.467 (0.466) $\pm$ 0.009
0.1625	10.1 ± 1.4	61 ± 7.8	4.3 ± 2.1	56.7 ± 7.8	0.464 (0.461) $\pm$ 0.009
0.1875	13.1 ± 1.6	76 ± 8.7	4.4 ± 2.1	71.6 ± 8.7	0.444 (0.446) $\pm$ 0.008
0.2125	12.8 ± 1.6	73 ± 8.5	4.6 ± 2.1	68.4 ± 8.5	0.440 (0.437) $\pm$ 0.009
0.2375	12.3 ± 1.6	72 ± 8.5	4.7 ± 2.2	67.3 ± 8.5	0.452 (0.447) $\pm$ 0.009
0.2625	12.2 ± 1.5	76 ± 8.7	4.9 ± 2.2	71.1 ± 8.7	0.478 (0.477) $\pm$ 0.009
0.2875	14.1 ± 1.7	79 ± 8.9	5.2 ± 2.3	73.8 ± 8.9	0.431 (0.427) $\pm$ 0.009
0.3125	15.5 ± 1.9	83 ± 9.1	5.7 ± 2.4	77.3 ± 9.1	0.408 (0.408) $\pm$ 0.008
0.3375	12.5 ± 1.7	70 ± 8.4	6.4 ± 2.5	63.6 ± 8.4	0.421 (0.417) $\pm$ 0.008
0.3625	12.5 ± 1.7	70 ± 8.4	7.5 ± 2.7	62.5 ± 8.4	0.409 (0.408) $\pm$ 0.008
0.3875	17.9 ± 2.1	93 ± 9.6	8.9 ± 3.0	84.1 ± 9.6	0.384 (0.384) $\pm$ 0.008
0.4125	8.6 ± 1.6	50 ± 7.1	10.8 ± 3.3	39.2 ± 7.1	0.369 (0.372) $\pm$ 0.008
0.4375	6.6 ± 1.4	44 ± 6.6	13.1 ± 3.6	30.9 ± 6.6	0.375 (0.383) $\pm$ 0.008
0.4625	9.9 ± 1.8	57 ± 7.5	15.9 ± 4.0	41.1 ± 7.5	0.329 (0.339) $\pm$ 0.007
0.4875	13.1 ± 2.2	68 ± 8.2	18.9 ± 4.4	49.1 ± 8.2	0.297 (0.308) $\pm$ 0.007
0.5125	25.2 ± 3.0	112 ± 10.6	22.1 ± 4.7	89.9 ± 10.6	0.286 (0.292) $\pm$ 0.007
0.5375	46.2 ± 4.6	153 ± 12.4	24.9 ± 5.0	128.1 ± 12.4	0.225 (0.227) $\pm$ 0.006
0.5625	61.7 ± 5.8	177 ± 13.3	26.8 ± 5.2	150.2 ± 13.3	0.198 (0.199) $\pm$ 0.006
0.5875	107.6 ± 9.1	219 ± 14.8	26.9 ± 5.2	192.2 ± 14.8	0.146 (0.146) $\pm$ 0.005

$\bar{p}p \to \pi^0\eta$ at $E_{cm} = 3469.9$ MeV ($\mathcal{L} = 2512.6\ 10^{31}\mathrm{s}^{-1}\mathrm{cm}^{-2}$)					
z	$d\sigma/dz$ (nb)	N_{tot}	N_{bkg}	$N_{\pi^0\pi^0}$	$a \times \epsilon$
-0.5875	79.0 ± 3.9	506 ± 22.5	24.3 ± 4.9	481.7 ± 22.5	0.279 (0.280) $\pm$ 0.004
-0.5625	49.7 ± 2.7	409 ± 20.2	25.0 ± 5.0	384.0 ± 20.2	0.348 (0.355) $\pm$ 0.005
-0.5375	29.3 ± 2.0	275 ± 16.6	23.8 ± 4.9	251.2 ± 16.6	0.387 (0.393) $\pm$ 0.005
-0.5125	15.3 ± 1.4	167 ± 12.9	21.5 ± 4.6	145.5 ± 12.9	0.424 (0.436) $\pm$ 0.005
-0.4875	10.7 ± 1.1	129 ± 11.4	18.8 ± 4.3	110.2 ± 11.4	0.457 (0.473) $\pm$ 0.006
-0.4625	7.6 ± 1.0	92 ± 9.6	16.1 ± 4.0	75.9 ± 9.6	0.443 (0.459) $\pm$ 0.005
-0.4375	7.2 ± 0.9	89 ± 9.4	13.7 ± 3.7	75.3 ± 9.4	0.469 (0.480) $\pm$ 0.006
-0.4125	7.6 ± 0.9	95 ± 9.8	11.7 ± 3.4	83.3 ± 9.8	0.495 (0.501) $\pm$ 0.006
-0.3875	8.5 ± 0.9	101 ± 10.1	10.1 ± 3.2	91.0 ± 10.1	0.489 (0.489) $\pm$ 0.006
-0.3625	10.6 ± 1.0	123 ± 11.1	8.8 ± 3.0	114.2 ± 11.1	0.494 (0.494) $\pm$ 0.006
-0.3375	10.0 ± 1.0	123 ± 11.1	8.0 ± 2.8	115.0 ± 11.1	0.533 (0.529) $\pm$ 0.006
-0.3125	10.9 ± 1.0	125 ± 11.2	7.4 ± 2.7	117.6 ± 11.2	0.498 (0.497) $\pm$ 0.006
-0.2875	9.3 ± 0.9	111 ± 10.5	7.0 ± 2.6	104.0 ± 10.5	0.519 (0.513) $\pm$ 0.006
-0.2625	10.4 ± 1.0	126 ± 11.2	6.7 ± 2.6	119.3 ± 11.2	0.528 (0.527) $\pm$ 0.006
-0.2375	9.9 ± 1.0	120 ± 10.9	6.5 ± 2.6	113.5 ± 10.9	0.527 (0.524) $\pm$ 0.006
-0.2125	9.1 ± 1.0	105 ± 10.2	6.4 ± 2.5	98.6 ± 10.2	0.500 (0.496) $\pm$ 0.006
-0.1875	8.2 ± 0.9	94 ± 9.7	6.2 ± 2.5	87.8 ± 9.7	0.492 (0.490) $\pm$ 0.006
-0.1625	6.4 ± 0.8	78 ± 8.8	6.2 ± 2.5	71.8 ± 8.8	0.513 (0.513) $\pm$ 0.006
-0.1375	5.3 ± 0.7	64 ± 8.0	6.1 ± 2.5	57.9 ± 8.0	0.505 (0.506) $\pm$ 0.006
-0.1125	3.7 ± 0.6	45 ± 6.7	6.0 ± 2.4	39.0 ± 6.7	0.482 (0.484) $\pm$ 0.006
-0.0875	2.3 ± 0.5	30 ± 5.5	6.0 ± 2.4	24.0 ± 5.5	0.483 (0.486) $\pm$ 0.006
-0.0625	1.3 ± 0.4	21 ± 4.6	6.0 ± 2.4	15.0 ± 4.6	0.504 (0.516) $\pm$ 0.006
-0.0375	1.7 ± 0.5	25 ± 5.0	6.0 ± 2.4	19.0 ± 5.0	0.496 (0.506) $\pm$ 0.006
-0.0125	1.3 ± 0.4	20 ± 4.5	6.1 ± 2.5	13.9 ± 4.5	0.483 (0.501) $\pm$ 0.006
0.0125	1.2 ± 0.4	19 ± 4.4	6.2 ± 2.5	12.8 ± 4.4	0.480 (0.495) $\pm$ 0.006
0.0375	1.5 ± 0.4	23 ± 4.8	6.4 ± 2.5	16.6 ± 4.8	0.509 (0.519) $\pm$ 0.006
0.0625	3.1 ± 0.6	41 ± 6.4	6.5 ± 2.6	34.5 ± 6.4	0.500 (0.513) $\pm$ 0.006
0.0875	2.4 ± 0.5	33 ± 5.7	6.7 ± 2.6	26.3 ± 5.7	0.496 (0.499) $\pm$ 0.006
0.1125	4.2 ± 0.7	52 ± 7.2	6.8 ± 2.6	45.2 ± 7.2	0.487 (0.493) $\pm$ 0.006
0.1375	5.3 ± 0.7	66 ± 8.1	6.9 ± 2.6	59.1 ± 8.1	0.509 (0.509) $\pm$ 0.006
0.1625	6.5 ± 0.8	79 ± 8.9	7.0 ± 2.6	72.0 ± 8.9	0.510 (0.510) $\pm$ 0.006
0.1875	7.9 ± 0.9	92 ± 9.6	7.0 ± 2.7	85.0 ± 9.6	0.491 (0.493) $\pm$ 0.006
0.2125	9.8 ± 1.0	108 ± 10.4	7.1 ± 2.7	100.9 ± 10.4	0.472 (0.471) $\pm$ 0.006
0.2375	10.7 ± 1.0	126 ± 11.2	7.2 ± 2.7	118.8 ± 11.2	0.512 (0.509) $\pm$ 0.006
0.2625	13.0 ± 1.1	145 ± 12.0	7.4 ± 2.7	137.6 ± 12.0	0.490 (0.487) $\pm$ 0.006
0.2875	12.3 ± 1.1	133 ± 11.5	7.8 ± 2.8	125.2 ± 11.5	0.469 (0.467) $\pm$ 0.006
0.3125	13.3 ± 1.2	144 ± 12.0	8.5 ± 2.9	135.5 ± 12.0	0.471 (0.468) $\pm$ 0.006
0.3375	11.2 ± 1.1	126 ± 11.2	9.6 ± 3.1	116.4 ± 11.2	0.477 (0.476) $\pm$ 0.006
0.3625	11.4 ± 1.2	122 ± 11.1	11.3 ± 3.4	110.7 ± 11.1	0.447 (0.444) $\pm$ 0.006
0.3875	10.2 ± 1.1	108 ± 10.4	13.7 ± 3.7	94.3 ± 10.4	0.423 (0.424) $\pm$ 0.005
0.4125	7.3 ± 1.0	86 ± 9.3	16.8 ± 4.1	69.2 ± 9.3	0.433 (0.437) $\pm$ 0.005
0.4375	5.8 ± 1.0	72 ± 8.5	20.7 ± 4.6	51.3 ± 8.5	0.401 (0.409) $\pm$ 0.005
0.4625	7.8 ± 1.2	89 ± 9.4	25.4 ± 5.0	63.5 ± 9.4	0.364 (0.375) $\pm$ 0.005
0.4875	9.0 ± 1.3	101 ± 10.1	30.7 ± 5.5	70.3 ± 10.1	0.352 (0.360) $\pm$ 0.005
0.5125	16.2 ± 1.7	152 ± 12.3	36.2 ± 6.0	115.8 ± 12.3	0.320 (0.328) $\pm$ 0.005
0.5375	31.2 ± 2.6	223 ± 14.9	41.4 ± 6.4	181.7 ± 14.9	0.266 (0.267) $\pm$ 0.004
0.5625	53.5 ± 3.7	312 ± 17.7	45.1 ± 6.7	266.9 ± 17.7	0.227 (0.229) $\pm$ 0.004
0.5875	78.1 ± 5.1	349 ± 18.7	46.2 ± 6.8	302.8 ± 18.7	0.178 (0.178) $\pm$ 0.003

Appendix H

The $\bar{p}p \to \eta\eta$ Cross Section Tables

The following list of tables reproduce the measured $\bar{p}p \to \eta\eta$ cross section (and the z-dependent quantities used to calculate it) at every energy point of the χ_{c0} sample. In particular: the z value of the center of the bin, the $\bar{p}p \to \eta\eta$ differential cross section ($\frac{d\sigma}{dz}$), the total number of events (N_{tot}) passing the $\eta\eta$ selection, the estimated number of instrumental background events (N_{bkg}), the number of $\eta\eta$ events ($N_{\eta\eta} \equiv N_{tot} - N_{bkg}$, with uncertainty conservatively taken as $\sqrt{N_{tot}}$). The last column reproduces the product of the acceptance and efficiency ($a \times \epsilon$) corrected for pileup; the uncertainty on $a \times \epsilon$ is determined by the number of Random Gate events available. The value of $a \times \epsilon$ given outside the brackets is determined by using a uniform $\pi^0\eta$ angular distribution. The value given inside the brackets is determined by using the estimate of the angular distribution corrected for the limited polar angle resolution, as described in Appendix B.

$\bar{p}p \to \eta\eta$ at $E_{cm} = 3339.5$ MeV ($\mathcal{L} = 629.4\ 10^{31}\mathrm{s}^{-1}\mathrm{cm}^{-2}$)					
z	$d\sigma/dz\,$(nb)	N_{tot}	N_{bkg}	$N_{\eta\eta}$	$a \times \epsilon$
0.0250	1.5 ± 1.1	5 ± 2.2	2.0 ± 1.4	3.0 ± 2.2	$0.407\ (0.467) \pm 0.006$
0.0750	4.9 ± 1.9	11 ± 3.3	2.3 ± 1.5	8.7 ± 3.3	$0.413\ (0.421) \pm 0.006$
0.1250	10.4 ± 2.6	21 ± 4.6	2.8 ± 1.7	18.2 ± 4.6	$0.419\ (0.414) \pm 0.006$
0.1750	9.2 ± 2.5	19 ± 4.4	3.1 ± 1.8	15.9 ± 4.4	$0.415\ (0.409) \pm 0.006$
0.2250	15.1 ± 3.1	29 ± 5.4	3.1 ± 1.8	25.9 ± 5.4	$0.405\ (0.405) \pm 0.006$
0.2750	13.7 ± 3.1	26 ± 5.1	3.1 ± 1.8	22.9 ± 5.1	$0.384\ (0.394) \pm 0.006$
0.3250	24.8 ± 4.1	43 ± 6.6	3.3 ± 1.8	39.7 ± 6.6	$0.368\ (0.377) \pm 0.006$
0.3750	34.1 ± 5.1	54 ± 7.3	4.1 ± 2.0	49.9 ± 7.3	$0.338\ (0.344) \pm 0.005$
0.4250	59.3 ± 7.3	79 ± 8.9	5.6 ± 2.4	73.4 ± 8.9	$0.293\ (0.291) \pm 0.005$
0.4750	100.3 ± 10.8	104 ± 10.2	7.6 ± 2.8	96.4 ± 10.2	$0.230\ (0.226) \pm 0.004$
0.5250	120.6 ± 13.9	97 ± 9.8	9.5 ± 3.1	87.5 ± 9.8	$0.173\ (0.171) \pm 0.004$
0.5750	156.9 ± 22.1	72 ± 8.5	10.0 ± 3.2	62.0 ± 8.5	$0.093\ (0.093) \pm 0.003$

Table H.1: This and the following tables: the cross section $\bar{p}p \to \eta\eta$.

$\bar{p}p \to \eta\eta$ at $E_{cm} = 3365.0$ MeV ($\mathcal{L} = 1423.7\ 10^{31}\mathrm{s}^{-1}\mathrm{cm}^{-2}$)					
z	$d\sigma/dz\,$(nb)	N_{tot}	N_{bkg}	$N_{\eta\eta}$	$a \times \epsilon$
0.0250	2.4 ± 0.9	14 ± 3.7	3.8 ± 2.0	10.2 ± 3.7	$0.428\ (0.447) \pm 0.004$
0.0750	6.6 ± 1.3	33 ± 5.7	4.3 ± 2.1	28.7 ± 5.7	$0.442\ (0.449) \pm 0.004$
0.1250	6.3 ± 1.3	32 ± 5.7	5.3 ± 2.3	26.7 ± 5.7	$0.439\ (0.439) \pm 0.004$
0.1750	9.5 ± 1.6	45 ± 6.7	5.8 ± 2.4	39.2 ± 6.7	$0.428\ (0.426) \pm 0.004$
0.2250	12.4 ± 1.8	57 ± 7.5	5.9 ± 2.4	51.1 ± 7.5	$0.429\ (0.428) \pm 0.004$
0.2750	13.4 ± 1.9	59 ± 7.7	5.8 ± 2.4	53.2 ± 7.7	$0.405\ (0.409) \pm 0.004$
0.3250	18.6 ± 2.3	77 ± 8.8	6.3 ± 2.5	70.7 ± 8.8	$0.388\ (0.392) \pm 0.004$
0.3750	31.7 ± 3.2	115 ± 10.7	7.8 ± 2.8	107.2 ± 10.7	$0.345\ (0.349) \pm 0.003$
0.4250	39.3 ± 3.8	127 ± 11.3	10.6 ± 3.3	116.4 ± 11.3	$0.304\ (0.306) \pm 0.003$
0.4750	79.6 ± 6.1	204 ± 14.3	14.4 ± 3.8	189.6 ± 14.3	$0.246\ (0.246) \pm 0.003$
0.5250	102.6 ± 8.3	194 ± 13.9	18.0 ± 4.2	176.0 ± 13.9	$0.178\ (0.177) \pm 0.002$
0.5750	172.2 ± 14.1	193 ± 13.9	18.9 ± 4.3	174.1 ± 13.9	$0.105\ (0.105) \pm 0.002$

$\bar{p}p \to \eta\eta$ at $E_{cm} = 3384.4$ MeV ($\mathcal{L} = 1521.6\ 10^{31}\mathrm{s}^{-1}\mathrm{cm}^{-2}$)					
z	$d\sigma/dz$ (nb)	N_{tot}	N_{bkg}	$N_{\eta\eta}$	$a \times \epsilon$
0.0250	2.0 ± 0.8	13 ± 3.6	3.3 ± 1.8	9.7 ± 3.6	$0.436\ (0.460) \pm 0.004$
0.0750	6.7 ± 1.3	35 ± 5.9	3.7 ± 1.9	31.3 ± 5.9	$0.441\ (0.448) \pm 0.004$
0.1250	7.2 ± 1.4	37 ± 6.1	4.6 ± 2.1	32.4 ± 6.1	$0.436\ (0.432) \pm 0.004$
0.1750	9.8 ± 1.6	49 ± 7.0	5.0 ± 2.2	44.0 ± 7.0	$0.434\ (0.429) \pm 0.004$
0.2250	10.0 ± 1.6	49 ± 7.0	5.1 ± 2.3	43.9 ± 7.0	$0.424\ (0.422) \pm 0.004$
0.2750	11.0 ± 1.7	52 ± 7.2	5.0 ± 2.2	47.0 ± 7.2	$0.409\ (0.411) \pm 0.004$
0.3250	16.0 ± 2.1	71 ± 8.4	5.4 ± 2.3	65.6 ± 8.4	$0.385\ (0.394) \pm 0.003$
0.3750	18.4 ± 2.3	75 ± 8.7	6.7 ± 2.6	68.3 ± 8.7	$0.349\ (0.356) \pm 0.003$
0.4250	35.8 ± 3.5	127 ± 11.3	9.2 ± 3.0	117.8 ± 11.3	$0.312\ (0.315) \pm 0.003$
0.4750	55.1 ± 4.8	157 ± 12.5	12.4 ± 3.5	144.6 ± 12.5	$0.252\ (0.251) \pm 0.003$
0.5250	91.5 ± 7.4	189 ± 13.8	15.5 ± 3.9	173.5 ± 13.8	$0.183\ (0.182) \pm 0.002$
0.5750	159.7 ± 12.6	200 ± 14.1	16.3 ± 4.0	183.7 ± 14.1	$0.111\ (0.110) \pm 0.002$

$\bar{p}p \to \eta\eta$ at $E_{cm} = 3384.8$ MeV ($\mathcal{L} = 3370.4\ 10^{31}\mathrm{s}^{-1}\mathrm{cm}^{-2}$)					
z	$d\sigma/dz$ (nb)	N_{tot}	N_{bkg}	$N_{\eta\eta}$	$a \times \epsilon$
0.0250	3.2 ± 0.6	42 ± 6.5	8.3 ± 2.9	33.6 ± 6.5	$0.438\ (0.457) \pm 0.002$
0.0750	5.4 ± 0.8	66 ± 8.1	9.4 ± 3.1	56.6 ± 8.1	$0.445\ (0.449) \pm 0.003$
0.1250	7.9 ± 0.9	92 ± 9.6	11.5 ± 3.4	80.5 ± 9.6	$0.443\ (0.441) \pm 0.003$
0.1750	11.2 ± 1.1	128 ± 11.3	12.7 ± 3.6	115.3 ± 11.3	$0.446\ (0.442) \pm 0.003$
0.2250	10.0 ± 1.1	112 ± 10.6	12.8 ± 3.6	99.2 ± 10.6	$0.430\ (0.429) \pm 0.002$
0.2750	11.7 ± 1.2	127 ± 11.3	12.7 ± 3.6	114.3 ± 11.3	$0.415\ (0.419) \pm 0.002$
0.3250	15.6 ± 1.4	158 ± 12.6	13.7 ± 3.7	144.3 ± 12.6	$0.391\ (0.398) \pm 0.002$
0.3750	25.1 ± 1.8	229 ± 15.1	17.0 ± 4.1	212.0 ± 15.1	$0.358\ (0.364) \pm 0.002$
0.4250	38.2 ± 2.4	301 ± 17.4	23.2 ± 4.8	277.8 ± 17.4	$0.312\ (0.313) \pm 0.002$
0.4750	65.1 ± 3.5	419 ± 20.5	31.5 ± 5.6	387.5 ± 20.5	$0.257\ (0.256) \pm 0.002$
0.5250	98.2 ± 5.1	459 ± 21.4	39.2 ± 6.3	419.8 ± 21.4	$0.186\ (0.184) \pm 0.002$
0.5750	164.0 ± 8.7	455 ± 21.3	41.2 ± 6.4	413.8 ± 21.3	$0.110\ (0.109) \pm 0.001$

$\bar{p}p \to \eta\eta$ at $E_{cm} = 3392.0$ MeV ($\mathcal{L} = 1431.1\ 10^{31}\text{s}^{-1}\text{cm}^{-2}$)					
z	$d\sigma/dz$ (nb)	N_{tot}	N_{bkg}	$N_{\eta\eta}$	$a \times \epsilon$
0.0250	3.0 ± 0.9	16 ± 4.0	2.9 ± 1.7	13.1 ± 4.0	$0.434\ (0.450) \pm 0.004$
0.0750	5.4 ± 1.2	27 ± 5.2	3.3 ± 1.8	23.7 ± 5.2	$0.439\ (0.444) \pm 0.004$
0.1250	9.7 ± 1.6	46 ± 6.8	4.0 ± 2.0	42.0 ± 6.8	$0.445\ (0.443) \pm 0.004$
0.1750	7.9 ± 1.4	38 ± 6.2	4.4 ± 2.1	33.6 ± 6.2	$0.439\ (0.435) \pm 0.004$
0.2250	11.5 ± 1.7	53 ± 7.3	4.5 ± 2.1	48.5 ± 7.3	$0.431\ (0.430) \pm 0.004$
0.2750	12.4 ± 1.8	55 ± 7.4	4.4 ± 2.1	50.6 ± 7.4	$0.414\ (0.416) \pm 0.004$
0.3250	17.2 ± 2.2	71 ± 8.4	4.8 ± 2.2	66.2 ± 8.4	$0.387\ (0.393) \pm 0.004$
0.3750	23.2 ± 2.7	87 ± 9.3	5.9 ± 2.4	81.1 ± 9.3	$0.353\ (0.357) \pm 0.004$
0.4250	29.1 ± 3.2	99 ± 9.9	8.1 ± 2.8	91.0 ± 9.9	$0.315\ (0.319) \pm 0.003$
0.4750	62.7 ± 5.2	169 ± 13.0	10.9 ± 3.3	158.1 ± 13.0	$0.255\ (0.257) \pm 0.003$
0.5250	95.9 ± 7.5	194 ± 13.9	13.6 ± 3.7	180.4 ± 13.9	$0.193\ (0.192) \pm 0.003$
0.5750	138.8 ± 12.4	158 ± 12.6	14.3 ± 3.8	143.7 ± 12.6	$0.107\ (0.106) \pm 0.002$

$\bar{p}p \to \eta\eta$ at $E_{cm} = 3400.1$ MeV ($\mathcal{L} = 1482.8\ 10^{31}\text{s}^{-1}\text{cm}^{-2}$)					
z	$d\sigma/dz$ (nb)	N_{tot}	N_{bkg}	$N_{\eta\eta}$	$a \times \epsilon$
0.0250	4.5 ± 1.0	24 ± 4.9	2.9 ± 1.7	21.1 ± 4.9	$0.458\ (0.471) \pm 0.003$
0.0750	5.4 ± 1.1	29 ± 5.4	3.3 ± 1.8	25.7 ± 5.4	$0.468\ (0.471) \pm 0.004$
0.1250	8.4 ± 1.4	43 ± 6.6	4.0 ± 2.0	39.0 ± 6.6	$0.463\ (0.462) \pm 0.004$
0.1750	12.3 ± 1.7	61 ± 7.8	4.4 ± 2.1	56.6 ± 7.8	$0.460\ (0.456) \pm 0.004$
0.2250	10.1 ± 1.6	50 ± 7.1	4.5 ± 2.1	45.5 ± 7.1	$0.452\ (0.450) \pm 0.003$
0.2750	14.1 ± 1.9	66 ± 8.1	4.4 ± 2.1	61.6 ± 8.1	$0.431\ (0.434) \pm 0.003$
0.3250	14.0 ± 1.9	63 ± 7.9	4.7 ± 2.2	58.3 ± 7.9	$0.410\ (0.415) \pm 0.003$
0.3750	25.5 ± 2.7	103 ± 10.2	5.9 ± 2.4	97.1 ± 10.2	$0.373\ (0.379) \pm 0.003$
0.4250	29.6 ± 3.1	106 ± 10.3	8.1 ± 2.8	98.0 ± 10.3	$0.327\ (0.330) \pm 0.003$
0.4750	52.5 ± 4.5	158 ± 12.6	10.9 ± 3.3	147.1 ± 12.6	$0.279\ (0.279) \pm 0.003$
0.5250	86.9 ± 6.9	189 ± 13.8	13.6 ± 3.7	175.4 ± 13.8	$0.201\ (0.201) \pm 0.002$
0.5750	151.0 ± 12.1	189 ± 13.8	14.3 ± 3.8	174.7 ± 13.8	$0.116\ (0.115) \pm 0.002$

$\bar{p}p \to \eta\eta$ at $E_{cm} = 3406.1$ MeV ($\mathcal{L} = 2680.5\ 10^{31}\mathrm{s}^{-1}\mathrm{cm}^{-2}$)					
z	$d\sigma/dz\,$(nb)	N_{tot}	N_{bkg}	$N_{\eta\eta}$	$a \times \epsilon$
0.0250	2.6 ± 0.6	28 ± 5.3	5.9 ± 2.4	22.1 ± 5.3	$0.445\ (0.468) \pm 0.003$
0.0750	4.4 ± 0.8	44 ± 6.6	6.7 ± 2.6	37.3 ± 6.6	$0.450\ (0.458) \pm 0.003$
0.1250	5.8 ± 0.9	56 ± 7.5	8.2 ± 2.9	47.8 ± 7.5	$0.452\ (0.450) \pm 0.003$
0.1750	8.5 ± 1.1	78 ± 8.8	9.1 ± 3.0	68.9 ± 8.8	$0.443\ (0.439) \pm 0.003$
0.2250	11.1 ± 1.2	98 ± 9.9	9.1 ± 3.0	88.9 ± 9.9	$0.439\ (0.436) \pm 0.003$
0.2750	11.0 ± 1.3	95 ± 9.8	9.0 ± 3.0	86.0 ± 9.8	$0.421\ (0.424) \pm 0.003$
0.3250	13.5 ± 1.4	110 ± 10.5	9.7 ± 3.1	100.3 ± 10.5	$0.398\ (0.405) \pm 0.003$
0.3750	19.8 ± 1.8	147 ± 12.1	12.1 ± 3.5	134.9 ± 12.1	$0.364\ (0.371) \pm 0.003$
0.4250	30.8 ± 2.4	200 ± 14.1	16.5 ± 4.1	183.5 ± 14.1	$0.321\ (0.324) \pm 0.002$
0.4750	54.3 ± 3.5	284 ± 16.9	22.4 ± 4.7	261.6 ± 16.9	$0.263\ (0.262) \pm 0.002$
0.5250	91.0 ± 5.4	349 ± 18.7	27.9 ± 5.3	321.1 ± 18.7	$0.193\ (0.192) \pm 0.002$
0.5750	129.1 ± 8.4	304 ± 17.4	29.3 ± 5.4	274.7 ± 17.4	$0.117\ (0.116) \pm 0.001$

$\bar{p}p \to \eta\eta$ at $E_{cm} = 3409.1$ MeV ($\mathcal{L} = 1134.5\ 10^{31}\mathrm{s}^{-1}\mathrm{cm}^{-2}$)					
z	$d\sigma/dz\,$(nb)	N_{tot}	N_{bkg}	$N_{\eta\eta}$	$a \times \epsilon$
0.0250	4.3 ± 1.2	19 ± 4.4	2.7 ± 1.6	16.3 ± 4.4	$0.479\ (0.492) \pm 0.004$
0.0750	5.6 ± 1.3	24 ± 4.9	3.1 ± 1.8	20.9 ± 4.9	$0.479\ (0.484) \pm 0.004$
0.1250	8.5 ± 1.6	35 ± 5.9	3.8 ± 1.9	31.2 ± 5.9	$0.482\ (0.478) \pm 0.004$
0.1750	9.2 ± 1.7	38 ± 6.2	4.1 ± 2.0	33.9 ± 6.2	$0.481\ (0.476) \pm 0.004$
0.2250	10.6 ± 1.8	42 ± 6.5	4.2 ± 2.0	37.8 ± 6.5	$0.468\ (0.465) \pm 0.004$
0.2750	11.8 ± 1.9	45 ± 6.7	4.1 ± 2.0	40.9 ± 6.7	$0.448\ (0.451) \pm 0.004$
0.3250	10.1 ± 1.9	38 ± 6.2	4.4 ± 2.1	33.6 ± 6.2	$0.424\ (0.433) \pm 0.004$
0.3750	23.5 ± 2.9	77 ± 8.8	5.5 ± 2.3	71.5 ± 8.8	$0.388\ (0.396) \pm 0.003$
0.4250	27.2 ± 3.4	81 ± 9.0	7.5 ± 2.7	73.5 ± 9.0	$0.347\ (0.351) \pm 0.003$
0.4750	47.8 ± 5.0	114 ± 10.7	10.2 ± 3.2	103.8 ± 10.7	$0.283\ (0.283) \pm 0.003$
0.5250	83.0 ± 7.7	143 ± 12.0	12.8 ± 3.6	130.2 ± 12.0	$0.205\ (0.204) \pm 0.002$
0.5750	125.7 ± 12.5	130 ± 11.4	13.4 ± 3.7	116.6 ± 11.4	$0.122\ (0.121) \pm 0.002$

$\bar{p}p \to \eta\eta$ at $E_{cm} = 3410.3$ MeV ($\mathcal{L} = 1596.6\ 10^{31}\mathrm{s}^{-1}\mathrm{cm}^{-2}$)					
z	$d\sigma/dz$ (nb)	N_{tot}	N_{bkg}	$N_{\eta\eta}$	$a \times \epsilon$
0.0250	4.1 ± 1.0	23 ± 4.8	2.8 ± 1.7	20.2 ± 4.8	$0.439\ (0.449) \pm 0.004$
0.0750	5.5 ± 1.1	30 ± 5.5	3.1 ± 1.8	26.9 ± 5.5	$0.442\ (0.445) \pm 0.004$
0.1250	7.1 ± 1.3	38 ± 6.2	3.9 ± 2.0	34.1 ± 6.2	$0.445\ (0.444) \pm 0.004$
0.1750	9.8 ± 1.5	51 ± 7.1	4.2 ± 2.1	46.8 ± 7.1	$0.440\ (0.438) \pm 0.004$
0.2250	10.0 ± 1.5	51 ± 7.1	4.3 ± 2.1	46.7 ± 7.1	$0.431\ (0.429) \pm 0.004$
0.2750	12.0 ± 1.7	59 ± 7.7	4.2 ± 2.1	54.8 ± 7.7	$0.417\ (0.419) \pm 0.004$
0.3250	15.2 ± 1.9	71 ± 8.4	4.6 ± 2.1	66.4 ± 8.4	$0.397\ (0.401) \pm 0.003$
0.3750	21.0 ± 2.4	90 ± 9.5	5.7 ± 2.4	84.3 ± 9.5	$0.364\ (0.369) \pm 0.003$
0.4250	31.2 ± 3.1	116 ± 10.8	7.7 ± 2.8	108.3 ± 10.8	$0.316\ (0.318) \pm 0.003$
0.4750	51.3 ± 4.4	158 ± 12.6	10.5 ± 3.2	147.5 ± 12.6	$0.263\ (0.264) \pm 0.003$
0.5250	91.7 ± 6.9	206 ± 14.3	13.1 ± 3.6	192.9 ± 14.3	$0.193\ (0.193) \pm 0.002$
0.5750	148.7 ± 11.7	196 ± 14.0	13.8 ± 3.7	182.2 ± 14.0	$0.114\ (0.112) \pm 0.002$

$\bar{p}p \to \eta\eta$ at $E_{cm} = 3413.8$ MeV ($\mathcal{L} = 1953.9\ 10^{31}\mathrm{s}^{-1}\mathrm{cm}^{-2}$)					
z	$d\sigma/dz$ (nb)	N_{tot}	N_{bkg}	$N_{\eta\eta}$	$a \times \epsilon$
0.0250	5.9 ± 1.1	37 ± 6.1	3.5 ± 1.9	33.5 ± 6.1	$0.424\ (0.433) \pm 0.004$
0.0750	8.6 ± 1.3	53 ± 7.3	3.9 ± 2.0	49.1 ± 7.3	$0.428\ (0.431) \pm 0.004$
0.1250	8.6 ± 1.3	53 ± 7.3	4.8 ± 2.2	48.2 ± 7.3	$0.426\ (0.424) \pm 0.004$
0.1750	12.5 ± 1.6	75 ± 8.7	5.3 ± 2.3	69.7 ± 8.7	$0.424\ (0.422) \pm 0.004$
0.2250	12.1 ± 1.6	72 ± 8.5	5.3 ± 2.3	66.7 ± 8.5	$0.417\ (0.416) \pm 0.003$
0.2750	12.6 ± 1.6	72 ± 8.5	5.3 ± 2.3	66.7 ± 8.5	$0.399\ (0.402) \pm 0.003$
0.3250	15.9 ± 1.9	85 ± 9.2	5.7 ± 2.4	79.3 ± 9.2	$0.373\ (0.379) \pm 0.003$
0.3750	21.4 ± 2.3	105 ± 10.2	7.0 ± 2.7	98.0 ± 10.2	$0.341\ (0.347) \pm 0.003$
0.4250	29.9 ± 2.9	128 ± 11.3	9.6 ± 3.1	118.4 ± 11.3	$0.297\ (0.300) \pm 0.003$
0.4750	52.4 ± 4.1	189 ± 13.8	13.1 ± 3.6	175.9 ± 13.8	$0.253\ (0.254) \pm 0.003$
0.5250	88.6 ± 6.5	226 ± 15.0	16.3 ± 4.0	209.7 ± 15.0	$0.180\ (0.179) \pm 0.002$
0.5750	133.9 ± 10.3	212 ± 14.6	17.1 ± 4.1	194.9 ± 14.6	$0.111\ (0.110) \pm 0.002$

$\bar{p}p \to \eta\eta$ at $E_{cm} = 3415.0$ MeV ($\mathcal{L} = 2352.1\ 10^{31}\mathrm{s}^{-1}\mathrm{cm}^{-2}$)					
z	$d\sigma/dz$ (nb)	N_{tot}	N_{bkg}	$N_{\eta\eta}$	$a \times \epsilon$
0.0250	4.6 ± 0.8	40 ± 6.3	5.0 ± 2.2	35.0 ± 6.3	$0.450\ (0.465) \pm 0.003$
0.0750	5.9 ± 0.9	50 ± 7.1	5.7 ± 2.4	44.4 ± 7.1	$0.459\ (0.464) \pm 0.003$
0.1250	9.3 ± 1.2	75 ± 8.7	6.9 ± 2.6	68.1 ± 8.7	$0.453\ (0.451) \pm 0.003$
0.1750	12.7 ± 1.4	100 ± 10.0	7.6 ± 2.8	92.4 ± 10.0	$0.450\ (0.446) \pm 0.003$
0.2250	14.4 ± 1.5	111 ± 10.5	7.7 ± 2.8	103.3 ± 10.5	$0.444\ (0.441) \pm 0.003$
0.2750	11.5 ± 1.4	87 ± 9.3	7.6 ± 2.8	79.4 ± 9.3	$0.424\ (0.426) \pm 0.003$
0.3250	13.9 ± 1.5	101 ± 10.1	8.2 ± 2.9	92.8 ± 10.1	$0.406\ (0.412) \pm 0.003$
0.3750	21.5 ± 2.0	141 ± 11.9	10.2 ± 3.2	130.8 ± 11.9	$0.367\ (0.374) \pm 0.003$
0.4250	30.7 ± 2.5	177 ± 13.3	13.9 ± 3.7	163.1 ± 13.3	$0.324\ (0.327) \pm 0.003$
0.4750	46.2 ± 3.4	220 ± 14.8	18.8 ± 4.3	201.2 ± 14.8	$0.267\ (0.268) \pm 0.002$
0.5250	86.7 ± 5.5	297 ± 17.2	23.5 ± 4.8	273.5 ± 17.2	$0.196\ (0.194) \pm 0.002$
0.5750	116.5 ± 8.4	247 ± 15.7	24.7 ± 5.0	222.3 ± 15.7	$0.119\ (0.117) \pm 0.002$

$\bar{p}p \to \eta\eta$ at $E_{cm} = 3415.9$ MeV ($\mathcal{L} = 2466.5\ 10^{31}\mathrm{s}^{-1}\mathrm{cm}^{-2}$)					
z	$d\sigma/dz$ (nb)	N_{tot}	N_{bkg}	$N_{\eta\eta}$	$a \times \epsilon$
0.0250	6.7 ± 1.0	54 ± 7.3	3.8 ± 1.9	50.2 ± 7.3	$0.435\ (0.440) \pm 0.003$
0.0750	7.8 ± 1.1	63 ± 7.9	4.3 ± 2.1	58.7 ± 7.9	$0.439\ (0.442) \pm 0.003$
0.1250	7.9 ± 1.1	65 ± 8.1	5.2 ± 2.3	59.8 ± 8.1	$0.443\ (0.442) \pm 0.003$
0.1750	10.6 ± 1.2	84 ± 9.2	5.8 ± 2.4	78.2 ± 9.2	$0.435\ (0.434) \pm 0.003$
0.2250	13.8 ± 1.4	104 ± 10.2	5.8 ± 2.4	98.2 ± 10.2	$0.420\ (0.419) \pm 0.003$
0.2750	11.5 ± 1.3	87 ± 9.3	5.7 ± 2.4	81.3 ± 9.3	$0.412\ (0.414) \pm 0.003$
0.3250	17.4 ± 1.7	121 ± 11.0	6.2 ± 2.5	114.8 ± 11.0	$0.384\ (0.388) \pm 0.003$
0.3750	20.5 ± 1.9	135 ± 11.6	7.7 ± 2.8	127.3 ± 11.6	$0.360\ (0.364) \pm 0.003$
0.4250	29.5 ± 2.4	170 ± 13.0	10.5 ± 3.2	159.5 ± 13.0	$0.315\ (0.318) \pm 0.003$
0.4750	53.5 ± 3.6	249 ± 15.8	14.2 ± 3.8	234.8 ± 15.8	$0.258\ (0.258) \pm 0.002$
0.5250	74.9 ± 5.0	263 ± 16.2	17.7 ± 4.2	245.3 ± 16.2	$0.193\ (0.192) \pm 0.002$
0.5750	124.2 ± 8.5	260 ± 16.1	18.6 ± 4.3	241.4 ± 16.1	$0.116\ (0.114) \pm 0.002$

$\bar{p}p \to \eta\eta$ at $E_{cm} = 3418.0$ MeV ($\mathcal{L} = 1215.4\ 10^{31}\mathrm{s}^{-1}\mathrm{cm}^{-2}$)					
z	$d\sigma/dz$ (nb)	N_{tot}	N_{bkg}	$N_{\eta\eta}$	$a \times \epsilon$
0.0250	4.9 ± 1.1	22 ± 4.7	1.8 ± 1.3	20.2 ± 4.7	$0.467\ (0.488) \pm 0.004$
0.0750	6.6 ± 1.3	29 ± 5.4	2.0 ± 1.4	27.0 ± 5.4	$0.480\ (0.483) \pm 0.004$
0.1250	9.4 ± 1.6	40 ± 6.3	2.5 ± 1.6	37.5 ± 6.3	$0.476\ (0.473) \pm 0.004$
0.1750	13.3 ± 1.9	55 ± 7.4	2.8 ± 1.7	52.2 ± 7.4	$0.472\ (0.466) \pm 0.004$
0.2250	19.9 ± 2.3	79 ± 8.9	2.8 ± 1.7	76.2 ± 8.9	$0.460\ (0.457) \pm 0.003$
0.2750	14.5 ± 2.0	57 ± 7.5	2.7 ± 1.7	54.3 ± 7.5	$0.446\ (0.447) \pm 0.003$
0.3250	13.6 ± 2.0	52 ± 7.2	3.0 ± 1.7	49.0 ± 7.2	$0.423\ (0.429) \pm 0.003$
0.3750	25.6 ± 2.9	88 ± 9.4	3.7 ± 1.9	84.3 ± 9.4	$0.385\ (0.392) \pm 0.003$
0.4250	28.0 ± 3.2	86 ± 9.3	5.0 ± 2.2	81.0 ± 9.3	$0.342\ (0.344) \pm 0.003$
0.4750	51.1 ± 4.8	128 ± 11.3	6.8 ± 2.6	121.2 ± 11.3	$0.283\ (0.282) \pm 0.003$
0.5250	70.5 ± 6.7	130 ± 11.4	8.5 ± 2.9	121.5 ± 11.4	$0.206\ (0.205) \pm 0.002$
0.5750	134.3 ± 11.8	151 ± 12.3	8.9 ± 3.0	142.1 ± 12.3	$0.127\ (0.126) \pm 0.002$

$\bar{p}p \to \eta\eta$ at $E_{cm} = 3422.1$ MeV ($\mathcal{L} = 2152.3\ 10^{31}\mathrm{s}^{-1}\mathrm{cm}^{-2}$)					
z	$d\sigma/dz$ (nb)	N_{tot}	N_{bkg}	$N_{\eta\eta}$	$a \times \epsilon$
0.0250	5.0 ± 0.9	37 ± 6.1	3.2 ± 1.8	33.8 ± 6.1	$0.445\ (0.457) \pm 0.003$
0.0750	6.0 ± 1.0	44 ± 6.6	3.6 ± 1.9	40.4 ± 6.6	$0.453\ (0.458) \pm 0.003$
0.1250	7.8 ± 1.1	56 ± 7.5	4.4 ± 2.1	51.6 ± 7.5	$0.453\ (0.451) \pm 0.003$
0.1750	11.0 ± 1.4	76 ± 8.7	4.9 ± 2.2	71.1 ± 8.7	$0.443\ (0.440) \pm 0.003$
0.2250	13.9 ± 1.5	93 ± 9.6	5.0 ± 2.2	88.0 ± 9.6	$0.436\ (0.434) \pm 0.003$
0.2750	13.1 ± 1.5	87 ± 9.3	4.9 ± 2.2	82.1 ± 9.3	$0.428\ (0.429) \pm 0.003$
0.3250	15.2 ± 1.7	95 ± 9.8	5.3 ± 2.3	89.7 ± 9.8	$0.398\ (0.402) \pm 0.003$
0.3750	17.3 ± 1.8	103 ± 10.2	6.5 ± 2.6	96.5 ± 10.2	$0.375\ (0.380) \pm 0.003$
0.4250	33.3 ± 2.7	169 ± 13.0	8.9 ± 3.0	160.1 ± 13.0	$0.325\ (0.328) \pm 0.003$
0.4750	47.5 ± 3.6	201 ± 14.2	12.1 ± 3.5	188.9 ± 14.2	$0.271\ (0.271) \pm 0.002$
0.5250	71.5 ± 5.2	222 ± 14.9	15.1 ± 3.9	206.9 ± 14.9	$0.198\ (0.198) \pm 0.002$
0.5750	131.5 ± 9.1	248 ± 15.8	15.9 ± 4.0	232.1 ± 15.8	$0.122\ (0.121) \pm 0.002$

$\bar{p}p \to \eta\eta$ at $E_{cm} = 3426.0$ MeV ($\mathcal{L} = 1800.1\ 10^{31}\mathrm{s}^{-1}\mathrm{cm}^{-2}$)					
z	$d\sigma/dz$ (nb)	N_{tot}	N_{bkg}	$N_{\eta\eta}$	$a \times \epsilon$
0.0250	4.5 ± 1.0	28 ± 5.3	3.2 ± 1.8	24.8 ± 5.3	$0.440\ (0.452) \pm 0.003$
0.0750	5.8 ± 1.1	36 ± 6.0	3.6 ± 1.9	32.4 ± 6.0	$0.453\ (0.457) \pm 0.004$
0.1250	8.8 ± 1.3	53 ± 7.3	4.4 ± 2.1	48.6 ± 7.3	$0.449\ (0.449) \pm 0.004$
0.1750	11.9 ± 1.5	69 ± 8.3	4.8 ± 2.2	64.2 ± 8.3	$0.443\ (0.440) \pm 0.003$
0.2250	10.5 ± 1.5	61 ± 7.8	4.9 ± 2.2	56.1 ± 7.8	$0.436\ (0.433) \pm 0.003$
0.2750	15.9 ± 1.8	86 ± 9.3	4.8 ± 2.2	81.2 ± 9.3	$0.416\ (0.415) \pm 0.003$
0.3250	12.6 ± 1.7	67 ± 8.2	5.2 ± 2.3	61.8 ± 8.2	$0.396\ (0.399) \pm 0.003$
0.3750	20.9 ± 2.2	103 ± 10.2	6.4 ± 2.5	96.6 ± 10.2	$0.372\ (0.377) \pm 0.003$
0.4250	22.4 ± 2.5	99 ± 9.9	8.8 ± 3.0	90.2 ± 9.9	$0.323\ (0.328) \pm 0.003$
0.4750	43.7 ± 3.8	157 ± 12.5	11.9 ± 3.5	145.1 ± 12.5	$0.267\ (0.270) \pm 0.003$
0.5250	71.8 ± 5.7	189 ± 13.8	14.9 ± 3.9	174.1 ± 13.8	$0.197\ (0.197) \pm 0.002$
0.5750	118.9 ± 9.5	192 ± 13.9	15.6 ± 4.0	176.4 ± 13.9	$0.122\ (0.121) \pm 0.002$

$\bar{p}p \to \eta\eta$ at $E_{cm} = 3430.1$ MeV ($\mathcal{L} = 1438.2\ 10^{31}\mathrm{s}^{-1}\mathrm{cm}^{-2}$)					
z	$d\sigma/dz$ (nb)	N_{tot}	N_{bkg}	$N_{\eta\eta}$	$a \times \epsilon$
0.0250	5.0 ± 1.1	23 ± 4.8	1.8 ± 1.3	21.2 ± 4.8	$0.424\ (0.432) \pm 0.004$
0.0750	7.0 ± 1.3	32 ± 5.7	2.0 ± 1.4	30.0 ± 5.7	$0.435\ (0.440) \pm 0.004$
0.1250	8.5 ± 1.5	38 ± 6.2	2.5 ± 1.6	35.5 ± 6.2	$0.429\ (0.429) \pm 0.004$
0.1750	11.8 ± 1.8	51 ± 7.1	2.7 ± 1.7	48.3 ± 7.1	$0.422\ (0.421) \pm 0.004$
0.2250	11.6 ± 1.7	50 ± 7.1	2.8 ± 1.7	47.2 ± 7.1	$0.422\ (0.419) \pm 0.004$
0.2750	14.6 ± 2.0	60 ± 7.8	2.7 ± 1.7	57.3 ± 7.8	$0.404\ (0.403) \pm 0.004$
0.3250	14.9 ± 2.0	59 ± 7.7	2.9 ± 1.7	56.1 ± 7.7	$0.384\ (0.387) \pm 0.004$
0.3750	19.2 ± 2.4	70 ± 8.4	3.6 ± 1.9	66.3 ± 8.4	$0.348\ (0.355) \pm 0.004$
0.4250	22.1 ± 2.8	72 ± 8.5	5.0 ± 2.2	67.0 ± 8.5	$0.307\ (0.312) \pm 0.004$
0.4750	51.3 ± 4.8	132 ± 11.5	6.8 ± 2.6	125.2 ± 11.5	$0.250\ (0.251) \pm 0.003$
0.5250	63.6 ± 6.1	128 ± 11.3	8.4 ± 2.9	119.6 ± 11.3	$0.194\ (0.193) \pm 0.003$
0.5750	117.7 ± 10.8	143 ± 12.0	8.9 ± 3.0	134.1 ± 12.0	$0.119\ (0.117) \pm 0.002$

$\bar{p}p \to \eta\eta$ at $E_{cm} = 3469.9$ MeV ($\mathcal{L} = 2512.6\ 10^{31}\mathrm{s}^{-1}\mathrm{cm}^{-2}$)					
z	$d\sigma/dz$ (nb)	N_{tot}	N_{bkg}	$N_{\eta\eta}$	$a \times \epsilon$
0.0250	5.3 ± 0.8	48 ± 6.9	3.4 ± 1.8	44.6 ± 6.9	$0.474\ (0.483) \pm 0.003$
0.0750	6.1 ± 0.9	55 ± 7.4	3.8 ± 2.0	51.2 ± 7.4	$0.476\ (0.479) \pm 0.003$
0.1250	8.9 ± 1.1	77 ± 8.8	4.7 ± 2.2	72.3 ± 8.8	$0.472\ (0.469) \pm 0.003$
0.1750	9.0 ± 1.1	78 ± 8.8	5.2 ± 2.3	72.8 ± 8.8	$0.467\ (0.463) \pm 0.003$
0.2250	9.2 ± 1.1	79 ± 8.9	5.2 ± 2.3	73.8 ± 8.9	$0.463\ (0.458) \pm 0.003$
0.2750	8.6 ± 1.1	72 ± 8.5	5.2 ± 2.3	66.8 ± 8.5	$0.444\ (0.445) \pm 0.003$
0.3250	9.7 ± 1.2	79 ± 8.9	5.6 ± 2.4	73.4 ± 8.9	$0.426\ (0.435) \pm 0.003$
0.3750	9.2 ± 1.2	71 ± 8.4	6.9 ± 2.6	64.1 ± 8.4	$0.391\ (0.402) \pm 0.003$
0.4250	14.9 ± 1.6	101 ± 10.1	9.4 ± 3.1	91.6 ± 10.1	$0.346\ (0.353) \pm 0.002$
0.4750	32.6 ± 2.6	180 ± 13.4	12.8 ± 3.6	167.2 ± 13.4	$0.292\ (0.295) \pm 0.002$
0.5250	59.3 ± 4.1	241 ± 15.5	16.0 ± 4.0	225.0 ± 15.5	$0.218\ (0.218) \pm 0.002$
0.5750	83.6 ± 6.3	213 ± 14.6	16.8 ± 4.1	196.2 ± 14.6	$0.136\ (0.135) \pm 0.002$

Bibliography

[1] S. Bagnasco *et al.* [E835 Collaboration], "New Measurements Of The Resonance Parameters Of The Chi/C0(1(3)P(0)) State Of Charmonium," Phys. Lett. B **533**, 237 (2002).

[2] M. Gell-Mann, "A Schematic Model Of Baryons And Mesons," Phys. Lett. **8**, 214 (1964).

[3] G. Zweig, "An SU(3) Model For Strong Interaction Symmetry And Its Breaking. 2," CERN-TH-412

[4] D. E. Groom *et al.*, [Particle Data Group] "The European Physical Journal," **C15** 1, (2000)

[5] J. D. Bjorken and S. L. Glashow, "Elementary Particles And SU(4)," Phys. Lett. **11**, 255 (1964).

[6] S. L. Glashow, J. Iliopoulos and L. Maiani, "Weak Interactions With Lepton - Hadron Symmetry," Phys. Rev. D **2**, 1285 (1970).

[7] N. Cabibbo, "Unitary Symmetry And Leptonic Decays," Phys. Rev. Lett. **10**, 531 (1963).

[8] J. J. Aubert *et al.*, "Experimental Observation Of A Heavy Particle J," Phys. Rev. Lett. **33**, 1404 (1974).

[9] J. E. Augustin *et al.*, "Discovery Of A Narrow Resonance In E+ E- Annihilation," Phys. Rev. Lett. **33**, 1406 (1974).

[10] C. Bacci and et al., "Preliminary Result Of Frascati (Adone) On The Nature Of A New 3.1-Gev Particle Produced In E+ E- Annihilation," Phys. Rev. Lett. **33**, 1408 (1974) [Erratum-ibid. **33**, 1649 (1974)].

[11] G. S. Abrams *et al.*, "The Discovery Of A Second Narrow Resonance In E+ E- Annihilation," Phys. Rev. Lett. **33**, 1453 (1974).

[12] S. Okubo, "Phi Meson And Unitary Symmetry Model," Phys. Lett. **5**, 165 (1963).

[13] J. Iizuka, "Systematics And Phenomenology Of Meson Family," Prog. Theor. Phys. Suppl. **37**, 21 (1966).

[14] E. Eichten, K. Gottfried, T. Kinoshita, K. D. Lane and T. M. Yan, "Charmonium: 1. The Model," Phys. Rev. D **17**, 3090 (1978) [Erratum-ibid. D **21**, 313 (1980)].

[15] E. Eichten, K. Gottfried, T. Kinoshita, K. D. Lane and T. M. Yan, "Charmonium: Comparison With Experiment," Phys. Rev. D **21**, 203 (1980).

[16] D. Gromes, "Bethe-Salpeter Equation With Confining Kernel: Correct Nonrelativistic Limit And The Constant To Be Added To The Linear Potential," Z. Phys. C **11**, 147 (1981).

[17] E. Eichten and F. Feinberg, "Spin Dependent Forces In QCD," Phys. Rev. D **23**, 2724 (1981).

[18] R. Cester and P. A. Rapidis, "Charmonium formation in $\bar{p}p$ annihilations," Ann. Rev. Nucl. Part. Sci. **44**, 329 (1994).

[19] W. Kwong, P. B. Mackenzie, R. Rosenfeld and J. L. Rosner, "Quarkonium Annihilation Rates," Phys. Rev. D **37**, 3210 (1988).

[20] T. A. Armstrong *et al.* [E760 Collaboration], "Study of the eta(c) (s wave singlet) state of charmonium formed in anti-p p annihilations and a search for the eta(c)-prime (s wave doublet)," Phys. Rev. D **52**, 4839 (1995).

[21] J. Z. Bai *et al.* [BES Collaboration], "Measurement of Branching Fractions for $B \to \eta_c K(^*)$ Decays," Phys. Rev. Lett. **90**, 071801 (2003)

[22] J. Z. Bai *et al.* [BES Collaboration], "Measurements of the mass and full-width of the eta/c meson," Phys. Lett. B **555**, 174 (2003) [arXiv:hep-ex/0301004].

[23] C. Edwards *et al.*, "Observation an an η_c' Candidate State with Mass 3592 ± 5 MeV," Phys. Rev. Lett. **48**, 70 (1982).

[24] M. Ambrogiani *et al.* [E835 Collaboration], "Search for the eta/c' (2(1)S(0)) charmonium resonance," Phys. Rev. D **64**, 052003 (2001).

[25] S. K. Choi *et al.* [BELLE collaboration], "Observation of the eta/c(2S) in exclusive B → K K(S) K- pi+ decays," Phys. Rev. Lett. **89**, 102001 (2002) [Erratum-ibid. **89**, 129901 (2002)] [arXiv:hep-ex/0206002].

[26] K. Abe *et al.* [Belle Collaboration], "Observation of double c anti-c production in e+ e- annihilation at s**(1/2) approx. 10.6-GeV," Phys. Rev. Lett. **89**, 142001 (2002) [arXiv:hep-ex/0205104].

[27] T. A. Armstrong *et al.* [E835 Collaboration], "Precision measurements of charmonium states formed in $\bar{p}p$ annihilation," Phys. Rev. Lett. **68**, 1468 (1992).

[28] M. Ambrogiani *et al.* [E835 Collaboration], "Study of the chi/c0 (1(3)P(0)) state of charmonium formed in anti-p p annihilations," Phys. Rev. Lett. **83**, 2902 (1999).

[29] D. P. McGinnis *et al.*, "Beam Decelerations with Variable Momentum Compaction in the Fermilab Antiproton Accumulator," Fermilab Report (2003), submitted to Elsevier Science.

[30] T. A. Armstrong *et al.* [E835 Collaboration], FNAL Proposal P-835-REV (1992).

[31] S. Van Der Meer, "An Introduction To Stochastic Cooling," Quarks, Leptons, and their Constituents, Erice 1984, Proceedings, 325-348.

[32] C. N. Yang, "Selection Rules For The Dematerialization Of A Particle Into Two Photons," Phys. Rev. **77**, 242 (1950).

[33] T. A. Armstrong *et al.* [Fermilab E760 Collaboration], "Two-body neutral final states produced in antiproton - proton annihilations at 2.911 GeV $\leq \sqrt{s} \leq$ 3.686 GeV," Phys. Rev. D **56**, 2509 (1997).

[34] J. Z. Bai *et al.* [BES Collaboration], "Radiative Decay of the $\psi(2S)$ into two Pseudoscalar Mesons," Phys. Rev. D **67**, 032004 (2003).

[35] M. Jacob and G. C. Wick, "On The General Theory Of Collisions For Particles With Spin," Annals Phys. **7**, 404 (1959) [Annals Phys. **281**, 774 (2000)].

[36] "Design Report: Tevatron I Project", Fermilab Report (1984), unpublished.

[37] J. Peoples, Jr., in Low Energy Antimatter, "Proceedings of the Workshop on the Design of a Low Energy Antimatter Facility", Madison, Wisconsin, 1985, edited by D. Cline (World Scientific, Singapore, 1986), p. 144.

[38] M. Church, "Stochastic Cooling at Fermilab", Nuclear Instruments & Methods in Physics Research Section A-Accelerators Spectrometers, Detectors and Associated Equipment (1997), V391, N1, P172-175.

[39] K. Hagiwara *et al.* [Particle Data Group Collaboration], "Review Of Particle Physics", Phys. Rev. D **66**, 010001 (2002).

[40] S.J. Werkema, "Precision Measurement of the Accumulator Beam Energy", Fermilab Pbar Note 633 (2000).

[41] D.A. Edwards and M.J. Syphers, "An Introduction to the Physics of High Energy Accelerators", New York, Wiley (1993).

[42] T.A. Armstrong *et al.*, "Measurement of the J/ψ and ψ' resonance parameters in $\bar{p}p$ annihilation", Phys. Rev. D **47**, 772 (1993).

[43] D. Allspach *et al.* , "The variable density gas jet internal target for experiment 835 at Fermilab", Nucl. Instrum. Meth. A **410**, 195 (1998).

[44] D. Allspach *et al.* , "Result of the October 1999 Hydrogen Jet Measurements", Fermilab Report (1999), unpublished.

[45] M. Ambrogiani *et al.* [E835 Collaboration], "Experiment E835 at Fermilab", Submitted to Nucl. Instrum. Meth. A, April 2003.

[46] S. Bagnasco *et al.*, "A Straw Chambers' Tracker For The High Rate Experiment 835 At The Fermilab Accumulator", Nucl. Instrum. Meth. A **409**, 75 (1998).

[47] P. Rumerio, "Design, test and operation of a system of proportional straw chambers for the E835 experiment at Fermilab", Laurea Degree Thesis, University of Torino, Italy (1996), in Italian.

[48] M. Ambrogiani *et al.*, "Construction And Performance Of A Cylindrical Scintillating Fiber Detector For Experiment 835 At Fnal", IEEE Trans. Nucl. Sci. **44**, 460 (1997).

[49] M. Ambrogiani *et al.*, "Results From The E835 Scintillating Fiber Detector", Nucl. Instrum. Meth. A **419**, 632 (1998).

[50] C. Biino *et al.*, "A Large Acceptance Threshold Cerenkov Counter For Experiment 760 At Fermilab. Fnal-760 Experiment", Nucl. Instrum. Meth. A **317**, 135 (1992).

[51] S. Bagnasco *et al.*, "The Threshold Gas Cherenkov Counter Of Charmonium Experiment 835 At Fermilab", Nucl. Instrum. Meth. A **424**, 304 (1999).

[52] L. Bartoszek, "The Mechanical design of the E760 lead glass calorimeter. FNAL 760 experiment", Nucl. Instrum. Meth. A **301**, 47 (1991).

[53] J.E. Fast, "Two Photon Decays of Charmonium States Produced in Proton-Antiproton Annihilation", Ph.D. Thesis, University of California, Irvine (1992).

[54] K.E. Gollwitzer, "The Charmonium 1P1 State (h_c) Produced in Antiproton-Proton Annihilations", Ph.D. Thesis, University of California, Irvine (1992).

[55] T. A. Armstrong *et al.* [E760 Collaboration], "Study of the eta(c) (s wave singlet) state of charmonium formed in anti-p p annihilations and a search for the eta(c)-prime (s wave doublet)", Phys. Rev. D **52**, 4839 (1995).

[56] M.D. Stancari, "Two Photon Decay Widths of Charmonium Resonances Formed in Proton-Antiproton Annihilations", Ph.D. Thesis, University of California, Irvine (1999).

[57] T. K. Pedlar, "Study of Two Photon Decays of Charmonium Resonances Formed in Proton-Antiproton Annihilations", Ph.D. Thesis, Northwestern University (1999).

[58] S. Bagnasco *et al.*, "FCAL II: Design and Construction", E835 Internal Memo 378 (1997).

[59] M. Graham *et al.*, "FCAL2000 Calibration", E835 Internal Memo 413 (2001).

[60] T. A. Armstrong *et al.* [E760 Collaboration], "Precision Measurements Of Anti-Proton Proton Forward Elastic Scattering Parameters In The 3.7-Gev/C To 6.2-Gev/C Region", Phys. Lett. B **385**, 479 (1996).

[61] S. Trokenheim, M. Sarmiento, K. K. Seth and L. Bartoszek, "A P Anti-P Luminosity Monitor For Fermilab Experiment E760", Nucl. Instrum. Meth. A **355**, 308 (1995).

[62] W. Baldini, D. Bettoni, R. Calabrese, E. Luppi, R. Mussa and G. Stancari, "The Charged Trigger Of The Experiment E835 At Fermilab", Nucl. Instrum. Meth. A **449**, 331 (2000).

[63] R. Ray, J. L. Rosen, M. Masuzawa and J. Zhao, "A Trigger for the Fermilab E760 lead glass calorimeter", Nucl. Instrum. Meth. A **307**, 254 (1991).

[64] S. Jin and J. L. Rosen, "E835 Neutral Trigger", E835 Internal Memo 375 (2001).

[65] J. J. Kasper, "Search for Two Omega Decays of Charmonium Resonances Produced in Proton-Antiproton Annihilations", Ph.D. Thesis, Northwestern University (2002).

[66] G. Oleynik *et al.*, "Fermilab DART run control", IEEE Trans. Nucl. Sci. **43**, 20 (1996).

[67] T. Vidnovic and P. Rumerio, "E835′ Neutral DST Format and Production Streaming", E835 Internal Memo 409 (2000).

[68] T. Vidnovic, "E835′ Neutral DST Production Efficiency", E835 Internal Memo 425 (2001).

[69] O. I. Dahl, T. B. Day and F. T. Solmitz, "SQUAW: Kinematic Fitting Program," Technical Report P-126, University of California Lawrence Radiation Laboratory (1965).

[70] M. M. Obertino, "Studio dei Decadimenti dello Stato $^3P_0(\chi_{c0})$ del Charmonio: $chi_{c0} \to J/\psi\,\gamma \to e^+e^-\,\gamma$ and $chi_{c0} \to \gamma\gamma$ nell'Ambito dell'Esperimento E835 del Femilab", Ph.D. Thesis, University of Torino, Italy (2001), in Italian.

[71] F. James and M. Roos, "MINUIT, Function Minimization and Error Analysis," CERN D506 (Long Writeup). Available from the CERN Program Library OFFICE, CERN-IT Division, CERN, CH-1211, Geneva 21, Switzerland.

[72] T. Vidnovic III, Ph.D. Thesis, "Di-Neutral Pion Production in the Triplet P-Wave States of Charmonium," University of Minnesota, Fermilab-Thesis-2002-17

[73] J. Z. Bai *et al.* [BES Collaboration], "Radiative decay of the $\psi(2S)$ into two pseudoscalar mesons," Phys. Rev. D **67**, 032004 (2003).

[74] R. A. Lee, "Radiative Decays Of The Psi-Prime To All Photon Final States," SLAC-0282

[75] J. L. Rosen, "Heavy Hadronic Molecules," American Institute of Physics, Conference Proceedings **185**, Particles and Fields Series **36**, *Glueballs, Hybrids and Exotic Hadrons*, Upton, NY, 29 Aug - 1 Sep 1988

[76] J. D. Richman, "An Experimenter's Guide to the Helicity Formalism," California Institute of Technology, CALT-68-1148 (1984).